Investigation of the hydro-mechanical behaviour of compacted bentonite/claystone mixture

Zhixiong Zeng

Thèse présentée pour obtenir le grade de

Docteur de l'Ecole nationale des ponts et chaussées

Spécialité : Géotechnique

par

Zhixiong Zeng

Etude du comportement hydromécanique du mélange de bentonite/argilite compacté

Date : 12 Mai 2021

Jury

Prof. Cristina Jommi	Delft University of Technology (Netherlands)	Présidente
Prof. Wei-Min Ye	Tongji University (China)	Rapporteur
Prof. Farimah Masrouri	Université de Lorraine (France)	Rapportrice
Dr. María Victoria Villar	CIEMAT (Spain)	Examinatrice
Dr. Chun-Liang Zhang	GRS (Germany)	Examinateur
Dr. Nathalie Conil	INERIS (France)	Examinatrice
Dr. Jean Talandier	ANDRA (France)	Examinateur
Prof. Yu-Jun Cui	Ecole des Ponts ParisTech (France)	Directeur de thèse

Dissertation presented for the degree of

Doctor of Ecole nationale des ponts et chaussées

Specialty: Geotechnical Engineering

by

Zhixiong Zeng

Investigation of the hydro-mechanical behaviour of compacted bentonite/claystone mixture

Date: 12 May 2021

Jury

Prof. Cristina Jommi	Delft University of Technology (Netherlands)	Présidente
Prof. Wei-Min Ye	Tongji University (China)	Rapporteur
Prof. Farimah Masrouri	Université de Lorraine (France)	Rapportrice
Dr. María Victoria Villar	CIEMAT (Spain)	Examinatrice
Dr. Chun-Liang Zhang	GRS (Germany)	Examinateur
Dr. Nathalie Conil	INERIS (France)	Examinatrice
Dr. Jean Talandier	ANDRA (France)	Examinateur
Prof. Yu-Jun Cui	Ecole des Ponts ParisTech (France)	Directeur de thèse

Acknowledgements

This dissertation was carried out at Laboratoire Navier of Ecole des Ponts ParisTech. It was financed by the China Scholarship Council (CSC) and the French National Radioactive Waste Management Agency (Andra). I would like to take this opportunity to acknowledge all the persons who directly or indirectly contributed to the accomplishment of this dissertation.

First of all, I would like to express my deepest gratitude to my supervisor Prof. Yu-Jun Cui for his professional guidance and constant encouragement, which enable me to overcome all the problems I faced in the course of experiments and the preparation of the dissertation. I thank him for sharing his great experience and giving me a lot of helpful advices. The precious scientific training guided by him enriched me and will benefit me throughout my life.

I would also like to extend my sincere appreciation to my co-supervisors at Andra, Dr. Jean Talandier and Dr. Nathalie Conil (now at INERIS), whose excellent guidance, precious ideas and useful advice have greatly contributed to the accomplishment of my research work.

Besides, I wish to thank the jury members: Prof. Wei-Min Ye, Prof. Farimah Masrouri, Prof. Cristina Jommi, Dr. María Victoria Villar and Dr. Chun-Liang Zhang for their interest in my work and the time spent reviewing the manuscript. Their insightful comments and constructive suggestions helped greatly improve this dissertation.

I am also grateful to my friends and colleages at CERMES for their encouragement, support and all the happy time we spend together. The experimental tests conducted during this PhD could not have been possible without the great help of the technical team of the laboratory. My special thanks go to Emmanuel De Laure for his uncountable support and guidance in the lab, and to Marine Lemaire, Xavier Boulay, Baptiste Chabot and Loïc Lesueur for their professional and friendly help.

I also sincerely appreciate the constant encouragement, help, advices and concerns from my former supervisor and my friends at the Institute of Rock and Soil Mechanics, Chinese Academy of Sciences, Prof. Ling-Wei Kong, Dr. Min Wang and Dr. Wei Li throughout this journey.

Last but certainly not least, I want to express all my love and gratitude to my parents, my girlfriend, my sister and my brother in law for always being there for me, giving me their love and backing me up, through thick and thin.

Résumé

Dans le concept français de stockage géologique profond, il est prévu que les galeries souterraines soient implantées dans une formation argileuse: le Callovo-Oxfordien (COx). Un mélange de bentonite et d'argilite excavée en blocs compactés est étudié comme matériau de scellement/remblai par l'Agence nationale pour la gestion des déchets radioactifs (ANDRA). Lorsque le stockage sera fermé, les blocs compactés vont gonfler, comblant les vides technologiques, limitant la propagation de la zone endommagée par l'excavation et le transfert de radionucléides vers la biosphère. Pour évaluer l'adéquation du matériau proposé, un programme de laboratoire a été établi dans le cadre de ce travail de thèse pour caractériser le comportement hydromécanique du mélange compacté de bentonite et d'argilite sous différentes conditions environnementales.

Des essais de compression, de pression de gonflement, de conductivité hydraulique et de porosimétrie d'intrusion au mercure ont été effectués sur les mélanges compactés de bentonite/argilite pour différentes fractions de bentonite, densités sèches et teneurs en eau afin d'évaluer la performance de ces matériaux. En considérant l'interaction entre la bentonite et l'argilite pendant l'hydratation, l'indice des vides de l'argilite et la fraction volumétrique dans le mélange, la pression de gonflement des grains d'argilite a été déterminée indirectement. En outre, deux méthodes analytiques ont été proposées pour prévoir la pression de gonflement et la conductivité hydraulique des mélanges bentonite/argilite. De plus, la pression de gonflement et la conductivité hydraulique des mélanges bentonite/argilite ont été évaluées sur la base de la distribution de la taille des pores après hydratation.

Par la suite, le gonflement aéolotrope du mélange bentonite/argilite compacté avec présence de vides technologiques a été déterminé expérimentalement. Les vides technologiques axiaux pourraient diminuer l'orientation du grain et réduire l'aéolotropie. En revanche, les vides radiaux augmenteraient l'hétérogénéité et renforceraient l'aéolotropie.

De plus, le processus d'homogénéisation de blocs compactés avec des vides technologiques a été évalué expérimentalement et théoriquement. Les évolutions des pressions de gonflement axiales et radiales et de la conductivité hydraulique avec le temps ont été étudiées, ainsi que la détermination des variations de la teneur en eau, de la densité sèche, de la succion et de la microstructure. Une attention particulière a été accordée à l'effet du frottement aux interfaces

et une méthode analytique a été proposée pour estimer la distribution finale de densité sèche des échantillons avec des vides technologiques.

Pour étudier l'influence de la composition de l'eau d'hydratation sur les mélanges bentonite/argilite, différents types de bentonite compactées à plusieurs densités sèches ont été hydratés avec de l'eau déminéralisée, de l'eau de site synthétique représentative de l'eau interstitielle du COx et de l'eau cimentaire. La pression de gonflement, la conductivité hydraulique et la microstructure ont été systématiquement déterminées. L'hydratation avec de l'eau de site synthétique et de l'eau cimentaire conduisent a une légère diminution de la pression de gonflement et une augmentation de la conductivité hydraulique en raison des échanges cationiques et de la dissolution de la montmorillonite.

Enfin, l'écoulement de l'eau dans le mélange de bentonite/argilite non saturé a été étudié en effectuant des essais d'infiltration et de rétention d'eau en conditions de volume constant et en suivant l'évolution de la microstructure. Sur la base de l'évolution de la structure des pores lors de l'hydratation, les conductivités hydrauliques de l'eau liquide et de la vapeur d'eau ont été évaluées en fonction de la saturation. Un modèle numérique a été développé pour évaluer les contributions respectives des flux de vapeur et d'eau liquide.

Mots clés : Mélange de bentonite et d'argilite; comportement hydromécanique; microstructure; vides technologiques; comportement à long terme; chimie de l'eau

Abstract

In the French concept of deep geological disposal, the underground repository is planned to be constructed in Callovo-Oxfordian (COx) claystone formation. To reduce the excavation wastes, a mixture of MX80 bentonite and excavated COx claystone in compacted blocks has been proposed as a candidate sealing/backfill material by the French National Radioactive Waste Management Agency (Andra). When the repository is closed, the compacted blocks are expected to swell, filling up the technological voids, resisting the propagation of excavation-damaged zone and preventing the release of radionuclides into the biosphere. To assess the suitability of the proposed material, a laboratory programme was set up in this PhD study to characterize the hydro-mechanical behaviour of compacted bentonite/claystone mixture under different environmental conditions.

Compression, swelling pressure, hydraulic conductivity and mercury intrusion porosimetry (MIP) tests were performed on the compacted MX80 bentonite/COx claystone mixtures with various bentonite fractions, dry densities and water contents for the preliminary performance assessment of the material. By considering the interaction between bentonite and claystone during hydration, the claystone void ratio and volumetric fraction in the mixture were deduced and the swelling pressure of claystone grains was indirectly determined. Moreover, two analytical methods were proposed to predict the swelling pressure and hydraulic conductivity of bentonite/claystone mixtures. Additionally, based on the pore size distribution after hydration, the swelling pressure and hydraulic conductivity of bentonite/claystone mixtures were further evaluated.

Afterwards, the aeolotropic swelling behaviour of compacted MX80 bentonite/COx claystone mixture with axial/radial technological voids was experimentally determined. Results show that axial technological voids could decrease the grain orientation and reduce the aeolotropy. By contrast, radial technological voids would increase the heterogeneity and enhance the aeolotropy.

In addition, the homogenization process of compacted blocks with technological voids was experimentally and theoretically evaluated. The evolutions of axial and radial swelling pressures and hydraulic conductivity over time were investigated, together with the determination of the variations of water content, dry density, suction and microstructure distribution. Particular attention was paid to the effect of boundary friction between the samples

and porous stones and an analytical method was proposed to estimate the final dry density distribution of samples with technological voids.

To account for the influences of the pore water in COx claystone and the cementitious solution due to concrete degradation, compacted bentonite/claystone mixtures with various bentonite types, dry densities and technological voids were hydrated with deionised water, synthetic site solution and cementitious solution and the swelling pressure, hydraulic conductivity and microstructure were determined. Results show that the synthetic site solution and cementitious solution slightly decreased the swelling pressure and increased the hydraulic conductivity due to the cation exchange and montmorillonite dissolution.

Finally, water flow in the unsaturated MX80 bentonite/COx claystone mixture was investigated by carrying out infiltration and water retention tests under constant-volume conditions alongside microstructure observation. The hydraulic conductivity was experimentally determined. Based on the evolving pore structure upon hydration, two-phase hydraulic conductivities were predicted and a numerical model was developed to investigate the contribution of vapour and liquid water flux.

Keywords: Bentonite/claystone mixture; hydro-mechanical behaviour; microstructure; technological voids; long-term behaviour; water chemistry

Publications

Journal papers

1 Zeng, Z.X., Cui, Y.J., Zhang, F., Conil, N., Talandier, J., 2019. Investigation of swelling pressure of bentonite/claystone mixture in the full range of bentonite fraction. Applied Clay Science, 178, 105137.

2 Zeng, Z.X., Cui, Y.J., Zhang, F., Conil, N., Talandier, J., 2020. Effect of technological voids on the swelling behaviour of compacted bentonite/claystone mixture. Canadian Geotechnical Journal. 57(12), 1881-1892.

3 Zeng, Z.X., Cui, Y.J., Conil, N., Talandier, J., 2020. Experimental investigation and modeling of the hydraulic conductivity of saturated bentonite–claystone mixture. International Journal of Geomechanics, 20(10), 04020184.

4 Zeng, Z.X., Cui, Y.J., Conil, N., Talandier, J., 2020. Effects of technological voids and hydration time on the hydro-mechanical behaviour of compacted bentonite/claystone mixture. Géotechnique. https://doi.org/10.1680/jgeot.19.P.220.

5 Zeng, Z.X., Cui, Y.J., Talandier, J., 2020. Evaluating the influence of soil plasticity on hydraulic conductivity based on a general capillary model. Engineering Geology, 278, 105826.

6 Zeng, Z.X., Cui, Y.J., Conil, N., Talandier, J., 2020. Experimental study on the aeolotropic swelling behaviour of compacted bentonite/claystone mixture with axial/radial technological voids. Engineering Geology, 278, 105846.

7 Zeng, Z.X., Cui, Y.J., Conil, N., Talandier, J., 2021. Analysis of boundary friction effect on the homogenization process of compacted bentonite/claystone mixture with technological voids upon hydration. Acta Geotechnica, 16(2), 525-533.

8 Zeng, Z.X., Cui, Y.J., Talandier, J. Investigation of the hydraulic conductivity of an unsaturated compacted bentonite/claystone mixture. Géotechnique. https://doi.org/10.1680/jgeot.20.P.321.

9 Zeng, Z.X., Cui, Y.J., Talandier, J. Compaction and sealing properties of bentonite/claystone mixtures: Impacts of bentonite fraction, water content and dry density. Under Review in Engineering Geology.

10 Zeng, Z.X., Cui, Y.J., Talandier, J. Evaluation of swelling pressure of bentonite/claystone mixtures from pore size distribution. Under Review in Acta Geotechnica.

11 Zeng, Z.X., Cui, Y.J., Talandier, J. An insight into the grain interaction in bentonite/claystone mixtures. Under Review in Acta Geotechnica.

12 Zeng, Z.X., Cui, Y.J., Talandier, J. Investigating the swelling pressure of highly compacted bentonite/sand mixtures under constant-volume conditions. Under Review in Acta Geotechnica.

13 Zeng, Z.X., Cui, Y.J., Talandier, J. Long-term effect of water chemistry on the hydro-mechanical behaviour of compacted bentonite/claystone mixture with technological voids. Under Review in Engineering Geology.

14 Zeng, Z.X., Cui, Y.J., Talandier, J. Effect of water chemistry on the hydro-mechanical behaviour of compacted mixtures of claystone and Na^{+}/Ca^{2+} bentonites. Under Review in Journal of Rock Mechanics and Geotechnical Engineering.

Conference communications

1 Zeng, Z.X., Cui, Y.J., Conil, N., Talandier, J., 2020. Investigating the contribution of claystone to the swelling pressure of its mixture with bentonite. E-UNSAT2020, October 19-21, Lisbon, Portugal.

Contents

General introduction

General context

Energy touches all aspects of human life (Harris et al., 2018). It is estimated that 85% of the world global energy consumption involves fossil-based fuels, such as coal, natural gas, and oils (Ağbulut, 2019). To cater the need for rapid decarbonisation of the world's energy supply, the use of nuclear energy has been receiving an increasing concern. During the nuclear energy activities, radioactive wastes are inevitably generated, albeit on a very small scale compared to the large amount of wastes generated from the fossil fuels. The radioactive wastes can be clarified into several categories according to their activity and their period (i.e. half-life) (IAEA, 2009). Among them, the most harmful wastes to environment and human health are the high-level and intermediate-level ones. A safe long-term treatment of the high-level and intermediate-level radioactive wastes has become an important issue for the nuclear energy industry in many countries.

In this context, several countries (Belgium, China, France, Germany, Japan, Sweden, etc.) are considering deep geological disposal as a possible solution for high-level and intermediate-level radioactive wastes (OECD/NEA, 1995; NEA, 2008; NDA, 2013; Sellin and Leupin, 2013). This involves placing the wastes in an underground facility, at several hundreds of meters in a relatively impermeable rock, in order to isolate the wastes from the biosphere for a very long period. In general, a multi-barrier principle is adopted in different programs of different countries. This multi-barrier system consists of natural geological barrier (host rock) and engineered barrier (waste container, and sealing/backfill elements).

In France, the Cigeo project (Industrial Centre for Geological Disposal) is being conducted by the French National Radioactive Waste Management Agency (Andra). Cigeo's facilities will be situated in Meuse/Haute-Marne. Located at a depth of approximately 500 m, the radioactive waste repository will be built in the middle of a clay layer named Callovo-Oxfordian (COx) claystone, a 150-m-thick layer (Figure 1). This choice is driven by its very low permeability and high retention capacity for radionuclides (Andra, 2005).

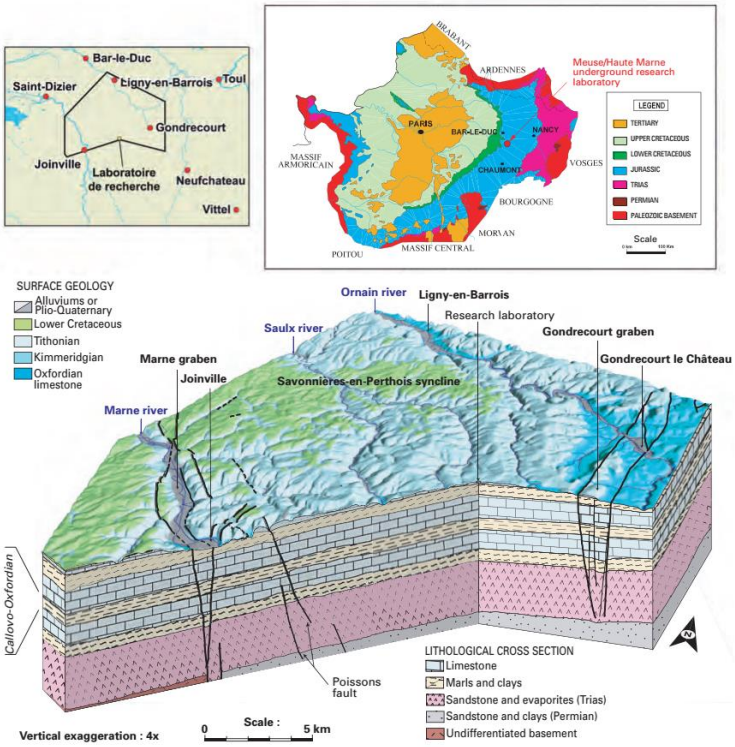

Figure 1. Geological map of the Meuse/Haute-Marne area in eastern France (Andra, 2005).

Cigeo's underground facility will consist of separate disposal zones for high-level and intermediate-level radioactive wastes connected by drift and shaft and will cover at the end a surface area of approximately 15 km² (Figure 2). High-level radioactive waste canisters will be disposed in metal-lined cells of at least 80 m in length and around 70 cm in diameter. Intermediate-level radioactive wastes will be disposed in cells that are a few hundred meters long and a few dozen meters in diameter.

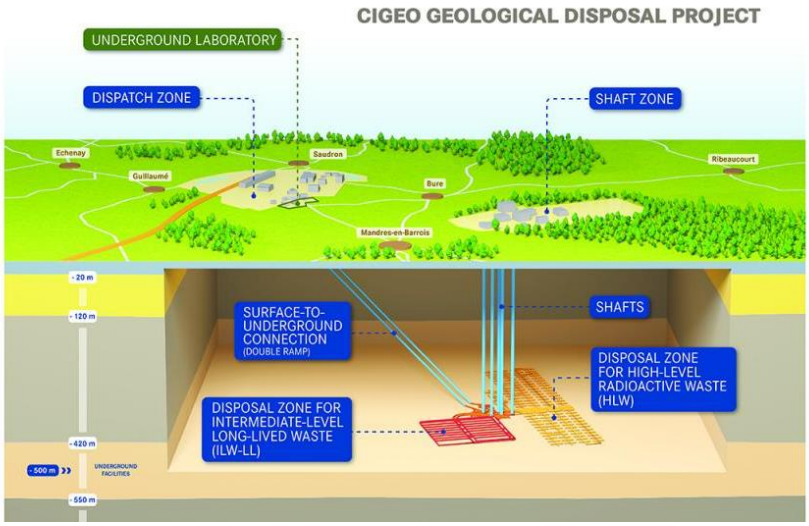

Figure 2. Schematic representation of the Industrial Centre for Geological Disposal, Cigeo (Loi n°2006-739).

To seal the drifts and shafts, bentonites are considered as the most appropriate material thanks to their high swelling characteristic, low permeability and good radionuclides retention capacity (Figure 3) (Pusch, 1979; 1982; Yong et al., 1986). In many cases, bentonites are blended with other additives, such as sand (Villar and Rivas, 1994; Sun et al., 2009; 2013; Wang et al. 2013a; 2013b), granite (Yong et al., 1986; Börgesson et al., 2003) and claystone (Wang et al., 2012; 2014; Middelhoff et al., 2020), to reduce the cost and improve the thermo-mechanical performance (Mollins et al., 1996; Sivapullaiah et al., 2000). After the repository closure, the sealing materials will be saturated by groundwater from the host rock. They are expected to develop a swelling pressure high enough to limit the propagation of excavation-damaged zone (Middelhoff et al., 2020) and a low hydraulic conductivity to prevent the release of radionuclides into the biosphere (Zhang, 2014). Therefore, it appears important to understand the hydro-mechanical behaviour of bentonite-based materials in the design and fabrication of deep geological repositories.

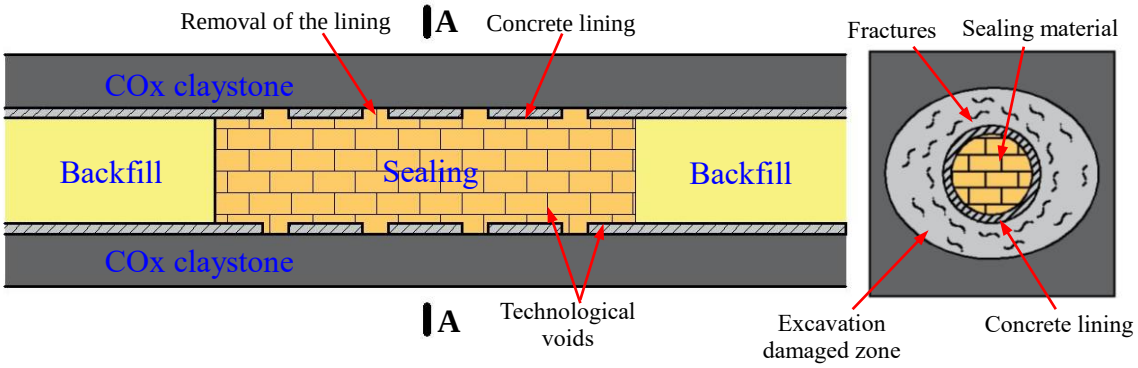

Figure 3. Sealing element in drifts in the French concept of radioactive waste disposal. (a) longitudinal profile and (b) cross section A-A.

Problem statement and objectives of the present work

For several years now, Andra has been conducting programs to define a range of potential materials for repository closure. This work is included in these programs with a focus on "reworked materials". To ensure chemical-mineralogical compatibility with the host rock and lower the costs, a compacted mixture composed of excavated COx claystone and a minor fraction of bentonite is proposed as a candidate sealing material (Zhang, 2014; Zhang and Kröhn, 2019; Middelhoff et al., 2020). This program aims at defining an appropriate protocol for fabricating and constructing blocks that can fulfil the following specifications:

(i) Having a hydraulic conductivity lower than or equal to 10^{-11} m/s;

(ii) Having a swelling capacity to fill up all the technological voids;

(iii) Having a final swelling pressure in the range from 1 to 2 MPa with consideration of the influence of environmental factors;

(iv) Limiting the deformation of retaining structures and preventing the propagation of fractured zone;

(v) Maintaining their properties over the long term.

To satisfy these specifications, the following questions arise.

(i) Since the swelling pressure and hydraulic conductivity of bentonite-based materials are generally mineral density-dependent at least in the short term, which final dry density and bentonite fraction can fulfil the specifications in terms of swelling pressure and hydraulic conductivity? Additionally, the technological voids can remain between the surrounding rock and compacted blocks and between blocks during the construction of the compacted block. Upon hydration, the compacted blocks will swell and fill these technological voids, resulting in a decrease in the block density and influencing the hydro-mechanical behaviour of compacted blocks. Therefore, which initial dry density corresponds to the required final dry density while taking into account the technological voids?

(ii) For the industrial fabrication of the compacted blocks, what compaction pressure is required?

(iii) Since the compacted blocks are uniaxially compacted, a more significant swelling in the axial direction is expected. What will be the swelling aeolotropy upon wetting?

(iv) After the galleries are closed, the sealing materials will be saturated with the pore water of the host rock, which is rich in salts. Additionally, the concrete structure will decay, producing cement solution. How do they affect the hydro-mechanical performance of the materials?

(v) The compacted blocks are commonly laid in dry state. With hydration, how does their hydraulic conductivity change with time?

This study is motivated by a better understanding of the hydro-mechanical of compacted bentonite/claystone mixture. The main objectives include:

(i) Characterization of the compaction and sealing properties of mixtures with different bentonite fractions, dry densities and water contents.

(ii) Investigating the effect of technological voids on the aeolotropic swelling behaviour.

(iii) Investigating the effects of technological voids and hydration time on the swelling pressure, hydraulic conductivity and microstructure.

(iv) Understanding the influences of site water, cement solution, bentonite type and dry

density on the swelling pressure, hydraulic conductivity, microstructure and mineralogy.

(v) Experimental and theoretical characterization of the unsaturated hydraulic property of the compacted blocks.

Outline of the thesis

The objectives of the thesis are addressed in seven chapters.

The first chapter is devoted to a literature review. Bentonite-based materials have been largely studied in the framework of radioactive waste disposal, and an overview of the knowledge of these studies is made. Emphasis is put on the basic microstructure of bentonite-based materials, the microstructural evolution upon hydration and the hydro-mechanical behaviour. The effects of bentonite fraction, dry density, water content, technological voids and water chemistry on the hydro-mechanical behaviour of bentonite-based materials are also presented.

The second chapter is devoted to the compaction and sealing properties of MX80 bentonite/COx claystone mixtures, which correspond to six published or submitted papers. The first one, submitted to Engineering Geology, presents an experimental study on the compaction and sealing properties under the effects of water content and bentonite fraction variations during mixing and humidifying processes as well as the dry density variation induced by natural fractures and technological voids. The second paper, submitted to Acta Geotechnica, addresses the interaction mechanism between the bentonite and claystone grains in the mixtures. The bentonite and claystone void ratios and the bentonite volumetric fraction in the mixtures were determined by considering the interaction between bentonite and claystone in the development of swelling pressure. Subsequently, the swelling pressure of crushed claystone grains was indirectly determined and then compared with that estimated from the measured vertical swelling pressure of intact COx claystone. The determined value was found to be comparable to that estimated from the relationship between the vertical swelling pressure and void ratio for intact COx claystone, confirming the identified swelling mechanism of bentonite/claystone mixtures. Moreover, based on the claystone void ratio in the mixtures, two analytical methods were proposed to predict the swelling pressure and hydraulic conductivity of bentonite/claystone mixture in the full range of bentonite fraction. The swelling pressure prediction is presented in a paper published in Applied Clay Science and the hydraulic conductivity prediction corresponds to a paper published in International Journal of Geomechanics. Additionally, mercury intrusion porosimetry (MIP) tests were also performed

on the specimens after hydration, allowing the determination of the pore size distribution and the evaluation of the swelling pressure and hydraulic conductivity of bentonite/claystone mixtures from the pore size distribution. The obtained results are presented in two paper. The first one, submitted to Acta Geotechnica, presents the relationship between the swelling pressure and inter-particle distance. The second one, published in Engineering Geology, addresses the influence of soil plasticity on the hydraulic conductivity based on a general capillary model.

The third chapter presents two experimental studies, presented in two papers, aiming at investigating the aeolotropic swelling behaviour of compacted MX80 bentonite/COx claystone mixture with technological voids. In the first paper published in Engineering Geology, the swelling pressure of the specimens without voids was first measured in both axial and radial directions by constant-volume method and the effect of dry density on the aeolotropic swelling behaviour was studied. Meanwhile, the axial/radial technological voids were designed and the swelling behaviour of the specimens with axial/radial voids was investigated in both axial and radial directions. In the second paper published in Canadian Geotechnical Journal, the water content, dry density and microstructure features at different positions were further investigated, helping the interpretation of the swelling behaviour of compacted mixture with technological voids.

The fourth chapter discusses the homogenization process of compacted bentonite/claystone mixture with technological voids. Firstly, a series of infiltration tests were carried out on compacted MX80 bentonite/COx claystone mixture at different times. The evolutions of swelling pressures and hydraulic conductivity of compacted blocks with different technological voids were evaluated. Moreover, the dry density, water content, suction and microstructure features at different positions after various times were determined, enabling interpretation of the hydro-mechanical behaviour of the compacted mixture with the presence of technological voids. Particular attention was paid to the effect of boundary friction between the specimens and porous stones. An analytical method was proposed to estimate the final dry density distribution of specimens with technological voids. The experimental results on the effects of technological voids and hydration time on the hydro-mechanical behaviour of bentonite/claystone mixture are presented in a paper published in Géotechnique. The results on the estimation of final dry density distribution are presented in a paper published in Acta Geotechnica.

The fifth chapter consists of two papers and analyses the effect of water chemistry on the hydro-mechanical of bentonite/claystone mixture. The specimens with various bentonites, dry densities and technological voids were hydrated with site water or cement solution. The swelling pressure and hydraulic conductivity during hydration, and microstructure features after hydration were determined to interpret the influence mechanism of cation and hydroxide. The experimental results are presented in the first paper submitted to Journal of Rock Mechanics and Geotechnical Engineering. The second paper, submitted to Engineering Geology, investigates the swelling pressures and hydraulic conductivities of compacted MX80 bentonite/COx claystone mixture with various technological voids and hydrated with deionised water and synthetic site solution for 10 and 590 days. The long-term effects of pore water chemistry and technological voids on the hydro-mechanical behaviour of compacted bentonite/claystone mixture were determined.

The sixth chapter presents an experimental and theoretical study on the two-phase water transfer in the compacted MX80 bentonite/COx claystone mixture. Firstly, infiltration and water retention tests under constant-volume conditions were carried out on a compacted bentonite/claystone mixture, allowing the water hydraulic conductivity of the mixture to be determined based on the instantaneous profile method. The microstructure of the mixture at different suctions was also investigated using MIP tests. Based on the test results, a novel method was proposed to predict the hydraulic conductivity for both vapour and liquid phases. Finally, a numerical model was set up to verify the feasibility of the proposed method. The results of this chapter are presented in a paper submitted to Géotechnique and now it is under the second revision.

The general conclusions are presented at the end, together with some perspectives for the future research.

Chapter 1. Literature review

1.1 Introduction

Bentonite-based materials have been chosen as sealing/backfill materials in deep geological repository for high-level radioactive wastes thanks to their high swelling capacity, low permeability and favourable radionuclide migration retardation properties (Pusch, 1979; 1982; Dixon et al., 1985; Komine and Ogata, 1994; 1999). In the past decades, the hydro-mechanical behaviour of bentonite-based materials has been largely studied by many researchers in the context of radioactive waste disposal. This chapter provides an overview of the knowledge concerning the hydro-mechanical behaviour of bentonite-based materials. The swelling behaviour of bentonite-based materials is first described in Section 1.2. A comprehensive literature study was conducted on water transfer property of the bentonite-based materials and presented in Section 1.3.

1.2 Swelling behaviour of bentonite-based materials

Bentonites are composed of large amount of clay minerals, in particular montmorillonite. Upon contact with pore water from the host rock, the bentonite-based materials are expected to swell and fill the technological voids between the blocks of compacted bentonite-based materials or between the blocks and the host rock. Afterwards, swelling pressure will develop when the technological voids are fully filled (Tang et al., 2011a; 2011b; Wang et al., 2012; Bian et al., 2019a). This swelling pressure must be high enough to limit the propagation of excavation-damaged zone in the Cigéo concept. Meanwhile, it must be lower than the in situ minor stress and the yield stress supported by the confinement elements (Saba et al., 2014a; Cui, 2017). In this section, we first present the basic microstructure, the microstructural evolution upon hydration and the corresponding swelling mechanism of compacted bentonite-based materials. Then, the influences of dry density, water content, swelling direction, technological voids and water chemistry on the swelling behaviour of compacted bentonite-based materials are discussed.

1.2.1 Microstructure of bentonite-based materials

Physically, the swelling property of bentonites is related to the montmorillonite structure (Mitchell, 1976; 1993). The montmorillonite is a “TOT” or “2:1” layer mineral consisting of an

alumina octahedral sheet sandwiched between two silica tetrahedral sheets (Figure 1-1). Mostly, this ideal structure can be affected by the exchange reaction, known as isomorphous substitution. Al^{3+} in octahedral sheet can be isomorphously substituted by divalent cations (e.g. Mg^{2+} and Fe^{2+}) and Si^{4+} in tetrahedral sheet can be substituted by Al^{3+}, resulting a permanent negative lattice charge on the faces. This negative surface charge is balanced by the cations adsorbed on the clay mineral crystal surfaces in the presence of water. The thickness of the "TOT"/"2:1" unit layer is roughly 9.6 Å while the thickness of the interlamellar space depends on the hydration state (Mitchell, 1993; Pusch and Yong, 2006; Villar et al., 2012).

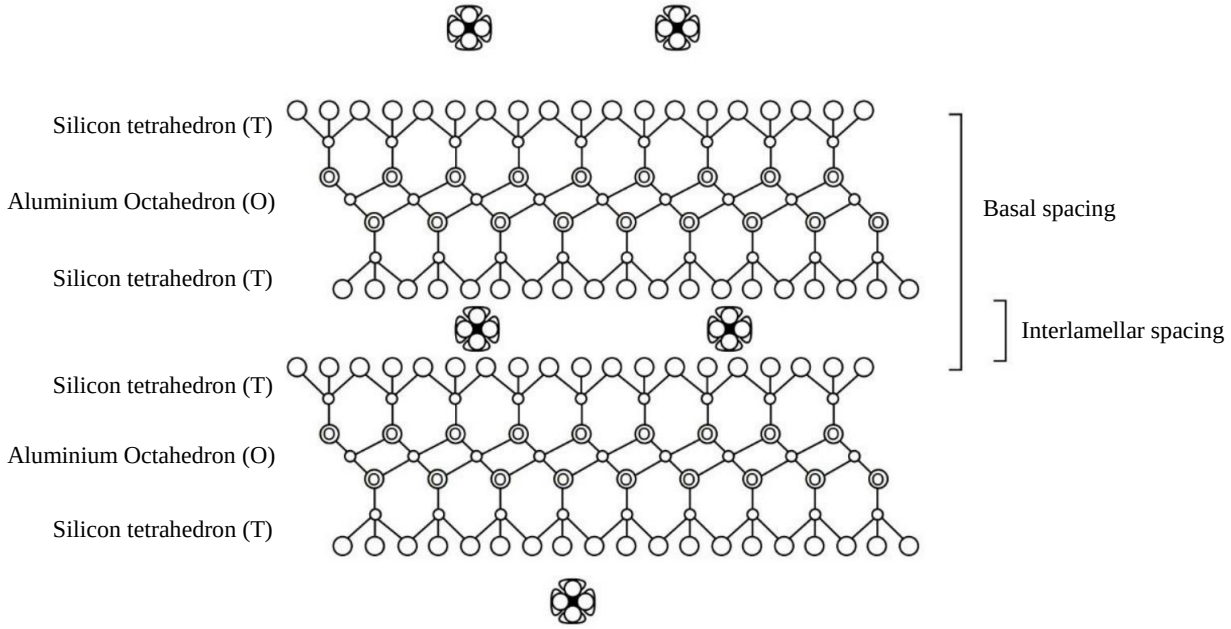

Figure 1-1. Representation of montmorillonite structure (modified after Pusch and Yong, 2006 and Dardé, 2019).

In a particle, the montmorillonite unit layers are disposed one above another in a face-to-face orientation, as illustrated in Figure 1-2. The number of layers varies between 10 and several hundred, depending on the hydration conditions (Saiyouri et al., 1998; 2000). For the bentonite-based materials, when the compaction characteristics (dry density and water content) are not too close to the saturation hyperbola in the Proctor diagram, clay particles will aggregate together and form an aggregate microstructure (Delage et al., 2006).

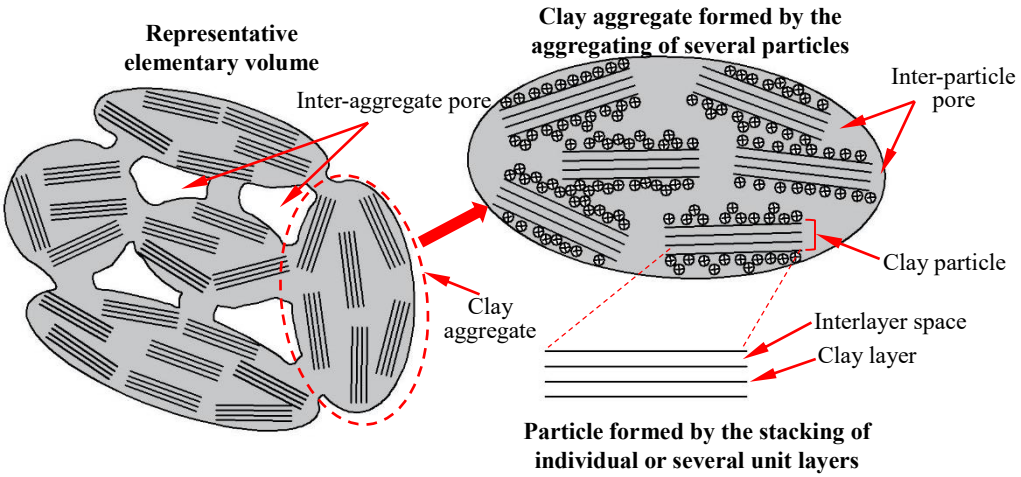

Figure 1-2. Fabric units and pore spaces of compacted bentonites (modified after Liu (2013) and Mašín and Khalili (2015)).

Thereby, three pore populations can be expected in the compacted bentonite-based materials (Delage et al., 2006):

(a) planar interlayer spaces between the elementary clay layers, inside the clay particles;

(b) interparticle voids between the particles, inside the aggregates;

(c) inter-aggregate pores between the aggregates made up of clay particles.

In the past decades, the pore structure of compacted bentonite-based materials was investigated by many researchers (Agus and Schanz, 2005; Delage et al., 2006; Lloret and Villar, 2007; Romero and Simms, 2008; Wang et al., 2013a; Molinero-Guerra et al., 2017; Sun et al., 2019a). Mercury intrusion porosimetry (MIP) is a common technique used to quantitatively determine the pore size distribution of bentonite-based materials by assuming parallel, cylindrical and nonintersecting pores of different radii (Romero and Simms, 2008; Molinero-Guerra et al., 2017). The inter-particle and inter-aggregate pores can be well verified by the presence of two peaks of the pore size distribution curve. Unfortunately, the interlayer spaces are not detectable due to the limited range of the pressure applied in the MIP tests. According to the results of Lloret and Villar (2007) on compacted FEBEX bentonite and Wang et al. (2013a) on MX80 bentonite/sand mixture (Figure 1-3), compaction could significantly decrease the inter-aggregate pores whereas the intra-aggregate pores remained unaffected.

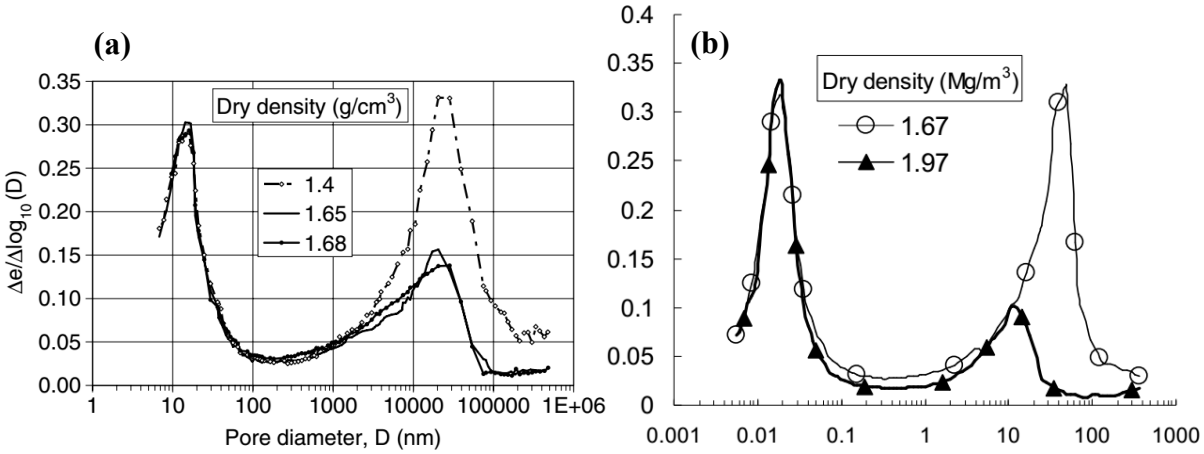

Figure 1-3. Pore size distribution of compacted (a) FEBEX bentonite (Lloret and Villar, 2007) and (b) MX80 bentonite/sand mixture (Wang et al., 2013a).

This was confirmed by Romero and Simms (2008) when they directly observed the microstructure of compacted FEBEX bentonite using scanning electron microscopy techniques (Figure 1-4). Obviously, larger inter-granular pores could be observed on the specimen with a smaller dry density.

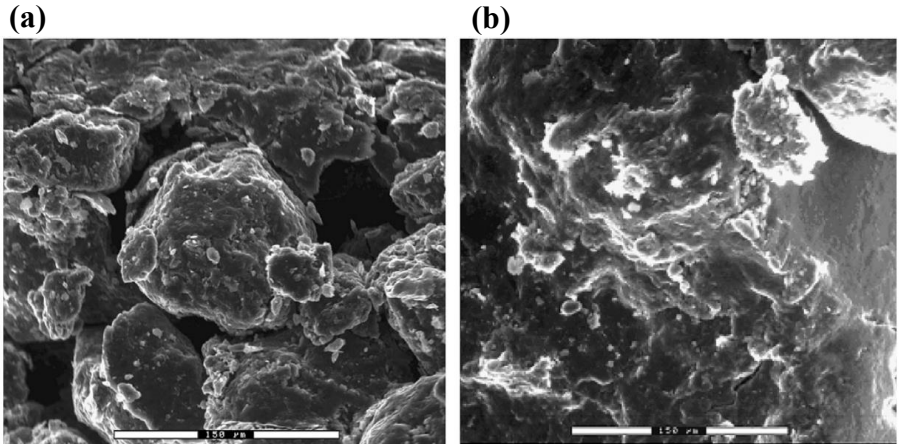

Figure 1-4. Micrographs of compacted FEBEX bentonite with a hygroscopic water content. (a) ρ_d=1.40 Mg/m^3; (b) ρ_d=1.65 Mg/m^3 (Romero and Simms, 2008).

1.2.2 Microstructural evolution upon hydration

Upon hydration, water molecules are expected to progressively placed on the clay unit surfaces, layer by layer up to four layers, with an increase in the interlayer spaces, as shown in Figure 1-5 (van Olphen, 1977; Saiyouri et al., 1998; 2000; Delage et al., 2006; Bian et al., 2019a). The corresponding distance between the unit layers starts from 9.6 Å with no water, and to 12.6, 15.6, 18.6 and 21.6 Å with one, two, three and four layers of adsorbed water molecules, respectively.

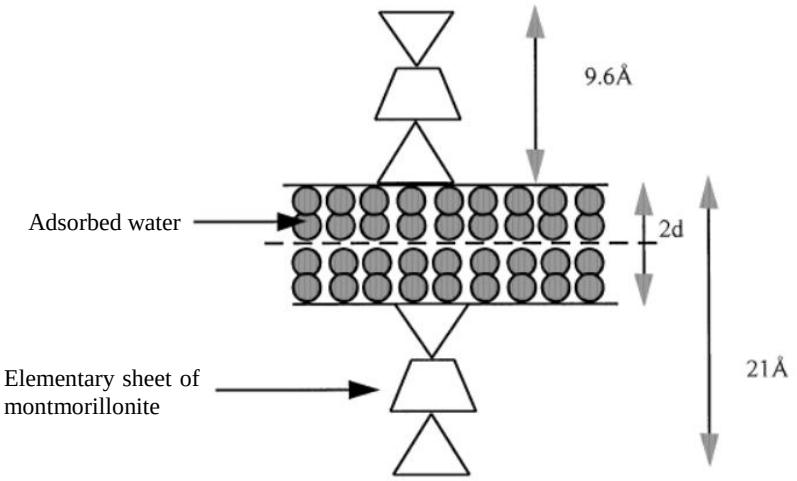

Figure 1-5. Schematic distance between two layers of montmorillonite (Saiyouri et al., 2000).

The placement of water molecules is highly dependent on suction. Figure 1-6 shows the variations of the layer number of adsorbed water molecules and the distance between the unit layers with suction. MX80 bentonite presents only one water layer when the suction is larger than 50 MPa. A second water layer is adsorbed when it decreases from 50 to 7 MPa. A third layer and a fourth layer are adsorbed as the suction decrease to below 7 MPa and 60 kPa, respectively.

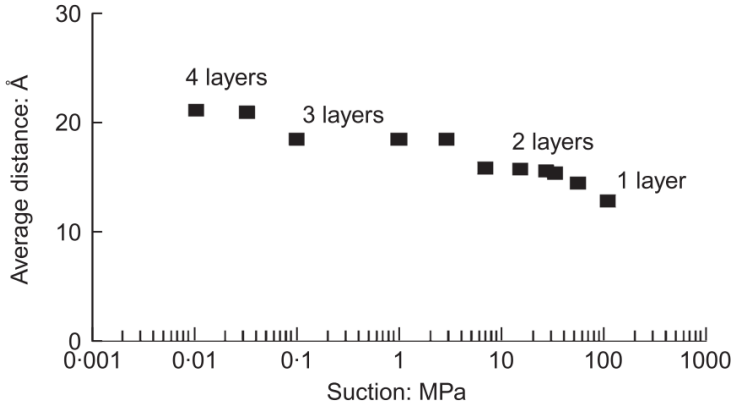

Figure 1-6. Variations of the layer number of adsorbed water molecules and the distance between montmorillonite layers with suction for MX80 bentonite (Saiyouri et al., 1998).

Moreover, clay aggregates will be divided into thinner particles as the suction decreases, leading to a decrease in the intra-aggregate pore size. As shown in Figure 1-7, a particle is composed of more than 100 layers in a dry specimen while the number of layers per particle decreases until reaching only 10 layers with the increasing water content.

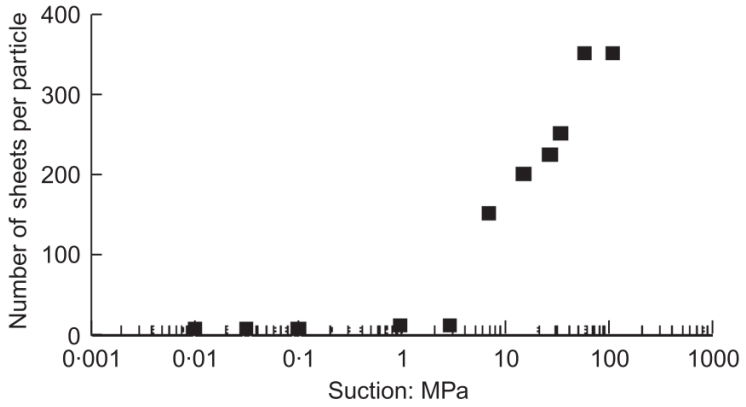

Figure 1-7. Variation of the number of layers per particle with suction for MX80 bentonite (Saiyouri et al., 1998)

In the past decades, the microstructural evolution of bentonite-based materials upon hydration has been experimentally investigated by many researchers (Montes-Hernandez et al., 2003; Agus and Schanz, 2005; Cui et al., 2002a; Wang et al., 2013b; 2014; Keller et al., 2014; Saba et al., 2014a; Seiphoori et al., 2014; Massat et al., 2016; Molinero-Guerra et al., 2018). Agus and Schanz (2005) compared the microstructure features of Calcigel bentonite/sand mixtures with an initial dry density of 2 Mg/m^3 before and after hydration under free-swell conditions. They found that the specimens in the initial state exhibited a clear bimodal porosity with peaks at about 15 and 10 μm. By contrast, a monomodal pore size distribution was observed with a single peak identified at approximately 0.6 μm after hydration, and the non-intruded pore volume increased significantly. Wang et al. (2013b) investigated the microstructural changes of MX80 bentonite/sand mixture with an initial dry density of 1.67 Mg/m^3 during the hydration process under constant-volume conditions through MIP tests. The results are presented in Figure 1-8. It clearly shows that when the suction decreased from 65 to 12.6 MPa, the inter-aggregate pore volume decreased slightly due to the exfoliated clay particles, without significantly changing the intra-aggregate pores. As the suction decreases to lower values than 4.2 MPa, the inter-aggregate pore volume increased again with the appearance of fissure-like 2-dimensional (2-D) pores due to the division of clay particles while the intra-aggregate pore volume decreased. Similar observation was made by Cui et al. (2002a) on Kunigel bentonite/sand mixture.

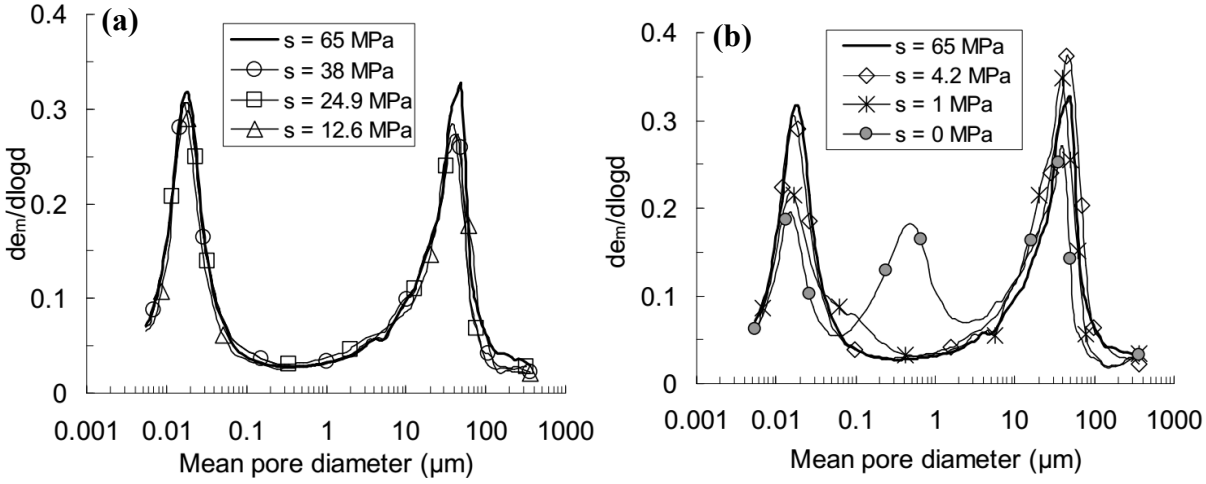

Figure 1-8. Pore size distributions of bentonite-sand mixture wetted with different suctions under constant volume conditions. (a) 12.6-65 MPa suction and (b) 4.2–0 MPa suction (Wang et al., 2013b).

Additionally, the clogging of inter-aggregate pores was studied using X-ray computed tomography (μCT) (Massat et al., 2016) and imaging methods (ESEM or SEM) (Wang et al., 2013b). Using μCT, Massat et al. (2016) determined the evolution of inter-aggregate porosity of Kunipia-G bentonite (at a dry density of 1.40 Mg/m^3) upon hydration under constant-volume conditions. The inter-aggregate porosity at different hydration times was deduced from μCT images and the results are summarised in Figure 1-9. Upon hydration, the inter-aggregate porosity of the specimens decreased progressively during hydration. Moreover, the smaller the distance from the hydration end, the more rapid the decrease of inter-aggregate porosity.

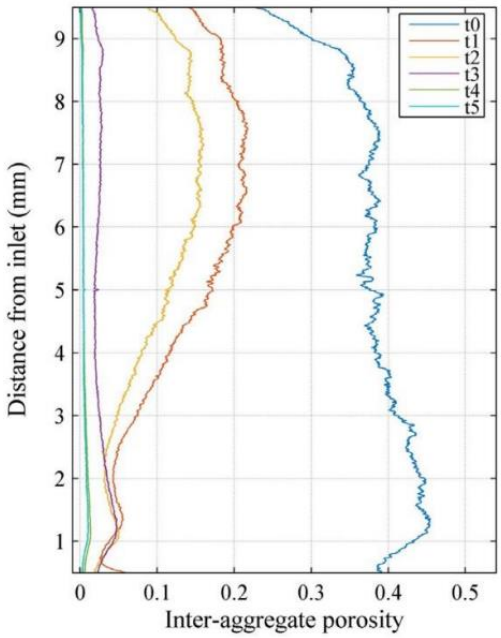

Figure 1-9. Profile of inter-aggregate porosity deduced from μCT images at different times (t_1=7.1 days, t_2=8.8 days, t_3=15.8 days, t_4=19.7 days, and t_5=39.8 days) (Massat et al., 2016).

1.2.3 Swelling mechanism

As remarked above, the swelling behaviour of bentonite-based materials is mainly ascribed to the special microstructure of the montmorillonite mineral characterised by a stack of the "TOT" unit layer (see Figure 1-1). Saiyouri et al. (2000), Liu (2013) and Sun et al. (2015) suggested that the swelling of clay minerals comprised two main processes: crystalline and osmotic swelling. The crystalline swelling is a process whereby 0-4 discrete layers of water molecules are placed along the clay layers inside the particles (Saiyouri et al., 2000; Delage et al., 2006; Liu, 2013). The adsorption energy of the water layers on the clay surface is the principal driving power of the crystalline swelling (Mollins, 1996). Commonly, the crystalline swelling occurs at low relative humidity (Dardé, 2019). Due to the isomorphous substitution in the crystal lattice, the surfaces of the clay layers are negatively charged. Water molecules will enter the interlayer space, hydrate counter-ions and form hydration spheres around the cations as well as hydrogen-bonding with the oxygen at the clay mineral surfaces (Sposito and Prost, 1982; Dardé, 2019). This process causes an increase in the interlayer spacing and pushes clay layers apart. Pusch (1982) indicated that the swelling pressure of compacted MX80 bentonite with a high dry density is mainly governed by the crystalline swelling due to the poor development of diffuse double layers.

The adsorption of water between individual clay layers is accompanied by the subdivision of clay particles (Saiyouri et al., 2000; 2004; Tripathy et al., 2004). Moreover, when the cations are attracted to the negatively charged clay particles, the concentration of adsorbed cations near the surface of clay particles is much higher than that far from the surface (Tripathy et al., 2004). This allows the diffuse double layers to develop on a parallel assembly of clay particles. In that case, the osmotic swelling represented by the interaction of clay particles becomes dominant. It includes the attractive (van der Waals) and repulsive (diffuse double layer) forces between the clay particles, both of which are highly dependent on the inter-particle distance (Liu, 2013). In the previous works, the inter-particle distance was commonly estimated from the total clay void ratio (or the inter-particle water volume) and the specific surface area (Komine and Ogata, 2004; Schanz and Tripathy, 2009; Saiyouri et al., 2000). However, the used specific surface area was in general a total value, which included the interlayer zones and the inter-particle zones (Mašín and Khalili, 2015). Additionally, it was assumed that the specific surface could decrease owing to the reduction of unit layer number inside the clay particles during the crystalline swelling process (Saiyouri et al., 2000; Schanz and Tripathy, 2009). To address these issues, Liu (2013) and Sun et al. (2015) introduced an empirical parameter related to the average

number of the unit layers per clay particle and empirically determined the inter-particle distance from the total void ratio, the thickness of unit layers and the distance between the unit layers.

1.2.4 Swelling deformation and swelling pressure

Upon the contact with pore water of host rock, bentonite-based materials can develop significant capacity of swelling or swelling pressure if expansion is constrained. Basically, the swelling strain and swelling pressure developments upon hydration are highly correlated with the microstructure evolution (Villar, 1999; Cui et al., 2002b; Cuisinier and Masrouri, 2005; Baille et al., 2009; Massat et al., 2016). The final swelling strain and swelling pressure are highly dependent on the bentonite content, dry density and water content (Sun et al., 2009; 2013; Cui et al., 2012; Wang et al., 2012; Chen et al., 2016a).

1.2.4.1 Swelling strain

Cuisinier and Masrouri (2005) performed suction-controlled stepwise hydration tests on a bentonite/silt mixture (a proportion of 60/40 in dry mass) at a dry density of 1.27 Mg/m^3. They found that the specimens swelled slowly at a suction above 4 MPa and swelled rapidly at a suction below 4 MPa. This phenomenon is consistent with the threshold identified by Wang et al. (2013b) on the microstructural evolution of compacted MX80 bentonite/sand mixture. Villar (1999) conducted stepwise hydration tests on Febex bentonite specimens with a dry density of 1.70 Mg/m^3 under various constant stresses. The results show that the wetting of specimens under a low vertical stress was characterised by a significant and monotonous swelling whereas the specimens under larger stresses would first collapsed and then swelled. Obviously, this collapse behaviour is also related to the initial dry density. Cui et al. (2002b) compacted Foca7 bentonite at vertical stresses of 10.2, 12.24, 18.36 and 22.24 MPa and hydrated the compacted the compacted specimens under constant stresses. The variation of void ratio with hydration is illustrated in Figure 1-10. A higher collapse behaviour was observed on the specimen with a larger initial void ratio, albeit under a smaller vertical stress.

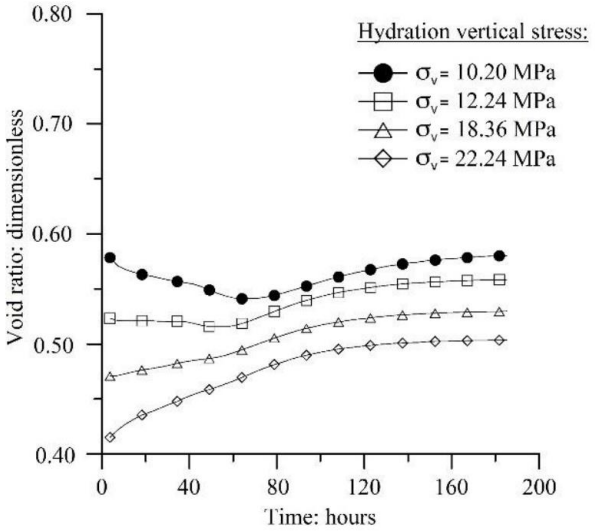

Figure 1-10. Hydration of FoCa7 bentonite specimens under constant stresses (Cui et al., 2002b).

The final swelling strain is dependent on the applied vertical stress, initial dry density and initial water content. Generally, the final swelling strain increased as the initial dry density increased. By contrast, with the increases of the applied vertical stress and the initial water content, the final swelling strain decreased (Komine and Ogata, 1994; Sun et al., 2009; 2013; Cui et al., 2012). Sun et al. (2009; 2013) performed a series of swelling deformation tests on Kunigel-V1 bentonite/sand and GMZ bentonite/sand mixtures. They defined the final montmorillonite void ratio as the volume ratio of water to montmorillonite and obtained its relationship to the vertical stress. For the specimens with a higher bentonite fraction and under a smaller vertical stress, the relationship could be well described using a straight line in a semi-logarithmic plot (Figure 1-11a). By contrast, when the vertical pressure was large enough and the bentonite fraction in the mixture was small, the measured plots deviated from the straight line due to the formation of skeleton void ratio (Figure 1-11b).

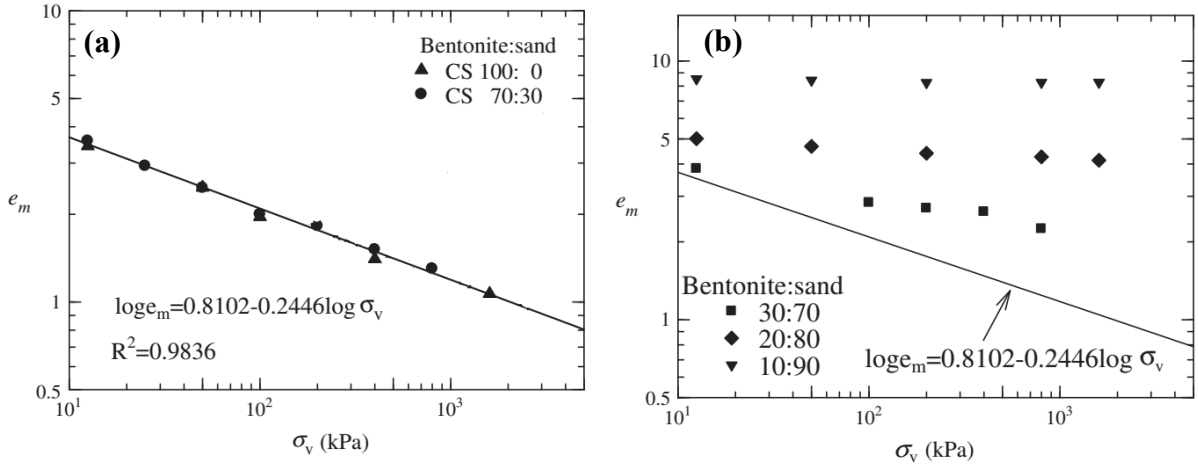

Figure 1-11. Relationship between the final montmorillonite void ratio and vertical stress of GMZ bentonite/sand mixtures with (a) high bentonite fractions and (b) low bentonite fractions (modified after Sun et al., 2013).

1.2.4.2 Swelling pressure

The swelling pressure of expansive clays can be experimentally measured in the laboratory by swell-consolidation, zero-swell, constant-volume and load-swell method methods (Sridharan et al., 1986; Basma et al., 1995; Abdullah et al., 1999; Tang et al., 2011b; Wang et al., 2012; Yigzaw et al., 2016; Dardé, 2019). In the swell-consolidation tests, the specimens are hydrated under free-swelling conditions in an oedometer ring and then incrementally loaded to recover its initial void ratio. The swelling pressure is defined as the load required to reach its initial void ratio. In the zero-swell tests, the specimens are wetted on an oedometer ring and the vertical load is added so as to prevent any vertical swelling once the specimens start to swell. The required maximum load is the corresponding swelling pressure. In the constant-volume tests, the specimens are installed in a constant-volume cell and the stress is measured using a pressure sensor. In the load-swell tests, several identical specimens are wetted under various vertical stresses, allowing the determination of the volumetric strain curve. The swelling pressure corresponds to the stress at the intersection of the volumetric strain curve with the no volume change line. Normally, different methods can give different values of swelling pressure due to the difference in the loading and wetting conditions in each method (Tang et al., 2011; Wang et al., 2012).

Baille et al. (2009) studied the swelling pressure development of compacted Bavaria bentonite with hydration using constant-volume method (Figure 1-12). They found a non-monotonic swelling pressure development for the specimens with very high dry densities and very low initial water contents. It was suggested that the initial hydration of bentonite-based materials

was accompanied by homogeneous swelling of aggregates. During this process, the aggregate structure would be persistent. With further hydration, the clay aggregates would soften and the aggregate structure collapsed.

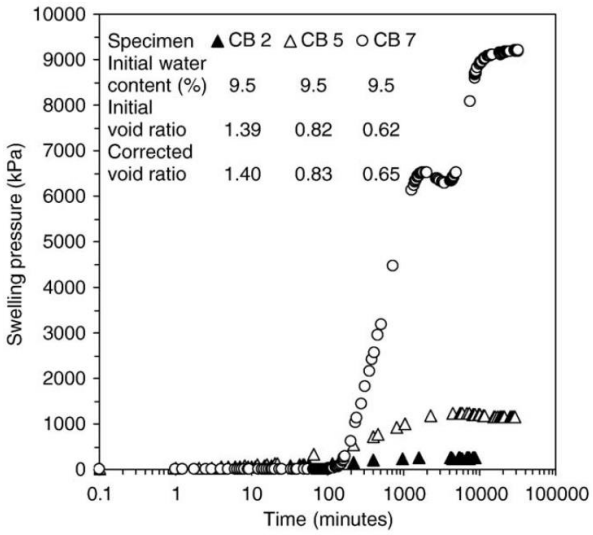

Figure 1-12. Evolution of swelling pressure of compacted Bavaria bentonite specimens (Baille et al., 2009).

To investigate the occurrence of transient peak, Massat et al. (2016) determined the evolution of inter-aggregate porosity in a specimen of Kunipia-G bentonite (dry density of 1.40 Mg/m^3) hydrated under constant-volume conditions using μCT. As shown in Figure 1-13, the transient drop was consistent with the collapse of inter-aggregate pores. Similar phenomenon was drawn by Saba et al. (2014a) while they investigated the swelling pressure kinetics of MX80 bentonite/sand mixtures (a proportion of 70/30 in dry mass).

In addition to the swelling pressure development, the final swelling pressure is also one of the major concerns. It has been documented that the final swelling pressure of bentonite-based materials can be influenced by many factors, such as bentonite fraction in the mixture, dry density and water content (Agus and Schanz, 2008; Villar and Lloret, 2008; Cui et al., 2012; Ye et al., 2013; Rao and Ravi, 2015; Lang et al., 2018). Generally, the higher the initial dry density and the bentonite fraction, the larger the swelling pressure (Agus and Schanz, 2008; Cui et al., 2012). However, there is no consensus on the influence of water content on the swelling pressure of bentonite-based materials: Komine and Ogata (1994) and Villar and Lloret (2008) have not detected significant influence when they compared the swelling pressures of Kunigel-V1 and FEBEX bentonites at different initial water contents; by contrast, Ye et al. (2013), Rao and Ravi (2015) and Lang et al. (2018) found that the swelling pressure decreased with the

increase of water content, especially for the specimens with high dry density.

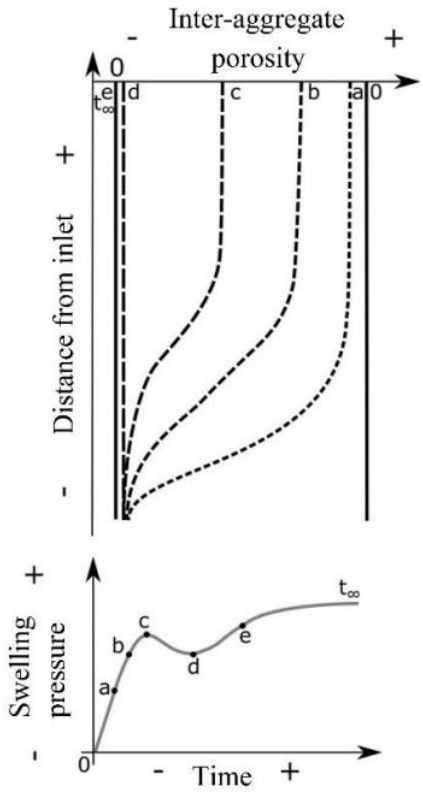

Figure 1-13. Schematic evolution of inter-aggregate porosity and swelling pressure upon specimen hydration.

To understand the swelling mechanism of bentonite/sand mixture, a number of studies have addressed the final swelling pressure of different types of bentonites and their mixtures with sand, such as Kunigel-V1 bentonite (Sun et al., 2009), MX80 bentonite (Karnland et al., 2008; Saba et al., 2013; Manca et al., 2015), Calcigel bentonite (Agus and Schanz, 2008), Tsukinuno bentonite (Komine and Ogata, 1999) and GMZ bentonite (Ye et al., 2007; Cui et al., 2012; Sun et al., 2015; 2017). Commonly, the bentonite/sand mixture was assumed to be an ideal mixture in which the hydrated bentonite grains were uniformly distributed forming a matrix, while the sand grains constituted impervious inclusion. This allowed the determination of the local variables in the mixture, such as montmorillonite void ratio (Sun et al., 2009; Sun et al., 2015; 2017), dry density of bentonite (Dixon et al., 1985; Lee et al., 1999; Agus and Schanz, 2008), effective dry density of montmorillonite (Dixon et al., 2002; Powell et al., 2013), and initial degree of saturation of montmorillonite (Rao and Ravi, 2015). Figure 1-14 presents the variations of swelling pressure of bentonite/sand mixture with the dry density for MX80 (Karland et al., 2008; Saba, 2013), Calcigel (Agus and Schanz, 2008), Tsukinuno (Komine and Ogata, 1999), and GMZ (Cui et al., 2012; Ye et al., 2017) bentonites. It appears that a unique

relationship was identified for each bentonite/sand mixture regardless of the bentonite fraction. This phenomenon suggested that the final swelling pressure is totally governed by the final bentonite dry density.

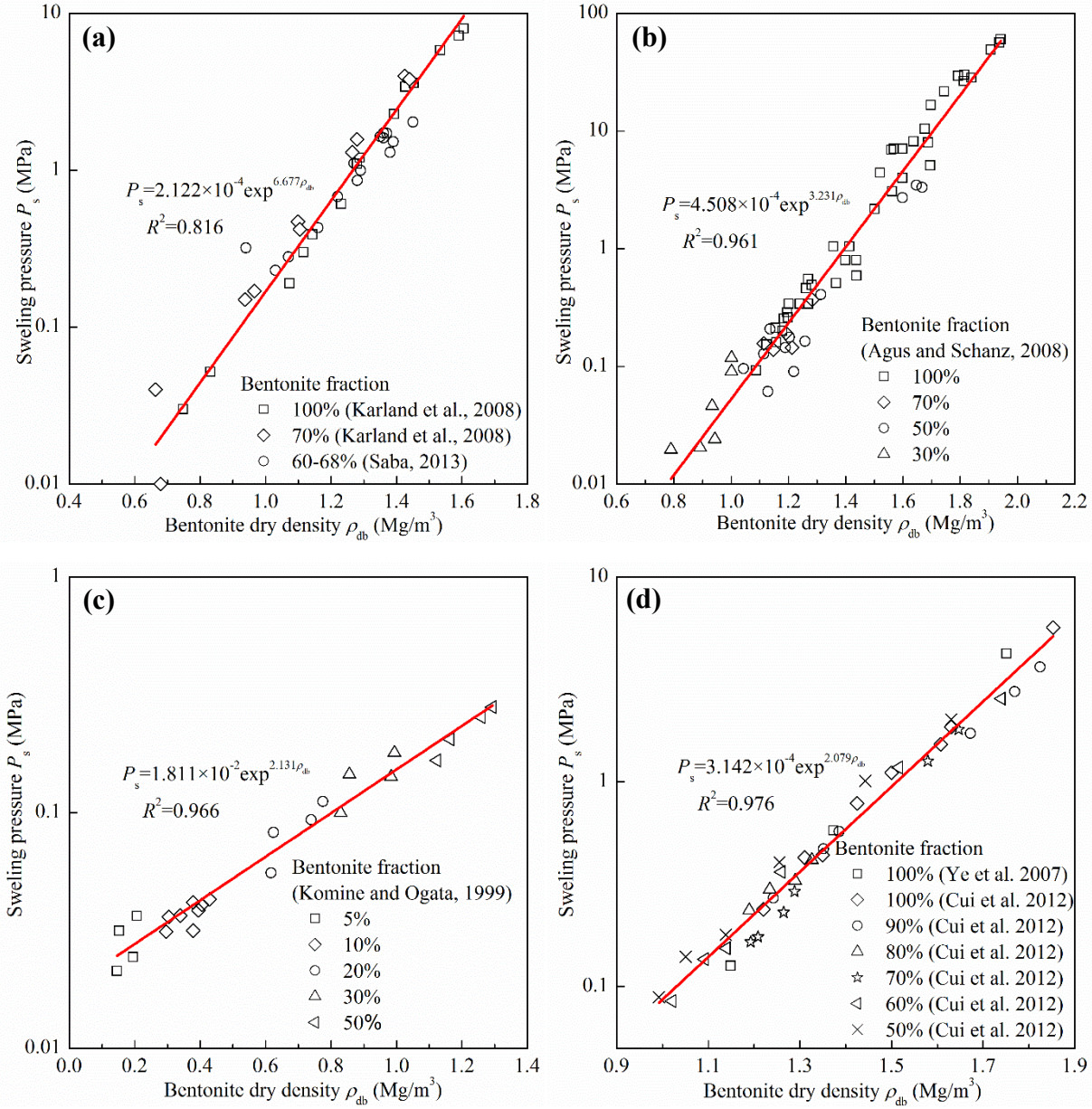

Figure 1-14. Relationship between swelling pressure and bentonite dry density for bentonite/sand mixtures: (a) MX80 bentonite; (b) Calcigel bentonite; (c) Tsukinuno bentonite; (d) GMZ bentonite.

In the case of bentonite/crushed claystone mixture, Wang et al. (2012) indicated that the relationship between the swelling pressure and bentonite dry density agreed well with that for the bentonite/sand mixture. They stated that the water content of claystone could be assumed to be constant during hydration and all water added was adsorbed by bentonite. In that case, the contribution of claystone to swelling pressure could be ignored and the claystone behaved as

inert sand. However, it should be noted that their study focused on the mixture with a low claystone fraction (30% in dry mass). The crushed claystone contains clay minerals and the interaction between clay minerals and water will occur during wetting, which can become more significant when the claystone fraction becomes predominant component.

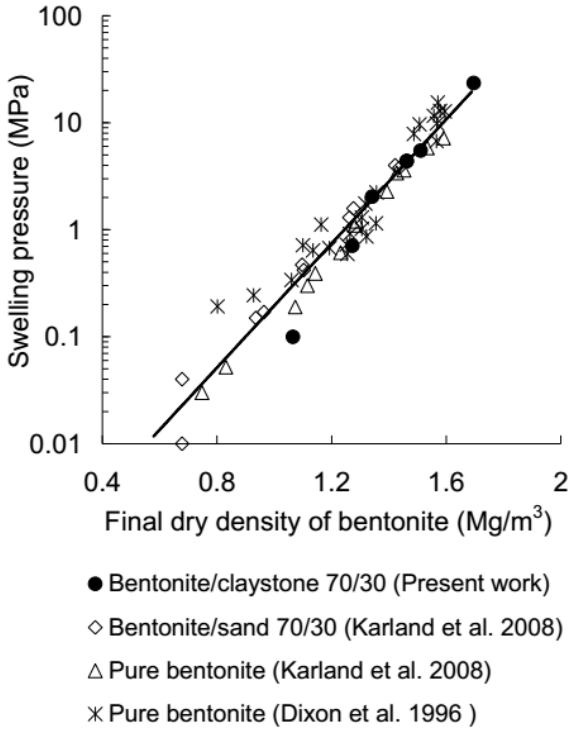

Figure 1-15. Relationship between the final swelling pressure and final bentonite dry density for MX80 bentonite/claystone mixture (Wang et al., 2012).

1.2.5 Anisotropic swelling behaviour

Even though numerous investigations have been carried out on the swelling behaviour of compacted bentonite-based materials in the context of radioactive waste disposal, the laboratory measurement of swelling pressure was generally carried out only in the axial direction (Saba et al., 2014a). In many cases, the swelling pressures in different directions were considered as the same.

Recently, some researchers attempted to determine the difference between the swelling pressures in different directions (Lee et al., 2001; 2012; Saba et al., 2014a; Jia et al., 2019). Lee et al. (2012) measured both the axial and radial swelling pressures of compacted Korean bentonite with a dry density of 1.5-1.7 Mg/m^3 and observed a significant difference between the axial and radial swelling pressures. Additionally, the higher the dry density, the larger the difference. This anisotropic swelling behaviour could be attributed to the fabrication process of

compacted block, in which bentonite powders were uniaxially compacted (Saba, 2013). As shown in Figure 1-16, the MX80 bentonite grains mostly had an irregular shape with one dimension at least 2.5 times larger than the thickness (Saba, 2013). When poured in the compaction mould, the grains would favour an anisotropic arrangement with a larger face side in the horizontal direction to find a stable position. Moreover, this anisotropy could be enhanced by the subsequent uniaxial static compaction (Saba, 2013). Upon hydration, the compacted bentonite exhibited a more significant swelling in the axial direction than that in the radial one.

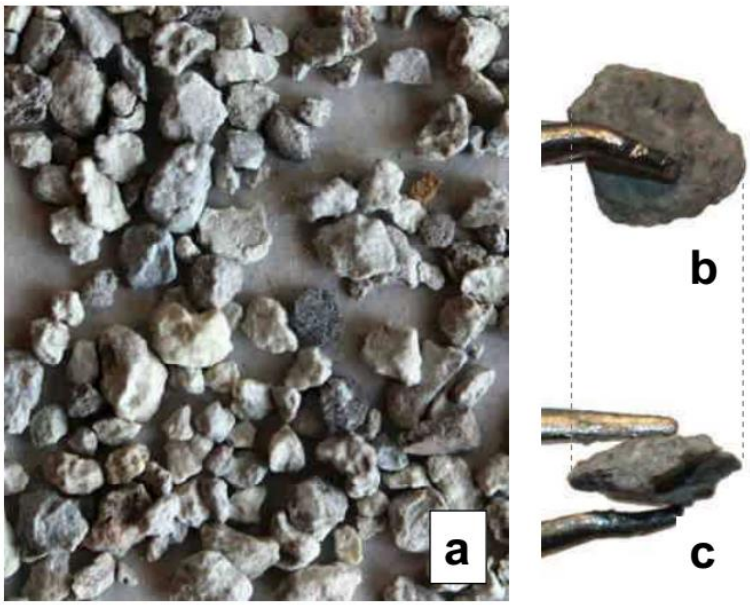

Figure 1-16. (a) MX80 bentonite grains. Zoom on a single bentonite grain rotated in two different directions. (b) Top view and (c) side view (after Saba, 2013).

To further characterise the anisotropic swelling bahviour, Saba et al. (2014a) defined an anisotropy coefficient as the ratio of radial to axial swelling pressures. For the compacted GMZ bentonite, Jia et al. (2019) found that the anisotropy coefficient decreased from 1.0 to 0.76 owing to the increasingly oriented arrangement of bentonite grains when the dry density increased from 1.46 to 1.71 Mg/m^3. Saba et al. (2014a) studied the axial and radial swelling pressures of compacted MX80 bentonite/sand mixture with a wide range of bentonite dry density. They indicated that the anisotropy coefficient was mainly related to the bentonite dry density: at low bentonite dry densities (lower than 1.16 Mg/m^3), the anisotropy coefficient increased with increasing bentonite dry density; at medium dry densities (from 1.16 to 1.3 Mg/m^3), the coefficient was near 1.0; at high bentonite dry densities (larger than 1.3 Mg/m^3), the anisotropy coefficient decreased with increasing bentonite dry density (Figure 1-17).

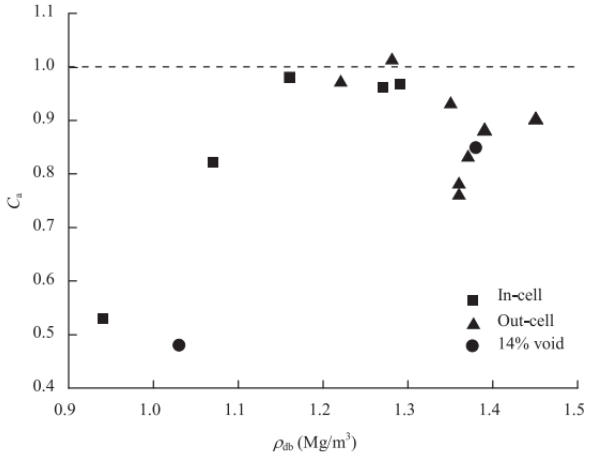

Figure 1-17. Variation of the anisotropy coefficient with bentonite dry density for MX80 bentonite/sand mixture (Saba et al., 2014a).

Using microfocus μCT, Saba et al. (2014b) found the concentrated macropores in the side part while investigating the microstructure of bentonite/sand mixture (a proportion of 70/30 in dry mass). Figure 1-18a shows a typical horizontal μCT cross section of the compacted bentonite/sand mixture specimen (the maximum grain size is 2 mm, the dry density is 1.8 Mg/m^3, the water content is 10% and the disk diameter is 50 mm). The image analysis and treatment were then carried out using ImageJ, allowing the porosity at different positons to be calculated. The variation of the macroporosity with respect to the radius of the ring selected is also shown in the Figure 1-18b. It appears that the macroporosity increased with the increasing radius. This phenomenon could be explained as follows. When poured in the compaction mould, many large grains would fall into the side part of the mould due to the gravitational effect. Consequently, more macro-pores could exist in the side part of specimens with the help of the friction with the mould wall (Saba et al., 2014b; Than et al., 2016).

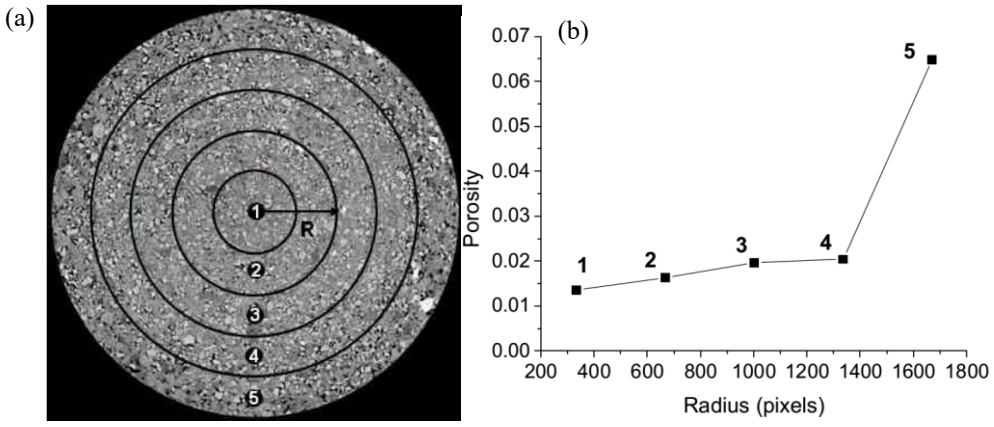

Figure 1-18. (a) μ-CT observations and (b) variation of the macro porosity with respect to the radius of the ring selected (after Saba et al., 2014b).

Based on the μCT results, Saba et al. (2014a) attributed the first increase of anisotropy coefficient to the swelling and splitting of bentonite upon hydration. They indicated that the swelling of bentonite grains could lead to microstructure collapse and thus reduce the initial anisotropy induced by uniaxial compaction. At very low dry densities, the bentonite grains swelled and split up, but they could not fill up the macro-pores in the side part. At medium bentonite dry densities, the microstructure collapse would eliminate the initial anisotropy, developing an isotropic microstructure. At high bentonite dry densities, the initial anisotropy would remain because the smaller macro-pore space prevented the microstructure collapse.

1.2.6 Effect of technological voids on swelling bahviour

In the deep underground radioactive waste repositories, sealing elements can be fabricated in different shapes, such as blocks, pellets or both (Andra, 2005). When the pre-compacted blocks are installed in the shifts and drafts, technological voids inevitably remain among the blocks, between the blocks and the canisters and between the blocks and the host rock (Villar et al., 2005; Villar and Lloret, 2008; Li et al., 2010; Wang et al., 2013a) (Figure 1-19). These technological voids are estimated at 6.6, 12 and 14% of the total volume of the galleries in the FEBEX mock-up test (Martin et al., 2006), PGZ2 in situ tests in the Underground Research Laboratory (URL) at Bure (Gatabin et al., 2016) and SEALEX in situ test (Wang et al., 2013a; Saba et al., 2014a), respectively. Upon the intrusion of groundwater from the host rock, the compacted blocks will swell and fill up the technological voids, closing the preferential pathways (Villar and Lloret, 2008). After that, their swelling will occur under constant-volume conditions. In the long term, they are expected to exhibit a swelling pressure high enough to limit the convergence of the galleries after the concrete lining failure (Cuisinier et al., 2008) and a hydraulic conductivity low enough to retard the water transfer-related phenomena (Castellanos et al., 2008).

A number of studies have been performed to investigate the hydration process of the compacted sealing materials with technological voids at both laboratory and field scales (Villar et al., 2005; Gens et al., 2011; Wang et al., 2013a; Saba et al., 2014b; 2014c; Mokni et al., 2016; Bian et al., 2019a; 2019b; 2020; Jia et al., 2019). It was found that the compacted sealing materials near the technological voids quickly swelled, filling up the technological voids, while those far from the technological voids swelled slowly. These processes led to a heterogeneous distribution of dry density, with a lower dry density in the external area and a larger dry density in the inner area.

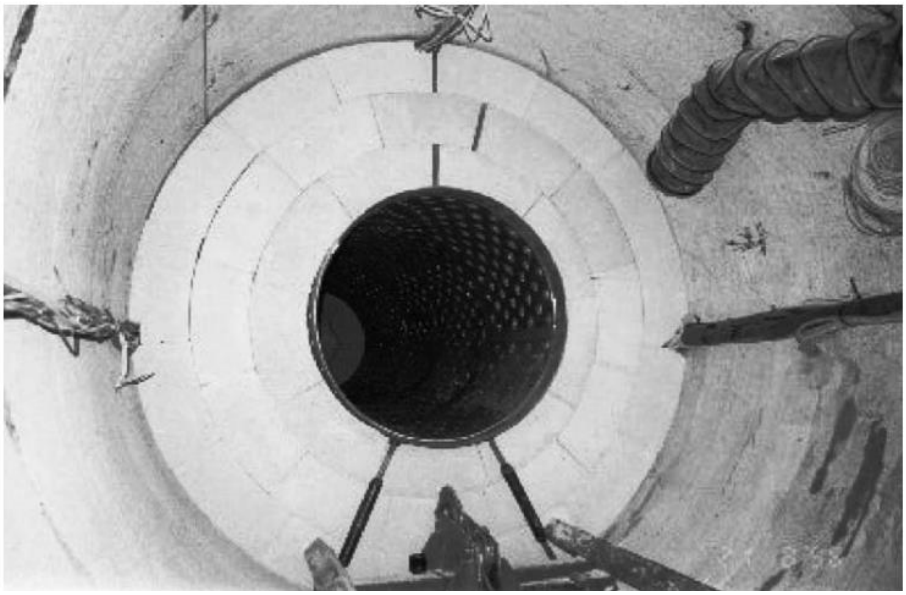

Figure 1-19. Geometry of Technological voids in the FEBEX Project (Villar et al., 2005).

To further understand the swelling process of compacted block with initial technological voids, Bian et al. (2019a) performed a series of infiltration tests on compacted MX80 bentonite with technological voids (above 11.3% to 11.6% of final specimen volume) at different times and the evolution of dry density distribution of compacted blocks was determined. The results are summarised in Figure 1-20. It could be observed that the dry density of soils corresponding to the initial technological voids increased with hydration time while that far from the technological voids decreased gradually. As a result, the dry density gradient would decrease and the bentonite approached a relatively homogeneous state. Bian et al. (2019a) divided the heterogeneous specimens into two zones according to the expected final dry density: a compression zone where the dry density was lower than the expected final value and a swelling zone at which the dry density was larger than the expected final value. They assumed that the swelling zone would undergo further swelling over time while the compression zone would be compressed by the swelling pressure of the swelling zone.

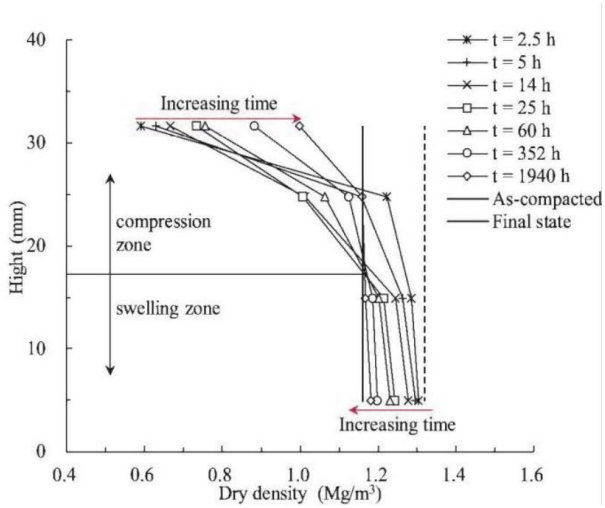

Figure 1-20. Variation of dry density distribution of the specimens with initial technological voids with respect to hydration time (Bian et al., 2019a).

Similar phenomenon was observed in large-scale testing in a tunnel (FEBEX test) by Gens et al. (2018) and Villar et al. (2019) when they compared the water content and dry density distributions of compacted bentonite blocks after 5- and 18-year hydrations (Figure 1-21). Interestingly, they found that the heterogeneous distribution of dry density of compacted bentonite was still persistent after 18 years, although it was reduced significantly.

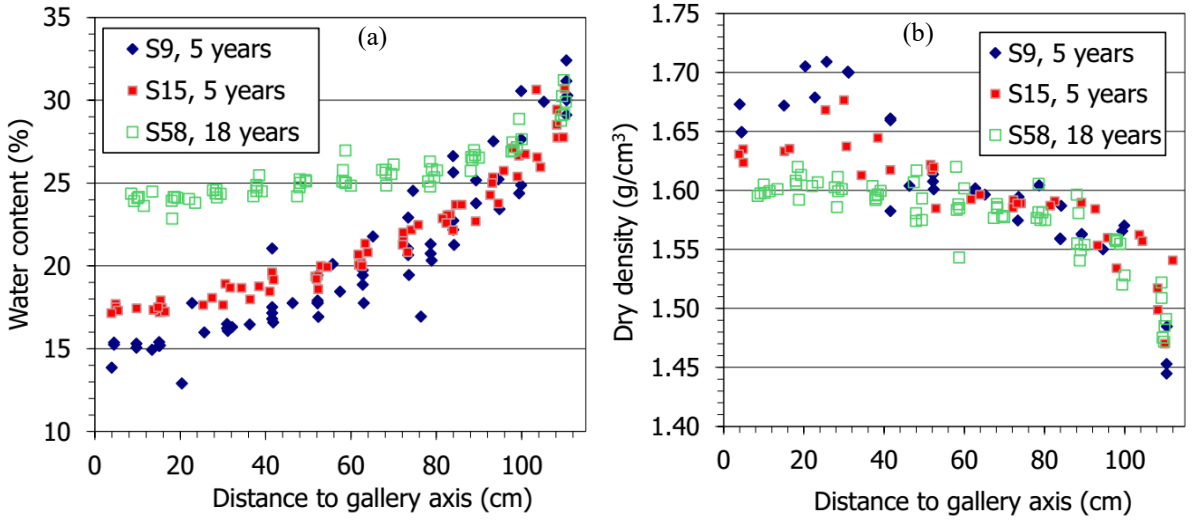

Figure 1-21. Comparison between the water content and dry density distributions of the bentonite barrier along the gallery axis after 5 and 18 years: (a) water content and (b) dry density (Villar et al., 2019).

Basically, the hydration process of compacted blocks is directly related to their microstructural changes (Wang et al., 2014; Bian et al., 2019a). Bian et al. (2019a) investigated the microstructural change of compacted bentonite with initial technological voids using MIP technique, alongside with the determination of dry density, water content and suction. They

found that the increase of global void ratio of bentonite after swelling was accompanied by a significant increase in inaccessible and medium pores, with a decrease in large pores. The change in microstructure was mainly due to the compression in large and medium-pores and due to the progressive development of inter-particle porosity. By contrast, in the swelling zone, the global void ratio of bentonite slightly increased due to a slight decrease of dry density, which could be represented by an increase in large pores. Over time, as the suction decreased to about 14 MPa (suction higher than 9 MPa), the soil swelling was mainly due to the significant increase in the inaccessible pores; as the suction further reduced to about 3 MPa (suction lower than 9 MPa), the soil swelling mainly resulted from a significant increase in medium pores. Note, however, that their work was limited to the microstructural changes of compacted bentonite during the saturation process only. After the full saturation of the compacted blocks, the water exchanges between intra-aggregate and inter-aggregate pores would continue, resulting in a decrease of inter-aggregate porosity and in an increase of very thin porosity due to more water infiltration into the interlayer space inside the aggregates (Delage et al., 2006; Ye et al., 2013; Wang et al., 2014).

The effect of technological voids on the swelling pressure of compacted sealing/backfill materials has been widely investigated (Villar et al., 2005; Gen et al., 2011; Wang et al., 2013a; Saba et al., 2014a; 2014b; Bian et al., 2019a; Jia et al., 2019; Watanabe and Yokoyama, 2021). For the compacted bentonite/sand mixtures with 14% initial technological voids, Wang et al. (2013a) and Saba et al. (2013) found that the swelling pressure of compacted MX80 bentonite/sand mixture (proportion of 70/30 in dry mass) was mainly governed by the expected final dry density, irrespective of the heterogeneity (Figure 1-22).

As far as the effect swelling anisotropy was concerned, Saba et al. (2014a) suggested that 14% radial technological voids had a negligible effect on the anisotropy coefficient. Jia et al. (2019) performed several swelling pressure tests on compacted GMZ bentonite with 13.3-26.7% axial voids. They found that an axial void of more than 16.7% could induce a lower axial swelling pressure without significant change of radial swelling pressure, resulting in an anisotropy coefficient higher than that without voids even though the global dry density was the same.

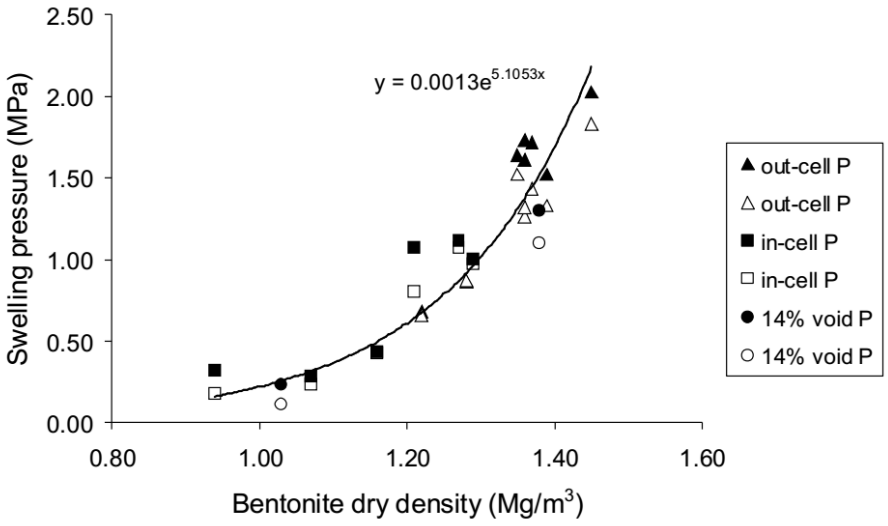

Figure 1-22. Variation of swelling pressures with bentonite dry density under different test conditions (Saba, 2013).

1.2.7 Effect of water chemistry on swelling behaviour

In the underground radioactive waste disposal repositories, the pore water in the surrounding rock generally has a certain salinity (Deng et al., 2011; Nguyen et al., 2013; Wang et al., 2014). After the galleries are closed, the pore water will infiltrate into the galleries and interact with the sealing materials. Additionally, the concrete lining will degrade and produce alkaline solution (Sun et al., 2018; Chen et al., 2019). Therefore, it is important to evaluate the impact of water chemistry on the hydro-mechanical properties of the sealing materials.

1.2.7.1 Effect of saline solution

The influence of saline solution on the swelling behaviour of bentonite has been largely reported in the previous studies (Rao and Shivananda, 2005; Karnland et al., 2006; Rao et al., 2006; Castellanos et al., 2008; Komine et al., 2009; Zhu et al., 2013; Ye et al., 2014a; Chen et al., 2018). Castellanos et al. (2008) performed a series of swelling deformation tests on the compacted FEBEX bentonite (initial dry density of 1.65 Mg/m^3) under different vertical stresses. They found that the final swelling strain decreased significantly as the salt concentration increased (Figure 1-23).

Komine et al. (2009) compared the swelling pressures of several reference bentonites (Kunigel-V1, Volclay, Kunibond, Neokunibond and MX80 bentonites) hydrated with synthetic seawater and deionised water. A significantly lower swelling pressure was observed on the specimens hydrated with synthetic seawater compared to that hydrated with

deionised water. Zhu et al. (2013) and Chen et al. (2018) investigated the influence of cation type on the swelling pressure of GMZ bentonite at a dry density 1.7 Mg/m^3 using constant-volume method and observed a more significant decrease of swelling pressure for the specimens hydrated with NaCl solution compared to that hydrated with $CaCl_2$ solution at a same concentration (Figure 1-24).

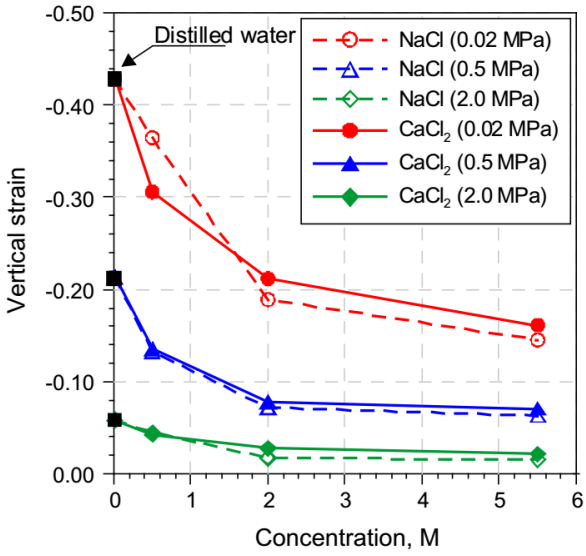

Figure 1-23. Final swelling strains of compacted FEBEX bentonite at dry density of 1.65 Mg/m^3 under different vertical stresses (Castellanos et al., 2008).

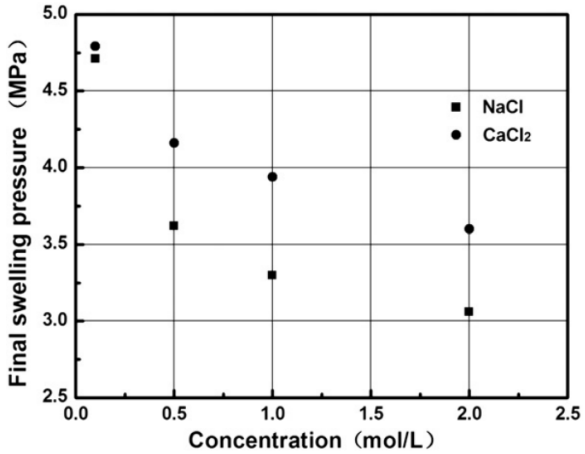

Figure 1-24. Final swelling pressure of GMZ bentonite compacted at a dry density of 1.7 Mg/m^3 and wetted under constant-volume conditions with different solutions (Zhu et al., 2013).

As mentioned above, the hydration of bentonite-based materials includes crystalline and osmotic swelling processes. It was reported that the cations in the pore water might significantly affect the chemical compositions of clays through cation exchanges (Yukselen-Aksoy et al., 2008) and influence the crystalline swelling process (Wang et al., 2014).

Commonly, the ease of a cation of one type to replace a cation of another type depends on the valence, proportion of different cation types, and the cation size. Given that other factors are the same, the higher the valence of the cation, the higher the replacing power. A typical replaceability order is: $Na^+<K^+<Mg^{2+}<Ca^{2+}$ (Mitchell, 1993; Mata, 2003; Wang et al., 2014). According to this order, for Febex, Kunigel-V1, Volclay, Neokunibond, MX80, and GMZ bentonites (Table 1-1), they would change from sodium (Na-) to other types (i.e. K-, Mg- or Ca-) after interaction with the cations in permeating solution. When the GMZ bentonite was hydrated with $CaCl_2$ solution, it could be transformed into Ca-bentonite. Zhu et al. (2013) assumed that the interlayer space of the Ca-bentonite would be larger that of the Na-bentonite when only two water layers were sandwiched between clay layers for both Na- and Ca- bentonites at a dry high density of 1.7 Mg/m^3. Thus, a larger swelling pressure was observed on the specimens hydrated with $CaCl_2$ solution (Figure 1-24). Additionally, the cations in the pore water can also influence the thickness of diffuse double layer during the osmotic swelling process (Siddiqua et al., 2011; Castellanos et al., 2008; Zhu et al., 2013). The thickness of the diffuse double layer is associated with the swelling strain of the bentonite-based materials (Komine and Ogata, 2003; 2004). Additionally, the thickness of diffuse double layer is related to the difference between the net inter-particle repulsive stress and the attractive stress, which directly represents the swelling pressure (Barbour and Fredlund, 1989; Mitchell, 1993; Ye et al., 2014a). In general, as the concentration of the saline solution increased, the thickness of the diffuse double layer and the net repulsive stress decreased (Yong and Warkentin, 1975; Mitchell, 1976; Tripathy et al., 2004) and lower swelling strain and swelling pressure could be expected.

Table 1-1. Main physical properties of common bentonites.

Bentonite	Specific surface area (m^2/g)	Total cation exchange capacity (meq/100 g)	Na^+ (meq/100 g)	K^+ (meq/100 g)	Mg^{2+} (meq/100 g)	Ca^{2+} (meq/100 g)
Febex[a]	725	96-102	24-27	2-3	31-32	35-42
Kunigel-V1[b]	-	48	40.5	0.9	2.0	58.7
Volclay[b]	-	69	56.6	1.6	13.2	29.3
Kunibond[b]	-	80	11.9	1.9	8.2	58.5
Neokunibond[b]	-	76	62.0	1.9	6.3	33.3
MX80[c]	-	80	67.0	1.0	8.0	8.0
GMZ[d]	570	77.3	43	2.5	12	29
Foca7	454	69	2.6	-	-	62.9

[a]: Castellanos et al. (2008); [b]: Komine et al. (2009); [c]: Karnland et al. (2006); [d]: Ye et al. (2012)

1.2.7.2 Effect of alkaline solution

In the deep underground disposal repositories, cement is used to construct the concrete

lining. The cement (Ordinary Portland Cement) will degrade during the long-term operation of the repositories and generate alkaline solution. According to the hydration of Ordinary Portland cement and the degradation characteristic of concrete, the chemical environment of groundwater during concrete degradation includes three stages (e.g. Berner, 1992; Glasser and Atkins, 1994; Faucon et al., 1998; Sánchez et al., 2006). At the initial stage, the pH of the leached pore water may rise above 13 at 25 ℃ due to the release of Na-K-OH into the fresh cement pore water. Afterwards, the hydroxides are eliminated. At second stage, the pH (equal to 12–12.5 at 25 ℃) is controlled by the dissolution of portlandite and the main characteristic composition of cement water is Ca^{2+}. At the third stage, the cement degradation produces the mineral of silicates and aluminates such as C-(A)-S-H with a pH below 12 (Savage et al., 2002; Karnland et al., 2007; Wang, 2009; Heikola et al., 2013).

In the past decades, the influence of alkaline solution on the swelling behaviour of bentonite-based materials was studied by several researchers (Karnland et al., 2007; Herbert et al., 2008; Lee et al., 2012; Ye et al., 2014b; Chen et al., 2016b, 2019; Sun et al., 2018, 2019b, 2020; Liu et al. 2020a). Chen et al. (2016b) studied the influence of NaOH solution on the swelling pressure of compacted GMZ bentonite. They found that the final swelling pressure of GMZ bentonite decreased significantly with the increase of NaOH solution concentration (Figure 1-25).

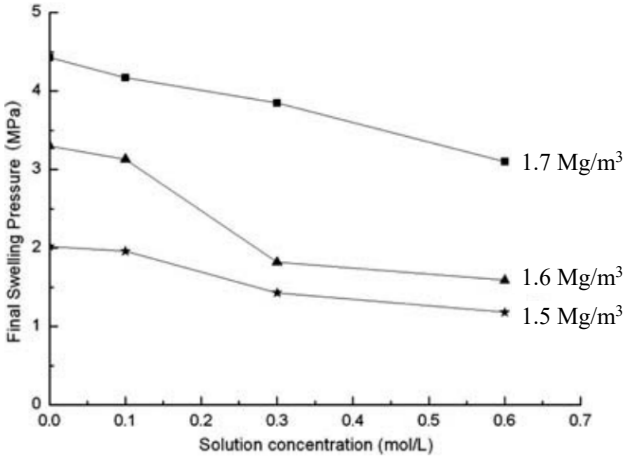

Figure 1-25. Variation of the final swelling pressure with alkaline concentration of specimens with different dry densities (Chen et al., 2016b).

Karnland et al. (2007) performed constant-volume swelling pressure tests on compacted Wyoming MX80 bentonite (dry density of 1.57 Mg/m^3) hydrated with 0.1, 0.3 and 1.0 M NaOH, and saturated $Ca(OH)_2$ solutions. The results show that 0.3 M (pH=13.3) and 1.0 M (pH=13.8) NaOH solutions significantly reduced the swelling pressure of the bentonite

while 0.1 M NaOH (pH=12.9) and saturated $Ca(OH)_2$ solutions (pH=12.4) did not significantly change the swelling pressure of compacted MX80 bentonite. Fernández et al. (2006) studied the influence of saturated $Ca(OH)_2$ solution on the mineralogy of La Serrata bentonite. They found that saturated $Ca(OH)_2$ solution had a negligible influence on the mineralogy of compacted La Serrata bentonite at 25–60 ℃ over a period of 1 year except for the cation exchange. Sun et al. (2018; 2019b) investigated the swelling pressures ofn GMZ bentonite specimens (dry densities of 1.50 and 1.7 Mg/m^3) hydrated with Beishan site water (pH=8.5), Young Concrete Water (pH=13) and Evolved Concrete Water (pH=12) for about 60 days. As shown in Figure 1-26, a remarkably lower swelling pressure was observed on specimens hydrated with Young Concrete Water. To further understand the mechanism, X-Ray diffractometry (XRD), MIP and scanning electron microscope tests were carried out on the specimens before and after hydration. The results demonstrate the dissolution of montmorillonite and the formation of some zeolites and calcium hydrated silicates in the GMZ bentonite upon saturation with alkaline solutions. On the whole, the montmorillonite content decreased linearly as the pH increased (Figure 1-27). Additionally, the generated secondary minerals on the surface of montmorillonite could lead to the clogging of inter-aggregate pores (Sun et al., 2019b).

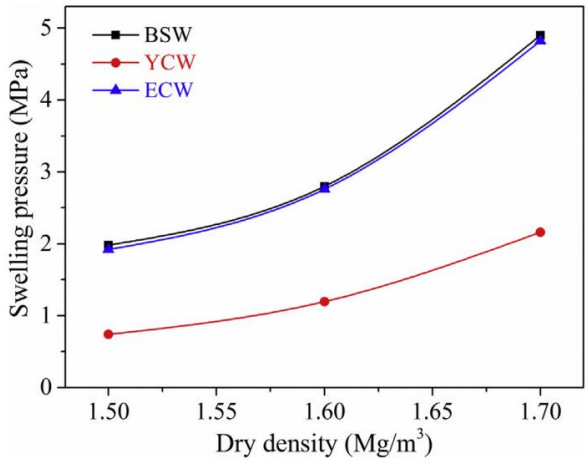

Figure 1-26. Variation of final swelling pressure with initial dry density of GMZ bentonite saturated with synthetic Beishan Site Water (BSW), Young Cement Water (YCW) and Evolved Cement Water (ECW) (Sun et al., 2018).

Note that the influence of alkaline solution on the swelling pressure is dependent on the specimen dry density and temperature (Ye et al., 2014b; Chen et al., 2019). Generally, the higher the temperature, the more significant the decrease of swelling pressure (Figure 1-28). The results of XRD tests indicate that the increase of temperature could accelerate the

dissolution of montmorillonite (Figure 1-29) and the formation of secondary minerals in GMZ01 bentonite saturated with alkaline solutions.

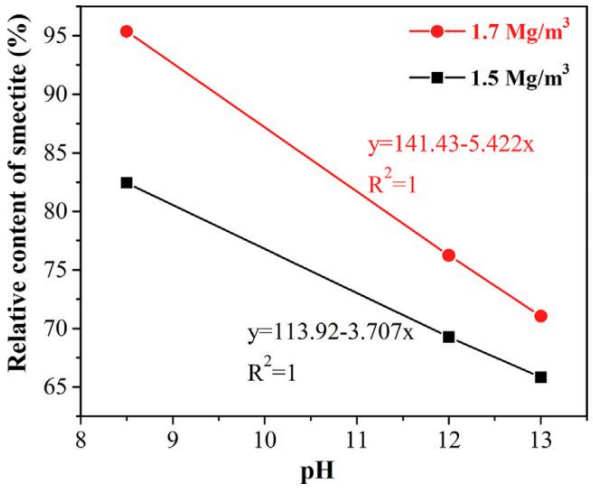

Figure 1-27. Variation of dissolved montmorillonite with pH of GMZ bentonite (Sun et al., 2019b).

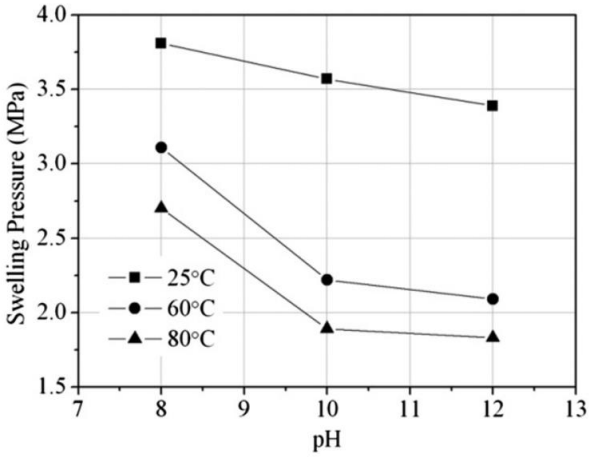

Figure 1-28. Variation of swelling pressure with pH value of GMZ bentonite at various temperatures (Ye et al., 2014b).

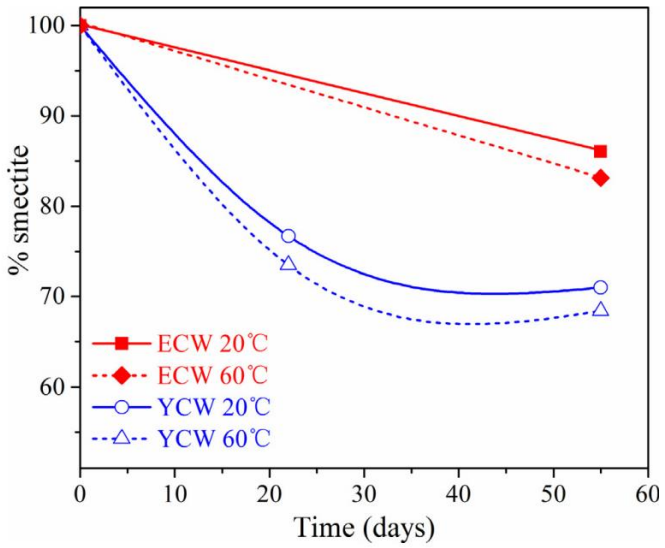

Figure 1-29. Variation of dissolved montmorillonite with pH of GMZ bentonite at various temperatures (Chen et al., 2019).

1.3 Water transfer in bentonite-based materials

In many cases, the bentonite-based materials are compacted in blocks at hygroscopic water content (Seiphoori et al., 2014; Chen et al., 2016c) and then placed in the drifts and shafts. When the local groundwater conditions are progressively recovered, the compacted bentonite-based materials in contact with the host rock are first hydrated by the pore water of the host rock. Afterwards, the water will infiltrate through the material pores and hydrate the inner part of the compacted blocks. In that case, water transfer in compacted bentonite-based materials occurs in both vapour and liquid phases (Börgesson et al., 2001; Kröhn, 2003). After the full saturation of the blocks, water transfer occurs in liquid phase and advective phenomena becomes dominant. Considering the complexity of the water flow through the sealing elements, a good understanding of the water transfer property of the compacted bentonite-based materials is essential for the assessment of the performance of the repository system.

In this section, firstly, the experimental evidence of the water transfer processes through compacted bentonite-based materials is presented and the water transfer mechanisms and the modelling approaches in both the unsaturated and saturated states are described. Then, the effects of technological voids and water chemistry on the water transfer processes are discussed.

1.3.1 Water transfer in unsaturated bentonite-based materials

When placed in the gallery, the compacted bentonite-based materials are initially unsaturated at very high suctions. The unsaturated hydraulic parameter (hydraulic diffusivity or

conductivity) is an important factor to be accounted for in addition to the saturated hydraulic parameter.

Compared to the saturated hydraulic parameter, the unsaturated one is difficult to be directly measured from a steady-state test since the water content changes when water is transported through the soils (Börgesson et al., 2001). Very often, the instantaneous profile method is used for this purpose by carrying out infiltration tests in columns. Kanno et al. (1999), Kröhn (2003), Börgesson et al. (2001) and Zhang et al. (2014) performed infiltration tests on compacted pure bentonite or bentonite/sand mixture. At different times, the specimens were extracted and sliced for the determination of water contents at different locations. To improve the accuracy, Daniel (1982), Lemaire et al. (2004), Cui et al. (2008), Ye et al. (2009) and Wang et al. (2013b) continuously measured the water content or suction profiles of soil columns upon wetting using either dual-energy γ radiation technique or relative humidity sensors installed at various locations. According to the suction and water content profiles, the unsaturated hydraulic conductivity was determined based on the Darcy's law. Cui et al. (2008), Ye et al. (2009), Wang et al. (2013b) and Liu et al. (2020b) found that the hydraulic conductivity decreased, followed by a rapid increase, and then approached the saturated hydraulic conductivity (Figure 1-30).

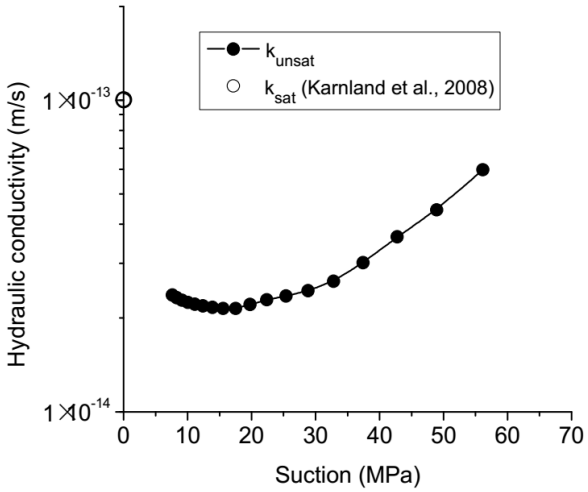

Figure 1-30. Variation of hydraulic conductivity with suction decrease (Wang et al., 2013b).

Commonly, the hydration of compacted bentonite-based materials was accompanied by microstructure changes. As shown in Figure 1-8, the large pores were progressively clogged by the exfoliated clay particles at the beginning of hydration; contrastingly, while saturation was approached, large-pore volume increased again due to the formation of 2-D pores by the division of clay aggregates due to swelling. While relating the large-pore changes to the hydraulic conductivity changes, Wang et al. (2013b) suggested that the hydraulic conductivity

changed following the same trend as the large-pore quantity during water hydration and the water transfer was primarily governed by the network of macro-pores in the full suction range. However, in their analyses, the apparent hydraulic conductivity was considered and the portions of water flow in liquid and vapour phases were not distinguished.

In the past decades, the contribution of vapour and liquid water flux to the global water transfer has been addressed by several researchers. Kröhn et al. (2003) and (2019) assumed that bentonite was exclusively hydrated by vapour diffusion in the pore space and proposed a constant diffusion coefficient to characterise the water infiltration process. However, the calculated value of diffusion coefficient was found to be lower than the experimental one, suggesting that the contribution of liquid water flow could not be ignored. Additionally, the water diffusivity for both the vapour and liquid could vary with water content. To address this issue, Kanno et al. (1999), Börgesson et al. (2001) and Zhang et al. (2014) empirically divided the total water diffusivity into vapour and liquid water diffusivities by assuming that the vapour and liquid phases contributed equally to the minimum value of the observed water diffusivity. Börgesson et al. (2001) and Zhang et al. (2014) suggested that the water diffusivity could be well described as a function of water content using Eq. (1-1):

$$D_{total}=D_l(w)+D_v(w)=\frac{a_1(w-w_s)}{(w-b_1)(b_1-w_s)}+\frac{a_2 w}{b_2(w-b_2)} \quad (1\text{-}1)$$

where D_{total} is the total diffusivity (m^2/s); $D_v(w)$ is the vapor diffusivity (m^2/s); $D_l(w)$ is the liquid diffusivity(m^2/s); w is the water content; w_s is the saturated volumetric water content; a_1, a_2, b_1 and b_2 are the fitting parameters. Taking the compacted GMZ bentonite/sand mixture (a proportion of 70/30 in dry mass) with a dry density of 1.70 Mg/m^3 as an example, the water diffusivity depended on water content, expressed as a U-shaped curve (Figure 1-31). As the water content increased from 12% to 27%, the vapor diffusivity decreased from 1.06×10^{-9} to 5.99×10^{-12} m^2/s, while the liquid water diffusivity increased from 3.96×10^{-11} to 2.32×10^{-9} m^2/s.

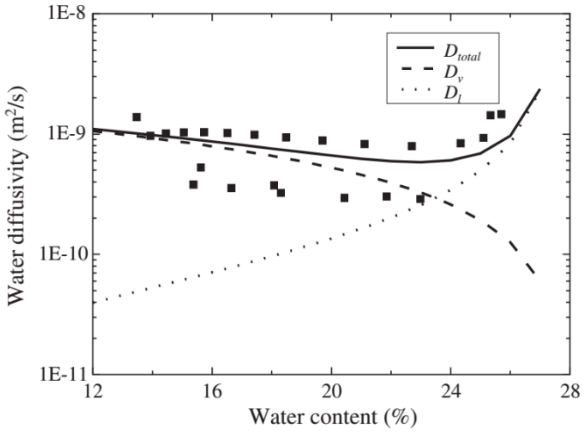

Figure 1-31. Separating water diffusivity of GMZ bentonite/sand mixture (a proportion of 70/30 in dry mass) with a dry density of 1.70 Mg/m^3 according to Eq. (1-1) (Zhang et al., 2014).

1.3.2 Water transfer in saturated bentonite-based materials

The saturated hydraulic conductivity is generally experimentally measured by monitoring the water inlet and/or outlet flows at constant or falling water head (Cui et al., 2008; Deng et al., 2011). Sometimes, it can also be indirectly determined from the consolidation curve based on the Terzaghi's consolidation theory (Terzaghi, 1943).

During the past decades, the saturated hydraulic conductivity was largely studied for different bentonite/sand mixtures (Kenney et al., 1992; Sivapullaiah et al., 2000; Komine et al., 2004; Wang et al., 2013a; Xu et al., 2016). It was found that the hydraulic conductivity of such mixtures increased with the decreasing bentonite fraction, in particular in the range of low bentonite fractions (Abichou et al., 2004). As the void space surrounded by sand grains was lower than the free-swell of bentonite, the void space was completely filled by bentonite. In that case, the hydraulic conductivity was dominated by the bentonite matrix (Komine et al., 2004; Wang et al., 2013a). In contrast, as the void space was larger than the free-swell of bentonite, the swollen bentonite could not fully occupy the void space. In that case, the hydraulic conductivity was influenced by the inter-sand structure (Shi and Yin, 2018).

Apart from the experimental measurement, some empirical, analytical and theoretical models were also developed to estimate the hydraulic conductivity of bentonite/sand mixtures. Commonly, the empirical models were established by fitting the measured hydraulic conductivity with the bentonite fraction and void ratio of the mixtures (Sivapullaiah et al., 2000; Xu et al., 2016). However, these empirical models were developed based on limited

data for some particular types of bentonites and the applicability of these empirical models to other bentonites needs further evaluation.

Some researchers proposed analytical models based on the intrinsic properties of sand and bentonite (Mollins et al., 1996; Komine et al., 2004). In their analyses, the bentonite/sand mixture was assumed to be an ideal mixture in which the hydrated bentonite was uniformly distributed forming a matrix, while the sand grains constituted impervious inclusion. Based on this assumption, the local variables in the mixture, such as the bentonite void ratio (Wang et al., 2013a) and swelling volumetric strain of montmorillonite (Komine et al., 2004) were defined. As shown Figure 1-32, the relationships between the overall hydraulic conductivity and the state variables of the pure MX80 bentonite and MX80 bentonite/sand mixture could be well described using a straight line. This allows the determination of hydraulic conductivity of bentonite-based materials using the correlations, if the bentonite proportion and the final dry density are known.

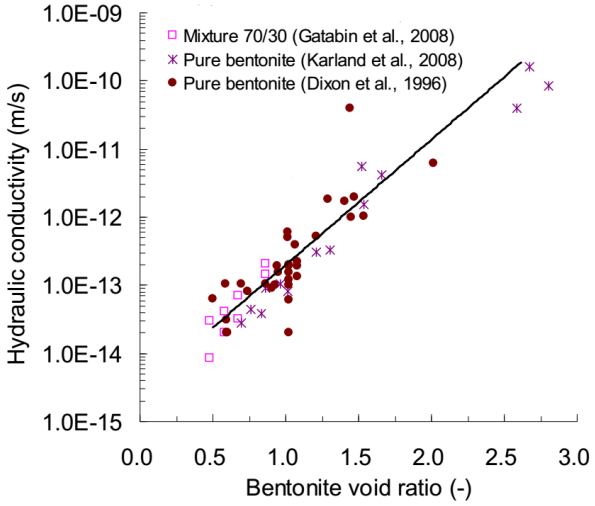

Figure 1-32. Relationship between hydraulic conductivity and bentonite void ratio (modified after Wang et al., 2013a).

Basically, the hydraulic conductivity is strongly related to the pore structure of soils. In the past decades, several theoretical models were also developed to characterise the saturated hydraulic conductivity. Taking the channels of water flow through a cross section as uniform tubes, Kozeny (1927) proposed a theoretical model known as Kozeny-Carman equation, which was further improved by Carman (1956):

$$k=C_F \frac{1}{S_s^2}\frac{\rho_w g}{\mu \rho_s^2}\frac{e^3}{1+e} \tag{1-2}$$

where k is the hydraulic conductivity; C_F is a dimensionless shape constant; S_s is the specific

surface area; ρ_w and μ are the density and viscosity of water, respectively; g is the gravitational acceleration. Its performance was validated for sand (Ren et al., 2016). For bentonite-based materials, which are generally characterized by an aggregated structure, pores can vary from very fine (intra-aggregate) to very coarse (inter-aggregate) (Wang et al., 2013a). The pore size distribution is a crucial factor to be accounted for. Based on the Poiseuille's equation for laminar flow through a cylindrical capillary, a capillary model was developed by Garcia-Bengochea et al. (1979) assuming parallel and cylindrical nonintersecting pores with different diameters:

$$k = \frac{\rho_w g n}{32\mu} \sum_{i=1}^{m} d_i^2 f(d_i) \tag{1-3}$$

where n is the porosity of soil; m is the total number of pore intervals; i is the counter from 1 to m; d_i and $f(d_i)$ are the pore diameter and volumetric probability corresponding to i, respectively. In addition to the pore size distribution, the pore interconnection between soil sections could also influence the water flow. Childs and Collis-George (1950) and Marshall (1958) introduced a probabilistic approach to address this issue. Figure 1-33a shows the water flow path through a capillary network in a soil fabric with two in-series sections having the same porosity n for a given length.

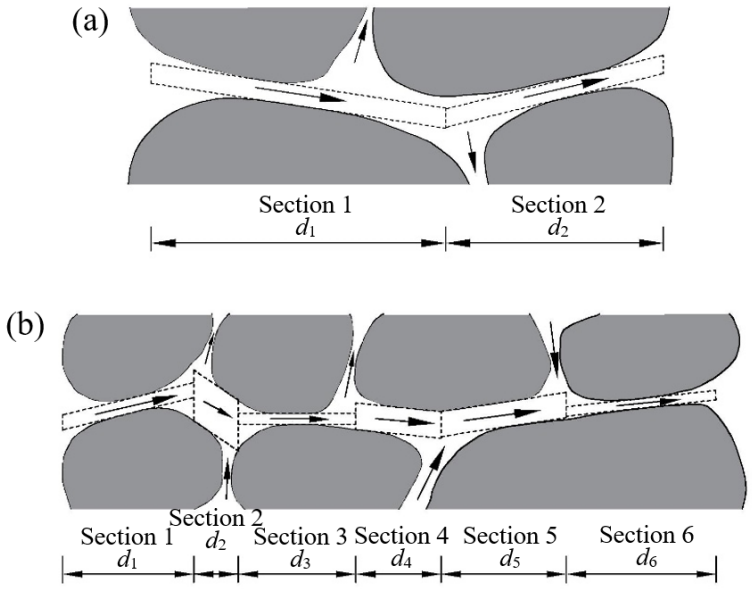

Figure 1-33. Typical water flow paths in soils consisting of (a) two sections and (b) six sections (modified after Watabe et al., 2006). Note: the grey areas represent the solid particle and the arrows indicate the water flow paths.

The probability that a pore of diameter d_1 from one section joins a pore of diameter d_2 of another section is $[nf(d_1)][nf(d_2)]$. According to the basic idea of Poiseuille's equation, the smallest capillary between two capillaries in series governs the water flow through the

capillaries (e.g. d_1 from a series of d_1 and d_2 in Figure 1-33a) (Watabe et al. 2006). Correspondingly, Garcia-Bengochea et al. (1979) derived the following equation (known as the Marshall Model) for hydraulic conductivity:

$$k=\frac{\rho_w g n^2}{32\mu}\sum_{i_1=1}^{m}\sum_{i_2=1}^{m}\bar{d}^2 f(d_{i_1})f(d_{i_2}) \tag{1-4}$$

where i_1 and i_2 are the counters from 1 to m; d_{i_1} and d_{i_2} are the pore diameters corresponding to i_1 and i_2, respectively; $\bar{d}$ is the smaller one of d_{i_1} and d_{i_2}; $f(d_{i_1})$ and $f(d_{i_2})$ are the volumetric probabilities of occurrence of pores with diameters d_{i_1} and d_{i_2}, respectively. When a more complex soil fabric is considered, the water flow path through a capillary network in the soil fabric is schematically shown in Figure 1-33b. The probability that a pore of diameter d_{i_1} from one section joins other pores of diameters $d_{i_2}, d_{i_3}, \cdots, d_{i_{N_p}}$ from other sections is $[nf(d_{i_1})][nf(d_{i_2})]\cdots\left[nf(d_{i_{N_p}})\right]$ (e.g. $[nf(d_1)][nf(d_2)][nf(d_3)][nf(d_4)][nf(d_5)][nf(d_6)]$ in Figure 1-33b) and the diameter of the dominant flow channel $\bar{d}$ is the smallest one of $d_{i_1}, d_{i_2}, \cdots, d_{i_{N_p}}$ (e.g. d_6 from a series of d_1, d_2, d_3, d_4, d_5 and d_6 in Figure 1-33b). N_p refers to the number of in-series pores in different sizes along a capillary water path for a given length. Under this circumstance, a general capillary model was proposed by Watabe et al. (2006; 2011):

$$k=\frac{\rho_w g n^{N_p}}{32\mu}\sum_{i_1=1}^{m}\sum_{i_2=1}^{m}\cdots\sum_{i_{N_p}=1}^{m}\bar{d}^2 f(d_{i_1})f(d_{i_2})\cdots f\left(d_{i_{N_p}}\right) \tag{1-5}$$

where $i_1, i_2, \cdots, i_{N_p}$ are the counters from 1 to m. The capillary and Marshall models correspond to Eq. (1-5) when N_p=1 and N_p=2, respectively. As a first attempt, Watabe et al. (2011) applied the general capillary model to the hydraulic conductivity prediction for glacial tills, sandy soils and clayey soils. They found that the N_p values which gave the best prediction for Québec glacial tills, sandy soils, clayey soils were 3, 4, and 5, respectively. Unfortunately, the best N_p values for predicting the hydraulic conductivity of bentonite-based materials were rarely investigated. This limits the application of such model.

1.3.3 Effect of technological voids on the water transfer

As mentioned earlier, the technological voids between the compacted blocks and the host rock or the canisters, and among the blocks bricks themselves are unavoidable during the emplacement of blocks (Villar et al., 2005; Villar and Lloret, 2008; Li et al., 2010; Wang et al., 2013a). When the underground radioactive waste repositories are closed, the groundwater will

be recovered and infiltrate into these technological voids (Chen et al., 2016c). When the compacted blocks are hydrated with the water in the technological voids, the compacted blocks will swell and fill up the technological voids. However, the part including initial technological voids will exhibit a lower dry density (Bian et al., 2019a) and the sealing elements will be heterogeneous over long time (Chen et al., 2014). The part with initial technological voids will act as a possible preferential flow pathway and facilitate water transfer through the sealing elements.

Wang et al. (2013a) performed a series of hydration tests the compacted MX80 bentonite/sand mixtures (proportion of 70/30 in dry mass) with 14% technological voids using oedometer cell. Radial technological voids were created between the specimens and cell wall. The hydraulic conductivity of specimens after about 40-h water hydration was then using the constant-head and the Casagrande's methods. As shown in Figure 1-34, the results are compared with constant-head permeability measurements by Gatabin et al. (2008) on homogeneous specimens at similar densities. It appears that the specimens with initial technological voids exhibited a hydraulic conductivity of one order of magnitude larger than those without voids after about 40-h water hydration. This phenomenon demonstrated the detrimental influence of the looser zone (initial technological voids) around the specimens.

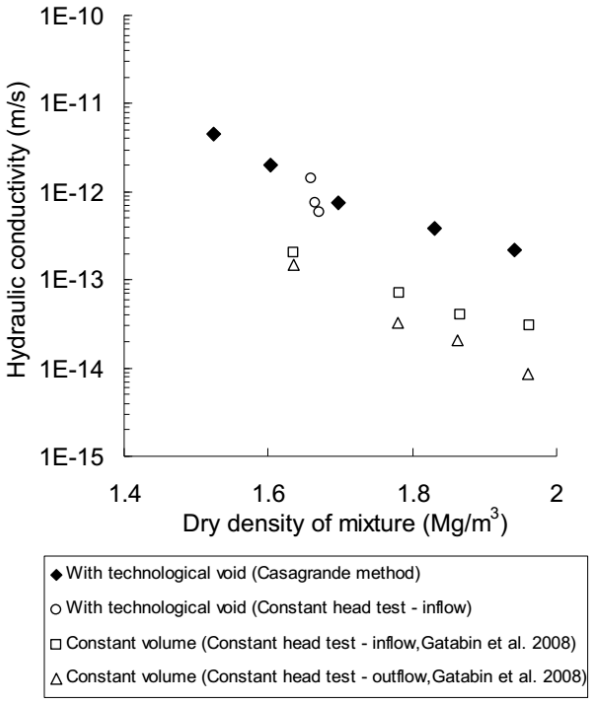

Figure 1-34. Hydraulic conductivities of compacted bentonite/sand mixture with and without technological voids (Wang et al. 2013a).

Furthermore, in the case of high water pressure, these discontinuities due to the presence of initial technological voids increase the risk of hydraulic fracturing (Gens et al., 2002; Marcial et al., 2006; Buzzi et al., 2008; Chen et al., 2014). Chen et al. (2014) examined the hydraulic fracturing behaviour of the interface between compacted MX80 bentonite and natural Boom Clay (host rock) with different initial gaps. The rate of water injection was fixed at 1 mm^3/s. The water injection pressure increased at the beginning of injection (Figure 1-35a). When water pressure reached the hydraulic resistance of the interface, hydraulic fracturing would take place and form a preferential channel for water flow. Meanwhile, the injected water pressure decreased drastically and the compacted bentonite continued to swell. A higher subsequent pressure was needed to produce a new hydraulic fracturing. Consequently, the hydraulic resistance became high enough so that no further fracturing occurred, suggesting that the technological gaps were sealed.

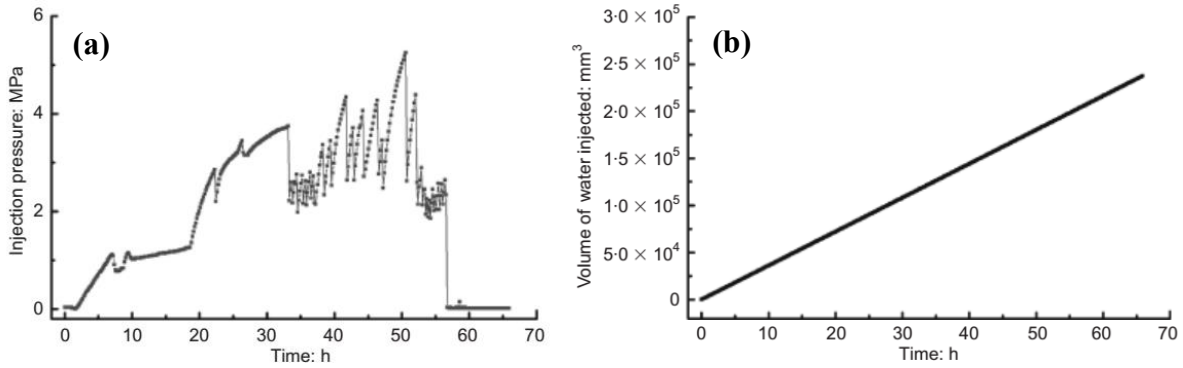

Figure 1-35. Changes in (a) injection pressure and (b) volume of water injected (Chen et al., 2014).

1.3.4 Effect of water chemistry on the water transfer

The hydraulic conductivity of compacted bentonite-based materials is associated with their pore structure. As mentioned above, the saline solution can change the montmorillonite type by cation exchange during the hydration and significantly decrease the thickness of diffuse double layer. Both of them can alter the size of the available channel for water flow (Olsen, 1962; Dunn, 1985; Pusch, 2001; Villar et al., 2006; Castellanos et al., 2008; Chen et al., 2015). Mesri and Olson (1971) observed a lower hydraulic conductivity for the montmorillonite saturated with a lower electrolyte concentration in the pore water. They suggested that the thicker diffuse double layer was associated with dilute solutions, leading to less available void space for water flow. According to the diffuse double layer theory, the thickness of diffuse double layer decreased as the concentration of saline solution in the pores increased (Yong and Warkentin, 1975; Zhu et al., 2013). At a given void ratio, a higher hydraulic conductivity could be expected for the

specimens with a higher cation concentration due to the poor development of diffuse double layers (Castellanos et al., 2008). Similarly, Karnland et al. (1992) found that the hydraulic conductivity of MX80 bentonite increased half an order of magnitude when the salinity of pore water increased from 0% to 3.5%. Zhu et al. (2014) studied the influence of cation types on hydraulic conductivity of GMZ01 bentonite (Figure 1-36). When the concentration of NaCl and $CaCl_2$ solutions increased from 0.1 to 2.0 M, the hydraulic conductivity of GMZ01 bentonite increased by 3.25 and 1.54 times, respectively. Moreover, at same concentrations, the hydraulic conductivity of GMZ01 bentonite infiltrated with NaCl solutions was higher than that infiltrated with $CaCl_2$ solutions. They attributed this phenomenon to the less significant swelling of the specimens saturated with NaCl solutions compared to those with $CaCl_2$ solutions. As a result, less clogging of macro-pores was expected for the specimens saturated with NaCl solutions and a relatively higher hydraulic conductivity was observed.

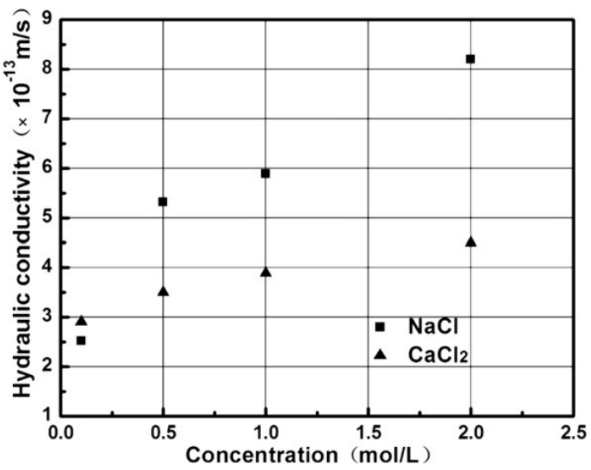

Figure 1-36. Influence of cation concentration on hydraulic conductivity of GMZ01 bentonite (Zhu et al., 2013).

When the bentonite-based materials are hydrated with alkaline solution, the montmorillonite can be dissolved and form secondary minerals, consequently influencing the hydraulic conductivity (Nakayama et al., 2004; Karnland et al., 2007; Cuisinier et al., 2008; Chen et al., 2016b). Ye et al. (2014b) investigated the influence of pH value of NaOH solutions on the hydraulic conductivity of GMZ bentonite at various temperatures. As shown in Figure 1-37, at a given temperature, the hydraulic conductivity increased as the pH value of NaOH solution increased due to the dissolution of montmorillonite in GMZ bentonite (Karnland et al., 2007; Yamaguchi et al., 2007). When the effective montmorillonite dry density decreased, the overall sizes of the pipelines between the soil particles increased, resulting in an increase in hydraulic conductivity. Furthermore, at the same pH value of NaOH solution, a larger hydraulic

conductivity was observed at a higher temperature. Ye et al. (2014b) attributed this phenomenon to the elevated viscosity of the permeating fluid (Bouazza et al., 2008) and the increasing effective cross-section area of pore space due to the more significant dissolution of montmorillonite (Cuisinier et al., 2008; Nakayama et al., 2004).

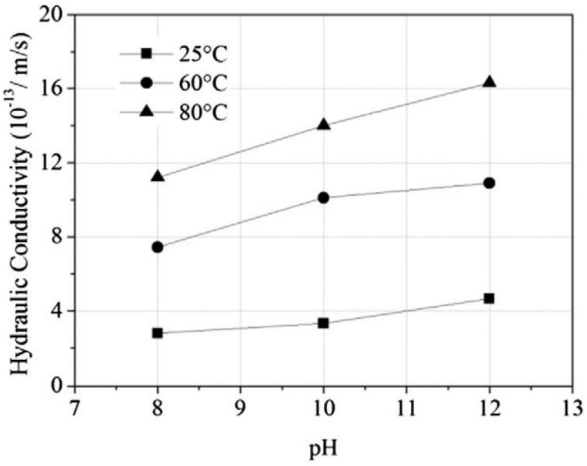

Figure 1-37. Influence of pH value of NaOH solutions on the hydraulic conductivity GMZ01 bentonite at different temperatures (Ye et al., 2014b).

1.4 Conclusions

This chapter firstly introduces the microstructure features and swelling mechanism of compacted bentonite-based materials upon hydration. Then, the swelling behaviour, swelling anisotropy and water transfer property in both unsaturated and saturated states are reviewed. The effects of technological voids and water chemistry on the hydro-mechanical behaviour of compacted bentonite-based materials are also presented. The following conclusions can be drawn:

Previous studies indicated that the claystone in the MX80 bentonite/claystone mixture at a proportion of 70/30 in dry mass acted as inert sand, making a negligible contribution to the global swelling pressure. For the bentonite/claystone mixture with a higher claystone fraction, the claystone can absorb water and swell. However, the swelling mechanism of bentonite/claystone mixtures with bentonite fractions lower than 70% has not been well understood. Furthermore, the permeability of claystone can be significantly higher than that of inert sand. In that case, the models which only consider the relationship between the hydraulic conductivity and bentonite properties in the mixture become no longer valid.

The aforementioned works allowed a good understanding of the effect of technological voids

on the anisotropic swelling behaviour of bentonite-based materials, but they were limited to the technological voids between the compacted blocks of bentonite-based materials and rigid boundaries. No studies have been reported on the effect of technological voids among compacted blocks, in particular the compacted blocks of bentonite/claystone mixture. Moreover, the mechanism of swelling behaviour of compacted blocks with axial/radial technological voids was not investigated.

Although the effects of technological voids on the heterogeneous dry density distribution of compacted blocks were identified in several studies, the final dry density distribution together with the swelling pressure and hydraulic conductivity of the compacted blocks with technological voids over long time have not been comprehensively studied.

Even though the effects of saline solution and alkaline solution on the hydro-mechanical behaviour of compacted bentonite or bentonite/sand mixtures have been widely reported, there is no systemtical study on the effect of complex groundwater of repository on the hydro-mechanical behaviour of compacted bentonite/claystone mixture.

The unsaturated hydraulic conductivity of compacted bentonite-based materials was shown to change with suction decrease. However, the portions of water flow in liquid and vapour phases were not well distinguished and the corresponding fundamental physics of vapour and liquid flows were not examined.

Chapter 2. Compaction and sealing properties

INTRODUCTION

The French concept of underground radioactive waste disposal in the COx claystone formation considers a mixture composed of excavated COx claystone and bentonite as a candidate sealing material to ensure the mineralogical and physico-chemical compatibility with the surrounding claystone. One of the possibilities is to pre-compact the bentonite/claystone mixture into blocks and then installed into shafts and drifts. After the repository closure, the main function of compacted blocks is to fill up the technological voids and limit the underground water fluxes. Afterwards, a swelling pressure is expected to develop against the surrounding claystone, confining the excavation damaged zone and reducing the water flow via this zone. To this end, it is necessary to investigate the compaction property of bentonite/claystone mixture for helping the fabrication process and the sealing property of the compacted mixture for helping the material suitability assessment.

A series of one-dimensional compaction tests were first performed on the MX80 bentonite/COx claystone mixtures with various bentonite fractions and water contents, to study the effects of bentonite fraction and water content on the compression and rebound indices and the needed demoulding pressure. Afterwards, constant-volume swelling pressures and hydraulic conductivities of the compacted blocks with different bentonite fractions, water contents and dry densities were experimentally determined to study the sealing performance of the mixtures. The results are presented in the form of a paper submitted to “Engineering Geology”.

By considering the interaction between bentonite and claystone during hydration, the claystone void ratio and volumetric fraction in the mixture were obtained. According to the relationship between the volumetric fraction and the stress applied by the swollen bentonite, the swelling pressure of claystone grains was indirectly determined. In parallel, the mean swelling pressure of claystone grain was estimated according to the relationship between the vertical swelling pressure and the void ratio of intact COx claystone. The estimated results were then compared with the indirectly determined one. This part corresponds to a paper submitted to “Acta Geotechnica”.

By comparing the claystone void ratio in the mixtures before and after hydration, an inhibition factor was proposed to describe the inhibition effect of bentonite on the swelling of claystone. Then, a method was proposed to predict the swelling pressure of the mixtures based on the relationship between the inhibition factor and bentonite fraction. Moreover, in light of binary structures of the mixtures with various bentonite fractions, an analytical method was proposed to predict the swelling pressure and hydraulic conductivity of bentonite/claystone mixtures. The results of this part are presented in two papers. The first one about the swelling pressure prediction was published in "Applied Clay Science"; the second one about the hydraulic conductivity prediction was published in "International Journal of Geomechanics". The articles are presented here in their original versions.

The pore structure of the specimens before and after hydration was also investigated using MIP. The total surface area of inter-particle pores was calculated assuming parallel and cylindrical pores, allowing the average the inter-particle distance to be obtained. Then, the relationship between the macroscopic swelling behaviour and inter-particle distance was determined. The results are presented in a paper submitted to Acta Geotechnica. In addition, the general capillary model considering N_p pores in series was applied to evaluate the hydraulic conductivities of bentonite/claystone mixtures together with those of other soils compiled from literature. The effect of plasticity index on the best N_p value was quantitatively determined, allowing an improved general capillary model to be proposed for the hydraulic conductivity estimation of different soils. These results correspond to a paper published in "Engineering Geology" and the article is presented here in its original version.

Zeng, Z.X., Cui, Y.J., Talandier, J. 2020. Submitted to Engineering Geology.

Compaction and sealing properties of bentonite/claystone mixture: Impacts of bentonite fraction, water content and dry density

Zhixiong Zeng[1], Yu-Jun Cui[1], Jean Talandier[2]

Abstract: Compacted block composed of 70% crushed Callovo-Oxfordian claystone and 30% MX80 bentonite has been proposed as a possible material for sealing a potential repository of radioactive waste. In this study, the compaction property of the bentonite/claystone mixtures with various bentonite fractions and water contents were first investigated to define an appropriate protocol for the fabrication of blocks. Results show that the increase of bentonite fraction decreased the overall compressibility and the achievable dry density at a given stress. As the water content increased, the compressibility at a relatively low vertical stress increased due to the increasing deformability of aggregates and the decreasing inter-aggregate friction; contrarily, at a high vertical stress, a lower compressibility was observed for the samples with a higher water content because a larger stress was required to squeeze water within aggregates. During demoulding, the required demoulding pressure increased with the increase of bentonite fraction and decreased with the increasing water content. Then, to assess the suitability of the material, the swelling pressures and hydraulic conductivities of the compacted blocks were determined. It was found that the swelling pressure increased and the hydraulic conductivity decreased with the increases of bentonite fraction and dry density. By contrast, as the water content increased, more water was intercalated in the interlayer spaces and the inter-aggregate pore volume decreased, resulting in reductions of the swelling pressure and hydraulic conductivity.

Keywords: bentonite/claystone mixture; bentonite fraction; water content; dry density; compaction and sealing properties

1 Introduction

In the French concept of radioactive waste disposal at great depth, the Callovo-Oxfordian (COx) claystone is considered by the French National Radioactive Waste Management Agency (Andra) as a potential host rock (Andra, 2005). The underground repository will be excavated in the COx formation and the radioactive waste canisters are to be placed in the disposal cells that consist of horizontal cased microtunnels of 70 cm in diameter and at least 80 m in length

1 Laboratoire Navier/CERMES, Ecole des Ponts ParisTech, 6 et 8 avenue Blaise Pascal, 77455 Marne La Vallée cedex 2, France
2 Andra, 1/7, rue Jean Monnet, 92298 Châtenay-Malabry cedex, France

(Menaceur et al., 2015). Note that this concept is different from that of China, in which the containers are embedded in GMZ bentonite-based materials and granite (Ye et al., 2010). A mixture composed of excavated COx claystone and bentonite is recently proposed as a candidate sealing material to ensure the chemical-mineralogical compatibility with the host rock and to lower the costs (Zhang, 2014; Zhang and Kröhn, 2019; Middelhoff et al., 2020; Zeng et al., 2020a; 2020b). To seal drifts and shafts, this material is industrially fabricated into blocks at a high dry density and then transported and emplaced in the drifts and shafts. (Andra, 2005). Swelling of the blocks can be expected upon the intrusion of groundwater from the host rocks, which can resist the propagation of excavation-damaged zone (Middelhoff et al., 2020) and prevent the release of radionuclides into the biosphere (Zhang, 2014). To this end, it is necessary to investigate the compaction property of bentonite/claystone mixture for practical fabrication and the sealing property of the compacted mixture for the suitability assessment of material.

In practice, the bentonite and claystone powders are first pre-mixed and humidified to reduce the compaction energy and the fabrication cost. During the mixing and humidifying processes, particle segregation and water-induced aggregation are unavoidable, which leads to uneven distributions of water content and bentonite fraction and thus influences the compaction and sealing properties of the mixture. Additionally, it has been admitted that there are excavation-induced fractures in the host rock as well as gaps between the surrounding rock between compacted blocks and joints between blocks (Bian et al., 2019; Zeng et al., 2020a; 2020b). Upon wetting, the block density will decrease in these zones, resulting in great variations of swelling pressure and hydraulic conductivity.

In the past decades, some studies addressed the compression behaviour (Zhang and Kröhn, 2019), swelling pressure (Tang et al., 2011a, 2011b; Wang et al., 2012; 2014; Zeng et al., 2019; Middelhoff et al., 2020) and hydraulic conductivity (Zeng et al., 2020c) of crushed COx claystone or its mixture with bentonite. Zhang and Kröhn (2019) compared the compressibility of crushed COx claystone and two COx claystone/MX80 bentonite mixtures (proportions of 60/40 and 80/20 in dry mass) and reported that the achievable dry density under a given load decreased with the increase of bentonite fraction. Zeng et al. (2019; 2020c; 2020d) experimentally determined the swelling pressure and hydraulic conductivity of MX80 bentonite/COx claystone mixtures with different bentonite fractions and dry densities and found that the swelling pressure increased while the hydraulic conductivity decreased as the sample dry density increased. However, there has been few published data on the effect of water content

on the compaction and sealing properties of the mixture. Moreover, the information of the rebound behaviour upon unloading and the needed pressure for demoulding are quite scarce.

The aim of present study is to comprehensively investigate the effects of bentonite fraction (B), dry density (ρ_d) and water content (w) on the compaction and sealing properties of the MX80 bentonite/COx claystone mixture. A series of one-dimensional compaction tests were first performed on the mixtures with various bentonite fractions and water contents, to study the effects of bentonite fraction and water content on the compression and rebound indices and the needed demoulding pressure. Afterwards, constant-volume swelling pressures and hydraulic conductivities of the compacted blocks with different bentonite fractions, water contents and dry densities were experimentally determined to study the sealing performance of the mixtures. The microstructure of the compacted samples was analysed in relation to the compaction and sealing properties of the mixtures.

2 Materials and methods

2.1 Materials

The soils tested in this study were MX80 bentonite and COx claystone mixtures. The MX80 bentonite is a commercial bentonite extracted from Wyoming, USA. The physical and mineralogical properties of the bentonite are summarized and compared with other reference bentonites in Table 1. The COx claystone was taken at approximately 490 m depth from the Underground Research Laboratory (URL) in Bure, France. The claystone contains 40%-45% interstratified illite/smectite, 30% carbonates and 25–30% quartz and feldspar (Fouché et al., 2004). The liquid limit is 41%, the plastic limit is 24% and the specific gravity is 2.70 (Zeng et al., 2020e). To acquire relatively homogeneous and representative samples in the laboratory, the bentonite and claystone were crushed into powders with particle size smaller than 2.0 mm. As shown in Fig. 1, the mean particle sizes D_{50} of the bentonite and claystone determined by dry-sieving method are 0.55 and 0.58 mm, respectively. The size distributions of bentonite and claystone grains larger than about 0.3 mm are quite close.

To simulate the working environments of compacted blocks, the saturation water used in the swelling pressure and hydraulic conductivity tests was synthetic pore water of COx claystone. The synthetic pore water was prepared by mixing the relevant chemical components (Table 2) with de-ionized water until full dissolution. It has the same chemical composition as the site water in Bure.

Table 1. Physical and mineralogical properties of bentonites

Soil property	MX80 bentonite (Zeng et al., 2020e)	GMZ bentonite (Liu and Wen, 2003)	Kunigel-V1 bentonite (Nakashima, 2004; Sun et al., 2009)
Specific gravity	2.76	2.66	2.79
Liquid limit (%)	494	313	473.9
Plastic limit (%)	46	38	24.6
Plasticity index (%)	448	275	447.3
Main minerals (%)	Montmorillonite (86%) Quartz (7) Carbonate and feldspar (7%)	Montmorillonite (75.4%) Kaolinite (0.8%) Quartz (11.7%) Cristobalite (7.3%) Feldspar (4.3%) Calcite (0.5%)	Montmorillonite (47%) Chalcedony (37%) Plagioclase (4%) Analcime (3%) Calcite (2%) Dolomite (2%) Quartz (0.6%) Pyrite (0.6%)

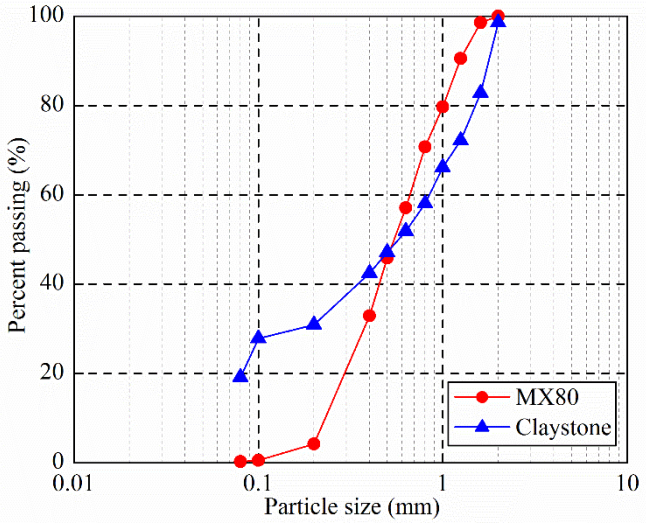

Fig. 1. Grain size distributions of MX80 bentonite and COx claystone

Table 2. Chemical composition of the synthetic pore water

Component	NaCl	$NaHCO_3$	KCl	$CaSO_4 \cdot 2H_2O$	$MgSO_4 \cdot 7H_2O$	$CaCl_2 \cdot 2H_2O$	Na_2SO_4
Content (g/L)	1.950	0.130	0.035	0.630	1.020	0.080	0.700

2.2 Compaction tests

According to the preliminary studies of Zeng et al. (2020a; 2020b; 2020e), the compacted mixture of 70% MX80 bentonite and 30% COx claystone at a dry density of 2.0 Mg/m^3 can meet the requirements in terms of hydraulic conductivity and swelling pressure. To account for the detrimental influence of variable bentonite/claystone mass ratio, another two MX80 bentonite/COx claystone mixtures with 20 and 25% bentonite were prepared in this study. The bentonite and claystone powders were mixed at proportions of 20/80, 25/75 and 30/70 for more than 10 min using a stirrer. The equilibrium gravimetric water contents of the bentonite and claystone powders under laboratory conditions (a relative humidity of about 60%) were 11.4%

and 6.1%, respectively. The corresponding water contents of the mixtures with 20, 25 and 30% bentonite were 7.2, 7.4 and 7.7%, respectively. Some of the mixtures were humidified by spraying de-ionized water to reach various moulding water contents of approximately 9.0, 11.0 and 12.5%, as shown in Table 3. The wet mixtures were then conserved in hermetic containers for more than 24 h for moisture homogenization. The compaction tests were performed using a set-up shown in Fig. 2. Prior to compaction, the inner wall of the compaction mould having an inner diameter of 50 mm was first coated with grease and the mixtures were then poured into the compaction mould (with inner and outer diameters of 50 and 90 mm). After installation of the piston, the compaction mould was placed on the top plate of the displacement shaft and adjusted to connect the top of the piston to the force transducer. Afterwards, the mixtures were statically compressed at a constant displacement rate of 0.05 mm/min. The displacement and compression force were monitored using a linear variable differential transformer (LVDT) and a force transducer, respectively. To study the rebound behaviour, the samples were unloaded at the dry density of 1.7 Mg/m^3 and then reloaded. This unloading/reloading cycle was repeated at dry densities of 1.8, 1.9 and 2.0 Mg/m^3. After compressed to a dry density of 2.1 Mg/m^3, the samples were unloaded to zero. Additionally, another sample for each case was prepared and compressed directly at a constant displacement rate of 0.05 mm/min without unloading/reloading cycles. The samples had a final height of 10 mm and the corresponding dry density was 2.0 Mg/m^3.

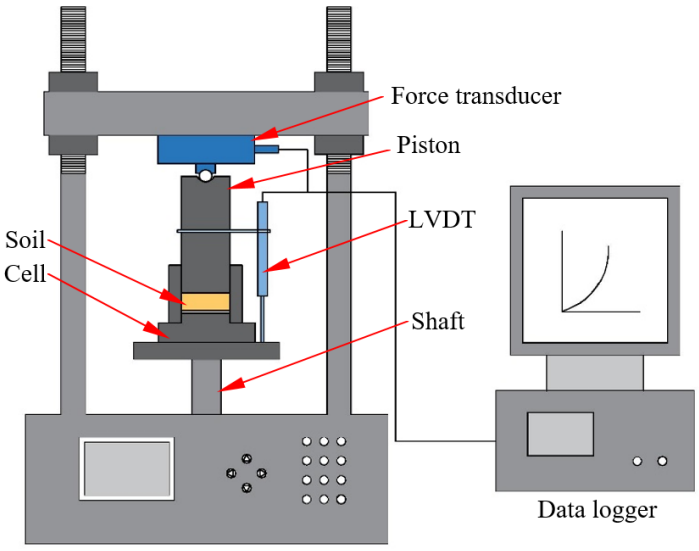

Fig. 2. Schematic diagram of the one-dimensional compression test

After unloading, a residual stress was expected to exist in radial direction, which influenced the demoulding behaviour (Saba et al., 2014; Eriksson, 2017). The needed demoulding pressure

could also be a major concern for the practical fabrication of blocks. In this study, the compacted samples at a dry density of 2.0 Mg/m^3 were extracted from the compaction mould by pushing the bottom of the samples at a constant displacement rate of 5 mm/min and the needed demoulding force was recorded using a force transducer (Fig. 3).

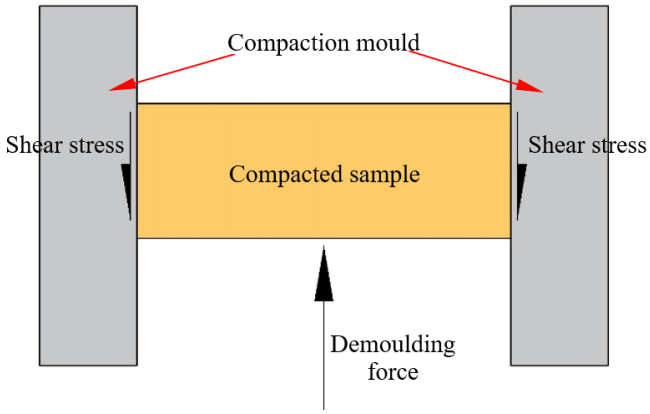

Fig. 3. Schematic diagram of the sample demoulding

2.3 Swelling pressure and hydraulic conductivity tests

According to the results from PGZ2 in situ tests in the Andra URL, the technological gaps were estimated at 12% of the volume of gallery (Gatabin et al., 2016). Taking into account 10 and 20% technological gaps, the compacted blocks at an initial dry density of 2.0 Mg/m^3 would swell upon hydration, filling up the technological gaps, and the final dry densities of sealing material were 1.8 and 1.6 Mg/m^3, respectively (Zeng et al., 2020e). In this study, to account for the effect of the technological gaps on the sealing property, the compacted samples with various dry densities of 1.6, 1.8 and 2.0 Mg/m^3 were prepared according to the compaction properties of the mixtures (Table 3). Then, they were transferred into the testing cell (having the same diameter as the compaction mould), following the guidelines provided by AFNOR (1995). Subsequently, the assembled cell was positioned in a stainless steel frame and the top cap was locked by a screw to prevent the axial deformation (Fig. 4). After that, the water inlet was connected to the synthetic pore water reservoir and the sample was hydrated with synthetic pore water at a constant water head of 1.0 m. The swelling pressure was monitored by a force transducer mounted under the cell base.

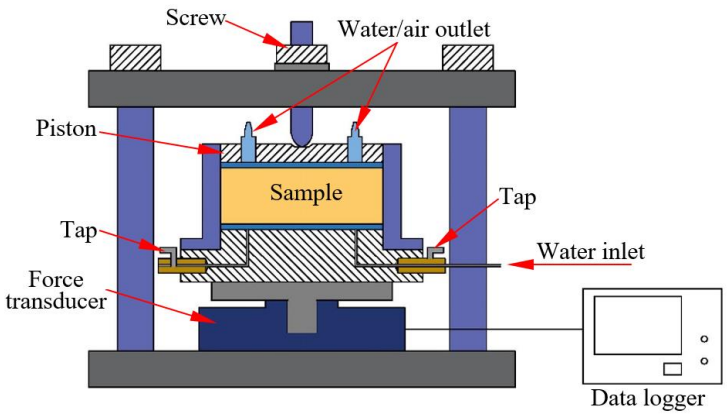

Fig. 4. Schematic diagram of the constant-volume cell for swelling pressure and hydraulic conductivity tests

Table 3. Experimental programme

No.	Bentonite fraction (%)	Water content (%)	Target dry density for P_s and k_w tests (Mg/m^3)	Degree of saturation (%)
T01	20	7.2	2.0	54.9
T02	20	8.9	2.0	67.8
T03	20	11.1	2.0	84.6
T04	20	12.6	2.0	96.0
T05	25	7.4	2.0	56.2
T06	25	9.1	2.0	69.1
T07	25	11.1	2.0	84.3
T08	25	12.5	2.0	95.0
T09	30	7.7	2.0	58.3
T10	30	9.1	2.0	68.9
T11	30	11.0	2.0	83.3
T12	30	12.5	2.0	94.7
T13	30	7.7	1.8	41.0
T14	30	9.1	1.8	48.5
T15	30	11.0	1.8	58.6
T16	30	12.5	1.8	66.6
T17	30	7.7	1.6	30.0
T18	30	9.1	1.6	35.4
T19	30	11.0	1.6	42.8
T20	30	12.5	1.6	48.6

Once the swelling pressure stabilized, the hydraulic conductivity tests were conducted according to AFNOR (2008). The details of the experimental setup can be found in Zeng et al. (2020c; 2020d). The applied water pressures were 40, 100 and 200 kPa for the samples with dry densities of 1.6, 1.8 and 2.0 Mg/m^3, respectively and the corresponding hydraulic gradients were 400, 1000 and 2000. Note that the water injected pressures for all the samples were lower than 1/10 of the swelling pressures to minimize the microstructure disturbance. After the stabilization of the flow rate, the hydraulic conductivity was calculated based on the Darcy's law.

2.4 Microstructure investigation

To interpret the compaction and sealing properties, the microstructure features of compacted samples with various dry densities (1.8 and 2.0 Mg/m^3) and water contents (7.7 and 12.5%) was investigated using mercury intrusion porosimetry (MIP). The compacted samples were first cut into small cubes with a side approximately equal to 1 cm and then freeze-dried. Afterwards, an autopore IV 9500 mercury intrusion porosimeter was employed to explore the pore structures. The mercury pressure increased by steps from 3.6 kPa to 228 MPa, corresponding to a maximum entrance diameter of 350 μm and a minimum entrance diameter of 5.5 nm. For each pressure increment, the intruded volume of mercury was monitored for the determination of pore size distribution.

3 Experimental results

3.1 Compression and rebound behaviour

The variations of void ratio (e) versus the logarithm of vertical stress (σ_v) for the mixtures with different bentonite fractions and water contents are shown in Fig. 5. It can be observed that the e-σ_v curves are similar for the samples with (represented by solid lines) and without (represented by dash lines) unloading/reloading cycles. As the water content increased, the initial void ratio increased since the grain would swell after absorbing water and led to a larger bulk volume. Upon loading, steeper e-σ_v curves were observed in general at higher water contents, suggesting that the increase of water content contributed to the soil compaction. After unloading, the mixtures with different water contents followed almost the same slope. When the water content increased from 7.5 to 12.5%, the vertical stress required to achieve a dry density of 2.0 Mg/m^3 (corresponding to a void ratio 0.36) decreased from 48.0 to 44.8 MPa for the mixture with 30% bentonite and from 43.1 to 35.7 MPa for the mixture with 25% bentonite. By contrast, for the mixture with 20% bentonite, it decreased from 37.7 to 31.3 MPa. A comparison of the e-σ_v curves for the mixtures with various bentonite fractions showed a slight increase of initial void ratio with the increasing bentonite fraction, but this effect was less significant than that of water content. Additionally, a larger vertical stress was needed to achieve a given void ratio at a higher bentonite fraction.

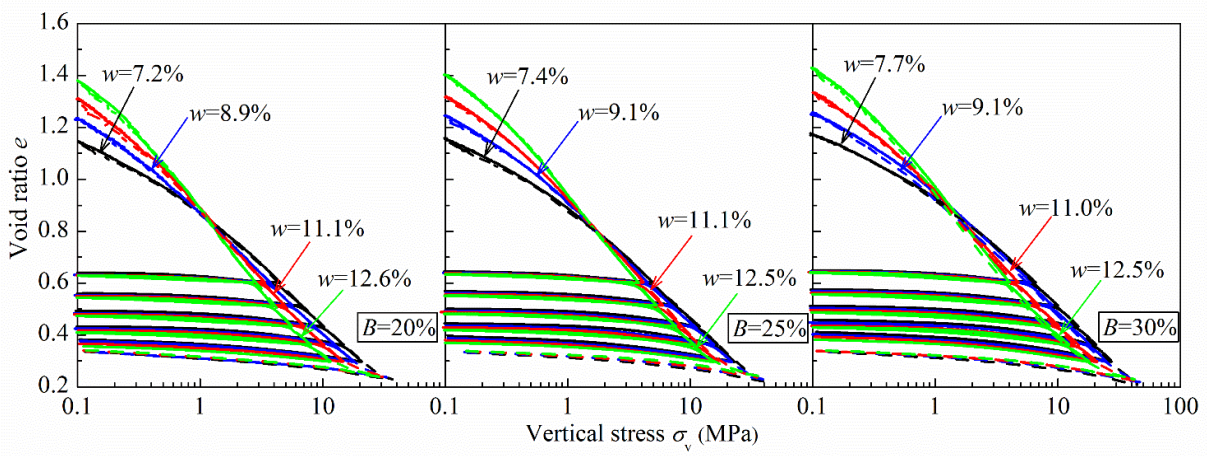

Fig. 5. Variation of void ratio with applied vertical stress during the compression and decompression phases. Note: the solid lines correspond to the samples with unloading/reloading cycles while the dash lines represent the samples without unloading/reloading cycles

To further analyse the compaction property, the compression index (C_c^*) at different stresses was determined, which corresponded to the slope of the e- $\log\sigma_v$ curves without unloading/reloading cycles ($de/d\log\sigma_v$). In a similar fashion, the rebound index (C_s^*) was determined by linearizing the e-$\log\sigma_v$ plot along the unloading paths at different vertical stresses. The variation of the compression index with vertical stress is depicted in Fig. 6. An inversed "U-shape" relationship between C_c^* and logarithm of σ_v was observed and a critical vertical stress could be identified, suggesting two stages during the compaction: (i) when the vertical stress increased from 0 to the critical value, the compression index increased; (ii) the compression index turned to decrease when the vertical stress was larger than the critical value. Taking the mixtures with a bentonite fraction of 30% as examples, the critical vertical stresses of samples with water contents of 7.7, 9.1, 11.0 and 12.5% were equal to 14.28, 8.63, 1.83 and 1.61 MPa, respectively. Moreover, a higher C_c^* at a lower vertical stress (lower than the critical value) was observed for the mixtures with a larger water content, while the mixtures at a lower water content exhibited a higher C_c^* at a higher vertical stress (larger than the critical value). Fig. 7 summarizes the relationship between the rebound index and vertical stress for the mixtures with different water contents and bentonite fractions. On the whole, the rebound index increased with the increasing vertical stress, regardless of the water content. At a given vertical stress, a higher rebound index was observed on the mixtures with a larger bentonite fraction.

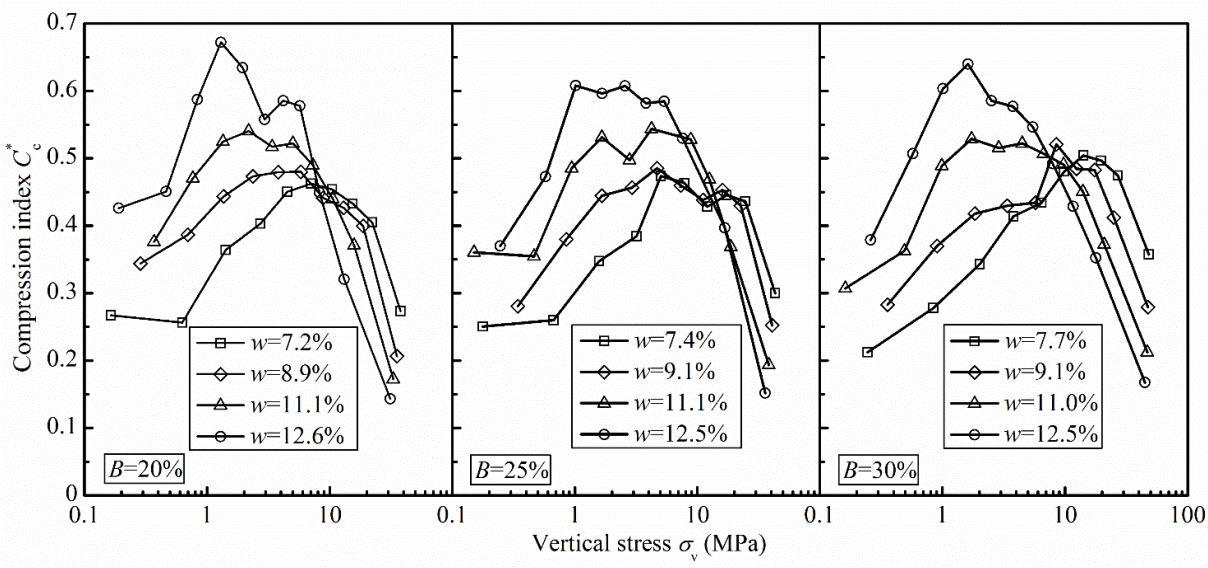

Fig. 6. Variation of compression index with vertical stress

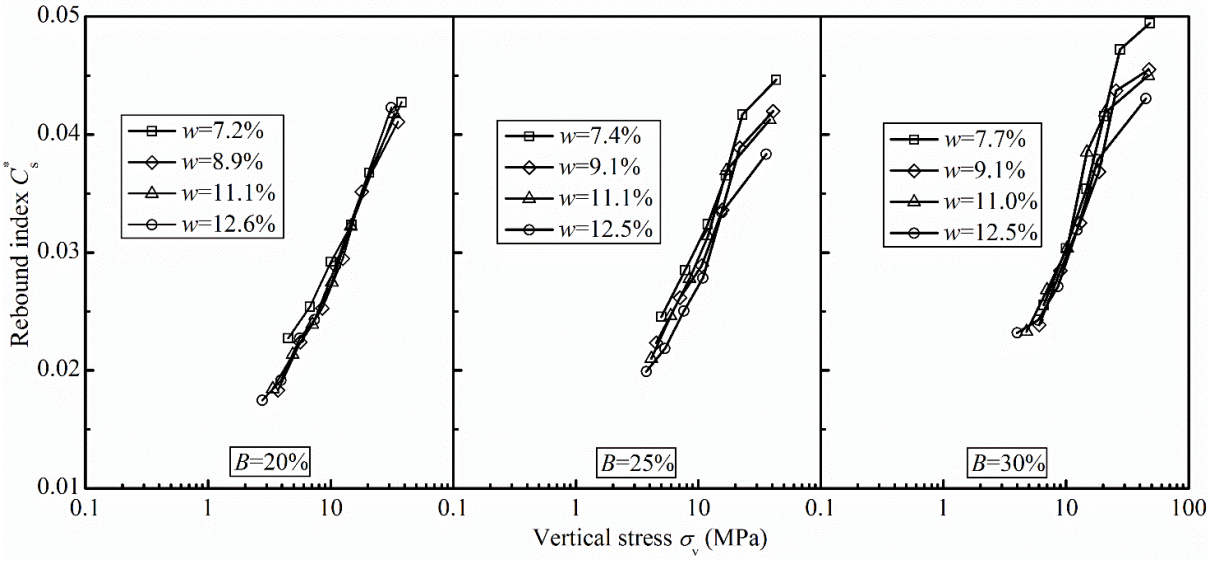

Fig. 7. Variation of rebound index with vertical stress

3.2 Demoulding pressure

After unloaded to zero, the samples were extracted from the cell. The variation of the demoulding pressure with displacement is shown in Fig. 8. Note that the demoulding pressure was calculated by dividing the demoulding force by the contact surface area of the samples with the compaction mould. On the whole, all the samples first experienced a rapid increase of demoulding pressure until reaching the maximum static friction stress at about 0.2 mm displacement. After that, the demoulding pressure decreased, becoming relatively stable beyond 1.0 mm displacement. In that case, the demoulding pressure was equal to the sliding friction stress. The maximum demoulding pressures of samples with various bentonite fractions and water contents are summarized in Fig. 9. For the samples with the same bentonite fraction, the

maximum demoulding pressure decreased as the water content increased. Additionally, at a given water content, the higher the bentonite fraction, the larger the required demoulding pressure.

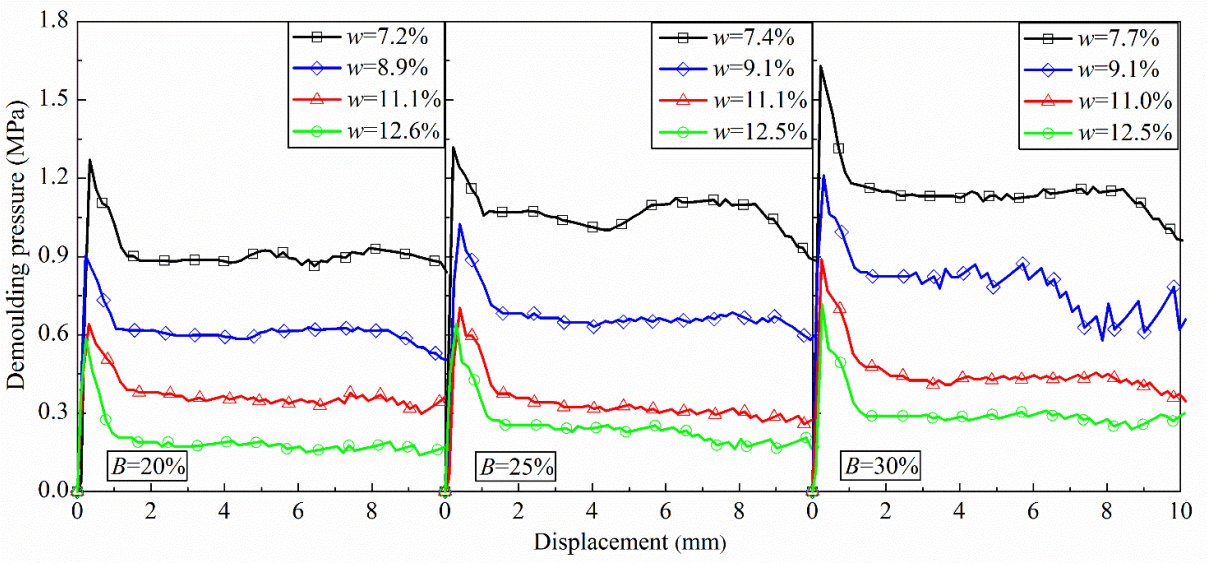

Fig. 8. Variation of demoulding pressure with displacement

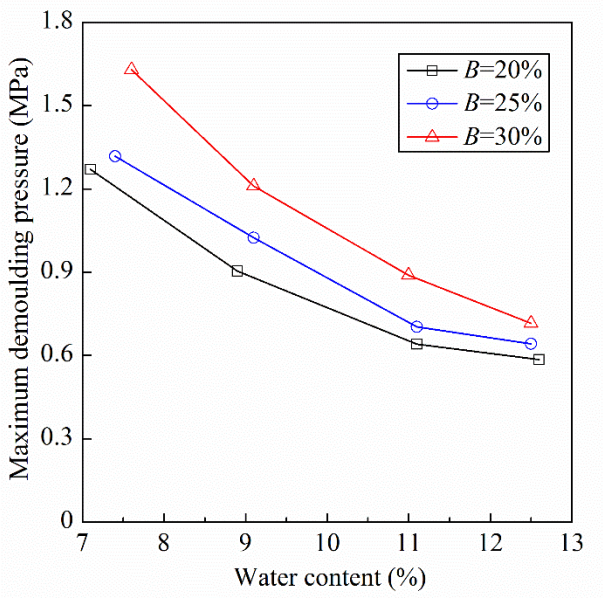

Fig. 9. Variation of maximum demoulding pressure with water content

3.3 Swelling pressure

The effects of bentonite fraction, dry density and water content on the swelling pressure kinetics of bentonite/claystone samples are depicted in Fig. 10. The swelling pressure increased slowly at the first 1-9 min of hydration, and then further increased at a higher increasing rate until about 300-1000 min hydration. Afterwards, for the samples at dry densities of 1.8 and 2.0 Mg/m^3, the

swelling pressure turned to stabilization (Fig. 10a and 10b); by contrast, for the samples with a dry density of 1.6 Mg/m^3, the swelling pressure reached a peak value and then decreased slightly probably due to the significant collapse of loose aggregate structure (Delage et al., 2006; Zeng et al., 2019) (Fig. 10b). On the whole, the variations of swelling pressure were of "gentle-sharp-gentle" feature with the increase of the logarithm of time. Sridharan and Gurtug (2004) and Chen et al. (2016) proposed to divide the swelling pressure curves into three stages: (i) a small initial swelling stage, (ii) a large primary swelling stage and (iii) a small secondary swelling stage. At given bentonite fraction and dry density, the effect of water content on the increasing rates of all stages was insignificant but the time needed to reach stabilization and the stabilized swelling pressure decreased considerably with the increasing water content and degree of saturation (Table 3). By contrast, a higher increasing rate of primary swelling could be identified for the samples with larger bentonite fraction and dry density. Moreover, more time was needed to reach equilibrium conditions for the samples with larger bentonite fraction and dry density. The final swelling pressures of samples with various bentonite fractions, dry densities and water contents are presented in Fig. 11. As the water content increased, a noticeable decrease of final swelling pressure was observed for the samples, which was consistent with the observation by Ye et al. (2013) on GMZ bentonite and by Lang et al. (2018) on Calcigel bentonite. Additionally, a comparison of the swelling pressures of samples with different dry densities indicated that the samples with a larger dry density exhibited a more significant decrease with the increase of water content. The similar phenomenon was reported by Rao and Ravi (2015) on the compacted Barmer bentonite/sand mixture.

3.4 Hydraulic conductivity

According to Zeng et al. (2020d), the saturation degree of samples was very close to 1. Subsequently, the hydraulic conductivity was determined on the saturated samples. Fig. 12a shows the influences of bentonite fraction and water content on the hydraulic conductivity of samples at a dry density of 2.0 Mg/m^3. When the water content increased from about 7.5 to 12.5%, the hydraulic conductivity was found to decrease from 1.80×10^{-12} to 6.13×10^{-13} m/s, from 1.42×10^{-12} to 6.05×10^{-13} m/s and from 7.62×10^{-13} to 5.37×10^{-13} m/s, respectively for the samples with 20, 25 and 30% bentonite. For the samples with a lower bentonite fraction, a higher value of hydraulic conductivity at a given water content and a more significant decrease were observed. The effects of water content and dry density on the hydraulic conductivity of samples with 30% bentonite are illustrated in Fig. 12b. For the samples at dry densities of 1.6, 1.8 and 2.0 Mg/m^3, the hydraulic conductivity decreased by 58.8, 53.1 and 29.5%, respectively,

when the water content increased from approximately 7.7 to 12.5%. The lower the dry density, the more significant the decrease of hydraulic conductivity with the increasing water content.

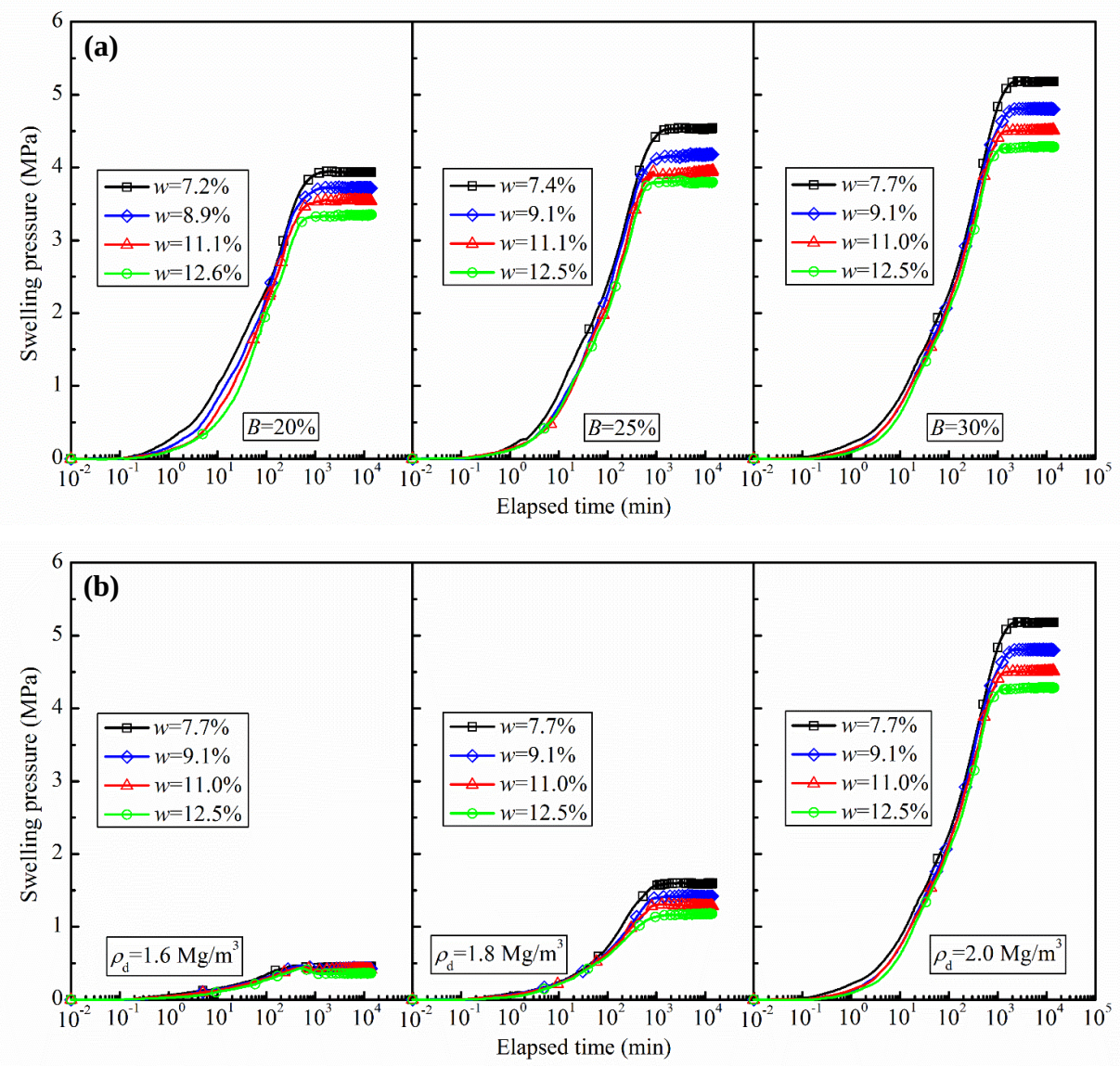

Fig. 10. Evolution of swelling pressure with elapsed time during hydration for the samples with (a) the same dry density of 2.0 Mg/m^3 and different bentonite fractions and water contents, and (b) the same bentonite fraction of 30% and different dry densities and water contents

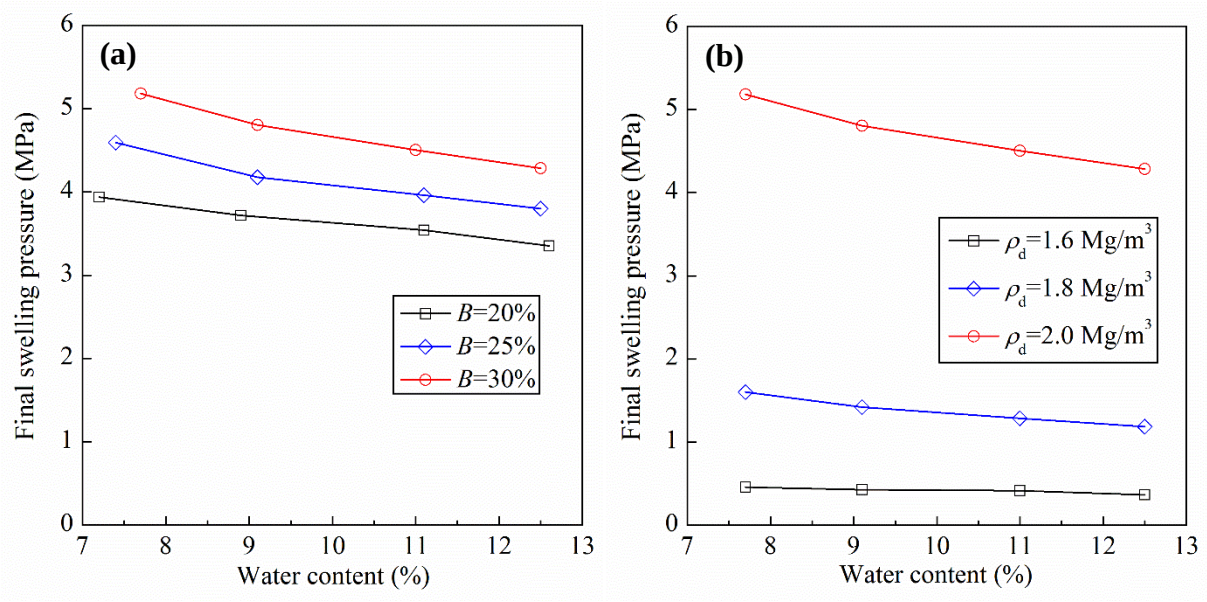

Fig. 11. Variation of swelling pressure with water content for the samples with (a) the same dry density of 2.0 Mg/m^3 and different bentonite fractions, and (b) the same bentonite fraction of 30% and different dry densities

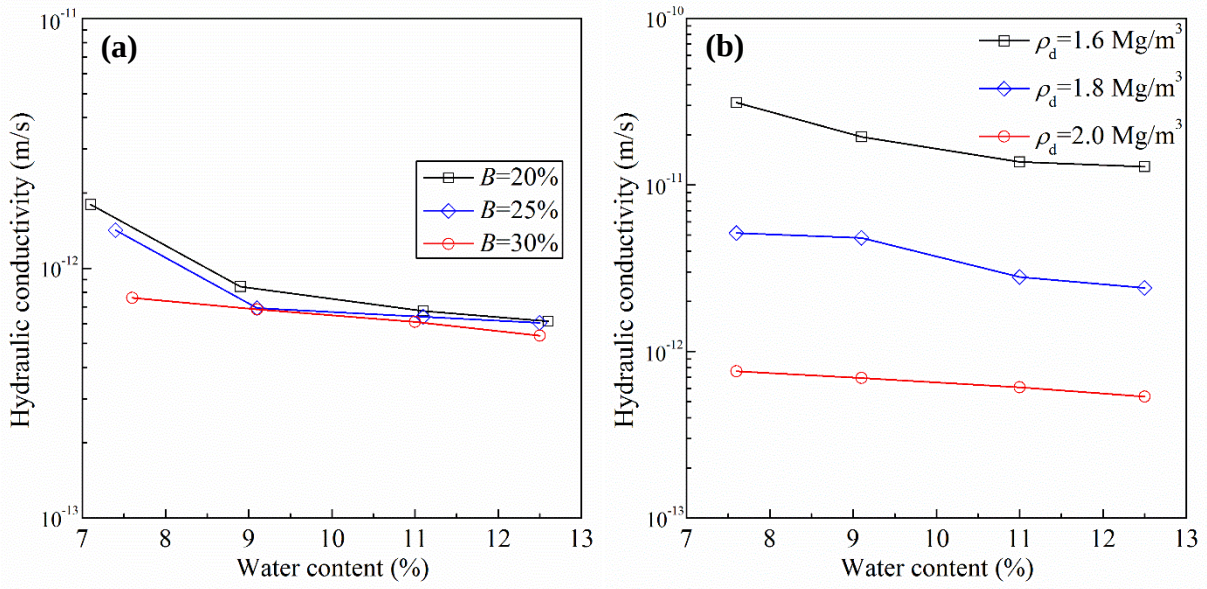

Fig. 12. Variation of hydraulic conductivity with water content for the samples with (a) the same dry density of 2.0 Mg/m^3 and different bentonite fractions, and (b) the same bentonite fraction of 30% and different dry densities

3.5 Microstructure features

Fig. 13 depicts the results of MIP tests carried out on the compacted bentonite/claystone mixtures with various dry densities and water contents. From the cumulative curves (Fig. 13a), it appears that the final intruded mercury void ratios of all the samples were lower than the global void ratios, indicating a significant undetectable porosity with a diameter smaller than 5.5 nm (corresponding to the inter-particle and inter-layer spaces) (Delage et al., 2006). When

the water content increased, more water molecules were placed along the clay monolayers. These processes gave rise to increases in the volume of pores with a diameter smaller than 5.5 nm; in that case, a larger difference between the final intruded mercury void ratio and global void ratio was observed for the samples with a higher water content (Fig. 13a). From the density function curves (Fig. 13b), a bimodal porosity distribution could be observed for all the samples, with two pore populations corresponding to: (i) intra-aggregate pores with an average pore diameter of 0.02 μm; (ii) inter-aggregate pores with an average pore diameter of 5 μm. In this study, the moulding water contents (7.7 and 12.5%) were lower than the optimum one (18.2%) (Middelhoff et al., 2020). As indicated by Delage et al. (1996; 2006), the soils compacted dry of optimum could be described by a typical aggregate microstructure. Fig. 13b also shows that the increase of dry density significantly reduced the volume of inter-aggregate pores between 0.1 and 350 μm, with no obvious changes in the intra-aggregate pore volume. At a given dry density, a lower inter-aggregate pore volume was observed for the samples with a higher water content, while the effect of water content on the intra-aggregate pore volume was almost negligible.

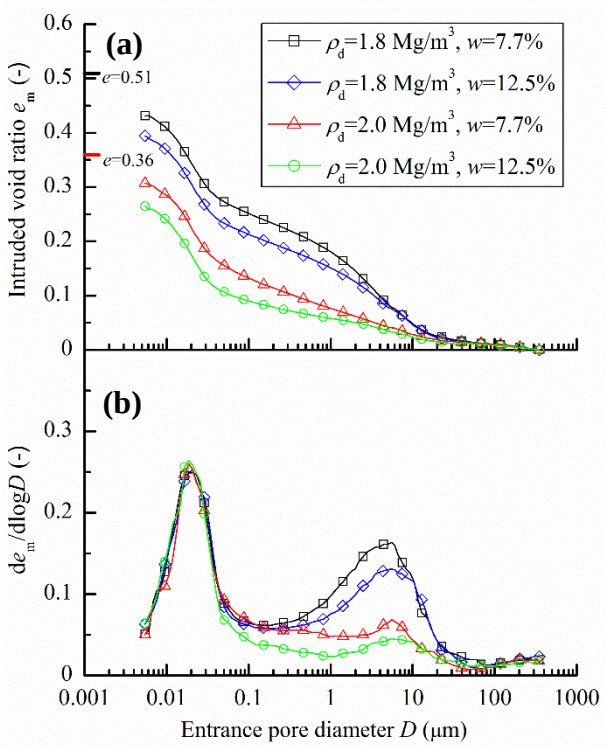

Fig. 13. Pore size distribution curves of compacted samples with 30% bentonite: (a) cumulative curves and (b) density function curves

4 Discussion

4.1 Effect of water content on the compression property

As commented above, the effect of water content on the compressibility was highly dependent on the applied vertical stress: at a relatively low vertical stress, the compressibility of the mixture increased with increasing water content; on the contrary, at a high vertical stress, a lower compressibility was observed for the mixtures with a higher water content. This phenomenon is consistent with the observations by Tang et al. (2009) on remoulded high-plasticity soils and by Kochmanová and Tanaka (2011) on Kunigel-VI and NSF clays. When the mixtures were poured into the compaction mould, large pores (inter-aggregate pores) were produced between the granules of bentonite and claystone powders. Most water was stored within the aggregates while the inter-aggregate pores were mainly filled with air. As the external vertical stress increased and exceeded the inter-aggregate friction and compression strength of aggregates, the aggregates rearrangement and deformation occurred, resulting in a rapid compaction of the air-filled pores. Therefore, an increase of C_c^* with the vertical stress was observed at low vertical stresses. With the further increase of vertical pressure, the volume of the air-filled pores became small and the water within aggregates began to be squeezed. Compared to air that could flow easily, the water needed a higher stress to be squeezed. Thereby, the slope of e-logσ_v curve was smaller than that at a low vertical stress and a decrease of C_c^* was observed at high vertical stresses. This explained the U-shape of $C_c^* - \log\sigma_v$ curve in a wide range of vertical stress. At low vertical stresses, the inter-aggregate friction and the deformability of aggregate were strongly related to the water content. The increase of water content would soften the soil aggregates as well as the bond between them, leading to an increase of C_c^* (Tang et al., 2009). As high vertical stresses, for the mixtures with a higher water content, a higher stress was required to squeeze water and a lower C_c^* could be expected.

4.2 Effects of water content and bentonite fraction on the required demoulding pressure

After compaction, the required demoulding pressure of samples with a dry density of 2.0 Mg/m^3 decreased with the increase of water content and increased with increase of bentonite fraction (Fig. 9). When the axial compaction pressure decreased to zero, the radial stress would remain thanks to the mechanical stiffness of the compacted samples. This residual stress in the radial direction was highly dependent on the maximum compression pressure previously applied on the samples. The larger the maximum compression pressure, the higher the residual stress in the radial direction. As remarked above, the maximum compression pressure increased with the

increase of bentonite fraction and decreased with the increase of water content. Thereby, a larger residual stress would be expected for the samples with a larger bentonite fraction and lower water content. During demoulding, the residual stress acted as the normal stress perpendicular to the shear direction, influencing the friction stress along the cell wall. This explained why a larger required demoulding was observed for the samples with a higher bentonite fraction and lower water content.

4.3 Effects of water content and dry density on the swelling pressure and hydraulic conductivity

From Fig. 11, the swelling pressure of bentonite/claystone mixtures increased with the increase of dry density and decreased with the increase of water content. It has been well documented that the swelling pressure at a given water content followed a linear relationship with the expansive mineral dry density of the samples (Middelhoff et al., 2020). The higher the expansive mineral dry density, the larger the swelling pressure. By contrast, the water content dependence of swelling pressure could be explained by the pore structure of compacted samples (Sridharan, 1986; Baille et al., 2010). When water was added, increasing water molecules were placed along the clay surface, which could be evidenced by the larger undetected undetectable pore volume using MIP technique for the samples with a higher water content (Fig. 13b). Upon hydration, less water would be further intercalated between the clay layers and the swelling of aggregates were less significant. As a result, a lower swelling pressure was observed for the samples with a higher water content.

Unlike the swelling pressure, the hydraulic conductivity decreased with the increase of water content and dry density (Fig. 12). According to Cuisinier et al. (2011) and Wang et al. (2013), water transfer through compacted soils mainly depended on the inter-aggregate pore volume. As remarked above, the increase of dry density by compaction mainly reduced the inter-aggregate pore volume (Fig. 13). Expectedly, the higher the dry density, the lower the inter-aggregate pore volume and the smaller the hydraulic conductivity. For the samples with a higher water content, a lower inter-aggregate pore volume could be expected due to the larger deformability of the aggregates and the lower inter-aggregate friction. Additionally, as mentioned above, the samples with a higher water content had a larger undetectable pore volume due to the placement of more water molecules along the clay layers (Fig. 13), which were largely immobilized and made a negligible contribution to the water flow (Pusch et al., 1990; Saiyouri et al., 2004). Both of them reduced the effective pore space for water flow through the compacted samples and resulted in a lower hydraulic conductivity.

5 Conclusions

The effects of bentonite fraction, dry density and water content on the compaction and sealing properties of the MX80 bentonite/COx claystone mixture have been investigated by carrying out a series of compaction, swelling pressure, hydraulic conductivity and MIP tests. From the experimental results, the following conclusions can be drawn.

At a relatively low vertical stress, the compressibility of samples increased with increasing water content due to the larger deformability of aggregates and the lower inter-aggregate friction; on the contrary, at a high vertical stress, a lower compressibility was observed with samples at a higher water content because a larger stress was required to squeeze water within aggregates. As the bentonite fraction increased, the overall compressibility and the achievable compacted density at a given stress decreased considerably. During demoulding, a larger pressure was required for the samples with a larger bentonite fraction and lower water content because of the larger residual stress normal to the cell wall after compaction.

The swelling pressure of bentonite/claystone mixture increased with the increase of dry density and bentonite fraction thanks to the increasing expansive mineral dry density. By contrast, it decreased as the water content increased due to the decreasing water adsorption capability. Additionally, the higher the bentonite fraction and dry density of samples, the larger the decrease of swelling pressure with the increase of water content.

As the water content increased, the hydraulic conductivity of bentonite/claystone mixture decreased due to the decreasing inter-aggregate pore volume and the increasing interlayer space. Additionally, more significant decrease of hydraulic conductivity with the increasing water content was observed for the samples with lower bentonite fraction and dry density.

Acknowledgments

The authors wish to acknowledge the supports from the French National Radioactive Waste Management Agency (Andra), the China Scholarship Council (CSC) and Ecole des Ponts ParisTech (ENPC).

References

AFNOR. 1995. Sols: reconnaissance et essais: essai de gonflement à l'oedomètre, détermination des déformations par chargement de plusieurs éprouvettes. French standard XP P 94-091. Association

française de normalisation (AFNOR), Paris.

AFNOR, 2008. De´termination a` l'oedoperme´ame`tre des caracte´ristiques de gonflement – Flux et perme´abilite´ des ge´osynthe´tiques bentonitiques (GSB). (Oedopermeameter Determination of Swelling Characteristics – Flux and Permeability of Geosynthetic Clay Liners (GCL)). French standard NF P 84 705. French Association for Normalization, Paris.

Andra, 2005. Dossier 2005 Argile - Synthesis: Evaluation of the Feasibility of a Geological Repository in an Argillaceous Formation (Meuse/Haute-Marne Site). French National Radioactive Waste Management Agency, Chatenay-Malabry CEDEX 241 pp. Accessed 22 November 2018.

Baille, W., Tripathy, S. and Schanz, T., 2010. Swelling pressures and one-dimensional compressibility behaviour of bentonite at large pressures. Applied Clay Science, 48(3), 324-333.

Bian, X., Cui, Y.J., Zeng, L.L. and Li, X.Z., 2019. Swelling behavior of compacted bentonite with the presence of rock fracture. Engineering Geology, 254, 25-33.

Chen, Y.G., Zhu, C.M., Ye, W.M., Cui, Y.J. and Chen, B., 2016. Effects of solution concentration and vertical stress on the swelling behavior of compacted GMZ01 bentonite. Applied Clay Science, 124, 11-20.

Cuisinier, O., Auriol, J.C., Le Borgne, T. and Deneele, D., 2011. Microstructure and hydraulic conductivity of a compacted lime-treated soil. Engineering geology, 123(3), 187-193.

Delage, P., Audiguier, M., Cui, Y.J. and Howat, M.D., 1996. Microstructure of a compacted silt. Canadian Geotechnical Journal, 33(1), 150-158.

Delage, P., Marcial, D., Cui, Y.J. and Ruiz, X., 2006. Ageing effects in a compacted bentonite: a microstructure approach. Géotechnique, 56(5), 291-304.

Eriksson, P. Compaction Properties of Bentonite Clay; SKB Technol. Rep. TR-16-16, Svensk Karnbra¨nslehantering AB, 2017; 1−39.

Fouché, O., Wright, H., Le Cléac'h, J.M. and Pellenard, P., 2004. Fabric control on strain and rupture of heterogeneous shale samples by using a non-conventional mechanical test. Applied Clay Science, 26(1-4), 367-387.

Gatabin, C., Talandier, J., Collin, F., Charlier, R. and Dieudonné, A.C., 2016. Competing effects of volume change and water uptake on the water retention behaviour of a compacted MX-80 bentonite/sand mixture. Applied Clay Science, 121, 57-62.

Kochmanová, N. and Tanaka, H., 2011. Influence of the Soil Fabric on the Mechanical Behaviour of Unsaturated and Saturated Clay. Soils and Foundations, 51(2), 275-286.

Lang, L.Z., Baille, W., Tripathy, S. and Schanz, T., 2018. Experimental study on the influence of preliminary desiccation on the swelling pressure and hydraulic conductivity of compacted bentonite. Clay Minerals, 53(4), 733-744.

Liu, Y.M., Wen, Z.J., 2003. An investigation of the physical properties of clayey materials used in nuclearwaste disposal at great depth. Miner. Rocks 23, 42–45 (in Chinese).

Menaceur, H., Delage, P., Tang, A.M. and Conil, N., 2015. The thermo-mechanical behaviour of the Callovo-Oxfordian claystone. International Journal of Rock Mechanics and Mining Sciences, 78, pp.290-303.

Middelhoff, M., Cuisinier, O., Masrouri, F., Talandier, J. and Conil, N., 2020. Combined impact of selected material properties and environmental conditions on the swelling pressure of compacted claystone/bentonite mixtures. Applied Clay Science, doi: 10.1016/j.clay.2019.105389

Nakashima, Y., 2004. Nuclear magnetic resonance properties of water-rich gels of Kunigel-V1 bentonite. Journal of Nuclear Science and Technology, 41(10), 981-992.

Pusch R, Karnland O, Hokmark H (1990) GMM - a general microstructural model for qualitative and quantitative studies of smectite clays. Swedish Nuclear Fuel and Waste Management Company, Stockholm, Sweden.

Rao, S.M. and Ravi, K., 2015. Influence of initial degree of saturation on swell pressures of compacted Barmer bentonite specimens. Annals of Nuclear Energy, 80, 303-311.

Saba, S., Barnichon, J.D., Cui, Y.J., Tang, A.M. and Delage, P., 2014. Microstructure and anisotropic swelling behaviour of compacted bentonite/sand mixture. Journal of Rock Mechanics and Geotechnical Engineering, 6(2), 126-132.

Saiyouri, N., Tessier, D. and Hicher, P.Y., 2004. Experimental study of swelling in unsaturated compacted clays. Clay minerals, 39(4), pp.469-479.

Sridharan, A., Rao, A.S. and Sivapullaiah, P.V., 1986. Swelling pressure of clays. Geotechnical Testing Journal, 9(1), 24-33.

Sridharan, A. and Gurtug, Y., 2004. Swelling behaviour of compacted fine-grained soils. Engineering geology, 72(1-2), 9-18.

Sun, D.A., Cui, H. and Sun, W.J., 2009. Swelling of compacted sand–bentonite mixtures. Applied Clay Science, 43(3-4), 485-492.

Tang, A.M., Cui, Y.J., Eslami, J. and Défossez, P., 2009. Analysing the form of the confined uniaxial compression curve of various soils. Geoderma, 148(3-4), 282-290.

Tang, C.S., Tang, A.M., Cui, Y.J., Delage, P., Schroeder, C. and Shi, B., 2011a. A study of the hydro-mechanical behaviour of compacted crushed argillite. Engineering geology, 118(3-4), 93-103.

Tang, C.S., Tang, A.M., Cui, Y.J., Delage, P., Schroeder, C. and De Laure, E., 2011b. Investigating the swelling pressure of compacted crushed-Callovo-Oxfordian claystone. Physics and Chemistry of the Earth, Parts A/B/C, 36(17-18), 1857-1866.

Wang, Q., Tang, A.M., Cui, Y.J., Delage, P. and Gatmiri, B., 2012. Experimental study on the swelling behaviour of bentonite/claystone mixture. Engineering Geology, 124, 59-66.

Wang, Q., Cui, Y.J., Tang, A.M., Barnichon, J.D., Saba, S. and Ye, W.M., 2013. Hydraulic conductivity and microstructure changes of compacted bentonite/sand mixture during hydration. Engineering Geology, 164, 67-76.

Wang, Q., Cui, Y.J., Tang, A.M., Delage, P., Gatmiri, B. and Ye, W.M., 2014. Long-term effect of water chemistry on the swelling pressure of a bentonite-based material. Applied Clay Science, 87, 157-162.

Ye, W.M., Lai, X.L., Liu, Y., Chen, Y.G. and Cui, Y.J., 2013. Ageing effects on swelling behaviour of compacted GMZ01 bentonite. Nuclear Engineering and Design, 265, 262-268.

Ye, W.M., Chen, Y.G., Chen, B., Wang, Q. and Wang, J., 2010. Advances on the knowledge of the

buffer/backfill properties of heavily-compacted GMZ bentonite. Engineering Geology, 116(1-2), 12-20.

Zeng, Z.X., Cui, Y.J., Zhang, F., Conil, N. and Talandier, J., 2019. Investigation of swelling pressure of bentonite/claystone mixture in the full range of bentonite fraction. Appl. Clay Sci. https://doi: 10.1016/j.clay.2019.105137.

Zeng, Z.X., Cui, Y.J., Zhang, F., Conil, N. and Talandier, J., 2020a. Effect of technological voids on the swelling behaviour of compacted bentonite/claystone mixture. Can. Geotech. J. 57(12), 1881-1892.

Zeng, Z.X., Cui, Y., Conil, N. and Talandier J., 2020b. Analysis of boundary friction effect on the homogenization process of compacted bentonite/claystone mixture with technological voids upon hydration. Acta Geotech. https://doi.org/10.1007/s11440-020-01048-x.

Zeng, Z.X., Cui, Y.J., Conil, N. and Talandier, J., 2020c. Experimental investigation and modelling of the hydraulic conductivity of saturated bentonite/claystone mixture. International Journal of Geomechanics. https://doi.org/10.1061/(ASCE)GM.1943-5622.0001817.

Zeng, Z.X., Cui, Y.J., Conil, N. and Talandier, J., 2020d. Experimental study on the aeolotropic swelling behaviour of compacted bentonite/claystone mixture with axial/radial technological voids. Engineering Geology. https://doi.org/10.1016/j.enggeo.2020.105826.

Zeng, Z.X., Cui, Y.J., Conil, N. and Talandier, J., 2020e. Effects of technological voids and hydration time on the hydro-mechanical behaviour of compacted bentonite/claystone mixture. Géotechnique. https://doi.org/10.1680/jgeot.19.P.220.

Zhang, C.L., 2014. Characterization of excavated claystone and claystone–bentonite mixtures as backfill/seal material. Geological Society, London, Special Publications, 400(1), 323-337.

Zhang, C.L. and Kröhn, K.P., 2019. Sealing behaviour of crushed claystone–bentonite mixtures. Geomechanics for Energy and the Environment, 17, 90-105.

Zeng, Z.X., Cui, Y.J., Talandier, J. 2021. Submitted to Acta Geotechnica.

An insight into grain interaction in bentonite/claystone mixtures

Zhixiong Zeng[1], Yu-Jun Cui[1], Jean Talandier[2]

Abstract: This paper investigates the swelling mechanism of Callovo-Oxfordian (COx) claystone grain in its mixtures with bentonite which are potential candidate for engineered barriers in the French high-level radioactive waste disposal. The swelling pressures of MX80 bentonite/COx claystone mixtures with various bentonite fractions and dry densities were first experimentally determined by carrying out infiltration tests under constant-volume conditions. According to the experimental results, the claystone void ratio after hydration in the mixtures was estimated by taking into account the bentonite–claystone grain interaction. Then, the volume change of claystone grain under different pressures applied by swollen bentonite was determined. The volumetric strain of claystone grain was found to decrease linearly with the increase of pressure. This allowed the indirect determination of the swelling pressure of claystone grain. The determined value was found to be comparable to that estimated from the relationship between the void ratio and the swelling pressure in the direction perpendicular to the stratification of intact COx claystone, confirming the identified swelling mechanism of bentonite/claystone mixtures.

Keywords: bentonite/claystone mixture; claystone void ratio; volumetric strain; swelling pressure of claystone grain

1 Introduction

The French Radioactive Waste Management Agency (Andra) is currently envisaging to construct a geological repository for high-level radioactive waste in the Callovo-Oxfordian (COx) claystone formation [1]. The disposal galleries are planned to be excavated at a depth of 490 m in the 150-m-thick layer of COx claystone. To seal or backfill these galleries after the emplacement of waste canisters, pure bentonite or bentonite/sand mixture may be employed. To reduce the excavation wastes and to have lower costs, excavated COx claystone has been proposed to partially or completely replace the commercial bentonite as sealing/backfilling material. Once the galleries are closed, the crushed claystone or its mixture with bentonite is expected to exhibit a swelling pressure high enough to stabilize the surrounding rock mass [7,

1 Laboratoire Navier/CERMES, Ecole des Ponts ParisTech, 6 et 8 avenue Blaise Pascal, 77455 Marne La Vallée cedex 2, France
2 Andra, 1/7, rue Jean Monnet, 92298 Châtenay-Malabry cedex, France

13, 18].

Over the last few decades, the swelling pressure of pure bentonite and bentonite/sand mixtures were widely studied [3-5, 9]. It was found that the swelling pressure increased linearly with the increase of dry density in a semi-logarithmic plane. Additionally, for each specific bentonite, the relationship between the swelling pressure and the final bentonite dry density could be described by a unique relationship, regardless of sand fraction [2, 11]. The swelling pressure of bentonite/sand mixtures was principally dominated by the matrix of bentonite, while the sand grains remained inert without any contribution to the global swelling pressure. Unlike the inert sand, the COx claystone contains a significant amount of clay minerals. Upon contact with water, both the bentonite and claystone grains adsorbed water and the interaction between them could occur. Zeng et al. [13] argued that the swelling of claystone was conditioned by the swollen bentonite due to the much higher swelling capacity of bentonite. However, this swelling mechanism of claystone grain in its mixtures with bentonite has not been analysed in-depth.

In this paper, a series of constant-volume swelling pressure tests were performed on the MX80 bentonite/COx claystone mixtures with various bentonite fractions and dry densities. By considering the interaction between bentonite and claystone in the development of global swelling pressure, the claystone void ratio in the mixture after hydration was calculated and the relationship between the claystone grain volume change and the pressure applied by swollen bentonite was determined. Subsequently, the swelling pressure of crushed claystone grains was indirectly determined and then compared with that estimated from the measured swelling pressure in the direction perpendicular to the stratification of intact COx claystone.

2 Materials and methods

The mixtures of MX80 bentonite and COx claystone powders were used in this study. The MX80 bentonite was taken from Wyoming, USA. Prior to the experiment, the bentonite was crushed to powders with a maximum grain size of 2 mm. The COx claystone was extracted from the Bure Underground Research Laboratory. The subsequent processing of excavated COx claystone comprised the crushing and sieving passing through 2.0 mm sieve. Then, the processed COx claystone powders were stored in hermetic containers. The physico-chemical properties of the tested materials are listed in Table 1. The initial suctions of the bentonite and

claystone powders were also measured by hygrometer WP4, equal to 101 and 27 MPa, respectively. As shown in Fig. 1, the grain size distributions of the bentonite and claystone determined by dry-sieving method are quite close, with mean particle sizes D_{50} of 0.55 and 0.58 mm, respectively. Using a pycnometer with a non-aromatic hydrocarbon fluid (Kerdane), the apparent volume of soil grains at a given dry mass was measured and the respective average dry densities of bentonite and claystone grains were thus determined, equal to 2.00 and 2.31 Mg/m^3.

Table 1. Physico-chemical properties of MX80 bentonite and COx claystone

Soil property	MX80 bentonite	COx claystone
Water content (%)	11.4	6.1
Specific gravity	2.76	2.70
Liquid limit (%)	494	41
Plastic limit (%)	46	24
Clay-size fraction (%)	86	26
Main clay minerals	Smectite	Interstratified illite/smectite

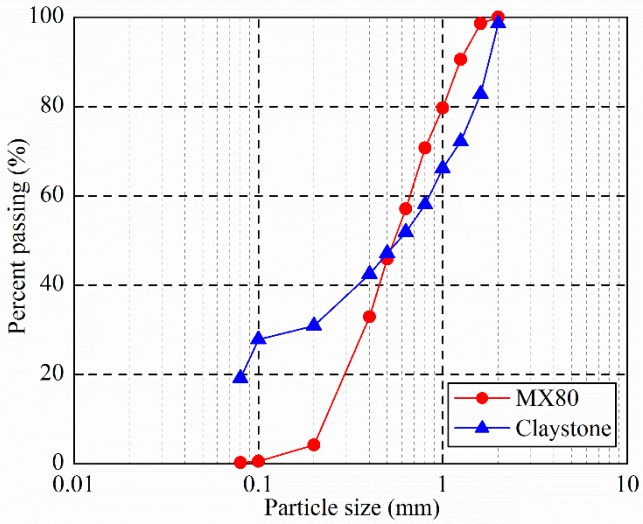

Fig. 1. Grain size distributions of MX80 bentonite and COx claystone

The bentonite and claystone powders at various proportions of 70/30, 50/50, 30/70, 20/80, 10/90 in dry mass were first mixed thoroughly. As shown in Table 2, the corresponding bentonite fractions (B) of the mixtures were 70, 50, 30, 20 and 10%. Subsequently, the mixtures and pure claystone were statically compacted at a control rate of 0.05 mm/min to reach various target dry densities. The diameter and height of the compacted samples were 50 and 10 mm, respectively. After compaction, the samples were transferred to the stainless steel cell (50 mm in diameter) and the two sides of samples were covered by two filter papers and two porous

discs (Fig. 2). At the top, the samples were restrained by a piston blocked using screws. Synthetic site water was injected from the bottom of the cell at constant water head of about 1 m (the corresponding water pressure was about 10 kPa). The synthetic site water has the same chemical composition as the site water in Bure and it was prepared by mixing the relevant chemical components (Table 3) with deionised water until full dissolution. The samples were hydrated under constant-volume conditions and the expelled air/water flowed through the air/water outlets at the top. During the hydration, the vertical force was monitored using a force transducer (accuracy ±0.01 kN) installed under the cell. Note that the maximum vertical displacement of the apparatus was quite small, estimated at 0.0049 mm. Thus, the volume change of samples due to the deformation of apparatus was ignored.

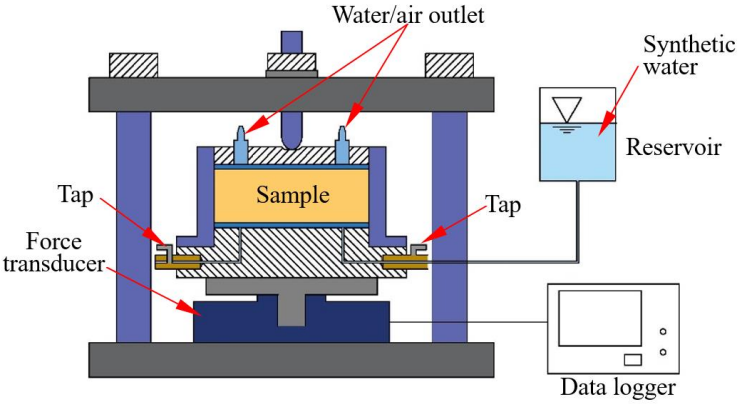

Fig. 2. Layout of the experimental setup for swelling pressure tests

3 Experimental results and discussion

3.1 Global swelling pressure of mixtures

Fig. 3 depicts the typical evolution of the global swelling pressure of samples with various bentonite fractions and dry densities. On the whole, the global swelling pressure of the samples with high bentonite fractions (larger than 50%) and high dry densities (larger than 1.50 Mg/m^3) increased with elapsed time and then tended to stabilise. By contrast, the swelling pressure of the samples with low bentonite fractions (smaller than 20%) and low dry densities (smaller than 1.77 Mg/m^3) increased quickly at the beginning and reached a peak. Then, it decreased and tended to stabilise.

Table 2. Test program and main results

Test No.	Bentonite fraction B (%)	Dry density of sample ρ_{dm} (Mg/m^3)	Initial water content w_m (%)	Claystone void ratio e_c	Volumetric strain of claystone grain ε_v (%)	Final swelling pressure P_s (MPa)
S01	70	1.38	9.8	0.08	-7.8	0.43
S02	70	1.50	9.8	0.13	-2.9	1.11
S03	70	1.63	9.8	0.07	-8.1	2.53
S04	70	1.71	9.8	0.02	-12.4	3.94
S05	50	1.27	8.8	0.49	27.4	0.13
S06	50	1.56	8.8	0.30	11.5	0.85
S07	50	1.73	8.8	0.18	1.1	2.10
S08	50	1.76	8.8	0.19	2.2	2.91
S09	30	1.50	7.7	0.18	26.2	0.22
S10	30	1.60	7.7	0.47	20.6	0.46
S11	30	1.68	7.7	0.41	16.4	0.78
S12	30	1.79	7.7	0.36	10.8	1.59
S13	30	1.89	7.7	0.30	5.0	2.72
S14	30	1.99	7.7	0.23	0.9	5.23
S15	20	1.60	7.2	0.18	27.3	0.26
S16	20	1.69	7.2	0.49	20.5	0.44
S17	20	1.77	7.2	0.41	15.8	0.70
S18	20	1.88	7.2	0.35	11.8	1.93
S19	10	1.61	6.6	0.31	33.7	0.14
S20	10	1.68	6.6	0.56	28.7	0.23
S21	10	1.78	6.6	0.50	21.5	0.39
S22	10	1.90	6.6	0.42	15.5	1.07
S23	0	1.80	6.1	0.35	28.3	0.15
S24	0	1.90	6.1	0.50	21.8	0.47
S25	0	1.99	6.1	0.42	16.3	0.79

Table 3. Chemical composition of the synthetic site water

Component	NaCl	$NaHCO_3$	KCl	$CaSO_4 \cdot 2H_2O$	$MgSO_4 \cdot 7H_2O$	$CaCl_2 \cdot 2H_2O$	Na_2SO_4
Content (g/L)	1.950	0.130	0.035	0.630	1.020	0.080	0.700

The swelling pressure tests ended after 25-150 h and the samples became saturated according the results of Zeng et al. [14]. The variation of final swelling pressure with respect to the dry density of samples is presented in Fig. 4 and compared with the results from other researchers [3, 10, 11]. It is observed that the final swelling pressure of samples increased linearly with the increase of dry density in a semi-logarithmic plane. At the same dry density, the swelling pressure of pure bentonite was 100 times larger than that of pure claystone. For the bentonite/claystone mixtures, the higher the bentonite fraction, the larger the final swelling pressure.

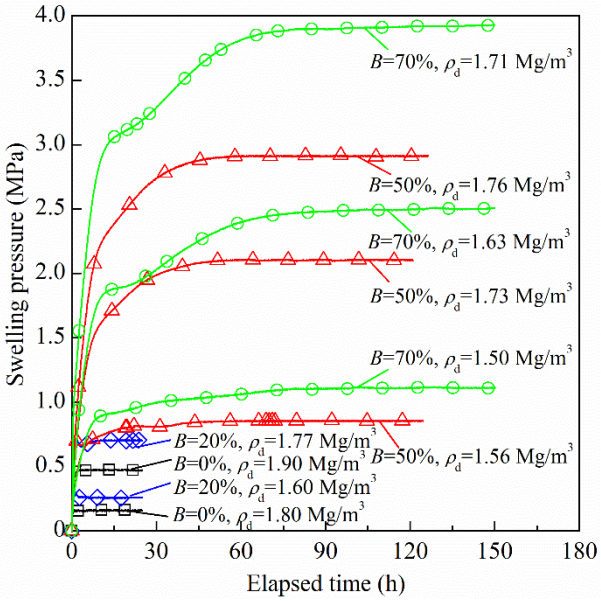

Fig. 3. Typical evolutions of the global swelling pressure of samples with various bentonite fractions and dry densities

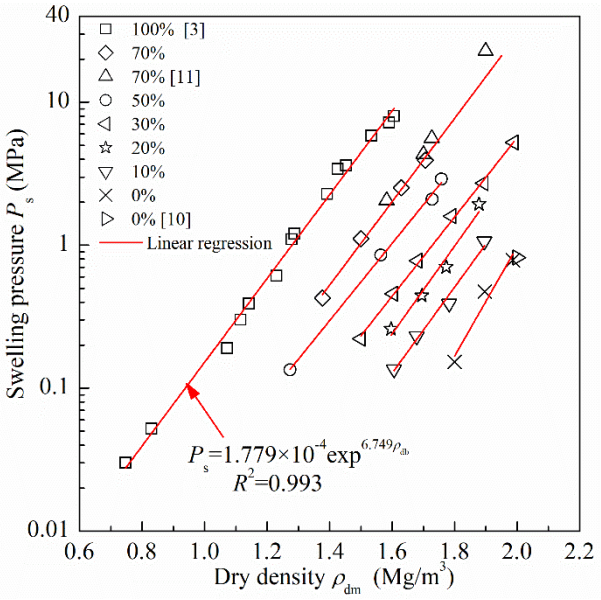

Fig. 4. Variation of the final swelling pressure with sample dry density

3.2 Volume change behaviour of claystone grains in the mixtures

When the bentonite/claystone mixtures were hydrated, the bentonite grains are expected to rapidly swell and fill up the voids in the mixtures, thanks to their extremely high swelling capacity, while the claystone grains are expected to adsorb water under the pressure applied by the swollen bentonite [13, 15]. This implies that the pressure at the interface of bentonite and claystone was governed by the bentonite property. Note that the water pressure was quite low and the pressure at the interface of bentonite and claystone could be considered as an effective stress. To clarify the role of the claystone in the mixture, an additional assumption was made:

the pressure at the interface of bentonite and claystone was equal to the global swelling pressure (Fig. 5a and b), as suggested by Yang et al. [12] when dealing with the consolidation behaviour of a lumpy granular soil under one-dimensional condition. Thereby, given the measured global swelling pressure of mixture (P_s in MPa), the final bentonite dry density in the mixture (ρ_{db} in Mg/m^3) can be estimated according to the relationship between the swelling pressure and the final dry density of pure bentonite (Fig. 4):

$$P_s=1.779\times10^{-4}\exp^{6.749\rho_{db}} \quad (1)$$

Based on the binary composition of the mixture, the final claystone dry density (ρ_{dc} in Mg/m^3) in the mixture can be deduced using Eq. (2):

$$\rho_{dc}=\frac{\rho_{db}\rho_{dm}(1-B/100)}{\rho_{db}-\rho_{dm}(B/100)} \quad (2)$$

where ρ_{dm} is the final mixture dry density (expressed in Mg/m^3) and ρ_{db} is the final bentonite dry density (expressed in Mg/m^3).

For pure claystone (B=0), the COx claystone swelled and filled up the voids between grains, becoming continuous (Fig. 5c). Thus, the final COx claystone dry density after saturation is equal to the global dry density.

Correspondingly, the final claystone void ratio e_c in the mixture and pure claystone can be determined:

$$e_c=\frac{G_{sc}\rho_w}{\rho_{dc}}-1 \quad (3)$$

where G_{sc} is the specific gravity of claystone and ρ_w is the water unit mass.

In order to describe the volume change behaviour of claystone grain after hydration, the claystone volumetric strain (ε_v) was determined using Eq. (4):

$$\varepsilon_v=\frac{e_c-e_c^0}{(1+e_c^0)}=\frac{\rho_{dc}^0}{\rho_{dc}}-1 \quad (4)$$

where e_c^0 is the initial void ratio of claystone grain and ρ_{dc}^0 is the initial dry density (equal to 2.31 Mg/m^3). According to Eqs. (1), (2), (3) and (4), the claystone void ratios and the volumetric strains of claystone for all the samples with various bentonite fractions and dry densities were calculated and the calculated results are summarized in Table 2. For further analysis, the results of Wang et al. [11] were collected and analysed in the same fashion. Fig. 6 depicts the variation of volumetric strain with the pressure applied by the swollen bentonite. It appears that the

volumetric strain of claystone decreased with the increase of pressure, regardless of the bentonite fraction. Moreover, the claystone grains swelled under low pressures and collapsed under high pressures.

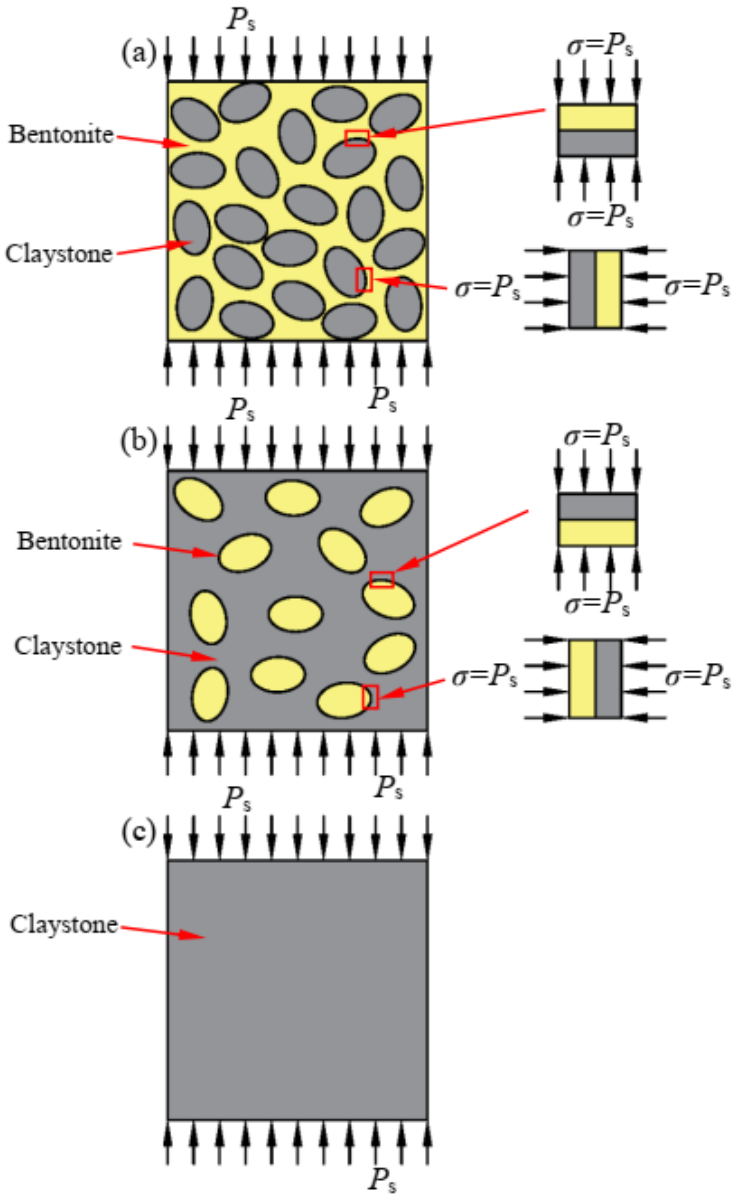

Fig. 5. Structure sketch of the samples after saturation: (a) mixtures with a large bentonite fraction, (b) mixtures with a small bentonite fraction, and (c) pure claystone. Note: the zones for bentonite and claystone after full saturation include voids in them

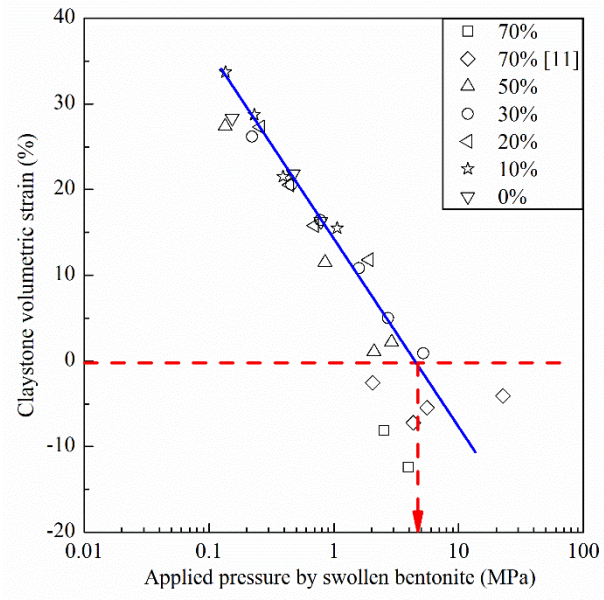

Fig. 6. Relationship between the claystone volumetric strain and the applied pressure by swollen bentonite

3.3 Swelling pressure of claystone grains

To further verify the swelling mechanism of claystone in its mixtures with bentonite, the swelling pressure of claystone grain was indirectly determined and then compared with that measured on intact COx claystone. According to the load-swell method, the volume changes of claystone grains subjected to various stresses were measured. This allowed the indirect determination of the swelling pressure of claystone grains. The swelling pressure corresponds to the stress at the intersection of the volumetric strain curve (represented by the blue solid line in Fig. 6) with the no volume change line (represented by the dash line in Fig. 6). A swelling pressure of about 4.9 MPa was thus determined for the claystone grain. Note that this swelling pressure referred to a mean value of those in all directions.

Using constant-volume, load-swell and Cui' methods, Zhang et al. [19] performed a series of swelling pressure tests on intact COx claystone, which had a similar water content to the crushed claystone powders used in this study (6.1%). They found that there was a good relationship between the swelling pressure ($P_{s\text{-}per}$ in MPa) and void ratio (e) (Fig. 7):

$$P_{s\text{-}per}=1.365\times10^{6}\exp^{-71.562e} \quad (5)$$

According to Eq. (5), the intact COx claystone with a void ratio of 0.17 corresponded to a swelling pressure of 7.11 MPa. It is worth noting that this swelling pressure was measured in the direction perpendicular to the stratification of claystone and did not represent the mean value. The measured swelling pressure corresponded to an effective stress because the pore

water pressure could be ignored during the testing [17]. Moreover, in the swelling pressure test, the intact claystone was placed in oedometer cell and it swelled under zero lateral deformation condition or K_0 condition. According to the empirical relationship proposed by Mayne & Kulhawy [6], the earth pressure coefficient at rest K_0 (ratio of horizontal and vertical effective stresses) for over-consolidated soil can be estimated using Eq. (6):

$$K_0=(1-\sin\varphi_c)\mathrm{OCR}^{\sin\varphi_c} \tag{6}$$

where OCR and φ_c are the over-consolidation ratio and the effective internal friction angle, respectively. The over-consolidation ratio is defined as the ratio of pre-consolidation stress to the current vertical stress. Based on the results from oedometer compression test on intact COx claystone, in which the loading direction was perpendicular to the stratification of claystone [8], the pre-consolidation stress was estimated at 8.5 MPa and the OCR value at 1.20 under a vertical swelling pressure of 7.11 MPa. Zhang et al. [16] investigated the shear strength of intact COx claystone by carrying out triaxial compression tests and found that the internal friction angle of intact COx claystone was about 24°. From the over-consolidation ratio and the effective internal friction angle, the K_0 value was estimated at 0.64. Substituting the swelling pressure in the direction perpendicular to the stratification and K_0 value into Eq. (7) yields the mean swelling pressure ($P_{\text{s-mean}}$ in MPa):

$$P_{\text{s-mean}}=P_{\text{s-per}}\frac{1+2K_0}{3} \tag{7}$$

The estimated mean swelling pressure of intact COx claystone was 5.39 MPa, which was quite close to the value of 4.9 MPa indirectly determined from the swelling pressure tests on the bentonite/claystone mixtures. This confirmed the reliability of the assumptions made above and the relevance of the identified swelling mechanism for claystone in its mixtures with bentonite. Upon hydration, the bentonite grains in the mixtures would swell rapidly due to their high swelling capacity while the claystone grains adsorbed water and then swelled or collapsed under the pressure applied by the previously swollen bentonite. The identified mechanism can be extended to other binary mixtures composed of two clays with extremely different swelling capacities.

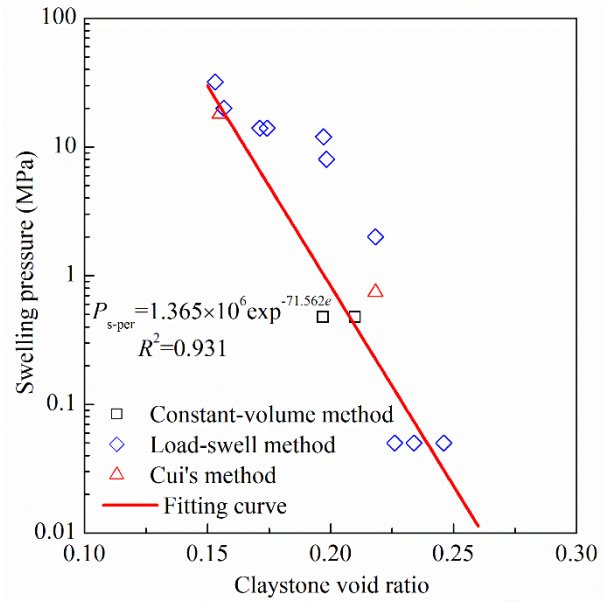

Fig. 7. Swelling pressure versus claystone void ratio of intact claystone (modified after Zhang et al. [19])

4 Conclusions

The swelling pressures of MX80 bentonite/COx claystone mixtures with various bentonite fractions and dry densities were experimentally investigated in the laboratory. By considering the interaction between bentonite and claystone grains during hydration, the claystone void ratio in the mixtures after hydration was estimated based on the relationship between the swelling pressure and dry density of pure bentonite. Comparison of the claystone void ratio after hydration with the initial one allowed the volumetric strains of claystone grains under different stresses to be obtained. It was found that the volumetric strain decreased linearly with the increase of pressure applied by the swollen bentonite. According to this relationship, the mean swelling pressure of claystone grain was indirectly determined.

Additionally, the mean swelling pressure of claystone grain was estimated according to the relationship between the void ratio and the swelling pressure in the direction perpendicular to the stratification of intact COx claystone. The estimated value was found to be comparable to that indirectly determined from the swelling pressure tests on bentonite/claystone mixtures. This confirmed the identified swelling mechanism of COx claystone grain in its mixtures with bentonite: the claystone grains adsorbed water under the pressure applied by the previously swollen bentonite.

Notably, the swelling pressure of claystone with a specified water content was determined in

this study. The influence of initial water content on the swelling pressure of claystone powders will be investigated in further studies.

Acknowledgments

The authors thank the Chinese Scholar Council (CSC) and the French National Radioactive Waste Management Agency (Andra) for the financial supports.

References

1. Andra (2005). Dossier 2005 Argile - Synthesis: Evaluation of the Feasibility of a Geological Repository in an Argillaceous Formation (Meuse/ Haute-Marne Site). French National Radioactive Waste Management Agency, Chatenay-Malabry CEDEX 241 pp. Accessed 22 November 2018

2. Agus SS, Schanz T (2008) A method for predicting the swelling pressure of compacted bentonites. Acta Geotech 3(2): 125

3. Karnland O, Nilsson U, Weber H, Wersin P (2008) Sealing ability of Wyoming bentonite pellets foreseen as buffer material–laboratory results. Phys Chem Earth Parts A/B/C 33: S472–S475

4. Komine H, Ogata N (1994) Experimental study on swelling characteristics of compacted bentonite. Can Geotech J 31(4): 478–490

5. Komine H, Ogata N (1999) Experimental study on swelling characteristics of sandbentonite mixture for nuclear waste disposal. Soils Found 39(2): 83–97

6. Mayne PW, Kulhawy FH (1982) Ko-OCR Relationships in Soil. Journal of the Soil Mechanics and Foundations Division 108(6): 851-872

7. Middelhoff M, Cuisinier O, Masrouri F, Talandier J, Conil N (2020) Combined impact of selected material properties and environmental conditions on the swelling pressure of compacted claystone/bentonite mixtures. Appl Clay Sci 184: 105389

8. Mohajerani M, Delage P, Monfared M, Tang AM, Sulem J, Gatmiri B (2011) Oedometric compression and swelling behaviour of the Callovo-Oxfordian argillite. Int J Rock Mech Min Sci 48(4): 606-615

9. Sun DA, Cui H, Sun WJ (2009) Swelling of compacted sand-bentonite mixtures. Appl Clay Sci 43(3–4): 485–492

10. Tang CS, Tang AM, Cui YJ, Delage P, Schroeder C, De Laure E (2011) Investigating the pressure of compacted crushed-Callovo-Oxfordian claystone. Phys Chem Earth Parts A/B/C 36(17-18): 1857-1866

11. Wang Q, Tang AM, Cui YJ, Delage P, Gatmiri B (2012) Experimental study on the swelling behaviour of bentonite/claystone mixture. Eng Geol 124: 59–66

12. Yang LA, Tan TS, Tan SA, Leung CF (2002) One-dimensional self-weight consolidation of a lumpy clay fill. Géotechnique 52(10): 713-725

13. Zeng ZX, Cui YJ, Zhang F, Conil N, Talandier J (2019) Investigation of swelling pressure of bentonite/claystone mixture in the full range of bentonite fraction. Appl Clay Sci https://doi.org/10.1016/j.clay.2019.105137

14. Zeng ZX, Cui YJ, Conil N, Talandier J (2020a) Effects of technological voids and hydration time on the hydro-mechanical behaviour of compacted bentonite/claystone mixture. Géotechnique https://doi.org/10.1680/jgeot.19.P.220

15. Zeng ZX, Cui YJ, Conil N, Talandier J (2020b) Experimental Investigation and Modeling of the Hydraulic Conductivity of Saturated Bentonite–Claystone Mixture. Int J Geomech https://doi.org/10.1061/(ASCE)GM.1943-5622.0001817

16. Zhang CL, Czaikowski O, Rothfuchs T (2010) Thermo-Hydro-Mechanical behaviour of the Callovo-Oxfordian clay rock. In: Final report

17 Zhang CL, Wieczorek K, Xie ML (2010) Swelling experiments on mudstones. J Rock Mech Geotech Eng 2(1): 44-51

18. Zhang CL, Kröhn KP (2019) Sealing behaviour of crushed claystone–bentonite mixtures. Geomech Energy Environ 17: 90-105

19. Zhang F, Cui YJ, Conil N, Talandier J (2020) Assessment of swelling pressure determination methods with intact Callovo-Oxfordian claystone. Rock Mech Rock Eng 53(4): 1879-1888

Zeng, Z.X., Cui, Y.J., Zhang, F., Conil, N., Talandier, J. 2019. Applied Clay Science, 178, 105137.

Investigation of swelling pressure of bentonite/claystone mixture in the full range of bentonite fraction

Zhixiong Zeng[1], Yu-Jun Cui[1], Feng Zhang[1], Nathalie Conil[2], Jean Talandier[3]

Abstract: MX80 bentonite/Callovo-Oxfordian (COx) claystone mixture has been proposed as a sealing/backfill material in a deep geological repository of radioactive waste in France. A good understanding of the swelling behaviour of this mixture is essential when evaluating the long-term performance of the repository. In this work, the swelling pressure of MX80 bentonite/COx claystone mixture was investigated by the constant-volume method for a full range of bentonite fraction. Results show that the swelling of claystone in the mixture can be inhibited by bentonite and its contribution to the global swelling pressure depends on the bentonite fraction. For the mixture with more than 70% bentonite, claystone behaves as an inert material, and its contribution to the global swelling pressure can be ignored. However, for the mixture with less bentonite, the swelling of claystone will significantly contribute to the global swelling pressure. A method was proposed allowing the swelling pressure of bentonite/claystone mixture to be predicted in the full range of bentonite fraction.

Keywords: bentonite/claystone mixture; swelling pressure; bentonite dry density; inhibition effect; prediction method

1 Introduction

Deep geological disposal has been adopted for radioactive waste in many countries such as China, Belgium, France, Germany, Japan, Sweden, etc. (Gray et al., 1984; Dixon et al., 1985; Sellin and Leupin, 2013). To ensure the isolation of radioactive waste from the surrounding environment, bentonite-based materials are often considered as possible sealing/backfill materials because of their favorable swelling characteristics and low permeability (Pusch, 1982; Dixon et al., 1985; Komine and Ogata, 1994; 1999; Villar and Lloret, 2008). Once the disposal galleries are closed, pore water from the host rock will progressively infiltrate into the sealing/backfill materials. They will swell and seal the technological voids between the blocks of compacted bentonite-based materials or between the blocks and the canisters/the host rock

1 Laboratoire Navier/CERMES, Ecole des Ponts ParisTech, 6 et 8 avenue Blaise Pascal, 77455 Marne La Vallée cedex 2, France
2 Centre de Meuse/Haute-Marne, RD 960, 55290 Bure, France
3 1/7, rue Jean Monnet, 92298 Châtenay-Malabry cedex, France

(Bian et al., 2018). Afterwards, swelling pressure will develop (Pusch, 1982; Wang et al., 2012). This swelling pressure must be high enough to ensure the good sealing performance, but lower than the in situ minor stress in the host rock (Saba et al., 2014). Therefore, the swelling pressure of bentonite-based materials becomes a key factor in the design of deep geological repositories.

In the past decades, pure bentonite or bentonite/sand mixture was widely investigated as a sealing/backfill material for the easy control of its swelling pressure (Komine and Ogata, 1994; 1999). A number of studies have been conducted on the swelling pressure of different compacted bentonites and their mixture with sand, such as Kunigel-V1 bentonite (Sun et al., 2009), MX80 bentonite (Karnland et al., 2008; Saba et al., 2014), Calcigel bentonite (Agus and Schanz, 2008), Tsukinuno bentonite (Komine and Ogata, 1999) and GMZ bentonite (Ye et al., 2007; Cui et al., 2012; Sun et al., 2015; 2017). The swelling pressure of bentonite/sand mixture has been characterized quantitatively based on the montmorillonite void ratio (Sun et al., 2009; Sun et al., 2015; 2017), dry density of bentonite (Dixon et al., 1985; Lee et al., 1999; Agus and Schanz, 2008), effective dry density of montmorillonite (Dixon et al., 2002; Powell et al., 2013), and initial degree of saturation of montmorillonite (Rao and Ravi, 2015).

The French National Radioactive Waste Management Agency (Andra) proposed to use a mixture of bentonite and excavated Callovo-Oxfordian (COx) claystone as the sealing/backfill material. This aims to reduce the excavation waste and to better ensure the compatibility of chemistry with the host rock (Tang et al., 2011; Wang et al., 2012; 2014). Wang et al. (2012) worked on a MX80 bentonite/crushed COx claystone mixture at a proportion of 70/30 in dry mass and found that the unique relationship between the swelling pressure and bentonite dry density could be extended to this mixture, the contribution of claystone to swelling pressure being negligible. However, the swelling mechanism of bentonite/claystone mixtures with bentonite fractions lower than 70% has not been well understood.

In this study, the swelling pressure of MX80 bentonite/crushed COx claystone mixture with different dry densities and bentonite fractions was studied. The role of claystone in the development of swelling pressure of the mixture was analyzed, allowing an inhibition factor to be defined for describing the effect of bentonite on the swelling of claystone. A novel method was then proposed to predict the swelling pressure of bentonite/claystone mixture in the full range of bentonite fraction.

2 Materials and experimental methods

2.1 Materials

The commercial MX80 bentonite tested in this study was extracted from Wyoming, USA. Table 1 summarizes the basic physical and chemical properties of MX80 bentonite. The maximum grain size of the bentonite powder is 2 mm and the clay-size fraction (< 2 μm) represents 84%. The density of bentonite grains was measured to be 2.00 Mg/m^3 by immersing clay powders into a non-aromatic hydrocarbon fluid (Kerdane) using a pycnometer. The initial suction measured by hygrometer WP4 was 101 MPa.

The COx claystone was extracted at around 490 m depth from the Underground Research Laboratory (URL) at Bure, France. The claystone contains 40-45% clay minerals (mainly interstratified illite/smectite), 30% carbonates and 2-30% quartz and feldspar, with a specific gravity of 2.70 (Fouché et al., 2004). It was crushed into fine powders with grain size less than 2.0 mm. More than 30% grains were smaller than 2 μm. The density of the claystone grains is 2.31 Mg/m^3. The initial suction measured by hygrometer WP4 was 27 MPa.

Table 1. Physical and chemical properties of MX80 bentonite (data from Tang et al. (2008), Saba (2013) and Wang et al. (2014))

Soil property	Description
Specific gravity	2.76-2.77
Consistency limit	
Liquid limit (%)	520-575
Plastic limit (%)	42-53
Plasticity index (%)	478-522
Cation exchange capacity (CEC) (meq/100 g)	78-85
Main exchangeable cations (meq/100 g)	
Na^+	60-67
K^+	1
Mg^{2+}	3-4
Ca^{2+}	5-8
Main minerals	
Montmorillonite (%)	70-92
Quartz (%)	3-15

In this study, synthetic water (see Table 2 for the recipe of preparation), which has the same chemical composition as the site groundwater from the URL in Bure, was used for hydration. The total mass of dissolved solids is 4.545 g/L, which corresponds to a salinity (ratio of salt mass to solution mass) lower than 0.5%.

Table 2. Recipe for preparing the synthetic water

Components	NaCl	$NaHCO_3$	KCl	$CaSO_4$▪$2H_2O$	$MgSO_4$▪$7H_2O$	$CaCl_2$▪$2H_2O$	Na_2SO_4	Total
Content (g/L)	1.950	0.130	0.035	0.630	1.020	0.080	0.700	4.545

2.2 Sample preparation

A series of tests were conducted on compacted claystone and MX80 bentonite/claystone mixtures with bentonite fractions of 10, 20, 30, 50, and 70% in dry mass. The bentonite and claystone, with initial water contents of 11.4% and 6.1%, respectively, were mixed for more than 10 min to reach a homogeneous state. Subsequently, samples were statically compacted in a cylindrical mold at a constant displacement rate of 0.05 mm/min to reach the target dry density (Table 3). This rate was chosen to ensure zero air over pressure in soil during compaction. After decompression, the samples had a diameter of 50 mm and a height of 10 mm.

Table 3. Test program and main results

Test No.	Bentonite fraction B (%)	Dry density of sample ρ_{dm} (Mg/m^3)	Initial water content w_m (%)	Bentonite dry density ρ_{db} (Mg/m^3)	Claystone void ratio e_c	Expected claystone void ratio e_c^e	Inhibition factor η	Final swelling pressure P_s (MPa)
01	70	1.38	9.8	1.15	0.08	0.42	0.81	0.43
02	70	1.50	9.8	1.29	0.13	0.34	0.60	1.11
03	70	1.63	9.8	1.42	0.07	0.28	0.74	2.53
04	70	1.71	9.8	1.48	0.02	0.25	0.91	3.94
05	50	1.27	8.8	0.98	0.49	0.52	0.06	0.13
06	50	1.56	8.8	1.26	0.30	0.36	0.16	0.85
07	50	1.73	8.8	1.39	0.18	0.29	0.38	2.10
08	50	1.76	8.8	1.44	0.19	0.27	0.28	2.91
09	30	1.50	7.7	1.06	0.47	0.47	0.00	0.22
10	30	1.60	7.7	1.16	0.41	0.41	0.00	0.46
11	30	1.68	7.7	1.24	0.36	0.37	0.02	0.78
12	30	1.79	7.7	1.35	0.30	0.31	0.06	1.59
13	30	1.89	7.7	1.43	0.23	0.28	0.18	2.72
14	30	1.99	7.7	1.52	0.18	0.23	0.23	5.23
15	20	1.60	7.2	1.08	0.49	0.46	-0.06	0.26
16	20	1.69	7.2	1.16	0.41	0.41	0.01	0.44
17	20	1.77	7.2	1.23	0.35	0.38	0.06	0.70
18	20	1.88	7.2	1.38	0.31	0.30	-0.02	1.93
19	10	1.61	6.6	0.98	0.56	0.52	-0.08	0.14
20	10	1.68	6.6	1.06	0.50	0.47	-0.07	0.23
21	10	1.78	6.6	1.14	0.42	0.42	0.01	0.39
22	10	1.90	6.6	1.29	0.35	0.34	-0.02	1.07
23	0	1.80	6.1	-	-	-	0	0.15
24	0	1.90	6.1	-	-	-	0	0.47
25	0	1.99	6.1	-	-	-	0	0.79

2.3 Experimental methods

Twenty-five swelling pressure tests were carried out using a constant-volume cell at a temperature of 20±1°C. The details about the constant-volume cell can be found in Saba et al. (2014). The compacted samples were pushed into the testing cell from the mold and placed between two porous stones and filter papers. The top cap was locked by a screw. The samples were hydrated from bottom through the water inlet connected to the synthetic water reservoir. The swelling pressure was monitored by a force transducer mounted below the test cell and all data were collected by a data logger. The maximum deformations of the apparatus and filter papers in this study were estimated to be 0.0049 and 0.0169 mm, corresponding to a small reduction of 2.3% in maximum swelling pressure. Thus, the volume change of samples throughout the water-uptake process was ignored.

3 Experimental results

3.1 Swelling pressure kinetics

The evolution of swelling pressure for samples with different bentonite fractions and dry densities is presented in Fig. 1. On the whole, for the samples with high bentonite fractions (larger than 50%) and high dry densities (larger than 1.50 Mg/m^3), the swelling pressure increased rapidly and then reached stabilization. For the samples with low bentonite fractions (smaller than 20%) and low dry densities (smaller than 1.78 Mg/m^3), the swelling pressure started with a fast increase followed by a peak value, a decrease and then reached stabilization. The presence of these peaks is related to the collapse of macro-pores between soil grains (Pusch, 1982; Komine and Ogata, 1994). The lower the dry density, the larger the volume of the macro-pores among grains (Lloret and Villar, 2007). At the same dry density, more macro-pores are expected in the samples with larger fractions of claystone, because of the higher unit mass of claystone (2.31 Mg/m^3) as compared with that of bentonite (2.00 Mg/m^3). It can also be observed that the time required to reach stabilization decreased with the decrease of dry density and bentonite fraction, which can be explained by the higher hydraulic conductivity of samples with a lower dry density and a larger claystone fraction.

3.2 Relationship between final swelling pressure and dry density of the mixture

Fig. 2 depicts the changes of final swelling pressure (P_s) with the dry density of samples. The results of Karnland et al. (2008) on pure MX80 bentonite, Tang et al. (2011) on pure COx claystone, Wang et al. (2012) and Zhang and Kröhn (2019) on MX80 bentonite/COx claystone mixture are also presented. The swelling pressure values remarkably agree even though the

tested materials were from different batches, suggesting that the influence of MX80 bentonite and claystone batches was not enough as to be relevant in the swelling pressure tests. For a given bentonite fraction, the final swelling pressure increased with increasing dry density. At the same dry density, the final swelling pressure of bentonite/claystone mixture after saturation was much lower than that of pure bentonite, indicating that the addition of claystone reduced the global swelling capability.

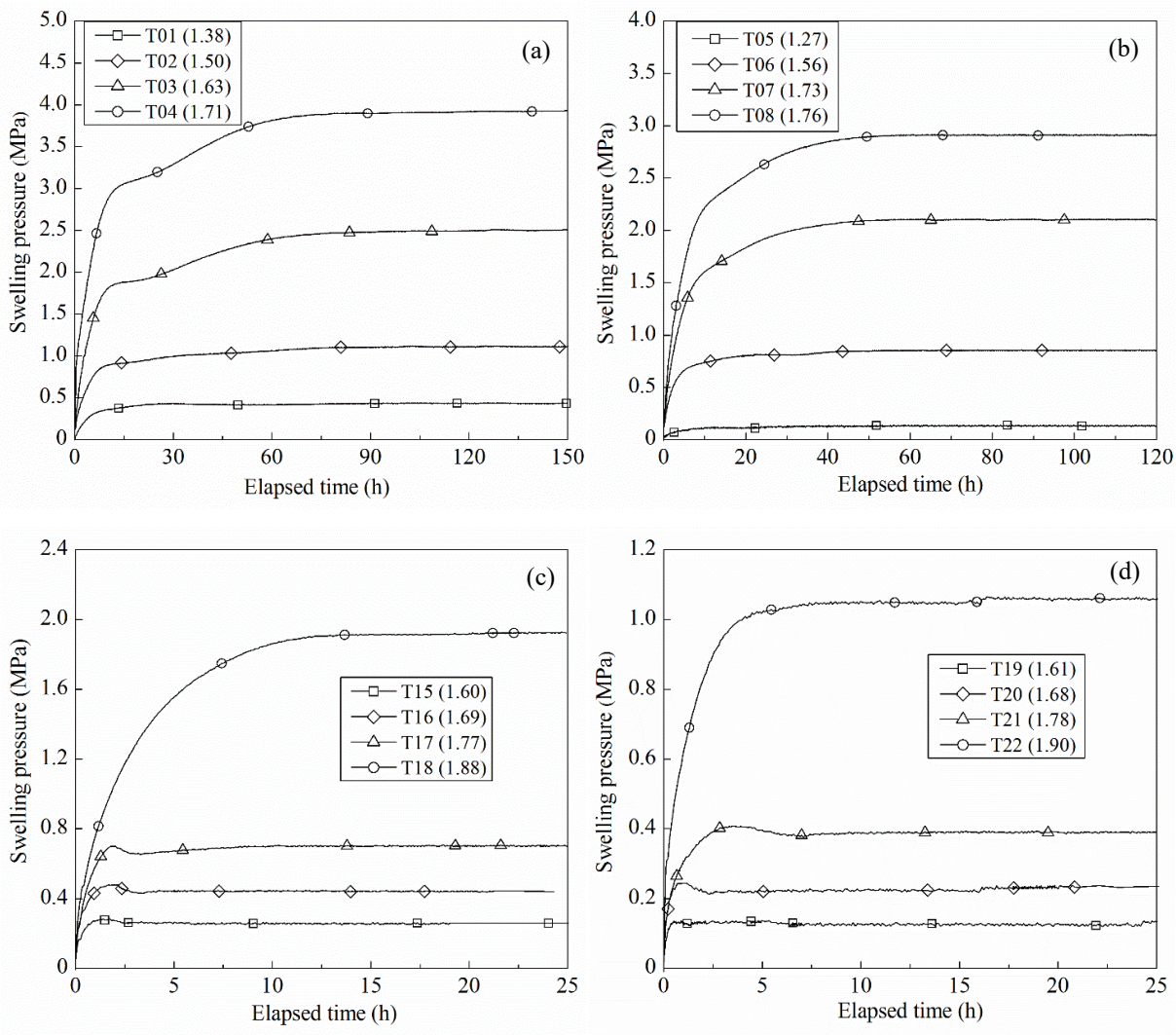

Fig. 1. Evolution of swelling pressure of bentonite/claystone mixture with bentonite fractions of (a) 70%; (b) 50%; (c) 20%; (d) 10%

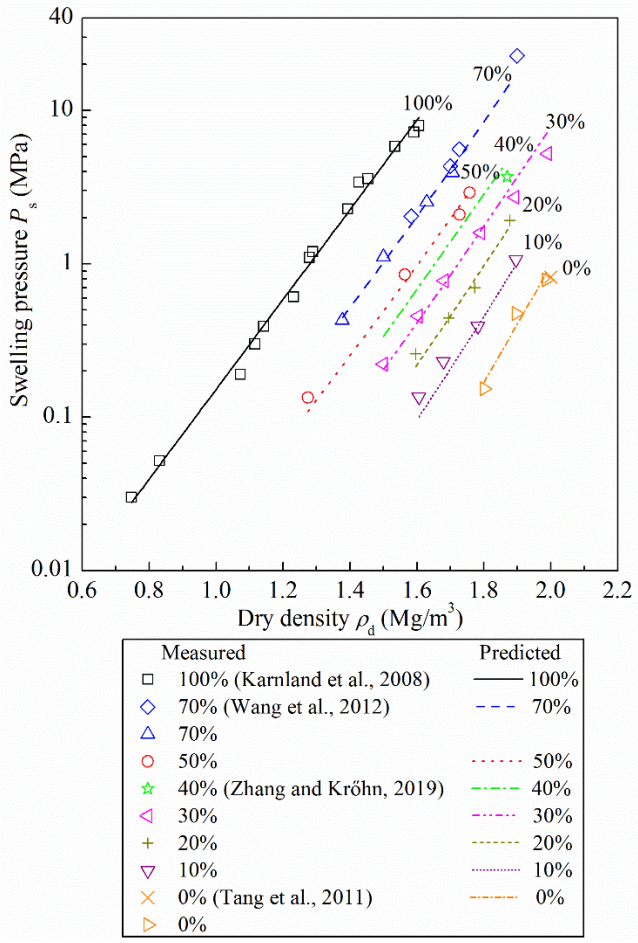

Fig. 2. Measured and predicted swelling pressures as function of the dry density of samples. Note: the legend indicates the bentonite fraction

4 Interpretation and discussion

4.1 Contribution of claystone to swelling pressure

As shown in Fig. 3a, each bentonite-based mixture after the full bentonite hydration process can be divided into four parts: bentonite, voids in bentonite, additive (crushed COx claystone or sand) and voids in additive (Wang et al., 2012; Deng et al., 2017). The bentonite dry density (ρ_{db}) can be formulated by the following equation:

$$\rho_{db}=\frac{(B/100)\rho_m G_{sa}\rho_w}{G_{sa}\rho_w(1+w_m/100)-\rho_m(1-B/100)(1+G_{sa}w_a)}=\frac{(B/100)\rho_{dm} G_{sa}\rho_w}{G_{sa}\rho_w-\rho_{dm}(1-B/100)(1+G_{sa}w_a)} \quad (1)$$

where ρ_m (Mg/m^3) is the mixture density; ρ_{dm} (Mg/m^3) is the dry density of the mixture; ρ_w is the water unit mass; B (%) is the bentonite fraction (in dry mass) in the mixture; w_m is the water content of the mixture; w_a is the water content of additive; G_{sa} is the specific gravity of additive.

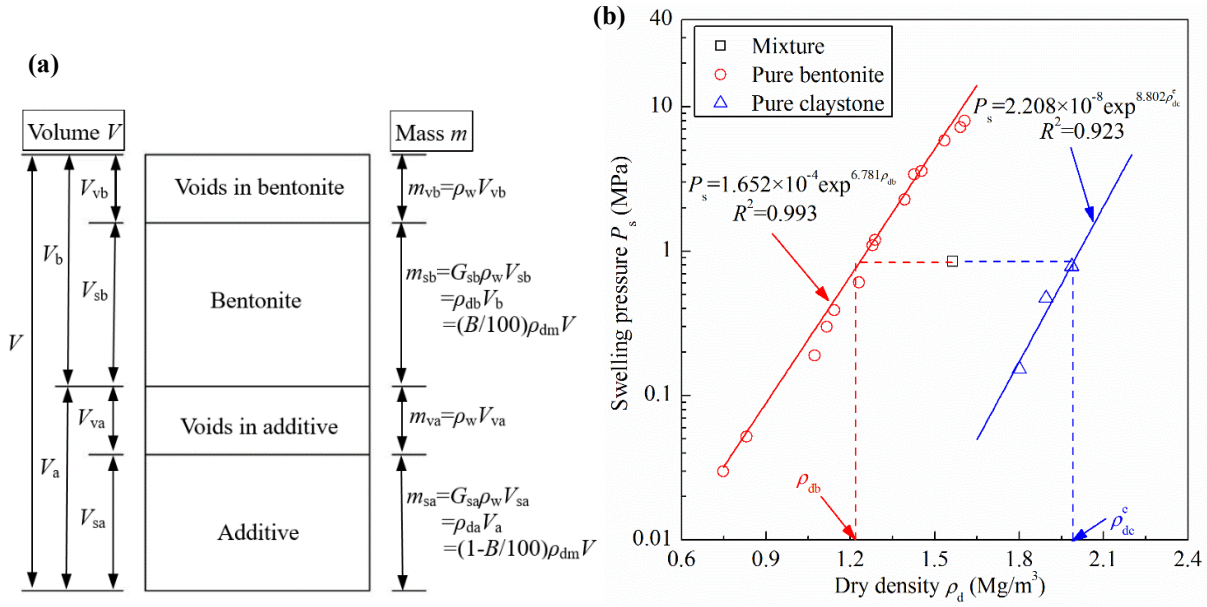

Fig. 3. Composition of bentonite/additive mixture (a) and calculation of bentonite dry density and expected claystone dry density of bentonite/claystone mixture (b)

For bentonite/sand mixtures, the water content of inactive sand is regarded as zero and the bentonite dry density can be calculated directly using Eq. (1). A unique relationship has been identified between swelling pressure and dry density of Avonseal (Gray et al., 1984), Calcigel (Agus and Schanz, 2008), GMZ (Cui et al., 2012) and MX80 (Saba, 2013) bentonites regardless of the bentonite fraction. For the MX80 bentonite/claystone mixture, the bentonite dry density of samples cannot be calculated directly since the water content of claystone after saturation is unknown. In terms of swelling pressure, the swelling capacity of pure bentonite is more than 100 times larger than that of pure claystone at the same dry density (Fig. 3b) and the initial suction of pure bentonite is about 4 times higher than that of pure claystone. During wetting, the bentonite in the mixture swelled rapidly and came in full contact with the claystone while the volume change of the claystone was influenced by the swelling pressure from bentonite. To determine the bentonite and claystone dry densities, the final pressure at the interface of bentonite and claystone grains was assumed to be equal to the global swelling pressure. This assumption was also adopted by Yang et al. (2002) when investigating the consolidation behavior of lumpy granular soil under one-dimensional condition. In this case, the bentonite dry density in the mixture can be estimated according to the relationship between the swelling pressure of pure bentonite and its dry density (Fig. 3b):

$$P_s=1.652\times10^{-4}\exp^{6.781\rho_{db}} \quad (2)$$

At a certain global swelling pressure P_s, the corresponding bentonite dry density ρ_{db} in the bentonite/claystone mixture can be back-calculated through the unique relationship for pure

bentonite. The claystone dry density ρ_{dc} in the mixture, the ratio of solid mass of claystone to the volume occupied by claystone (Fig. 3a), can be calculated using Eq. (3):

$$\rho_{dc}=\frac{m_{sc}}{V\text{-}V_b}=\frac{V\rho_{dm}(1\text{-}B/100)}{V\text{-}\frac{V\rho_{dm}(B/100)}{\rho_{db}}}=\frac{\rho_{db}\rho_{dm}(1\text{-}B/100)}{\rho_{db}\text{-}\rho_{dm}(B/100)} \quad (3)$$

where m_{sc} is the solid mass of claystone; V is the total volume of the mixture; V_b is the volume of bentonite.

Then, the claystone void ratio e_c in the mixture can be deduced using Eq. (4):

$$e_c=\frac{G_{sc}\rho_w}{\rho_{dc}}\text{-}1 \quad (4)$$

where G_{sc} is the specific gravity of claystone. The calculated e_c is summarized in Table 3.

If the claystone can swell without the influence of bentonite, the expected claystone dry density ρ_{dc}^{e} needed to achieve the above swelling pressure P_s can be similarly obtained from the correlation between the swelling pressure of pure claystone and its dry density (Fig. 3b):

$$P_s=2.208\times10^{-8}\exp^{8.802\rho_{dc}^{e}} \quad (5)$$

Correspondingly, the expected claystone void ratio e_c^e can be deduced using Eq. (6):

$$e_c^e=\frac{G_{sc}\rho_w}{\rho_{dc}^{e}}\text{-}1 \quad (6)$$

During wetting, the stress states of claystone grains in bentonite/claystone mixture and pure claystone are different. In the former, the wetting of claystone is under the pressure imposed by the swelling of bentonite and the water absorption of claystone is restrained (Attom and Barakat, 2000). By contrast, in the latter, the pressure between claystone grains gradually increases with wetting. Therefore, at a given global swelling pressure, e_c in the bentonite/claystone mixture should be smaller than e_c^e, which is corroborated by the calculated result in Table 3. The difference between e_c and e_c^e physically represents the inhibition degree of bentonite on the swelling of claystone. On the whole, the larger the bentonite fraction, the larger the difference and the greater the inhibition effect.

For further analysis of the interaction between bentonite and claystone in swelling pressure development, an inhibition factor η is defined as follows:

$$\eta=\frac{e_c^e\text{-}e_c}{e_c^e}=1\text{-}\frac{e_c}{e_c^e} \quad (7)$$

The calculated inhibition factor values for the samples tested are summarized in Table 3. Fig. 4a depicts the variation of η with bentonite fraction. For pure bentonite, the value of inhibition

factor is 1; for pure claystone, it equals 0. The inhibition factor increases with the increasing bentonite fraction, following a nonlinear relationship. This relationship can be well described by the following expression with a squared correlation coefficient $R^2 = 0.972$:

$$\eta = \frac{1}{1+e^{10.664(0.595-B/100)}} \tag{8}$$

From Fig. 4a, two inflection points of the sigmoidal curve can be identified, at approximately 40% and 70% bentonite fractions. The inhibition effect of bentonite on the swelling of claystone can be divided into three zones according to these two critical values, that is, Zone I, $100 \geqslant B \geqslant 70$; Zone II, $70 > B \geqslant 40$; Zone III, $40 > B \geqslant 0$. Fig. 4b shows the sketch of bentonite/claystone mixture before and after full saturation in the three zones.

In Zone I, $100 \geqslant B \geqslant 70$, the inhibition factor η is larger than 0.73. The fully swollen bentonite grains form a matrix and claystone grains disperse into the matrix. The claystone grains behave as an inert material and their swelling is almost completely inhibited by bentonite. After wetting, the claystone void ratio e_c in the mixture (Table 3) is even slightly less than the initial void ratio of claystone grain (0.17), due to the collapse of claystone under the swelling pressure induced by bentonite.

In Zone II, $70 > B \geqslant 40$, the inhibition factor η is between 0.11 and 0.73. The swelling of claystone grains is partially restrained by bentonite and the claystone can swell in volume and fill up some voids in the mixture. In this case, partially swelling of the claystone will contribute to the global swelling pressure.

In Zone III, $40 > B \geqslant 0$, the inhibition factor η is smaller than 0.11. Both claystone and bentonite grains swell upon wetting. The fully swollen bentonite grains disperse in the skeleton formed by the swollen claystone. The claystone void ratio e_c in the mixture is very close to the expected claystone void ratio e_c^e, suggesting that the global swelling pressure is governed by claystone.

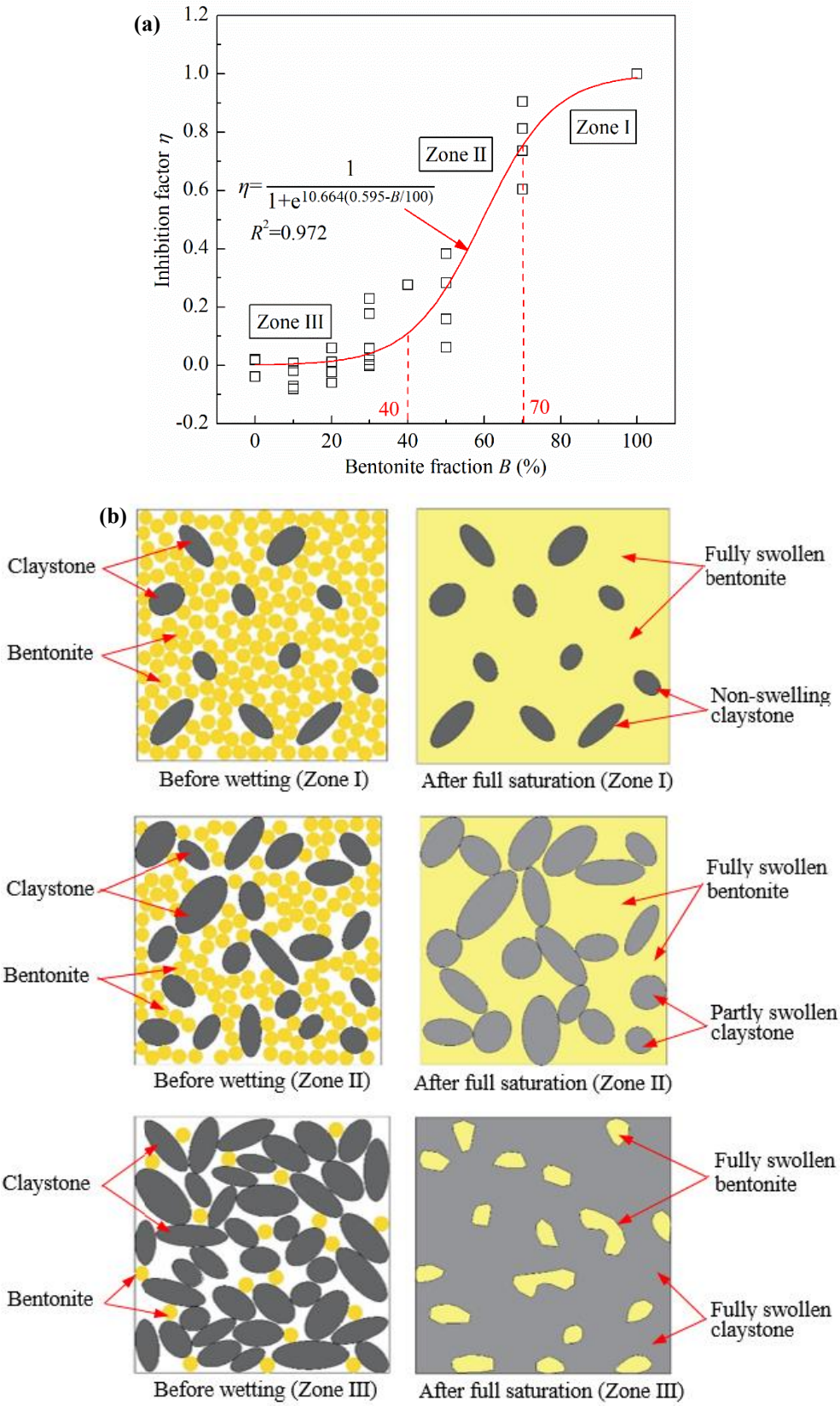

Fig. 4. Evolution of inhibition factor with bentonite fraction (a) and swelling mechanism of bentonite/claystone mixture in three zones (b). Note: the zones for bentonite and claystone after full saturation include voids in them

4.2 Estimation of swelling pressure of bentonite/claystone mixture

According to the inhibition factor determined above and the relationships between swelling pressure and dry density for pure bentonite and claystone, the swelling pressure of samples with different bentonite fractions and dry densities can be computed following an iteration procedure. Fig. 5 is a flowchart showing how to predict the swelling pressure of MX80 bentonite/COx claystone mixture in the full range of bentonite fraction. The general outline of this procedure is summarized as follows:

(a) to assign an initial value of swelling pressure P_0;

(b) to back-calculate the expected claystone dry density based on Eq. (5) and to determine the corresponding expected claystone void ratio using Eq. (6);

(c) to determine the inhibition factor using Eq. (8) and to compute the claystone void ratio in the bentonite/claystone mixture using Eq. (7);

(d) to apply Eq. (4) to calculate the claystone dry density and to back-calculate the bentonite dry density using Eq. (3);

(e) to compute the swelling pressure P_1 according to Eq. (2);

(f) to judge the absolute error between P_1 and P_0: if $|P_1-P_0|$ is smaller than a certain tolerance α (0.0001 MPa in this study), P_1 is the predicted value of swelling pressure; else, to assign $P_0 = P_1$ and to go to step (a) for a new iteration.

The predicted and the measured swelling pressures are compared in Fig. 2, as a function of the dry density of the mixture, showing a good agreement. This agreement shows the performance of the proposed method as well as the relevance of the identified swelling mechanism.

5 Conclusions

The swelling pressure of MX80 bentonite/COx claystone mixture with different bentonite fractions was investigated by carrying out constant-volume swelling pressure tests. The obtained results allow the following conclusions to be drawn:

The swelling of claystone in the mixture can be inhibited by bentonite and the contribution of claystone to the global swelling pressure depends on the bentonite fraction (B). An inhibition factor was introduced as a function of the bentonite fraction to describe the inhibition effect. According to two inflection points (40% and 70%), the inhibition effect can be divided into three zones ($100 \geqslant B \geqslant 70$; Zone Ⅱ, $70 > B \geqslant 40$; Zone Ⅲ, $40 > B \geqslant 0$). In Zone I, the swelling of claystone is almost totally inhibited by bentonite; in Zone II, the swelling of claystone grains is

partially restrained by bentonite and the claystone can swell and contribute to the global swelling pressure of the mixture; in Zone III, claystone fully swells upon wetting and the claystone governs the global swelling pressure.

A predictive method was proposed, allowing the swelling pressure of the mixture with different bentonite fractions and dry densities to be calculated. The good agreement between the calculated and measured swelling pressure values showed the performance of the proposed method as well as the relevance of the identified swelling mechanism.

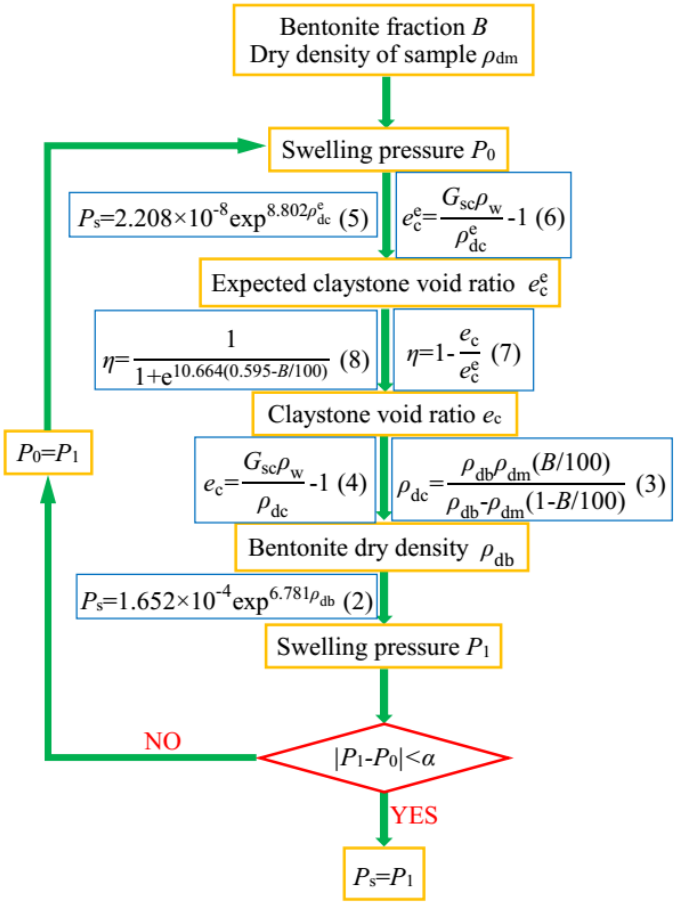

Fig. 5. Flowchart for swelling pressure prediction for bentonite/claystone mixture in the full range of bentonite fraction

Acknowledgments

The authors thank the China Scholarship Council (CSC). The support provided by the French National Radioactive Waste Management Agency (Andra) is also greatly acknowledged.

References

Agus, S.S., Schanz, T., 2008. A method for predicting the swelling pressure of compacted

bentonites. Acta Geotech. 3(2), 125.

Attom, M.F., Barakat, S., 2000. Investigation of three methods for evaluating swelling pressure of soils. Environ. Eng. Geosci. 6(3), 293-299.

Bian, X., Cui, Y.J., Li, X.Z., 2018. Voids effect on the swelling behaviour of compacted bentonite. Géotechnique, 1-13.

Cui, S.L., Zhang, H.Y., Zhang, M., 2012. Swelling characteristics of compacted GMZ bentonite–sand mixtures as a buffer/backfill material in China. Eng. Geol. 141, 65-73.

Deng, Y.F., Wu, Z.L., Cui, Y.J., Liu, S.Y., Wang, Q., 2017. Sand fraction effect on hydro-mechanical behavior of sand-clay mixture. Appl. Clay Sci. 135, 355-361.

Dixon, D.A., Gray, M.N., Thomas, A.W., 1985. A study of the compaction properties of potential clay-sand buffer mixtures for use in nuclear fuel waste disposal. Eng. Geol. 21(3/4):247-255.

Dixon, D.A., Chandler, N.A., Baumgartner, P., 2002. The influence of groundwater salinity and influences on the performance of potential backfill materials. Proceedings of the 6th International Workshop on Design and Construction of Final Reposito- ries, Backfilling in Radioactive Waste Disposal, Brussels, Belgium, 11–13 March 2002. ONDRAF/NIRAS, Brussels, Belgium (Transactions, Session IV, paper 9).

Fouché, O., Wright, H., Le Cléac'h, J.M., Pellenard, P., 2004. Fabric control on strain and rupture of heterogeneous shale samples by using a non-conventional mechanical test. Appl. Clay Sci. 26(1-4), 367-387.

Gray, M.N., Cheung, S.C.H., Dixon, D.A., 1984. Swelling pressures of compacted bentonite/sand mixtures. Mat. Res. Soc. Symp, 44, 523-530.

Karnland, O., Nilsson, U., Weber, H., Wersin, P., 2008. Sealing ability of Wyoming bentonite pellets foreseen as buffer material–laboratory results. Phys. Chem. Earth Parts A/B/C, 33, S472-S475.

Komine, H., Ogata, N., 1994. Experimental study on swelling characteristics of compacted bentonite. Can. Geotech. J. 31(4), 478-490.

Komine, H., Ogata, N., 1999. Experimental study on swelling characteristics of sand-bentonite mixture for nuclear waste disposal. Soils Found. 39(2), 83-97.

Lee, J.O., Cho, W.J., Chun, K.S., 1999. Swelling pressures of a potential buffer material for high-level waste repository. J. Korean Nucl. Soc. 31(2), 139-150.

Lloret, A., Villar, M.V., 2007. Advances on the knowledge of the thermo-hydro-mechanical behaviour of heavily compacted “FEBEX” bentonite. Phys. Chem. Earth Parts A/B/C 32(8-14), 701-715.

Powell, J.S., Siemens, G.A., Take, W.A., Remenda, V.H., 2013. Characterizing the swelling potential of Bearpaw clayshale. Eng. Geol. 158, 89-97.

Pusch, R., 1982. Mineral–water interactions and their influence on the physical behavior of

highly compacted Na bentonite. Can. Geotech. J. 19(3), 381-387.

Rao, S.M., Ravi, K., 2015. Influence of initial degree of saturation on swell pressures of compacted Barmer bentonite specimens. Ann. Nucl. Eng. 80, 303-311.

Saba, S., 2013. Hydro-mechanical behaviour of bentonite-sand mixture used as sealing materials in radioactive waste disposal galleries (Doctoral dissertation, Université Paris-Est).

Saba, S., Barnichon, J. D., Cui, Y. J., Tang, A. M., Delage, P., 2014. Microstructure and anisotropic swelling behaviour of compacted bentonite/sand mixture. J. Rock Mech. Geotech. Eng. 6(2), 126-132.

Sellin, P., Leupin, O.X., 2013. The use of clay as an engineered barrier in radioactive-waste management–a review. Clays Clay Miner. 61(6), 477-498.

Sun, D.A., Cui, H., Sun, W.J., 2009. Swelling of compacted sand-bentonite mixtures. Appl. Clay Sci. 43(3-4), 485-492.

Sun, W.J., Wei, Z.F., Sun, Da., Liu, S.Q., Fatahi, B., Wang, X.Q., 2015. Evaluation of the swelling characteristics of bentonite-sand mixtures. Eng. Geol. 199, 1-11.

Sun, W.J., Zong, F.Y., Sun, D.A., Wei, Z.F., Schanz, T., Fatahi, B., 2017. Swelling prediction of bentonite-sand mixtures in the full range of sand content. Eng. Geol. 222, 146-155.

Tang, A.M., Cui, Y.J., Le, T.T., 2008. A study on the thermal conductivity of compacted bentonites. Appl. Clay Sci. 41 (3-4), 181–189.

Tang, C.S., Tang, A.M., Cui, Y.J., Delage, P., Schroeder, C., De Laure, E., 2011. Investigating the pressure of compacted crushed-Callovo-Oxfordian claystone. Phys. Chem. Earth Parts A/B/C 36 (17-18), 1857-1866.

Villar, M.V., Lloret, A., 2008. Influence of dry density and water content on the swelling of a compacted bentonite. Appl. Clay Sci. 39(1-2), 38-49.

Wang, Q., Tang, A.M., Cui, Y.J., Delage, P., Gatmiri, B., 2012. Experimental study on the swelling behaviour of bentonite/claystone mixture. Eng. Geol. 124, 59-66.

Wang, Q., Cui, Y.J., Tang, A.M., Delage, P., Gatmiri, B., Ye, W.M., 2014. Long-term effect of water chemistry on the swelling pressure of a bentonite-based material. Appl. Clay Sci. 87, 157-162.

Yang, L.A., Tan, T.S., Tan, S.A., Leung, C.F., 2002. One-dimensional self-weight consolidation of a lumpy clay fill. Géotechnique 52(10), 713-725.

Ye, W.M., Schanz, T., Qian, L.X., Wang, J., Arifin, Y., 2007. Characteristics of swelling pressure of densely compacted Gaomiaozi bentonite GMZ01. Chin. J. Rock Mech. Eng. 26 (S2), 3861–3865 (in Chinese).

Zhang, C.L., Kröhn, K.P., 2019. Sealing behaviour of crushed claystone–bentonite mixtures. Geomech. Energy Environ. 17, 90-105.

Zeng, Z.X., Cui, Y.J., Conil, N., Talandier, J. 2020. International Journal of Geomechanics, 20(10), 04020184.

Experimental investigation and modelling of the hydraulic conductivity of saturated bentonite/claystone mixture

Zhixiong Zeng[1], Yu-Jun Cui[1], Nathalie Conil[2], Jean Talandier[3]

Abstract: Mixtures composed of MX80 bentonite and crushed Callovo-Oxfordian (COx) claystone have been considered as one of the promising sealing/backfill materials in the French deep geological disposal for radioactive waste. One of the key issues about these mixtures is the hydraulic conductivity. In this study, the swelling pressure and hydraulic conductivity of bentonite/claystone mixtures with different bentonite fractions and dry densities were determined by carrying out infiltration tests under constant-volume conditions. The results indicated that as the bentonite fraction and dry density increased, the overall swelling pressure increased while the hydraulic conductivity decreased. Based on the assumption that the stress between bentonite and claystone grains was equal to the overall swelling pressure, the void ratios and volumetric fractions of bentonite and claystone in the mixture were determined. According to the relationships between hydraulic conductivity and void ratio for pure bentonite and claystone, the overall hydraulic conductivities of the bentonite/claystone mixtures were then calculated using five analytical models (Parallel, Series, Maxwell-Eucken 1, Maxwell-Eucken 2 and EMT models) corresponding to different potential composite structures, allowing appreciation of the composite structures of bentonite/claystone mixtures with various bentonite fractions: for specimens with more than 70% bentonite, the bentonite formed a matrix with the claystone being dispersed in it; for specimens with less than 40% bentonite, the matrix was formed by swollen claystone, with the bentonite dispersed into the matrix; for the specimens with 40-70% bentonite, the bentonite and claystone were randomly distributed, without being continuous or dispersed. Based on the defined composite structure of bentonite/claystone mixture, a new method was proposed for estimating the overall hydraulic conductivity. Comparison between estimation and measurement showed the relevance of the proposed method.

Keywords: bentonite/claystone mixture; hydraulic conductivity; bentonite fraction; dry density; prediction method

1 Laboratoire Navier/CERMES, Ecole des Ponts ParisTech, 6 et 8 avenue Blaise Pascal, 77455 Marne La Vallée cedex 2, France
2 Centre de Meuse/Haute-Marne, RD 960, 55290 Bure, France
3 1/7, rue Jean Monnet, 92298 Châtenay-Malabry cedex, France

1 Introduction

Bentonite is mainly composed of montmorillonite and exhibits high swelling capacity, low hydraulic conductivity and large absorption capacity (Pusch, 1979; Sivapullaiah et al., 2000). It has been extensively used to construct isolating barriers, such as liner in the municipal solid waste landfill (Mollins et al., 1996; Du et al., 2009), cutoff wall in the contaminated site remediation system (Sivapullaiah et al., 2000; Du et al., 2015) and engineered barrier in the radioactive waste repository (Pusch, 1980; Geneste et al., 1990; Komine et al., 2004; 2010). In many cases, bentonite is blended with other additives, such as sand (Villar and Rivas, 1994), granite (Yong et al., 1986; Börgesson et al., 2003) and claystone (Wang et al., 2012; Zeng et al., 2019; Middelhoff et al., 2020), to reduce the cost and improve the thermo-mechanical performance (Mollins et al., 1996; Sivapullaiah et al., 2000). However, the inclusion of additives into the bentonite can also influence its hydraulic behaviour. A good understanding of such influence is of importance in the design of isolating barriers.

During the past decades, the hydraulic conductivities of different bentonite/sand mixtures were experimentally determined using constant-head or falling-head methods (Kenney et al., 1992; Komine et al., 2004; Xu et al., 2016). It was found that the hydraulic conductivity of such mixtures increased with the decreasing bentonite fraction, in particular in the range of low bentonite fractions. As the void space surrounded by sand grains was lower than the free-swell of bentonite, the void space was completely filled by bentonite. In that case, the hydraulic conductivity was dominated by the bentonite matrix. In contrast, as the void space was larger than the free-swell of bentonite, the swollen bentonite could not fully occupy the void space. In that case, the hydraulic conductivity was influenced by the inter-sand structure. Apart from the experimental measurement, some empirical and analytical models were also developed to estimate the hydraulic conductivity of bentonite/sand mixtures. The empirical models were established by fitting the measured hydraulic conductivity with the bentonite fraction and void ratio of the mixtures (Cho et al., 2000; Sivapullaiah et al., 2000; Xu et al., 2016). However, these empirical models were developed based on limited data for some particular soils and the transferability to other soils has not been demonstrated. Some researchers proposed analytical models based on the intrinsic properties of sand and bentonite (Kenney et al., 1992; Mollins et al., 1996; Komine et al., 2004). In these analyses, the bentonite/sand mixture was assumed to be an ideal mixture in which the hydrated bentonite was uniformly distributed forming a matrix, while sand grains constituted

impervious inclusion. Based on this assumption, the local variables in the mixture, such as the bentonite void ratio (Wang et al., 2013) and swelling volumetric strain of montmorillonite (Komine et al., 2004) were defined and the relationships between the overall hydraulic conductivity and local variables were obtained.

Recently, the excavated Callovo-Oxfordian (COx) claystone and bentonite mixtures were proposed as a sealing/backfill material in the French deep geological disposal for high-level radioactive waste by the French National Radioactive Waste Management Agency (Andra) (Zeng et al., 2019; 2020). After the installation, these mixtures will absorb groundwater from the host rock and gradually become saturated, and exhibit a hydraulic conductivity low enough to retard the water transfer-related phenomena. Unlike inert sand, the claystone could absorb water and swell or collapse (Zeng et al., 2019). Thereby, the determination of the void ratio and volumetric fraction of bentonite should consider the volume change of claystone. Furthermore, the permeability of claystone could be significantly higher than that of inert sand. In this case, the models which only consider the relationship between the hydraulic conductivity and bentonite properties in the mixture (such as bentonite void ratio and volumetric strain of montmorillonite) became no longer valid.

In this study, a series of infiltration tests under constant-volume conditions were performed on the compacted MX80 bentonite/COx claystone mixtures and the effects of bentonite fraction and dry density on the swelling pressure and hydraulic conductivity were investigated. By considering the interaction between bentonite and claystone in the development of swelling pressure, the bentonite and claystone void ratios and the bentonite volumetric fraction in the mixture were computed. Five analytical models corresponding to different potential binary composite structures were then applied to calculate the hydraulic conductivities of specimens. By comparing the measured and calculated results using different models, the composite structures of bentonite/claystone mixtures with different bentonite fractions were identified. Finally, a new method considering the composite structure of the mixture was proposed for estimating the overall hydraulic conductivity.

2 Materials and Methods

2.1 Materials

The materials used in this study included MX80 bentonite and COx claystone. The MX80 bentonite was extracted from Wyoming, USA. The physical and mineralogical properties of the

bentonite are shown in Table 1. The proportion of montmorillonite is dominant (86%). The liquid limit is 494%, the plastic limit is 46% and the specific gravity is 2.76. These data are in satisfactory agreement with those collected from other works (Karnland et al., 2008; Tang et al., 2008; Seiphoori et al., 2014; Saba et al., 2014). The COx claystone was taken from the Underground Research Laboratory (URL) at around 490 m depth in Bure, France. It has a liquid limit of 41%, a plastic limit of 24% and a specific gravity of 2.70. It is composed of 40-45% clay minerals being dominated by interstratified illite/smectite, 30% carbonates and 25-30% quartz and feldspar (Fouché et al., 2004). Prior to the experiments, both the bentonite and claystone were crushed to have the same maximum grain size of 2.0 mm. The grain size distributions of the bentonite and claystone were determined by dry-sieving and hydrometer methods (Fig. 1). The mean grain diameters D_{50} determined by dry-sieving are 0.55 and 0.58 mm for the bentonite and claystone, respectively. These close grain size distributions of dry bentonite and claystone contribute to a homogeneous state during the mixing process. The clay-size fractions (< 2 μm) determined by hydrometer method are 86% and 26% for the bentonite and claystone, respectively.

Table 1. Physical and mineralogical properties of MX80 bentonite

Soil property	Present work	Tang et al. (2008)	Seiphoori et al. (2014)	Saba et al. (2014)	Karnland et al. (2008)
Specific gravity	2.76	2.76	2.74	2.77	-
Liquid limit (%)	494	520	420	575	-
Plastic limit (%)	46	42	65	53	-
Plasticity index (%)	448	478	355	522	-
Main minerals (%)					
Montmorillonite	86	92	85		80
Quartz	7	3	-		2-3

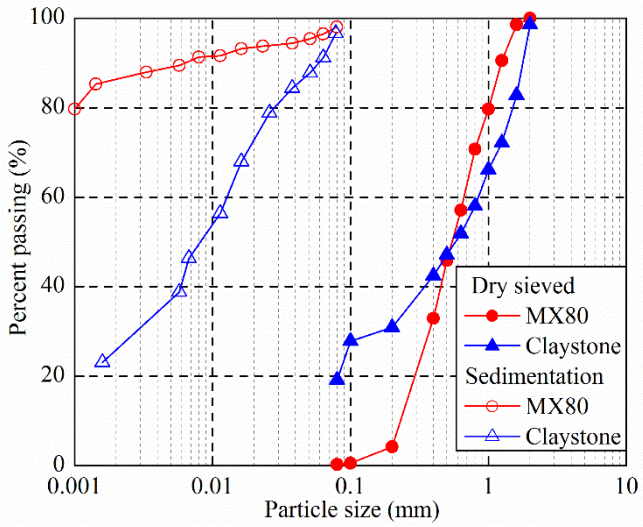

Fig. 1. Grain size distributions of MX80 bentonite and crushed COx claystone

The saturation water used in this study was synthetic water, which was prepared according to the recipe given by Andra, respecting the chemical composition of the site water at the Andra URL, as compiled in Table 2.

Table 2. Chemical composition of the synthetic water

Component	NaCl	$NaHCO_3$	KCl	$CaSO_4$▪$2H_2O$	$MgSO_4$▪$7H_2O$	$CaCl_2$▪$2H_2O$	Na_2SO_4
Content (g/L)	1.950	0.130	0.035	0.630	1.020	0.080	0.700

2.2 Specimen preparation

The bentonite and claystone powders were mixed with different proportions of 0/100, 10/90, 20/80, 30/70, 50/50 and 70/30 in dry mass. Note that the bentonite and claystone powders were air-dried prior to mixing and the corresponding water contents are 11.4% and 6.1% for the bentonite and claystone powders, respectively. The corresponding bentonite fraction B (%) was calculated by Eq. (1):

$$B=\frac{m_b}{m_b+m_c} \tag{1}$$

where m_b and m_c are the dry masses of bentonite and claystone, respectively. The calculated bentonite fractions of the different mixtures were 0, 10, 20, 30, 50 and 70%, respectively, as shown in Table 3. According to the target dry density (Table 3) and dimensions (50 mm in diameter and 10 mm in height) of specimens, a pre-determined amount of wet soils were weighed and spooned into a stainless steel mould of 50 mm inner diameter. Subsequently, the soils were compacted at a constant displacement rate of 0.05 mm/min, to reach the target height.

2.3 Experimental procedure

The compacted specimens were placed in a steel cell between two porous stones and filter papers. On the top, the piston was blocked by a screw to ensure the constant-volume condition (Fig. 2). At the bottom of the cell, a force transducer was installed to monitor the axial swelling pressure. The specimens were hydrated from the bottom through the water inlet connected to the synthetic water reservoir and the expelled air/water flowed through the air/water outlets at the top. A data logger was used for swelling pressure recording (Fig. 2a). After stabilisation of swelling pressure, the specimens were saturated and the water inlet was connected to a Pressure/Volume controller for the hydraulic conductivity tests. As the synthetic water could corrode the Pressure/Volume controller, a Water/Solution converter (a flexible rubber was used to separate the synthetic and distilled water) was adopted with one end connected to the Pressure/Volume controller and the other end to the bottom of the cell (Fig. 2b). The injected water volume was recorded automatically by the data logger. The applied water pressure ranged

from 10 to 200 kPa, approximately equal to the 1/10 of the maximum swelling pressure of different specimens, defining a hydraulic gradient (ratio of the water head to the specimen height) between 100 and 2000. As reported by Pusch (1980) and Dixon et al. (1999), this range of hydraulic gradient has a negligible influence on the hydraulic conductivity. Additionally, the application of this pressure aimed to minimize the influence of possible microstructure disturbance owing to water injection on the hydraulic conductivity measurement. In total, twenty-five hydraulic conductivity tests were carried out at a temperature of 20±1°C (Table 3).

Table 3. Test program and main results

Test No.	Bentonite fraction B (%)	Dry density of specimen ρ_{dm} (Mg/m^3)	Initial water content w_m (%)	Bentonite void ratio e_b	Claystone void ratio e_c	Bentonite volumetric fraction ϕ_b	Final swelling pressure P_s (MPa)	Hydraulic conductivity k (m/s)
01	70	1.38	9.8	0.74	0.08	83.5	0.43	1.00×10^{-12}
02	70	1.50	9.8	0.76	0.13	81.1	1.11	3.51×10^{-13}
03	70	1.63	9.8	0.79	0.07	80.5	2.53	1.55×10^{-13}
04	70	1.71	9.8	0.88	0.02	80.6	3.94	9.91×10^{-14}
05	50	1.27	8.8	0.89	0.49	64.9	0.13	3.90×10^{-11}
06	50	1.56	8.8	0.97	0.30	62.3	0.85	2.11×10^{-12}
07	50	1.73	8.8	1.11	0.18	62.2	2.10	4.31×10^{-13}
08	50	1.76	8.8	1.13	0.19	61.1	2.91	3.90×10^{-13}
09	30	1.50	7.7	1.29	0.47	42.6	0.22	1.52×10^{-10}
10	30	1.60	7.7	1.42	0.41	41.4	0.46	3.12×10^{-11}
11	30	1.68	7.7	1.51	0.36	40.6	0.78	1.49×10^{-11}
12	30	1.79	7.7	1.67	0.30	39.9	1.59	5.14×10^{-12}
13	30	1.89	7.7	2.28	0.23	39.8	2.72	1.52×10^{-12}
14	30	1.99	7.7	2.63	0.18	39.2	5.23	7.62×10^{-13}
15	20	1.60	7.2	1.39	0.49	29.6	0.26	1.52×10^{-10}
16	20	1.69	7.2	1.13	0.41	29.3	0.44	3.97×10^{-11}
17	20	1.77	7.2	0.95	0.35	28.9	0.70	1.83×10^{-11}
18	20	1.88	7.2	0.86	0.31	27.3	1.93	7.21×10^{-12}
19	10	1.61	6.6	1.81	0.56	16.3	0.14	9.73×10^{-10}
20	10	1.68	6.6	1.20	0.50	15.8	0.23	2.46×10^{-10}
21	10	1.78	6.6	0.99	0.42	15.6	0.39	6.16×10^{-11}
22	10	1.90	6.6	0.92	0.35	14.7	1.07	2.05×10^{-11}
23	0	1.80	6.1	-	0.50	0	0.15	3.65×10^{-10}
24	0	1.90	6.1	-	0.42	0	0.47	6.92×10^{-11}
25	0	1.99	6.1	-	0.36	0	0.79	3.14×10^{-11}

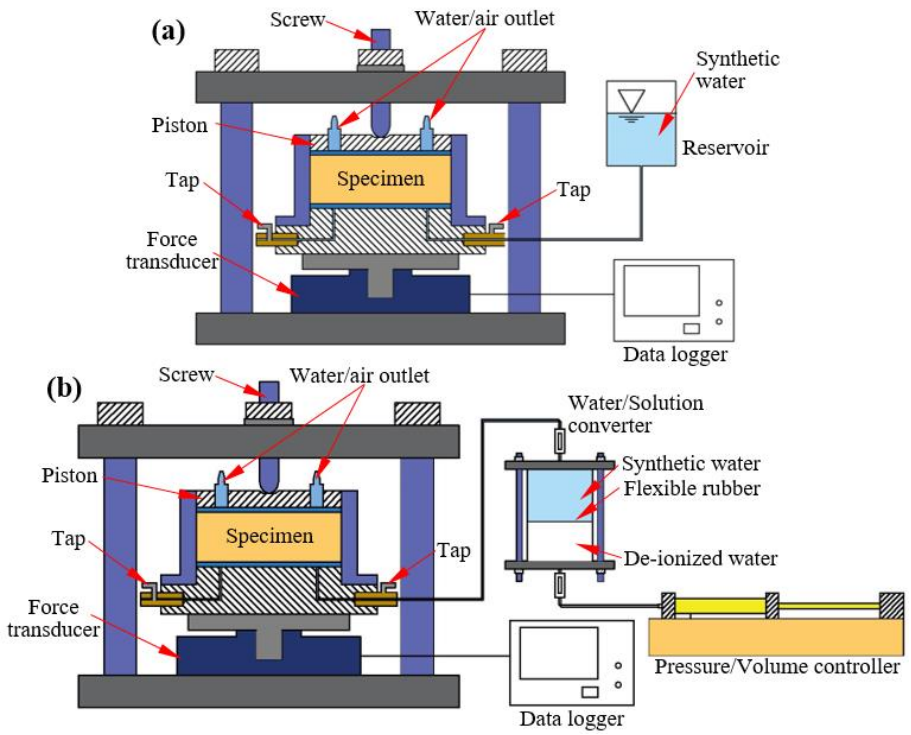

Fig. 2. Layout of the experimental setups for (a) swelling pressure and (b) hydraulic conductivity tests

According to the evolution of injected water volume, the water flow rate (ratio of the flow volume to elapsed time) was determined. When the flow rate became stable, the hydraulic conductivity test was finished. The hydraulic conductivity k (m/s) was calculated using the Darcy's law:

$$k=\frac{q}{iA} \tag{2}$$

where q (m^3/s) is the stable flow rate, i is the hydraulic gradient and A (m^2) is the cross-section area of the specimens.

3 Experimental results

3.1 Effects of bentonite fraction and dry density on the swelling pressure

The variation of swelling pressure with dry density is depicted in Fig. 3a. The results of Karnland et al. (2008) on pure MX80 bentonite and Tang et al. (2011) on pure COx claystone are also presented. On the whole, the swelling pressure increased linearly with the dry density (Fig. 3a). For the specimens with different bentonite fractions, the slopes of the fitted lines were almost the same. The relationship between the swelling pressure and bentonite fraction for the specimens with different dry densities is illustrated in Fig. 3b. Because of the lack of experimental results at given dry densities of 1.60, 1.70, 1.80, 1.90 and 2.00 Mg/m^3, the swelling pressures in Fig. 3b were estimated using linear interpolation and extrapolation

according to the relationships between swelling pressure and dry density (Fig. 3a). For the specimens at a given dry density, as the bentonite fraction increased, the swelling pressure increased.

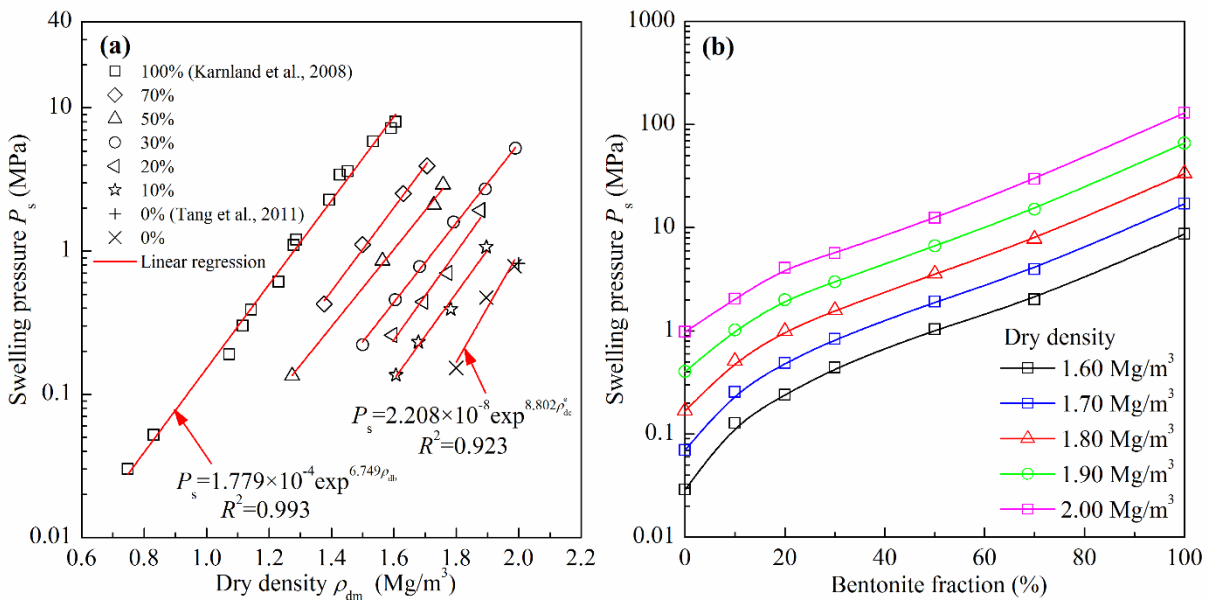

Fig. 3. Variations of swelling pressure with (a) dry density and (b) bentonite fraction

3.2 Effects of bentonite fraction and void ratio on the hydraulic conductivity

Fig. 4a depicts the variation of hydraulic conductivity with void ratio for the specimens with different bentonite fractions. For comparison, the results of Karnland et al. (2008) on pure MX80 bentonite are also added. To calculate the void ratio of the mixture, the overall specific gravity G_{sm} of the mixture was determined according to the specific gravities of bentonite G_{sb} and claystone G_{sc}:

$$G_{sm}=\frac{G_{sb}G_{sc}}{G_{sb}(1\text{-}B/100)+G_{sc}(B/100)} \tag{3}$$

From Fig. 4a, it could be observed that the hydraulic conductivity increased with the increasing void ratio of specimens. The relationships between the logarithm of hydraulic conductivity and the void ratio could be well described by line regression equations. The slope of the fitted lines decreased with the increase of bentonite fraction. According to the linear relationships for different bentonite fractions, the hydraulic conductivity of the specimens with different void ratios (0.72, 0.62, 0.53, 0.45 and 0.38) were estimated. The relationship between the hydraulic conductivity and bentonite fraction for specimens with different void ratios is presented in Fig. 4b. On the whole, for the specimens with the same void ratio, the lower the bentonite fraction, the larger the hydraulic conductivity, suggesting that addition of claystone reduced the sealing performance.

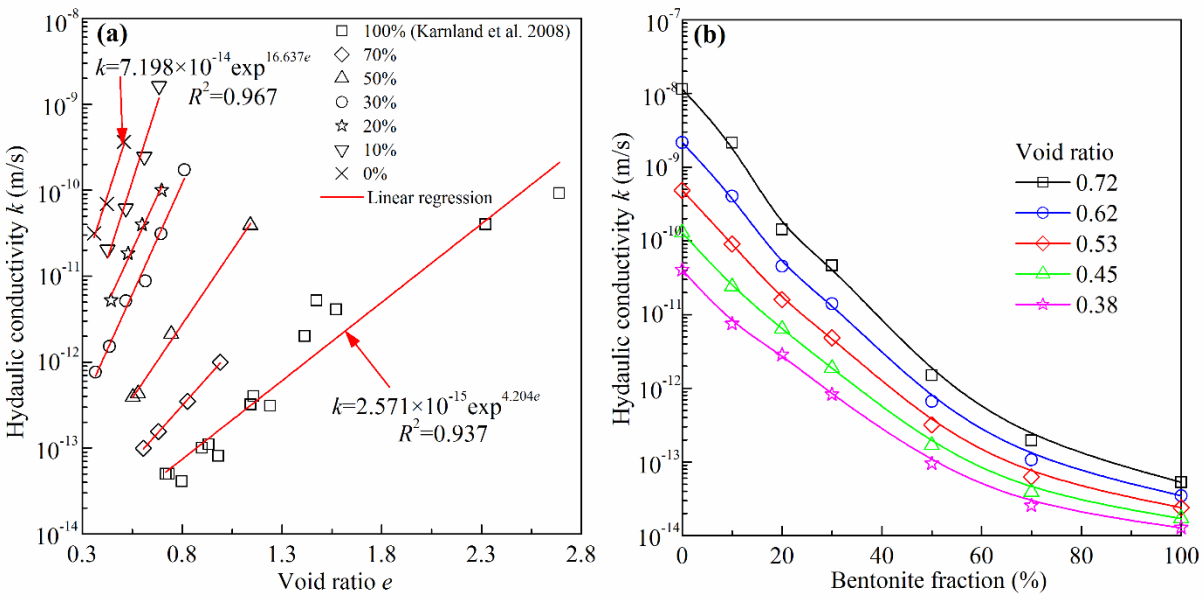

Fig. 4. Variations of hydraulic conductivity with (a) void ratio and (b) bentonite fraction

4 Modelling of hydraulic conductivity of bentonite/claystone mixture

4.1 Models for binary mixture

For a binary mixture, its overall hydraulic conductivity is contributed by each constituent (Wang and Pan, 2008). To estimate the overall hydraulic conductivity, many analytical models accounting for different binary composite structures were developed, such as the models of Parallel, Series, Maxwell-Eucken and EMT (Fig. 5). Of them, Parallel and Series models are based on two simple graded composite structures: (i) the two constituents are in parallel to the water flow direction (Fig. 5a), and (ii) the two constituents are in series in the water flow direction (Fig. 5b). For the mixtures with Parallel and Series composite structures, the overall hydraulic conductivity in the vertical direction ($k_{overall}$) can be estimated using Eqs. (4) and (5), respectively (Shi and Yin, 2018):

$$k_{overall}=\phi_1 k_1+(1-\phi_1)k_2 \tag{4}$$

$$k_{overall}=\frac{1}{\phi_1/k_1+(1-\phi_1)/k_2} \tag{5}$$

where k_1 is the hydraulic conductivity of constituent 1; k_2 the hydraulic conductivity of constituent 2; ϕ_1 is the volumetric fraction of constituent 1.

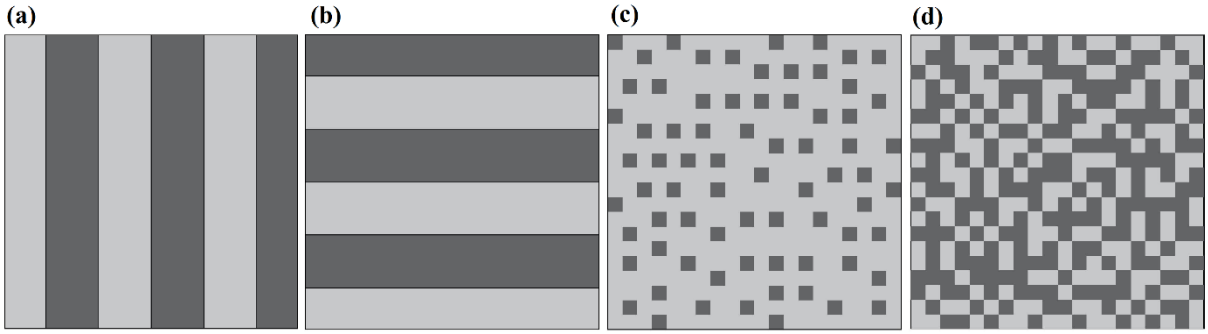

Fig. 5. Composite structure schematic of classical analytical models for hydraulic conductivity estimation of binary mixture. (a) Parallel model; (b) Series model; (c) Maxwell-Eucken model; (d) EMT model (Carson et al., 2005; Wang and Pan., 2008; Zhai et al., 2018). Note: the gray area represents constituent 1 and the dark is constituent 2

When constituent 2 is dispersed in the continuous matrix of constituent 1 and the particles of constituent 2 are quite separated from each other (Fig. 5c), the overall hydraulic conductivity can be expressed by the Maxwell-Eucken model (Dunn and Mehuys, 1984; Brakensiek, 1986):

$$k_{\text{overall}}=k_1\frac{2k_1+k_2-2(k_1-k_2)(1-\phi_1)}{2k_1+k_2+(k_1-k_2)(1-\phi_1)} \tag{6}$$

Note that Eq. (6) corresponds to the composite structure in which the continuous matrix is formed by constituent 1. When the distributions of continuous and dispersed constituents are inversed (constituent 1 is the matrix while constituent 2 is the inclusion), the expression of Maxwell-Eucken model can be written as:

$$k_{\text{overall}}=k_2\frac{2k_2+k_1+2(k_1-k_2)\phi_1}{2k_2+k_1-(k_1-k_2)\phi_1} \tag{7}$$

For convenience, the form of Eq. (6) is designated as Maxwell-Eucken 1 whereas that of Eq. (7) is denoted as Maxwell-Eucken 2.

For a composite structure with a completely random distribution of two constituents (Fig. 5d), the overall hydraulic conductivity can be modelled using the Effective Medium Theory (EMT) model (Dagan, 1979; Ma et al., 2014):

$$k_{\text{overall}}=\frac{1}{4}\left\{\left[(2-3\phi_1)k_2+(3\phi_1-1)k_1\right]+\sqrt{\left[(2-3\phi_1)k_2+(3\phi_1-1)k_1\right]^2+8k_1k_2}\right\} \tag{8}$$

Note that the particles in the Maxwell-Eucken and EMT models are assumed to be ellipsoidal and isotropic. For simplification, the particles are represented by rectangles in Fig. 5.

4.2 Calculation of bentonite volumetric fraction in the mixture

Upon wetting, the bentonite rapidly swelled and came in contact with claystone because the

swelling capacity of bentonite was 100 times larger than that of claystone (Fig. 3). By contrast, the claystone absorbed water and collapsed or swelled under the pressure exerted by the swollen bentonite (Zeng et al., 2019). After the hydration process, the bentonite/claystone mixture could be divided into the following four parts: solids in bentonite, voids in bentonite, solids in claystone and voids in claystone, as illustrated in Fig. 6. To determine the bentonite and claystone dry densities in the mixture, the following assumptions were made: (1) the bentonite could fully swell; (2) the stress at the interface of bentonite and claystone was equal to the overall swelling pressure, adopted by Yang et al. (2002) when investigating the consolidation behavior of lumpy granular soil under one-dimensional condition. As shown in Fig. 3a, the relationship between the swelling pressure and dry density for pure bentonite could be expressed as:

$$P_s=1.779\times10^{-4}\exp^{6.749\rho_{db}} \tag{9}$$

Therefore, the bentonite dry density in the mixture ρ_{db} could be back-calculated from the overall swelling pressure of the mixture using Eq. (9) based on the assumptions. According to the composition of the mixture, the claystone dry density in the mixture ρ_{dc} could be derived:

$$\rho_{dc}=\frac{\rho_{db}\rho_{dm}(1\text{-}B/100)}{\rho_{db}\text{-}\rho_{dm}(B/100)} \tag{10}$$

Correspondingly, the bentonite void ratio e_b and claystone void ratio e_c in the mixture could be obtained using Eqs. (11) and (12), respectively:

$$e_b=\frac{G_{sb}\rho_w}{\rho_{dc}}\text{-}1 \tag{11}$$

$$e_c=\frac{G_{sc}\rho_w}{\rho_{db}}\text{-}1 \tag{12}$$

where ρ_w is the water density. Then, the bentonite volumetric fraction ϕ_b, defined as the ratio of the bentonite volume (including solids and voids in bentonite) to the total volume of the mixture, could be determined:

$$\phi_b=\frac{V_b}{V_b+V_c}=\frac{(e_b+1)(B/100)/G_{sb}}{(e_b+1)(B/100)/G_{sb}+(e_c+1)(1\text{-}B/100)/G_{sc}}=\frac{\rho_{dm}(B/100)}{\rho_{db}} \tag{13}$$

The calculated e_b, e_c and ϕ_b for all the specimens are summarized in Table 3. Unlike the inert materials (sand or granite), the volume of claystone no longer kept constant after hydration - it varied with the bentonite fraction and dry density of the specimens. In general, the claystone void ratio decreased as the bentonite fraction and the specimen dry density increased.

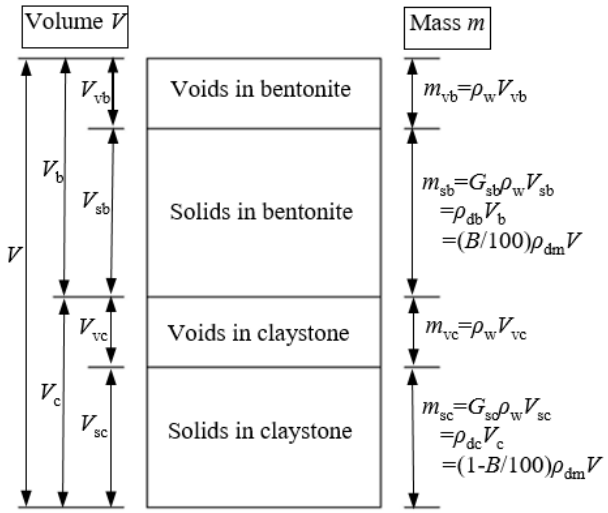

Fig. 6. Composition of bentonite/claystone mixture

4.3 Development of a new method of determining hydraulic conductivity for bentonite/claystone mixture

As shown in Fig. 4a, the changes of hydraulic conductivity could be expressed by straight lines in a semi-logarithm plot between logk_w and e. The linear regression equations for the hydraulic conductivities of pure bentonite (k_b) and claystone (k_c) are Eqs. (14) and (15), respectively:

$$k_b=2.571\times10^{-15}\exp^{4.204e} \quad (14)$$

$$k_c=7.198\times10^{-14}\exp^{16.637e} \quad (15)$$

Eqs. (14) and (15) allowed the local hydraulic conductivities of bentonite and claystone to be estimated according to the bentonite and claystone void ratios in the mixture. In addition to the hydraulic property and volumetric fraction of each constituent, the overall hydraulic conductivity of the mixture was highly related to the composite structure of the mixture. To clarify the composite structure of bentonite/claystone mixture, the Parallel, Series, Maxwell-Eucken 1, Maxwell-Eucken 2 and EMT models corresponding to the potential composite structures of the mixtures were used to calculate the overall hydraulic conductivity from k_b, k_c and the bentonite volumetric fraction ϕ_b. A comparison between the calculated and measured hydraulic conductivities of the mixtures using different models is presented in Fig. 7. Overall, the parallel model gave the highest value while the series model gave the lowest one for all the specimens (Fig. 7a). Except the Series and Maxwell-Eucken 1 models, the calculated results of other models fell in the range of 1/3 to 3 times $k_{measured}$. For clarity, Fig. 7b depicts the variation of $k_{calculated}/k_{measured}$ with the bentonite fraction. For the specimens with 10-50% bentonite, the results of Maxwell-Eucken 2 and EMT models were closer to the line of $k_{calculated}/k_{measured}=1$; for the specimens with 70% bentonite, all the models gave acceptable results. To quantitatively

determine the effectiveness of the five models, the mean absolute error (MSE) between the calculated and measured values in the semi-logarithm plot was defined:

$$\mathrm{MSE}=\frac{1}{N}\sum_{i=1}^{N}\left|\log k_{\mathrm{calculated}}-\log k_{\mathrm{measured}}\right|=\frac{1}{N}\sum_{i=1}^{N}\left|\log\left(k_{\mathrm{calculated}}/k_{\mathrm{measured}}\right)\right| \tag{16}$$

where N is the specimen number; i is a counter. The MSE value represented the performance of the models, and allowed the composite structures of the bentonite/claystone mixtures to be appreciated - when the model which accounts for a specific binary composite structure showed the lowest MSE value for the specimens with a certain bentonite fraction, the specimens should have the similar composite structure as the model. Table 4 summarizes the calculated results of MSE. The MSE value for different models was found to depend on the bentonite fraction: for the specimens with 70% bentonite, the MSE value of the Maxwell-Eucken 1 model was the lowest; for the specimens with 50% bentonite, the EMT gave the lowest MSE value; for the specimens with 30, 20, and 10% bentonite, the MSE value of Maxwell-Eucken 2 model was the lowest. This phenomenon was in accordance with the observation of Zeng et al. (2019) while analysing the interaction between bentonite and claystone based on the swelling pressure. The composite structures of bentonite/claystone mixtures could be divided into three zones (namely Zone I, 100%≥B≥70%; Zone II, 70%>B≥40%; Zone III, 40%>B≥0%). In Zone I, the swollen bentonite formed the continuous matrix while the claystone grains were dispersed constituent (Fig. 8a); in Zone III, the continuous matrix was formed by swollen claystone while the swollen bentonite was dispersed in the matrix (Fig. 8c); in Zone II, the bentonite and claystone were randomly distributed, with neither constituent being continuous or dispersed (Fig. 8b). Based on the composite structure of bentonite/claystone mixtures, a combined equation could be proposed for estimating the hydraulic conductivity of the mixture (k_{mix}):

$$k_{\mathrm{mix}}=\begin{cases} k_{\mathrm{b}}\dfrac{2k_{\mathrm{b}}+k_{\mathrm{c}}-2(k_{\mathrm{b}}-k_{\mathrm{c}})(1-\phi_{\mathrm{b}})}{2k_{\mathrm{b}}+k_{\mathrm{c}}+(k_{\mathrm{b}}-k_{\mathrm{c}})(1-\phi_{\mathrm{b}})} & (B\geq 70\%) \\ \dfrac{1}{4}\left\{\left[(2-3\phi_{\mathrm{b}})k_{\mathrm{c}}+\left(3\phi_{\mathrm{b}}-1\right)k_{\mathrm{b}}\right]+\sqrt{\left[(2-3\phi_{\mathrm{b}})k_{\mathrm{c}}+(3\phi_{\mathrm{b}}-1)k_{\mathrm{b}}\right]^{2}+8k_{\mathrm{b}}k_{\mathrm{c}}}\right\} & (70\%>B\geq 40\%) \\ k_{\mathrm{c}}\dfrac{2k_{\mathrm{c}}+k_{\mathrm{b}}-2(k_{\mathrm{c}}-k_{\mathrm{b}})(1-\phi_{\mathrm{b}})}{2k_{\mathrm{c}}+k_{\mathrm{b}}+(k_{\mathrm{c}}-k_{\mathrm{b}})(1-\phi_{\mathrm{b}})} & (B<40\%) \end{cases} \tag{17}$$

Table 4. MSE values of different analytical models for specimens with different bentonite fractions

Bentonite fraction *B* (%)	Parallel model	Series model	Maxwell-Eucken 1	Maxwell-Eucken 2	EMT model
70	0.036	0.010	0.003	0.005	0.004
50	0.294	0.228	0.089	0.043	0.004
30	0.089	1.129	0.602	0.008	0.021
20	0.049	1.381	0.688	0.001	0.003
10	0.054	1.489	0.711	0.008	0.009

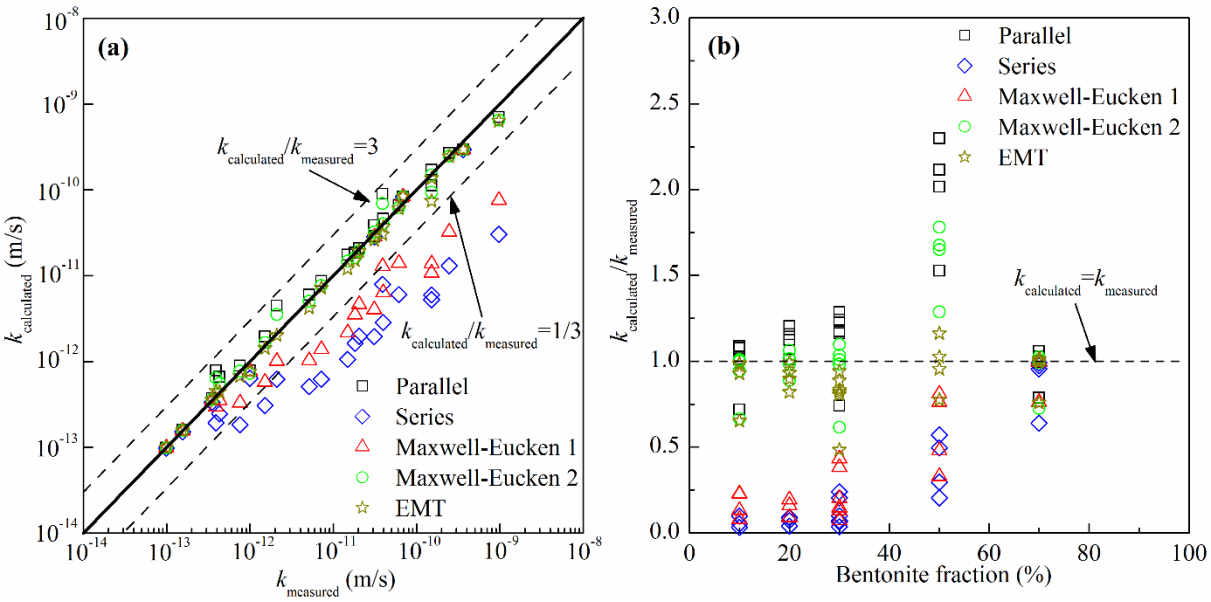

Fig. 7. Comparison between measured and calculated hydraulic conductivities using different models: (a) $k_{calculated}$ versus $k_{measured}$; (b) $k_{calculated}/k_{measured}$ versus bentonite fraction

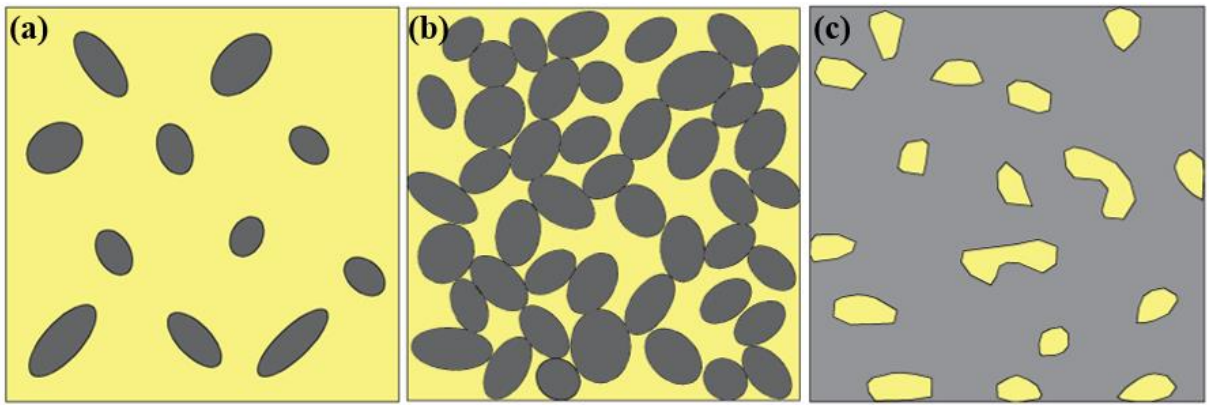

Fig. 8. Composite structure schematics of bentonite/claystone mixtures with different bentonite fractions: (a) 100%≥*B*≥70%; (b) 70%>*B*≥40%; (c) 40%>*B*≥0%. Note: the yellow and grey areas represent bentonite and claystone, respectively

4.4 Hydraulic conductivity estimation for bentonite/claystone mixture

As remarked previously, the hydration process of claystone was influenced by the swollen bentonite. At a given global swelling pressure, claystone void ratio in the bentonite/claystone mixture should be smaller than that without considering the inhibition effect of bentonite

(designated as expected claystone void ratio) (Zeng et al., 2019). To describe the influence of bentonite on the swelling of claystone, Zeng et al. (2019) defined an inhibition factor (η) as the relative difference between the claystone void ratio e_c and the expected claystone void ratio e_c^e:

$$\eta=\frac{e_c^e-e_c}{e_c^e}=1-\frac{e_c}{e_c^e} \tag{18}$$

The expected claystone void ratio e_c^e corresponded to the dry density needed for pure claystone to reach the same swelling pressure as the mixture (denoted as ρ_{dc}^e). It could be back-calculated according to the relationship between the swelling pressure and the dry density for pure claystone (Fig. 3a):

$$P_s=2.208\times10^{-8}\exp^{8.802\rho_{dc}^e} \tag{19}$$

Then, e_c^e could be computed using Eq. (20):

$$e_c^e=\frac{G_{sc}\rho_w}{\rho_{dc}^e}-1 \tag{20}$$

Then, the inhibition factor of all the specimens could be obtained. Zeng et al. (2019) found that the inhibition factor obeyed to a logistic function with the bentonite fraction:

$$\eta=\frac{1}{1+e^{10.664(0.595-B/100)}} \tag{21}$$

According to the expression of inhibition factor and the relationships between the swelling pressure and the dry density for pure bentonite and claystone, the swelling pressure and bentonite and claystone void ratios (e_b and e_c) in the mixtures with different bentonite fractions and dry densities could be computed after several iterations, as shown in Fig. 9. According to Eqs. (13), (14) and (15), the bentonite volumetric fraction ϕ_b and the hydraulic conductivities of bentonite and claystone (k_b and k_c) in the mixture were then determined. Substituting ϕ_b, k_b and k_c into Eq. (17), the hydraulic conductivity of the mixture could be computed, as shown in Fig. 9. The estimated results are shown in Fig. 10. A good agreement was obtained between the estimated and the measured hydraulic conductivity, showing the relevance of the proposed method.

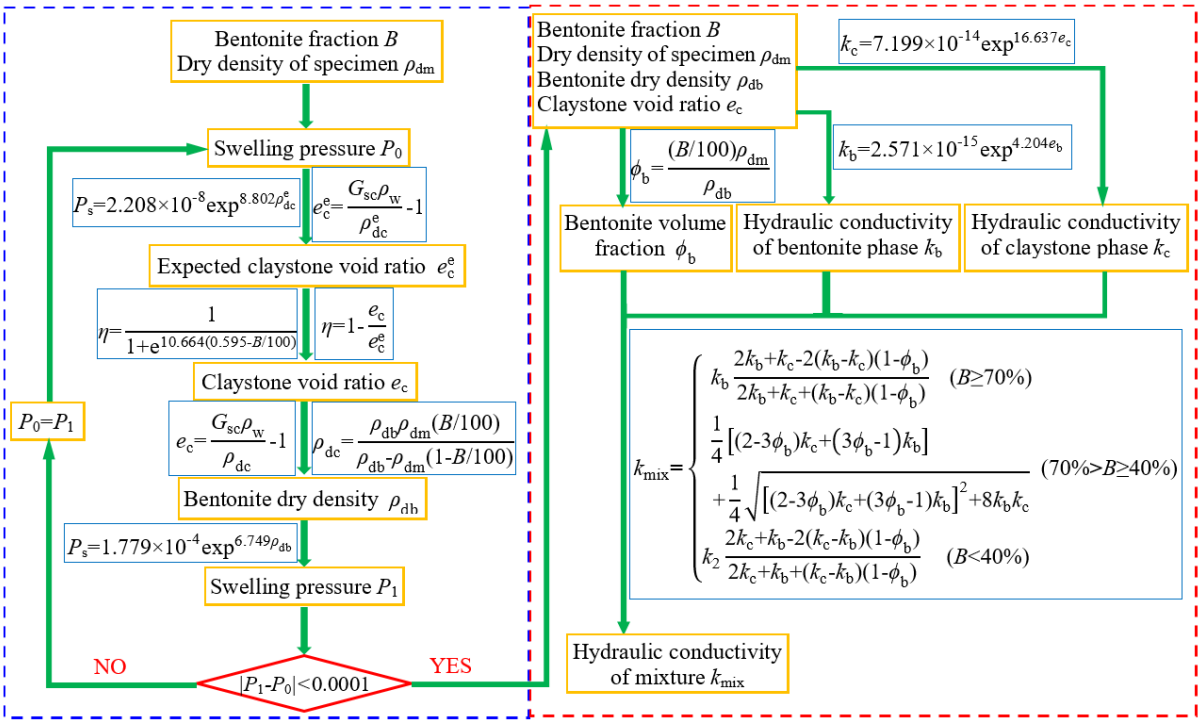

Fig. 9. Flowchart for the hydraulic conductivity estimation of bentonite/claystone mixtures with different bentonite factions and dry densities

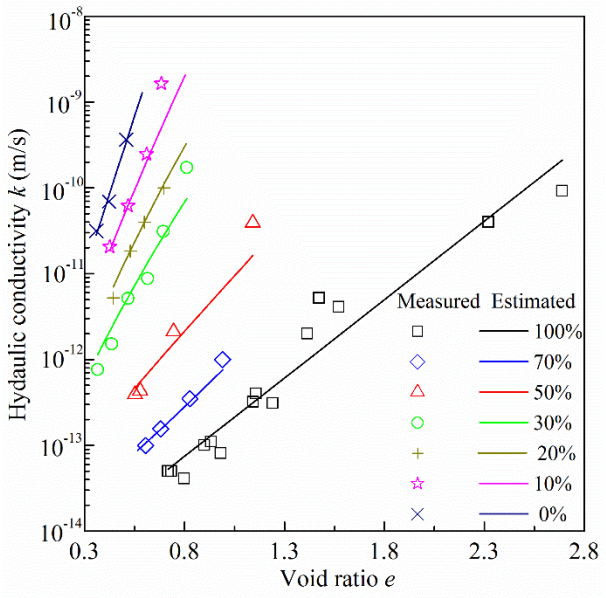

Fig. 10. Comparison between the experimental data and estimated results using the proposed method

5 Conclusions

In this study, the hydraulic conductivity of MX80 bentonite/COx claystone mixture was experimentally investigated considering the influences of bentonite fraction (B) and dry density. According to the experimental results, a new method was proposed to estimate the overall hydraulic conductivity of bentonite/claystone mixture. The following conclusions can be drawn:

(1) The hydraulic conductivity of bentonite/claystone increased with the decrease of specimen dry density and bentonite fraction, suggesting that addition of claystone reduced the sealing performance of the mixture.

(2) Statistical evaluation of the five analytical models (Parallel, Series, Maxwell-Eucken 1, Maxwell-Eucken 2 and EMT models) confirmed that the composite structure of bentonite/claystone mixture could be divided into three zones (Zone I, 100%≥B≥70%; Zone II, 70%>B≥40%; Zone III, 40%>B≥0%). In Zone I, the bentonite formed the continuous matrix, with claystone grain being the dispersed constituent; In Zone III, the continuous matrix was formed by swollen claystone while the bentonite was dispersed in the matrix; In Zone II, both bentonite and claystone bentonite and claystone were randomly distributed, with neither constituent being continuous or dispersed.

(3) According to the composite structures of bentonite/claystone mixtures with different bentonite fractions, a new method considering the bentonite/claystone interaction was proposed to estimate the overall hydraulic conductivity. The good agreement between the estimation and measurement indicated the relevance of the proposed method.

Notably, the particles were assumed to be ellipsoidal and isotropic in this study. The influences of irregular shape and anisotropic microstructure of particles on the overall hydraulic conductivity will be investigated in further work.

Acknowledgments

The authors are grateful to Ecole des Ponts ParisTech, the China Scholarship Council (CSC) and the French National Radioactive Waste Management Agency (Andra) for their financial supports.

References

Börgesson, L., L. E. Johannesson and D. Gunnarsson. 2003. “Influence of soil structure heterogeneities on the behaviour of backfill materials based on mixtures of bentonite and crushed rock.” Appl. Clay Sci. 23(1-4): 121-131. https://doi.org/10.1016/S0169-1317(03)00094-2.

Brakensiek, D. L., W. J. Rawls and G. R. Stephenson. 1986. “Determining the Saturated Hydraulic Conductivity of a Soil Containing Rock Fragments 1.” Soil Sci. Soc. Am. J. 50(3): 834-835. https://doi:10.2136/sssaj1986.03615995005000030053x.

Carson, J.K., S. J. Lovatt, D. J Tanner and A. C. Cleland. 2005. "Thermal conductivity bounds for isotropic, porous materials." Int. J. Heat Mass Transfer 48(11): 2150-2158. https://doi.org/10.1016/j.ijheatmasstransfer.2004.12.032.

Dagan, G. 1979. "Models of groundwater flow in statistically homogeneous porous formations." Water Resour. Res. 15(1): 47-63. https://doi.org/10.1029/WR015i001p00047.

Dixon, D. A., J. Graham and M. N. Gray. 1999. "Hydraulic conductivity of clays in confined tests under low hydraulic gradients." Can. Geotech. J. 36(5): 815-825. https://doi.org/10.1139/t99-057.

Du, Y. J., S. L. Shen, S. Y. Liu and S. Hayashi. 2009. "Contaminant mitigating performance of Chinese standard municipal solid waste landfill liner systems." Geotext. Geomembr. 27(3): 232-239. https://doi.org/10.1016/j.geotexmem.2008.11.007.

Du, Y.J., R. D. Fan, S. Y. Liu, K. R. Reddy and F. Jin. 2015. "Workability, compressibility and hydraulic conductivity of zeolite-amended clayey soil/calcium-bentonite backfills for slurry-trench cutoff walls." Eng. Geol. 195: 258-268. https://doi.org/10.1016/j.enggeo.2015.06.020.

Dunn, A. and G. Mehuys. 1984. "Relationship between gravel content of soils and saturated hydraulic conductivity in laboratory tests." Proceeding of the Symposium on Erosion and Productivity of Soils Containing Rock Fragment. Special Publication, vol. 13. Soil Science Society of America, 55–63. https://doi.org/10.2136/sssaspecpub13.c6.

Fouché, O., H. Wright, J. M. Le Cléac'h and P. Pellenard. 2004. "Fabric control on strain and rupture of heterogeneous shale samples by using a non-conventional mechanical test". Appl. Clay Sci. 26(1-4): 367-387. https://doi.org/10.1016/j.clay.2003.12.014.

Geneste, P., M. Raynal, R. Atabek, M. Dardaine, and J. Oliver. 1990. "Characterization of a French clay barrier and outline of the experimental programme." Eng. Geol. 28(3-4): 443-454. https://doi.org/10.1016/0013-7952(90)90027-X.

Karnland, O., U. Nilsson, H. Weber and P. Wersin. 2008. "Sealing ability of Wyoming bentonite pellets foreseen as buffer material–laboratory results." Phys. Chem. Earth Parts A/B/C 33: S472-S475. https://doi.org/10.1016/j.pce.2008.10.024.

Kenney, T. C., W. V. Veen, M. A. Swallow, and M. A. Sungaila. 1992. " Hydraulic conductivity of compacted bentonite–sand mixtures." Can. Geotech. J. 29 (3): 364–374. https://doi.org/10.1139/t92-042.

Komine, H. 2004. "Simplified evaluation on hydraulic conductivities of sand–bentonite mixture backfill." Appl. Clay Sci. 26(1-4): 13-19. https://doi.org/10.1016/j.clay.2003.09.006.

Komine, H. 2010. "Predicting hydraulic conductivity of sand–bentonite mixture backfill before and after swelling deformation for underground disposal of radioactive wastes." Eng. Geol. 114(3-4), 123-134. https://doi.org/10.1016/j.enggeo.2010.04.009.

Ma, L., Y. S. Xu, S. L. Shen and W. J. Sun. 2014. "Evaluation of the hydraulic conductivity of

aquifers with piles." Hydrol. J. 22(2): 371-382. https://doi.org/10.1007/s10040-013-1068-y.

Middelhoff, M., O. Cuisinier, F. Masrouri, J. Talandier and N. Conil. 2020. "Combined impact of selected material properties and environmental conditions on the swelling pressure of compacted claystone/bentonite mixtures." Appl. Clay Sci. https://doi: 10.1016/j.clay.2019.105389.

Mollins, L. H., D. I. Stewart and T. W. Cousens. 1996. "Predicting the properties of bentonite-sand mixtures." Clay Miner. 31(2): 243-252. https://doi.org/10.1180/claymin.1996.031.2.10.

Pusch, R. 1979. "Highly compacted sodium bentonite for isolating rock-deposited radioactive waste products." Nucl. Technol. 45(2): 153-157. https://doi.org/10.13182/NT79-A32305.

Pusch, R. 1980. "Permeability of highly compacted bentonite (No. SKBF/KBS-TR--80-16)." Svensk Kaernbraenslefoersoerjning AB.

Saba, S., Y. J. Cui, A. M. Tang and J. D. Barnichon. 2014. Investigation of the swelling behaviour of compacted bentonite–sand mixture by mock-up tests. Can. Geotech. J. 51(12): 1399-1412. https://doi.org/10.1139/cgj-2013-0377.

Seiphoori, A., A. Ferrari and L. Laloui. 2014. "Water retention behaviour and microstructural evolution of MX-80 bentonite during wetting and drying cycles". Géotechnique. 64(9): 721-734. https://doi.org/10.1680/geot.14.P.017.

Shi, X. S. and J. H. Yin. 2018. "Estimation of hydraulic conductivity of saturated sand–marine clay mixtures with a homogenization approach." Int. J. Geomech. 18(7): p.04018082. https://doi.org/10.1061/(ASCE)GM.1943-5622.0001190.

Sivapullaiah, P. V., A. Sridharan and V. K. Stalin. 2000. "Hydraulic conductivity of bentonite-sand mixtures". Can. Geotech. J. 37(2): 406-413. https://doi.org/10.1139/t99-120.

Tang, A. M., Y. J. Cui and T. T. Le. 2008. "A study on the thermal conductivity of compacted bentonites". Appl. Clay Sci. 41(3-4): 181–189. https://doi.org/10.1016/j.clay.2007.11.001.

Tang, C. S., A. M. Tang, Y. J. Cui, P. Delage, C. Schroeder and E. De Laure. 2011. "Investigating the pressure of compacted crushed-Callovo-Oxfordian claystone." Phys. Chem. Earth Parts A/B/C 36 (17-18): 1857-1866. https://doi.org/10.1016/j.pce.2011.10.001.

Villar, M. V. and P. Rivas. 1994. "Hydraulic properties of montmorillonite-quartz and saponite-quartz mixtures." Appl. Clay Sci. 9(1): 1-9. https://doi.org/10.1016/0169-1317(94)90011-6.

Wang, M. and N. Pan. 2008. "Predictions of effective physical properties of complex multiphase materials." Materials Science and Engineering: R: Reports, 63(1): 1-30. https://doi.org/10.1016/j.mser.2008.07.001.

Wang, Q., A. M. Tang, Y. J. Cui, P. Delage and B. Gatmiri. 2012. Experimental study on the

swelling behaviour of bentonite/claystone mixture. Eng. Geol. 124: 59-66. https://doi.org/10.1016/j.enggeo.2011.10.003.

Wang, Q., A. M. Tang, Y. J. Cui, P. Delage, J. D. Barnichon and W. M. Ye. 2013. "The effects of technological voids on the hydro-mechanical behaviour of compacted bentonite–sand mixture." Soils and Found. 53(2), 232-245. https://doi.org/10.1016/j.sandf.2013.02.004.

Xu, L., W. M. Ye, B. Chen, Y. G. Chen and Y. J. Cui. 2016. "Experimental investigations on thermo-hydro-mechanical properties of compacted GMZ01 bentonite-sand mixture using as buffer materials." Eng. Geol. 213, 46-54. https://doi.org/10.1016/j.enggeo.2016.08.015.

Yang, L. A., T. S. Tan, S. A. Tan, and C. F. Leung. 2002. "One-dimensional self-weight consolidation of a lumpy clay fill." Geotechnique, 52(10), 713-725.

Yong, R. N., P. Boonsinsuk and G. Wong. 1986. "Formulation of backfill material for a nuclear fuel waste disposal vault." Can. Geotech. J. 23(2), 216-228. https://doi.org/10.1139/t86-031.

Zeng, Z. X., Y. J. Cui, F. Zhang, N. Conil and J. Talandier. 2019. "Investigation of swelling pressure of bentonite/claystone mixture in the full range of bentonite fraction." Appl. Clay Sci. https://doi: 10.1016/j.clay.2019.105137.

Zeng, Z. X., Y. J. Cui, F. Zhang, N. Conil and J. Talandier. 2020. Effect of technological voids on the swelling behaviour of compacted bentonite/claystone mixture. Can. Geotech. J. https://doi.org/10.1139/cgj-2019-0339.

Zhai, S., P. Zhang, Y. Xian, J. Zeng and B. Shi. 2018. "Effective thermal conductivity of polymer composites: theoretical models and simulation models." Int. J. Heat Mass Transfer 117, 358-374. https://doi.org/10.1016/j.ijheatmasstransfer.2017.09.067.

Zeng, Z.X., Cui, Y.J., Talandier, J. 2020. Submitted to Acta Geotechnica.

Evaluation of swelling pressure of bentonite/claystone mixtures from pore size distribution

Zhixiong Zeng[1], Yu-Jun Cui[1], Jean Talandier[2]

Abstract: The swelling behaviour of expansive clays is strongly related to the interaction between clay particles. In this paper, a series of constant-volume swelling pressure and mercury intrusion porosimetry (MIP) tests were carried out on MX80 bentonite/Callovo-Oxfordian (COx) claystone mixtures with different bentonite fractions and dry densities. Results show that the swelling pressure increased linearly with the increase of dry density. Additionally, at a given dry density, the larger the bentonite fraction, the larger the swelling pressure. From the MIP results, the inter-particle pore volume decreased with the increases of bentonite fraction and dry density. To link the macroscopic swelling behaviour with the microstructure features, a new method was proposed, allowing the determination of the average inter-particle distance from the pore size distribution. Moreover, a linear relationship was identified between the swelling pressure and the average inter-particle distance, regardless of the bentonite fraction and montmorillonite content.

Keywords: bentonite/claystone mixture; bentonite fraction; swelling pressure; pore size distribution; inter-particle distance

1 Introduction

Expansive clays are composed of large amount of clay minerals, in particular smectite. Upon contact with water, they develop significant swell or swelling pressure. This swelling behaviour of expansive clays can cause severe distress to civil infrastructures, such as building and roads [5, 15-17, 29, 31]. In some applications, such clays can be greatly beneficial in the case of geological radioactive waste disposal where expansive clays (e.g. bentonite-based materials) are commonly used as sealing material. They are expected to fill up the technological voids and excavation fractures and to generate desired swelling pressure to limit the convergence of the excavation damaged zone [14, 20].

Over the past decades, the swelling behaviour of expansive clays has been extensively studied. It has been well admitted that the swelling behaviour of expansive clays could be influenced by

1 Laboratoire Navier/CERMES, Ecole des Ponts ParisTech, 6 et 8 avenue Blaise Pascal, 77455 Marne La Vallée cedex 2, France
2 Andra, 1/7, rue Jean Monnet, 92298 Châtenay-Malabry cedex, France

many factors, including mineralogical composition, index properties, dry density, water content, suction, salinity of pore water, etc. [3, 4, 10, 26-28]. This allowed many empirical relationships to be proposed by fitting the relationships between the swelling pressure/swell and influencing factors. In parallel, the fundamental swelling mechanism of expansive clays were also investigated at microscopic scales. Saiyouri et al. [19] suggested that the swelling of clay minerals comprised two main processes: crystalline and osmotic swelling. The crystalline swelling was a process whereby 0-4 discrete layers of water molecules were placed along the clay monolayers inside particles with a subdivision of the particles into thinner ones that are composed of less stacked clay layers [2, 9, 19]. The cations are attracted to the negatively charged clay particles due to the isomorphous substitution in the crystal lattice (Fig. 1) and the concentration of adsorbed cations near the surface of clay particles is much higher than that far from the surface [24]. This allows the diffuse double layers to be developed on a parallel assembly of clay particles. In that case, the osmotic swelling represented by the interaction of clay particles become dominant. It includes the attractive (van der Waals) and repulsive (diffuse double layer) forces between the clay particles, both of which are highly dependent on the inter-particle distance. To further clarify the swelling behaviour, the inter-particle distance was commonly estimated from the total clay void ratio (or the inter-particle water volume) and the specific surface area [8, 19, 21]. However, the used specific surface area was in general a total value, which included the interlayer zones apart from the inter-particle zones [12]. Moreover, it was assumed that the specific surface could decrease owing to the reduction of unit layer number inside the clay particles during the crystalline swelling process [19, 21]. To address these issues, Liu [9] introduced an empirical parameter related to the average number of the unit layers per clay particle and empirically determined the inter-particle distance from the total void ratio, the thickness of unit layers and the distance between the unit layers. However, the inter-particle distance has not been accurately determined and its relationship to the swelling pressure/deformation has not been well characterized.

In this study, constant-volume swelling pressure tests were performed on compacted MX80 bentonite/Callovo-Oxfordian (COx) claystone mixtures which has been proposed as possible sealing/backfilling materials in the French deep geological disposal for high-level radioactive waste [32]. The swelling pressures of the mixtures with different bentonite fractions (B) and dry densities (ρ_d) were experimentally determined. After the swelling tests, the pore size distributions were investigated using mercury intrusion porosimetry (MIP) and the inter-particle distance was estimated, enabling interpretation of the swelling pressure at a microscopic scale.

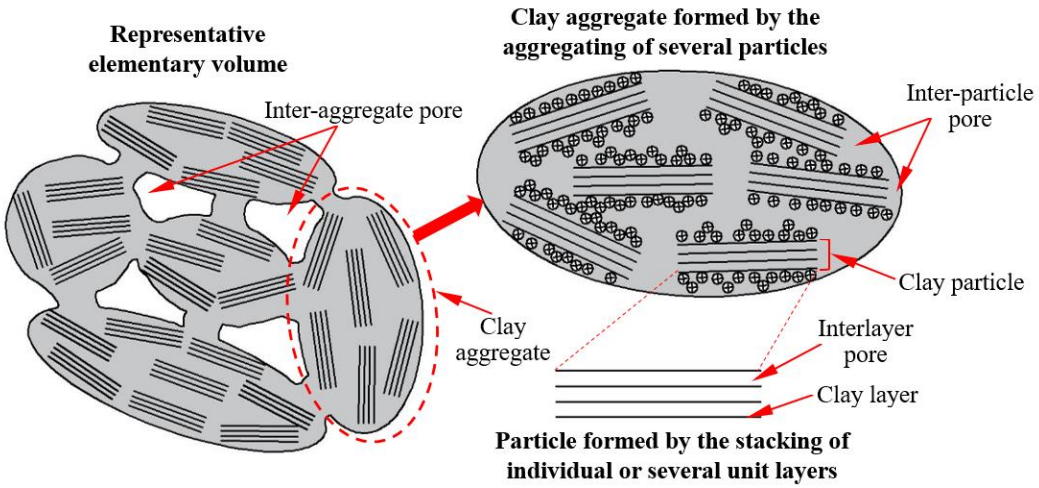

Fig. 1. Fabric units and pore spaces of compacted clay (modified after Liu [9] and Mašín and Khalili [12])

2 Materials and methods

The studied soils were the mixtures of MX80 bentonite and COx claystone. The MX80 bentonite was collected from Wyoming in the USA, while the COx claystone was sampled from the Underground Research Laboratory (URL) at around 490 m depth in Bure, France. The bentonite and claystone were then crushed to particles passing through the 2 mm sieve. The physical properties and mineralogical compositions of the bentonite and claystone are listed in Table 1. To simulate the working environment of the sealing/backfilling materials, synthetic site water, which has the same chemical composition as the site water in the URL, was used as saturation water in the swelling pressure tests. The details about the preparation of the synthetic water can be found in Zeng et al. [33].

The bentonite and claystone powders at their respective initial water contents were well mixed with different proportions of 0/100, 10/90, 20/80, 30/70, 50/50 and 70/30 in dry mass. The corresponding bentonite fractions of the mixtures are 0, 10, 20, 30, 50 and 70%. The samples of 50 mm diameter and 10 mm height were prepared by static compaction in a rigid steel ring using an axial press at a controlled rate of 0.05 mm/min. The target dry densities of the samples are shown in Table 2.

After compaction, the samples were transferred to the testing cell (50 mm in inner diameter), as shown in Fig. 2. The compacted samples were placed between two metallic porous stones and filter papers. On the top, a piston blocked with a screw was used to restrain the axial deformation during the hydration and a force transducer was installed under the cell to monitor

the axial swelling force. The samples were hydrated by synthetic water from the bottom of the cell at a water head of about 1.0 m and the swelling force during the hydration was recorded by a data logger. All tests were performed in a temperature controlled room (20±1 °C).

Table 1. Physical properties and mineralogical compositions of MX80 bentonite and COx claystone

Soil property	MX80 bentonite	COx claystone
Water content (%)	11.4	6.1
Specific gravity	2.76	2.70
Liquid limit (%)	494	41
Plastic limit (%)	46	24
Plasticity index (%)	448	17
Main minerals	Smectite (86%)	Interstratified illite/smectite (40-45%)[a]
	Quartz (7%)	Carbonate (30%)[a]
	Carbonate and feldspar (7%)	Quartz and feldspar (25-30%)[a]

[a] After Fouché et al. [6]

Table 2. Test program and main results

Test No.	Bentonite fraction B (%)	Dry density of sample ρ_{dm} (Mg/m^3)	Initial water content w_m (%)	Final swelling pressure P_s (MPa)
S01	70	1.38	9.8	0.43
S02	70	1.50	9.8	1.11
S03	70	1.63	9.8	2.53
S04	70	1.71	9.8	3.94
S05	50	1.27	8.8	0.13
S06	50	1.56	8.8	0.85
S07	50	1.73	8.8	2.10
S08	50	1.76	8.8	2.91
S09	30	1.50	7.7	0.22
S10	30	1.60	7.7	0.46
S11	30	1.68	7.7	0.78
S12	30	1.79	7.7	1.59
S13	30	1.89	7.7	2.72
S14	30	1.99	7.7	5.23
S15	20	1.60	7.2	0.26
S16	20	1.69	7.2	0.44
S17	20	1.77	7.2	0.70
S18	20	1.88	7.2	1.93
S19	10	1.61	6.6	0.14
S20	10	1.68	6.6	0.23
S21	10	1.78	6.6	0.39
S22	10	1.90	6.6	1.07
S23	0	1.80	6.1	0.15
S24	0	1.90	6.1	0.47
S25	0	1.99	6.1	0.79

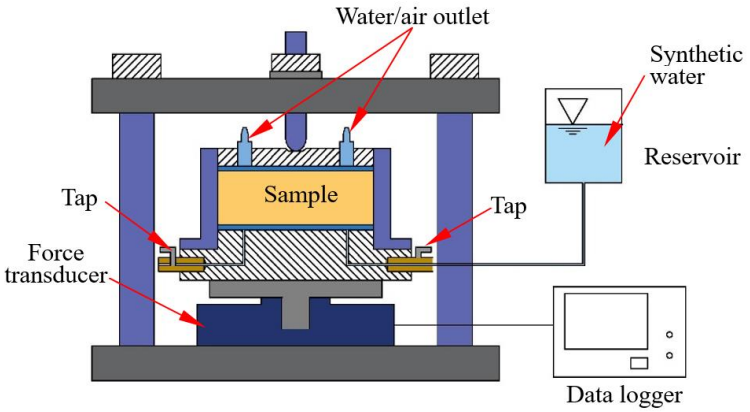

Fig. 2. Layout of the experimental setup for swelling pressure tests

After the swelling pressures tests, the samples were extracted from the cell and rapidly cut into several cubes (maximum volume of 1 cm^3). Prior to the MIP tests, the freeze-drying method was applied to dehydrate the samples [1]. Autopore IV 9500 mercury intrusion porosimeter was used to explore the pore structure of samples. The exploration was performed in two stages: a low-pressure phase with a working pressure from 3.6 to 200 kPa; a high-pressure phase with a working pressure from 0.2 to 228 MPa. The corresponding pore entrance diameter D (μm) at a mercury pressure p (MPa) could be calculated according to the Washburn equation:

$$D=\frac{4T_s\cos\alpha}{p} \quad (1)$$

where T_s is the interfacial tension (taken as 0.485 N/m); α is the contact angle between the mercury-air interface and soil (taken as 130°). According to Eq. (1), the applied working pressures correspond to a maximum entrance pore diameter of 350 μm and a minimum entrance diameter of 5.5 nm.

3 Experimental results and discussions

3.1 Swelling pressure

When water infiltrated into the samples, the swelling pressure increased and then tended to stabilization after 2.5-102 h [32]. The variations of stabilized swelling pressure with dry density for the samples with different bentonite fractions are shown in Table 2 and Fig. 3. For comparison, also presented in the same figure are the results collected from other studies on pure MX80 bentonite [7] and on pure COx claystone [23]. It clearly shows that the swelling pressure increased with the increase of dry density. There was a linear relationship between the logarithm of swelling pressure and dry density for samples with various bentonite fractions. Additionally, the slopes of the fitted lines were almost the same while the intercept of the fitted

lines increased with the increasing bentonite fraction. This suggests that the increase of the bentonite fraction enhanced the swelling capacity of the mixtures.

3.2 Pore size distribution

Fig. 4 presents the pore size distribution of the samples with different dry densities and bentonite fractions after hydration. The curves are illustrated in terms of cumulative and density functions in a semi-logarithmic plot. The cumulative curves were well ordered with respect to the dry density: the curve for a lower dry density lied above the curve for a higher dry density. From the density curves, a trimodal porosity was identified for samples after swelling, especially for those with low dry densities and low bentonite fractions. The three main pore populations were at a mean pore diameter of 10-22 μm for large pores, 0.17-0.52 μm for medium pores and around 0.025 μm for small pores. This was different from the sample in the as-compacted state, for which a typical bimodal porosity was observed, with intra-aggregate pores (inter-particle pores) and inter-aggregate pores [34]. When the as-compacted sample was hydrated with water, water molecules would infiltrate into the interlayer space and intercalated stepwise between the clay sheets, layer after layer up to 4 layers. In this process, the aggregates swelled and progressively invaded the initial inter-aggregate space. Consequently, an increase in inter-particle pore volume and a decrease in the inter-aggregate pore volume were expected, and a new population (medium pores) appeared with the transformation of some initial inter-particle and inter-aggregate pores into medium-pore size. In case of confined conditions, the swelling of clay minerals would be related to the dry density of clay minerals in the samples. For the samples with a larger bentonite fraction and dry density, a higher dry density of clay minerals could be expected and the swelling of aggregate was not allowed to be fully developed; for the samples with a lower bentonite fraction and dry density, a lower dry density of clay minerals would lead to more significant development of inter-particle space. This explained why a lower small-pore peak value and a larger medium-pore volume were observed for the samples with a lower bentonite fraction and dry density after saturation (Fig. 4).

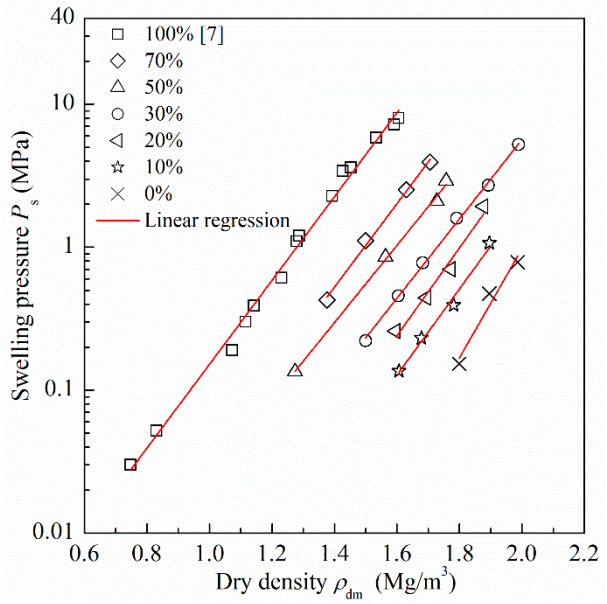

Fig. 3. Variation of the stabilized swelling pressure with sample dry density

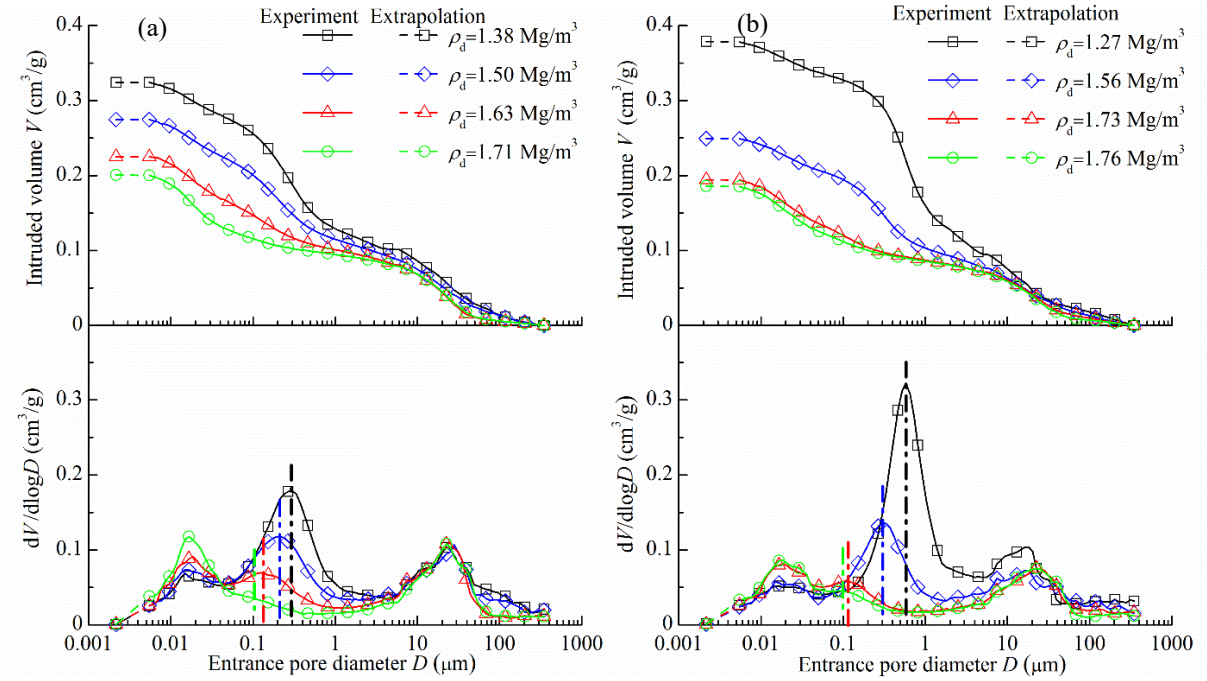

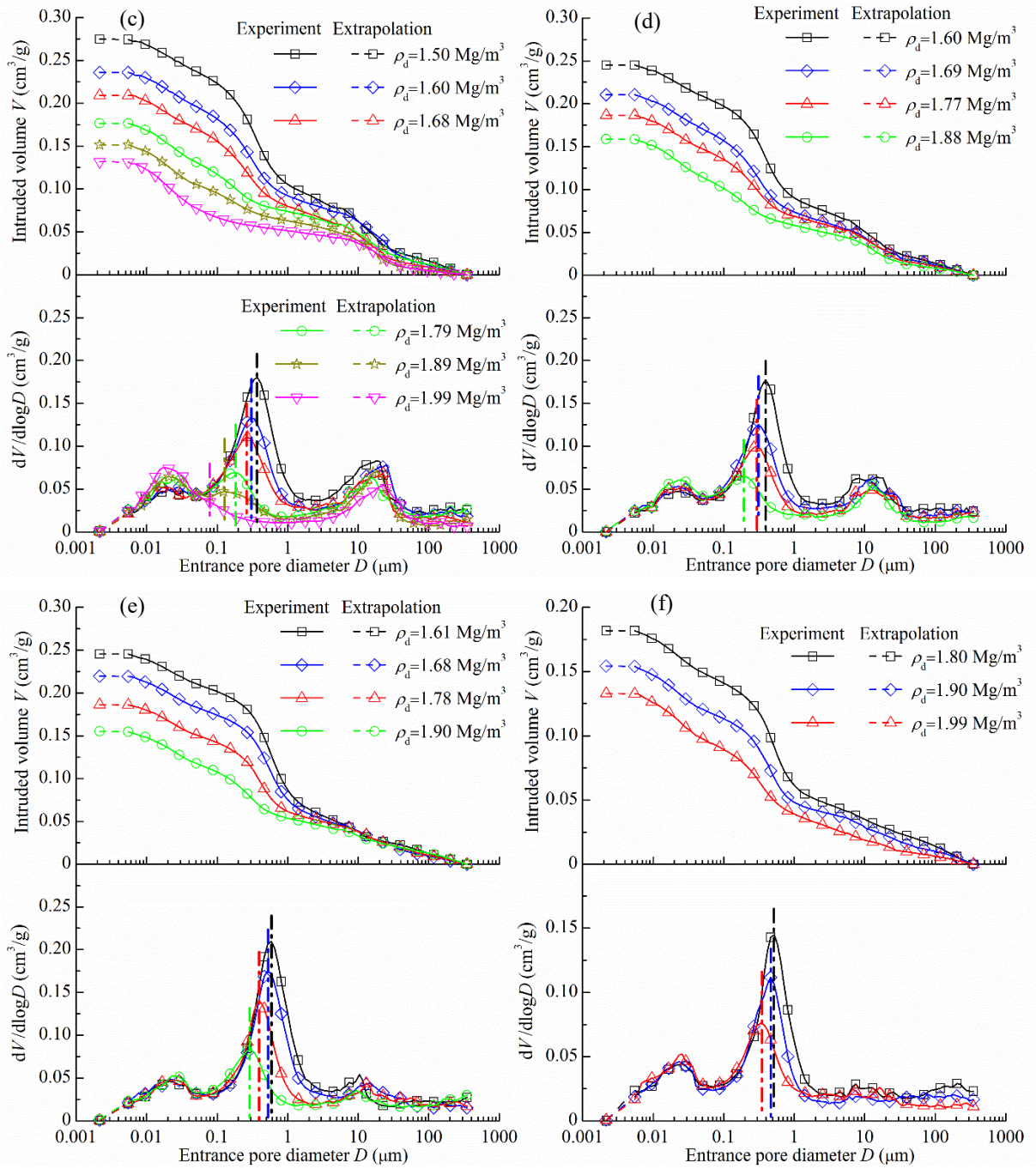

Fig. 4. Pore size distributions of samples with (a) 70%, (b) 50%, (c) 30%, (d) 20%, (e) 10% and (f) 0% bentonite. Note: the dash dot lines represent the delimiting diameters between inter-particle and inter-aggregate pores

3.3 Inter-particle distance and its relationship to swelling pressure

As discussed earlier, the inter-particle interactions are directly related to the swelling behaviour. For the bentonite/claystone mixtures, some inter-particle and inter-aggregate pores would merge into medium pores upon hydration, which added a degree of complexity while separating the inter-particle and inter-aggregate pores. Romero et al. [18] and Yuan et al. [30] suggested that the boundary between inter-particle and inter-aggregate pores would be taken at the merged

peak when they studied the microstructural behaviour of expansive clays hydrated under free-swell and confined conditions. Following their suggestions, the delimiting diameters between inter-particle and inter-aggregate pores are marked by dash dot lines in Fig. 4. The delimiting diameter ranged from 78.7 to 582.8 nm for the bentonite/claystone mixtures, and the larger the dry density and the bentonite fraction the lower the delimiting value. As the interlayer distance of clay minerals is approximately equal to 2.16 nm with 4 layers of water molecules, the inter-particle distance should be larger than 2.16 nm [19]. Imperfectly, the inter-particle pores with a dimeter ranging from 2.16 to 5.5 nm could not be covered by the used mercury intrusion porosimetry. In further analysis, the dV/dlog$D$ in the range of 2.16-5.5 nm was estimated using linear extrapolation according to the density function curves. Then, multiplying the dV/dlog$D$ by the pore dimeter yielded the inter-particle pore volume increment in the range of 2.16-5.5 nm. In Fig. 4, the estimated pore size distributions in the range of 2.16-5.5 nm is presented by dash lines. According to the cumulative curves and the delimiting values, the total inter-particle pore volume in 1 g dry soils ($V_{\text{inter-particle}}$ in cm^3/g) for the samples with different bentonite fractions and dry densities were determined and the obtained results are shown in Fig. 5a. On the whole, the inter-particle pore volume decreased as the dry density and bentonite fraction increased because of the inhibition effect of increasing clay mineral density on the swelling of aggregates. In Fig. 5b, the swelling pressure is plotted versus the inter-particle pore volume. It appears that the swelling pressure increased with the increase of $V_{\text{inter-particle}}$. The relationship between the swelling pressure and $V_{\text{inter-particle}}$ was dependent on the bentonite fraction. At the same $V_{\text{inter-particle}}$, the higher the bentonite fraction, the larger the swelling pressure. Upon the saturation of bentonite/claystone mixtures, clay minerals would form a matrix, the property of which governed the macroscopic swelling behaviour. By contrast, the inert quartz, carbonate or feldspar grains (mainly from the COx claystone) were embedded into the clay matrix [13]. Generally, the small intra-grain pore volume in inert minerals could be ignored [22] and the abovementioned inter-particle pores were resident in the clay matrix. Therefore, to achieve a given swelling pressure, a smaller $V_{\text{inter-particle}}$ was needed for the samples with larger contents of inert minerals.

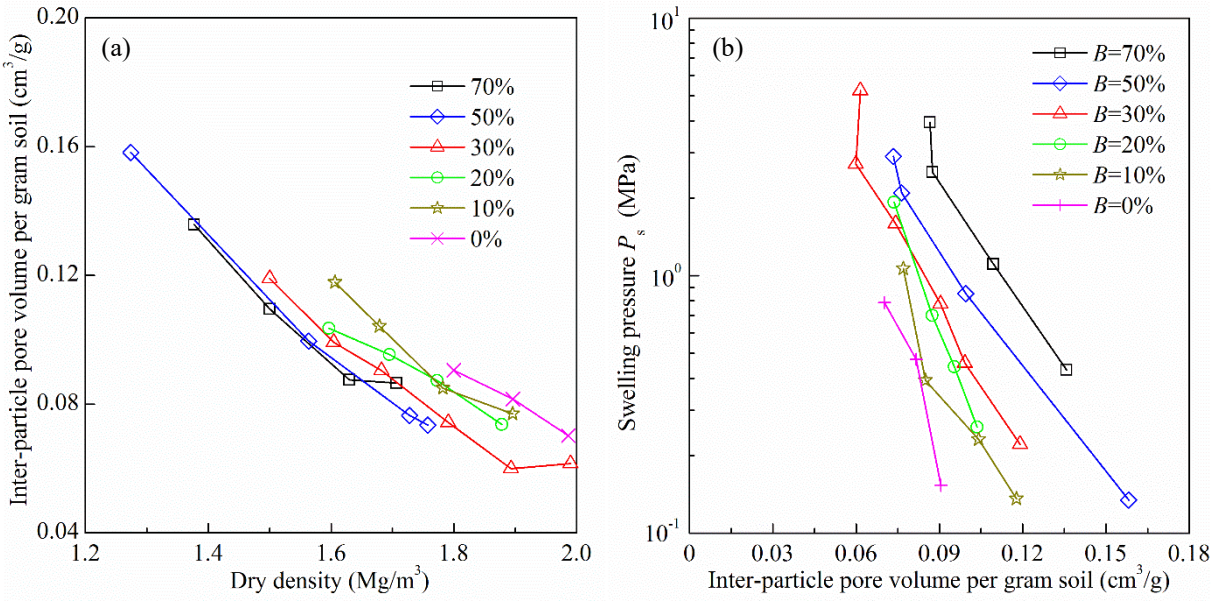

Fig. 5. Variation of the inter-particle pore volume with sample dry density (a) and variation of the swelling pressure with inter-particle volume (b)

To exclude the influence of inert minerals, the inter-particle distance of clay matrix was determined. For the inter-particle pores with a diameter of D_i (μm) in 1 g dry soil, the total length L_i (μm) could be determined by Eq (2) assuming that the pores were cylindrical [15]:

$$L_i=\frac{10^{12}V_i}{S_i}=\frac{4\times10^{12}V_i}{\pi D_i^2} \tag{2}$$

where S_i (μm^2) is the cross-section area of inter-particle pores with a diameter of D_i and V_i (cm^3) is the volume of inter-particle pores with a diameter of D_i in 1 g dry soils, which could be determined according to the cumulative curves (Fig. 4). Then, the surface area A_i (m^2) was calculated using Eq. (3):

$$A_i=10^{-12}\pi D_i L_i=\frac{4V_i}{D_i} \tag{3}$$

Correspondingly, the total surface area of inter-particle pores $A_{\text{inter-particle}}$ (m^2/g) could be computed:

$$A_{\text{inter-particle}}=\sum_{i=1}^{N}\frac{4V_i}{D_i} \tag{4}$$

where N is the number of pore intervals; i is the counter from 1 to N. According to the inter-particle pore volume and total surface area, the average inter-particle distance $\overline{D}$ (nm) could be estimated using Eq. (5) [11]:

$$\overline{D}=\frac{2\times10^3 V_{\text{inter-particle}}}{A_{\text{inter-particle}}} \tag{5}$$

The average inter-particle distances for the samples with various bentonite fractions and dry densities are summarized in Fig. 6a. Since the inter-particle pores only existed in the clay matrix, the obtained inter-particle distance represented the property of the clay matrix. It appears that the average inter-particle distance decreased with the increase of sample dry density. For the samples at the same dry density, the larger the bentonite fraction, the lower the average inter-particle distance. This phenomenon could be related to the high sensitivity of surface area to the small pores. For the samples with a larger bentonite fraction, the larger clay mineral density would restrain the swelling of clay aggregates upon hydration and a larger small-pore volume was expected, compared to those with a lower bentonite fraction. Thereby, a large surface area and a lower average distance were obtained according to Eqs. (3), (4) and (5).

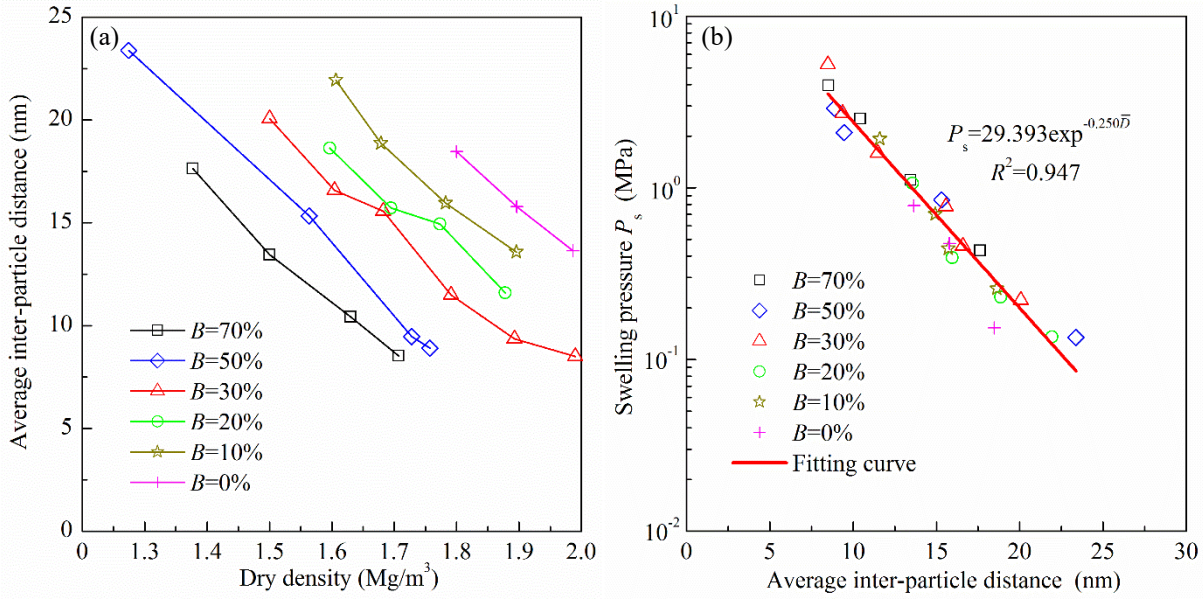

Fig. 6. Variation of the average inter-particle distance with sample dry density (a) and variation of the swelling pressure with average inter-particle distance (b)

Fig. 6b depicts the relationship between the swelling pressure and the average inter-particle distance. For all samples, the swelling pressure decreased with the increase of average inter-particle distance, whatever the bentonite fraction. A good correlation can be obtained between the swelling pressure (P_s) and the average inter-particle distance:

$$P_s=29.393\exp^{-0.250\overline{D}} \quad (6)$$

This indicated that the swelling pressure of bentonite/claystone mixtures could be well described by the average inter-particle distance upon hydration. Note however that the bentonite/claystone mixtures reported in this study were hydrated with synthetic water, which had a negligible effect on the swelling behaviour [25]. The influence of chemistry pore solution on relationship between the swelling pressure and inter-particle distance needs to be

investigated in-depth in further studies.

4 Conclusions

In this study, the swelling pressures and microstructure features of MX80 bentonite/COx claystone mixtures with different bentonite fractions and dry densities were experimentally determined, allowing the swelling pressure to be interpreted at a microscopic scale. According to the obtained results, the following conclusions were drawn.

The swelling pressure increased linearly with the sample dry density. As a given dry density, the swelling pressure increased as the bentonite fraction increased, confirming that the addition of bentonite enhanced the swelling pressure of the mixtures.

The bentonite/claystone mixtures after hydration exhibited a trimodal porosity, with a large pore population with a mean pore diameter of 10-22 μm, a medium pore population with a mean diameter of 0.17-0.52 μm and a small pore population with a mean diameter of 0.025 μm. As the bentonite fraction and dry density increased, the inter-particle pore volume decreased because of the inhibition effect of increasing clay mineral density on the swelling of aggregates.

According to the pore size distribution, the total surface area of inter-particle pores was calculated assuming parallel and cylindrical pores, and the average the inter-particle distance was defined as the ratio of the total volume to the total surface area of inter-particle pores. For the bentonite/claystone mixtures, a linear relationship between the swelling pressure and inter-particle distance was identified, regardless of the bentonite fraction, suggesting that the swelling behaviour was mainly dependent on the inter-particle distance after hydration.

Acknowledgments

The supports from the Chinese Scholar Council (CSC) and the French National Radioactive Waste Management Agency (Andra) are greatly acknowledged.

References

1. Delage P, Lefebvre G (1984) Study of the structure of a sensitive Champlain clay and its evolution during consolidation. Can Geotech J 21 (1): 21–35
2. Delage P, Marcial D, Cui YJ, Ruiz X (2006) Ageing effects in a compacted bentonite: a microstructure approach. Géotechnique 56(5): 291-304

3. Du JP, Zhou AN, Lin X, Bu Y, Kodikara J (2020) Revealing expansion mechanism of cement-stabilized expansive soil with different interlayer cations through molecular dynamics simulations. J Phys Chem C 124(27): 14672-14684

4. Du JP, Zhou AN, Lin X, Bu Y, Kodikara J (2021) Prediction of swelling pressure of expansive soil using an improved molecular dynamics approach combining diffuse double layer theory. Appl Clay Sci 203: 105998

5. Eyo EU, Ng'ambi S, Abbey SJ (2019) Effect of intrinsic microscopic properties and suction on swell characteristics of compacted expansive clays. Transp Geotech 18: 124-131

6. Fouché O, Wright H, Le Cléac'h JM, Pellenard P (2004) Fabric control on strain and rupture of heterogeneous shale samples by using a non-conventional mechanical test. Appl Clay Sci 26(1–4): 367–387

7. Karnland O, Nilsson U, Weber H, Wersin P (2008) Sealing ability of Wyoming bentonite pellets foreseen as buffer material–laboratory results. Phys Chem Earth Parts A/B/C 33: S472-S475

8. Komine H, Ogata N (2004) Predicting swelling characteristics of bentonites. J Geotech Geoenviron Eng 130(8): 818-829

9. Liu L (2013) Prediction of swelling pressures of different types of bentonite in dilute solutions. Colloids Surf A 434: 303-318

10. Ma TT, Yao CQ, Dong Y, Yi PP, Wei CF (2019) Physicochemical approach to evaluating the swelling pressure of expansive soils. Appl Clay Sci 172: 85-95

11. Madsen FT, Müller-Vonmoos M (1985) Swelling pressure calculated from mineralogical properties of a Jurassic opalinum shale, Switzerland. Clays Clay Miner 33(6): 501-509

12. Mašín D, Khalili N (2015) Swelling phenomena and effective stress in compacted expansive clays. Can Geotech J 53(1): 134-147

13. Menaceur H, Delage P, Tang AM, Talandier J (2016) The status of water in swelling shales: an insight from the water retention properties of the Callovo-Oxfordian claystone. Rock Mech Rock Eng 49(12): 4571-4586

14. Middelhoff M, Cuisinier O, Masrouri F, Talandier J, Conil N (2020) Combined impact of selected material properties and environmental conditions on the swelling pressure of compacted claystone/bentonite mixtures. Appl Clay Sci doi: 10.1016/j.clay.2019.105389.

15. Pedarla A, Puppala AJ, Hoyos LR, Chittoori B (2016) Evaluation of swell behavior of expansive clays from internal specific surface and pore size distribution. J Geotech Geoenviron Eng 142(2): 04015080

16. Puppala AJ, Pedarla A, Hoyos LR, Zapata C, Bheemasetti TV (2016) A semi-empirical swell prediction model formulated from 'clay mineralogy and unsaturated soil' properties. Eng Geol 200: 114-121

17. Puppala AJ, Pedarla A, Pino A, Hoyos LR (2017) Diffused double-layer swell prediction

model to better characterize natural expansive clays. J Eng Mech 143(9): 04017069

18. Romero E, DELLA VECCHIA G, Jommi C (2011) An insight into the water retention properties of compacted clayey soils. Géotechnique 61(4): 313-328
19. Saiyouri N, Hicher PY, Tessier D (2000) Microstructural approach and transfer water modelling in highly compacted unsaturated swelling clays. Mech CF Mater 5(1): 41-60
20. Sellin P, Leupin OX (2013) The use of clay as an engineered barrier in radioactive-waste management–a review. Clays Clay Miner 61(6): 477-498
21. Schanz T, Tripathy S (2009) Swelling pressure of a divalent-rich bentonite: Diffuse double-layer theory revisited. Water Resour Res doi: 10.1029/2007WR006495.
22. Souza RFC, Pejon OJ (2020) Pore size distribution and swelling behavior of compacted bentonite/claystone and bentonite/sand mixtures. Eng Geol 275: 105738
23. Tang CS, Tang AM, Cui YJ, Delage P, Schroeder C, De Laure E (2011) Investigating the pressure of compacted crushed-Callovo-Oxfordian claystone. Phys Chem Earth Parts A/B/C 36 (17-18): 1857-1866
24. Tripathy S, Sridharan A, Schanz T (2004) Swelling pressures of compacted bentonites from diffuse double layer theory. Can Geotech J 41(3): 437-450
25. Wang Q, Tang AM, Cui YJ, Delage P, Gatmiri B (2012) Experimental study on the swelling behaviour of bentonite/claystone mixture. Eng Geol 124: 59-66
26. Xiang GS, Xu YF, Xie S, Fang Y (2017) A simple method for testing the fractal dimension of compacted bentonite immersed in salt solution. Surf Rev Lett 24(03): 1750040.
27. Xiang GS, Ye WM, Xu YF, Jalal FE (2020) Swelling deformation of Na-bentonite in solutions containing different cations. Eng Geol 277: 105757.
28. Yuan SY, Liu XF, Sloan SW, Buzzi, O.P. (2016) Multi-scale characterization of swelling behaviour of compacted Maryland clay. Acta Geotech 11(4): 789-804
29. Yuan SY, Buzzi O, Liu XF, Vaunat J (2019) Swelling behaviour of compacted Maryland clay under different boundary conditions. Géotechnique, 69(6): 514-525
30. Yuan SY, Liu XF, Romero E, Delage P, Buzzi O (2020) Discussion on the separation of macropores and micropores in a compacted expansive clay. Géotechnique Lett doi: 10.1680/jgele.20.00056.
31. Zeng ZX, Kong LW (2019) Effect of wetting–drying–freezing–thawing cycles on the swelling behaviour of the Yanji mudstone. Environ Earth Sci 78(15): 435
32. Zeng ZX, Cui YJ, Zhang F, Conil N, Talandier J (2019) Investigation of swelling pressure of bentonite/claystone mixture in the full range of bentonite fraction. Appl Clay Sci doi: 10.1016/j.clay.2019.105137
33. Zeng ZX, Cui YJ, Zhang F, Conil N, Talandier J (2020). Effect of technological voids on the swelling behaviour of compacted bentonite/claystone mixture. Can Geotech J doi:

10.1139/cgj-2019-0339

34. Zeng ZX, Cui YJ, Conil N, Talandier J (2020). Effects of technological voids and hydration time on the hydro-mechanical behaviour of compacted bentonite/claystone mixture. Géotechnique. https://doi.org/10.1680/jgeot.19.P.220

Zeng, Z.X., Cui, Y.J., Talandier, J. 2020. Engineering Geology, 278, 105826.

Evaluating the influence of soil plasticity on hydraulic conductivity based on a general capillary model

Zhixiong Zeng[1], Yu-Jun Cui[1], Jean Talandier[2]

Abstract: Soil hydraulic conductivity depends not only on the state variables such as void ratio and pore size distribution, but also on its physical/geotechnical properties. In this study, Atterberg limits, hydraulic conductivity and mercury intrusion porosimetry (MIP) tests were performed on MX80 bentonite/Callovo-Oxfordian (COx) claystone mixtures. Based on the experimental results obtained in this study together with the test data compiled from literature, a general capillary model considering N_p pores in series was used to evaluate the influence of soil plasticity on the relationship between hydraulic conductivity and pore size distribution. It was found that the best pore interconnection parameter N_p was highly dependent on the soil property. The larger the plasticity index, the larger the best N_p value and the more complex the pore interconnection. The relationship between the best N_p value and plasticity index could be well described by an exponential equation. The general capillary model was then improved to estimate the hydraulic conductivity of different soils. The estimated values using the improved general capillary model were finally compared with the measured ones and the good agreement between the measurement and estimation revealed the good performance of the proposed model.

Keywords: bentonite/claystone mixture; plasticity index; pore size distribution; hydraulic conductivity; general capillary model

1 Introduction

Water flow through soils is a matter of concern in many geotechnical, agricultural and environmental engineering practices, for instance, in the coupled consolidation analysis of clay foundation improvement and land reclamation with dredged clay (Yin, 2009; Zeng et al., 2019a), in the design of isolating barriers in waste disposal facilities (Chapuis, 1990) as well as in the assessment of water infiltration rate and percolation depth into agricultural land (Saffih-Hdadi et al., 2009). Obviously, this percolation process is dominated by the hydraulic conductivity of soils based on Darcy' law. It is therefore essential to quantitatively evaluate the hydraulic conductivity of soils for the geotechnical, agricultural and environmental issues.

1 Laboratoire Navier/CERMES, Ecole des Ponts ParisTech, 6 et 8 avenue Blaise Pascal, 77455 Marne La Vallée cedex 2, France
2 Andra, 1/7, rue Jean Monnet, 92298 Châtenay-Malabry cedex, France

In general, the hydraulic conductivity of saturated soils is experimentally measured using constant-head or fall-head methods (Deng et al., 2011). It can also be indirectly determined from the consolidation curve based on the Terzaghi's consolidation theory (Terzaghi, 1943). It has been well documented that the hydraulic conductivity can be influenced by many factors, including the chemical properties of fluid, void ratio, mineralogy, grain size and shape, grain packing and orientation, pore size distribution and pore interconnection (Yin et al., 2009; Ren et al., 2016; Teng et al., 2019). Several investigators attempted to develop some empirical and theoretical models to predict the hydraulic conductivity from easily determinable physical characteristics of soils (Lapierre et al., 1990; Dolinar, 2009). In most empirical models, the hydraulic conductivity was related to the selected properties of soils, such as void ratio (Berilgen et al., 2006; Dolinar, 2009), effective grain size (Chapuis, 2004) and representative pore size (Deng et al., 2015). However, the applicability of these empirical models to other soils needs further evaluation. Taking the channels of water flow through a cross section as uniform tubes, Kozeny (1927) proposed a theoretical model known as Kozeny-Carman equation, which was further improved by Carman (1956):

$$k=C_{\mathrm{F}}\frac{1}{S_{\mathrm{s}}^2}\frac{\rho_{\mathrm{w}}g}{\mu\rho_{\mathrm{s}}^2}\frac{e^3}{1+e} \tag{1}$$

where k is the hydraulic conductivity; C_{F} is a dimensionless shape constant; S_{s} is the specific surface area; ρ_{w} and μ are the density and viscosity of water, respectively; g is the gravitational acceleration. Its performance was validated for sand (Ren et al., 2016). For clayey soils, which were generally characterized by an aggregated structure, pores could vary from very fine (intra-aggregate) to very coarse (inter-aggregate) (Kong et al., 2018). In that case, the pore size distribution became a crucial factor to be accounted for.

Based on the Poiseuille's equation for laminar flow through a cylindrical capillary, a capillary model was developed by Garcia-Bengochea et al. (1979) assuming parallel and cylindrical nonintersecting pores with different diameters:

$$k=\frac{\rho_{\mathrm{w}}gn}{32\mu}\sum_{i=1}^{m}d_{\mathrm{i}}^2 f(d_{\mathrm{i}}) \tag{2}$$

where n is the porosity of soil; m is the total number of pore intervals; i is the counter from 1 to m; d_i and $f(d_i)$ are the pore diameter and volumetric probability corresponding to i, respectively. In addition to the pore size distribution, the pore interconnection between soil sections could also influence the water flow. Childs and Collis-George (1950) and Marshall (1958) introduced a probabilistic approach to address this issue. Fig. 1a shows the water flow path through a

capillary network in a soil fabric with two in-series sections having the same porosity n for a given length. The probability that a pore of diameter d_1 from one section joins a pore of diameter d_2 of another section is $[nf(d_1)][nf(d_2)]$. According to the basic idea of Poiseuille's equation, the smallest capillary between two capillaries in series governs the water flow through the capillaries (e.g. d_1 from a series of d_1 and d_2 in Fig. 1a) (Watabe et al., 2006). Correspondingly, Garcia-Bengochea et al. (1979) derived the following equation (known as the Marshall Model) for hydraulic conductivity:

$$k=\frac{\rho_w g n^2}{32\mu}\sum_{i_1=1}^{m}\sum_{i_2=1}^{m}\bar{d}^2 f(d_{i_1})f(d_{i_2}) \tag{3}$$

where i_1 and i_2 are the counters from 1 to m; d_{i_1} and d_{i_2} are the pore diameters corresponding to i_1 and i_2, respectively; $\bar{d}$ is the smaller one of d_{i_1} and d_{i_2}; $f(d_{i_1})$ and $f(d_{i_2})$ are the volumetric probabilities of occurrence of pores with diameters d_{i_1} and d_{i_2}, respectively. When a more complex soil fabric is considered, the water flow path through a capillary network in the soil fabric is schematically shown in Fig. 1b. The probability that a pore of diameter d_{i_1} from one section joins other pores of diameters $d_{i_2}, d_{i_3}, \cdots, d_{i_{N_p}}$ from other sections is $[nf(d_{i_1})][nf(d_{i_2})]\cdots[nf(d_{i_{N_p}})]$ (e.g. $[nf(d_1)][nf(d_2)][nf(d_3)][nf(d_4)][nf(d_5)][nf(d_6)]$ in Fig. 1b) and the diameter of the dominant flow channel $\bar{d}$ is the smallest one of $d_{i_1}, d_{i_2}, \cdots, d_{i_{N_p}}$ (e.g. d_6 from a series of d_1, d_2, d_3, d_4, d_5 and d_6 in Fig. 1b). N_p refers to the number of in-series pores in different sizes along a capillary water path for a given length. Under this circumstance, a general capillary model was proposed by Watabe et al. (2006; 2011):

$$k=\frac{\rho_w g n^{N_p}}{32\mu}\sum_{i_1=1}^{m}\sum_{i_2=1}^{m}\cdots\sum_{i_{N_p}=1}^{m}\bar{d}^2 f(d_{i_1})f(d_{i_2})\cdots f(d_{i_{N_p}}) \tag{4}$$

where $i_1, i_2, \cdots, i_{N_p}$ are the counters from 1 to m. The capillary and Marshall models correspond to Eq. (4) when N_p=1 and N_p=2, respectively. As a first attempt, Watabe et al. (2011) applied the general capillary model to the hydraulic conductivity prediction for glacial tills, sandy soils and clayey soils. They found that the N_p value which gives the best prediction was not the same for different soils. However, the influence mechanism of soil property on the hydraulic conductivity was not investigated in-depth.

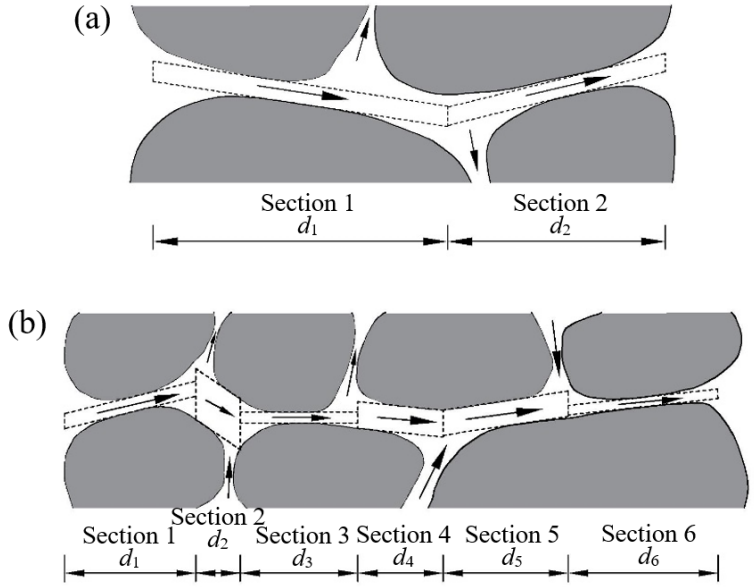

Fig. 1. Typical water flow paths in soils consisting of (a) two sections and (b) six sections (modified after Watabe et al. (2006)). Note: the grey areas represent the solid particle and the arrows indicate the water flow paths

In France, the clay-rich Callovo-Oxfordian (COx) sedimentary rock formation situated in the Meuse/Haute Marne site between 400 and 600 m depth was selected as the host rock to install the future repository for disposing radioactive wastes by the French National Radioactive Waste Management Agency (Andra) (Andra, 2005). The excavation of the underground tunnels for waste storage will produce a large amount of excess COx claystones to be dealt with. To reduce the financial costs and to better ensure the compatibility of chemistry with the host rock, the mixtures of the excavated COx claystone and MX80 bentonite were proposed to seal and backfill the underground drifts and shafts (Zeng et al., 2019b; 2020). After the installation in the repository, the selected mixtures are expected to exhibit permeability low enough to ensure the safety functions of the deep geological repository. Therefore, a comprehensive understanding of the permeability of bentonite/COx claystone mixtures with different bentonite fractions is essential to meet the performance target and to optimize the sealing/backfill element design.

In this study, a series of Atterberg limits, constant-head hydraulic conductivity and mercury intrusion porosimetry (MIP) tests were carried out on MX80 bentonite and COx claystone mixtures. The plasticity index, hydraulic conductivity and pore size distribution of the mixtures with various bentonite fractions were determined. The general capillary model was applied to evaluate the hydraulic conductivities of bentonite/claystone mixtures together with those of other soils compiled from literature. The effect of plasticity index on the best N_p value was

quantitatively determined, allowing an improved general capillary model to be proposed for the hydraulic conductivity estimation of different soils.

2 Materials and methods

2.1 Materials

The MX80 bentonite was taken from Wyoming in the USA, while the COx claystone was extracted at a depth of around 490 m in the Underground Research Laboratory (URL) operated by Andra. The bentonite and claystone were crushed to less than 2 mm. Their grain size distributions determined by dry-sieving and hydrometer methods are shown in Fig. 2. The fractions of fine grains (< 0.08 mm) determined by dry-sieving method are 19% and 0.3%, while the clay contents (< 2 μm) determined by hydrometer method are 86% and 26%, for bentonite and claystone respectively. Based on the X-ray diffraction analysis, the bentonite consists of montmorillonite (86%) and quartz (7%), whereas the claystone comprises interstratified illite/smectite (40-45%), carbonates (30%) as well as quartz and feldspar (25-30%).

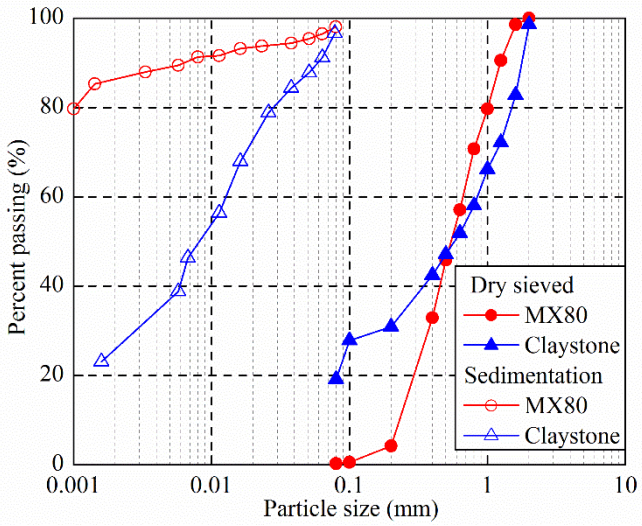

Fig. 2. Grain size distributions of MX80 bentonite and crushed COx claystone

Table 1 summarizes the chemical composition of the pore water extracted from the Andra URL. To simulate the working environment of the bentonite/claystone mixtures, synthetic water was used in the Atterberg limits and hydraulic conductivity tests. It was prepared by mixing the components (Table 1) with deionized water until full dissolution.

Table 1. Chemical composition of the synthetic water

Component	NaCl	$NaHCO_3$	KCl	$CaSO_4 \cdot 2H_2O$	$MgSO_4 \cdot 7H_2O$	$CaCl_2 \cdot 2H_2O$	Na_2SO_4
Content (g/L)	1.950	0.130	0.035	0.630	1.020	0.080	0.700

2.2 Determination of index properties

Prior to the experiments, the bentonite and claystone, at their initial water contents of 11.4% and 6.1%, were first mixed together with different proportions of 10/90, 20/80, 30/70, 50/50 and 70/30 in dry mass. Subsequently, the specific gravity (G_s) values of bentonite, claystone and their mixtures were measured using the pycnometer method in accordance with ASTM D854-10 (2010). Referring to ASTM D4318-10 (2014), the liquid limit (w_L) and plastic limit (w_P) were determined using percussion-cup and rolling test methods, respectively. Note that the bentonite, claystone and their mixtures were wetted with synthetic water in the Atterberg limits test. For comparison, the Atterberg limits of pure bentonite and claystone were also measured with de-ionized water.

2.3 Hydraulic conductivity tests

The hydraulic conductivity tests were performed on cylindrical samples of 50 mm diameter and 10 mm height. The pure claystone and mixtures were poured into a stainless steel ring and statically compacted at a controlled displacement rate of 0.05 mm/min to various dry densities. Subsequently, the compacted samples were transferred into the testing cell of 50 mm diameter and confined by a cap which was blocked using a screw to prevent axial swelling deformation during hydration (Fig. 3). Afterwards, synthetic water was supplied from the bottom of the cell and the swelling pressure during the hydration was monitored by the force transducer installed at the bottom of the cell. After stabilization of the swelling pressure, the constant-head method was adopted to determine the hydraulic conductivity of the compacted bentonite/claystone mixture in this study to gain good accuracy (Pedescoll et al., 2012; Sandoval et al., 2017). The constant water pressure applied at the bottom of samples was 10-200 kPa (about 1/10 of the stabilized swelling pressure), defining a hydraulic gradient ranging from 100 to 2000. The evolution of injected water volume with time was recorded. As the flow rate became steady, the tests were terminated and the corresponding hydraulic conductivity k (m/s) was computed according to Darcy' law:

$$k = \frac{q}{iA} \tag{5}$$

where q is the steady flow rate (m^3/s); i is the hydraulic gradient; A is the cross-section area of sample (m^2). All the tests were carried out at an ambient temperature of 20 ± 1 °C.

2.4 Mercury intrusion porosimetry tests

After the hydraulic conductivity tests, the samples were extracted from the cell for the analysis of pore size distribution by MIP. Freeze-drying method was applied for the sample preparation: the saturated samples were carefully cut into small cubes with a side approximately equal to 1 cm; each cube was rapidly immersed into liquid nitrogen previously vacuum-cooled below its freezing point (-196 °C) and then dehydrated in a vacuumed chamber for about 24 hours (Wang et al., 2014). After that, the samples were put into the low-pressure chamber of porosimeter with a working pressure from 3.6 to 200 kPa, prior to being transferred to the high-pressure chamber with a working pressure from 0.2 to 228 MPa (Bian et al., 2019). According to the Washburn equation, the pore entrance diameter d (μm) intruded by mercury at an applied pressure p (MPa) could be calculated, as follows:

$$d=\frac{4T_s\cos\alpha}{p} \tag{6}$$

where T_s is the interfacial tension (taken as 0.485 N/m); α is the contact angle between the mercury-air interface and soil (taken as 130°). The identified pore entrance diameter ranged from 350 to 0.006 μm.

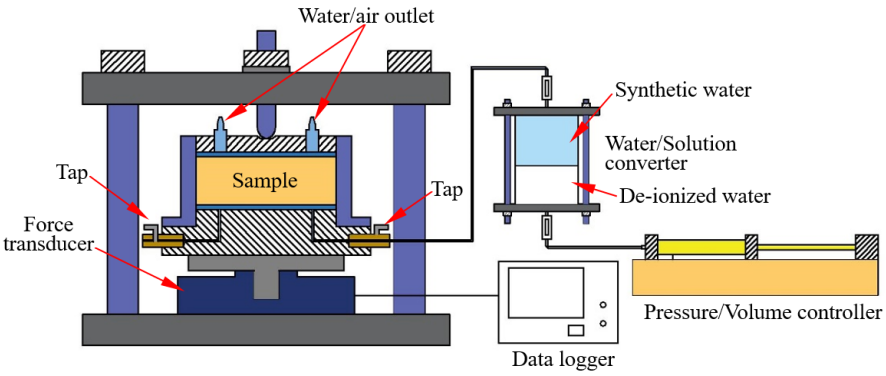

Fig. 3. Layout of the experimental setups for hydraulic conductivity tests

3 Experimental results

3.1 Index properties

The index properties of the bentonite, claystone and their mixtures are shown in Table 2. As the bentonite fraction increased from 0 to 100%, the liquid limit determined with synthetic water increased from 41 to 291% while the plastic limit increased from 23 to 53%. The variation of the corresponding plasticity index with bentonite fraction is illustrated in Fig. 4. It clearly showed that the plasticity index determined with synthetic water increased from 17 to 238% with the increase of bentonite fraction from 0 to 100%. From Fig. 4, it could also be observed

that the plasticity index of the mixtures lied below the dashed line, which could be expressed by the following equation:

$$I_{P\text{-}M}=I_{P\text{-}B}B/100+I_{P\text{-}C}(1\text{-}B/100) \quad (7)$$

where $I_{P\text{-}B}$ and $I_{P\text{-}C}$ and are the plasticity indices of bentonite and claystone, respectively; $I_{P\text{-}M}$ is the mean weighted plasticity index of the bentonite and claystone in the mixture. This was consistent with the observation of Pandian et al. (1995) on bentonite/clayey soil mixtures. It was suspected that the mixing of two clays with various particle sizes and non-uniform clay plate sizes influenced development of the diffuse double layer (Schanz et al., 2013) and a smaller thickness of diffuse double layer surrounding the clay particles was expected in the bentonite/claystone mixture (Sridharan et al., 1986). Accordingly, lower absorbed water on the external clay surface at the liquid limit (Sridharan et al., 1986; Dolinar et al., 2007) and a lower plasticity index were observed compared to the mean weighted value. With de-ionized water, the plasticity indices of bentonite and claystone were found to be 448 and 17%, respectively. The plasticity index of bentonite with synthetic water was significantly lower than that with de-ionized water. Yukselen-Aksoy et al. (2008) found that the saline water could considerably reduce the plasticity index of soils with a plastic index larger than 70%. This water chemistry effect could be explained by the diffuse double layer theory. For the soils treated with saline water, the distance between two particles was inversely with the square root of the salt concentration (Zhu et al., 2013). Thereby, a larger inter-particle spacing and a larger amount of adsorbed water could be expected for the bentonite with deionized water. As a result, a higher plastic index was observed compared to that with synthetic water.

Table 2. Index properties of MX80 bentonite, COx claystone and their mixtures

Soil property	Claystone	Bentonite/claystone mixtures with different bentonite fraction (B)					Bentonite
		B=10%	B=20%	B=30%	B=50%	B=70%	
Water content (%)	6.1	6.6	7.2	7.7	8.8	9.8	11.4
Specific gravity	2.70	2.71	2.71	2.72	2.73	2.74	2.76
Liquid limit (%)	40	54	73	98	140	208	291
Plastic limit (%)	23	25	27	29	34	41	53
Plasticity index (%)	17	29	46	69	106	167	238

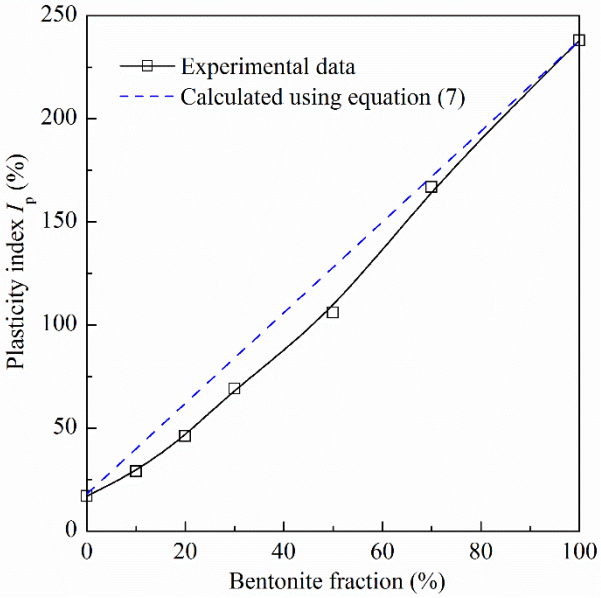

Fig. 4. Variation of plasticity index determined using synthetic water with bentonite fraction

3.2 Hydraulic conductivity

The hydraulic conductivities of the samples with different bentonite fractions and void ratios are summarized in Fig. 5. For comparison, the data of Karnland et al. (2008) on pure MX80 bentonite is also presented. For the samples with 70% bentonite, it decreased from 1.00×10^{-12} to 9.91×10^{-14} m/s as the void ratio decreased from 0.99 to 0.61; for the samples without bentonite, it decreased from 3.65×10^{-10} to 3.14×10^{-11} m/s as the dry density decreased from 0.50 to 0.36. Overall, there was a linear relationship between hydraulic conductivity and void ratio. Similar phenomenon was observed by Berilgen et al. (2006) and Dolinar (2009) when they studied the hydraulic conductivity of crystallized kaolinite and Ca-montmorillonite. As the bentonite fraction decreased from 100% to 0%, the slope of the fitting lines (represented by the solid lines in Fig. 5) kept almost constant, with a mean value of 6.577, while the intercept increased from $10^{-12.722}$ to $10^{-7.401}$. This phenomenon indicated that the addition of claystone significantly reduced the sealing performance of the mixture.

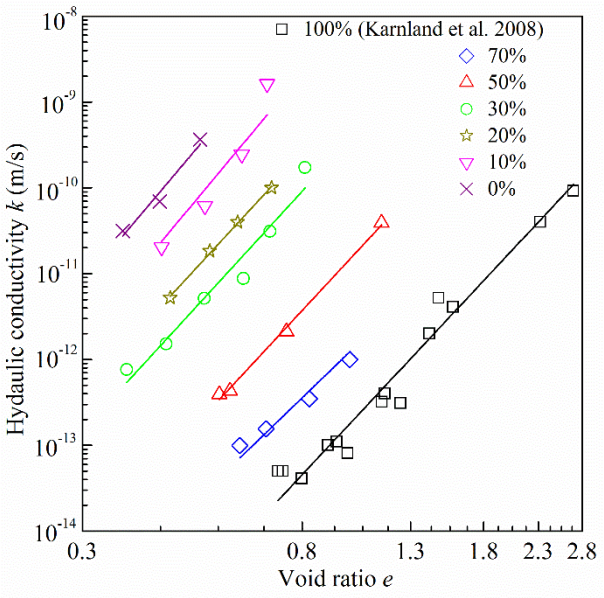

Fig. 5. Relationship between hydraulic conductivity and void ratio

3.3 Pore size distribution

Fig. 6 presents the pore size distribution curves of samples with various bentonite fractions and void ratios. On the whole, the cumulative curves of samples with larger void ratio lied above those of samples with lower void ratio (Fig. 6a, c, e, g, i and k). Regarding the density function curves, the samples with large bentonite fractions and low void ratios showed a typical bimodal pore size distribution, with small pores at 0.25 μm and large pores at 10-22 μm. For the samples with low bentonite fractions and large void ratios, another pore population at 0.17-0.52 μm (designated as medium pores) could be observed apart from the small-pore and large-pore populations (Fig. 6b, d, f, h, j and l). Following the definition of Bian et al. (2019) and Zeng et al. (2020), the pore sizes of 2 and 0.04 μm were adopted to delimit the large (2-350 μm), medium (0.04-2 μm) and small (0.006-0.04 μm) pores. According to the accumulative curves, the corresponding void ratios of large, medium and small pores were determined. Their variations with the total void ratio are illustrated in Fig. 7. It appeared that the large-pore and medium-pore void ratios decreased while the small-pore void ratio increased with the decrease of total void ratio. For the samples at the same total void ratio, as the bentonite fraction increased, the large-pore and small-pore void ratios increased whereas the medium-pore void ratio decreased. Additionally, the void ratios for various populations became more uniform, showing a more complex pore size distribution. This phenomenon could be explained as follows: as a rule, the samples compacted at dry state were characterized by a bimodal porosity, with small and large pores (Wang et al., 2014; Bian et al., 2019). When the clay particles were saturated with water, the water molecules would be successively placed on the clay surface, increasing

the inter-layer space (Wang et al., 2014; Bian et al., 2019). During this process, some initial small pores would become medium pores. Therefore, a decrease of the small-pore void ratio and an increase of the medium-pore void ratio could be expected after saturation. In the meanwhile, the placement of water molecules on the clay surface could also lead to clay particle exfoliation, clogging the large pores (Wang et al., 2014). Note that this process was strongly dependent on the dry density of soil. For the samples with low bentonite fraction, the void ratio of bentonite was relatively large and the placement of water molecules could be significant. Thereby, greater large-pore and medium-pore void ratios and smaller small-pore void ratio could be expected. On the contrary, with a high bentonite fraction, the void ratio of bentonite was relatively low; the limited void space did not allow full placement of water molecules, thereby limiting the microstructure change. For the samples with the same bentonite fraction, the decrease of total void ratio in the as-compacted state reduced the inter-aggregate pore volume (defined as the pores larger than 2 um by Wang et al. (2013)), but did not change the intra-aggregate pore volume. This explained why a greater large-pore (2-350 μm) void ratio was observed for the samples with a greater total void ratio after saturation, despite the much significant clogging process of large pores, thanks to the greater void ratio of bentonite.

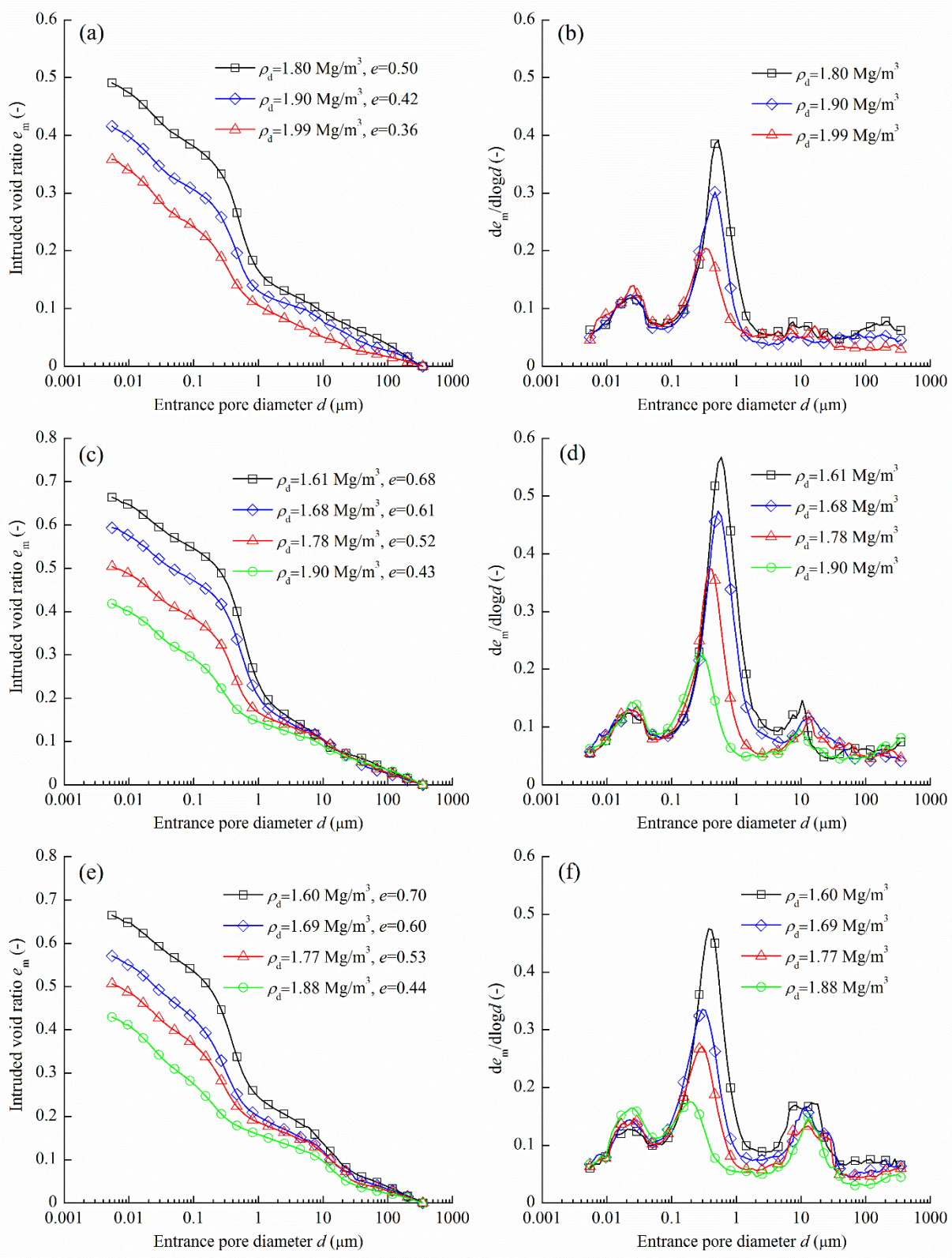
(a)
Intruded void ratio e_m (-)
Entrance pore diameter d (μm)
ρ_d=1.80 Mg/m^3, e=0.50
ρ_d=1.90 Mg/m^3, e=0.42
ρ_d=1.99 Mg/m^3, e=0.36
(b)
$de_m/d\log d$ (-)
Entrance pore diameter d (μm)
ρ_d=1.80 Mg/m^3
ρ_d=1.90 Mg/m^3
ρ_d=1.99 Mg/m^3
(c)
Intruded void ratio e_m (-)
Entrance pore diameter d (μm)
ρ_d=1.61 Mg/m^3, e=0.68
ρ_d=1.68 Mg/m^3, e=0.61
ρ_d=1.78 Mg/m^3, e=0.52
ρ_d=1.90 Mg/m^3, e=0.43
(d)
$de_m/d\log d$ (-)
Entrance pore diameter d (μm)
ρ_d=1.61 Mg/m^3
ρ_d=1.68 Mg/m^3
ρ_d=1.78 Mg/m^3
ρ_d=1.90 Mg/m^3
(e)
Intruded void ratio e_m (-)
Entrance pore diameter d (μm)
ρ_d=1.60 Mg/m^3, e=0.70
ρ_d=1.69 Mg/m^3, e=0.60
ρ_d=1.77 Mg/m^3, e=0.53
ρ_d=1.88 Mg/m^3, e=0.44
(f)
$de_m/d\log d$ (-)
Entrance pore diameter d (μm)
ρ_d=1.60 Mg/m^3
ρ_d=1.69 Mg/m^3
ρ_d=1.77 Mg/m^3
ρ_d=1.88 Mg/m^3

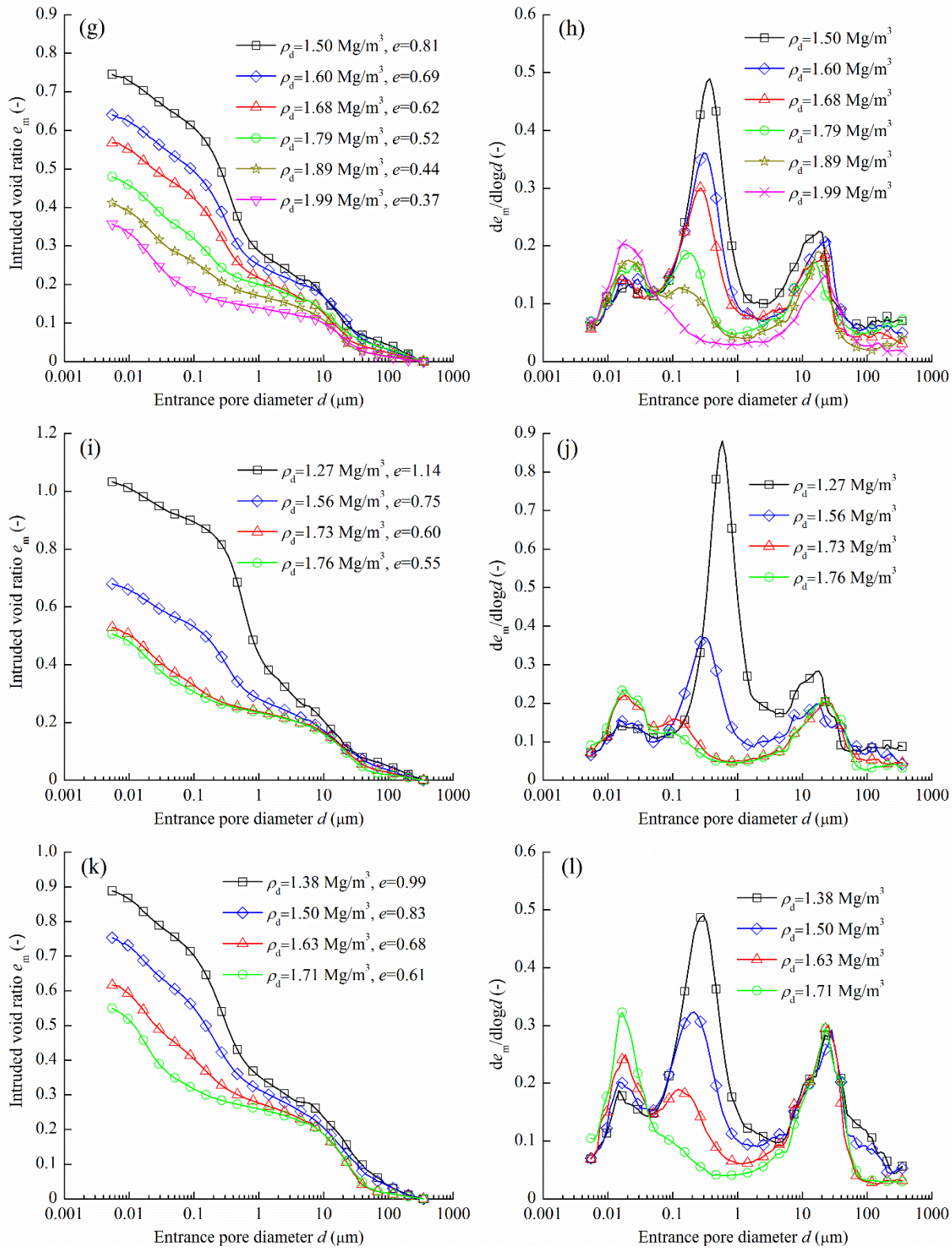

Fig. 6. Pore size distributions of samples: (a) cumulative curves of samples with 0% bentonite, (b) density function curves of samples with 0% bentonite, (c) cumulative curves of samples with 10% bentonite, (d) density function curves of samples with 10% bentonite, (e) cumulative curves of samples with 20% bentonite, (f) density function curves of samples with 20% bentonite, (g) cumulative curves of samples with 30% bentonite, (h) density function curves of samples with 30% bentonite, (i) cumulative curves of samples with 50% bentonite, (j) density function curves of samples with 50% bentonite, (k) cumulative curves of samples with 70% bentonite and (l) density function curves of samples with 70% bentonite

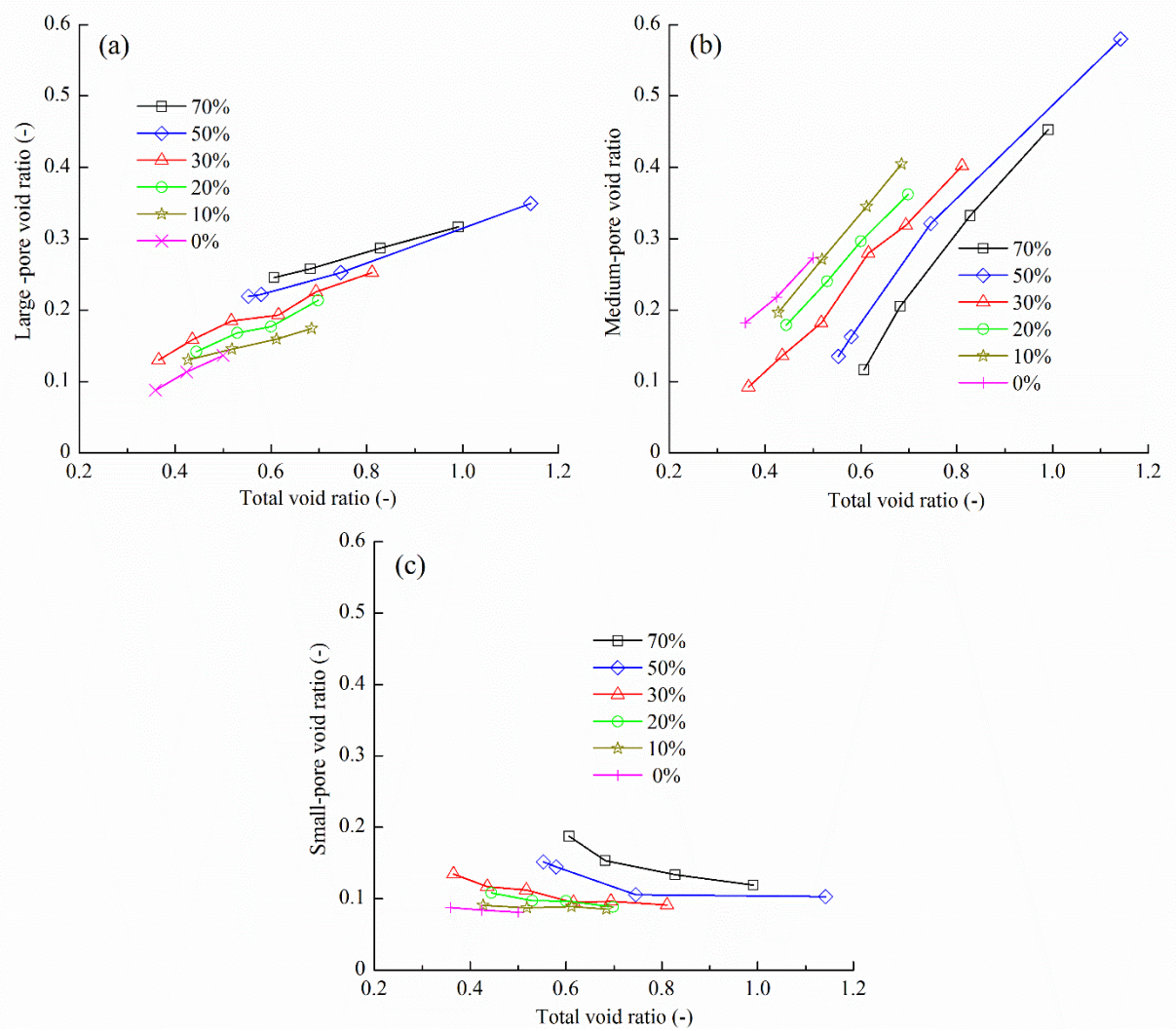

Fig. 7. Variations of (a) large-pore, (b) medium-pore and (c) small-pore void ratios with respect to total void ratio

4 Influence of plasticity index on hydraulic conductivity based on the general capillary model

From the general capillary model (Eq. (4)), the relationship between the hydraulic conductivity and the pore-size parameter (PSP) can be expressed by Eqs. (8) and (9) in the double-liner and double-logarithmic forms, respectively:

$$k=\frac{\rho_{\mathrm{w}} g}{32\mu}\mathrm{PSP} \tag{8}$$

$$\log(k)=\log(\frac{\rho_{\mathrm{w}} g}{32\mu})+\log(\mathrm{PSP}) \tag{9}$$

where PSP is calculated from the pore size distribution using Eq. (10):

$$\mathrm{PSP}=n^{N_{\mathrm{p}}}\sum_{i_1=1}^{m}\sum_{i_2=1}^{m}\cdots\sum_{i_{N_{\mathrm{p}}}=1}^{m}\bar{d}^{2}f(\mathrm{d}_{i_1})f(d_{i_2})\cdots f\left(d_{i_{N_{\mathrm{p}}}}\right) \tag{10}$$

The parameter N_p refers to the pore interconnection and reflects the pore tortuosity. To further analyse the influence of N_p, Eq. (10) with N_p=1, 2, 3, 4, 5, 6, 7, 8, 9 and 10 was applied to compute the PSP of MX80 bentonite/COx claystone mixtures, Louiseville clay (Lapierre et al., 1990), Shanghai muddy clay (Tang and Yan, 2015), Al-Ghat soil (Elkady et al., 2016), Wuhan clay (Zhao et al., 2016), Nanyang clay (Zhao et al., 2016), Maryland clay (Yuan et al., 2019) and Rajasthan monovalent bentonite (Jadda and Bag, 2020) using the respective pore size distributions. As an example, the details of calculating the PSP value with N_p= 4 for the compacted MX80 bentonite/claystone mixture with a bentonite fraction of 30% and void ratio of 0.62 are described in Appendix A. In Fig. 8, the measured hydraulic conductivity is presented versus the PSP value for N_p=1, 2, 3, 4, 5, 6, 7, 8, 9 and 10, together with estimated hydraulic conductivity using Eq. (8). For clarity, all the data are presented in the double-logarithmic plane and the relationship between the estimated hydraulic conductivity and PSP value can be described by a straight line with a slope of 1. For comparison, also plotted in Fig. 8 is the relationship between the measured hydraulic conductivity and PSP determined by Watabe et al. (2006; 2011) for Québec glacial tills (N_p=1, 2 and 3), sandy soils (N_p=2, 3, 4 and 5) and clayey soils (N_p=2, 3, 4 and 5). For all the samples, the larger the value of N_p, the lower the PSP value and the lower the estimated hydraulic conductivity using Eq. (8), suggesting that the samples with a more complex pore interconnection had a lower hydraulic conductivity. When the N_p value was lower than 4, the measured hydraulic conductivities of the MX80 bentonite/COx claystone mixtures appeared on the right-hand of the estimated line. It appeared that the theoretical estimations with N_p=5, 6, 6, 7, 9 and 10 were the best fit for the hydraulic conductivities of MX80 bentonite/COx claystone mixtures with 0%, 10%, 20%, 30%, 50% and 70% bentonite, respectively. This phenomenon indicated that the pore structure was more complex for the samples with a higher bentonite fraction, which was consistent with the MIP results. For the Louiseville clay, Québec glacial tills, sandy soils, clayey soils, Shanghai muddy clay, Al-Ghat soil, Wuhan clay, Nanyang clay, Maryland clay and Rajasthan monovalent bentonite, the theoretical equation showed the best performance for the hydraulic conductivity estimation when the N_p was equal to 5, 3, 4, 5, 4, 5, 4, 6, 6 and 10, respectively.

As an easily determinable property, the plasticity index I_P represents the water quantity adsorbed to the internal and external clay surfaces (Dolinar, 2009). Generally, the higher the clay fraction (< 2 μm), the larger the plasticity index (Seed, 1964; Shi and Herle, 2015). As illustrated in Fig. 1, N_p represents the number of in-series pores in various diameters for a given length. Obviously, the larger the clay fraction, the smaller the grain size, the more complex the

pore interconnection and the larger the N_p value. To quantitatively evaluate the influence of soil property on the N_p value, the best N_p values are plotted versus the plasticity index in Fig. 9 for various soils. Note that the plasticity indices of sandy and clayey soils reported by Watabe et al. (2011) ranged from 0 to 15.3 and from 20.5 to 30.7, respectively. In Fig. 9, the mean plasticity indices of 7.6 and 25.4 were considered for the sandy and clayey soils, respectively. This relationship could be expressed by the following exponential function, with a correlation coefficient of 0.940:

$$N_p=11.587-8.423\exp^{-0.0096I_p} \quad (11)$$

According to Eq. (11), the best N_p values of MX80 bentonite/COx claystone mixtures with 0%, 10%, 20%, 30%, 50% and 70% bentonite, Québec glacial tills, sandy soil, clayey soil, Louiseville clay, Shanghai muddy clay, Al-Ghat soil, Wuhan clay, Nanyang clay, Maryland clay and Rajasthan monovalent bentonite were found to be 4.50, 5.22, 6.18, 7.25, 8.55, 9.90, 5.75, 3.16, 3.76, 4.99, 4.65, 4.97, 4.63, 5.11, 6.16 and 10.20, respectively. Note that the value of N_p applied to Eq. (10) must be a natural number. In this study, two limit values of hydraulic conductivity were first determined using Eq. (8) and (10) with two adjacent natural numbers of the estimated N_p and then the hydraulic conductivity of samples was estimated by a linear interpolation. The relationship between the estimated and measured hydraulic conductivities for different soils is shown in Fig. 10. The estimated hydraulic conductivities agreed well with the measured values, with errors in the range from 1/5 to 5 times the measured values in most cases. This good agreement confirmed the performance of the proposed method in the estimation of hydraulic conductivity.

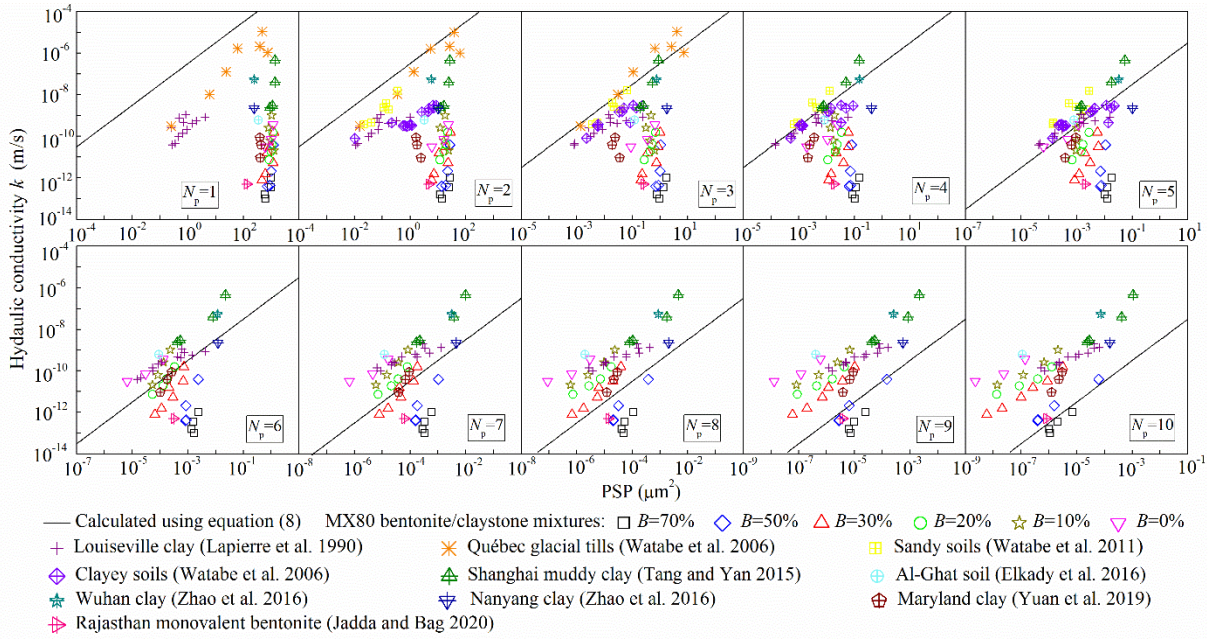

Fig. 8. Relationship between hydraulic conductivity and PSP

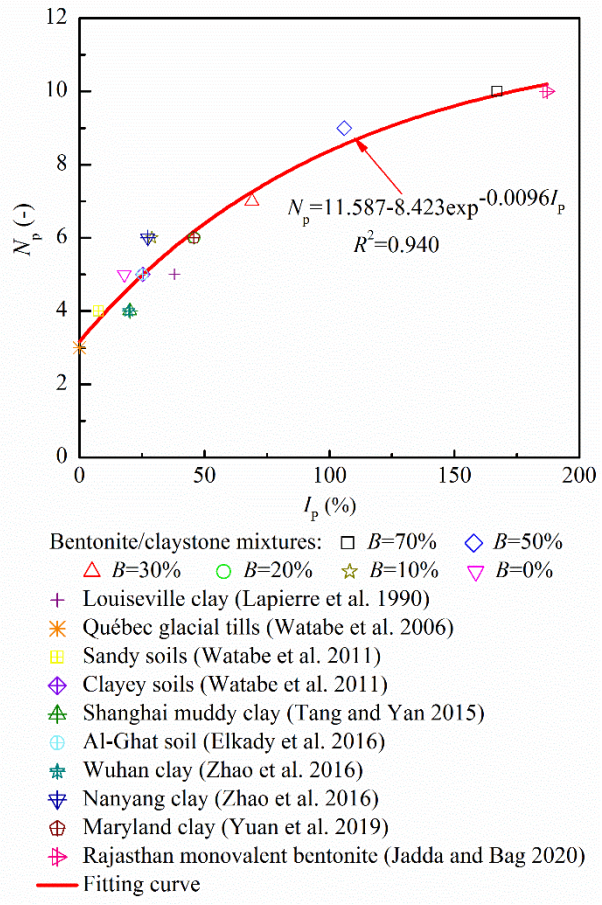

Fig. 9. Variation of N_p with plasticity index I_p

5 Conclusions

In this study, the hydraulic conductivity of bentonite/claystone mixtures with different bentonite fractions and void ratios were experimentally determined, together with the pore size distribution. The experimental results obtained and the data compiled from literature were interpreted using the general capillary model considering N_p pores in series, allowing the influence of plasticity index on the relationship between the hydraulic conductivity and the pore size distribution to be investigated. The following conclusions can be drawn.

(1) There was a liner relationship between the logarithms of hydraulic conductivity and void ratio. The slope of the fitting lines, kept almost constant for the samples with various bentonite fractions whereas the intercept increased with the decreasing bentonite fraction, suggesting that the addition of claystone reduced the sealing performance of the mixture.

(2) According to the microstructure investigation, the dry density of bentonite is lower for the samples with lower bentonite fractions and larger void ratios and therefore, a larger medium-pore (0.04-2 μm) volume but a lower small-pore (0.006-0.04 μm) volume was observed after

saturation due to the more significant swelling of bentonite.

(3) Based on the general capillary model, it was found that the higher the plasticity index, the larger the best value of N_p, indicating a more complex pore interconnection for the soils with higher plasticity. The relationship between N_p and plasticity index could be described by an exponential equation. Based on this equation, an improved general capillary model was proposed. The results estimated using this model were then compared with the measured ones and the good agreement of hydraulic conductivity between the measurement and estimation revealed the performance of the proposed model.

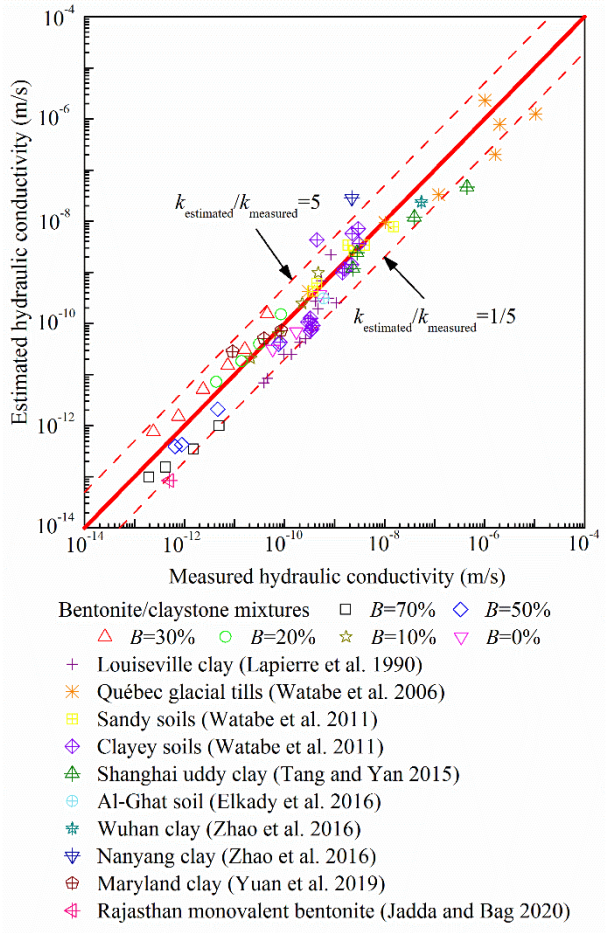

Fig. 10. Comparison between measured and estimated hydraulic conductivities using Eqs. (8), (10) and (11)

Acknowledgments

The authors are grateful to Ecole des Ponts ParisTech, the China Scholarship Council (CSC) and the French National Radioactive Waste Management Agency (Andra) for their financial supports.

Appendix A. The details of calculating the PSP value with N_p=4 for the bentonite/claystone mixture sample with a bentonite fraction is 30% and void ratio of 0.62

According to Eq. (10), the pores should be divided into discrete intervals before the calculation of PSP. Generally, the smaller the discretized intervals, the more precise the calculation of PSP. However, more discretized intervals will increase the computation time. After performing several trial computations, the pores were divided into 33 groups in this study, as shown in Fig. 1A. According to the cumulative pore volume curve of the bentonite/claystone mixture sample with a bentonite fraction of 30% and void ratio of 0.62, the volumetric probability ($f(d)$) of each group (corresponding to different average diameters of d) was calculated. The pore volumetric probability distribution of the sample is summarized in Fig. 1A. Afterwards, N_p=4, m=33, n=0.62/(1+0.62)=0.38 and the pore volumetric probability distribution were substituted into Eq. (10). Fig. 2A is a flowchart showing the process of calculating the PSP value with N_p=4. The corresponding PSP value of the sample was calculated to be 0.0225 μm^2.

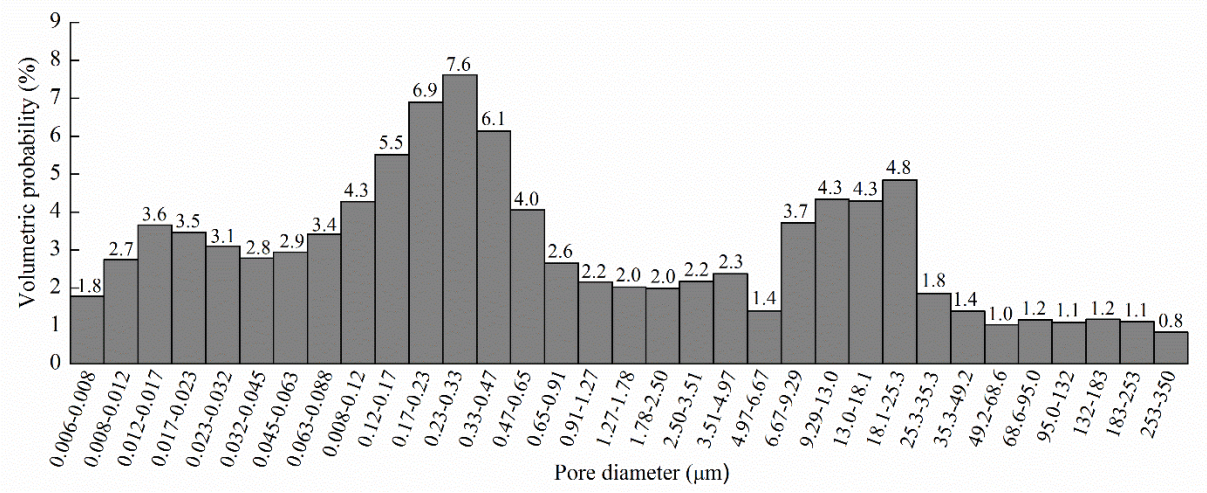

Fig. A1. Pore volumetric probability versus pore diameter for the sample with a bentonite fraction of 30% and void ratio of 0.62. The number above each bar indicates the pore volumetric probability in percent

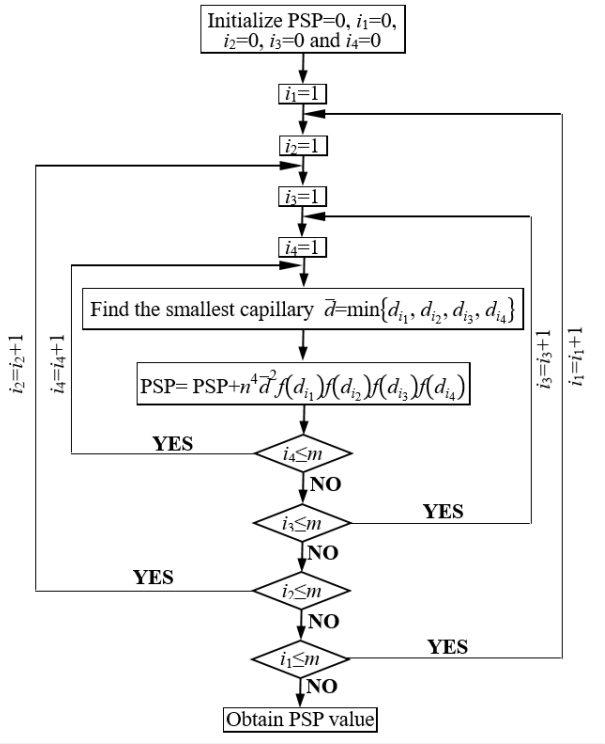

Fig. A2. The flowchart of calculating the PSP value using Eq. (10) with N_p=4

References

Andra, 2005. Dossier 2005 Argile - Synthesis: Evaluation of the Feasibility of a Geological Repository in an Argillaceous Formation (Meuse/Haute-Marne Site). French National Radioactive Waste Management Agency, Chatenay-Malabry CEDEX 241 pp. Accessed 22 November 2018.

ASTM D854-10, 2010. Standard test methods for specific gravity of soil solids by water pycnometer. Soil and Rock, West Conshohocken, Pennsylvania.

ASTM D4318-10, 2014. Standard Test Method for Liquid Limit, Plastic Limit, and Plasticity Index of Soils. Soil and Rock, West Conshohocken, Pennsylvania.

Berilgen, S.A., Berilgen, M.M., Ozaydin, I.K., 2006. Compression and permeability relationships in high water content clays. Applied Clay Science, 31(3-4), 249-261.

Bian, X., Cui, Y.J., Li, X.Z., 2019. Voids effect on the swelling behaviour of compacted bentonite. Géotechnique, 69(7): 593-605.

Carman P.C., 1956. Flow of gases through porous media. Butterworths, London.

Chapuis, R.P., 1990. Sand–bentonite liners: predicting permeability from laboratory tests. Canadian Geotechnical Journal, 27(1), 47-57.

Chapuis, R.P., 2004. Predicting the saturated hydraulic conductivity of sand and gravel using effective diameter and void ratio. Canadian geotechnical journal, 41(5), 787-795.

Childs, E.C., Collis-George, N., 1950. The permeability of porous materials. Proceedings of the

Royal Society of London. Series A. Mathematical and Physical Sciences, 201(1066), 392-405.

Deng, Y.F., Tang, A.M., Cui, Y.J., Li, X.L., 2011. Study on the hydraulic conductivity of Boom clay. Canadian Geotechnical Journal, 48(10), 1461-1470.

Deng, Y.F., Yue, X.B., Liu, S.Y., Chen, Y.G., Zhang, D.W., 2015. Hydraulic conductivity of cement-stabilized marine clay with metakaolin and its correlation with pore size distribution. Engineering geology, 193, 146-152.

Dolinar, B., Miŝiĉ, M., Trauner, L., 2007. Correlation between surface area and Atterberg limits of fine-grained soils. Clays and Clay Minerals, 55(5), 519-523.

Dolinar, B., 2009. Predicting the hydraulic conductivity of saturated clays using plasticity-value correlations. Applied clay science, 45(1-2), 90-94.

Elkady, T.Y., Shaker, A., Al-Shamrani, M., 2016. Hydraulic conductivity of compacted lime-treated expansive soils. In Geo-China 2016 (52-59).

Garcia-Bengochea, I., Altschaeffl, A.G., Lovell, C.W., 1979. Pore distribution and permeability of silty clays. Journal of the Geotechnical Engineering Division, 105(7), 839-856.

Jadda, K., Bag, R., 2020. Variation of swelling pressure, consolidation characteristics and hydraulic conductivity of two Indian bentonites due to electrolyte concentration. Engineering Geology, doi: 10.1016/j.enggeo.2020.105637.

Karnland, O., Nilsson, U., Weber, H., Wersin, P., 2008. Sealing ability of Wyoming bentonite pellets foreseen as buffer material–laboratory results. Phys. Chem. Earth Parts A/B/C, 33, S472-S475.

Kong, L.W., Zeng, Z.X., Bai, W., Wang, M., 2018. Engineering geological properties of weathered swelling mudstones and their effects on the landslides occurrence in the Yanji section of the Jilin-Hunchun high-speed railway. Bulletin of Engineering Geology and the Environment, 77(4), 1491-1503.

Kozeny, J., 1927. Uber kapillare Leitung des Wassers im Boden. Sitzungsber. Akad. Wiss. Wien 136:271–306.

Lapierre, C., Leroueil, S., Locat, J., 1990. Mercury intrusion and permeability of Louiseville clay. Canadian Geotechnical Journal, 27(6), 761-773.

Marshall, T.J., 1958. A relation between permeability and size distribution of pores. Journal of Soil Science, 9(1), 1-8.

Pandian, N.S., Nagaraj, T.S., Raju, P.N., 1995. Permeability and compressibility behavior of bentonite-sand/soil mixes. Geotechnical Testing Journal, 18(1), 86-93.

Pedescoll, A., Knowles, P.R., Davies, P., Garc á, J., Puigagut, J., 2012. A comparison of in situ constant and falling head permeameter tests to assess the distribution of clogging within horizontal subsurface flow constructed wetlands. Water, Air, & Soil Pollution, 223(5), 2263-2275.

Ren, X., Zhao, Y., Deng, Q., Kang, J., Li, D., Wang, D., 2016. A relation of hydraulic conductivity-void ratio for soils based on Kozeny-Carman equation. Engineering geology, 213, 89-97.

Saffih-Hdadi, K., Défossez, P., Richard, G., Cui, Y.J., Tang, A.M., Chaplain, V., 2009. A method for predicting soil susceptibility to the compaction of surface layers as a function of water content and bulk density. Soil and Tillage Research, 105(1), 96-103.

Sandoval, G.F., Galobardes, I., Teixeira, R.S., Toralles, B.M., 2017. Comparison between the falling head and the constant head permeability tests to assess the permeability coefficient of sustainable Pervious Concretes. Case studies in construction materials, 7, 317-328.

Schanz, T., Khan, M.I., Al-Badran, Y., 2013. An alternative approach for the use of DDL theory to estimate the swelling pressure of bentonites. Applied Clay Science, 83, 383-390.

Seed, H.B., Woodward, R.J., Lundgren, R. (1964). Fundamental aspects of the Atterberg limits. J. Soil Mech. Found. Div. ASCE 90(6), 75–105.

Shi, X.S., Herle, I., 2015. Compression and undrained shear strength of remoulded clay mixtures. Géotechnique Letters, 5(2), 62-67.

Sridharan, A., Rao, S.M., Murthy, N.S., 1986. Liquid limit of montmorillonite soils. Geotechnical Testing Journal, 9(3), 156-159.

Tang, Y.Q., Yan, J.J., 2015. Effect of freeze–thaw on hydraulic conductivity and microstructure of soft soil in Shanghai area. Environmental earth sciences, 73(11), 7679-7690.

Teng, J., Kou, J., Zhang, S., Sheng, D., 2019. Evaluating the Influence of Specimen Preparation on Saturated Hydraulic Conductivity Using Nuclear Magnetic Resonance Technology. Vadose Zone Journal, doi: 10.2136/vzj2018.09.0179.

Terzaghi, K., 1943. Theoretical soil mechanics. New York: Wiley.

Wang, Q., Tang, A.M., Cui, Y.J., Delage, P., Barnichon, J.D., Ye, W.M., 2013. The effects of technological voids on the hydro-mechanical behaviour of compacted bentonite–sand mixture. Soils and Foundations, 53(2), 232-245.

Wang, Q., Cui, Y.J., Tang, A.M., Li, X.L., Ye, W.M., 2014. Time-and density-dependent microstructure features of compacted bentonite. Soils and Foundations, 54(4): 657-666.

Watabe, Y., LeBihan, J.P., Leroueil, S., 2006. Probabilistic modelling of saturated/unsaturated hydraulic conductivity for compacted glacial tills. Géotechnique, 56(4), 273-284.

Watabe, Y., Yamada, K., Saitoh, K., 2011. Hydraulic conductivity and compressibility of mixtures of Nagoya clay with sand or bentonite. Géotechnique, 61(3), 211-219.

Yin, J.H., 2009. Influence of relative compaction on the hydraulic conductivity of completely decomposed granite in Hong Kong. Canadian geotechnical journal, 46(10), 1229-1235.

Yuan, S.Y., Liu, X.F., Buzzi, O., 2019. Effects of soil structure on the permeability of saturated Maryland clay. Géotechnique, 69(1), 72-78.

Yukselen-Aksoy, Y., Kaya, A., Ören, A.H., 2008. Seawater effect on consistency limits and compressibility characteristics of clays. Engineering Geology, 102(1-2), 54-61.

Zeng, L.L., Cai, Y.Q., Cui, Y.J., Hong, Z.S., 2019a. Hydraulic conductivity of reconstituted clays based on intrinsic compression. Géotechnique, 1-8.

Zeng, Z.X., Cui, Y.J., Zhang, F., Conil, N., Talandier, J., 2019b. Investigation of swelling pressure of bentonite/claystone mixture in the full range of bentonite fraction. Applied Clay Science. doi: 10.1016/j.clay.2019.105137.

Zeng, Z.X., Cui, Y.J., Zhang, F., Conil, N., Talandier, J., 2020. Effect of technological voids on the swelling behaviour of compacted bentonite/claystone mixture. Canadian Geotechnical Journal, doi: 10.1139/cgj-2019-0339.

Zhao L.Y., Xue Q., Wan Y., Liu L., 2016. A comparative study of anti-seepage performance of clays with high and low liquid limits under drying-wetting cycles. Rock and Soil Mechanics, 37(2), 446-452.

Zhu, C.M., Ye,W.M., Chen, Y.G., Chen, B., Cui, Y.J., 2013. Influence of salt solutions on the swelling pressure and hydraulic conductivity of compacted GMZ01 bentonite. Eng. Geol. 166, 74–80.

Chapter 3. Effect of technological voids on aeolotropic swelling behaviour

INTRODUCTION

In the underground repository, one of the typical approaches is to emplace the bentonite-based materials in the form of pre-compacted blocks in the drifts and shafts. Commonly, the bentonite-based materials are uniaxially compacted and the swelling behaviour of the compacted blocks in various directions can be different. Additionally, during the installation of compacted blocks, it is unavoidable to create technological voids in the form of axial voids between compacted blocks and radial voids between the compacted blocks and the host rock. After hydration, the dry density distribution is heterogeneous due to the presence of technological voids and influences the swelling pressures in various directions.

Accounting for these factors, this chapter in two parts investigates the aeleotropic swelling behaviour of the compacted MX80 bentonite/crushed COx claystone mixture with technological voids. In the first part, the swelling pressure of the specimens without voids was measured in both axial and radial directions by constant-volume method and the effect of dry density on the aeolotropic swelling behaviour was studied. Meanwhile, the axial/radial technological voids were designed and the swelling behaviour of the specimens with axial/radial voids was investigated in both axial and radial directions. In the second part, the water content, dry density and microstructure features at different positions after the infiltration tests were further investigated, to interpret the swelling behaviour of the compacted mixture with different axial technological voids.

The results are presented in two papers. The results on the aeolotropic swelling pressure of compacted bentonite/claystone with and without technological voids are presented in the first paper published in “Engineering Geology”. The details of the swelling mechanism of compacted bentonite/claystone mixture with technological voids are presented in the second paper published in “Canadian Geotechnical Journal”. The articles are presented here in their original versions.

Zeng, Z.X., Cui, Y.J., Conil, N., Talandier, J. 2020. Engineering Geology, 278, 105846.

Experimental study on the aeolotropic swelling behaviour of compacted bentonite/claystone mixture with axial/radial technological voids

Zhixiong Zeng[1], Yu-Jun Cui[1], Nathalie Conil[2], Jean Talandier[3]

Abstract: Pre-compacted blocks of MX80 bentonite/Callovo-Oxfordian (COx) claystone mixture are chosen as sealing/backfill materials in the French concept of deep geological disposal for radioactive waste. Creating technological voids is normally unavoidable during installation in the disposal galleries, in the form of axial voids between compacted blocks and radial voids between the compacted blocks and the host rock. In this work, the aeolotropic swelling behaviour of compacted mixture with axial/radial technological voids was experimentally investigated. Results showed that the aeolotropy coefficient (ratio of radial to axial pressures) of samples without voids increased from 0.46 to 0.88 with the increasing dry density from 1.6 to 2.0 Mg/m^3 due to the relatively concentrated macro-pores which defined a relatively lower local dry density in the side part. For the samples with axial/radial voids, their final axial swelling pressures were in agreement with the unique correlation with final dry density, regardless of the soil density heterogeneity. Samples with axial voids had a larger aeolotropy coefficient than samples without voids, due to the reduction of the orientation of clay particles upon hydration, while samples with radial voids had a smaller aeolotropy coefficient, due to the relatively lower dry density near the cell wall.

Keywords: bentonite/claystone mixture; axial/radial technological voids; swelling pressure; aeolotropy coefficient

1 Introduction

In many countries, deep geological disposal has been considered as a possible solution to store high-level radioactive wastes. (Pusch, 1982; Sellin and Leupin, 2013). In a promising concept, waste canisters are emplaced within galleries excavated in a low-permeability formation a few hundred metres below the surface. Bentonite-based materials are used to construct the sealing/backfill elements thanks to their favourable swelling characteristic, low permeability and good radionuclides retention capacity (Dixon et al., 1985). A typical approach is to emplace bentonite-based materials in the form of pre-compacted blocks between the host rock and waste

1 Ecole des Ponts ParisTech, Laboratoire Navier/CERMES, 6 et 8 avenue Blaise Pascal, 77455 Marne La Vallée cedex 2, France
2 Andra, Centre de Meuse/Haute-Marne, RD 960, 55290 Bure, France
3 Andra, 1/7, rue Jean Monnet, 92298 Châtenay-Malabry cedex, France

canisters. Creating axial technological voids between the compacted blocks, and radial technological voids between the compacted blocks and the host rock is normally unavoidable during such installation operation. After the disposal galleries are closed, the groundwater from the host rock will fill the technological voids and progressively infiltrate into the bentonite-based materials. They swell and form a gel, filling up the technological voids. Afterwards, swelling pressure develops progressively under constrained volume condition. This swelling pressure must be high enough to limit the convergence of the galleries in case of concrete lining failure (Cuisinier et al., 2008), but lower than the yield stress supported by the sealing plugs (Saba et al., 2014a). It is therefore crucial to investigate the swelling behaviour of compacted bentonite-based materials to achieve a reliable design of the repository.

Numerous investigations have been carried out on the swelling behaviour of compacted bentonite-based materials in the context of radioactive waste disposal (e.g. Komine and Ogata, 1994; 1999; Cho et al., 2000; Lee et al., 1999; Saba et al., 2014a). It was well documented that the final swelling pressure is dominated by bentonite dry density (Dixon et al., 1985; Lee et al., 1999; Wang et al., 2012). However, the laboratory measurement of swelling pressure was generally carried out only in the axial direction and the swelling pressures in different directions were considered as the same in many cases. Recently, some researchers attempted to determine the difference between the swelling pressures in different directions (Lee et al., 2001; 2012; Saba et al., 2014a; Jia et al., 2019). Lee et al. (2012) measured both the axial and radial swelling pressures of compacted Korean bentonite with a dry density of 1.5-1.7 Mg/m^3 and observed a larger difference between the axial and radial swelling pressures at a higher dry density. They attributed this phenomenon to the fabrication process of compacted block, in which bentonite powders were uniaxially compacted. To address this point, Saba et al. (2014a) defined an anisotropy coefficient as the ratio of radial to axial swelling pressures. For compacted GMZ bentonite, Jia et al. (2019) found that the anisotropy coefficient decreased from 1.0 to 0.76 owing to the increasingly oriented arrangement of bentonite grains when the dry density increased from 1.46 to 1.71 Mg/m^3. Saba et al. (2014a) studied the axial and radial swelling pressures of compacted MX80 bentonite/sand mixture with a wide range of bentonite dry density. They indicated that the anisotropy coefficient was mainly related to the bentonite dry density: at low bentonite dry densities (lower than 1.16 Mg/m^3), the anisotropy decreased with increasing bentonite dry density; at medium dry densities (from 1.16 to 1.3 Mg/m^3), the coefficient was near 1.0; at high bentonite dry densities (larger than 1.3 Mg/m^3), anisotropy increased with increasing bentonite dry density. They explained this phenomenon by the

swelling and splitting of bentonite upon hydration, which could lead to microstructure collapse and thus reduce the initial anisotropy induced by uniaxial compaction. At medium bentonite dry densities, the microstructure collapse eliminated the initial anisotropy, developing an isotropic microstructure. At high bentonite dry densities, the initial anisotropy would remain because the smaller macro-pore space prevented the microstructure collapse. At very low dry densities, the macro-pores were not fully filled by the swollen bentonite and the oriented microstructure was also preserved.

In the real deep geological repository, filling of technological voids will lead to a decrease in the dry density of compacted blocks and the swelling behaviour can change upon hydration. Moreover, the dry density distribution is not heterogeneous due to the presence of technological voids in short term, influencing the swelling pressures in various directions. Many studies on the swelling behaviour of compacted bentonite-based materials with technological voids were reported (Villar et al., 2005; Saba et al., 2014a; Bian et al., 2019a; 2019b; 2020; Jia et al., 2019; Zeng et al., 2020a; 2020b; 2020c). Wang et al. (2013) and Saba et al. (2014a) pointed out that the unique relationship between axial swelling pressure and final bentonite dry density could be extended to compacted MX80 bentonite/sand mixture (70% bentonite-30% sand in dry mass) with 14% radial technological voids. Moreover, Saba et al. (2014a) suggested that 14% radial technological voids had a negligible effect on the anisotropy coefficient. Jia et al. (2019) performed several swelling pressure tests on compacted GMZ bentonite with 13.3-26.7% axial voids. They concluded that a void of more than 16.7% could induce a lower axial swelling pressure without significant change of radial swelling pressure, resulting in an anisotropy coefficient higher than that without voids even though the global dry density was the same. Their works were however limited to the voids between compacted samples and the rigid cell wall, which simulated the host rock. The effect of axial technological voids between the blocks was not studied. Moreover, the mechanism of swelling behaviour of compacted blocks with axial/radial technological voids was not investigated.

This study investigated the aeolotropic swelling behaviour of compacted MX80 bentonite/Callovo-Oxfordian (COx) claystone mixture with technological voids. Unlike in Saba et al. (2014a), the term of "aeolotropy" was adopted to distinguish from the common term of ''anisotropy", which physically represents the intrinsic material property. To this end, the swelling pressure of the samples was measured in both axial and radial directions by the constant-volume method. Three set of experiments were performed to examine the effects of dry bulk density and voids: (i) initial dry density varied without voids; (ii) final dry density

varied using different initial axial technological voids; (iii) final dry density varied using different initial radial technological voids. After the swelling pressure tests, the water content and dry density at various positions were determined to interpret the aeolotropic swelling mechanism of the compacted mixture with different technological voids.

2 Materials and methods

2.1 Materials

The soil used in this study was a mixture of MX80 bentonite and crushed COx claystone (30/70 in dry mass), which was selected as a candidate buffer/backfill material for the Cigéo project by the French National Radioactive Waste Management Agency (Andra). The MX80 bentonite was extracted from Wyoming, USA. Its physical and mineralogical properties are presented in Table 1. The MX80 bentonite is of light gray colour, dominated by montmorillonite (86% in dry mass). The liquid limit is 494%, the plastic limit is 46% and the unit mass is 2.76 Mg/m^3, which are consistent with the results of Karnland et al. (2008), Tang et al. (2008), Seiphoori et al. (2014) and Saba et al. (2014). The crushed COx claystone used in this study was sampled from the Andra Underground Research Laboratory (URL) in Bure. The COx claystone has an interstratified illite/smectite content of 40-45% (Fouché et al., 2004) and a unit mass of 2.70 Mg/m^3. The grain size distributions of the bentonite and claystone powders determined by dry sieving and sedimentation (ASTM D422, 2007) are presented in Fig. 1. The D_{50} values of the dry bentonite and claystone powders are 0.55 and 0.58 mm, respectively. After saturation, the clay-size fractions of the bentonite and claystone are 86% and 26%, respectively.

The saturation water used in this study was synthetic water prepared according to the methods of Zeng et al. (2019).

Table 1. Physical and mineralogical properties of MX80 bentonite

Soil property	This work	Tang et al. (2008)	Seiphoori et al. (2014)	Saba et al. (2014)	Karnland et al. (2008)
Specific gravity	2.76	2.76	2.74	2.77	-
Consistency limit					
Liquid limit (%)	494	520	420	575	-
Plastic limit (%)	46	42	65	53	-
Plasticity index (%)	448	478	355	522	-
Main minerals					
Montmorillonite (%)	86	92	85	-	80
Quartz (%)	7	3	-	-	2-3

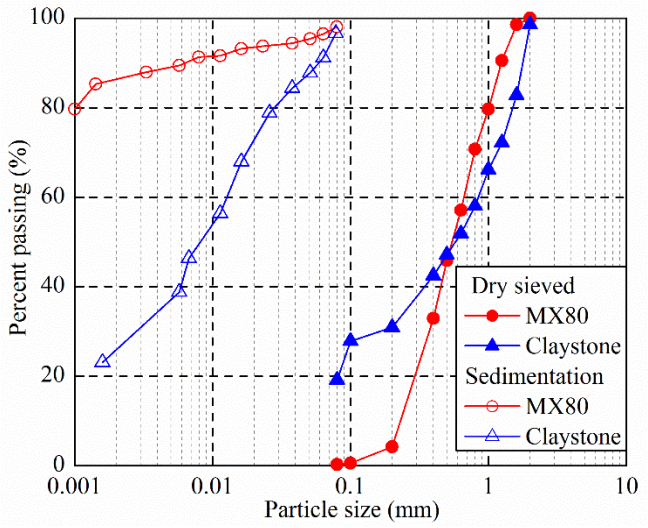

Fig. 1. Grain size distributions of MX80 bentonite and crushed COx claystone

2.2 Experimental technique and procedure

Fig. 2 depicts the experimental set-up used in this study. The test sample was installed in a stainless cell (50 mm in diameter) and placed between two porous stones (hydraulic conductivity is about 1.0×10^{-5} m/s) and filter papers (hydraulic conductivity is about 0.15 m/s). It was saturated from the bottom of the cell at a constant water pressure of 9.8 kPa and the expelled air/water flowed through the air/water outlets at the top. The confined saturation conditions for the sample were guaranteed by the cell wall and a metallic cap that was locked using a screw. A force transducer was mounted under the cell base. A total pressure sensor (6 mm in diameter) was installed through a port on the side of the cell and its measuring surface was flush with the cell wall to ensure satisfactory pressure measurement. Based on the cell design, the axial force at the top of samples was transmitted to the piston and then the force transducer while the total pressure sensor directly measured the radial pressure at one location around the perimeter of the sample. All data were automatically collected by a data logger. The whole set-up was placed in a constant temperature room (controlled at 20 ± 1 °C).

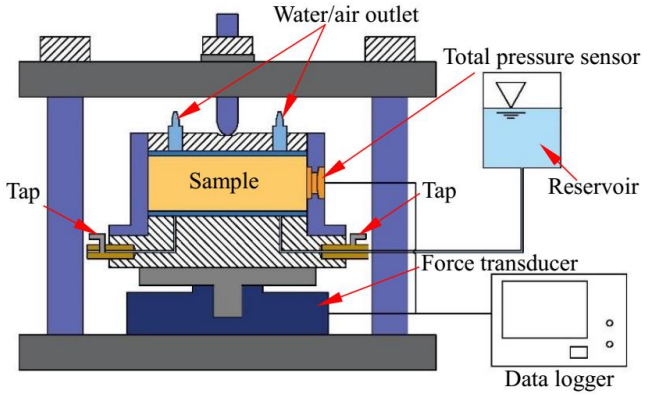

Fig. 2. Layout of the constant-volume cell

The soil was prepared by mixing the bentonite powder with claystone powder using a stirrer for more than 10 min. The initial gravimetric water contents of the bentonite and claystone powders were 11.4 and 6.1%, respectively. The water content of the obtained mixture was 7.7%. A pre-determined amount of mixture was weighed and poured into a cylindrical mould. The samples were prepared by compaction in the mould. Five disks (50 mm in diameter and 10 mm in height) were compacted to the dry densities of 1.6, 1.7, 1.8, 1.9 and 2.0 Mg/m^3, respectively, in order to investigate the effect of dry density on the aeolotropic swelling behaviour (Table 2). Additionally, another four disks at the same dimensions were compacted to a dry density of 2.0 Mg/m^3 to study the effect of radial voids. In the case of axial voids, twelve disks (49.80 mm in diameter and 5 mm in height) with a dry density of 2.0 Mg/m^3 were prepared.

Table 2. Experimental program and main results

Test No.	Technological voids		Global dry density (Mg/m^3)	Final axial swelling pressure (MPa)	Final lateral swelling pressure (MPa)
	Mode	Amount (%)			
T01	Without voids	0	2.0	5.18	4.55
T02		0	1.90	2.81	2.35
T03		0	1.80	1.60	1.14
T04		0	1.70	0.83	0.53
T05		0	1.60	0.46	0.21
T06	Axial voids	7.4	1.85	2.30	2.19
T07		9.6	1.81	1.59	1.53
T08		13.8	1.72	1.00	0.98
T09		18.5	1.63	0.53	0.53
T10	Radial voids	5	1.90	2.86	2.33
T11		10	1.80	1.62	1.14
T12		15	1.70	0.86	0.47
T13		20	1.60	0.52	0.20

For the tests without voids (T01 to 05), the samples were directly transferred into the test cell by connecting the ends of the two cells (the compaction mould and test cell). For tests T06 to 09, axial voids between the 5-mm disks were simulated by a pre-defined space between disks using bentonite grains (Fig. 3a). For each test, three identical disks were used. After the installation of the first disk, 0.10 g of bentonite grains of pre-defined sizes were scattered on the top of the disk. Then, the second disk, the second layer of bentonite grains and the third disk were emplaced in sequence. As a result, two identical layers of bentonite grains were sandwiched among three disks and two gaps were created between disks. In this study, four samples with different gaps of 0.60, 0.80, 1.20 and 1.70 mm (corresponding to the technological voids of 7.4%, 9.6%, 13.8% and 18.5%, respectively) were prepared using four groups of

bentonite grains (0.25-0.40, 0.63-0.80, 1.00-1.25 and 1.60-2.00 mm). Note that the total mass of bentonite grains was smaller than 0.5% of all disks' mass and thereby, their influence could be ignored. To facilitate the synthetic water to go into the technological voids at the beginning of hydration, the lateral surfaces of all the disks were covered by filter papers (about 0.10 mm thick), in addition to the filter papers at the top and bottom of samples (Fig. 3a). For tests T10 to 13 (Fig. 3b), four compacted disks with a dry density of 2.0 Mg/m^3 were extracted from the compaction mould and trimmed into smaller disks with the same height of 10 mm but with different diameters of 48.73, 47.43, 46.10 and 44.72 mm. The trimmed disks were positioned at the centre of test cell, keeping the initial gaps of 5, 10, 15 and 20% of the total volume respectively between the samples and cell wall. For all the tests (T01 to 13), the pressure sensor corresponded to the middle position of samples by changing the thickness of the porous stone at the bottom of samples. Note that for the tests with axial technological voids (T06 to 09), the testing surface of pressure sensor (6 mm in diameter) was in contact with the central disk (5 mm in thickness) and initial technological voids on the two sides of the central disk. Then, the synthetic water was injected from the bottom of the cell and the axial and radial pressures were measured during the hydration.

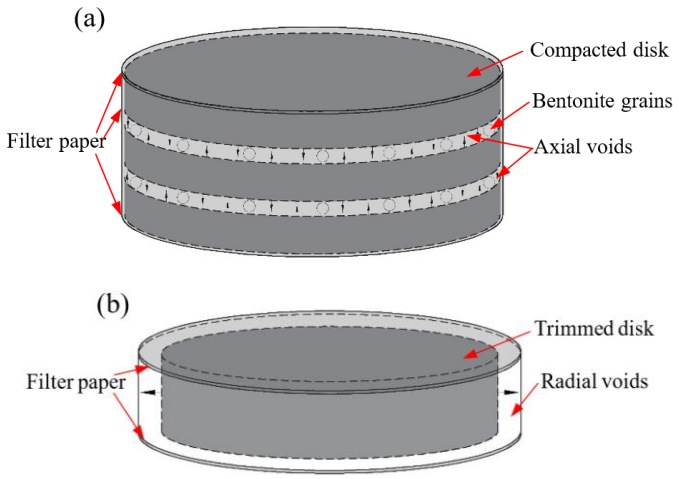

Fig. 3. Different technological voids considered: (a) axial voids and (b) radial voids

After the infiltration tests, the samples without voids (T01 to 05) and with radial voids (T10 to 13) were extracted from the cell by pushing the sample from the bottom. By contrast, for the tests with axial voids (T06 to 09), the samples were carefully trimmed from the cell by cutting the edge of sample, because the common extruding method may cause significant sample compaction and lead to misjudgment on the soil density distribution in the vertical direction. The samples with initial axial voids (T06 to 09) were divided into five parts termed part I, part

II, part III, part IV and part V, numbered sequentially from the top. As shown in Fig. 4a, parts II and IV corresponded to initial voids and a 1-mm thick surface disk from the two sides, while parts I, III and V were the three disks. The sample T01 and those with initial radial voids (T10 to 13) were divided into parts I, II and III. As shown in Fig. 4b, part I is a ring having inner and outer diameters of 40 and 50 mm, which included initial voids; part II is a ring with inner and outer diameters of 20 and 40 mm; part III is the rest of the cylinder within a diameter of 20 mm. Each part was cut into two pieces. One piece was oven-dried at 105 °C for a period of 24 h to determine the water content; the other piece was immersed into non-aromatic hydrocarbon fluid (Kerdane) to determine the dry density.

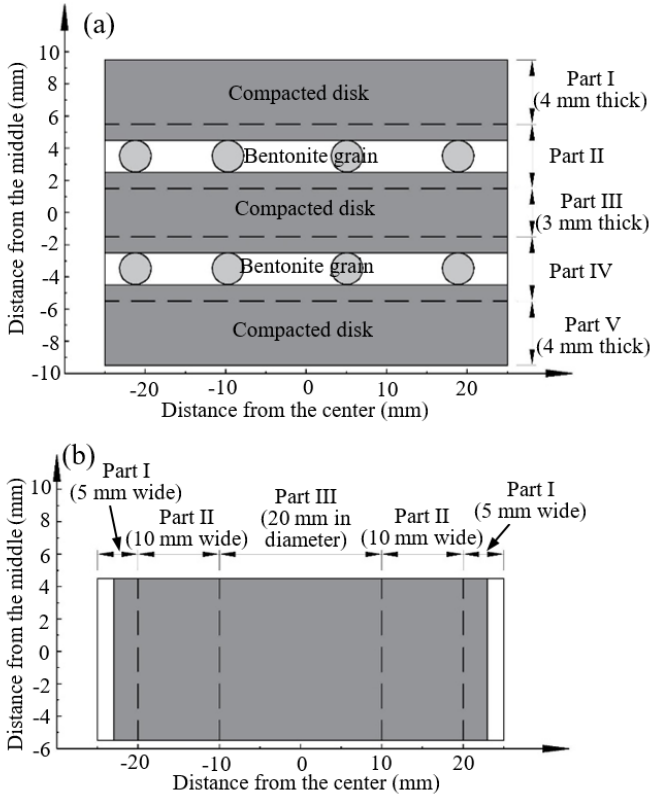

Fig. 4. Schematic view of sample cutting: (a) axial voids and (b) radial voids

3 Experimental results

3.1 Swelling behaviour of samples without technological voids

The evolutions of axial and radial swelling pressures with respect to elapsed time for the samples without voids (T01 to 05) are shown in Fig. 5. Both axial and radial swelling pressures started with a quick increase. For the samples with high dry densities (larger than 1.8 Mg/m^3), the axial swelling pressure increased and then reached stabilization at 5.18, 2.81 and 1.60 MPa after about 2600, 1860 and 1710 min for tests T01 to 03, respectively. For the samples with low

dry densities (smaller than 1.7 Mg/m^3), it increased until reaching peak values, then decreased and finally reached stabilization at 0.83 and 0.46 MPa at about 1580 and 1060 min for T04 and T05, respectively. The times needed to reach stabilization were comparable for the axial and radial swelling pressures. The final values of swelling pressures are summarized in Table 2. The larger the dry density, the larger the final axial and radial swelling pressures, in agreement with the observation by Zeng et al. (2019). Moreover, the difference between them increased with the increase of dry density.

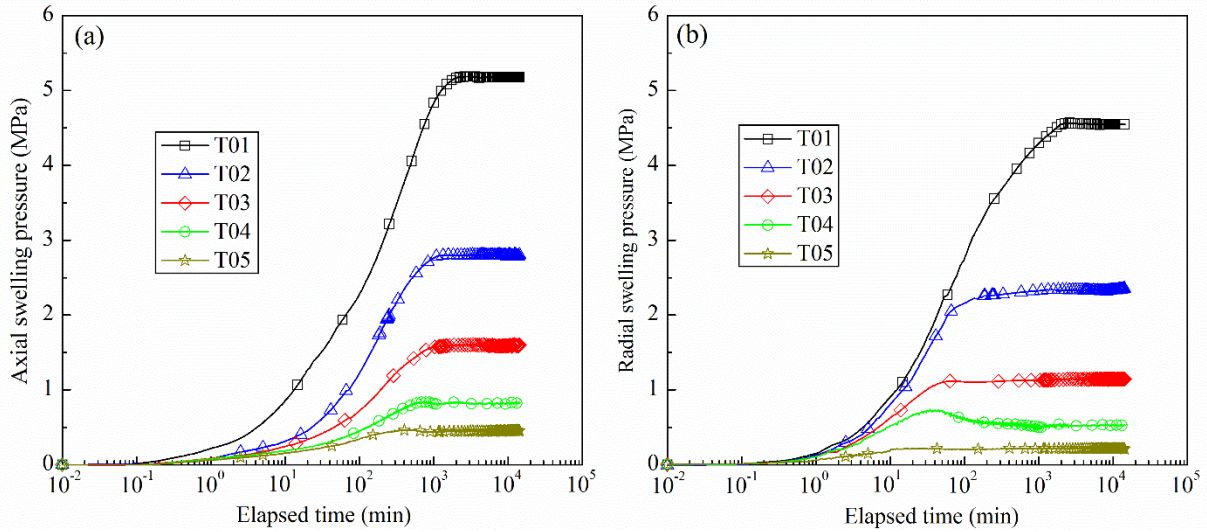

Fig. 5. Evolutions of axial and radial swelling pressures of samples without voids: (a) axial swelling pressure and (b) radial swelling pressure

3.2 Swelling behaviour of samples with axial technological voids

The evolutions of axial and radial swelling pressures of samples T06 to 09 with different axial technological voids are illustrated in Fig. 6. At the beginning of hydration, the axial swelling pressure kept zero. After 5.4, 6.6, 12.0 and 28.8 min for tests T06 to 09, respectively, the axial swelling pressure became measurable (Fig. 6a). With further hydration, the axial swelling pressure increased and then tended to stabilize at 2.30, 1.59, 1.00 and 0.53 MPa after 2940, 2720, 2250 and 2120 min for tests T06 to 09, respectively. Overall, the larger the axial technological voids, the lower the increasing rate. Unlike the axial swelling pressure, the radial swelling pressure started with a quick increase at almost the same rate for tests T06 to 09. Subsequently, the radial swelling pressure reached a peak value and then decreased. After about 390-min hydration, the radial swelling pressures increased again and then reached stabilization values of 2.19, 1.53, 0.98 and 0.53 MPa after 2920, 2720, 2290 and 2060 min for tests T06 to 09, respectively. The final axial and radial swelling pressures and the difference between them decreased with the increasing technological voids.

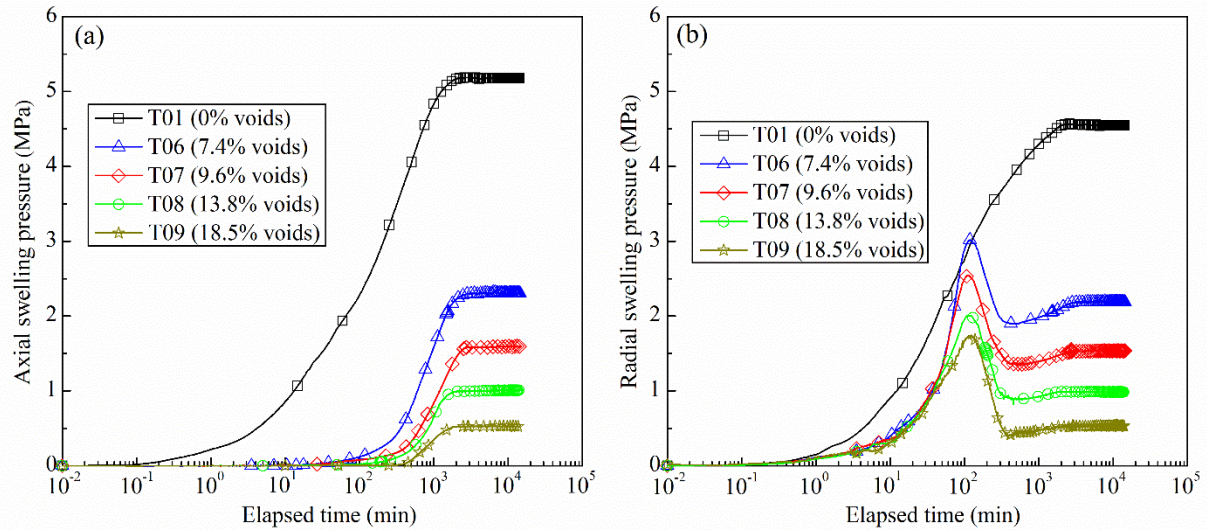

Fig. 6. Evolutions of axial and radial swelling pressures of samples with axial voids: (a) axial swelling pressure and (b) radial swelling pressure

At the end of tests, the samples were extracted from the cell and the dry density and water content of different parts were determined. Fig. 7 shows the distributions of dry density and water content of samples. It appeared that the distributions of dry density and water content were heterogeneous. Moreover, the larger the technological voids, the more heterogeneous the dry density and water content distributions. Parts II and IV which included initial voids had a lower dry density than the global one, whereas parts I, III and V had a higher dry density. The denser zone (parts I, III and V) could undergo further swelling, while the looser zone (parts II and IV) would be subjected to compression by the swelling pressure (Bian et al. 2019a). According to the measured dry density and water content, the saturation degree of each part was calculated to be 98.6-104.4% and the samples were almost saturated, confirming that no air was entrapped within the samples after 10-day hydration.

3.3 Swelling behaviour of samples with radial technological voids

The evolutions of axial and radial swelling pressures of samples T10 to 13 with different radial voids are depicted in Fig. 8. The axial swelling pressure increased rapidly upon hydration. For tests T10 and T11 (with less than 10% radial voids), the axial swelling pressure reached stabilization at 2.86 and 1.62 MPa after 500 and 440 min. For tests T12 and T13 (with more than 15% radial voids), the axial swelling pressure increased and then reached the peak values of 0.97 and 0.80 MPa at 99 and 41 min, respectively. Afterwards, the axial swelling pressure tended to be stable at about 0.86 and 0.52 MPa after 410 and 400 min, respectively. Regarding the radial pressure, it kept zero during the first 1.8, 4.8, 8.4 and 10.8 min of hydration for samples T10 to 13, respectively. After that, the radial swelling pressure started to increase and

then reached stabilization at 2.33, 1.14, 0.47 and 0.20 MPa after 480, 470, 460 and 400 min, respectively. On the whole, the increasing rate decreased with the increasing technological voids. As the technological voids increased, the axial and radial swelling pressures decreased, while the difference between them increased.

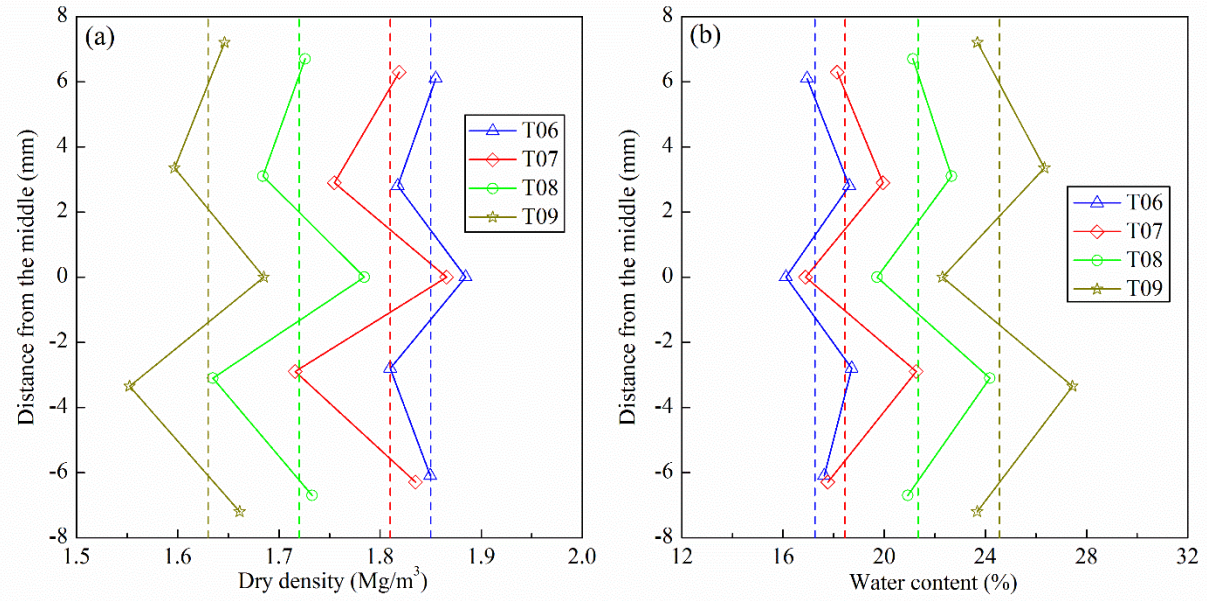

Fig. 7. Dry density and water content profiles for the samples with axial voids: (a) dry density and (b) water content. Note: the dash lines in the left graph represent the global dry density calculated using the total volume after filling technological voids instead of initial state while the dash lines in the right graph refer to the global water content corresponding to the global dry density and a 100% degree of saturation

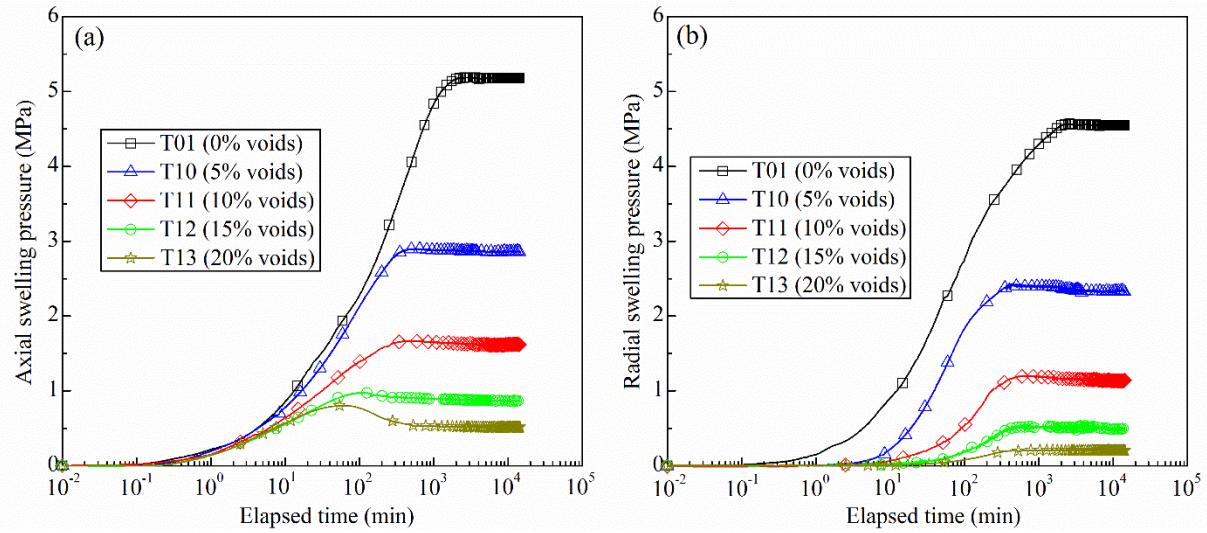

Fig. 8. Evolutions of axial and radial swelling pressures of samples with radial voids: (a) axial swelling pressure and (b) radial swelling pressure

The dry density and water content profiles of samples T10 to 13 after infiltration tests are depicted in Fig. 9. Heterogeneous distributions of dry density and water content were observed for all the samples, with a lower dry density and higher water content in part I (looser) while a higher dry density and lower water content in parts II and III (denser zone). This heterogeneity increased with the increasing technological voids. According to the measured dry density and water content, the saturation degree of each part was calculated and the calculated results varied from 98.4 to 101.5%, indicating that the samples were almost saturated even though the dry density distribution was still heterogeneous.

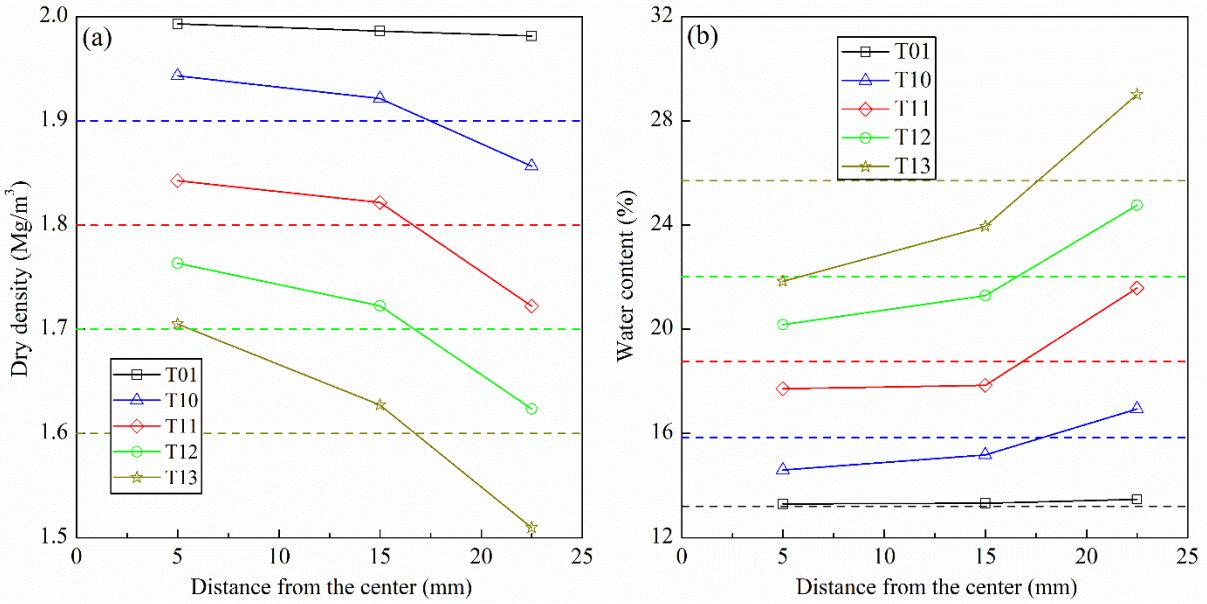

Fig. 9. Dry density and water content profiles for sample T01 and those with radial voids (T10 to13): (a) dry density and (b) water content. Note: the dash lines in the left graph represent the global dry density calculated using the total volume after filling technological voids instead of initial state while the dash lines in the right graph refer to the global water content corresponding to the global dry density and a 100% degree of saturation

4 Interpretation and discussion

4.1 Swelling pressure kinetics

As mentioned above, the swelling pressure kinetics of samples were highly dependent on the mode and amount of technological voids. For the samples with axial technological voids (T06 to 09), the axial voids were rapidly filled up by water with the help of lateral filter paper once the hydration started. Then, the compacted disks swelled under free-swell condition in the axial direction and under confined condition in the radial direction. The samples with different amount of axial voids (T06 to 09) were under the same condition. Therefore, the axial pressure kept zero while the radial one started with a quick increase at the same increasing rate until the

adjacent disks came into contact (Fig. 6a). Subsequently, the axial swelling pressure started to increase. However, the axial swelling of the central disk (corresponding to the radial pressure sensor) simultaneously led to a decrease in dry density in the vicinity of radial pressure sensor, resulting in a reduction of the radial pressure. When this reduction induced by the axial swelling of the central disk was larger than the increase of the radial swelling, peaks occurred on the radial swelling pressure curves (Fig. 6b). After the axial voids were filled up by the swollen soils, the radial swelling pressure increased again and then tended to stabilization. For the samples with radial technological voids (T10 to 13), the water rapidly filled up the radial technological voids upon hydration, allowing the trimmed disk to imbibe water from all the directions. In the axial direction, the axial swelling pressure increased quickly while the soils swelled in the radial direction, filling the radial technological voids. Owing to the significant radial swelling, a peak occurrence was identified on the axial swelling pressure curve of samples with large radial technological voids (T12 and T13) (Fig. 8a). Once the radial technological voids were filled by the swollen soils, the radial swelling pressure became measureable (Fig. 8b). Afterwards, the samples imbibed water from the top and bottom, and tended to homogeneity.

To clarify the effect of technological voids on the swelling pressure kinetics of samples, the evolutions of axial and radial swelling pressures of samples with the same initial dry density of 2.0 Mg/m^3 (T01 and T06 to 13) are shown in Figs. 6 and 8. Additionally, the evolutions of axial and radial swelling pressures of samples at a given global dry density (as an example, samples T03, T07 and T11 are selected and their global dry densities are 1.80, 1.81 and 1.80 Mg/m^3, respectively) are compared in Fig. 10. Compared to the samples with axial voids, a larger increasing rate of axial swelling pressure was observed for the samples with radial voids at the beginning of hydration (Fig. 6a and 8a). At the beginning of hydration, the samples with radial technological voids were wetted from all the direction while the samples without voids were wetted only from the bottom. As a result, the samples (T01 and T10 to T13) exhibited a similar increasing rate, regardless of the radial technological voids. With further hydration, the radial voids would be filled by the swollen soils, with a decrease of the dry density of compacted disk (T10 to T13) while the upper layers of samples without voids (T01) were gradually hydrated by the synthetic water and swelled. Hence, the increasing rate of axial swelling pressure for the sample without voids T01 became larger than that of the samples with radial voids. By contrast, for the samples with axial voids, the soils swelled axially in volume at the beginning of hydration due to the presence of axial voids. Upon the filling of axial voids, the samples

absorbed water from the lateral sides, in addition to the top and bottom. Therefore, a larger increasing rate was identified for the samples with axial voids compared to the samples with radial voids at the same global dry density (water imbibition from the top and bottom), as shown in Fig. 10a. As regards the radial pressure, even though the middle part of the sample without voids could not significantly imbibe water from the bottom at a short time owing to the low permeability of compacted disk, the middle part would be subjected to axial compression by the lower layers through the K_0 effect (Saba et al., 2014c). This explained the rapid increase of radial pressure (Figs. 6b and 8b), which accompanied the increasing axial swelling pressure. Owing to the smaller distance to the water inlet, the radial pressure even exhibited a slightly larger increasing rate than the axial one, which was determined at the top of the samples (Fig. 2). For the samples with axial voids, the pressure sensor was in contact with the central disk. Upon hydration, the central disk swelled axially, filling the technological voids with a decreasing dry density of the compacted disk. Thereby, a lower increasing rate of radial swelling pressure was observed, compared to the samples without voids (Fig. 6b). For the samples with radial voids, the radial swelling pressure would be measureable only after the filling of radial voids. This was why the samples with radial voids exhibited the lowest increasing rate of radial swelling pressure (Fig. 10b).

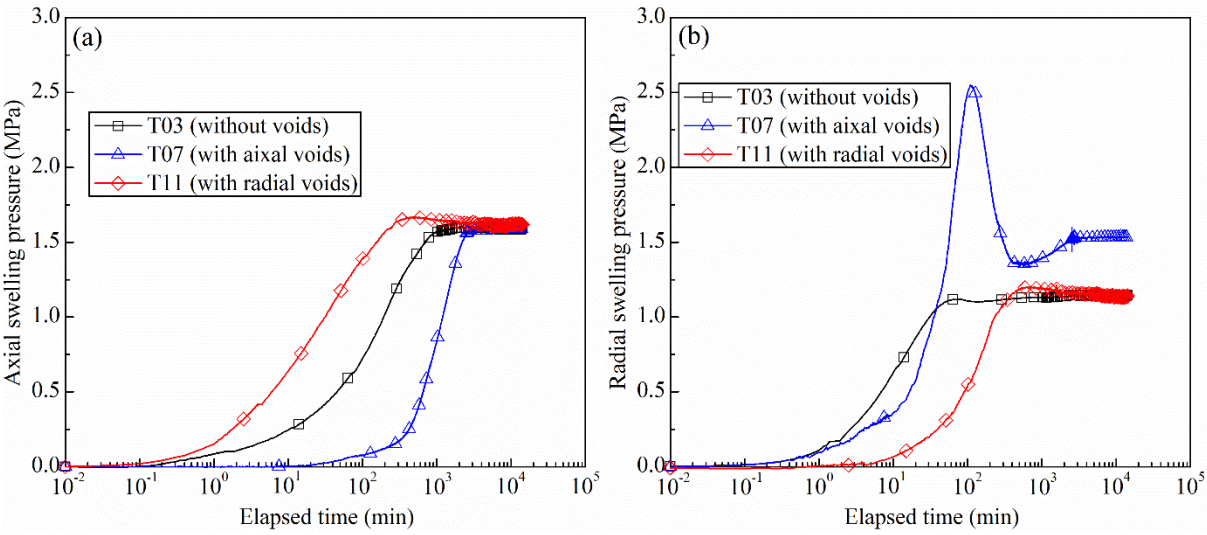

Fig. 10. Comparison of the swelling pressure kinetics of samples in different cases: (a) axial swelling pressure and (b) radial swelling pressure

4.2 Final axial and radial swelling pressures

4.2.1 Aeolotropic swelling pressure of samples without voids

In addition to the swelling pressure kinetics, the final swelling pressures of samples are of equal importance. Fig. 11 shows the relationships between the final axial and radial swelling pressures

and the global dry density for the samples without voids. The logarithm of axial and radial swelling pressures increased linearly with the increasing dry density. The relationships between the final axial swelling pressure ($P_{s\text{-}axial}$ in MPa), the final radial swelling pressure ($P_{s\text{-}radial}$ in MPa) and the dry density (ρ_d in Mg/m^3) for the samples without voids could be described by unique correlations with squared correlation coefficients of 0.999:

$$P_{s\text{-}axial}=2.030\times10^{-3}\rho_d^{11.313} \quad (1)$$

$$P_{s\text{-}radial}=5.112\times10^{-4}\rho_d^{13.122} \quad (2)$$

From Fig. 11, it could also be observed that the axial swelling pressure was larger than the radial one. To further analyse this aeolotropic behaviour, the ratio of measured radial to axial swelling pressures, which was termed as aeolotropy coefficient, for all the samples was calculated. The relationship between the aeolotropy coefficient and global dry density for the samples without voids is shown in Fig. 12. It appears that the aeolotropy coefficient increased from 0.46 to 0.88 as the dry density increased from 1.6 to 2.0 Mg/m^3. Similar experimental studies were conducted on compacted pure Korean bentonite with dry densities ranging from 1.5 to 1.7 Mg/m^3 by Lee et al. (2012) and on compacted MX80 bentonite/sand mixture (70/30 in dry mass) with bentonite dry densities from 0.94 to 1.45 Mg/m^3 by Saba et al. (2014a). With the increase of dry density, the aeolotropy coefficient increased until reaching a peak value at the turning point and then decreased (Fig. 13). This phenomenon could be due to the combined effects of the heterogeneous distribution of macro-pores in the radial direction and the oriented arrangement of grains (Fig. 14). When grains with a dimension significantly larger than others were poured in the compaction mould, they would favour an oriented arrangement with a larger face side in the horizontal direction, as shown by Saba (2013) in a quantitative study. Additionally, more macro-pores could exist in the side part of samples due to the friction between grains and the mould wall, which was verified by Saba et al. (2014b) and Than et al. (2016) through X-ray computed tomography (μCT). Both of them would lead to an aeolotropic swelling behaviour upon hydration. During the subsequent compaction process, the oriented arrangement of grains increased with the increasing dry density while the heterogeneity of macro-pores would be reduced because of the squeeze of small grains into the side part (Than et al., 2016). Fig. 15 shows a sketch of compacted bentonite (various dry densities) before and after saturation. For the samples at low dry densities, the bentonite grains swelled and split up, but they could not fill up the macro-pores, especially at the side part. As shown in Fig. 2, the pressure sensor in contact with the side part of samples measured a lower radial swelling pressure when there were more macro-pores present in this zone (Fig. 15a), giving rise to a

lower aeolotropy coefficient. For the samples at high dry densities, the grains could not fully swell due to the limited macro-pores between grains (Fig. 15c). Thus, the initial orientation would be preserved. For the samples at medium dry densities, the bentonite grains could swell and well fill the macro-pores (Fig. 15b), resulting in a relatively isotropic behaviour. Summarizing, the aeolotropic swelling behaviour for the samples at low dry densities could be mainly attributed to the heterogeneous distribution of macro-pores in the radial direction while the influence of grain orientation became dominant when the dry density of samples was larger than the turning point. Obviously, the swelling capacity of bentonite governed the filling process of macro-pores, influencing the turning point. Because of the lower montmorillonite content of Korean bentonite (70%) as compared with that of MX80 bentonite (86%), a larger turning point was observed for the Korean bentonite (Fig. 13). Furthermore, this turning point was also dependent on the property of studied material such as grain size and water content. For the sample with a larger size and lower water content, more macro-pores could be present in the side part owing to the larger friction with the mould wall. In that case, a larger turning point could be expected. In this work, the used material was a MX80 bentonite/COx claystone mixture with a claystone fraction as large as 70%. As the grain size of COx claystone was larger than that of MX80 bentonite while its water content was lower than that of MX80 bentonite, a higher concentration of macro-pores in the side parts could be expected in this bentonite/claystone mixture. Additionally, the swelling capacity of this mixture was quite low because the swelling capacity of major claystone is lower than 1% of that of bentonite (Zeng et al. 2019). Therefore, the heterogeneity of macro-pores in the radial direction was difficult to eliminate after hydration and a large turning point was obtained for this mixture. For the samples with dry densities ranging from 1.6 to 2.0 Mg/m^3, their aeolotropic swelling behaviour would be mainly influenced by the heterogeneity of macro-pores and only the increasing trend of aeolotropy coefficient with the increasing dry density was observed.

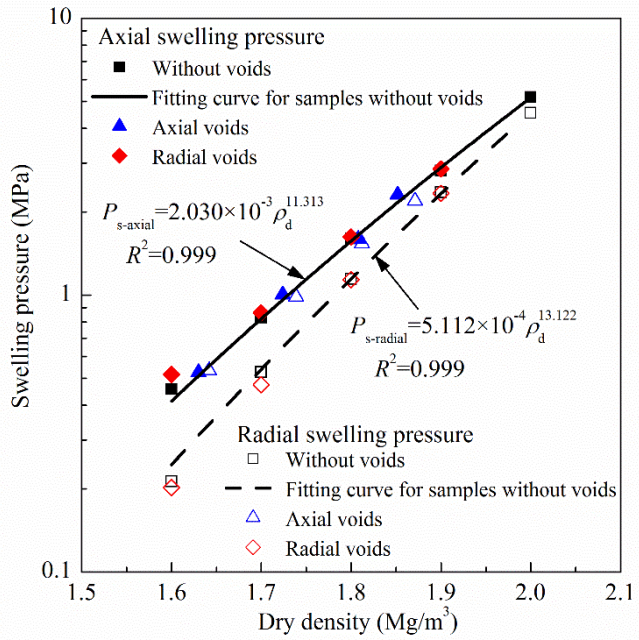

Fig. 11. Relationship between axial and radial swelling pressures and dry density

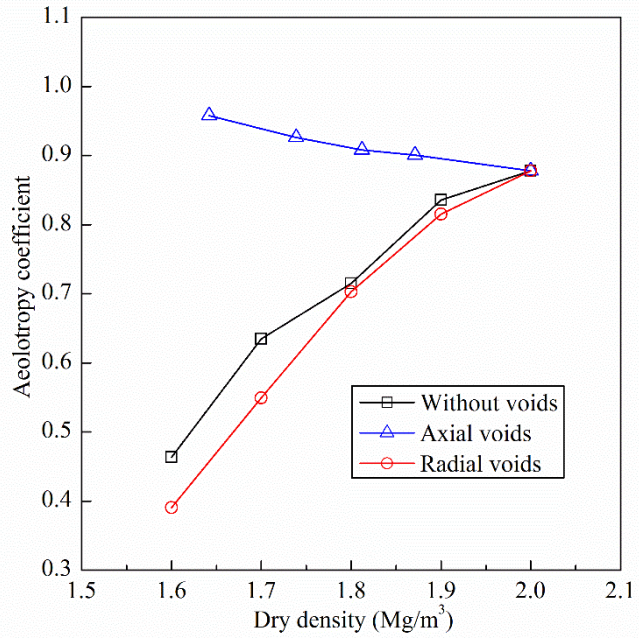

Fig. 12. Relationship between aeolotropy coefficient and dry density of bentonite/claystone mixture. Note: the aeolotropy coefficient of the samples with axial voids was determined according to the axial and radial swelling pressures of the soils in contact with the pressure sensor

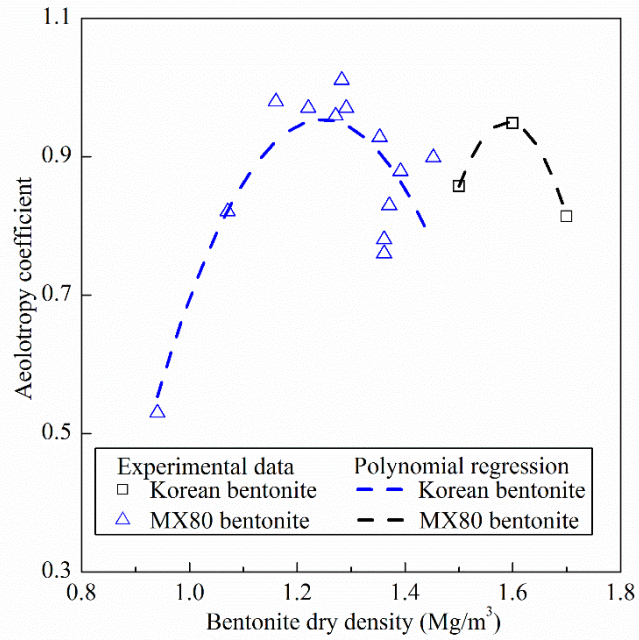

Fig. 13. Aeolotropy coefficient changes with bentonite dry density for different bentonites (data from Lee et al. (2012) and Saba et al. (2014a))

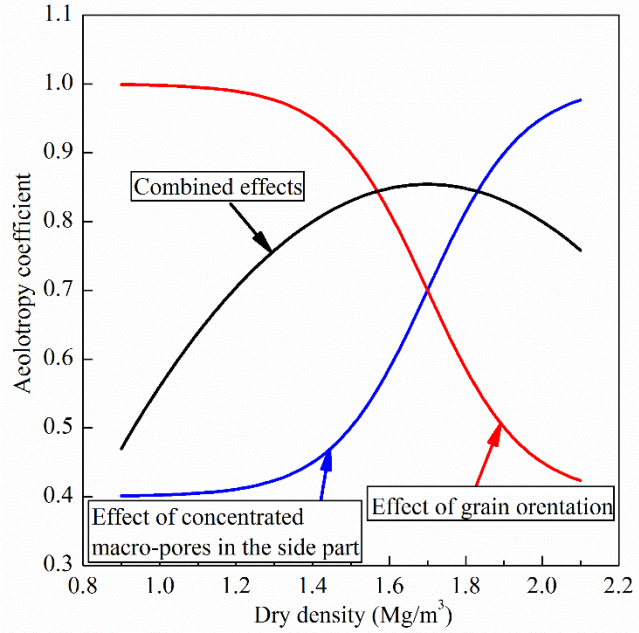

Fig. 14. Representation of the effects of grain orientation and concentrated macro-pores in the side part. Note: the curves in the figure are schematically drawn and do not represent measured values

4.2.2 Aeolotropic swelling pressure of samples with axial/radial voids

As far as the effect of technological voids was concerned, their presence led to the decreases of axial and radial swelling pressures (Table 2). The variations of the axial swelling pressure with the global dry density for the samples with axial/radial voids are also presented in Fig. 11. It could be observed that the axial swelling pressure for samples with axial/radial voids were in satisfactory agreement with that of samples without voids. This good agreement indicted that

the final axial swelling pressure of compacted disks were mainly dependent on the global dry density, irrespective of the heterogeneity due to the presence of technological voids and the mode of voids (axial/radial voids). The variation in the radial swelling pressure with dry density for the samples with radial voids and without voids is also illustrated in Fig. 11. For samples with axial voids, since the dry density distribution was heterogeneous along the sample height at the end of infiltration tests, the distribution of radial swelling pressure was expected to be non-uniform. As the pressure sensor was located at the middle of the samples and in contact with parts II, III and IV, and the areas of contact between the pressure sensor and parts II, III and IV (A_2, A_3 and A_4) were 5.23, 17.22 and 5.23 mm^2, the average dry density of soils ($\rho_{\text{d-sensor}}$ in Mg/m^3) in contact with the pressure sensor could be calculated using Eq. (3):

$$\rho_{\text{d-sensor}}=(\rho_{\text{d-II}}\times A_2+\rho_{\text{d-III}}\times A_3+\rho_{\text{d-IV}}\times A_4)/(A_2+A_3+A_4) \quad (3)$$

where $\rho_{\text{d-II}}$, $\rho_{\text{d-III}}$, $\rho_{\text{d-IV}}$ are the dry density of parts II, III and IV, respectively. The values of average dry density were calculated to be 1.87, 1.81, 1.74 and 1.64 Mg/m^3, for tests T06-09, respectively. Thereby, the radial swelling pressure versus the average soil dry density near the pressure sensor is shown in Fig. 11. It appears that the samples with axial voids exhibited a larger radial swelling pressure than those without voids at the same dry density, while the samples with radial voids showed a lower one, especially for those with more than 15% radial voids. The aeolotropy coefficients of the samples with axial/radial voids are also summarized in Fig. 12. Note that the aeolotropy coefficient for the samples with axial voids was determined according to the axial and radial swelling pressures of soils in the vicinity of the pressure sensor. The axial swelling pressures of soils in contact with the pressure sensor were estimated using Eq. (1). From Fig. 12, the samples with axial voids exhibited a larger aeolotropy coefficient than those without voids, whereas the samples with radial voids showed a lower one, albeit at the same dry density. The aeolotropic swelling mechanism of the compacted bentonite/claystone mixture with axial/radial voids is shown in Fig. 16. Upon hydration, the clay particles of the samples with axial voids swelled and split up, filling up the initial axial voids. This process allowed the rearrangement of clay particles and reduced the initial orientation of clay particles (Fig. 16a). Consequently, a less aeolotropic behaviour was observed for the samples with axial voids. Furthermore, larger axial voids would provide more spaces for the swelling of clay particles, leading to more pronounced reductions in the orientation of clay particles. This explained why the aeolotropy coefficient increased with the increasing axial technological voids (decreasing dry density). When the radial technological voids were considered, the radial sensor was in contact with the soils in the side part (part I) where the dry density was lower than the global one (Fig. 16b) and the measured radial swelling pressure was

lower than that of samples without voids, especially for the samples with more than 15% voids (Fig. 11). As shown in Fig. 10a, the larger initial voids, the more heterogeneous the dry density distribution. Hence, a larger reduction in the aeolotropy coefficient was observed for the samples with larger initial radial voids. In other words, radial voids would increase the heterogeneity of dry density in the radial direction, giving rise to a more pronounced aeolotropic beahviour; by contrast, the axial voids could decrease the initial orientation of clay particles, leading to a less pronounced aeolotropic behaviour.

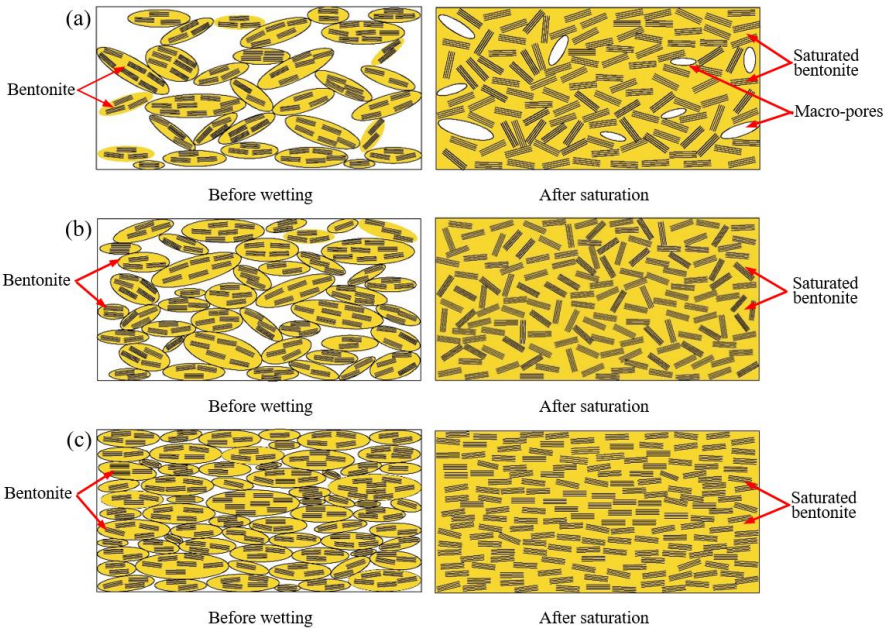

Fig. 15. Schematic view of aeolotropic swelling mechanism in compacted bentonite at: (a) low dry densities; (b) medium dry densities; (c) high dry densities

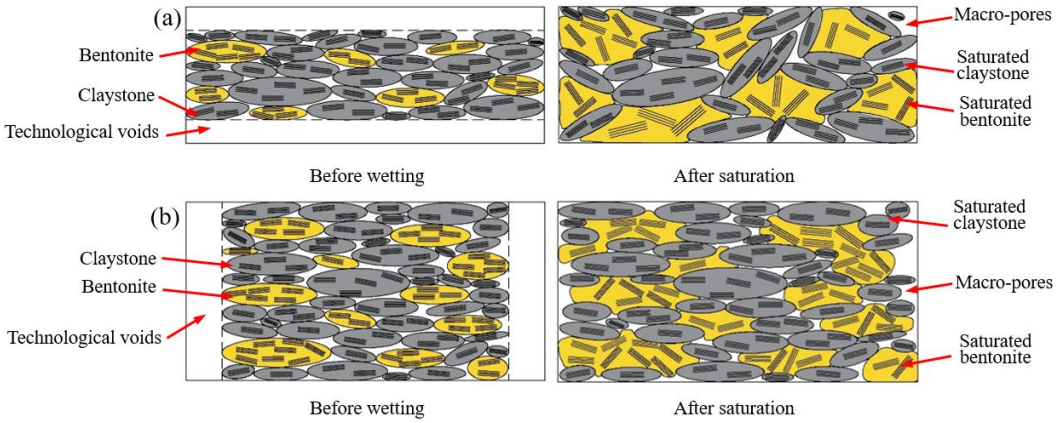

Fig. 16. Schematic view of aeolotropic swelling mechanism in compacted bentonite/claystone mixture with: (a) axial voids; (b) radial voids

As remarked above, the dry density distributions of samples with axial/radial voids were non-uniform at the end of infiltration tests. Over time, the soils in the looser zone would be

compressed by swelling pressure with an increase in dry density, whereas the soils in the denser zone underwent further swelling with a decrease in dry density, resulting in a relatively homogenous distribution. For the samples with axial technological voids, the swollen clay particles would become more oriented under the swelling pressure, leading to a decrease of aeolotropy coefficient. For the samples with radial voids, this homogenization process would reduce the concentration of macro-pores in the side part, resulting in an increase of aeolotropy coefficient. However, the dry density gradient could remain for longtime because of the friction between the samples and cell wall. To this end, the samples with axial voids would present a relatively higher aeolotropy coefficient in long term than those without voids whereas the samples with radial voids would show a lower one.

5 Conclusions

Constant-volume swelling pressure tests were performed on compacted MX80 bentonite/COx claystone mixture at different dry densities and the swelling pressures in both axial and radial directions were obtained, allowing the effect of dry density on the aeolotropic swelling behaviour to be determined. To study the effects of axial/radial voids on the aeolotropic swelling behaviour, swelling pressures of the samples with different axial/radial technological voids were measured, together with the determination of dry density and water content at different positions. From the experimental results, the following conclusions can be drawn.

The axial swelling pressure was dominated by global dry density, regardless of the presence of technological voids and the mode of technological voids (axial or radial voids). At the same dry density, the samples with axial technological voids had a larger radial swelling pressure than those without voids while the samples with radial voids exhibited a smaller one, especially for the samples with larger voids.

For the samples without voids, the aeolotropy coefficient (ratio of radial to axial swelling pressures) increased and then decreased with the increasing dry density due to the combined effects of the concentration of macro-pores in the border of samples and the orientation of clay particles. At low dry densities, the swelling aeolotropy was mainly conditioned by the former. As the dry density decreased, the heterogeneous distribution of macro-pores decreased while grain orientation increased. Therefore, the swelling aeolotropy was dominated by the latter, in case of high dry densities.

At the same dry density, the samples with axial voids exhibited a larger aeolotropy coefficient

than those without voids, thanks to the reductions of the orientation of clay particles. On the contrary, the samples with radial voids presented a lower one because of the lower dry density in the side part. Furthermore, the larger the technological voids, the more significant the influence of axial/radial voids on the aeolotropic swelling behaviour.

Acknowledgments

The authors are grateful to Ecole des Ponts ParisTech and the French National Radioactive Waste Management Agency (Andra). The first author also wishes to acknowledge the support of the China Scholarship Council (CSC).

References

American Society for Testing and Materials (ASTM), 2007. Standard Test Method for Particle-Size Analysis of Soils. Soil and Rock, West Conshohocken, PA. D422.

Bian, X., Cui, Y.J., and Li, X.Z., 2019a. Voids effect on the swelling behaviour of compacted bentonite. Géotechnique, 69(7): 593-605.

Bian, X., Cui, Y.J., Zeng, L.L. and Li, X.Z., 2019b. Swelling behavior of compacted bentonite with the presence of rock fracture. Engineering Geology, 254: 25-33.

Bian, X., Cui, Y.J., Zeng, L.L. and Li, X.Z., 2020. State of compacted bentonite inside a fractured granite cylinder after infiltration. Applied Clay Science. doi: 10.1016/j.clay.2020.105438.

Cho, W.J., Lee, J.O., Kang, C.H., 2000. Influence of temperature elevation on the sealing performance of a potential buffer material for a high-level radioactive waste repository. Annals of Nuclear Energy, 27(14), 1271-1284.

Cuisinier, O., Masrouri, F., Pelletier, M., Villieras, F., Mosser-Ruck, R., 2008. Microstructure of a compacted soil submitted to an alkaline plume. Applied Clay Science. 40 (1–4), 159–170.

Dixon, D.A., Gray, M.N., Thomas, A.W., 1985. A study of the compaction properties of potential clay-sand buffer mixtures for use in nuclear fuel waste disposal. Eng. Geol. 21(3/4):247-255.

Fouché, O., Wright, H., Le Cléac'h, J.M., Pellenard, P., 2004. Fabric control on strain and rupture of heterogeneous shale samples by using a non-conventional mechanical test. Appl. Clay Sci. 26 (1–4), 367–387.

Jia, L.Y., Chen, Y.G., Ye, W.M., Cui, Y.J. 2019. Effects of a simulated gap on anisotropic swelling pressure of compacted GMZ bentonite. Engineering geology, 248: 155-163.

Karnland, O., Nilsson, U., Weber, H., Wersin. P., 2008. Sealing ability of Wyoming bentonite

pellets foreseen as buffer material–laboratory results. Phys. Chem. Earth Parts A/B/C. 33, S472-S475.

Komine, H., Ogata, N., 1994. Experimental study on swelling characteristics of compacted bentonite. Can. Geotech. J. 31(4), 478-490.

Komine, H., Ogata, N., 1999. Experimental study on swelling characteristics of sand-bentonite mixture for nuclear waste disposal. Soils Found. 39(2), 83-97.

Lee, J.O., Cho, W.J., Chun, K.S., 1999. Swelling pressures of a potential buffer material for high-level waste repository. J. Korean Nucl. Soc. 31(2), 139-150.

Lee, J.O., Cho, W.J., Kang, C.H., Chun, K.S., 2001. Swelling and hydraulic properties of Ca-bentonite for the buffer of a waste repository (No. IAEA-CSP--6/C).

Lee, J.O., Lim, J.G., Kang, I.M., Kwon, S., 2012. Swelling pressures of compacted Ca-bentonite. Engineering Geology, 129, 20-26.

Pusch, R., 1982. Mineral–water interactions and their influence on the physical behavior of highly compacted Na bentonite. Can. Geotech. J. 19(3), 381-387.

Saba, S., 2013. Hydro-mechanical behaviour of bentonite-sand mixture used as sealing materials in radioactive waste disposal galleries (Doctoral dissertation, Université Paris-Est).

Saba, S., Barnichon, J. D., Cui, Y. J., Tang, A. M., Delage, P., 2014a. Microstructure and anisotropic swelling behaviour of compacted bentonite/sand mixture. J. Rock Mech. Geotech. Eng. 6(2), 126-132.

Saba, S., Delage, P., Lenoir, N., Cui, Y.J., Tang, A.M., Barnichon, J.D., 2014b. Further insight into the microstructure of compacted bentonite–sand mixture. Engineering geology, 168, 141-148.

Saba, S., Cui, Y.J., Tang, A.M., Barnichon, J.D., 2014c. Investigation of the swelling behaviour of compacted bentonite–sand mixture by mock-up tests. Canadian geotechnical journal, 51(12), 1399-1412.

Seiphoori, A., Ferrari, A., Laloui. L., 2014. Water retention behaviour and microstructural evolution of MX-80 bentonite during wetting and drying cycles. Géotechnique. 64(9), 721-734.

Sellin, P., Leupin, O.X., 2013. The use of clay as an engineered barrier in radioactive-waste management–a review. Clays Clay Miner. 61(6), 477-498.

Tang, A.M., Cui, Y.J., Le, T.T., 2008. A study on the thermal conductivity of compacted bentonites. Appl. Clay Sci. 41(3-4), 181–189.

Than, V.D., Aimedieu, P., Pereira, J.M., Roux, J.N., Bornert, M., Tang, A.M., 2016. Macro-microscopic one-dimensional compression of wet granular soils by experimental investigation. E3S Web of Conferences.

Villar, M.V., García-Siñeriz, J.L., Bárcena, I., Lloret, A., 2005. State of the bentonite barrier

after five years operation of an in situ test simulating a high level radioactive waste repository. Engineering Geology, 80(3-4), 175-198.

Wang, Q., Tang, A.M., Cui, Y.J., Delage, P., Gatmiri, B., 2012. Experimental study on the swelling behaviour of bentonite/claystone mixture. Eng. Geol. 124, 59-66.

Wang, Q., Tang, A.M., Cui, Y.J., Delage, P., Barnichon, J.D., Ye, W.M., 2013. The effects of technological voids on the hydro-mechanical behaviour of compacted bentonite–sand mixture. Soils and Foundations, 53(2), 232-245.

Zeng, Z.X., Cui, Y.J., Zhang, F., Conil, N., Talandier, J., 2019. Investigation of swelling pressure of bentonite/claystone mixture in the full range of bentonite fraction. Applied Clay Science. doi: 10.1016/j.clay.2019.105137.

Zeng, Z.X., Cui, Y.J., Zhang, F., Conil, N., Talandier, J., 2020a. Effect of technological voids on the swelling behaviour of compacted bentonite/claystone mixture. Can. Geotech. J. https://doi.org/10.1139/cgj-2019-0339.

Zeng, Z.X., Cui, Y., Conil, N. Talandier J., 2020b. Analysis of boundary friction effect on the homogenization process of compacted bentonite/claystone mixture with technological voids upon hydration. Acta Geotech. https://doi.org/10.1007/s11440-020-01048-x.

Zeng, Z.X., Cui, Y.J., Conil, N., Talandier, J., 2020c. Effects of technological voids and hydration time on the hydro-mechanical behaviour of compacted bentonite/claystone mixture. Géotechnique. https://doi.org/10.1680/jgeot.19.P.220.

Zeng, Z.X., Cui, Y.J., Zhang, F., Conil, N., Talandier, J. 2020. Canadian Geotechnical Journal. 57(12), 1881-1892.

Effect of technological voids on the swelling behaviour of compacted bentonite/claystone mixture

Zhixiong Zeng[1], Yu-Jun Cui[1], Feng Zhang[1], Nathalie Conil[2], Jean Talandier[3]

Abstract: The effect of technological voids on the swelling pressure of compacted MX80 bentonite-Callovo-Oxfordian (COx) claystone mixture was investigated by simulating the technological voids with a pre-defined space between the compacted disks of the mixture. Both axial and radial swelling pressures were monitored. After the tests, the microstructure of samples at different positions was investigated using Mercury Intrusion Porosimetry (MIP), together with the determination of dry density and water content. Results showed that two main processes, filling and homogenization, occurred during soil hydration. In the filling process, the initial technological voids were gradually filled and the axial swelling pressure tended to increase. In the homogenization process, the samples had a sealing zone and a swelling zone. The sealing zone was characterized by a lower dry density than the expected final dry density while the swelling zone was characterized by a larger one. From the MIP results, the sealing zone showed larger inaccessible-pore, medium-pore and large-pore void ratios and a lower small-pore void ratio than the swelling zone. Over time, the medium and large pores in the sealing zone were compressed, while the small pores in the swelling zone decreased. The stabilized axial swelling pressure followed a unique relationship with the expected final dry density. Moreover, the swelling pressure anisotropy was found to decrease as the technological voids increased.

Keywords: bentonite-claystone mixture; technological voids; swelling pressure; swelling anisotropy; microstructure

1 Introduction

In the context of deep geological disposal for radioactive waste, pre-compacted blocks of

1 Ecole des Ponts ParisTech, Laboratoire Navier/CERMES, 6 et 8 avenue Blaise Pascal, 77455 Marne La Vallée cedex 2, France
2 Andra, Centre de Meuse/Haute-Marne, RD 960, 55290 Bure, France
3 Andra, 1/7, rue Jean Monnet, 92298 Châtenay-Malabry cedex, France

bentonite-based materials are often considered as possible sealing and backfilling materials thanks to their high swelling capacity, low permeability and favourable radionuclide migration retardation properties (Pusch, 1982; Dixon et al., 1985; Komine and Ogata, 1994; 1999; Cui, 2017). When the compacted blocks are placed in the disposal galleries, radially technological voids between the blocks, the canisters, and the host rock, and axially technological voids between the blocks themselves are unavoidable (Wang et al., 2013a). Upon contact with pore water from the host rock, compacted blocks will swell and fill up the technological voids, leading to a decrease of dry density. After that, swelling pressure will develop both radially and axially (Pusch, 1982; Saba et al., 2014a). Previous studies (Villar et al., 2005; Gen et al., 2011; Wang et al., 2013a) showed that after the saturation process, the initial heterogeneity could remain to some extent, significantly affecting the hydromechanical behaviour of the sealing and backfilling materials. From the practical point of view, it is essential to well understand the swelling behaviour of compacted blocks upon hydration, in particular in case of presence of technological voids.

The effect of technological voids on the swelling behaviour of compacted sealing and backfilling materials has been widely investigated in both the laboratory and the field, in terms of swelling pressure, water content and dry density distributions (Villar et al., 2005; Gen et al., 2011; Wang et al., 2013a; Saba et al., 2014a; 2014b; Bian et al., 2019; Jia et al., 2019). It was found that the blocks that were close to the technological voids swelled with a quick reduction in dry density once the technological voids were filled with water, while the dry density far from the technological voids decreased slowly (Villar et al., 2005; Gen et al., 2011; Bian et al., 2019). The swelling allowed by the technological voids significantly affected the dry density distribution and swelling capacity (Jia et al., 2019). After the filling of technological voids, the filling material with low dry density was compressed by the swelling pressure generated by the further hydration of the part with large dry density. These processes led to a relatively homogeneous distribution of dry density, and a final swelling pressure equal to that of a compacted block without technological voids, but at the same final dry density (Wang et al., 2012; Saba et al., 2014a; Bian et al., 2019). Additionally, the block fabricated by uniaxial compaction was characterized by an anisotropic microstructure that would generate a lower swelling pressure in the radial direction (Lee et al., 2012; Saba et al., 2014a). With technological voids, the swelling anisotropy could remain to some extent after hydration and the final radial swelling pressure was mainly dominated by the final dry density, irrespective of whether there were technological voids or not (Saba et al., 2014a; Jia et al., 2019).

The aforementioned works allowed a good understanding of the effect of technological voids, but the studies were limited to the technological voids between the compacted blocks of bentonite-based materials and rigid boundaries. To the authors' knowledge, no studies have been reported on the effect of technological voids among compacted blocks, in particular the compacted blocks of bentonite and claystone mixture.

In this study, a series of infiltration tests under constant-volume condition were performed on compacted MX80 bentonite and Callovo-Oxfordian (COx) claystone mixture. The swelling pressure of compacted disks with different technological voids in between was measured in both axial and radial directions, allowing the effect of technological voids on the swelling anisotropy to be studied. Afterwards, the water content, dry density and microstructure features at different positions were investigated, helping the interpretation of the swelling behaviour of compacted mixture.

2 Materials and methods

2.1 Materials

The soil studied was a mixture of 30% (dry mass) MX80 bentonite and 70% (dry mass) crushed COx claystone mixture, which has been proposed as a candidate sealing and backfilling material by the French National Radioactive Waste Management Agency (Andra). The basic physical and chemical properties of the bentonite are summarized in Table 1. It has a montmorillonite content of 86%, a liquid limit of 494%, a plastic limit of 46% and a specific gravity of 2.76, which are in satisfactory agreement with the literature data (Tang et al., 2008; Seiphoori et al., 2014; Saba et al., 2014b). The cation exchange capacity (CEC) of the bentonite is 80 meq/100g, with Na^+ as the main exchange cation (Herbert et al., 2004; 2008; Karnland et al., 2006; Saba et al., 2014b). Fig. 1 shows the grain-size distribution determined using the conventional hydrometer method. It can be observed that the clay-size fraction (< 2 μm) is 86%.

The COx claystone was excavated from the Underground Research Laboratory (URL) in Bure and then crushed to pass through a 2 mm sieve. The main clay mineral of the COx claystone is interstratified illite-smectite (40-45%), the others being carbonates (30%), and quartz and feldspar (25-30%) (Fouché et al., 2004). The claystone has a liquid limit of 41%, a plastic limit of 24% and a specific gravity of 2.70. The grain-size distribution determined by sedimentation reveals the clay fraction (< 2 μm) represents 26%.

The water used in this study was synthetic water (see Table 2 for the recipe of preparation), which has the same chemical composition as the pore water of COx claystone from the Andra URL in Bure. It was prepared by mixing the corresponding chemical components with de-ionized water until full dissolution (Saba et al., 2014b).

Table 1. Physical and chemical properties of MX80 bentonite

Property	Present work	Tang et al. (2008)	Seiphoori et al. (2014)	Saba et al. (2014b)	Karnland et al. (2006)	Herbert et al. (2004, 2008)
Specific gravity	2.76	2.76	2.74	2.77	-	-
Liquid limit (%)	494	520	420	575	-	-
Plastic limit (%)	46	42	65	53	-	-
Plasticity index (%)	448	478	355	522	-	-
CEC (meq/100 g)	-	-		76	80	78-85
Na^+	-	-		63	67	62.4-66.8
K^+	-	-		-	1	0.2-1.3
Mg^{2+}	-	-		-	5	3-4
Ca^{2+}	-	-		-	8	6.6-7.4
Main minerals (%)						
Montmorillonite	86	92	85		92	94
Quartz	7	3	-		3	4

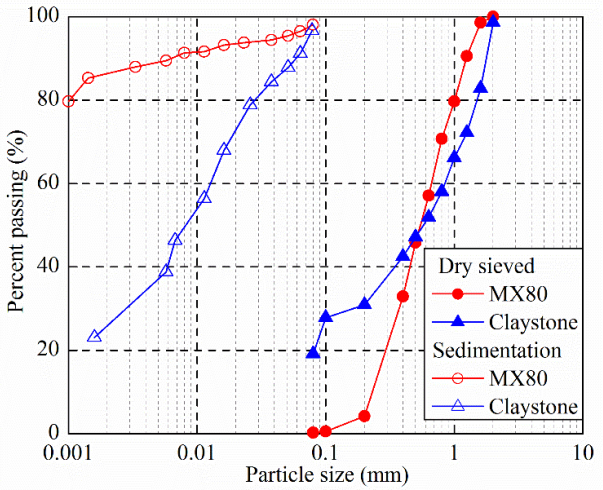

Fig. 1. Grain-size distribution of MX80 bentonite and crushed Callovo-Oxfordian (COx) claystone

Table 2. Recipe for the synthetic water preparation

Component	NaCl	$NaHCO_3$	KCl	$CaSO_4 \cdot 2H_2O$	$MgSO_4 \cdot 7H_2O$	$CaCl_2 \cdot 2H_2O$	Na_2SO_4
Content (g/L)	1.950	0.130	0.035	0.630	1.020	0.080	0.700

2.2 Test device

The layout of the experimental setup is presented in Fig. 2. The sample was placed between two porous stones in a stainless cell (50 mm in diameter). The synthetic water was injected through the bottom of the cell and the constant-volume condition was ensured by the top piston

blocked with a screw. A force transducer was installed under the cell for the axial swelling pressure measurement. A total pressure sensor (6 mm in diameter) was mounted in the cell, allowing the radial swelling pressure to be monitored at one location around the perimeter of the sample. All data were recorded by a data logger. Prior to the tests, the force transducer and the pressure sensor were calibrated. The force transducer was placed on a compression machine and a series of vertical forces were applied on the measuring face of the transducer. For the pressure sensor, it was inserted in a smaller cell with a sealing plug and a series of pressures were imposed by means of a pressure-volume controller.

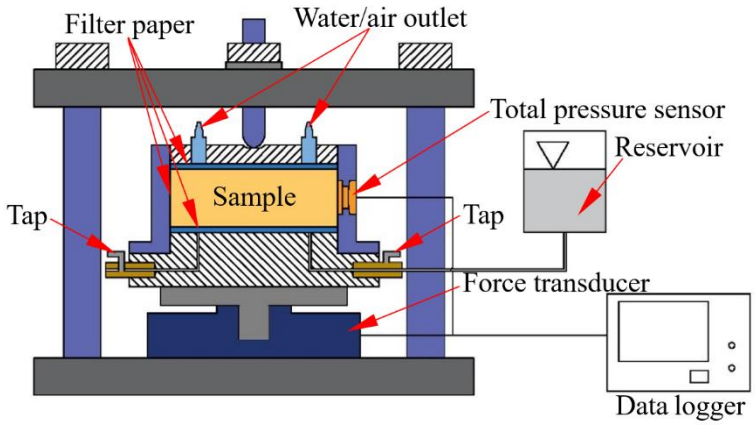

Fig. 2. Layout of the constant-volume cell for swelling pressure tests

The responses of the transducer and pressure sensor during loading-unloading paths were recorded and linear correlations between the applied force (pressure) and the output voltage were identified. Subsequently, the axial force and radial pressure were back-calculated.

2.3 Sample preparation

The bentonite and claystone powders, with initial water contents of 11.4% and 6.1%, respectively, were first mixed (30% bentonite-70% claystone in dry mass) for more than 10 min. The water content of the obtained mixture was 7.7%. Afterwards, soil disks were statically compacted using a rigid ring to reach the dimensions of 50 mm in diameter and 15 mm (for test T01) or 5 mm (for tests T02, T03, T04 and T05, see Table 3) in height, corresponding to a target dry density of 2.0 Mg/m^3.

2.4 Test procedure

For the tests with technological voids (T02, T03, T04, and T05), three identical disks with a height of 5 mm were used in each test. The lateral surfaces of all disks were first covered by filter papers. Next, the first disk was placed on a porous stone underlying a filter paper, and about 0.10 g of bentonite grains of pre-defined sizes were dispersed on the top of the first disk.

Similarly, the second disk, the second bentonite grain layer, and the third disk were installed successively. Consequently, two identical layers of bentonite grains were created among three identical disks, as shown in Fig. 3a. Note that the mass of bentonite grains represented about 0.5% of all disks' mass. Thus, their contribution to the global swelling could be ignored. In this study, four groups of bentonite grains (0.25-0.40, 0.63-0.80, 1.00-1.25 and 1.60-2.00 mm) were used to create different gaps of 0.60, 0.80, 1.20 and 1.70 mm thick, corresponding to technological voids of 7.4% (T02), 9.6% (T03), 13.8% (T04) and 18.5% (T05), respectively, as summarized in Table 3. For comparison, test T01 was carried out on a compacted disk with a height of 15 mm without technological voids (Fig. 3b). Note that the total pressure sensor was located at the middle position of each sample. For the tests with technological voids, the testing surface of pressure sensor was in contact with the central disk (5 mm in thickness) and initial technological voids on the two sides of the central disk. It is believed that upon hydration, the axial swell of the compacted disks allowed the full surface of the pressure sensor to be in contact with the soils. To ensure a good contact, an initial stress of 0.05 MPa was applied.

Table 3. Test program and main results

Test	Grain size (mm)	Initial dry density of disk (Mg/m^3)	Technological voids (%)	Expected final dry density (Mg/m^3)	Final axial swelling pressure (MPa)	Final radial swelling pressure (MPa)
T01	0	2.0	0	2.0	5.22	4.46
T02	0.25-0.40	2.0	7.4	1.85	2.30	2.19
T03	0.63-0.80	2.0	9.6	1.81	1.59	1.53
T04	1.00-1.25	2.0	13.8	1.72	1.00	0.98
T05	1.60-2.00	2.0	18.5	1.63	0.53	0.53

After completion of the infiltration tests, the samples were carefully extracted from the cell. Each sample was then divided into five layers, that is, layer I to layer V, as shown in Fig. 3. For test T01, the sample was equally cut into five layers (50 mm in diameter and 3 mm in height); for tests T02, T03, T04, and T05, layers II and IV referred to the parts corresponding to technological voids and two surface layers on the two sides of the samples (1 mm thick each), other parts being termed as layer I, layer III, and layer V, respectively. Subsequently, each layer was cut into several pieces for water content and dry density measurements as well as microstructure observation. Note that the entire operations (removal and cutting) were completed in less than 5 min to minimise water evaporation. The water content was measured by oven-drying the samples at 105 °C for 24 h and the dry density was determined based on the fluid displacement technique using a non-aromatic hydrocarbon liquid called Kerdane (Delage et al., 2008). The microstructure feature was investigated using mercury intrusion porosimetry

(MIP). To minimise the microstructure disturbance during dehydration, the samples were freeze-dried (Bian et al., 2019). They were rapidly frozen using liquid nitrogen previously vacuum-cooled at its freezing point (-210 °C) and then vacuumed in a chamber for 24 h sublimation (Wang et al., 2014). For the MIP tests, the mercury intrusion pressure was limited to the range from 3.6 kPa to 228 MPa, allowing the entrance pore diameters ranging from 350 μm to 0.006 μm to be identified.

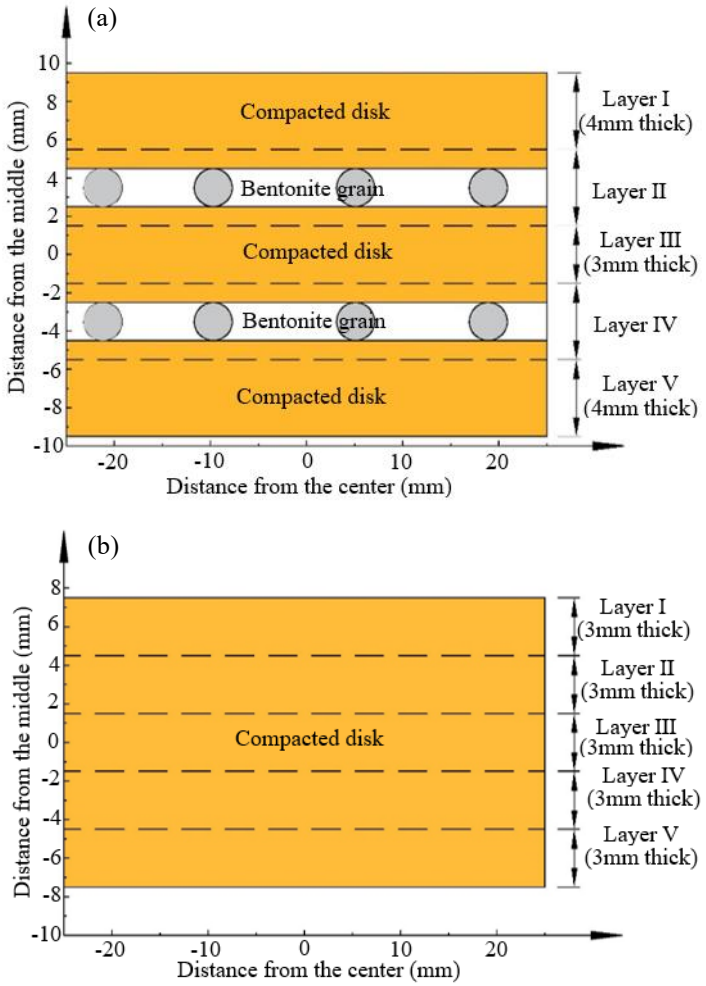

Fig. 3. Definition of sample layers: (a) T02, T03, T04, and T05, and (b) T01

3 Experimental results

3.1 Axial and radial swelling pressures

Fig. 4 depicts the evolution of axial welling pressure. For test T01, the axial swelling pressure started with a fast increase and then reached stabilization at 5.22 MPa (Fig. 4c). For tests T02, T03, T04, and T05 with technological voids, the axial pressures decreased slightly from the initial value (0.05 MPa) to about 0.047 MPa at the beginning of hydration (0.09, 0.11, 0.20, and 0.48 h for tests T02, T03, T04, and T05, respectively) (Fig. 4a). This phenomenon could be

attributed to the softening of bentonite grains during hydration. After that, the axial swelling pressures tended to increase at an increasing rate till the inflection points at 5.2, 6.2, 6.6, and 7.0 h for T02, T03, T04, and T05, respectively (Fig. 4a and b). The variation rates then decreased to zero after 49.0, 45.4, 37.5, and 35.3 h, with the axial swelling pressures reaching stabilization at 2.30, 1.59, 1.00, and 0.53 MPa for tests T02, T03, T04, and T05, respectively (Fig. 4b and c). On the whole, the larger the technological voids, the lower the variation rate and the lower the final axial swelling pressure.

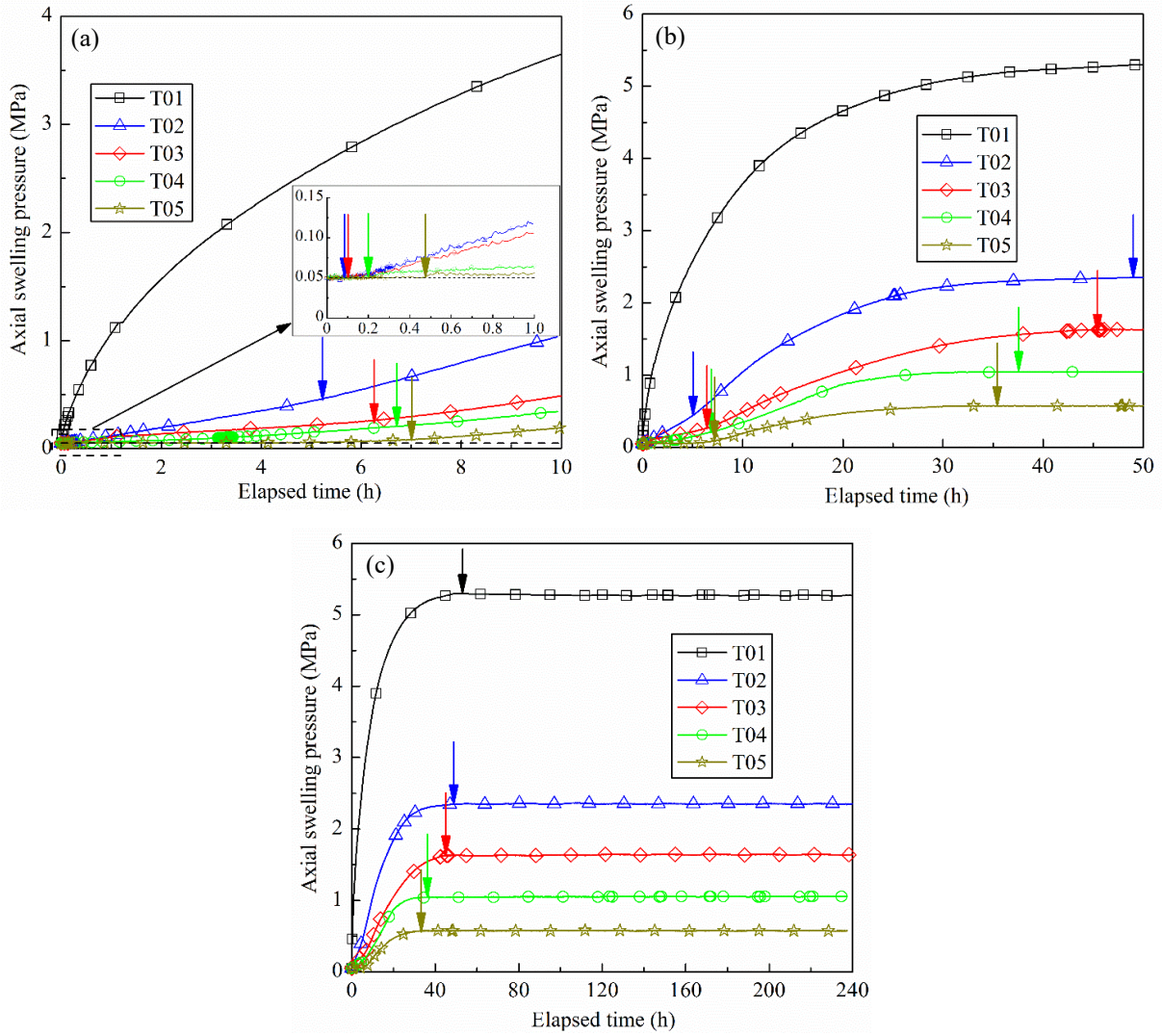

Fig. 4. Evolution of axial swelling pressure (a) in the first 10 h, (b) in the first 50 h, and (c) for the whole test duration. Note: the curves in the figure are drawn according to all the measurement points but only a few symbols in each curve are plotted for distinction purpose

The evolution of radial swelling pressure is shown in Fig. 5. A first quick increase was observed at the beginning for all tests, at almost the same rate (Fig. 5a). For test T01, the radial swelling pressure increased rapidly and then reached a stabilization value of 4.46 MPa (Fig. 5b and c). For tests T02, T03, T04 and T05, the radial swelling pressures, after the first quick increases,

reached the peak values of 3.02, 2.55, 2.01, and 1.74 MPa, respectively, after about 2 h, then decreased significantly until about 6.5 h hydration (Fig. 5a and b). Afterwards, they increased again, but slowly and reached stabilization at 2.19, 1.53, 0.98, and 0.53 MPa after 48.7, 45.3, 38.2, and 34.4 h, respectively (Fig. 5b and c). The times needed to decrease from the peaks to the minimum values coincided with the inflection points identified on the axial swelling pressure curves (Figs. 4a and 5a). Moreover, the times required to attain the stabilization of axial and radial swelling pressures are almost the same. The final values of axial and radial swelling pressures are summarized in Table 3 and the variations of the axial and radial swelling pressures with technological voids are presented in Fig. 6. It can be observed that both axial and radial swelling pressures decreased with increasing technological voids, indicating that the presence of technological voids reduced the swelling capacity of the mixture.

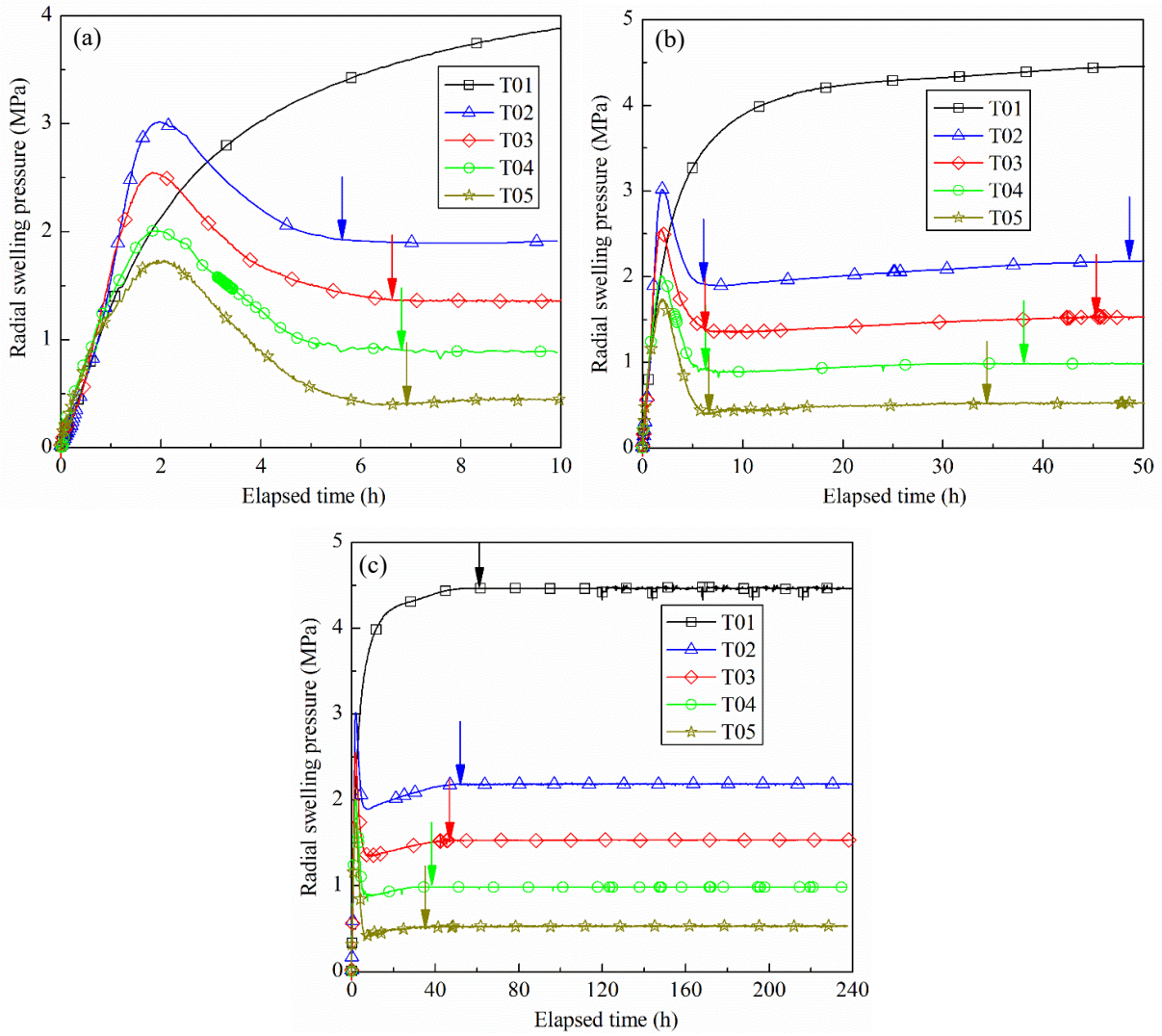

Fig. 5. Evolution of radial swelling pressure (a) in the first 10 h, (b) in the first 50 h, and (c) for the whole test duration

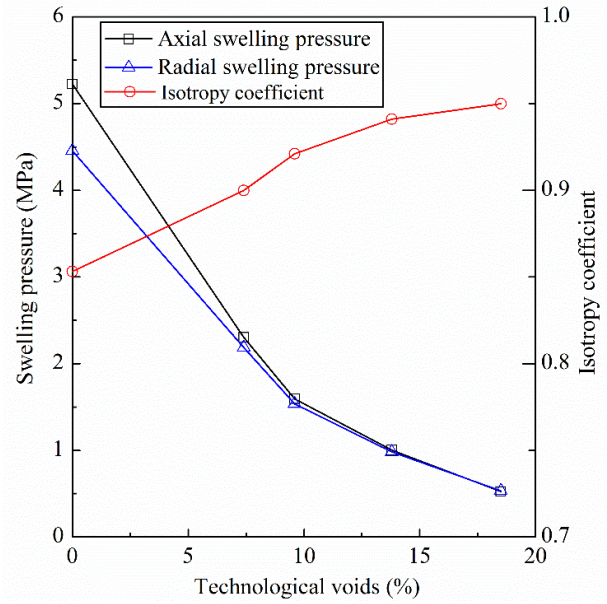

Fig. 6. Relationship between final swelling pressures, isotropy coefficient and technological voids

3.2 Water content and dry density profiles

The water content and dry density profiles are plotted in Fig. 7. Both water content and dry density profiles were almost symmetrical with respect to the horizontal plans in the middle of the samples. For sample T01, the water content and dry density were characterized by the increase and decrease trends with the increasing distance from the symmetry plan. For samples T02, T03, T04, and T05, the filling of technological voids led to heterogeneous distributions of water content and dry density, with larger water contents and lower dry densities for layers II and IV that included technological voids, but lower water contents and larger dry densities for layers I, III and V. Further examination showed that the dry density of layer III was larger than those of layers I and V. This could be attributed to the longer wetting path and slower swelling of layer III when the technological voids were closed. On the whole, the larger the technological voids, the more heterogeneous the distributions of water content and dry density. The expected final dry densities calculated using the total volume including technological voids are also presented in Fig. 7b. It appears that for sample T01 without technological voids, the measured values were quite close to the expected final value, while for other samples with technological voids the measured values are little different from the expected final one, revealing the effect of technological voids.

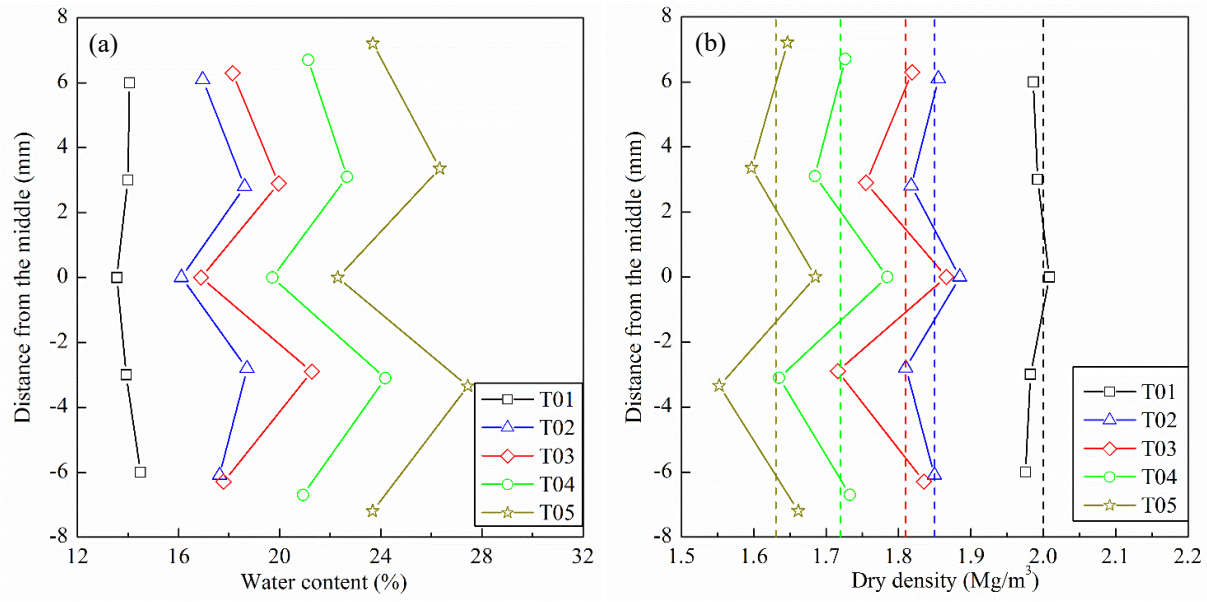

Fig. 7. Water content and dry density profiles after tests: (a) water content profile and (b) dry density profile

3.3 Microstructure distribution

Fig. 8 shows the results from MIP tests on samples T01, T02, T03, T04, and T05. The result of the as-compacted sample is also presented for comparison. For sample T01, the cumulative curves of all layers were almost the same; on the contrary, samples T02, T03, T04, and T05 exhibited significantly different microstructures: the cumulative curves of layers II and IV with technological voids lied above those of other layers, which was consistent with the dry density distributions. Note that the final intruded void ratio was slightly smaller than the corresponding ones determined on the large layer specimens. This was attributed to the inaccessible pores which could not be identified with the maximum pressure applied in the MIP tests (Tang et al., 2011; Wang et al., 2014).

From the pore size density function curves (Fig. 8b), it was observed that the as-compacted sample presented a typical bimodal porosity with a mean size of 0.02 μm for the small-pore population and a mean pore size of 5 μm for the large-pore population, respectively. After water saturation, the mean size of large-pore population increased sharply from 5 to 15-30 μm, while the mean size of small-pore population kept almost constant. For the samples with technological voids, a new pore population with a mean size of 0.1-0.3 μm appeared, leading to tri-modal pore size distribution curves (Fig. 8d, f, h and j).

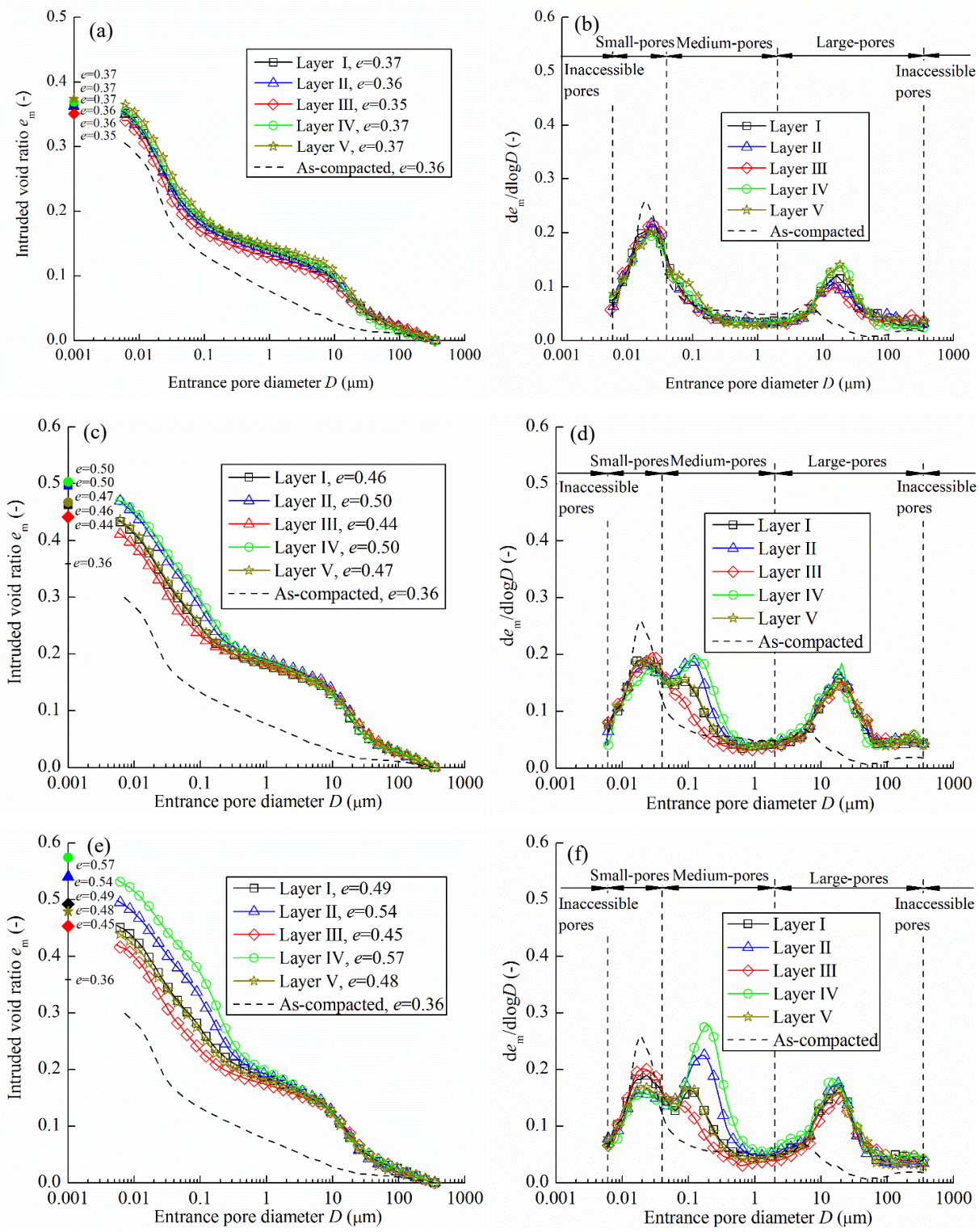
(a)
Intruded void ratio e_m (-)
Entrance pore diameter D (μm)
Layer I, e=0.37
Layer II, e=0.36
Layer III, e=0.35
Layer IV, e=0.37
Layer V, e=0.37
As-compacted, e=0.36
(b)
de_m/dlog$D$ (-)
Small-pores
Medium-pores
Large-pores
Inaccessible pores
Layer I
Layer II
Layer III
Layer IV
Layer V
As-compacted
(c)
Layer I, e=0.46
Layer II, e=0.50
Layer III, e=0.44
Layer IV, e=0.50
Layer V, e=0.47
As-compacted, e=0.36
(d)
(e)
Layer I, e=0.49
Layer II, e=0.54
Layer III, e=0.45
Layer IV, e=0.57
Layer V, e=0.48
As-compacted, e=0.36
(f)

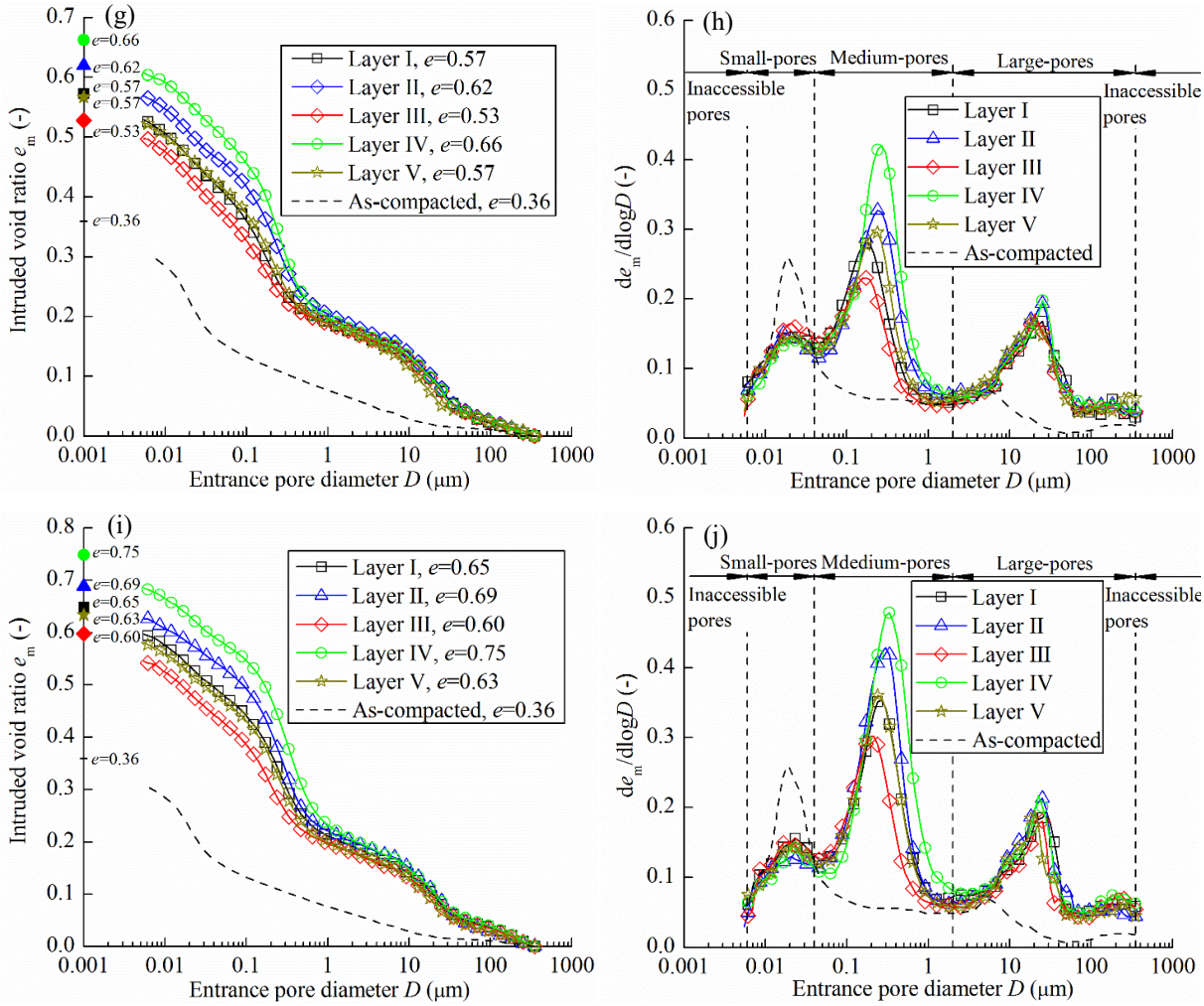

Fig. 8. Pore size distribution at different layers: (a) cumulative curves of T01, (b) density function curves of T01, (c) cumulative curves of T02, (d) density function curves of T02, (e) cumulative curves of T03, (f) density function curves of T03, (g) cumulative curves of T04, (h) density function curves of T04, (i) cumulative curves of T05, and (j) density function curves of T05

To further analyze the different microstructure features, four pore types were defined: inaccessible pores (< 0.006 μm and > 350 μm), small pores (0.006-0.04 μm), medium pores (0.04-2 μm) and large pores (2-350 μm), as shown in Fig. 8 (Wang et al., 2014; Bian et al., 2019). Fig. 9 presents the variations of void ratios corresponding to different pores with the distance from the middle of samples. It shows clearly that the void ratios for the four types of pores were almost the same for sample T01 without technological voids. By contrast, for the samples with technological voids (T02, T03, T04, and T05), larger inaccessible-pore, medium-pore and large-pore void ratios and a lower small-pore void ratio were observed for layers II and IV, which were characterized by higher water contents and lower dry densities.

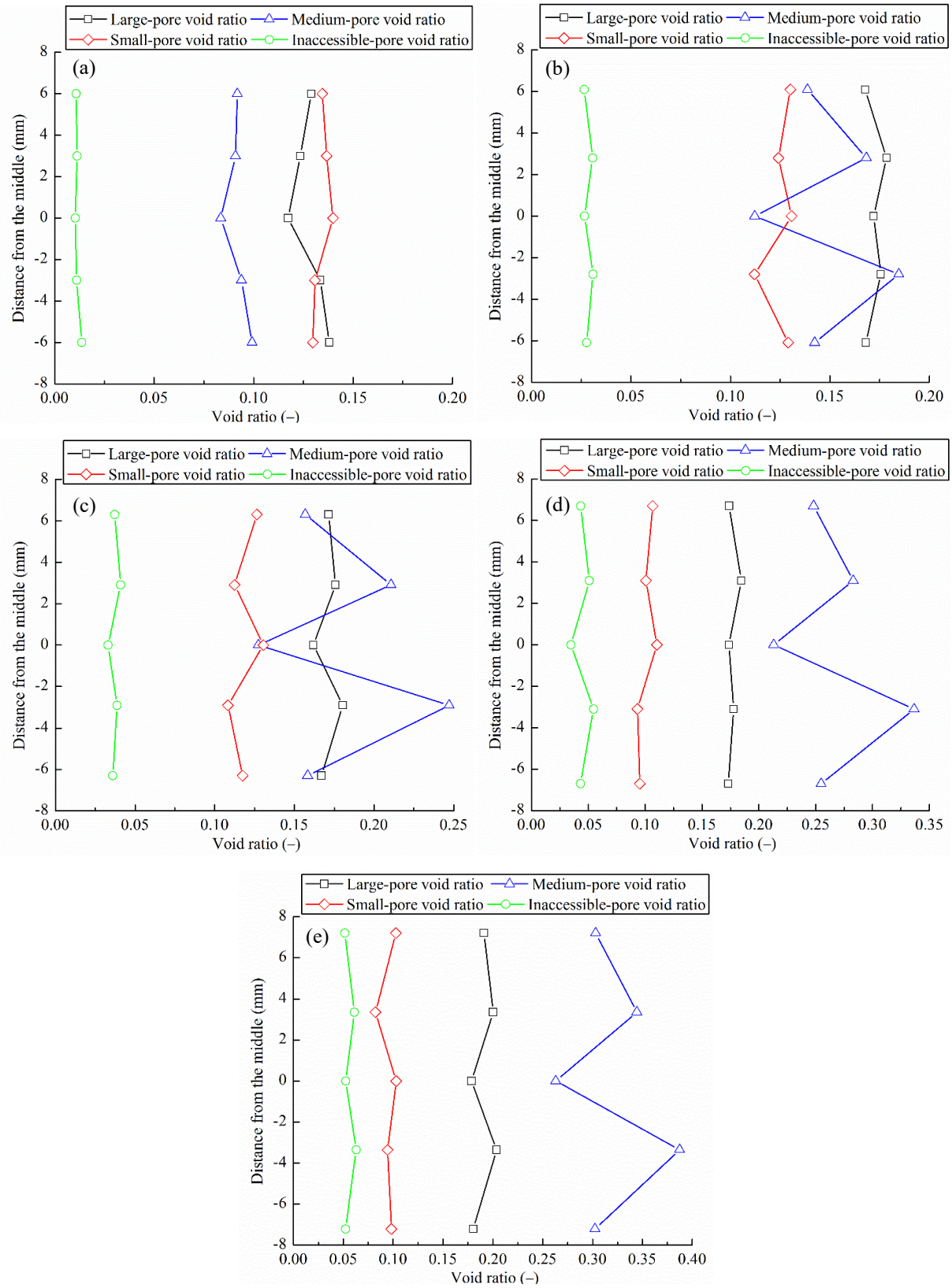

Fig. 9. Changes in inaccessible-pore, small-pore, medium-pore and large-pore void ratios (a) T01, (b) T02, (c) T03, (d) T04 and (e) T05

Fig. 10 compares the pore size distribution curves from different tests for different layers. The corresponding changes in the void ratio of different pore types are also presented in Fig. 11. It

can be seen that the technological voids increased the sizes of large-pores and medium-pores, without significantly modifying the size of small-pores. As the technological voids increased, the large-pore, medium-pore and inaccessible-pore void ratios increased, while the small-pore void ratio decreased slightly. Further examination showed that the variation of the medium-pore void ratio was the most pronounced, suggesting that the heterogeneous microstructure distribution due to the presence of technological voids was mainly related to changes in medium pores.

4 Interpretation and discussion

The evolution of axial and radial swelling pressures is basically linked to the microstructural changes (Saba et al., 2014a). According to the swelling pressures kinetics, the hydration of the samples with technological voids (T02, T03, T04, and T05) could be divided into four stages, namely stages I, II, III, and IV, respectively, as shown in Fig. 12 for sample T04 as an example. At stage I, the bentonite grains were softened, resulting in a slight decrease of axial pressure and at the same time, the disks swelled and started to fill the technological voids. At stage II, the adjacent disks came in contact with each other with more significant development of axial swelling pressure. During stages I and II, radial swelling pressure increased quickly and then decreased significantly, exhibiting a marked peak. This could be explained as follows: due to the presence of technological voids, the central disk, which was in contact with the radial pressure sensor, swelled significantly in the axial direction and reduced the soil dry density in the vicinity of radial sensor, resulting in a decrease of the radial swelling pressure. When the decrease in radial pressure due to the axial swelling was larger than the increase due to radial swelling, a peak on the radial swelling pressure curve appeared. When the technological voids were fully filled and sealed with further hydration, the soils were subjected to swelling under constant-volume condition, and the radial swelling pressure increased again at stage III and tended to be stable at stage IV. By contrast, the axial swelling pressure increased at a much higher rate at stage III and then reached stabilization at stage IV. During stages III and IV, the samples became more and more homogenous. Summarizing, stages I and II referred to a filling process of technological voids, while stages III and IV could be regarded as a homogenization process. During the homogenization process, the sample could be divided into two zones: (i) a swelling zone at which the soil with a dry density larger than the expected final one underwent further swelling and thus further decrease of dry density; (ii) a sealing zone where the soil with a dry density lower than the expected final one was subjected to compression imposed by the

further swelling of soil in the swelling zone (Bian et al., 2019). From Fig. 7b, it appears that layers I, III, and V corresponded to the swelling zone, while the sealing zone included layers II and IV where the technological voids were preset. For the sample with larger technological voids, a much longer time was required to reach the full homogenization owing to the lower swelling pressure of the sample, which could be evidenced by the lower increase rate of the axial swelling pressure (Fig. 4b and c).

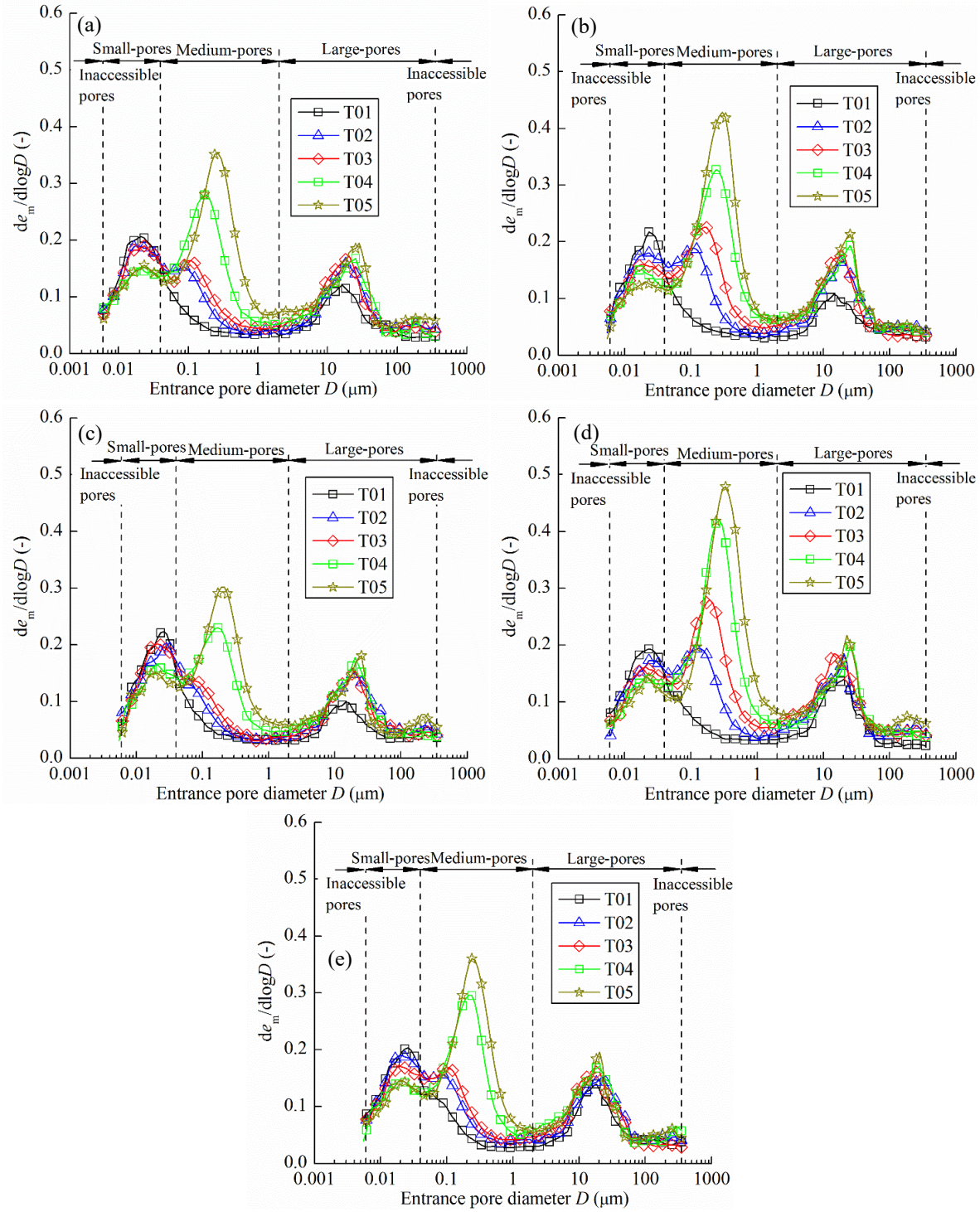

Fig. 10. Pore size distributions for (a) layer I, (b) layer II, (c) layer III, (d) layer IV, and (e) layer V

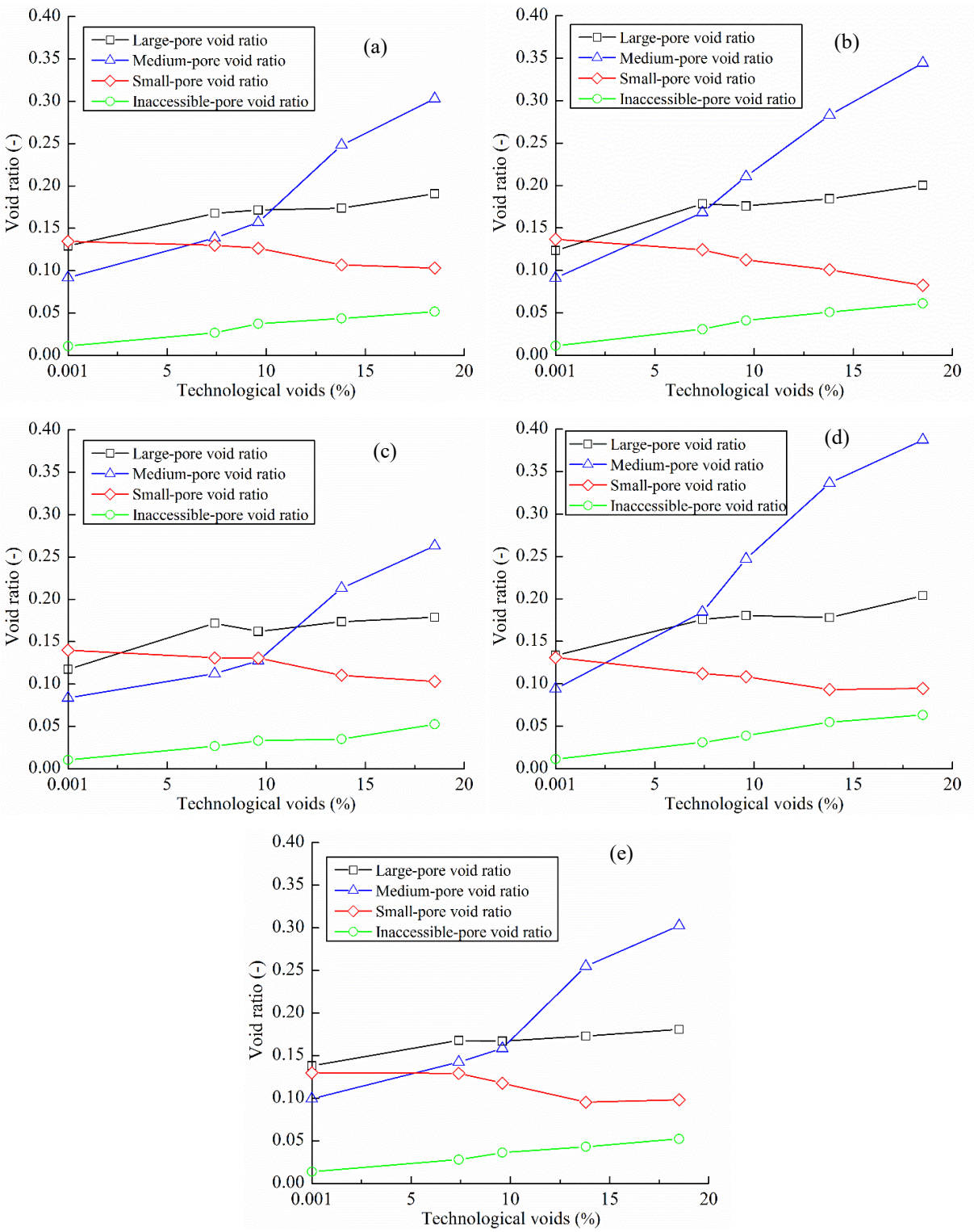

Fig. 11. Changes in inaccessible-pore, small-pore, medium-pore and large-pore void ratios with technological voids for (a) layer I, (b) layer II, (c) layer III, (d) layer IV and (e) layer V

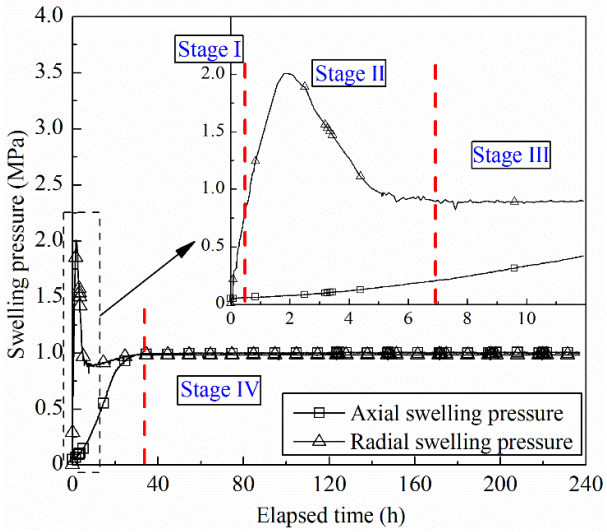

Fig. 12. Schematic diagram showing separation of the four swelling stages

From Figs. 7 and 9, it appears that the variations of small-pore void ratios along the samples exhibited a trend similar to that of dry density while those of inaccessible-pore, medium-pore and large-pore void ratios exhibited an opposite one, indicating a good correspondence between the microstructure and dry density. Fig. 13 displays the variations of the void ratios of inaccessible, small, medium and large pores with dry density. It clearly shows that the inaccessible-pore, medium-pore and large-pore volume increased with the decreasing dry density, while the small-pore volume decreased. Upon hydration, water molecules were adsorbed by clay particles, layer after layer up to four layers, resulting in an increase in interparticle space. This pore size change corresponded to the inaccessible pores and could not be detected by MIP (Wang et al., 2014). Obviously, this process highly depended on the soil dry density. The soils with low dry density allowed more water infiltration into the interlayer space, and therefore exhibited more inaccessible pores. Meanwhile, the enlargement of inter-particle space upon saturation could facilitate the exfoliation of clay particles and lead to large-pore filling. Additionally, fissure-like 2-dimensional (2-D) pores would appear owing to the division of soil aggregates, resulting in an increase of large-pore volume (Wang et al., 2014). The lower the dry density, the larger the 2-D pores, explaining the increase of the mean size of large pores with the increasing technological voids (Fig. 10). The increase of large-pore void ratio was the combined effect of the two aforementioned mechanisms. In addition to the absorption of water molecules in the interlayer space, the subdivision of particles into thinner ones could enlarge the interparticle pores inside the aggregates, resulting in a decrease of small-pore void ratio (Delage 2007). Regarding the creation of new pore population (medium pores), it was aided by the filling of large pores and enlargement of small pores.

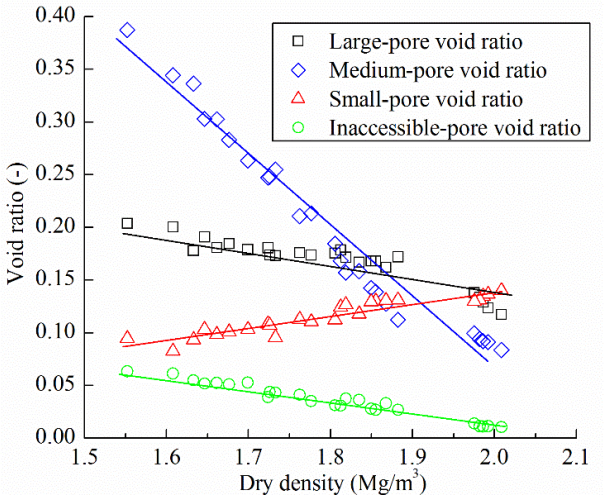

Fig. 13. Large-pore, medium-pore, small-pore and inaccessible-pore void ratios versus soil dry density

For the samples with technological voids, larger inaccessible-pore, medium-pore and large-pore void ratios and a lower small-pore void ratio were observed in the sealing zone (layers II and IV). As the hydration time increased, the medium pores and large pores in the sealing zone were compressed by swelling pressure, leading to decreases in medium-pore and large-pore void ratios. By contrast, in the swelling zone, the inaccessible-pore void ratio increased while the small-pore void ratio decreased due to more water driven into the interparticle pores with time (Wang et al., 2014). Consequently, these processes resulted in a more uniform microstructure.

As remarked earlier, the axial swelling pressures reached stabilization after 49.0, 45.4, 37.5, and 35.3 h hydration for tests T02, T03, T03, and T05, respectively, although the distributions of dry density and microstructure still changed with time. To address this remark, the measured axial swelling pressure is plotted versus the expected final dry density for all tests in Fig. 14. For comparison, the variation of axial swelling pressure with the dry density of the same material (30/70 MX80 bentonite-COx claystone mixture) without technological voids is also presented (Zeng et al., 2019). All data remarkably agreed, providing a unique relationship between the axial swelling pressure ($P_{\text{s-axial}}$) and the final dry density (ρ_{d}):

$$P_{\text{s-axial}}=1.564\times10^{-5}\exp^{6.390\rho_{\text{d}}} \quad (1)$$

This agreement confirmed that the axial swelling pressure at stabilization is not affected by the heterogeneity of the samples induced by technological voids. In other words, the technological voids played the same role as the macropores of the compacted samples without technological voids. As far as the difference of swelling pressures in the axial and radial directions was concerned, it could be observed that the radial swelling pressure (4.46 MPa) was significantly smaller than the axial swelling pressure (5.22 MPa) for the sample without technological voids

(Fig. 6). To further analyse this anisotropic behaviour, an isotropy coefficient was defined as the ratio of radial to axial swelling pressures. Because, for the samples with technological voids, the dry density distribution was still heterogeneous along the sample height at the end of infiltration tests (Fig. 7b), the measured value of radial swelling pressure could be dependent on the measurement position. Based on the division of the samples for dry density measurement (Fig. 3a), the testing surface of pressure sensor was in contact with the soils at layers II, III, and IV and the dry density of soils in the vicinity of the pressure sensor $\rho_{\text{d-sensor}}$ could be calculated using Eq. (2):

$$\rho_{\text{d-sensor}}=(\rho_{\text{d-III}}\times A_3+\rho_{\text{d-II}}\times A_2+\rho_{\text{d-IV}}\times A_4)/(A_2+A_3+A_4) \quad (2)$$

where $\rho_{\text{d-II}}$, $\rho_{\text{d-III}}$, and $\rho_{\text{d-IV}}$ are the dry densities of layers II, III, and IV; A_2, A_3, and A_4 are the areas of contact between the pressure sensor and layers II, III, and IV, respectively. In this study, A_2, A_3, and A_4 are equal to 17.22, 5.23, and 5.23 mm^2, respectively. According to the dry density distribution of soils, the values of dry density of soils in contact with the radial sensor were estimated to be 1.87, 1.81, 1.74, and 1.64 Mg/m^3 for tests T02, T03, T04, and T05, respectively. Correspondingly, the axial swelling pressures of the soils in contact with the pressure sensor were estimated to be 2.43, 1.67, 1.05, and 0.56 MPa from Eq. (1). The isotropy coefficients for the samples with technological voids were determined according to the axial and radial swelling pressures of the soils in contact with the pressure sensor. The relationship between the isotropy coefficient and technological voids is presented in Fig. 6. It appears that the samples with technological voids exhibited higher isotropy coefficients, compared to that without technological voids (0.85). Moreover, the larger the technological voids, the larger the isotropy coefficient. As explained by Lee et al. (2012), Saba et al. (2014a) and Jia et al. (2018), the anisotropic behaviour of compacted disks could be attributed to the microstructural anisotropy induced by the uniaxial compaction. After compaction, clay particles were preferentially oriented in the horizontal direction. Upon hydration, the samples exhibited more significant swelling in the axial direction. For the samples with technological voids, aggregates swelled and split up upon hydration, filling the technological voids and allowing the rearrangement of clay particles. This process led to a microstructural collapse and reduced the initial orientation of aggregates due to the uniaxial compaction (Saba, 2013).

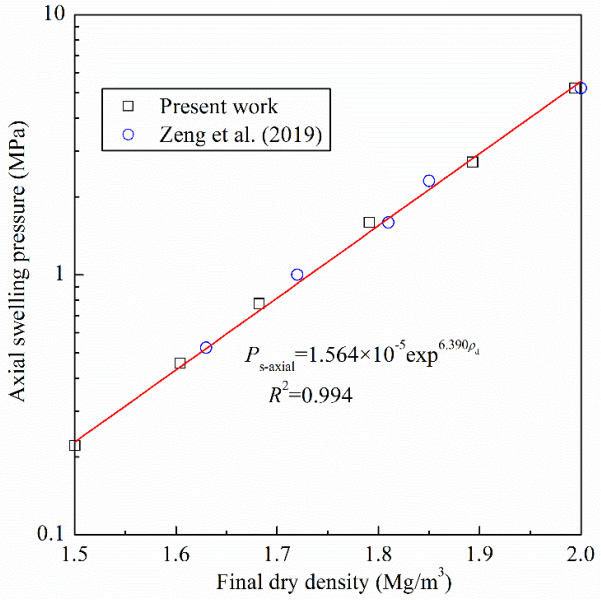

Fig. 14. Relationship between axial swelling pressure and final dry density

From a practical point of view, swelling pressure and hydraulic conductivity are two key parameters in the design of sealing and backfilling materials and in the assessment of their long-term sealing performance. Given that the presence of technological void can reduce the initial anisotropy and result in a relatively isotropic swelling, the corresponding axial and radial swelling pressure can be satisfactorily predicted according to the unique relationship elaborated between the axial swelling pressure and the expected final dry density when the initial state of compacted disks and the technological voids are known.

In general, water transfer is primarily dominated by the network of large pores (> 2 μm) (Wang et al., 2013b). As mentioned above, the large-pore void ratio is greater in the sealing zone corresponding to the technological voids and a larger hydraulic conductivity can be expected in this zone. Therefore, possible preferential flow in the radial direction can appear in the sealing zone and should be taken into account, at least in the short term. In the long term, these large pores can be compressed by swelling pressure, resulting in a decrease of hydraulic conductivity in the sealing zone.

5 Conclusions

The effect of technological voids on the swelling behaviour of compacted MX80 bentonite-COx claystone was investigated by carrying out infiltration tests under constant-volume condition and microstructure observation. From the experimental results, the following conclusions can be drawn.

Two main processes were identified from the kinetics of axial and radial swelling pressures of the samples with technological voids: (i) a filling process of technological voids and (ii) a homogenization process. During the homogenization process, there were sealing and swelling zones. The former referred to the initial technological voids zone, while the latter to the zone far from the initial technological voids zone.

At the end of tests, water content and dry density distributions were still heterogeneous, with a larger water content and a lower dry density in the sealing zone while a lower water content and higher dry density in the swelling zone. The sealing zone was characterized by larger inaccessible-pore (< 0.006 μm and > 350 μm), medium-pore (0.04-2 μm) and large-pore (2-350 μm) void ratios and a lower small-pore (0.006-0.04 μm) void ratio. It was believed that the difference in dry density and microstructure between the sealing and swelling zones decreased with the hydration time, rendering the sample more and more homogeneous.

The final axial and radial swelling pressures decreased with increasing technological voids. The relationship between the axial swelling pressures and the expected final dry density could be described by a unique correlation, which was in good agreement with that for compacted disks. The isotropy coefficient (ratio of radial to axial swelling pressures) increased with the increasing technological voids from 0 to 18.5%.

Acknowledgments

The authors thank the China Scholarship Council (CSC). The supports provided by Ecole des Ponts ParisTech and the French National Radioactive Waste Management Agency (Andra) are also greatly acknowledged.

References

Bian, X., Cui, Y.J., and Li, X.Z. 2019. Voids effect on the swelling behaviour of compacted bentonite. Géotechnique, 69(7): 593-605.

Cui, Y.J. 2017. On the hydro-mechanical behavior of MX80 bentonite-based materials. Journal of Rock Mechanics and Geotechnical Engineering, 9(3): 565-574.

Delage, P. 2007. Microstructure features in the behaviour of engineered barriers for nuclear waste disposal. Experimental unsaturated soil mechanics, 11-32.

Delage, P., Le, T.T., Tang, A.M., Cui, Y.J., and Li, X.L. 2008. Suction effects in deep Boom clay block samples. Géotechnique 57(2): 239–244.

Dixon, D.A., Gray, M.N., and Thomas, A.W. 1985. A study of the compaction properties of potential clay-sand buffer mixtures for use in nuclear fuel waste disposal. Eng. Geol. 21(3/4): 247-255.

Fouché, O., Wright, H., Le Cléac'h, J.M., and Pellenard, P. 2004. Fabric control on strain and rupture of heterogeneous shale samples by using a non-conventional mechanical test. Applied Clay Science, 26(1-4): 367-387.

Gens, A., Vállejan, B., Sánchez, M., Imbert, C., Villar, M. V., and Van Geetl, M. 2011. Hydromechanical behaviour of a heterogeneous compacted soil: experimental observations and modelling. Géotechnique 61(5): 367-386.

Herbert, H.J., Kasbohm, J., Moog, H.C., and Henning, K.H. 2004. Long-term behaviour of the Wyoming bentonite MX-80 in high saline solutions. Applied Clay Science, 26(1-4): 275-291.

Herbert, H.J., Kasbohm, J., Sprenger, H., Fernández, A.M., and Reichelt, C. 2008. Swelling pressures of MX-80 bentonite in solutions of different ionic strength. Physics and Chemistry of the Earth, Parts A/B/C, 33: S327-S342.

Jia, L.Y., Chen, Y.G., Ye, W.M., and Cui, Y.J. 2019. Effects of a simulated gap on anisotropic swelling pressure of compacted GMZ bentonite. Engineering geology, 248: 155-163.

Karnland, O., Olsson, S., and Nilsson, U. 2006. Mineralogy and sealing properties of various bentonites and smectite-rich clay materials. Technical Report No. TR-06-30. SKB, Swedish Nuclear Fuel and Waste Management Co.

Komine, H., and Ogata, N. 1994. Experimental study on swelling characteristics of compacted bentonite. Canadian Geotechnical Journal, 31(4): 478-490.

Komine, H., and Ogata, N. 1999. Experimental study on swelling characteristics of sand-bentonite mixture for nuclear waste disposal. Soils and Foundations, 39(2): 83-97.

Lee, J.O., Lim, J.G., Kang, I.M., and Kwon, S. 2012. Swelling pressures of compacted Ca-bentonite. Engineering Geology, 129: 20-26.

Pusch, R. 1982. Mineral–water interactions and their influence on the physical behavior of highly compacted Na bentonite. Canadian Geotechnical Journal, 19(3): 381-387.

Saba, S. 2013. Hydro-mechanical behaviour of bentonite-sand mixture used as sealing materials in radioactive waste disposal galleries (Doctoral dissertation, Université Paris-Est).

Saba, S., Barnichon, J. D., Cui, Y. J., Tang, A. M., and Delage, P. 2014a. Microstructure and anisotropic swelling behaviour of compacted bentonite/sand mixture. Journal of Rock Mechanics and Geotechnical Engineering, 6(2): 126-132.

Saba, S., Cui, Y.J., Tang, A.M., and Barnichon, J.D. 2014b. Investigation of the swelling behaviour of compacted bentonite–sand mixture by mock-up tests. Canadian Geotechnical Journal, 51(12): 1399-1412.

Seiphoori, A., Ferrari, A., and Laloui, L. 2014. Water retention behaviour and microstructural

evolution of MX-80 bentonite during wetting and drying cycles. Géotechnique, 64(9): 721-734.

Tang, A.M., Cui, Y.J., Le, T.T., 2008. A study on the thermal conductivity of compacted bentonites. Applied Clay Science, 41 (3-4): 181–189.

Tang, C.S., Tang, A.M., Cui, Y.J., Delage, P., Schroeder, C., and Shi, B. 2011. A study of the hydro-mechanical behaviour of compacted crushed argillite. Engineering Geology, 118(3-4): 93-103.

Villar, M.V., García-Siñeriz, J.L., Bárcena, I., and Lloret, A. 2005. State of the bentonite barrier after five years operation of an in situ test simulating a high level radioactive waste repository. Engineering Geology, 80(3-4): 175-198.

Wang, Q., Tang, A.M., Cui, Y.J., Delage, P., and Gatmiri, B. 2012. Experimental study on the swelling behaviour of bentonite/claystone mixture. Engineering Geology, 124: 59-66.

Wang, Q., Tang, A.M., Cui, Y.J., Delage, P., Barnichon, J.D. and Ye, W.M. 2013a. The effects of technological voids on the hydro-mechanical behaviour of compacted bentonite–sand mixture. Soils and Foundations, 53(2): 232-245.

Wang, Q., Cui, Y.J., Tang, A.M., Barnichon, J.D., Saba, S., and Ye, W.M. 2013b. Hydraulic conductivity and microstructure changes of compacted bentonite/sand mixture during hydration. Engineering Geology: 164, 67-76.

Wang, Q., Cui, Y.J., Tang, A.M., Li, X.L., and Ye, W.M. 2014. Time-and density-dependent microstructure features of compacted bentonite. Soils and Foundations, 54(4): 657-666.

Zeng, Z.X., Cui, Y.J., Zhang, F., Conil, N., and Talandier, J. 2019. Investigation of swelling pressure of bentonite/claystone mixture in the full range of bentonite fraction. Applied Clay Science. doi: 10.1016/j.clay.2019.105137.

Chapter 4. Effects of technological voids and hydration time

INTRODUCTION

During the installation of the compacted bentonite-based materials in the drifts and shafts, technological voids will remain between the compacted blocks and between the compacted blocks and the host rock. When underground water is recovered, the compacted blocks close to the technological voids swell quickly with a quick reduction of the dry density. This leads to a heterogeneous distribution with lower dry densities in the area affected by water and higher dry densities in the innermost area and influences the hydro-mechanical behaviour of the compacted blocks.

This chapter deals, firstly, with an experimental program aiming to study the effects of technological voids and hydration time on the hydro-mechanical behaviour of compacted MX80 bentonite/COx claystone mixture. The evolutions of swelling pressure and hydraulic conductivity of compacted blocks with different technological voids were investigated. To further interpret the hydro-mechanical behaviour of the specimens with technological voids, the dry density, water content, suction and microstructure features at different positions after different times were determined. Afterwards, with consideration of the effect of boundary friction between the specimens and porous discs, an analytical method was proposed to estimate the final dry density distribution of specimens with technological voids. The estimated results were then compared to the measured ones.

This chapter consists of two papers. The first one, published in “Géotechnique”, presents an experimental study on the effects of technological voids and hydration time on the hydro-mechanical behaviour of compacted bentonite/claystone mixture. The second paper, published in “Acta Geotechnica”, deals with the estimation of final dry density distribution of the compacted bentonite/claystone mixture with technological voids. The articles are presented here in their original versions.

Zeng, Z.X., Cui, Y.J., Conil, N., Talandier, J. 2020. Géotechnique. https://doi.org/10.1680/jgeot.19.P.220.

Effects of technological voids and hydration time on the hydro-mechanical behaviour of compacted bentonite/claystone mixture

Zhixiong Zeng[1], Yu-Jun Cui[1], Nathalie Conil[2], Jean Talandier[3]

Abstract: Pre-compacted MX80 bentonite/Callovo-Oxfordian (COx) claystone mixture has been considered as a promising sealing/backfilling material in deep geological repository for high-level radioactive waste in France. When the pre-compacted blocks are emplaced in the gallery, technological voids can remain. After the infiltration of groundwater from the host rock, they will swell freely, filling the technological voids and then undergo further hydration under constant-volume conditions. From the perspective of the storage safety, it is essential to understand the effects of technological voids and hydration time on the hydro-mechanical behaviour of such pre-compacted blocks. In this work, a series of infiltration tests at various hydration times were carried out on compacted MX80 bentonite/COx claystone mixture with different technological voids. The evolutions of the swelling pressures in axial and radial directions as well as the hydraulic conductivity were monitored while wetting. After the predetermined hydration times, the dry density, water content and suction at different positions were determined, together with the microstructure investigation using mercury intrusion porosimetry (MIP). It was observed that the soils close to initial voids swelled and filled the initial voids upon contact with water, with significant increases in large-pore and medium-pore void ratios. From the variation of dry density profile with time, compression and swelling zones could be identified: in the compression zone, the soils corresponding to the initial voids were subjected to compression, with decrease in large-pore and medium-pore void ratios over time, whereas in the swelling zone, the soils with a higher dry density than the expected final one underwent further swelling, with large-pore void ratio increasing untill saturation and then a slight decrease due to the water redistribution in the soil. Due to the soil density heterogeneity, the axial swelling pressure and hydraulic conductivity of samples with voids were slightly larger than those of samples without voids; contrarily, the radial swelling pressure was lower than that of the samples without voids.

Keywords: expansive soils; fabric/structure of soils; time dependence; laboratory tests; radioactive waste disposal

1 Ecole des Ponts ParisTech, Laboratoire Navier/CERMES, 6 et 8 avenue Blaise Pascal, 77455 Marne La Vallée cedex 2, France
2 Andra, Centre de Meuse/Haute-Marne, RD 960, 55290 Bure, France
3 Andra, 1/7, rue Jean Monnet, 92298 Châtenay-Malabry cedex, France

1 Introduction

Many European concepts of deep geological disposal for radioactive waste involve a multi-barrier system consisting of canisters, natural geological barrier (host rock), concrete lining and sealing/backfilling elements. In most cases, compacted blocks manufactured by uniaxial compaction are placed between host rock and canisters, and inevitably, technological voids remain among the blocks, between blocks and canisters and between blocks and host rock (Villar and Lloret, 2008; Wang et al., 2013a; Bian et al., 2019a). These technological voids are estimated at 6.6, 12 and 14% of the total volume of the galleries in the Febex mock-up test (Martin et al., 2006), PGZ2 in situ tests in the underground research laboratory (URL) at Bure (Gatabin et al., 2016) and Sealex in situ test (Wang et al., 2013a; Saba et al., 2014a), respectively. Upon the intrusion of groundwater from the host rock, compacted blocks will swell and fill up the technological voids, closing the preferential pathways (Villar and Lloret, 2008). After that, their swelling will occur under constant-volume conditions. In the long term, they are expected to exhibit a swelling pressure high enough to limit the convergence of the galleries after the failure of concrete lining (Cuisinier et al., 2008) and a hydraulic conductivity low enough to retard the water transfer-related phenomena (Castellanos et al., 2008). Hence, it is essential to well understand thoroughly the hydro-mechanical behaviour of the bentonite-based materials in the assessment of overall repository safety, when technological voids are present.

A number of studies were performed to investigate the effect of technological voids on the hydro-mechanical behaviour of compacted sealing/backfilling materials both in the laboratory and at field scale (Villar et al., 2005; Gens et al., 2011; Wang et al., 2013a; Saba et al., 2014b; 2014c; Mokni et al., 2016; Bian et al., 2019b; Jia et al., 2019). Once the hydration has started, a quick reduction of the dry density of compacted blocks close to the technological voids occurs, leading to a heterogeneous distribution of dry density, with lower dry densities in the area affected by water and higher dry densities in the innermost area (Villar and Lloret, 2008). Bian et al. (2019b) divided the heterogeneous samples into two zones according to the expected final dry density: a compression zone where the dry density was lower than the expected final value and a swelling zone in which the dry density was larger than the expected final value. Over time, the swelling zone would undergo further swelling while the compression zone would be compressed by the swelling pressure. As a result, the dry density gradient would decrease and approach a relatively homogeneous state (Bian et al., 2019b). It was also found that the samples with voids exhibited a hydraulic conductivity of one order of magnitude larger than those

without voids after about 40 h of water hydration. By contrast, the swelling pressure was mainly governed by the expected final dry density, irrespective of the heterogeneity when 14% technological voids were considered (Wang et al., 2013a; Saba et al., 2014b). To the authors' knowledge, the evolutions of the swelling pressures in various directions and hydraulic conductivity of the compacted blocks with technological voids over a long time period have not been comprehensively studied.

Basically, the macroscopic hydro-mechanical response of compacted blocks is directly related to their microstructure changes (Wang et al., 2014; Bian et al., 2019b). Bian et al. (2019b) conducted seven infiltration tests on compacted bentonite with initial voids and investigated the microstructure change with time using mercury intrusion porosimetry (MIP), together with the determination of dry density, water content and suction. They found that the variation of dry density at different positions was well correlated with the microstructure changes, but their work was limited to the microstructural changes of compacted bentonite during the saturation process only. After the full saturation of the compacted blocks, the water exchanges between intra-aggregate and inter-aggregate pores would continue, resulting in a decrease in inter-aggregate porosity and an increase in interlayer porosity due to more water infiltration into the interlayer space inside the aggregates (Delage et al., 2006; Wang et al., 2014). However, it should be pointed out that, although the ageing effect on the microstructure of compacted blocks was identified in several studies, there has been no investigation into the evolution of microstructure with the presence of technological voids over long time period.

In the present study, a series of infiltration tests were carried out on a compacted MX80 bentonite and Callovo-Oxfordian (COx) claystone mixture at different times. The evolutions of swelling pressure and hydraulic conductivity of compacted blocks with different technological voids were evaluated. Moreover, the dry density, water content, suction and microstructure features at different positions after different times were determined, enabling interpretation of the hydro-mechanical behaviour of the compacted mixture with the presence of technological voids.

2 Materials and methods

2.1 Materials

The soil studied is a mixture of MX80 bentonite and COx claystone with a proportion of 30/70 in dry mass, which has been considered as a promising sealing/backfilling material by the

French National Radioactive Waste Management Agency (Andra). The bentonite is a commercial bentonite from Wyoming, USA and its physical and chemical properties are summarized in Table 1. The COx claystone was obtained at about 490 m depth from the Andra URL at Bure, France. The claystone consists of 40-45% clay minerals with predominance of interstratified illite/smectite, 30% carbonates and 25-30% quartz and feldspar (Fouché et al., 2004). It has a liquid limit of 41%, a plastic limit of 24% and an average specific gravity of 2.70. The bentonite and claystone were obtained as granulated powders at water contents of 11.4 and 6.1%, respectively. The grain size distribution curves of MX80 bentonite and COx claystone determined by dry sieving and sedimentation are displayed in Fig. 1. The size of bentonite grains determined by dry sieving was very close to that of claystone grains. Once deflocculated in water, the clay-size fractions (< 2 μm) were determined, and were equal to 86 and 26% for bentonite and claystone, respectively (Zeng et al., 2020a).

Table 1. Physical and chemical properties of MX80 bentonite (the CEC data compiled from Kiviranta and Kumpulainen (2011))

Soil property	Description
Specific gravity	2.76
Consistency limit	
Liquid limit (%)	496
Plastic limit (%)	46
Plasticity index (%)	448
Cation exchange capacity (CEC) (meq/100 g)	84
Main exchange capacity (meq/100 g)	
Na^+	58
K^+	2
Mg^{2+}	8
Ca^{2+}	25
Main minerals	
Montmorillonite (%)	86
Quartz (%)	7

Synthetic water, which has the same chemical composition as the site water, was used for hydration. It was prepared by mixing the chemical components with de-ionised water, according to the recipe shown in Table 2 (Zeng et al., 2019). Note that even though this recipe was different that of Wang et al. (2013b), the ion compositions of the synthetic water prepared according to the two recipes were quite close.

2.2 Experimental set-up

Fig. 2 presents the experimental set-up used in this study. It consists of a stainless cell of dia. 50 mm. The test sample was installed between two porous stones and filter papers. The sample

was saturated from the bottom and the constant-volume condition was ensured by the stainless cell and a top piston, which was fixed with a screw. A force transducer under the cell and a total pressure sensor in the cell were installed for the axial and radial pressure measurements, respectively.

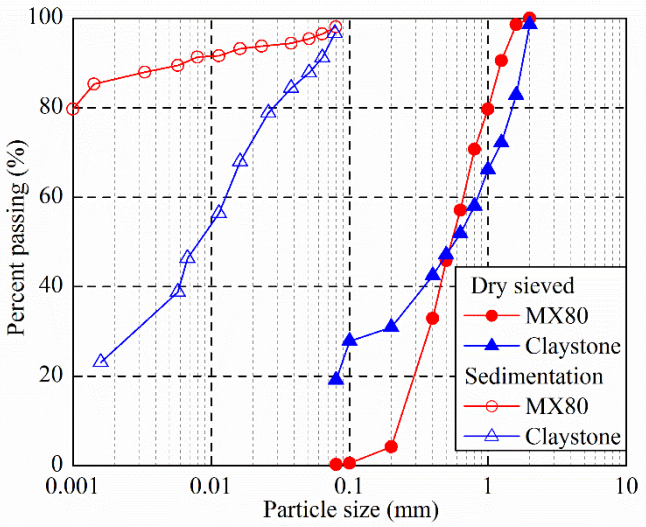

Fig. 1. Grain size distribution of MX80 bentonite and crushed COx claystone (Zeng et al., 2020a)

Table 2. Recipe for the synthetic water preparation

Component	NaCl	$NaHCO_3$	KCl	$CaSO_4 \cdot 2H_2O$	$MgSO_4 \cdot 7H_2O$	$CaCl_2 \cdot 2H_2O$	Na_2SO_4
Content (g/L)	1.950	0.130	0.035	0.630	1.020	0.080	0.700

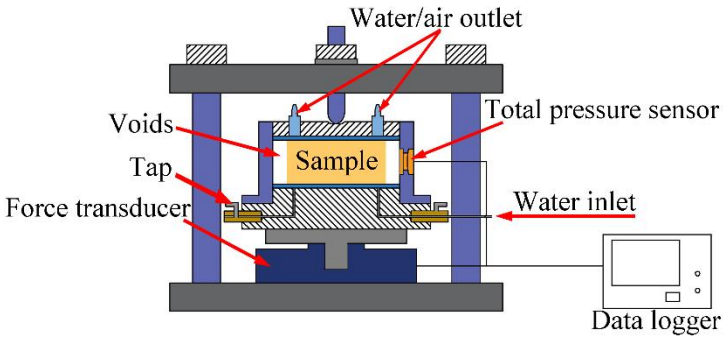

Fig. 2. Layout of the constant-volume cell for swelling pressure and hydraulic conductivity tests

2.3 Sample preparation and test procedure

The bentonite and claystone powders (30% bentonite - 70% claystone in dry mass) were carefully mixed for more than 10 min to obtain a relatively homogeneous state. The obtained mixture had a water content of 7.7%. Next, a predetermined amount of mixture was poured into a rigid ring (50 mm in dia.) and statically compacted at a controlled displacement rate of 0.05 mm/min. The target height of samples was 10 mm and the dry densities were 1.6, 1.8 and 2.0 Mg/m^3 (Table 3).

To study the effect of technological voids, 14 samples (T01 to T14) with a dry density of 2.0 Mg/m^3 were trimmed to different diameters of 47.43 and 44.72 mm (Fig. 3). When the samples were installed and centered in the cell, there were initial voids between the samples and the inner wall of cell, corresponding to 10 and 20% of the total volume for the samples with diameters of 47.43 and 44.72 mm, respectively. Before hydration, an initial axial pressure of 0.05 MPa was applied onto the samples to ensure good contact. For each case, seven identical samples were prepared and hydrated using synthetic water for 0.5, 5, 15, 60, 240, 720 and 2160 h to study the time effect. The expected final dry densities were 1.8 and 1.6 Mg/m^3 for the samples with initial diameters of 47.43 and 44.72 mm, respectively. For comparison, three 50 mm dia. samples with dry densities of 1.6, 1.8 and 2.0 Mg/m^3 (T15 to T17) were hydrated with synthetic water for 2160 h. The evolutions of both axial and radial pressures were determined during hydration. For the tests with less than 60 h of hydration (T01 to T04 and T08 to T11), the samples were hydrated using a Pressure/Volume controller to record the volume of injected synthetic water. For the tests with more than 240-h hydration (T05 to T07 and T12 to T17), the samples were first hydrated under a water head of about 1 m until the predetermined hydration times (see Table 3). After that, the synthetic water injection was continued using a Pressure/Volume controller under constant pressures of 0.04, 0.1 and 0.2 MPa (less than 1/10 of the swelling pressure) for the samples with expected final dry densities of 1.6, 1.8 and 2.0 Mg/m^3, respectively.

After the infiltration tests, the samples with initial technological voids were carefully taken out of the test cell by slowly pushing the sample from the bottom to minimise soil disturbance. Then, they were divided into three parts, namely part I, part II and part III, as shown in Fig. 4. Part I, including the initial voids, referred to a ring with inner and outer diameters of 40 and 50 mm. Part II corresponded to a ring with inner and outer diameters of 20 and 40 mm and the rest of cylinder with a diameter of 20 mm belonged to part III. Each part was cut into several pieces for the determination of water content, dry density and suction as well as the microstructural investigation. The water content of soils was determined by oven-drying at 105°C for a period of 24 h and the soil volume was determined by hydrostatic weighing after immersing the soil into a non-aromatic hydrocarbon fluid (Kerdane) (Bian et al., 2019b). The suction was measured with a chilled mirror dew point tensiometer (Decagon WP4). The microstructure was determined using the MIP technique. To ensure the quality of microstructure investigation, the samples (about 1.5 g) were first freeze-dried prior to MIP testing. The applied pressure ranged from 3.6×10^{-3} to 228 MPa, allowing the exploration of pore diameters from 350 to 0.006 μm.

Table 3. Experimental programme

Test	Technological voids (%)	Duration (h)	Initial dry density of block (Mg/m^3)	Expected final dry density (Mg/m^3)	MIP
T01	20	0.5	2.0	1.6	√
T02	20	5	2.0	1.6	√
T03	20	15	2.0	1.6	√
T04	20	60	2.0	1.6	√
T05	20	240	2.0	1.6	√
T06	20	720	2.0	1.6	√
T07	20	2160	2.0	1.6	√
T08	10	0.5	2.0	1.8	√
T09	10	5	2.0	1.8	√
T10	10	15	2.0	1.8	√
T11	10	60	2.0	1.8	√
T12	10	240	2.0	1.8	√
T13	10	720	2.0	1.8	√
T14	10	2160	2.0	1.8	√
T15	0	2160	2.0	2.0	-
T16	0	2160	1.8	1.8	-
T17	0	2160	1.6	1.6	-

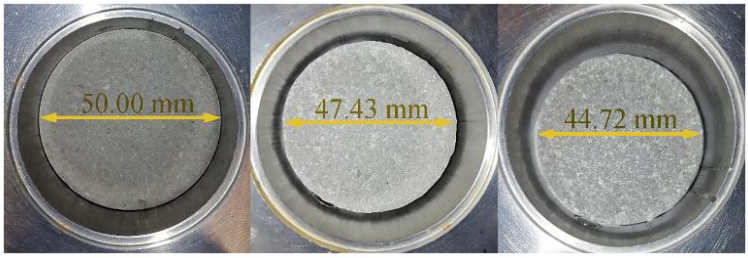

Fig. 3. Preparation of samples with and without voids

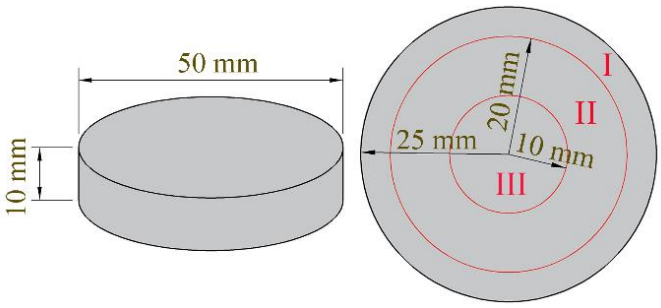

Fig. 4. Schematic view of the sample cutting

3 Experimental results

3.1 Axial and radial swelling pressures

As the hydration started, the synthetic water would fill up the technological voids and infiltrate into the compacted block from top, bottom and lateral sides. The compacted block was under a

free-swell condition in the radial direction and a confined condition in the axial direction. Fig. 5 depicts the evolution of axial swelling pressure of samples with different technological voids over various times. It clearly shows that the curves of identical samples for different hydration times were quite close, indicating a good repeatability of the infiltration tests. For test T15 without voids, the axial swelling pressure increased rapidly and then tended to stabilisation at 58.3 h (Fig. 5a). For the samples with 10% voids (T08 to T14), the axial swelling pressure started with a quick increase and reached stabilisation after 7.4 h (Fig. 5b). For the samples with 20% voids (T01 to T07), the swelling pressure increased at the beginning of hydration, reaching a peak value of 0.80 MPa at 0.68 h. Then, it decreased to about 0.57 MPa at 5.8 h and tended to stabilise (Fig. 5c). The occurrence of peaks could be attributed to the fact that the radial swelling of compacted block would decrease the dry density of compacted block and reduce the axial pressure. When the reduction of axial pressure due to the radial swelling was larger than the increase of axial swelling, the peaks appeared. The final axial swelling pressures after 2160-h hydration were 1.63 and 0.53 MPa for the samples with 10 and 20% technological voids, respectively. The larger the technological voids, the lower the final axial swelling pressure.

The evolution of radial swelling pressure with respect to elapsed time for all the samples is shown in Fig. 6. For test T15 without voids, the radial swelling pressure increased rapidly and then reached stabilisation after 54.0 h (Fig. 6a). For the samples with voids (T01 to T14), the radial pressure kept zero at the beginning of hydration. With further radial swelling, the soils came in contact with the sensor, and the radial swelling pressures became detectable after 0.08 and 0.18 h for the samples with 10 and 20% voids. Afterwards, they increased and then tended to stabilise after 7.5 and 5.7 h, respectively (Fig. 6b and c). The final radial swelling pressure decreased with the increase of technological voids.

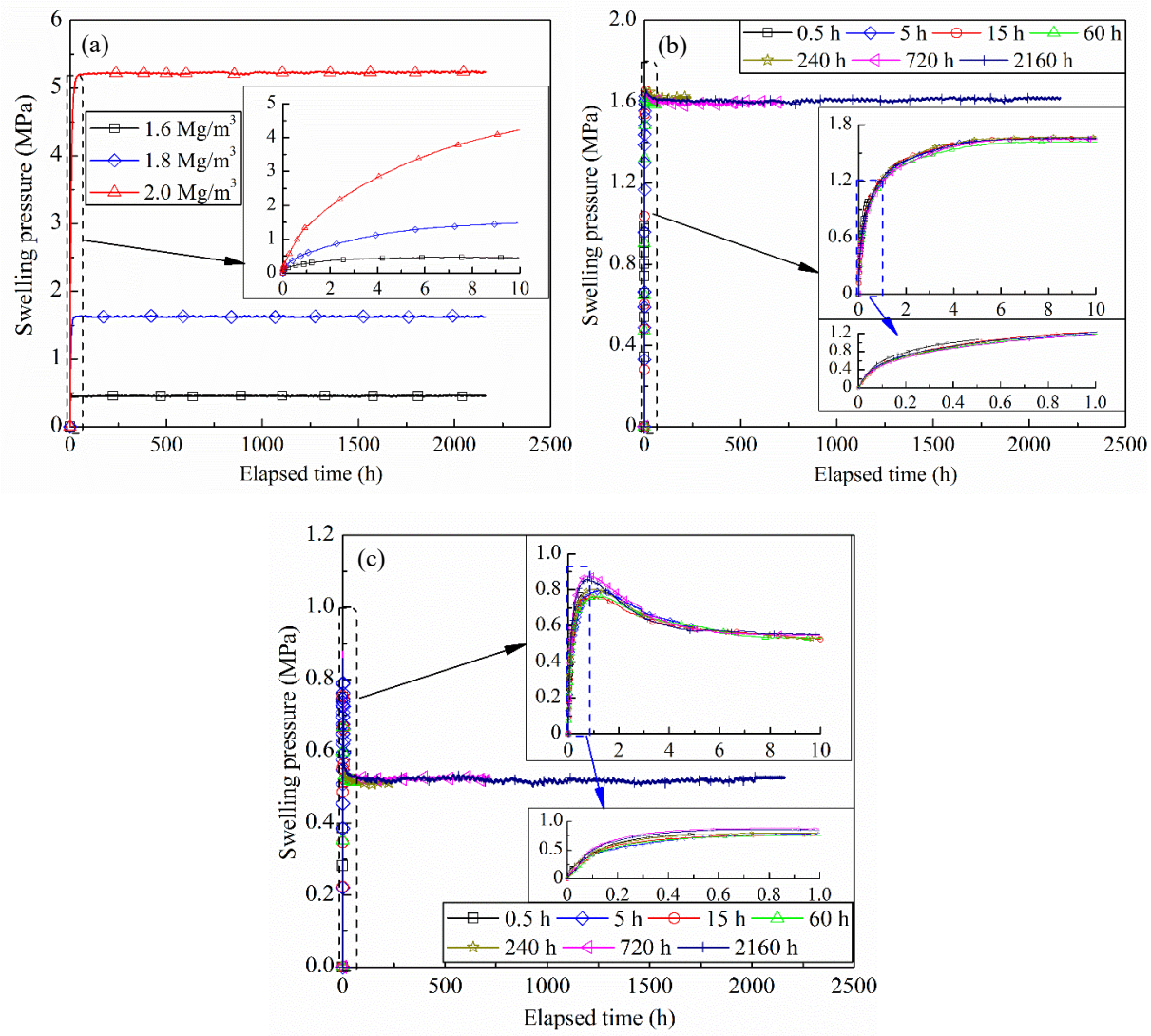

Fig. 5. Evolution of axial swelling pressure of samples: (a) without voids; (b) with 10% voids; (c) with 20% voids

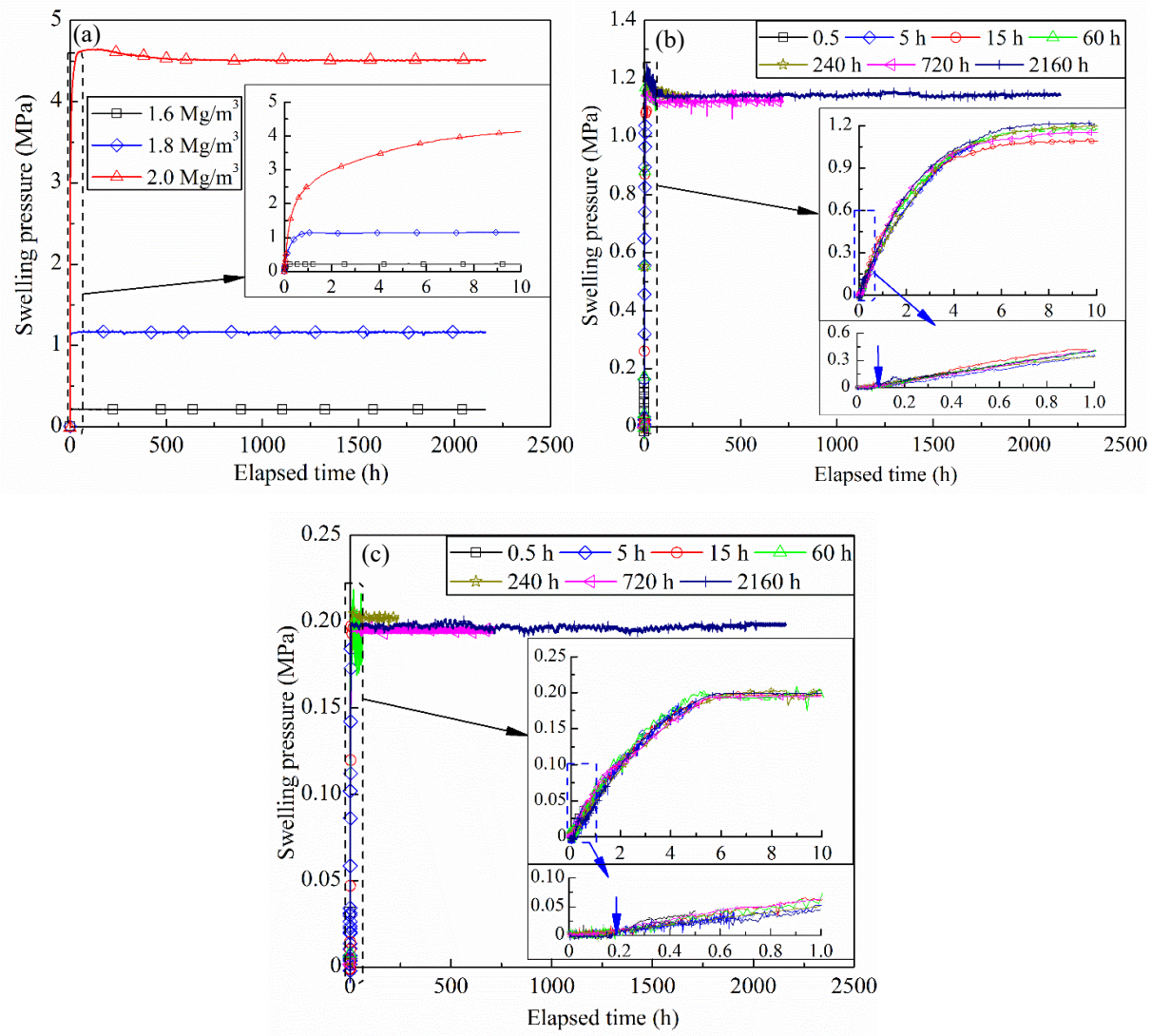

Fig. 6. Evolution of radial swelling pressure of samples: (a) without voids; (b) with 10% voids; (c) with 20% voids

3.2 Hydraulic conductivity

The theoretical water volumes required for saturating the samples (3.91 and 5.66 cm^3 for the samples with 10 and 20% voids, respectively) were lower than one-tenth of the total volumes of injected synthetic water after 5 h (78.05 and 87.27 cm^3 for the samples with 10 and 20% voids, respectively). Therefore, the hydraulic conductivity was determined according to the variation of synthetic water inflow recorded by the pressure/volume controller, without considering the synthetic water volume for saturating the samples. The evolutions of calculated hydraulic conductivities of samples with initial voids are presented in Fig. 7. Overall, a bi-linear decrease of hydraulic conductivity was clearly identified with the elapsed time in spite of the data scatter. A critical time could be thus defined: the slope before the critical time was noticeably larger than that after the critical time. The values of 7.5 and 5.8 h could be determined

at the intersection of two lines for the samples with 10 and 20% voids, respectively. Note that these critical times were very close to those required to reach stabilisation of the axial and radial swelling pressures, indicating a good compatibility between the hydraulic and mechanical parameters. It could be suspected that, before the critical times, the technological voids and the subsequent swollen soil with a larger void ratio around the sample governed the synthetic water flow. The progressively increasing radial swelling pressure compressed the swollen soil gradually and led to a decrease in hydraulic conductivity. By contrast, after the critical times, the swollen soil was subjected to consolidation under almost constant pressure and the hydraulic conductivity was decreasing but at a lower decreasing rate. As far as the final hydraulic conductivity was concerned, the final values of the samples without voids were 6.94×10^{-13}, 2.12×10^{-12} and 1.11×10^{-11} m/s for dry densities of 2.0, 1.8 and 1.6 Mg/m^3, respectively, while slightly higher hydraulic conductivities of 2.32×10^{-12} and 1.19×10^{-11} m/s were observed for the samples with 10 and 20% voids (corresponding to the expected final dry densities of 1.8 and 1.6 Mg/m^3, respectively).

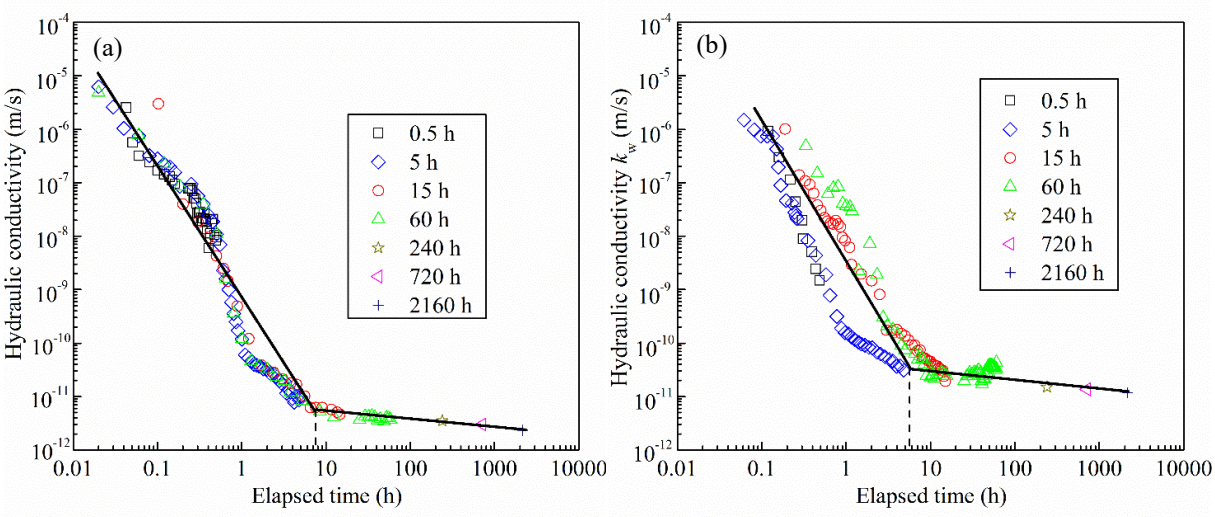

Fig. 7. Evolutions of hydraulic conductivities of samples: (a) with 10% voids; (b) with 20% voids

3.3 Water content, dry density and suction profiles

The water content and dry density profiles of the samples at different hydration times are depicted in Figs. 8 and 9. The water content and dry density exhibited rather heterogeneous distributions, with a higher water content and a lower dry density for part I, which included the initial voids. With the decrease of the distance from the center, the water content decreased and the dry density increased. Over time, the water content of part I including initial voids decreased while those of parts II and III far from the initial voids increased, leading to a decrease in water content gradient (Fig. 8). By contrast, the dry density of part I increased while those of parts II

and III decreased with time, approaching the expected final dry density (Fig. 9). Further examination of the evolutions of water content and dry density profiles showed a larger variation rate during the first 5 h but a lower one after 15 h, which was consistent with the phenomenon observed in the evolution of hydraulic conductivity. The dramatic decrease of dry density of part II and III especially during the first 5 h for the samples with 20% voids confirmed that the peak occurrence on the axial swelling pressure curve was related to the swelling of compacted block in the radial direction. Additionally, according to the measured water content and dry density, the degree of saturation of each part was calculated by considering a water density of 1.0 Mg/m^3 and the calculated results are summarized in Fig. 10. For part I, the degree of saturation quickly increased from 58% to larger than 98% after 0.5 h. By contrast, the degree of saturation of parts II and III increased during the first 5 h of hydration and then kept within the range of 98 to 102%.

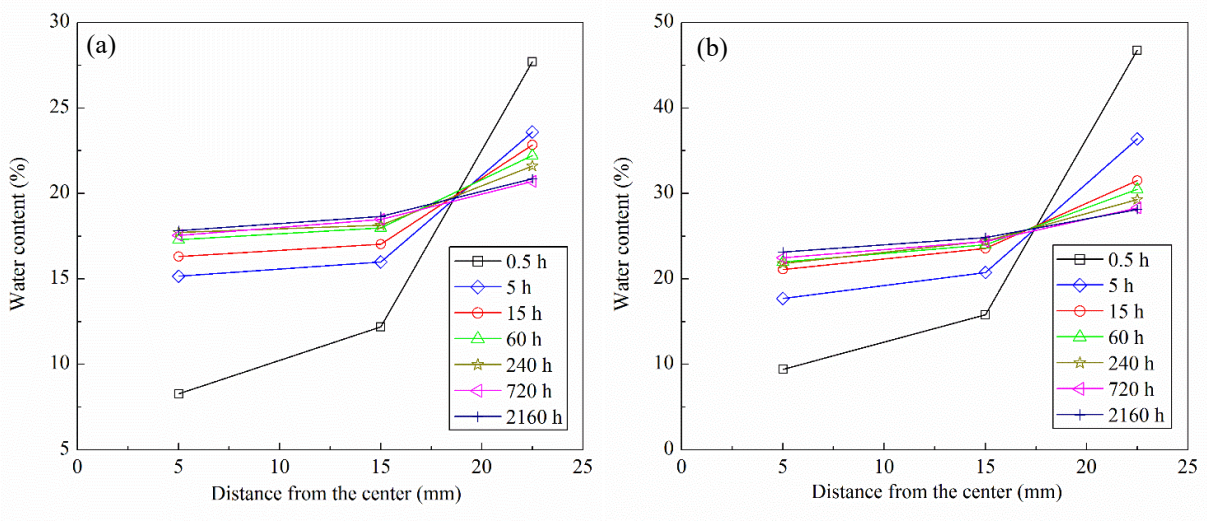

Fig. 8. Water content profiles after tests: (a) with 10% voids; (b) with 20% voids

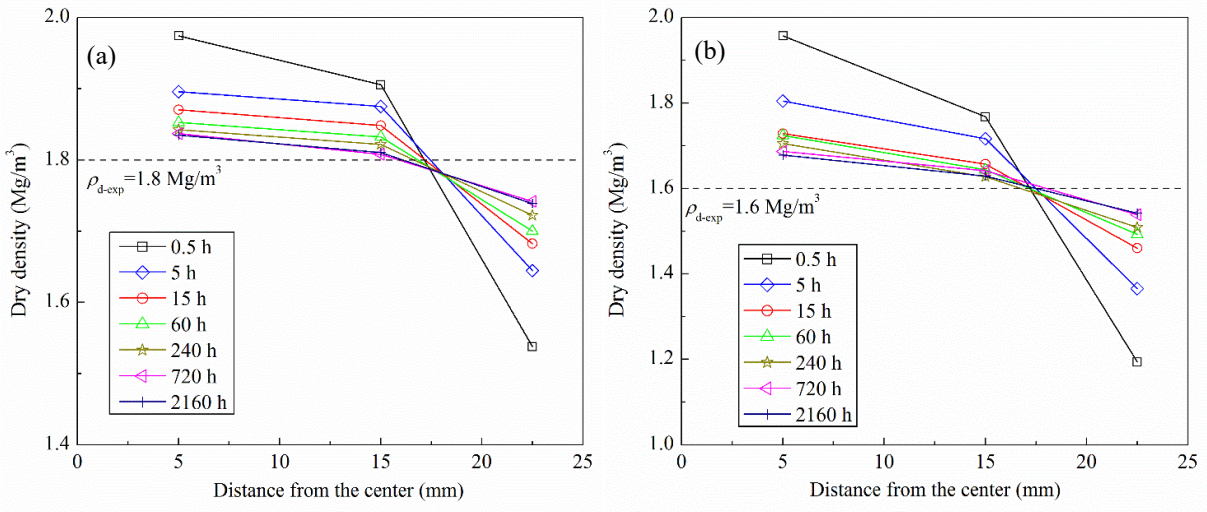

Fig. 9. Dry density profiles after tests: (a) with 10% voids; (b) with 20% voids

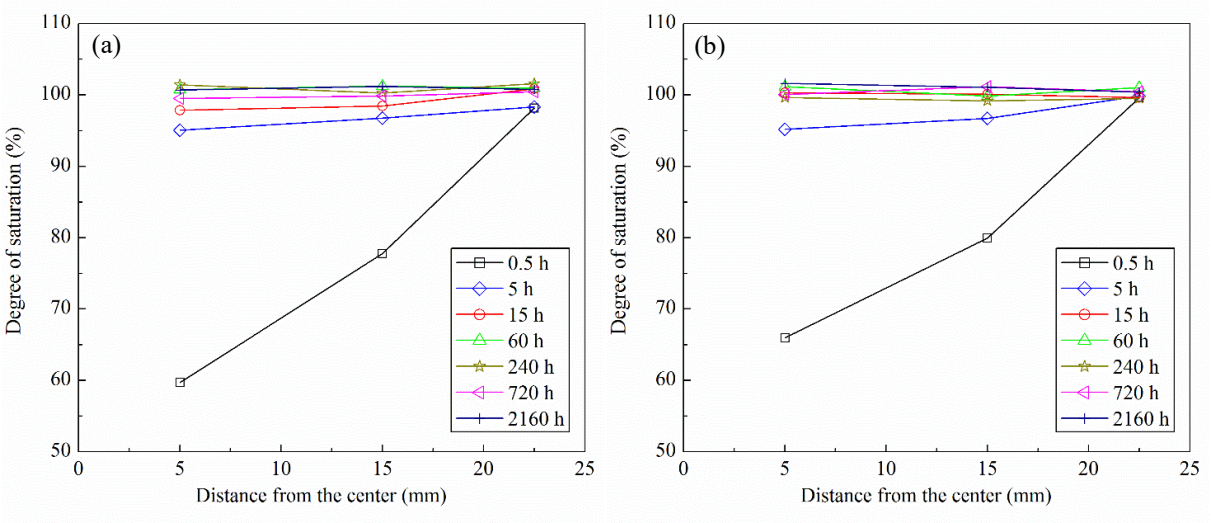

Fig. 10. Degree of saturation profiles after tests: (a) with 10% voids; (b) with 20% voids

The variation of suction profile with time for samples with technological voids is presented in Fig. 11. A drastic decrease of suction from 74.3 MPa at the as-compacted state to below 1.0 MPa after 0.5 h of hydration could be observed for part I, which included initial voids. The suction decrease was much less significant for parts II and III. For the samples with 10% voids, the suctions of parts II and III decreased to 1.50 and 1.38 MPa at 5 h, respectively (Fig. 11a), whereas the suctions of parts II and III for the samples with 20% voids decreased to 1.00 and 1.06 MPa at 5 h, respectively (Fig. 11b). Afterwards, the suctions of parts II and III went down below 1.0 MPa and reached stabilisation after 15 h.

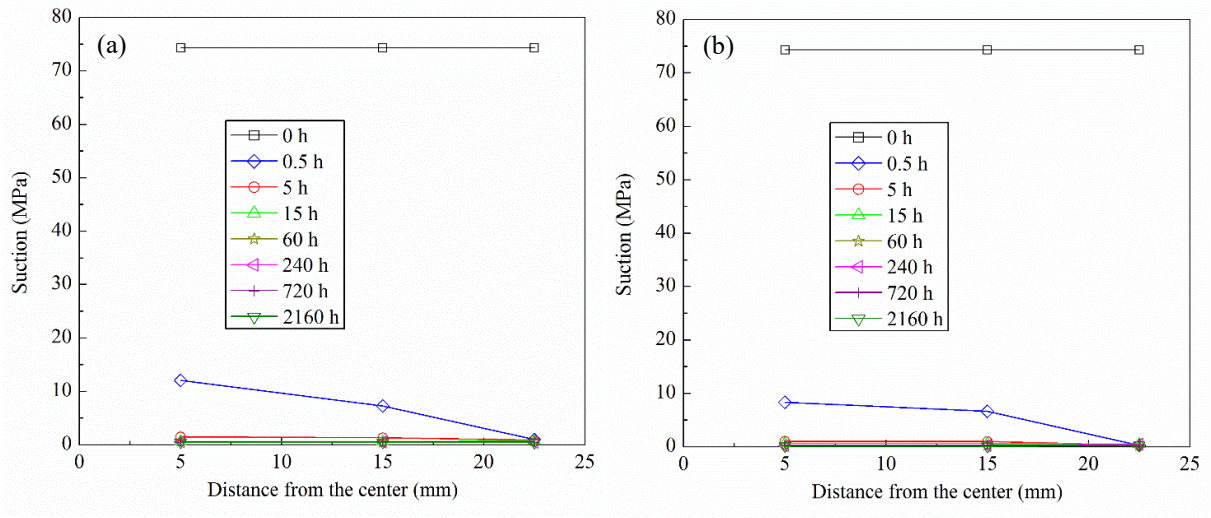

Fig. 11. Suction profiles before and after tests: (a) with 10% voids; (b) with 20% voids

3.4 Microstructure distribution

Figs. 12 and 13 present the pore size distribution of the samples with 10 and 20% voids, respectively, together with that of the as-compacted sample at a dry density of 2.0 Mg/m^3. For

the samples with technological voids, the cumulative curves of part I at a longer time lied below those at a shorter time while the cumulative curves of parts II and III at a longer time lied above those at a shorter time (Figs. 12 and 13). A comparison between different parts showed that the total cumulative curves along the y-axis were distributed in the following order: parts I, II and III, the same order as the increasing dry density. Moreover, the difference between different parts decreased with time. For all the curves, it could be observed that the final value of intruded mercury volume was lower than the soil void ratio. This phenomenon was due to the limited range of the pressure applied in the MIP tests. Some pores with a size smaller than 0.006 μm or larger than 350 μm could not be determined and they were termed as 'inaccessible-pores' in further analysis.

Regarding the density function curves, a typical bimodal porosity for the as-compacted sample with a dry density of 2.0 Mg/m^3 was observed: inter-aggregate pores with a mean pore size of 5 μm and intra-aggregate pores with a mean pore size of 0.02 μm. After hydration, in addition to the two main populations for the as-compacted sample, a new pore population ranging from 0.04 to 2 μm was formed (Figs. 12 and 13). Following the suggestion of Wang et al. (2014) and Bian et al. (2019b), four pore populations were defined: inaccessible-pores (< 0.006 μm and > 350 μm), small-pores (0.006-0.04 μm), medium-pores (0.04-2 μm) and large-pores (2-350 μm). Over time, the medium-pore size of part I decreased, whereas those of parts II and III increased. The large-pore size of part I decreased, while those of parts II and III increased during the first 5 h of hydration and then decreased slightly after 15 h. Consequently, the microstructure of parts I, II and III approached a relatively uniform state. Additionally, the void ratio of each pore population at different times was calculated and the variations of the void ratios corresponding to the four pore populations with time are shown in Figs. 14 and 15. For the samples with technological voids, the large-pore and medium-pore void ratios of part I decreased with time after an initial strong increase, while the inaccessible-pore void ratio increased slightly, without significant changes in small-pore void ratio. For parts II and III, the medium-pore and inaccessible-pore void ratios increased with hydration time while the small-pore void ratio decreased. The larger-pore void ratio of parts II and III increased during the first 5 h of hydration and then started to decrease after 15 h. A comparison between the different parts showed that larger inaccessible-pore, medium-pore and large-pore void ratios and a lower small-pore void ratio were observed for part I, which included initial technological voids.

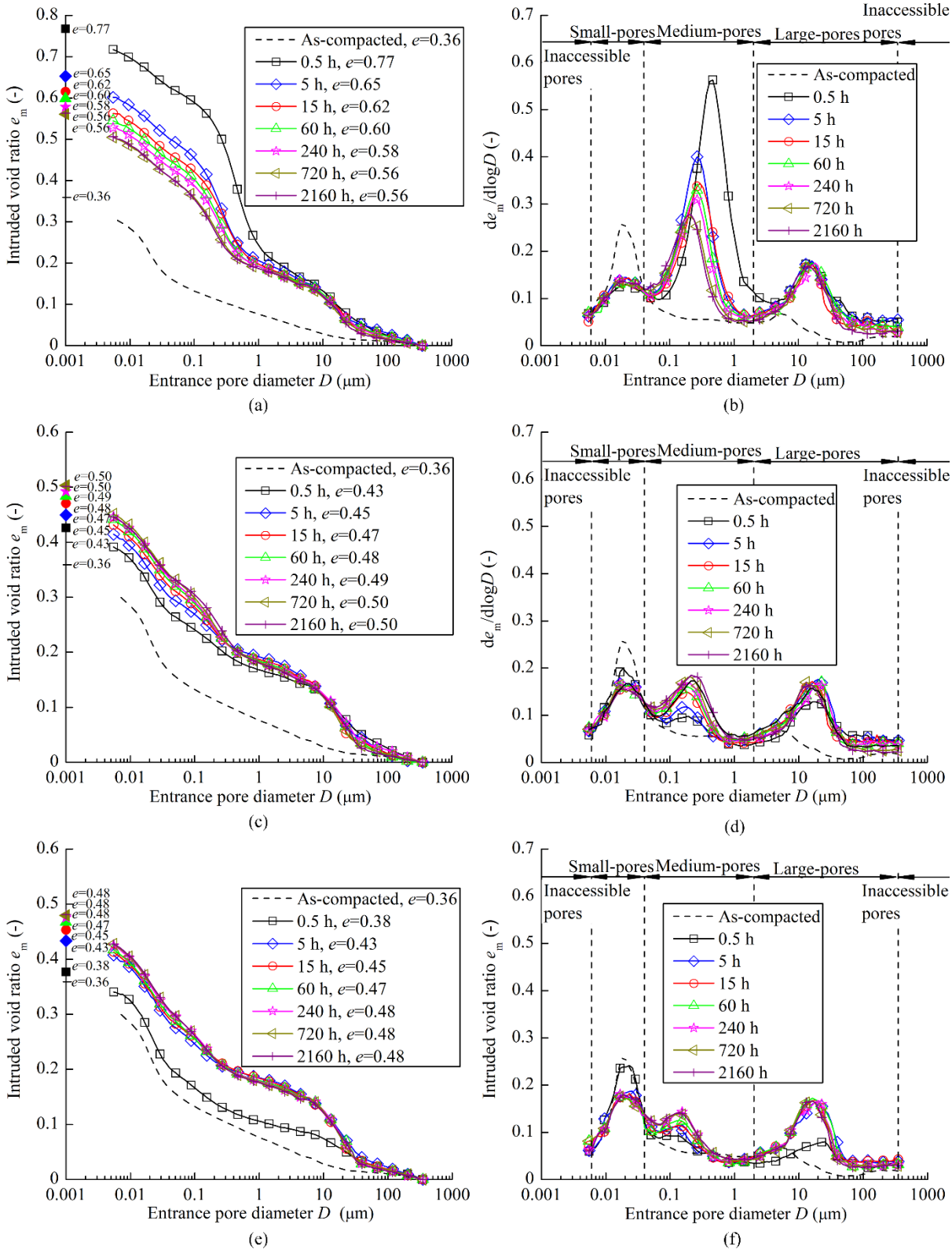

Fig. 12. Pore size distribution of different parts for the samples with 10% voids: (a) cumulative curves of part I; (b) density function curves of part I; (c) cumulative curves of part II; (d) density function curves of part II; (e) cumulative curves of part III; (f) density function curves of part III

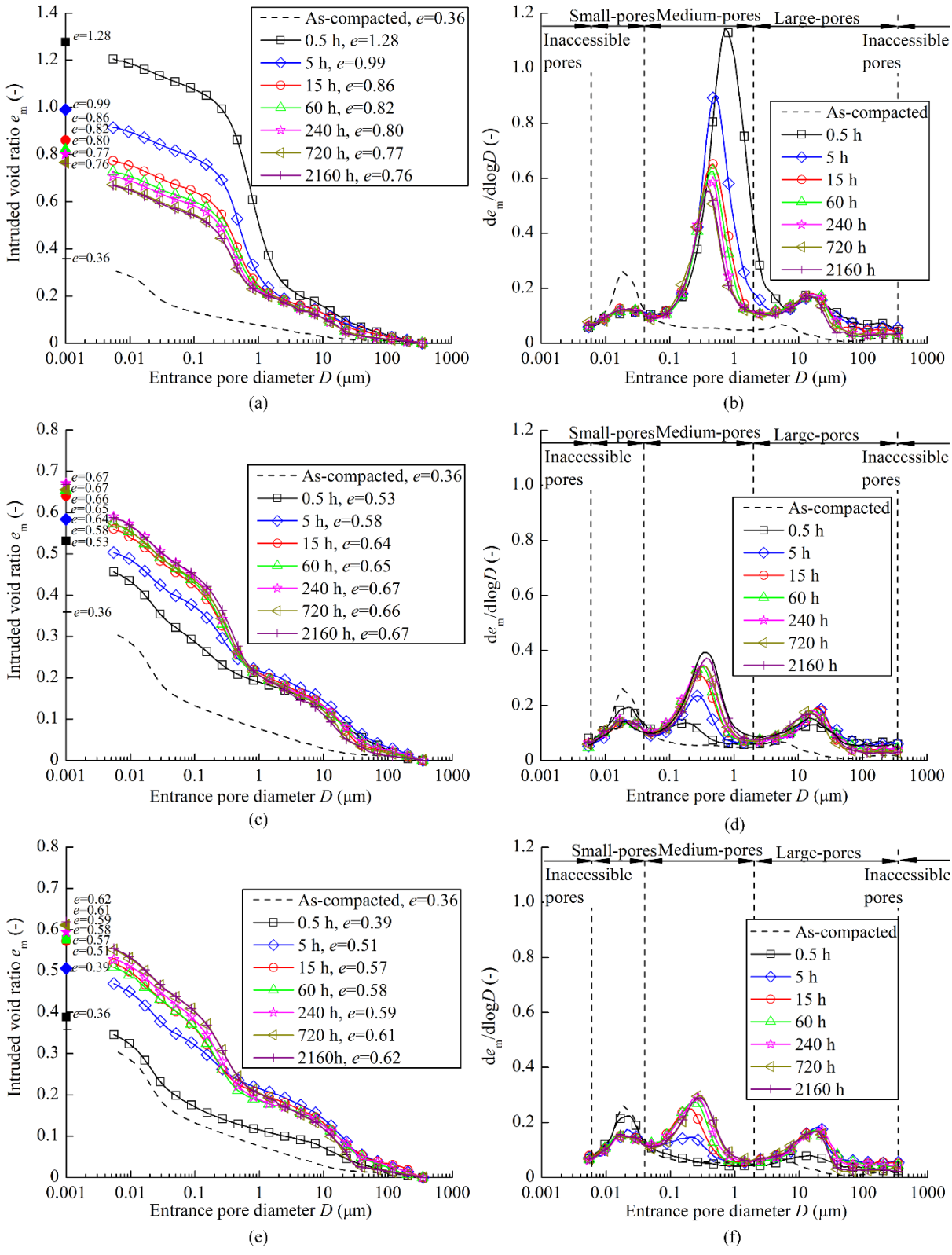

Fig. 13. Pore size distribution of different parts for the samples with 20% voids: (a) cumulative curves of part I; (b) density function curves of part I; (c) cumulative curves of part II; (d) density function curves of part II; (e) cumulative curves of part III; (f) density function curves of part III

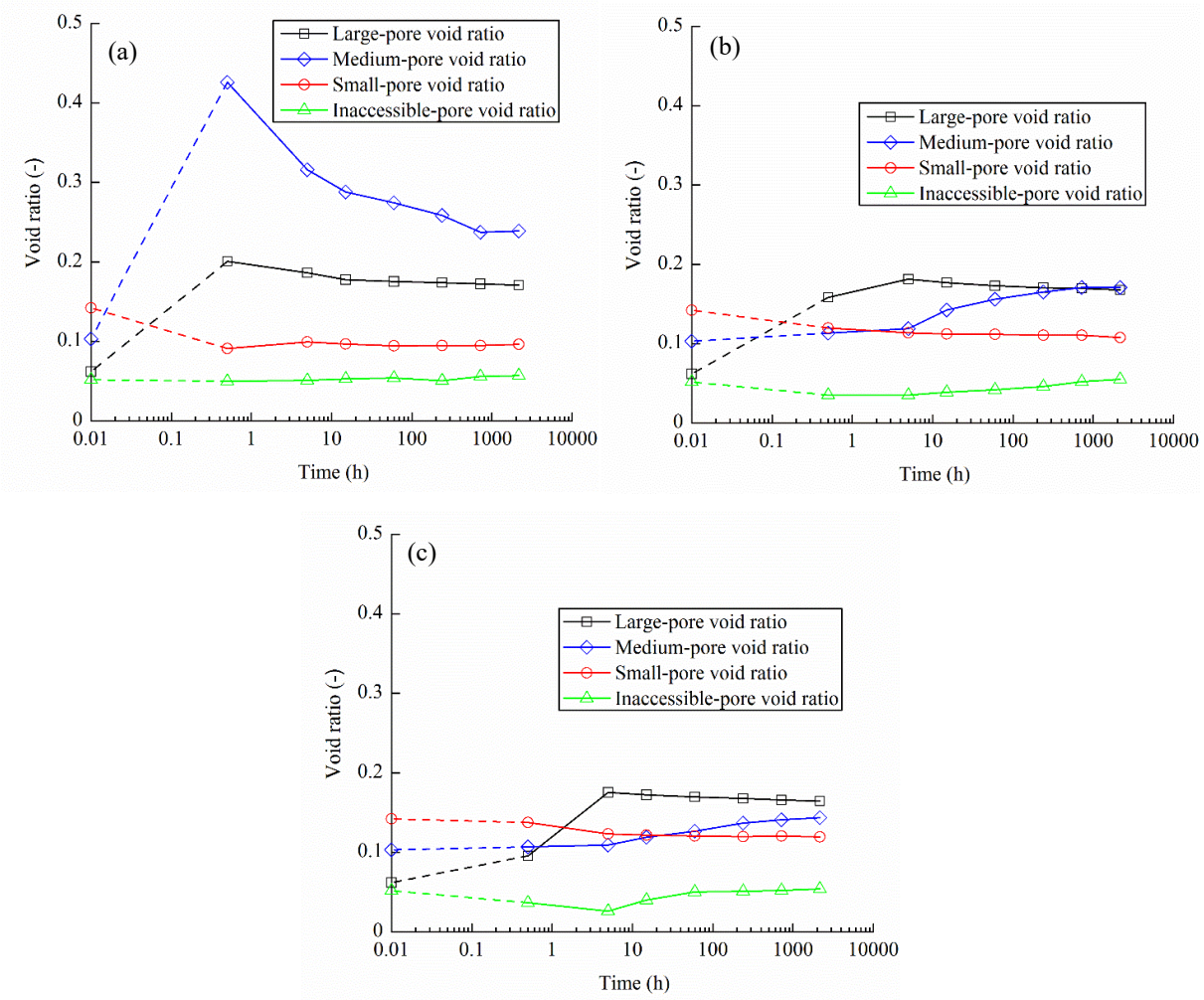

Fig. 14. Changes in inaccessible-pore, small-pore, medium-pore and large-pore void ratios with time for the samples with 10% voids: (a) part I; (b) part II; (c) part III

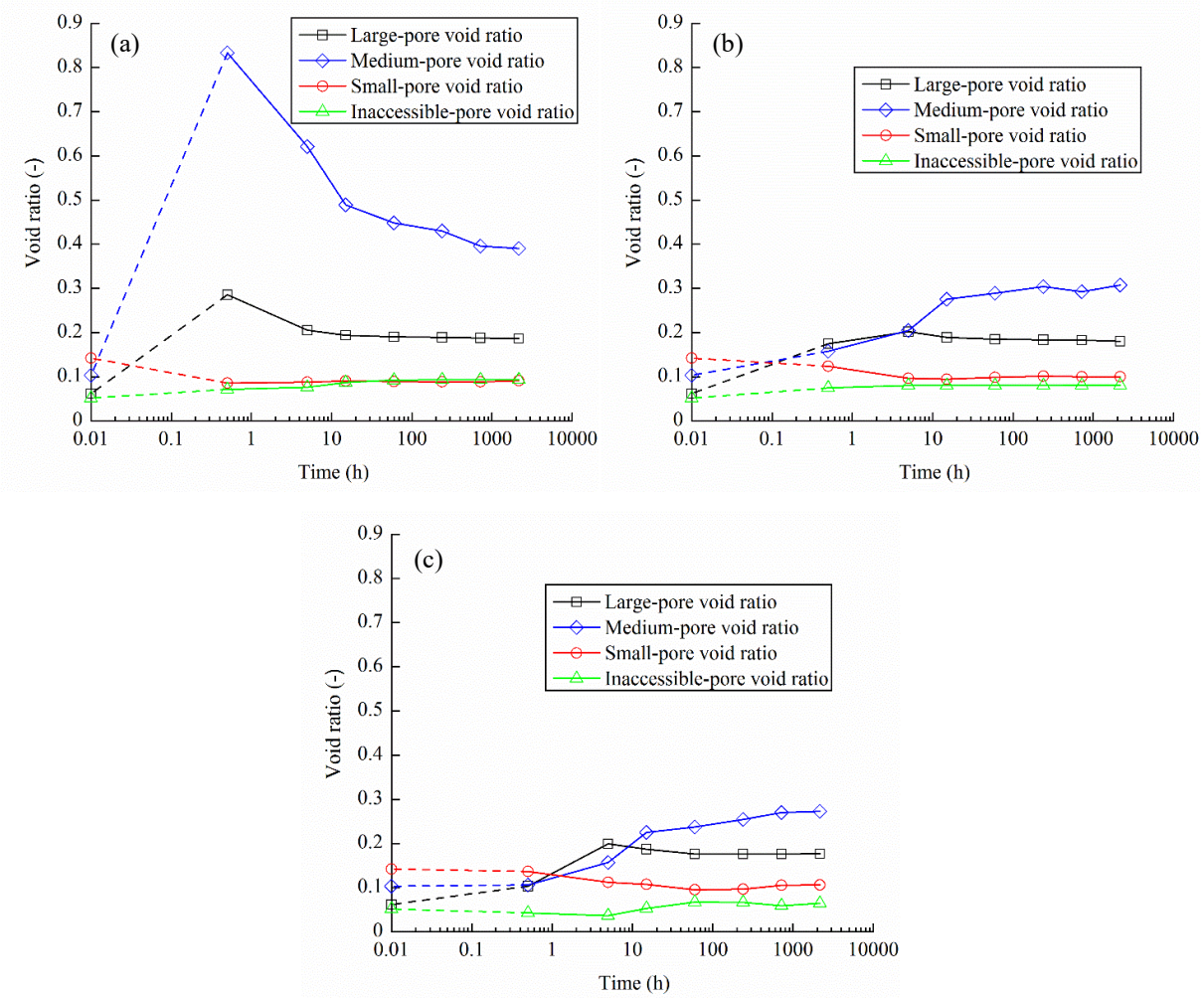

Fig. 15. Changes in inaccessible-pore, small-pore, medium-pore and large-pore void ratios with time for the samples with 20% voids: (a) part I; (b) part II; (c) part III

4 Discussions

4.1 Swelling behaviour of samples with technological voids

As shown in Fig. 6b and c, the radial swelling pressure of the samples with technological voids started to increase after a certain time. This phenomenon implied two stages during the hydration of samples with voids: a filling stage corresponding to the filling up of initial voids by the swollen soil, leading to heterogeneous distributions of water content and dry density; and a homogenization stage corresponding to the decreasing water content and dry density gradients, which allowed the samples to approach a relatively homogeneous state. As noted earlier, the filling stage lasted 0.08 and 0.18 h for the samples with 10 and 20% voids, respectively. After that, the samples could be divided into two zones: compression and swelling zones based on the dry density distribution (Bian et al., 2019b). In this study, parts II and III corresponded to the swelling zone which would undergo further swelling, resulting in a decrease of dry density, whereas part I including the initial voids corresponded to the

compression zone, which would be subjected to compression, leading to an increase of dry density over time. Consequently, the dry density of three parts gradually reached the expected final state over time. For the samples with larger technological voids, a lower swelling pressure was generated and thus a lower homogenization rate was observed (Fig. 9).

4.2 Microstructural mechanism

4.2.1 Compression zone

At the filling stage, the soils adjacent to the voids swelled with a rapid decrease in suction from 74.3 MPa to below 1.0 MPa (Fig. 11). Water molecules were expected to progressively placed on the clay surface, layer by layer up to four layers, with an increase in the inter-layer space, which was inaccessible by the MIP observation (Saiyouri et al., 1998; 2000). During this process, the clay particles could exfoliate upon saturation and form a gel, progressively filling the inter-aggregate pores with a decrease in pore volume (Bian et al., 2020). Moreover, clay aggregates would be divided into thinner particles as the suction was lower than 9.0 MPa, leading to an increase in the intra-aggregate pore size (Cui et al., 2002; Wang et al., 2013b). With the transformations of inter-aggregate and intra-aggregate pores into the medium-pore population, a significant increase in the medium-pore void ratio was observed. Additionally, fissure-like 2-dmensional (2D) pores with a mean pore size of 20 μm appeared, explaining the increased void ratio of large pores (Wang et al., 2014; Zeng et al., 2016). At the homogenization stage, the large pores and medium pores of the compression zone were compressed gradually by the swelling pressure, leading to decreases in large-pore and medium-pore void ratios.

4.2.2 Swelling zone

At the filling stage, the soils inside the compacted block were subjected to slower hydration due to the larger radial distance to the hydration front, as compared to those in the external part, with gradual increases in large-pore and medium-pore void ratios and a decrease in small-pore void ratio. After the filling stage, the water gradually infiltrated into the swelling zone (parts II and III) and the suction of the swelling zone decreased to 1.0-1.5 MPa at 5 h (Fig. 11). The large-pore and medium-pore void ratios increased and the small-pore void ratio decreased significantly due to the further radial swelling of compacted block, especially for the samples with 20% voids, which explained the peak occurrence of axial swelling pressure (Fig. 5c). While reaching saturation at 15 h with suction approaching zero, the soils exhibited a slow swelling, with a slight decrease in dry density. Over time, increases in the medium-pore and inaccessible-pore void ratios and decreases in the large-pore and small-pore void ratios were

observed. This phenomenon could be explained by the water redistribution in the soil (Delage et al., 2006; Ye et al., 2013; Wang et al., 2014). The inter-aggregate pores were first filled due to their high permeability, but the water filling the inter-aggregate pores was not necessarily in equilibrium with that inside the aggregates in terms of water potential (Alonso et al., 2011; Wang et al., 2014). Over time, this water in the inter-aggregate pores was driven to the intra-aggregate pores, leading to further sub-division of the clay particles and filling up of large pores by clay exfoliation. Obviously, this process was soil dry density dependent (Wang et al., 2014). More pronounced microstructure changes after saturation occurred in the swelling zone of the samples with 20% technological voids (Fig. 15).

4.3 Axial and radial swelling pressures

The relationships between the final axial and radial swelling pressures after 2160 h of hydration and the expected final dry density for the samples with and without technological voids are shown in Fig. 16. From Fig. 16a, it appears that there was a unique relationship between the axial swelling pressure (P_a in MPa) and the dry density (ρ_d in Mg/m^3) for the samples without voids:

$$P_a=a_1\exp^{b_1\rho_d}=2.591\times10^{-5}\exp^{6.117\rho_d} \quad (1)$$

where a_1 and b_1 are the fitting parameters. For the samples with 10 and 20% voids, the final axial swelling pressures were 1.63 and 0.53 MPa, respectively, which were slightly larger than those of samples without voids (1.62 and 0.45 MPa for the samples at dry densities of 1.8 and 1.6 Mg/m^3). The higher axial swelling pressure for the sample with voids could be attributed to its significantly heterogeneous distribution of dry density (Fig. 9). According to the cell design, the axial force of samples is transmitted to the piston and then the force transducer (Saba et al., 2014c). Thereby, the measured axial swelling pressure corresponded to the global pressure at the top of samples. From Eq. (1), the axial swelling pressures of parts I, II and III could be estimated and the global axial swelling pressure of samples with voids ($P_{a\text{-void}}$) can be approximated by the arithmetic mean value of three parts, as follows:

$$P_{a\text{-void}}=\frac{A_1P_{a1}+A_2P_{a2}+A_3P_{a3}}{A}=\frac{A_1a_1\exp^{b_1\rho_{d1}}+A_2a_1\exp^{b_1\rho_{d2}}+A_3a_1\exp^{b_1\rho_{d3}}}{A} \quad (2)$$

where P_{a1}, P_{a2} and P_{a3} are the axial swelling pressures of parts I, II and III; ρ_{d1}, ρ_{d2} and ρ_{d3} are the dry densities of parts I, II and III; A_1, A_2 and A_3 are the cross-sectional areas of parts I, II and III, respectively; A is the total cross-sectional area of the samples, equal to the sum of A_1, A_2 and A_3. The relationship between the expected final dry density ($\rho_{d\text{-exp}}$) and the dry densities of the three parts is described using the following expression:

$$\rho_{\text{d-exp}}=\frac{A_1\rho_{\text{d1}}+A_2\rho_{\text{d2}}+A_3\rho_{\text{d3}}}{A} \tag{3}$$

By substituting Eq. (3) into Eq. (2), $P_{\text{a-void}}$ can be rewritten as a function of two variables: ρ_{d1} and ρ_{d2}, as follows:

$$P_{\text{a-void}}=a_1\frac{A_1\exp^{b_1\rho_{\text{d1}}}+A_2\exp^{b_1\rho_{\text{d2}}}+A_3\exp^{b_1(A\rho_{\text{d-exp}}-A_1\rho_{\text{d1}}-A_2\rho_{\text{d2}})/A_3}}{A} \tag{4}$$

To find the critical points of $P_{\text{a-void}}$, the first- and second-order partial derivatives $\partial P_{\text{a-void}}/\partial\rho_{\text{d1}}$, $\partial P_{\text{a-void}}/\partial\rho_{\text{d2}}$, $\partial^2 P_{\text{a-void}}/\partial\rho^2_{\text{d1}}$, $\partial^2 P_{\text{a-void}}/\partial\rho^2_{\text{d1}}$ and $\partial^2 P_{\text{a-void}}/(\partial\rho_{\text{d1}}\partial\rho_{\text{d2}})$ are calculated:

$$\frac{\partial P_{\text{a-void}}}{\partial\rho_{\text{d1}}}=\frac{a_1b_1A_1\exp^{b_1\rho_{\text{d1}}}}{A}-\frac{a_1b_1A_1\exp^{b_1(A\rho_{\text{d-exp}}-A_1\rho_{\text{d1}}-A_2\rho_{\text{d2}})/A_3}}{A} \tag{5}$$

$$\frac{\partial P_{\text{a-void}}}{\partial\rho_{\text{d2}}}=\frac{a_1b_1A_2\exp^{b_1\rho_{\text{d2}}}}{A}-\frac{a_1b_1A_2\exp^{b_1(A\rho_{\text{d-exp}}-A_1\rho_{\text{d1}}-A_2\rho_{\text{d2}})/A_3}}{A} \tag{6}$$

$$\frac{\partial^2 P_{\text{a-void}}}{\partial\rho^2_{\text{d1}}}=\frac{a_1b_1^2A_1\exp^{b_1\rho_{\text{d1}}}}{A}+\frac{a_1b_1^2A_1^2\exp^{b_1(A\rho_{\text{d-exp}}-A_1\rho_{\text{d1}}-A_2\rho_{\text{d2}})/A_3}}{AA_3} \tag{7}$$

$$\frac{\partial^2 P_{\text{a-void}}}{\partial\rho^2_{\text{d2}}}=\frac{a_1b_1^2A_2\exp^{b_1\rho_{\text{d2}}}}{A}+\frac{a_1b_1^2A_2^2\exp^{b_1(A\rho_{\text{d-exp}}-A_1\rho_{\text{d1}}-A_2\rho_{\text{d2}})/A_3}}{AA_3} \tag{8}$$

$$\frac{\partial^2 P_{\text{a-void}}}{\partial\rho_{\text{d1}}\partial\rho_{\text{d2}}}=\frac{a_1b_1^2A_1A_2\exp^{b_1(A\rho_{\text{d-exp}}-A_1\rho_{\text{d1}}-A_2\rho_{\text{d2}})/A_3}}{AA_3} \tag{9}$$

Setting both $\partial P_{\text{a-void}}/\partial\rho_{\text{d1}}$ and $\partial P_{\text{a-void}}/\partial\rho_{\text{d2}}$ equal to zero yields:

$$\begin{cases}\dfrac{\partial P_{\text{a-void}}}{\partial\rho_{\text{d1}}}=\dfrac{a_1b_1A_1\exp^{b_1\rho_{\text{d1}}}}{A}-\dfrac{a_1b_1A_1\exp^{b_1(A\rho_{\text{d-exp}}-A_1\rho_{\text{d1}}-A_2\rho_{\text{d2}})/A_3}}{A}=0\\ \dfrac{\partial P_{\text{a-void}}}{\partial\rho_{\text{d2}}}=\dfrac{a_1b_1A_2\exp^{b_1\rho_{\text{d2}}}}{A}-\dfrac{a_1b_1A_2\exp^{b_1(A\rho_{\text{d-exp}}-A_1\rho_{\text{d1}}-A_2\rho_{\text{d2}})/A_3}}{A}=0\end{cases} \tag{10}$$

In Eq. (10), $\rho_{\text{d1}}=\rho_{\text{d-exp}}$ and $\rho_{\text{d2}}=\rho_{\text{d-exp}}$; thus, $(\rho_{\text{d-exp}}, \rho_{\text{d-exp}})$ is a critical point of $P_{\text{a-void}}$.

$$\left[\frac{\partial^2 P_{\text{a-void}}}{\partial\rho^2_{\text{d1}}}(\rho_{\text{d-exp}},\rho_{\text{d-exp}})\right]\left[\frac{\partial^2 P_{\text{a-void}}}{\partial\rho^2_{\text{d2}}}(\rho_{\text{d-exp}},\rho_{\text{d-exp}})\right]-\left[\frac{\partial^2 P_{\text{a-void}}}{\partial\rho_{\text{d1}}\partial\rho_{\text{d2}}}(\rho_{\text{d-exp}},\rho_{\text{d-exp}})\right]^2$$

$$=\frac{A_1A_2}{AA_3}a_1^2b_1^4\exp^{2b_1\rho_{\text{d-exp}}}>0 \tag{11}$$

and

$$\frac{\partial^2 P_{\text{a-void}}}{\partial\rho^2_{\text{d1}}}(\rho_{\text{d-exp}},\rho_{\text{d-exp}})=\frac{A_1(A_1+A_3)}{AA_3}a_1b_1^2\exp^{b_1\rho_{\text{d-exp}}}>0 \tag{12}$$

Therefore, the function $P_{\text{a-void}}$ has a local minimum at $(\rho_{\text{d-exp}}, \rho_{\text{d-exp}})$ and the local minimum value is $a_1\exp^{b_1\rho_{\text{d-exp}}}$. This means that the global axial swelling pressures of heterogeneous samples are larger than those of homogeneous samples when ρ_{d1}, ρ_{d2} and ρ_{d3} are not equal to $\rho_{\text{d-exp}}$. Moreover, the greater the difference between ρ_{d1}, ρ_{d2}, ρ_{d3} and $\rho_{\text{d-exp}}$, the larger the difference

between the axial swelling pressures of samples with and without voids. This explains the significant difference between the measured axial swelling pressures of the sample with 20% voids and that without voids at the same expected final dry density of 1.6 Mg/m^3.

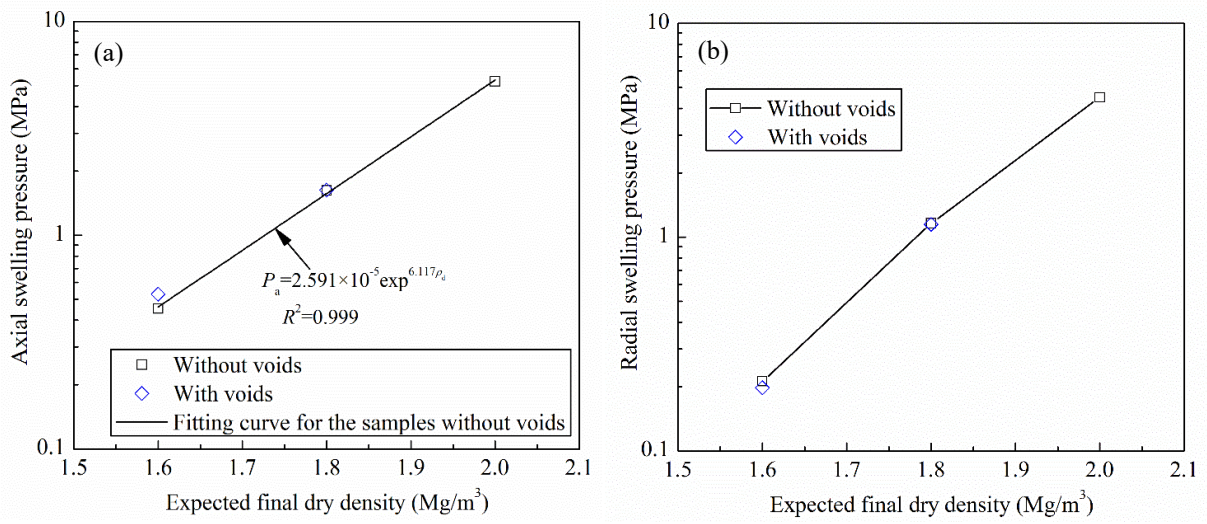

Fig. 16. Relationship between the final swelling pressures and final dry density: (a) axial swelling pressure; (b) radial swelling pressure

Note that the above analytical analysis about the effect of heterogeneity on the axial swelling pressure was preliminary because of the difficulties in the continuous measurement of dry density along the radial direction. Eq. (2) can underestimate the difference of axial swelling pressures between the samples with and without voids, because the dry density distribution of each part was similarly heterogeneous. Based on the measured mean dry densities of parts I, II and III after 2160 h of hydration, the axial swelling pressures of samples with 10 and 20% voids were estimated at 1.58 and 0.50 MPa, respectively. By contrast, the axial swelling pressures of samples without voids at dry densities of 1.8 and 1.6 Mg/m^3 were estimated at 1.57 and 0.46 MPa, respectively. The estimated differences of axial swelling pressures between samples with and without voids are lower than the measured ones, especially for the sample with an expected final dry density of 1.6 Mg/m^3.

As far as the final radial swelling pressure was concerned, a much lower swelling pressure was measured in the radial direction than that in the axial direction, as displayed in Fig. 16b. This aeolotropic behaviour of compacted block could be ascribed to the sample preparation method (Lee et al., 2012; Saba et al., 2014a; Jia et al., 2019). During the uniaxial compaction, the aggregates tended to orientate perpendicular to the compaction direction. Thus, a larger swelling pressure could be expected in the axial direction upon hydration. From Fig. 16b, it could also be observed that the samples with technological voids exhibited a lower radial

swelling pressure than that of the samples without voids, even though the expected final dry density was the same, especially for the sample with 20% voids. For the samples with technological voids, the radial sensor directly measured the local radial pressure of part I (Fig. 2), which corresponded to the initial voids and had a lower dry density than the expected final one (Fig. 9). Additionally, at the heterogeneous stage, the radial swelling of the swelling zone (parts II and III) could be restrained by the friction stress between the filter papers and top and bottom surfaces of samples, resulting in a lower radial pressure sensed at the lateral surface of the samples. These explained why a slightly lower radial swelling pressure was observed for the samples with technological voids.

4.4 Hydraulic conductivity

In addition to the swelling pressure, the hydraulic conductivity is also a key parameter in the design and development of the sealing/backfilling materials. The measured hydraulic conductivities at 2160 h are plotted versus the expected final dry density for all the samples in Fig. 17. In a standard fashion, the hydraulic conductivity of the samples without voids decreased with the increase of dry density and the following relationship between the hydraulic conductivity (k_w in m/s) and the dry density (ρ_d in Mg/m^3) could be derived:

$$k_w=a_2\exp^{b_2\rho_d}=6.761\times10^{-7}\exp^{-6.995\rho_d} \quad (13)$$

where a_2 and b_2 are the fitting parameters. Note that the hydraulic conductivity of samples without voids reached stabilisation after 2160 h of hydration, even though it gradually decreased with time during the first several hundred hours, as reported by Zhu et al. (2013). As mentioned above, the hydraulic conductivity of the samples with technological voids decreased with time and approached that of the samples without voids. This was because part I had a lower dry density, acting as possible preferential flow pathway and facilitated water transfer around the samples and a higher hydraulic conductivity was measured for the samples with technological voids than those without technological voids, at the same expected final dry density. After 2160 h of hydration, the measured hydraulic conductivities of samples with and without initial voids were quite close (Fig. 17). However, owing to the friction between the filter papers and sample, the heterogeneous distribution of dry density could be persistent in the long term (Zeng et al., 2020b) and the hydraulic conductivity could not decrease below that of the samples without voids.

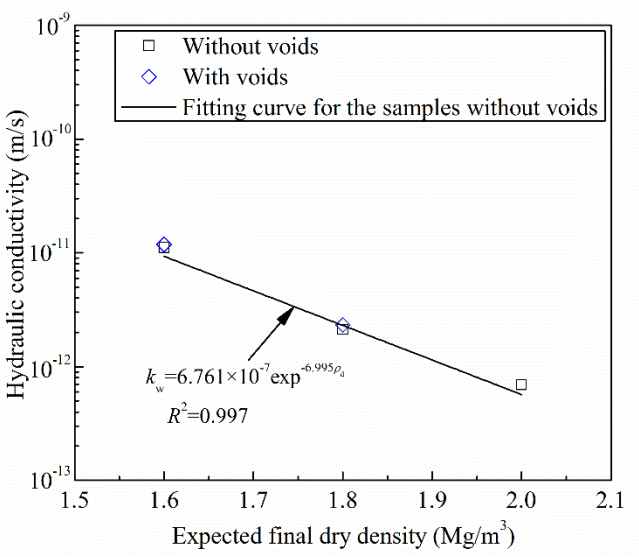

Fig. 17. Relationship between the final hydraulic conductivity and expected final dry density

5 Conclusions

Infiltration tests at different hydration times were performed on compacted bentonite/claystone mixture with various technological voids. The evolutions of axial and radial swelling pressures and hydraulic conductivity with time were investigated, together with the determination of the variations of water content, dry density, suction and microstructure feature at different positions. The results obtained allow the following conclusions to be drawn.

The filling of technological voids led to a sharp decrease in the dry density of soil close to the initial voids and a relatively slow decrease in that far from the voids. After that, a compression zone and a swelling zones could be identified: (i) the compression zone was characterized by a lower dry density than the expected final one; (ii) the swelling zone was represented by a higher dry density than the expected final one. Over time, the soil in the swelling zone underwent further swelling, while that in the compression zone was compressed by the swelling pressure, resulting in a decrease of dry density gradient.

In the compression zone, the global void ratio increased significantly after swelling at the filling stage, with increases in large-pore, medium-pore and inaccessible-pore void ratios but a decrease in small-pore void ratio. Over time, the large and medium pores were compressed by almost constant swelling pressure. By contrast, the volume of large pores of the swelling zone increased until the suction decreased to below 1 MPa and then it decreased from 15 h to 2160 h owing to the water redistribution in the soil. These processes resulted in a relatively uniform microstructure distribution.

After 2160 h of hydration, the water content and dry density distributions of samples with technological voids still remained heterogeneous. Due to this heterogeneity, the samples with initial voids exhibited slightly larger axial swelling pressure and hydraulic conductivity than those without voids at the same expected final dry density; on the contrary, their radial swelling pressure was slightly lower than that of the samples without voids.

Acknowledgments

The authors thank the China Scholarship Council (CSC). The supports provided by Ecole des Ponts ParisTech and the French National Radioactive Waste Management Agency (Andra) are also greatly acknowledged.

References

Alonso, E.E., Romero, E. & Hoffmann, C. (2011). Hydromechanical behaviour of compacted granular expansive mixtures: experimental and constitutive study. Géotechnique 61, No. 4, 329-344.

Bian, X., Cui, Y.J., Zeng, L.L. & Li, X.Z. (2019a). Swelling behavior of compacted bentonite with the presence of rock fracture. Engineering Geology 254, 25-33.

Bian, X., Cui, Y.J. & Li, X.Z. (2019b). Voids effect on the swelling behaviour of compacted bentonite. Géotechnique 69, No. 7, 593-605.

Bian, X., Cui, Y.J., Zeng, L.L. & Li, X.Z. (2020). State of compacted bentonite inside a fractured granite cylinder after infiltration. Applied Clay Science. doi: 10.1016/j.clay.2020.105438

Castellanos, E., Villar, M.V., Romero, E., Lloret, A. & Gens, A. (2008). Chemical impact on the hydro-mechanical behaviour of high-density FEBEX bentonite. Physics and Chemistry of the Earth, Parts A/B/C 33, S516-S526.

Cui, Y. J., Loiseau, C. & Delage, P. (2002). Microstructure changes of a confined swelling soil due to suction controlled hydration. In Unsaturated soils: proceedings of the 3rd international conference on unsaturated soils, UNSAT 2002 (eds J. F. T. Juca, T. M. P. de Campos and F. A. M. Marinho), vol. 2, pp. 593–598. Lisse, the Netherlands: Balkema.

Cuisinier, O., Masrouri, F., Pelletier, M., Villieras, F. & MosserRuck, R. (2008). Microstructure of a compacted soil submitted to an alkaline plume. Appl. Clay Sci. 40, No. 1–4, 159–170.

Delage, P., Marcial, D., Cui, Y.J. & Ruiz, X. (2006). Ageing effects in a compacted bentonite: a microstructure approach. Géotechnique 56, No. 5, 291-304.

Fouché, O., Wright, H., Le Cléac'h, J.M. & Pellenard, P. (2004). Fabric control on strain and rupture of heterogeneous shale samples by using a non-conventional mechanical test.

Applied Clay Science 26, No. 1-4, 367-387.

Gatabin, C., Talandier, J., Collin, F., Charlier, R. & Dieudonné, A.C. (2016). Competing effects of volume change and water uptake on the water retention behaviour of a compacted MX-80 bentonite/sand mixture. Applied Clay Science 121, 57-62.

Gens, A., Vállejan, B., Sánchez, M., Imbert, C., Villar, M. V. & Van Geetl, M. (2011). Hydromechanical behaviour of a heterogeneous compacted soil: experimental observations and modelling. Géotechnique 61, No. 5, 367-386.

Jia, L.Y., Chen, Y.G., Ye, W.M. & Cui, Y.J. (2019). Effects of a simulated gap on anisotropic swelling pressure of compacted GMZ bentonite. Engineering Geology 248, 155-163.

Kiviranta, L. & Kumpulainen, S. (2011). Quality control and characterization of bentonite materials, Posiva Working Report 2011-84. Olkiluoto, Eurajoki, Finland: Posiva Oy. See https://www.posiva.fi/files/1994/WR_2011-84_web.pdf

Lee, J.O., Lim, J.G., Kang, I.M. & Kwon, S. (2012). Swelling pressures of compacted Ca-bentonite. Engineering Geology 129, 20-26.

Martin, P.L., Barcala, J.M. & Huertas, F. (2006). Large-scale and long-term coupled thermo-hydro-mechanic experiments with bentonite: the FEBEX mock-up test. J. Iberian Geol. 32, No. 2, 259-282

Mokni, N., Barnichon, J.D., Dick, P. & Nguyen, T.S. (2016). Effect of technological macro voids on the performance of compacted bentonite/sand seals for deep geological repositories. International Journal of Rock Mechanics and Mining Sciences 88, 87-97.

Saba, S., Delage, P., Lenoir, N., Cui, Y.J., Tang, A.M. & Barnichon, J.D. (2014a). Further insight into the microstructure of compacted bentonite–sand mixture. Engineering geology 168, 141-148.

Saba, S., Barnichon, J.D., Cui, Y.J., Tang, A.M. & Delage, P. (2014b). Microstructure and anisotropic swelling behaviour of compacted bentonite/sand mixture. Journal of Rock Mechanics and Geotechnical Engineering 6, No. 2, 126-132.

Saba, S., Cui, Y.J., Tang, A.M. & Barnichon, J.D. (2014c). Investigation of the swelling behaviour of compacted bentonite–sand mixture by mock-up tests. Canadian Geotechnical Journal 51, No. 12, 1399-1412.

Saiyouri, N., Hicher, P. & Tessier, D. (1998). Microstructural analysis of highly compacted clay swelling. In Proceedings of the 2nd international conference on unsaturated soils, vol. 1, pp. 119–124. Beijing, China: International Academic Publisher.

Saiyouri, N., Hicher, P.Y. & Tessier, D. (2000). Microstructural approach and transfer water modelling in highly compacted unsaturated swelling clays. Mechanics of Cohesive-frictional Materials: An International Journal on Experiments, Modelling and Computation of Materials and Structures 5, No. 1, 41-60.

Villar, M.V., García-Siñeriz, J.L., Bárcena, I. & Lloret, A. (2005). State of the bentonite barrier

after five years operation of an in situ test simulating a high level radioactive waste repository. Engineering Geology 80, No. 3-4, 175-198.

Villar, M.V. & Lloret, A. (2008). Influence of dry density and water content on the swelling of a compacted bentonite. Applied Clay Science 39, No. 1-2, 38-49.

Wang, Q., Tang, A.M., Cui, Y.J., Delage, P., Barnichon, J.D. & Ye, W.M. (2013a). The effects of technological voids on the hydro-mechanical behaviour of compacted bentonite–sand mixture. Soils and Foundations 53, No. 2, 232-245.

Wang, Q., Cui, Y.J., Tang, A.M., Barnichon, J.D., Saba, S. & Ye, W.M. (2013b). Hydraulic conductivity and microstructure changes of compacted bentonite/sand mixture during hydration. Engineering Geology 164, 67-76.

Wang, Q., Cui, Y.J., Tang, A.M., Li., X.L. & Ye, W.M. (2014). Time-and density-dependent microstructure features of compacted bentonite. Soils and Foundations 54, NO. 4, 657-666.

Ye, W.M., Lai, X.L., Liu, Y., Chen, Y.G. & Cui, Y.J. (2013). Ageing effects on swelling behaviour of compacted GMZ01 bentonite. Nuclear Engineering and Design 265, 262-268.

Zeng, L.L., Cui, Y.J., Conil, N., Zghondi, J., Armand, G. & Talandier, J. (2016). Experimental study on swelling behaviour and microstructure changes of natural stiff Teguline clays upon wetting. Canadian Geotechnical Journal 54, No. 5, 700-709.

Zeng, Z.X., Cui, Y.J., Zhang, F., Conil, N. & Talandier, J. (2019). Investigation of swelling pressure of bentonite/claystone mixture in the full range of bentonite fraction. Applied Clay Science. doi: 10.1016/j.clay.2019.105137.

Zeng, Z.X., Cui, Y.J., Zhang, F., Conil, N. & Talandier, J. (2020a). Effect of technological voids on the swelling behaviour of compacted bentonite/claystone mixture. Canadian Geotechnical Journal. doi: 10.1139/cgj-2019-0339.

Zeng, Z.X., Cui, Y.J, Conil, N. & Talandier J. (2020b). Analysis of boundary friction effect on the homogenization process of compacted bentonite/claystone mixture with technological voids upon hydration. Acta Geotech., in press, https://doi.org/10.1007/s11440-020-01048-x.

Zhu, C.M., Ye, W.M., Chen, Y.G., Chen, B. & Cui, Y.J. (2013). Influence of salt solutions on the swelling pressure and hydraulic conductivity of compacted GMZ01 bentonite. Engineering Geology 166, 74-80.

Zeng, Z.X., Cui, Y.J., Conil, N., Talandier, J. 2021. Acta Geotechnica, 16(2), 525-533.

Analysis of boundary friction effect on the homogenization process of compacted bentonite/claystone mixture with technological voids upon hydration

Zhixiong Zeng[1], Yu-Jun Cui[1], Nathalie Conil[2], Jean Talandier[3]

Abstract: Pre-compacted MX80 bentonite/Callovo-Oxfordian (COx) claystone mixture has been proposed to backfill and seal the underground galleries for radioactive waste disposal in France. While emplacing these pre-compacted blocks, technological voids are created between the blocks and the host rock and among the blocks themselves. It is expected that homogenization process will take place over time for the structure constructed with pre-compacted blocks upon hydration. This study investigated the boundary friction effect on such a process. Results showed that after the filling of technological voids, the soil far from the technological voids would swell further while those near the voids would be compressed under the swelling pressure generated by the soil behind, resulting in an increase of homogeneity in terms of dry density distribution. However, this homogenization process would stop after a certain time. Further examination showed that the homogenization process ended when the maximum boundary friction force became equal to or higher than the vector sum of swelling forces in the radial direction. Based on the force equilibrium and the mass conservation, the final dry density distribution was estimated. Comparison between the estimation and the measurement showed a good agreement, indicating the relevance of the identified mechanism related to boundary friction.

Keywords: bentonite/claystone mixture; technological voids; friction effect; final dry density distribution

1 Introduction

In many countries, compacted bentonite-based materials have been selected to backfill and seal the underground galleries for high-level radioactive waste disposal, thanks to their high swelling characteristic, low permeability and good radionuclides retention capacity (Pusch, 1982; Yong and Boonsinsuk, 1986; Komine and Ogata, 1994; 1999; Sellin and Leupin, 2013). Once the galleries are closed, the pore water from the host rock will infiltrate into the

1 Ecole des Ponts ParisTech, Laboratoire Navier/CERMES, 6 et 8 avenue Blaise Pascal, 77455 Marne La Vallée cedex 2, France
2 Andra, Centre de Meuse/Haute-Marne, RD 960, 55290 Bure, France
3 Andra, 1/7, rue Jean Monnet, 92298 Châtenay-Malabry cedex, France

technological voids existing between the blocks and the host rock and among the blocks themselves, hydrating the compacted blocks from outside (Saba, 2013; Villar and Lloret, 2007; 2008; Wang et al., 2013). The compacted sealing/backfill materials near the technological voids quickly swell, filling up the technological voids, while those far from the technological voids swell slowly. These processes lead to a lower dry density in the external zone and a larger dry density in the inner zone (Bian et al., 2019; Jia et al., 2019; Villar and Lloret, 2008). Under this circumstance, the overall dry density does not fully characterize the hydro-mechanical performance of sealing/backfill materials and the dry density distribution becomes significant factor to be accounted for (Gens et al., 2011; 2018).

The dry density distribution of compacted bentonite-based materials with technological voids is strongly dependent on the hydration time. Bian et al. (2019) studied the variation of dry density distribution of compacted bentonite during the saturation process. They indicated that the soils after the filling of initial voids could be divided into a compression zone in which the dry density of soils was lower than the overall one and a swelling zone with a higher dry density. Over time, the soils in the swelling zone were subjected to further swelling, while the soils in the compression zone were compressed by the swelling pressure from the swelling zone. By means of large-scale testing in a tunnel (FEBEX test), the dry density distributions of compacted bentonite after 5- and 18-year hydrations were compared by Gens et al. (2018) and Villar et al. (2019). They found that the heterogeneous distribution of dry density of compacted bentonite was still persistent after 18 years. Therefore, the question that arises was whether this compacted bentonite with technological voids would reach a homogeneous state in long term.

To address this question, a series of infiltration tests were performed on a compacted MX80 bentonite/Callovo-Oxfordian (COx) claystone mixture with different technological voids and the evolution of dry density distribution was determined. Particular attention was paid to the effect of boundary friction between the samples and porous discs. An analytical method was proposed to estimate the final dry density distribution of samples with technological voids.

2 Materials and methods

A mixture of MX80 bentonite and crushed COx claystone was used, at a proportion of 30/70 in dry mass. This mixture was proposed as a candidate sealing/backfill material by the French National Radioactive Waste Management Agency (Andra). The MX80 bentonite was collected from Wyoming, USA, while the COx claystone was extracted from the Andra Underground

Research Laboratory (URL), in Bure, France. Both the bentonite and claystone were first crushed and passed through 2 mm sieve. The mean particle size D_{50} of bentonite and claystone fragments are 0.55 and 0.58 mm, respectively (Fig. 1). The basic physical and mineralogical properties of the bentonite and claystone are listed in Table 1. The bentonite has a hygroscopic water content of 11.4%, a liquid limit of 494%, a plastic limit of 46% and a specific gravity of 2.76. The claystone is characterized by a hygroscopic water content of 6.1%, a liquid limit of 41%, a plastic limit of 24% and a specific gravity of 2.70. Mineralogy analysis showed that the main minerals of bentonite and claystone are montmorillonite (86%) and interstratified illite/smectite (40-45%), respectively.

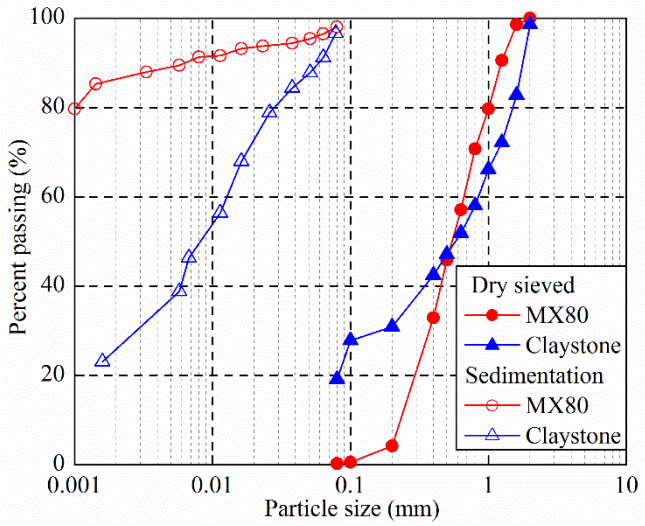

Fig. 1. Grain size distributions of MX80 bentonite and crushed COx claystone

Table 1. Physical and mineralogical properties of MX80 bentonite and COx claystone

Soil property	MX80 bentonite	COx claystone
Specific gravity	2.76	2.70
Liquid limit (%)	494	41
Plastic limit (%)	46	24
Plasticity index (%)	448	17
Main minerals	Montmorillonite (86%)	Interstratified illite/smectite (40-45%)[a]
	Quartz (7%)	Carbonates (30%)[a]

[a] Fouché et al. (2004)

The bentonite was firstly mixed thoroughly with claystone, at initial water contents. The water content of the obtained mixture was 7.7%. Afterwards, the mixture was statically compacted in a rigid mould of 50 mm inner diameter. The target thickness of the compacted disks was 10 mm and the dry density ranged from 1600 to 2000 kg/m^3 (Table 2). To study the effect of technological voids, fourteen disks with a dry density of 2000 kg/m^3 were compacted and trimmed into different diameters of 47.43 mm (tests T01-07) and 44.72 mm (tests T08-14).

Subsequently, they were placed between two metallic porous discs and filter papers, and then positioned at the center of the testing cell of 50 mm inner diameter (Fig. 2). The gaps between the sample and the cell wall (Fig. 3a) corresponded to 10% and 20% of the total volume for samples T01-07 and T08-14, respectively. The corresponding overall final dry densities are 1800 and 1600 kg/m^3, respectively. On the top, the piston was blocked by a screw to prevent axial displacement. Afterwards, the samples were hydrated from the bottom of the cell with synthetic water, which has the same chemical composition as the pore water in the host rock in Bure (see Table 3 for the recipe of preparation). A force transducer was placed under the bottom of the cell and a radial pressure sensor (0.006 m in diameter) was mounted at the cell, allowing the axial force and the radial pressure to be measured, respectively. For each case, seven identical samples were hydrated for 0.5, 5, 15, 60, 240, 720 and 2160 h to investigate the evolution of dry density distribution. The samples after the prescribed hydration times were extracted from the cell and divided into three parts (I, II and III), as shown in Fig. 3b. Each part was cut into small pieces for the dry density measurement based on the fluid displacement technique using a non-aromatic hydrocarbon fluid (Kerdane) (Delage et al., 2008) and a mean value was considered in further analysis. For comparison, other five disks (T15-19) were compacted to different dry densities of 1600, 1700, 1800, 1900 and 2000 kg/m^3 in a compaction mould (50 mm in inner diameter) and then directly transferred into the test cell (having the same inner diameter with compaction mould) to avoid the gap between the samples and the cell wall. Subsequently, the disks were hydrated with synthetic water under constant-volume conditions for 2160 h and both the axial and radial swelling pressure were recorded.

3 Experimental results

3.1 Axial and radial swelling pressures

The axial and radial swelling pressures of the samples without voids increased and then reached stabilization after 3-58 h (Zeng et al., 2019). The final axial and radial swelling pressures of samples without voids are summarized in Table 2. As the dry density increased, both the axial and radial swelling pressures increased. When the swelling pressures were displayed as a function of dry density in a semi-logarithmic plot (Fig. 4), unique relationships were obtained:

$$P_a = a_1 \exp^{b_1 \rho_d} = 25.824 \exp^{6.102\times10^{-3}\rho_d} \quad (1)$$

$$P_r = a_2 \exp^{b_2 \rho_d} = 1.199 \exp^{7.598\times10^{-3}\rho_d} \quad (2)$$

where P_a and P_r are the axial and radial swelling pressures (Pa), respectively; ρ_d is the dry density of sample (kg/m^3); a_1, a_2, b_1 and b_2 are fitting parameters.

Table 2. Experimental program and main results

Test	Technological void (%)	Duration (h)	Initial dry density of disk (kg/m^3)	Overall dry density (kg/m^3)	Final axial swelling pressure ($\times 10^6$ Pa)	Final radial swelling pressure ($\times 10^6$ Pa)
T01	20	0.5	2000	1800	1.07	0.20
T02	20	5	2000	1800	1.63	1.07
T03	20	15	2000	1800	1.63	1.08
T04	20	60	2000	1800	1.58	1.13
T05	20	240	2000	1800	1.62	1.14
T06	20	720	2000	1800	1.59	1.12
T07	20	2160	2000	1800	1.62	1.15
T08	0	0.5	2000	1600	0.78	0.04
T09	10	5	2000	1600	0.59	0.19
T10	10	15	2000	1600	0.52	0.20
T11	10	60	2000	1600	0.51	0.20
T12	10	240	2000	1600	0.51	0.20
T13	10	720	2000	1600	0.53	0.20
T14	10	2160	2000	1600	0.53	0.20
T15	0	2160	1600	1600	0.45	0.21
T16	0	2160	1700	1700	0.83	0.53
T17	0	2160	1800	1800	1.62	1.16
T18	0	2160	1900	1900	2.81	2.35
T19	0	2160	2000	2000	5.24	4.51

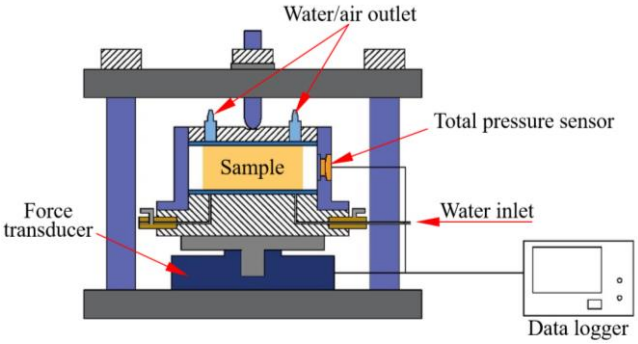

Fig. 2. Layout of the constant-volume cell

Table 3. Recipe for the synthetic water preparation

Component	NaCl	$NaHCO_3$	KCl	$CaSO_4 \cdot 2H_2O$	$MgSO_4 \cdot 7H_2O$	$CaCl_2 \cdot 2H_2O$	Na_2SO_4
Content (g/L)	1.950	0.130	0.035	0.630	1.020	0.080	0.700

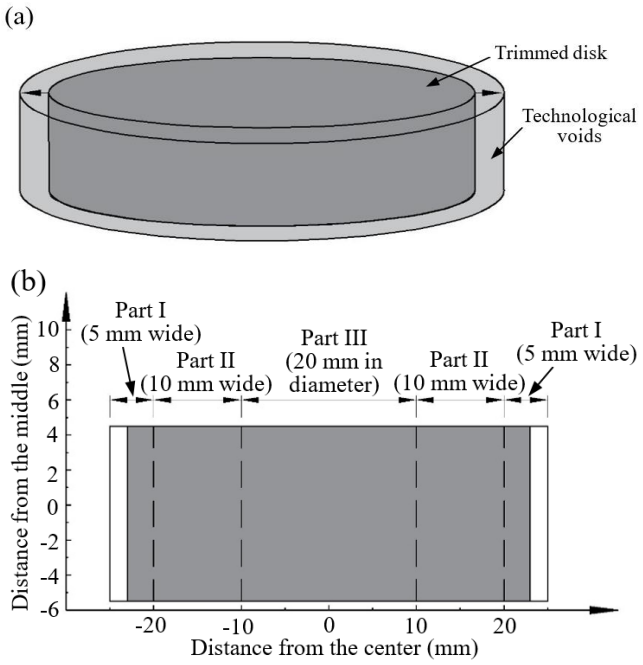

Fig. 3. Schematic view of the design of technological voids and the cutting of samples after hydration tests

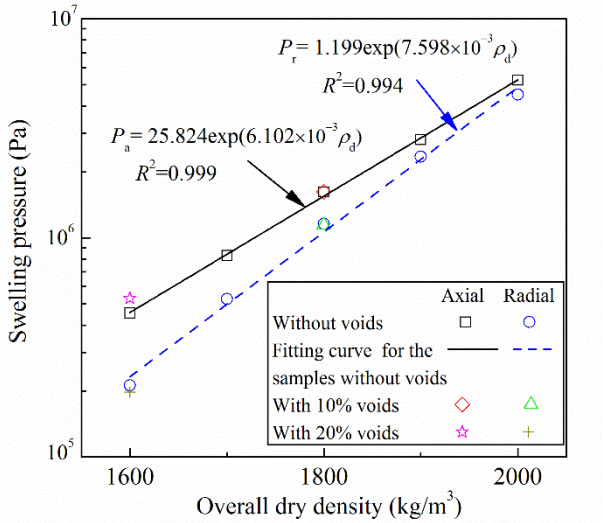

Fig. 4. Relationships between the axial and radial swelling pressures and overall dry density. Note: the equations were derived from the data of samples without voids

For the samples with technological voids, the final axial and radial swelling pressures are summarized in Table 2. It appeared that the final axial and radial swelling pressures tended to be stable after 60 h. The final axial and radial swelling pressures are also plotted in Fig. 4 for samples T07 and T14 after 2160-h hydration. Comparison with the case without voids showed that the samples with technological voids had a slightly higher axial swelling pressure but a lower radial one, especially for the sample with 20% voids.

3.2 Dry density profiles of samples with technological voids

The dry density profiles of samples with technological voids after various hydration times are depicted in Fig. 5. After filling of technological voids, the dry density, assumed to be axisymmetrically distributed, was characterized by a decreasing trend of dry density from the center of samples. The dry density of part I which corresponded to the initial technological voids was lower than the overall dry density $\rho_{\text{d-overall}}$, whereas those of parts II and III were higher than $\rho_{\text{d-overall}}$. Over time, part I was subjected to compression with an increase in dry density, while parts II and III further swelled with a decrease in dry density, suggesting the occurrence of a homogenization process. In Fig. 6, the variations of dry densities of the three parts are plotted on the scale of logarithm of hydration time. It appeared that the dry density evolutions for all the three parts followed an exponential function. For the sample with 10% technological voids, the asymptotic values for parts I, II and III are 1762.9, 1788.0 and 1824.6 kg/m^3, respectively; for the sample with 20% technological voids, the asymptotic values for parts I, II and III are 1575.9, 1612.7 and 1668.3 kg/m^3, respectively. As the asymptotic values of dry densities were not the same for parts I, II and III, it could be deduced that the heterogeneous distribution of dry density would remain forever.

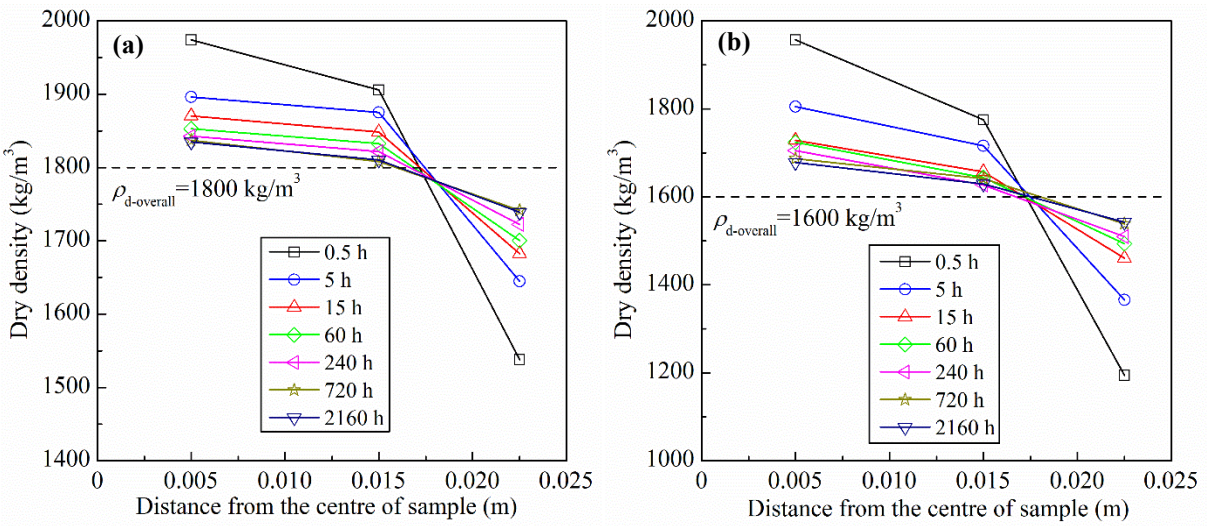

Fig. 5. Dry density profiles for samples with (a) 10% voids and (b) 20% voids

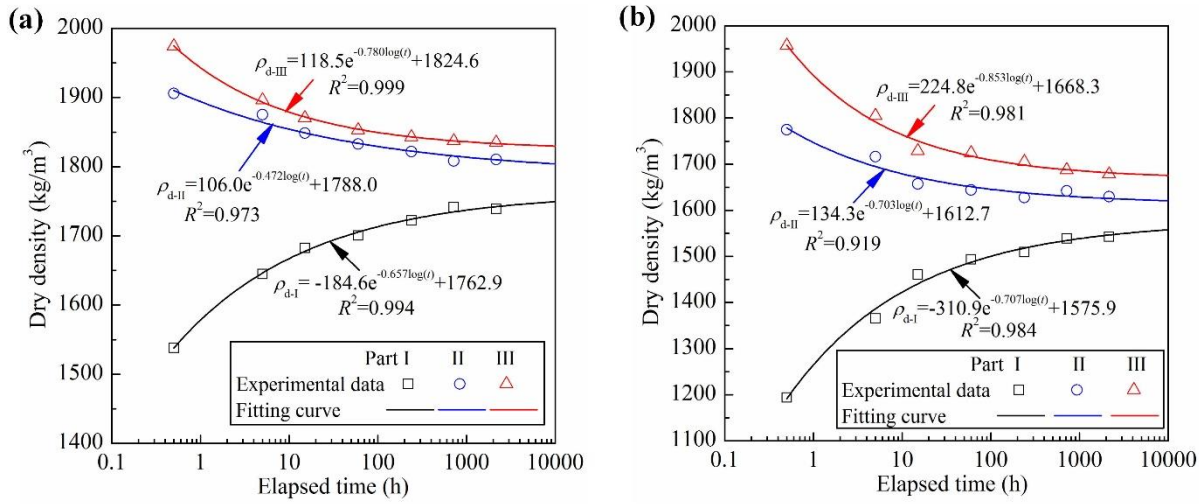

Fig. 6. Variations of dry density of different parts over time for samples with (a) 10 % voids and (b) 20% voids

4 Discussion

During the homogenization process, the part with higher dry density further swelled, while those with lower dry density was compressed. These displacement processes were accompanied by the boundary friction between the samples and the porous discs, which restricted the radial displacement (Zhong et al., 2015). Fig. 7 depicts the horizontal stresses of an element (0.01 m in thickness) of a cylindrical sample. The vector sum of swelling forces (F_s) and friction force (two sides) can be defined using Eq. (3):

$$F_s=P_r Tr\mathrm{d}\theta-(P_r+\frac{\partial P_r}{\partial r}\mathrm{d}r)T(\mathrm{d}r+r)\mathrm{d}\theta+P_\theta T\mathrm{d}r\sin\frac{\mathrm{d}\theta}{2}+(P_\theta+\frac{\partial P_\theta}{\partial\theta}\mathrm{d}\theta)T\mathrm{d}r\sin\frac{\mathrm{d}\theta}{2} \quad (3)$$

where P_r and P_θ are the swelling pressures (Pa) in the r and θ directions, respectively; T is the sample thickness (0.01 m); dr and dθ are the radius and angle increments of the element. Since the cross section area of the element is infinitely small, the friction stress (S_f) on this element can be assumed to be linearly distributed and the force (two sides) (F_f) in the radial direction can be expressed as:

$$F_f=2\left[\frac{1}{2}S_f+\frac{1}{2}(S_f+\frac{\partial S_f}{\partial r}\mathrm{d}r)\right]r\mathrm{d}r\mathrm{d}\theta \quad (4)$$

Once F_s cannot exceed maximum F_f, radial displacement stops. According to the force equilibrium in the r direction, the sum of all the forces in radial direction should be equal to zero:

$$F_s-F_f=0 \quad (5)$$

Substitution of Eqs. (3) and (4) into Eq. (5) gives:

$$P_{\mathrm{r}}Tr\mathrm{d}\theta-(P_{\mathrm{r}}+\frac{\partial P_{\mathrm{r}}}{\partial r}\mathrm{d}r)T(\mathrm{d}r+r)\mathrm{d}\theta+2P_{\theta}T\mathrm{d}r\sin\frac{\mathrm{d}\theta}{2}+\frac{\partial P_{\theta}}{\partial\theta}T\mathrm{d}r\,\mathrm{d}\theta\sin\frac{\mathrm{d}\theta}{2}$$

$$-2(S_{\mathrm{f}}+\frac{1}{2}\frac{\partial S_{\mathrm{f}}}{\partial r}\mathrm{d}r)r\mathrm{d}r\mathrm{d}\theta=0 \tag{6}$$

By substituting $\partial P_{\theta}/\partial\theta=0$ (the pressure in θ direction kept constant under axisymmetric conditions) and neglecting the three-order derivatives and taking $\sin(\mathrm{d}\theta/2)\approx\mathrm{d}\theta/2$, Eq. (6) was simplified as:

$$T\frac{P_{\theta}-P_{\mathrm{r}}}{r}-T\frac{\partial P_{\mathrm{r}}}{\partial r}-2S_{\mathrm{f}}=0 \tag{7}$$

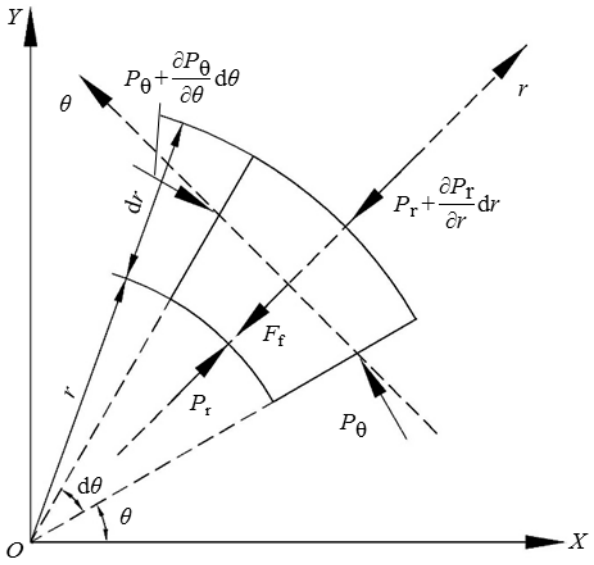

Fig. 7. Horizontal stresses of a cylindrical element of samples with technological voids

For further analyzing the final state of samples, the axial and radial swelling pressure were determined according to the following assumptions: (1) the samples are fully saturated when approaching the final equilibrium state and the axial and radial swelling pressures of the element follow Eqs. (1) and (2), respectively; (2) the element is the transversely isotropic and P_{r} and P_{θ} have the same function with dry density; (3) the dry density is uniformly distributed along the axial direction and can be described using an exponential function with $r = 0$ as the symmetry axis (Bian et al., 2019):

$$\rho_{\mathrm{d}}=a_3\exp^{b_3 r} \tag{8}$$

where a_3 is the soil dry density at the center of samples and b_3 is the homogeneity coefficient reflecting the dry density distribution. The larger the absolute value of b_3, the more heterogeneous the dry density distribution; $b_3 = 0$ indicates the homogenous distribution of dry density.

Based on the assumptions, P_a, P_r and P_θ can be determined from Eqs. (1) and (2):

$$P_a=a_1\exp^{a_3 b_1 \exp^{b_3 r}} \tag{9}$$

$$P_r=P_\theta=a_2\exp^{a_3 b_2 \exp^{b_3 r}} \tag{10}$$

After substitution of Eqs. (8) and (10) into Eq. (7), the friction stress is formulated based on two parameters, a_3 and b_3:

$$S_f=\frac{a_2 a_3 b_2 b_3 T}{2}\exp^{b_3 r}\exp^{a_3 b_2 \exp^{b_3 r}} \tag{11}$$

To determine parameters a_3 and b_3, two additional equations are required.

Physically, the friction stress between the soil and the porous discs for all the elements should be less than or equal to the limiting one. Moreover, there is at least one element at which the friction stress is exactly equal to the limiting one. Generally, the limiting friction stress (S_f^l) depends not only on the stress perpendicular to the interface but also on the material properties:

$$S_f^l=P_a\tan\phi+c \tag{12}$$

where ϕ and c are the friction angle (°) and the cohesion (Pa) for the interface between the samples and the porous discs, respectively. In the final state, the relationship between the friction stress and the limiting friction stress can be expressed as:

$$S_f\leq S_f^l \tag{13}$$

By substituting Eqs. (11) and (12) into Eq. (13), the following expression can be derived:

$$-\frac{1}{c}\left[\frac{a_2 a_3 b_2 b_3 T}{2}\exp^{b_3 r}\exp^{a_3 b_2 \exp^{b_3 r}}+a_1\tan\phi\exp^{a_3 b_1 \exp^{b_3 r}}\right]\leq 1 \tag{14}$$

The left-hand side is defined as $f(r)$. As discussed above, there is at least one element with the limiting friction stress. Thus, the maximum of $f(r)$ from 0 to R (the radius of sample) should be equal to 1:

$$\text{Max}\, f(r)=\text{Max}\left\{-\frac{1}{c}\left[\frac{a_2 a_3 b_2 b_3 T}{2}\exp^{b_3 r}\exp^{a_3 b_2 \exp^{b_3 r}}+a_1\tan\phi\exp^{a_3 b_1 \exp^{b_3 r}}\right]\right\}=1 \tag{15}$$

Additionally, based on mass conservation, the integral of ρ_d over the horizontal cross-section of samples should be equal to the product of overall dry density and surface area:

$$\int_0^{2\pi}\int_0^R (a_3\exp^{b_3 r}) r\,\mathrm{d}r\,\mathrm{d}\theta=\pi R^2\rho_{\text{d-overall}} \tag{16}$$

It can be further developed as:

$$-\frac{2a_3}{b_3^2 R^2}(b_3 R\exp^{b_3 R}-\exp^{b_3 R}+1)=\rho_{\text{d-overall}} \tag{17}$$

Combining Eqs. (15) and (17) yields:

$$\begin{cases} \text{Max } f(r)=1 \\ -\dfrac{2a_3}{b_3^2 R^2}(b_3 R\exp^{b_3 R}-\exp^{b_3 R}+1)=\rho_{\text{d-overall}} \end{cases} \tag{18}$$

According to the experimental results of Potyondy (1961), the friction angle and cohesion between clay and smooth steel could be taken as 6.5 ° and 6699 Pa. These values were taken here to represent the boundary/soil interface properties. Based on Eq. (18), parameters a_3 and b_3 could be computed following an iteration procedure. The values of a_3 for the samples with 10% and 20% voids were found to be 1835.5 and 1649.2, respectively; the values of b_3 for the samples with 10% and 20% voids were -1.174 and -1.820, respectively. By substituting the values of a_3 and b_3, the dry density distributions in the final state could be estimated, as illustrated in Fig. 8a. It appeared clearly that the dry density distributions of samples were still heterogeneous in the final state. Additionally, the sample with 20% voids had a larger absolute value of b_3 and a more significant heterogeneity could be observed in that case. Also plotted in Fig. 8a are the asymptotic values which were obtained by fitting the dry density evolution curves using exponential functions (Fig. 6). It appeared that the estimated dry density distribution agreed well with the fitting results. According to Eqs. (11) and (12), the friction stress and limiting friction stress at different positions could be calculated. As shown in Fig. 8b, both the friction stress and limiting friction stress decreased with the increasing radius. Additionally, the friction stress was equal to the limiting friction stress at the center of samples and the difference between them increased with the increasing radius. Based on Eqs. (7) and (12), the friction stress and limiting friction stress were dependent on the radial swelling pressure gradient and axial swelling pressure, respectively. Upon hydration, the soils in the external zone swelled to fill the technological voids, with a quick decrease of dry density. With further swelling of the soils in the internal parts, the radial swelling pressure gradient induced by the dry density gradient would lead to the radial displacement of soils, increasing the dry density and the axial swelling pressure of the soils adjacent to periphery. As a result, a larger limiting friction stress was observed compared to the friction stress. Meanwhile, the dry density gradient of soils close to the center would increase and a further radial displacement took place. When the friction stress at the center of the sample became equal to the limiting friction stress, the homogenization process would stop.

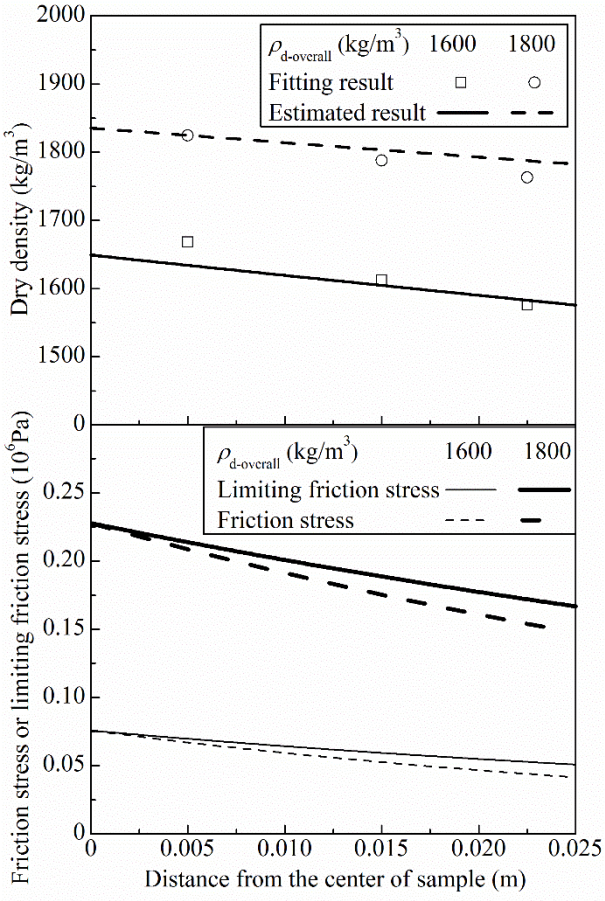

Fig. 8. (a) estimated final dry density and (b) friction stress and limiting friction stress distributions of samples with technological voids

From the estimated dry density distribution curves in Fig. 8a, the dry densities at the border (r = 0.025 m) for the samples with 10 and 20% voids were found to be 1782 and 1576 kg/m^3, respectively. Using Eq. (2), the corresponding radial swelling pressures could be estimated at 0.92 and 0.19 MPa, respectively, which were lower than the measured values (Table 2). This was due to the fact that the present study only focused on the influence of boundary friction on the mean dry density distribution along the radial direction, without considering the dry density distribution along the axial direction. Indeed, since the friction stress directly acted on the two surfaces of samples, it significantly affected the dry density distribution in the zones close to the surfaces of the samples. This influence was expected to be the minimum in the middle part. Thereby, the dry density would display an inversely U-shaped distribution along the axial direction. As shown in Fig. 2, the radial pressure sensor was in contact with the middle part of sample (a circular area with a diameter of 0.006 m), which had a dry density closer to the overall one. This explained the slight difference between the measured radial swelling pressures of the samples with and without voids (Fig. 4).

In a real repository, the backfill/sealing elements can be several meters in diameter and a few tens of meters in axial length. The radial technological voids between the compacted blocks and the host rock and the axial technological voids between the compacted blocks can be created during the construction of backfill/sealing elements. In the case of radial technological voids, the heterogeneous dry density distributions in the radial direction at the two ends of the backfill/sealing elements will remain owing to the interface friction with the concrete plugs, while that in the intermediate section of the backfill/sealing elements can achieve a relatively homogenous state in the radial direction. As far as the axial technological voids are concerned, the interface friction with the host rock will impede the axial homogenization process, resulting in a heterogeneous distribution of dry density in the axial direction. Henceforth, these heterogeneities in terms of dry density distribution must be taken into account in the assessment of long-term performance and safety of deep geological repositories.

5 Conclusions

The boundary friction effect on the evolution of dry density distribution was investigated on compacted bentonite/claystone mixture with different technological voids upon hydration. Results showed that the initial heterogeneity due to the presence of technological voids decreased with time. Further analysis of the dry density evolution curves for different parts indicated that this heterogeneity would remain forever.

The final heterogeneity could be attributed to the effect of friction stress between the sample and the porous discs. When the vector sum of swelling forces in the radial direction was lower than or equal to the limiting friction force for all elements, the homogenization process would stop. According to the force equilibrium in the final state and the mass conservation, the final dry density distributions of samples were estimated. The good agreement between the estimated and measured dry density distributions showed the relevance of the identified mechanism for the final heterogeneous dry density distribution.

Acknowledgments

The authors are grateful to Ecole des Ponts ParisTech, the China Scholarship Council (CSC) and the French National Radioactive Waste Management Agency (Andra) for their financial supports.

References

Bian X, Cui YJ, Li XZ (2019). Voids effect on the swelling behaviour of compacted bentonite. Géotechnique 69(7):593-605

Delage P, Le TT, Tang AM, Cui YJ, Li XL (2008) Suction effects in deep Boom clay block samples. Géotechnique 57(2):239–244

Fouché O, Wright H, Le Cléac'h JM, Pellenard P (2004) Fabric control on strain and rupture of heterogeneous shale samples by using a non-conventional mechanical test. Appl Clay Sci 26(1-4):367-387

Gens A, Vállejan B, Sánchez M, Imbert C, Villar MV, Van Geetl M (2011) Hydromechanical behaviour of a heterogeneous compacted soil: experimental observations and modelling. Géotechnique 61(5):367-386

Gens A, Pomaro B, Sánchez M, Villar MV (2018) On the hydration of unsaturated barriers for high-level nuclear waste disposal. In Unsaturated Soils: UNSAT 2018: The 7th International Conference on Unsaturated Soils, 55-60

Jia LY, Chen YG, Ye WM, Cui YJ (2019) Effects of a simulated gap on anisotropic swelling pressure of compacted GMZ bentonite. Eng Geol 248:155-163

Komine H, Ogata N (1994) Experimental study on swelling characteristics of compacted bentonite. Can Geotech J 31(4):478-490

Komine H, Ogata N (1999) Experimental study on swelling characteristics of sand-bentonite mixture for nuclear waste disposal. Soils Found 39(2):83-97

Potyondy JG (1961) Skin friction between various soils and construction materials. Géotechnique 11(4):339-353

Pusch R (1982) Mineral–water interactions and their influence on the physical behavior of highly compacted Na bentonite. Can Geotech J 19(3):381-387

Saba S (2013) Hydro-mechanical behaviour of bentonite-sand mixture used as sealing materials in radioactive waste disposal galleries (Doctoral dissertation, Université Paris-Est)

Sellin P, Leupin OX (2013) The use of clay as an engineered barrier in radioactive-waste management–a review. Clays Clay Miner 61(6):477-498

Villar MV, Lloret A (2007) Dismantling of the first section of the FEBEX in situ test: THM laboratory tests on the bentonite blocks retrieved. Phys. Chem. Earth Parts A/B/C 32(8-14):716-729

Villar MV, Lloret A (2008) Influence of dry density and water content on the swelling of a compacted bentonite. Appl Clay Sci 39(1-2):38-49

Villar MV, Iglesias RJ, García-Siñeriz JL, Lloret A, Huertas F (2019) Physical evolution of a bentonite buffer during 18 years of heating and hydration. Eng Geol doi: 10.1016/j.enggeo.2019.105408

Wang Q, Tang AM, Cui YJ, Delage P, Barnichon JD, Ye WM (2013) The effects of technological voids on the hydro-mechanical behaviour of compacted bentonite–sand mixture. Soils Found 53(2):232-245

Yong RN, Boonsinsuk P, Wong G (1986) Formulation of backfill material for a nuclear fuel waste disposal vault. Can Geotech J 23(2):216-228

Zeng ZX, Cui YJ, Zhang F, Conil N, Talandier J (2019) Investigation of swelling pressure of bentonite/claystone mixture in the full range of bentonite fraction. Appl Clay Sci doi: 10.1016/j.clay.2019.105137

Zhong WZ, Rusinek A, Jankowiak T, Abed F, Bernier R, Sutter G (2015) Influence of interfacial friction and specimen configuration in Split Hopkinson Pressure Bar system. Tribol Int 90:1-14

Chapter 5. Effect of water chemistry

INTRODUCTION

The pore water of COx claystone formation in Bure, which is chosen as the possible host rock for underground radioactive water disposal, is relatively rich in salts (Gaucher et al., 2006; Wileveau and Bernier, 2008). In addition, the cement in contact with groundwater for a long period can degrade and release a large number of K^+, Na^+, Ca^{2+} and OH^-, resulting in a high-pH alkaline solution (Anh et al., 2017; Savage et al., 2002; Karnland et al., 2007; Sun et al., 2018). Over the long time lifespan of the repository, the sealing/backfill materials can interact with the cations and hydroxide, and in turn influence their hydro-mechanical performance. To this end, it is essential to account for the effect of such water chemistry on the hydro-mechanical behaviour of bentonite-based materials for the long-term safety assessment of the repository.

In this chapter, a series of tests was performed to investigate the effects of water chemistry on the hydro-mechanical behaviour of bentonite/claystone mixtures. The results are presented in this chapter in the form of two papers.

The first part presents the results of infiltration tests on the compacted mixtures of COx claystone and two types of bentonites (Na^+ MX80 and Ca^{2+} Sardinia bentonites) using deionised water, synthetic site solution and cement solution. Emphasis was put on the hydro-mechanical responses of specimens with different bentonite nature and dry densities. This part corresponds to a paper submitted to “Journal of Rock Mechanics and Geotechnical Engineering”.

The second part, submitted to “Engineering Geology”, compares the swelling pressures and hydraulic conductivities of compacted MX80 bentonite/COx claystone mixture with various technological voids and hydrated with deionised water and synthetic site solution for 10 and 590 days. The dry density, water content and microstructure features at various positions of the specimen were then determined to better understand the influence mechanism of pore water chemistry and technological voids.

Zeng, Z.X., Cui, Y.J., Talandier, J. 2021. Submitted to Journal of Rock Mechanics and Geotechnical Engineering.

Effect of water chemistry on the hydro-mechanical behaviour of compacted mixtures of claystone and Na^+/Ca^{2+} bentonites for deep geological repositories

Zhixiong Zeng[1], Yu-Jun Cui[1], Jean Talandier[2]

Abstract: In the French deep geological disposal for radioactive wastes, compacted bentonite/claystone mixtures have been considered as possible sealing materials. After emplacement in place, such mixtures are hydrated by the site solution as well as the cement solution produced by the degradation of concrete. In this study, the effects of synthetic site solution and cement solution on the hydro-mechanical behaviour of compacted mixtures of claystone and two types of bentonites (Na^+ MX80 and Ca^{2+} Sardinia bentonites) were investigated by carrying out a series of swelling pressure, hydraulic conductivity and Mercury Intrusion Porosimetry (MIP) tests. It was found that for the MX80 bentonite/claystone mixture hydrated with synthetic site solution, the swelling capacity was reduced compared to the case with deionised water owing to the transformation of Na-montmorillonite to multi-cation dominant montmorillonite by cation exchanges. For the Sardinia bentonite/claystone mixture, the similar increasing rate of swelling pressure was observed during the crystalline swelling process for different solutions, suggesting insignificant cation exchanges. Additionally, the cations in the synthetic site solution could reduce the thickness of diffuse double layer and the osmotic swelling for both MX80 bentonite/claystone and Sardinia bentonite/claystone mixtures. The large-pore volume increased consequently and enhanced water flow. In the cement solution, the hydroxide could also dissolve the montmorillonite, reducing the swelling pressure, and increased the large-pore volume, facilitating the water flow. Furthermore, the decrease of swelling pressure and the increase of hydraulic conductivity were more significant in the case of low dry density because of more intensive interaction between montmorillonite and hydroxide thanks to the high permeability.

Keywords: bentonite/claystone mixture; synthetic site solution; cement solution; bentonite type; swelling pressure; hydraulic conductivity

1 Ecole des Ponts ParisTech, Laboratoire Navier/CERMES, 6 et 8 avenue Blaise Pascal, 77455 Marne La Vallée cedex 2, France
2 Andra, 1/7, rue Jean Monnet, 92298 Châtenay-Malabry cedex, France

1 Introduction

Deep geological repository has been accepted as a solution for the long-term storage of high-level radioactive wastes in many countries (Sellin and Leupin, 2013). To ensure the long-term safe isolation of radioactive wastes in deep geological formations, bentonite-based materials are commonly used as sealing materials (Pusch, 1982; Dixon et al., 1985; Villar and Lloret, 2008; Ye et al., 2010), while cement (in mortar or concrete) is used to construct the tunnel retaining structures and tunnel plugs/seals (Sánchez et al., 2006). After the repositories are closed, the bentonite-based materials will be hydrated by the pore water of the host rock and swell, filling the technological voids and restricting the release of radionuclides from the radioactive wastes to the surrounding environment. It has been reported that the pore water of the host rock considered in several countries is of certain salinity (Deng et al., 2011; Nguyen et al., 2013; Wang et al., 2014; Sun et al., 2018). In addition, the cement in contact with groundwater for a long period can degrade and release a large number of Ca^{2+} and OH^{-}, resulting in a high-pH alkaline solution (Savage et al., 2002; Karnland et al., 2007; Anh et al., 2017; Sun et al., 2018). In the performance assessment of the storage repositories, it appears essential to account for the effect of such water chemistry on the hydro-mechanical behaviour of bentonite-based materials.

In the past decades, the influence of saline solution on the hydro-mechanical behaviour of bentonite-based materials was studied by many researchers (Karnland et al., 2006; Rao et al., 2006; Castellanos et al., 2008; Komine et al., 2009; Zhu et al., 2013). It was found that the pore water salinity could significantly decrease the swelling pressure (Komine et al., 2009; Zhu et al., 2013) and increase the hydraulic conductivity (Castellanos et al., 2008; Schanz and Tripathy, 2009; Zhu et al., 2013; Du et al., 2021). Yukselen-Aksoy et al. (2008) and Zhu et al. (2013) reported that the cations in the pore water might alter the mineralogical compositions through cation exchanges and influence the crystalline swelling process, resulting in a lower swelling pressure. Additionally, the cations in the pore water could decrease the thickness of diffuse double layer, affecting the osmotic swelling behaviour (Siddiqua et al., 2011; Castellanos et al., 2008; Zhu et al., 2013). At a given void ratio, a larger large-pore volume could be expected for the specimen hydrated with a saline solution, leading to a higher hydraulic conductivity.

In addition to the saline solution, alkaline solution can also significantly influence the hydro-mechanical behaviour of bentonite-based materials (Karnland et al., 2007; Herbert et al., 2008; Lee et al., 2012; Chen et al., 2016; Sun et al., 2018, 2019, 2020; Liu et al., 2020). Chen et al.

(2016) experimentally determined the swelling pressures and hydraulic conductivities of GMZ bentonite hydrated with various NaOH solutions and found that the final swelling pressure decreased and the hydraulic conductivity increased significantly with the increase of NaOH solution concentration. Karnland et al. (2007) investigated the constant-volume swelling pressures of compacted Wyoming MX80 bentonite hydrated with NaOH and $Ca(OH)_2$ solutions and found that 0.1 M NaOH (pH=12.9) or saturated $Ca(OH)_2$ solutions (pH=12.4) did not significantly change the swelling pressure of compacted MX80 bentonite. In contrast, Sun et al. (2018; 2019) compared the swelling pressures and mineralogical compositions of GMZ bentonite hydrated with Beishan site solution (pH=8.5), young concrete water (pH=13) and evolved concrete water (pH=12) and observed a remarkably lower swelling pressure in the case of young concrete water. They explained this phenomenon by the dissolution of montmorillonite upon saturation with alkaline solutions and the formation of some less active zeolites and calcium hydrated silicates. Additionally, the montmorillonite content decreased linearly as the pH increased (Sun et al., 2019).

In France, Callovo-Oxfordian (COx) claystone has been considered as a potential geological host rock for high-level radioactive waste disposal. To reduce the excavation waste and ensure the mineralogical compatibility, a mixture of crushed COx claystone and bentonite in the form of pre-compacted blocks has been proposed as a possible sealing material by the French National Radioactive Waste Management Agency (Andra) (Wang e al., 2014; Zeng et al., 2019; Middelhoff, 2020). Wang et al. (2014) carried out a series of constant-volume swelling pressure tests on compacted MX80 bentonite/COx claystone mixture with a bentonite fraction of 70% (dry density of 1.7 Mg/m^3) and observed a slight decrease of swelling pressure with the synthetic site solution after 700 days of hydration. Cuisinier et al. (2009) studied the microstructure of compacted COx claystone at a dry density of 1.61 Mg/m^3 hydrated with portlandite-saturated solution for 1 year using mercury intrusion porosimetry (MIP) and scanning electron microscopy (SEM) techniques and found an increase of macro-pore void ratio after the fluid circulation. By contrast, Middelhoff (2020) indicated that the swelling pressure after about 7 days and the hydraulic conductivity after 1 year were hardly affected by the site solution and cement solution for the compacted MX80 bentonite/COx claystone mixture (a proportion of 30/70 in dry mass) at a dry density of 1.72 Mg/m^3. Up to now, there was no consensus regarding the effects of site solution and cement solution on the hydro-mechanical behaviour of bentonite/claystone mixture. Additionally, to the authors' knowledge, the responses of the mixtures of COx claystone and different bentonites upon hydration with site

solution and cement solution have not been systematically studied.

In this study, a series of infiltration tests using deionised water, synthetic site solution and cement solution were performed on compacted mixtures of COx claystone and Na^+ MX80 and Ca^{2+} Sardinia bentonites at different dry densities. The effects of synthetic site solution and cement solution on the swelling pressure and hydraulic conductivity were analysed. Moreover, the microstructure features before and after hydration were also determined using MIP technique, enabling the interpretation of the physico-chemical interaction between different bentonite/claystone mixtures and different fluids involved.

2 Materials and methods

2.1 Materials

According to the preliminary results of Zeng et al. (2020a), the bentonite/claystone mixtures with a proportion of 30/70 in dry mass were used in this study to fulfill the requirements of Andra in terms of swelling pressure and hydraulic conductivity with a dry density of 1.72-1.82 Mg/m^3. To investigate the effect of bentonite type, two bentonites, MX80 and Sardinia bentonites, were considered. The MX80 bentonite is a Na-bentonite, extracted from Wyoming in the United States while the Sardinia bentonite is a Ca-bentonite, taken from Monte Furros, Italy. The main physical and chemical characteristics of the two bentonites are presented in Table 1. The COx claystone was sampled from the Andra Underground Research Laboratory (URL) in Bure. It is composed of 40–45% interstratified illite/smectite, 30% carbonates, and 25%–30% quartz and feldspar. The COx claystone is characterized by a liquid limit of 41%, a plastic limit of 24% and a specific gravity of 2.70. Prior to testing, the bentonites and claystone were crushed to have a maximum grain size of 2.0 mm. The grain size distributions of the bentonites and claystone determined by dry sieving are presented in Fig. 1. The mean grain diameters (D_{50}) of the MX80 bentonite, Sardinia bentonite, COx claystone are 0.55, 1.06 and 0.58 mm, respectively.

Synthetic site solution and cement solution were used for the infiltration tests. These solutions respectively represent the site water at a depth of -490 m and the alkaline solution after the degradation of concrete, and were prepared according to the recipe provided by Andra (Table 2). The chemical compositions of the solutions are summarized in Table 3. The pH values of the two solutions were measured, equal to 8.6 and 12.5, respectively. In addition, deionised water was also employed as a reference case.

Table 1. Physical and chemical properties of MX80 and Sardinia bentonites

Soil property	MX80	Sardinia
Specific gravity	2.76	2.54[b]
Consistency limit		
Liquid limit (%)	494	143[b]
Plastic limit (%)	46	69[b]
Plasticity index (%)	448	74[b]
Cation exchange capacity (CEC) (meq/100 g)	80[a]	65[c]
Main minerals	Montmorillonite (86%)	Montmorillonite (60-90%)[d]
	Quartz (7%)	Illite (10-14%)[d]

[a]: Karnland et al. (2006); [b]: Vitale et al. (2016); [c]: Cara et al. (2000); [d]: Pusch and Karnland (1988)

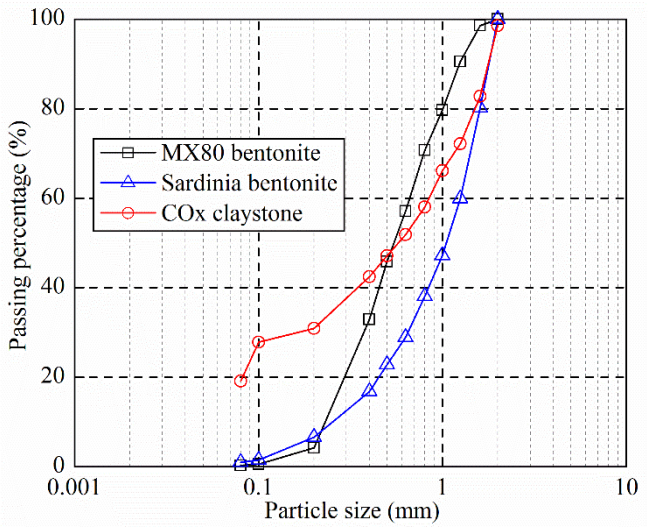

Fig. 1. Grain size distribution of MX80 and Sardinia bentonites and crushed COx claystone

Table 2. Recipe for the synthetic site solution and cement solution preparation

Content (g/L)	NaCl	$NaHCO_3$	KCl	$CaSO_4 \cdot 2H_2O$	$MgSO_4 \cdot 7H_2O$	$CaCl_2 \cdot 2H_2O$	Na_2SO_4	$Ca(OH)_2$
Site solution	1.950	0.130	0.035	0.630	1.020	0.080	0.700	-
Cement solution	1.286	-	0.596	-	-	-	-	1.408

Table 3. Composition of the synthetic site solution and cement solution

Compound (mmol/L)	Na^+	K^+	Ca^{2+}	Mg^{2+}	Cl^-	$SO4^{2-}$	CO_3^{2-}
Site solution	44.6	0.47	4.2	4.1	34.8	12.7	1.58
Cement solution	22.2	8.05	19	-	30.2	-	-

2.2 Experimental methods

The bentonite and claystone powders with a proportion of 30/70 in dry mass were first mixed for more than 10 min. The gravimetric water contents of the MX80 bentonite, Sardinia bentonite and claystone under laboratory conditions (a relative humidity of about 60%) were determined by oven-drying at 105°C for 24 h, equal to 11.4, 16.0 and 6.1%, respectively. Accordingly, the respective water contents of the MX80 bentonite/claystone and Sardinia bentonite/claystone mixtures were 7.7 and 9.1%, respectively. Based on the target dry density, a pre-determined amount of mixtures were poured into a rigid steel ring with an inner diameter of 50 mm and

statically compacted at a constant displacement rate of 0.05 mm/min. The final height of compacted specimens was 10 mm. For the MX80 bentonite/claystone mixture, nine specimens with dry densities of 1.6, 1.8 and 2.0 Mg/m^3 were compacted, three for each dry density (Table 4); for the Sardinia bentonite/claystone mixture, six specimens with dry densities of 1.6 and 1.8 Mg/m^3 were prepared. Afterwards, the compacted specimens were transferred into a testing cell with an inner diameter of 50 mm (Fig. 2) and placed between two porous stones and filter papers. A circular cap with a diameter of 50 mm was placed at the top of the specimens and then blocked using a screw to prevent axial swelling. After that, deionised water, synthetic site solution or cement solution was injected into the specimens from the bottom of the cell under a water head of about 1 m and the axial swelling force was monitored using a force transducer installed under the testing cell. For all the specimens, the hydration lasted for 90 days. All the tests were performed at constant ambient temperature (20 ± 1 °C).

Table 4. Experimental programme

Test No.	Bentonite type	Dry density (Mg/m^3)	Injected water	MIP
T01	MX80	1.6	Deionised water	√
T02	MX80	1.6	Site solution	√
T03	MX80	1.6	Cement solution	√
T04	MX80	1.8	Deionised water	√
T05	MX80	1.8	Site solution	√
T06	MX80	1.8	Cement solution	√
T04	MX80	2.0	Deionised water	√
T05	MX80	2.0	Site solution	√
T06	MX80	2.0	Cement solution	√
T04	Sardinia	1.6	Deionised water	√
T05	Sardinia	1.6	Site solution	√
T06	Sardinia	1.6	Cement solution	√
T04	Sardinia	1.8	Deionised water	√
T05	Sardinia	1.8	Site solution	√
T06	Sardinia	1.8	Cement solution	√

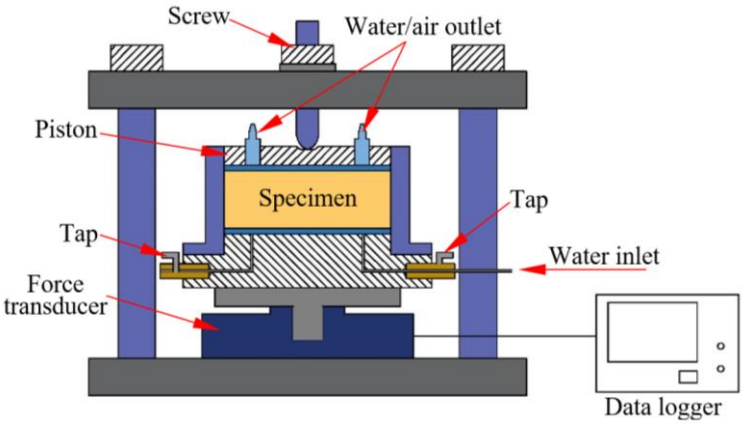

Fig. 2. Schematic diagram of the constant-volume cell for swelling pressure and hydraulic conductivity tests

At the end of the swelling pressure tests, the solution injection was continued for more than 24 h using a pressure/volume controller under constant pressures. To minimise the disturbance of the microstructure and avoid hydraulic fracturing, the water injection pressure was lower than 1/10 of the final swelling pressure. For the MX80 bentonite/claystone mixtures at 1.6, 1.8 and 2.0 Mg/m^3 dry densities, the injection pressures were respectively 0.04, 0.10 and 0.20 MPa, while those for the Sardinia bentonite/claystone mixtures at 1.6 and 1.8 Mg/m^3 dry densities were 0.03 and 0.10 MPa, respectively. During the solution injection, the solution volume injected into the specimens was recorded. After stabilization of the flow rate, the specimens were regarded as saturated and the saturated hydraulic conductivity was calculated based on the Darcy's law:

$$k=\frac{q}{iA} \tag{1}$$

where q is the flow rate (m^3/s); i is the hydraulic gradient; A is the cross-section (m^2).

After the infiltration tests, the specimens were taken out of the cell for microstructure observation. The specimens were first cut into small pieces (about 1 cm^3 in volume). Afterwards, the pieces were immersed in slush nitrogen (-210°C) obtained by previously submitting it to vacuum for instantaneous freezing, and then lyophilized in a vacuumed chamber (Delage et al., 1996). For the MIP test, the freeze-dried pieces were put in a low pressure chamber with a working pressure from 3.6 to 2000 kPa and then a high pressure chamber with a working pressure from 0.2 to 228 MPa, enabling identification of pore entrance diameter 350 to 0.006 μm (the diameter at the narrowest position).

3 Experimental results

3.1 Swelling pressure

The evolutions of swelling pressure for different dry densities are depicted in Fig. 3. On the whole, the curves can be divided into two stages: a relatively large primary swell (stage I) and a small secondary swell (stage II). In stage I, the swelling pressure increased quickly. The overall increasing rate for the MX80 bentonite/claystone mixture hydrated with synthetic site solution and cement solution was slightly lower than that of the specimens hydrated with deionised water. Moreover, the synthetic site and cement solutions reduced the elapsed time required to complete stage I. By contrast, the increasing rate for the Sardinia bentonite/claystone mixture was almost the same regardless of the permeating solutions. In stage II, for the MX80 bentonite/claystone mixture with large dry densities (1.8 and 2.0 Mg/m^3), the swelling pressure tended to stabilization. By contrast, for the MX80 bentonite/claystone mixture at a low dry density (1.6 Mg/m^3) and the Sardinia bentonite/claystone mixtures at dry densities of 1.6 and 1.8 Mg/m^3, the swelling pressure reached a peak, decreased sharply and then tented to stabilization. The specimens at a low dry density and hydrated with cement solution exhibited a more remarkable decrease of swelling pressure after reaching a peak. Moreover, at a given dry density, the decrease of swelling pressure after reaching a peak was more significant for the Sardinia bentonite/claystone mixture compared to the MX80 bentonite/claystone mixture. The final swelling pressures of the specimens at various dry densities and hydrated with different solutions are summarized in Fig. 4. There were reasonable linear relationships between the final swelling pressure and the dry density for the specimens hydrated with different solutions. In case of high dry densities (1.8 and 2.0 Mg/m^3), the final swelling pressure was almost independent of the permeating solution. In case of low dry density (1.6 Mg/m^3), the synthetic site solution and cement solution more or less reduced the swelling pressure. Additionally, from Fig. 4, a slightly lower final swelling pressure could be observed on the Sardinia bentonite/claystone mixture comparted to the MX80 bentonite/claystone mixture, especially in the case of low dry density of 1.6 Mg/m^3.

3.2. Saturated hydraulic conductivity

At the end of swelling pressures tests, the saturated hydraulic conductivities were determined for various dry densities and the results are presented in Fig. 5. For the specimens hydrated with a given solution, the hydraulic conductivity decreased with the increase of dry density. The synthetic site solution and cement solution increased the hydraulic conductivity for both the

MX80 bentonite/claystone and the Sardinia bentonite/claystone mixtures. This is consistent with the results of Villar (2006) and Chen et al. (2016) while studying the effects of saline and alkaline solutions on the hydraulic conductivity of MX80 bentonite/granite mixture (a proportion of 30/70 in dry mass) and GMZ bentonite, respectively. Additionally, larger increases of hydraulic conductivity due to the water chemistry were observed on the specimens hydrated with cement solution. The lower the dry density of specimens, the more significant the influences of synthetic site solution and cement solution on the saturated hydraulic conductivity. In addition, compared to the MX80 bentonite/claystone mixture, the compacted Sardinia bentonite/claystone mixture exhibited a larger hydraulic conductivity at the same dry density.

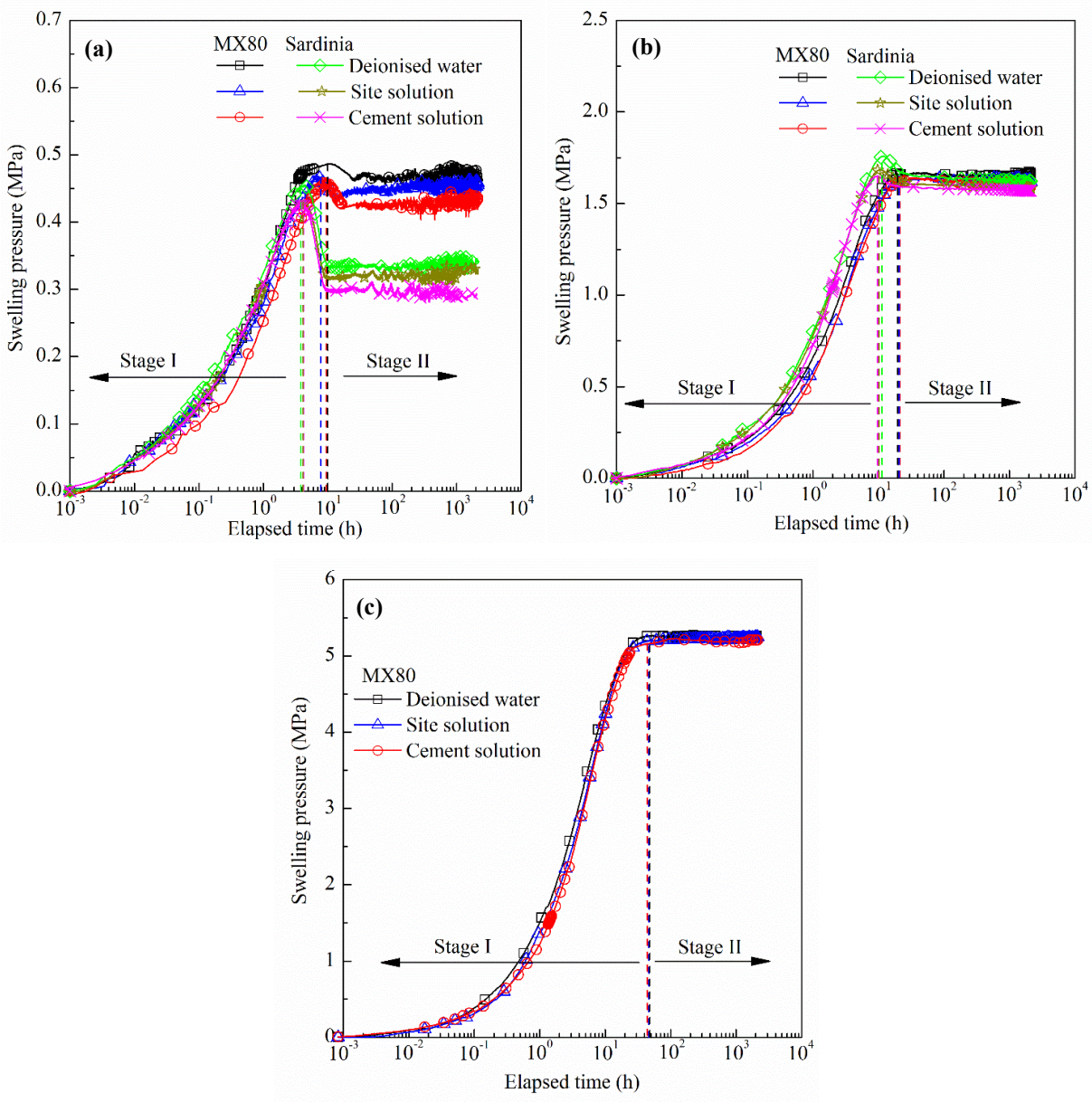

Fig. 3. Evolution of axial swelling pressure of specimens at different dry densities. (a) 1.6 Mg/m^3, (b) 1.8 Mg/m^3 and (c) 2.0 Mg/m^3

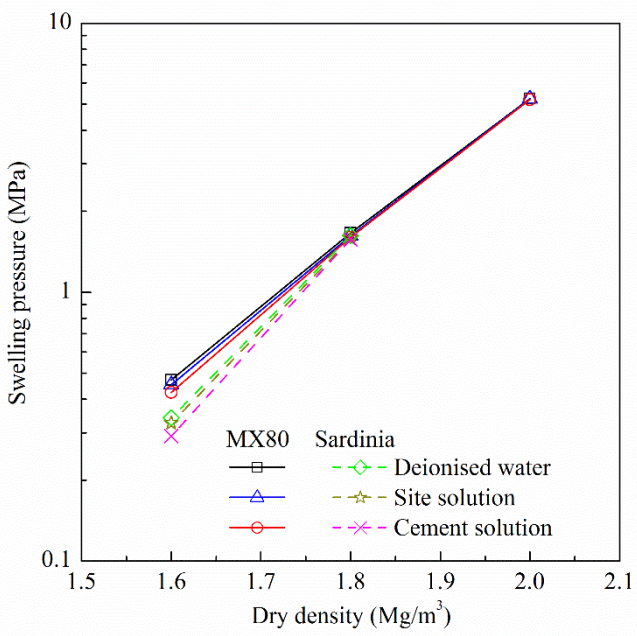

Fig. 4. Final swelling pressure versus dry density

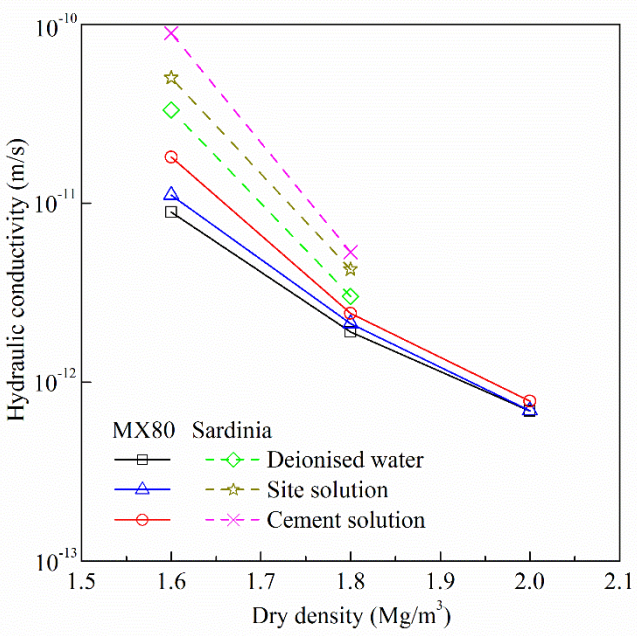

Fig. 5. Hydraulic conductivity versus dry density

3.3 Microstructure observation

Figs. 6 and 7 illustrate the pore size distributions of the specimens before and after hydration. From the cumulative curves (Figs. 6a and 7a), it could be observed that the final value of intruded mercury void ratio was lower than the global void ratio. This difference indicated the existence of a large amount of porosity which was inaccessible with the maximum pressure applied in the MIP tests. From the density curves (Figs. 6b and 7b), the as-compacted specimens exhibited a typical bimodal porosity, allowing two main pore populations to be defined: a

population of intra-aggregate pores (small pores) with a mean pore diameter of 0.02 μm and a population of inter-aggregate pores (large pores) with a mean pore diameter of 5 μm. This is consistent with the observation of Delage et al. (1996; 2006) who found that the soils compacted dry of optimum could be described by a typical aggregate microstructure. After hydration, the mean pore diameter of large pores increased to about 25 μm. By contrast, the mean pore diameter of small pores remained unchanged but the peak value decreased remarkably. For the specimens at low dry densities (1.6 and 1.8 Mg/m^3), a new pore population with a mean diameter of 0.2-0.5 μm (defined as medium pores) appeared between the large and small pores. Following the suggestion of Bian et al. (2019) and Zeng et al. (2020b), the respective delimiting diameters between the large and medium pores and between the medium and small pore were taken as 2 and 0.04 μm, respectively. To further investigate the effects of synthetic site solution and cement solution on the pore structure of bentonite/claystone mixtures, the void ratios of four populations were determined based on the delimiting values and the cumulative curves. The results are summarized in Figs. 8 and 9. It can be clearly observed that the synthetic site solution and cement solution increased the larger-pore and small-pore void ratios and decreased the medium-pore void ratio. Similar phenomenon was observed by Wang et al. (2014) and Liu et al. (2020) while investigating the effect of saline solution on the pores structure of compacted MX80 bentonite/claystone (70/30 in dry mass) and the effect of NaOH solution on the pore structure of compacted GMZ bentonite, respectively. Moreover, the cement solution had a more remarkable influence on the pore structure changes than the synthetic site solution. Comparison of the pore structures of two bentonite/claystone mixtures shows that at a given dry density, the Sardinia bentonite/claystone mixture exhibited a lower large-pore void ratio and larger medium-pore and small-pore void ratios than the MX80 bentonite/claystone mixture.

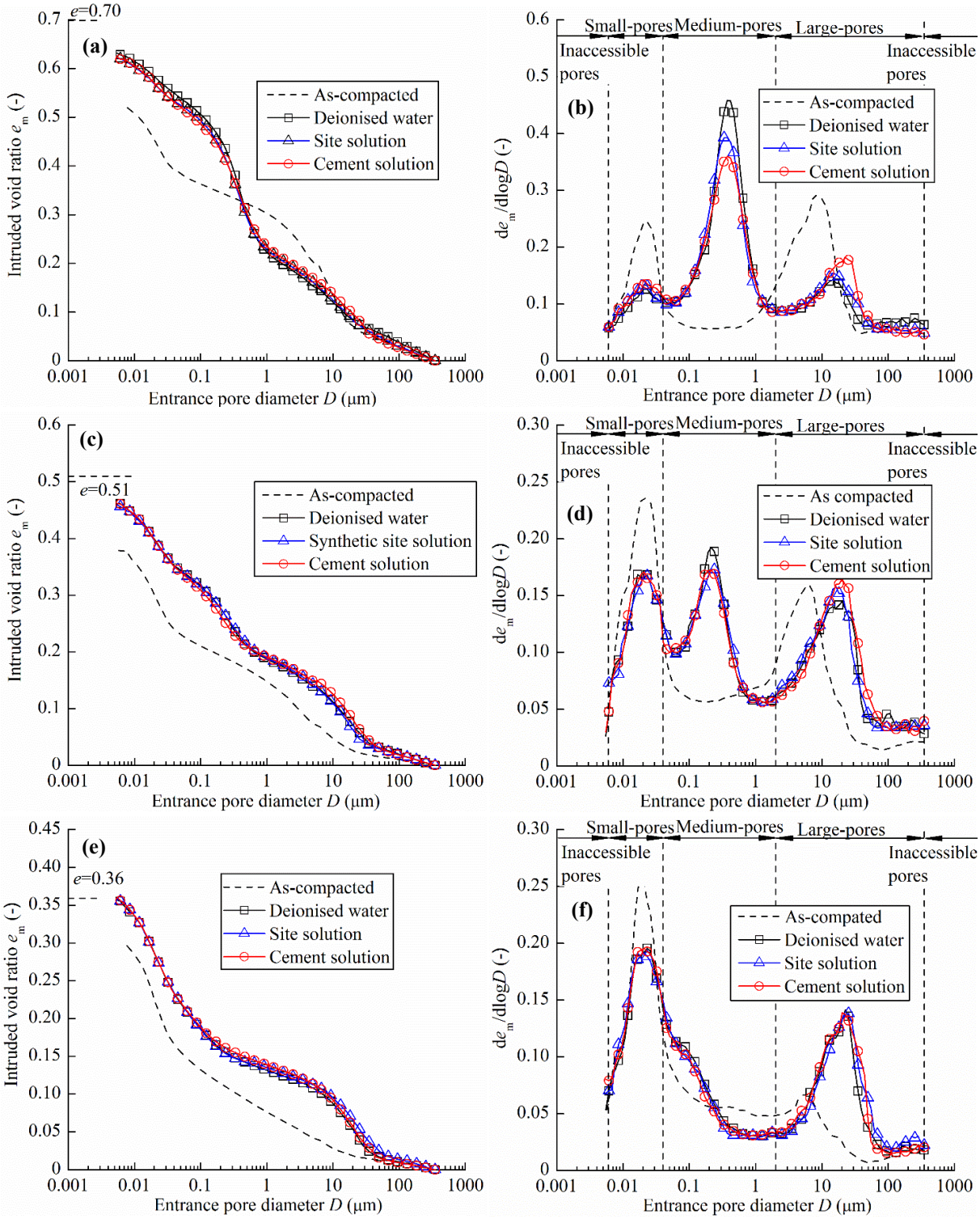

Fig. 6. Pore size distribution of MX80 bentonite/claystone mixtures: (a) cumulative curves of specimens at a dry density of 1.6 Mg/m^3, (b) density function curves of specimens at a dry density of 1.6 Mg/m^3, (c) cumulative curves of specimens at a dry density of 1.8 Mg/m^3, (d) density function curves of specimens at a dry density of 1.8 Mg/m^3, (e) cumulative curves of specimens at a dry density of 2.0 Mg/m^3 and (f) density function curves of specimens at a dry density of 2.0 Mg/m^3

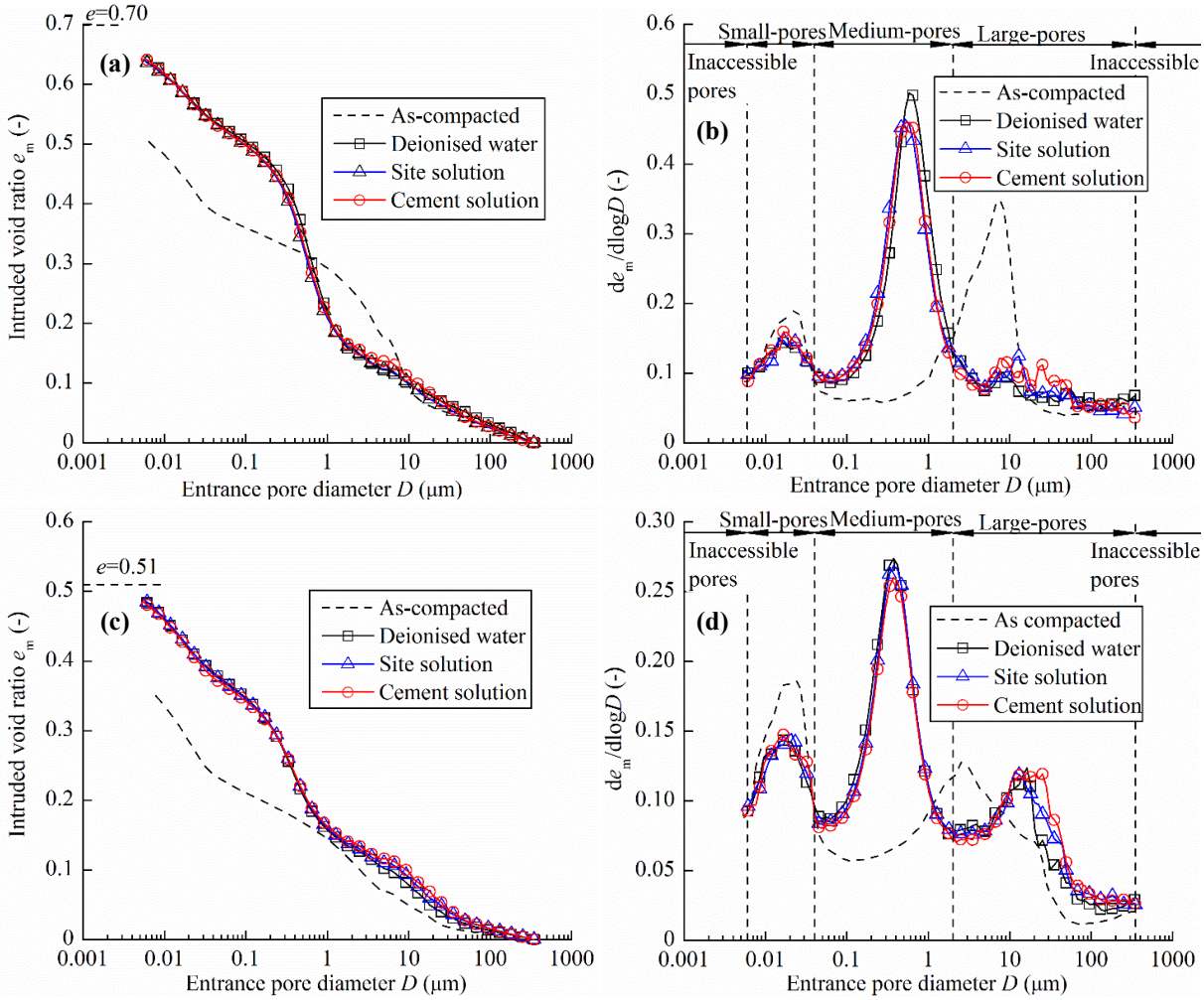

Fig. 7. Pore size distribution of Sardinia bentonite/claystone mixtures: (a) cumulative curves of specimens at a dry density of 1.6 Mg/m^3, (b) density function curves of specimens at a dry density of 1.6 Mg/m^3, (c) cumulative curves of specimens at a dry density of 1.8 Mg/m^3 and (d) density function curves of specimens at a dry density of 1.8 Mg/m^3

4 Interpretation and discussion

4.1 Effects of synthetic site solution and cement solution on hydro-mechanical behaviour

When the clay minerals in the bentonite/claystone mixtures were wetted with water, their hydration could be described by crystalline and osmotic swelling processes (Mitchell, 1993). At a low relative humidity, crystalline hydration is the predominant mechanism with water molecules being progressively adsorbed on the clay surfaces layer by layer, leading to an increase of the intra-aggregate pore volume. Meanwhile, the swollen aggregates invaded the inter-aggregate pores and reduced the inter-aggregate-pore volume. Obviously, this process depended on the global dry density. The lower the dry density, the more significant the swelling of aggregates. With the transformation of intra-aggregate and inter-aggregate pores to the medium-pore population, a remarkable increase of medium-pore void ratio occurred (Figs. 8

and 9). During the crystalline swelling process, the clay particles would be divided into smaller ones and fissure-like 2-dimensional (2-D) pores with a mean pore size of 20 μm appeared. The variation of large-pore volume after hydration was due to the combined effects of the invasion of swollen clay particles and the appearance of 2-D pores. As the suction decreased down to 4 MPa, the crystalline swelling reached a nearly steady state and a significant amount of water would be stored in inter-particle pores (Saiyouri et al., 2000). Due to the difference of cation concentration between the pore water and the clay particle surface, diffuse double layer would develop on a parallel assembly of clay particles (Liu, 2013) and osmotic swelling took place.

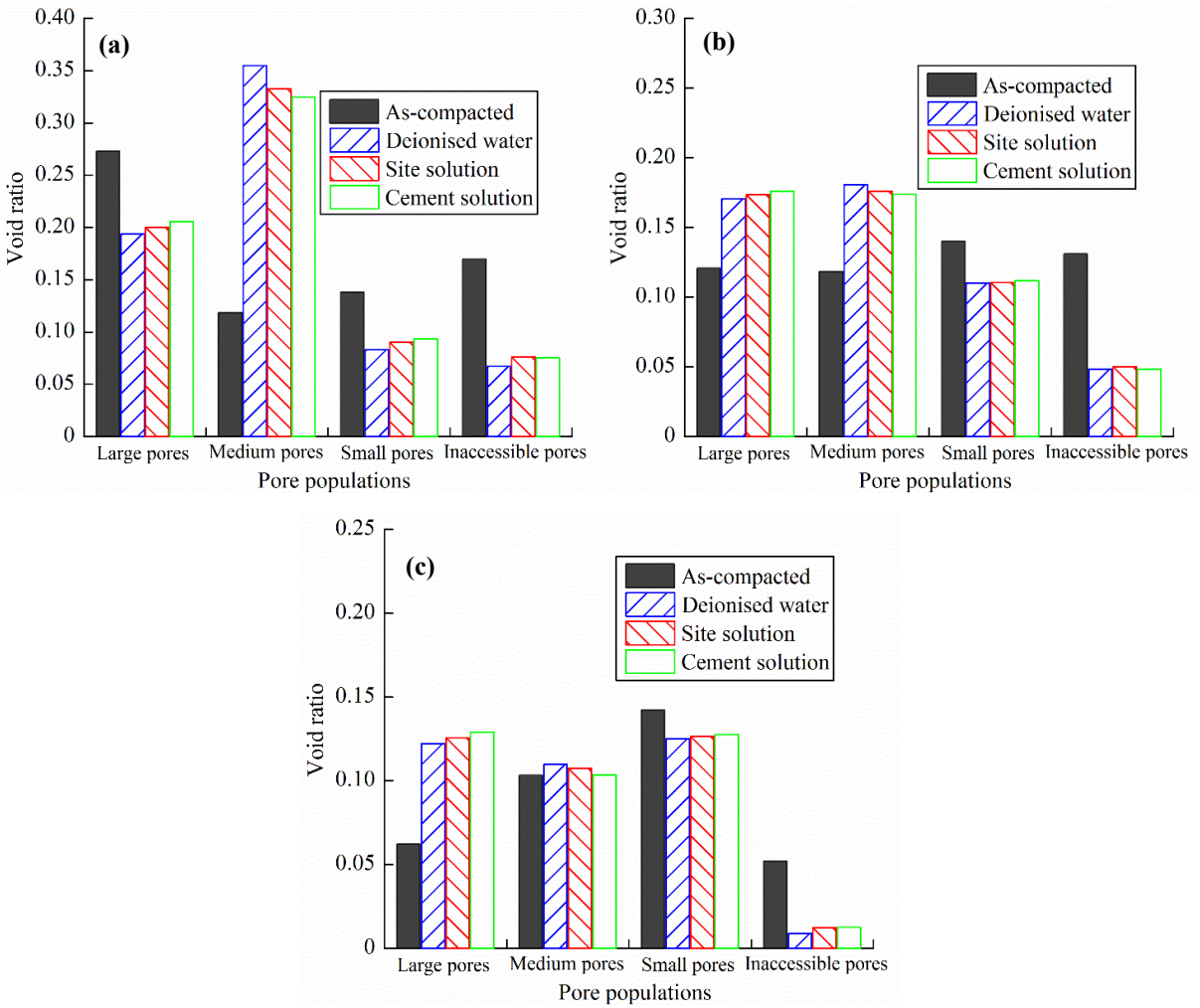

Fig. 8. Changes in inaccessible-pore, small-pore, medium-pore and large-pore void ratios for the compacted MX80 bentonite/claystone mixtures. (a) 1.6 Mg/m^3, (b) 1.8 Mg/m^3 and (c) 2.0 Mg/m^3

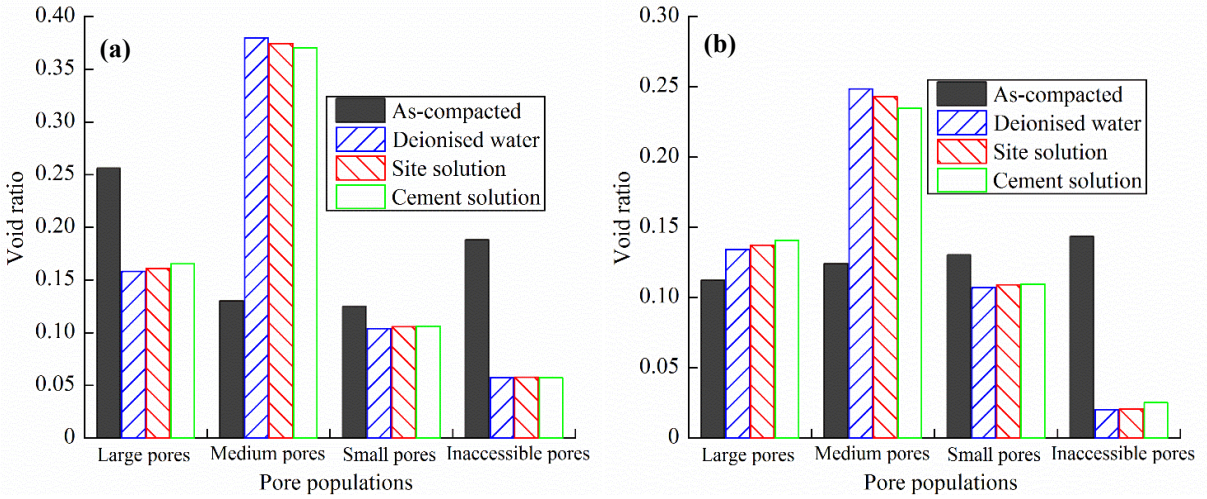

Fig. 9. Changes in inaccessible-pore, small-pore, medium-pore and large-pore void ratios for the compacted Sardinia bentonite/claystone mixtures. (a) 1.6 Mg/m^3 and (b) 1.8 Mg/m^3

Generally, the maximum number of water molecule layers intercalated between the unit layers depends on the clay type and the available cations in the permeating water (Marcial et al., 2002; Liu, 2013). If the cation in the pore water is characterized by a high replacing power, cation exchanges can take place and the clay type will change. A typically competitive order that has been commonly admitted is: $Na^+<K^+<Mg^{2+}<Ca^{2+}$ (Mitchell, 1993; Mata, 2003; Sun et al., 2018). As shown in Table 3, the synthetic site solution and cement solution used in this study contain a certain amount of K^+, Mg^{2+} or Ca^{2+} cations. According to the X-Ray diffractometry (XRD) results on GMZ bentonite by Sun et al. (2019), Na-montmorillonite would be transformed to Mg-/Ca- dominant montmorillonite and Ca- dominant montmorillonite after the interaction with synthetic site solution and cement solution, respectively. During the crystalline swelling process, the water adsorption capacity of Na-montmorillonite was larger than that for Ca-montmorillonite (Liu, 2013; Du et al., 2020; Yotsuji et al., 2021). Therefore, this transformation of Na-montmorillonite would decrease the swelling capacity of the montmorillonite. Additionally, as the cation concentration of pore water increased, the repulsive force between the diffuse double layer and the thickness of the diffuse double layer decreased (Yong and Warkentin, 1975; Mitchell, 1976). Consequently, a lower swelling pressure was observed for the specimens hydrated with synthetic site solution (Fig. 4). At a given global void ratio, this decreased distance between clay particles leads to an increase of the large-pore void ratio. As a result, a larger hydraulic conductivity was observed for the specimens hydrated with synthetic site solution (Fig. 5) (Cuisinier et al., 2011).

Apart from the cations, the hydroxide in the cement solution can also greatly influence the

hydro-mechanical behaviour of the bentonite/claystone mixtures. Upon contact with hydroxide, the montmorillonite might be dissolved, forming secondary minerals with much lower swelling capacity, such as analcime and calcium hydrated silicates gels (Sun et al., 2018; 2019). As result, the swelling capacity was reduced (Fig. 4). The produced calcium hydrated silicates gels were characterized by a large amount of small pores (Wang et al., 2017), leading to an increase of small-pore void ratio of the specimens hydrated with cement solution (Figs. 8 and 9) (Sun et al., 2019; Liu et al., 2020). By contrast, the dissolution of montmorillonite would lead to an increase of the large-pore volume (Chen et al., 2016). Compared to the specimens hydrated with synthetic site solution, the specimens could be affected by the hydroxide in addition to the cations. Thus, the specimens hydrated with cement solution exhibited a larger large-pore volume and a higher hydraulic conductivity compared with those hydrated with synthetic site solution (Fig. 5).

4.2 Effects of bentonite type and dry density on hydro-mechanical behaviour

Basically, the synthetic site solution and cement solution can influence the hydro-mechanical behaviour of bentonite-based materials mainly by means of cation exchanges, osmotic effect and montmorillonite dissolution. After the MX80 bentonite/claystone and Sardinia bentonite/claystone mixtures were in contact with synthetic site solution, cation exchanges could occur in the MX80 bentonite/claystone mixture, with the transformation of some Na-montmorillonite to Mg-, and Ca- montmorillonite, while the Sardinia bentonite/claystone mixture would be immune to the cation exchange. This would reduce the swelling capacity of MX80 bentonite/claystone mixture. Thus, a slightly smaller increasing rate of swelling pressure for this mixture in stage I for MX80 bentonite/claystone mixture, as compared to that hydrated with deionised water (Fig. 3a and b). Thanks to the higher permeability, the interaction between clay minerals and solution became more intensive for the MX80 bentonite/claystone mixture at a lower dry density upon the hydration with the synthetic site solution. By contrast, the cations in the synthetic site solution would exert an influence on the osmotic swelling of both the MX80 bentonite/claystone and the Sardinia bentonite/claystone mixtures at low dry densities. In general, the clay particles of Na-montmorillonite after crystalline swelling are thinner than those of Ca-montmorillonite (Saiyouri et al., 2004). It was reported that the clay particles are composed of 2–20 (and even more) aligned unit layers in Ca-montmorillonite, but only of 1–5 unit layers in Na-montmorillonite (Liu, 2013). Therefore, during the osmotic swelling process, few double layer development could be expected in the Ca-montmorillonite, as compared to the Na-montmorillonite. The weaker osmotic swelling of Sardinia bentonite/claystone mixture

could not compensate the reduction of swelling pressure induced by the collapse of aggregate structure. Thus, a more significant decrease was observed in stage II at low dry densities (Fig. 3a and b). Additionally, the cations in the synthetic site solution could reduce the repulsive force and the thickness of diffuse double layer, resulting in a lower swelling pressure and a higher hydraulic conductivity for the specimens hydrated with synthetic site solution (Figs. 4 and 5). For the specimens at high dry densities, the low amount of inter-particle water was insufficient to form the diffuse double layer (Pusch and Yong, 2006) and the effect of cations on the swelling pressure and hydraulic conductivity of the highly compacted MX80 bentonite/claystone and Sardinia bentonite/claystone mixtures was less significant.

5 Conclusions

The effects of synthetic site solution and cement solution on the hydro-mechanical behaviour of compacted Na^+ MX80 bentonite/claystone and Ca^{2+} Sardinia bentonite/claystone mixtures were investigated by carrying out a series of swelling pressure and hydraulic conductivity tests together with microstructure observation. The results obtained allow the following conclusions to be drawn:

For the MX80 bentonite/claystone mixture, the cations in synthetic site solution could transform the Na-montmorillonite to multi-cation dominant montmorillonite, reducing the swelling capacity of the mixture. By contrast, for the Sardinia bentonite/claystone mixture, the cations in synthetic site solution did not significantly change the Ca-montmorillonite during the crystalline swelling. Thus, an insignificant effect was identified on the swelling pressure.

During the osmotic swelling, the presence of cations reduced the repulsive force by diffuse double layer and thus swelling pressure for both the MX80 bentonite/claystone and Sardinia bentonite/claystone mixtures. Additionally, a smaller thickness of diffuse double layer and a greater large-pore volume could be expected for the specimens hydrated with synthetic site solution. Thus, a slightly higher saturated hydraulic conductivity was obtained in that case, as compared to the case of deionised water. Furthermore, a more significant influence of synthetic site solution was observed on the specimens at a lower dry density thanks to the well-developed diffuse double layer.

In addition to the cations, the hydroxide also reduced the swelling pressure of both the MX80 bentonite/claystone and Sardinia bentonite/claystone mixtures. The hydroxide led to a slight increase of large-pore volume and thus an increase of saturated hydraulic conductivity.

Moreover, the lower the dry density, the more intensive the interaction between the montmorillonite and hydroxide and the more significant the changes in swelling pressure and hydraulic conductivity, due to the higher permeability.

Over the experiment time scale of 90 days, only a slight deterioration of sealing performance of the bentonite/claystone mixture was identified due to the low cation concentration and the low ionic strength of permeating solutions. The effect of water chemistry in the very long-term lifespan of the underground radioactive waste repository needs to be investigated in further work.

Acknowledgments

The research work was supported by Ecole des Ponts ParisTech and the French National Radioactive Waste Management Agency (Andra). The first author is grateful to the China Scholarship Council for the grant scholarship.

References

Anh, H.N., Ahn, H., Jo, H.Y., Kim, G.Y., 2017. Effect of alkaline solutions on bentonite properties. Environmental Earth Sciences, 76(10), 374.

Bian, X., Cui, Y.J., Li, X.Z., 2019. Voids effect on the swelling behaviour of compacted bentonite. Géotechnique, 69(7), 593-605.

Cara, S., Carcangiu, G., Padalino, G., Palomba, M., Tamanini, M., 2000. The bentonites in pelotherapy: chemical, mineralogical and technological properties of materials from Sardinia deposits (Italy). Applied Clay Science, 16(1-2), 117-124.

Castellanos, E., Villar, M.V., Romero, E., Lloret, A., Gens, A., 2008. Chemical impact on the hydro-mechanical behaviour of high-density FEBEX bentonite. Physics and Chemistry of the Earth, Parts A/B/C 33, S516-S526.

Chen, B., Guo, J.X., Zhang, H.X., 2016. Alteration of compacted GMZ bentonite by infiltration of alkaline solution. Clay Minerals, 51(2), 237-247.

Cuisinier, O., Deneele, D., Masrouri, F., 2009. Shear strength behaviour of compacted clayey soils percolated with an alkaline solution. Engineering geology, 108(3-4), 177-188.

Cuisinier, O., Auriol, J.C., Le Borgne, T., Deneele, D., 2011. Microstructure and hydraulic conductivity of a compacted lime-treated soil. Engineering geology, 123(3), 187-193.

Delage, P., Audiguier, M., Cui, Y.J., Howat, M.D., 1996. Microstructure of a compacted silt. Canadian Geotechnical Journal, 33(1), 150-158.

Delage, P., Marcial, D., Cui, Y.J., Ruiz, X., 2006. Ageing effects in a compacted bentonite: a

microstructure approach. Géotechnique, 56(5), 291-304.

Deng, Y.F., Tang, A.M., Cui, Y.J., Nguyen, X.P., Li, X.L., Wouters, L., 2011. Laboratory hydro-mechanical characterisation of Boom Clay at Essen and Mol. Physics and Chemistry of the Earth, Parts A/B/C, 36(17-18), 1878-1890.

Dixon, D.A., Gray, M.N., Thomas, A.W., 1985. A study of the compaction properties of potential clay-sand buffer mixtures for use in nuclear fuel waste disposal. Eng. Geol. 21(3/4): 247-255.

Du, J.P., Zhou, A.N., Lin, X., Bu, Y., Kodikara, J., 2020. Revealing expansion mechanism of cement-stabilized expansive soil with different interlayer cations through molecular dynamics simulations. The Journal of Physical Chemistry C, 124(27), 14672-14684.

Du, J.P., Zhou, A.N., Lin, X., Bu, Y., Kodikara, J., 2021. Prediction of swelling pressure of expansive soil using an improved molecular dynamics approach combining diffuse double layer theory. Applied Clay Science, 203, 105998.

Gaucher, É. C., Blanc, P., Bardot, F., Braibant, G., Buschaert, S., Crouzet, C., Altmann, S. 2006. Modelling the porewater chemistry of the Callovian–Oxfordian formation at a regional scale. Comptes Rendus Geoscience, 338(12-13), 917-930.

Heikola, T., Kumpulainen, S., Vuorinen, U., Kiviranta, L., Korkeakoski, P., 2013. Influence of alkaline (pH 8.3–12.0) and saline solutions on chemical, mineralogical and physical properties of two different bentonites. Clay Minerals, 48(2), 309-329.

Herbert, H., Kasbohm, J., Sprenger, H., Fernández, A.M., Reichelt, C., 2008. Swelling pressures of MX-80 bentonite in solutions of different ionic strength. Phys. Chem. Earth, 33, S327–S342.

Karnland, O., Olsson, S., Nilsson, U., 2006. Mineralogy and sealing properties of various bentonites and smectite-rich clay materials. Technical Report No. TR-06-30. SKB, Swedish Nuclear Fuel and Waste Management Co.

Karnland, O., Olsso, S., Nilsson, U., Sellin, P., 2007. Experimentally determined swelling pressures and geochemical interactions of compacted Wyoming bentonite with highly alkaline solutions. Phys. Chem. Earth, 32(1–7), 275–286.

Komine, H., Yasuhara, K., Murakami, S., 2009. Swelling characteristics of bentonites in artificial seawater. Can. Geotech. J., 46, 177–189.

Lee, J.O., Lim, J.G., Kang, I.M., Kwon, S., 2012. Swelling pressures of compacted Cabentonite. Eng. Geol. 129-130, 20–26.

Liu, L., 2013. Prediction of swelling pressures of different types of bentonite in dilute solutions. Colloids and Surfaces A: Physicochemical and Engineering Aspects, 434, 303-318.

Liu, L.N., Chen, Y.G., Ye, W.M., Cui, Y.J., Wu, D.B., 2020. Swelling pressure deterioration of compacted GMZ bentonite and its structural damage under heat combined with hyperalkaline conditions. Geomechanics and Geoengineering, 1-12.

Mata, C., 2003. Hydraulic behaviour of bentonite based mixtures in engineered barriers: the Backfill and Plug Test at the A ¨ spo ¨ HRL (Sweden). (Ph.D. Thesis) Universitat Polite'cnica de Catalunya, Barcelona (257 pp.).

Marcial, D., Delage, P., Cui, Y.J., 2002. On the high stress compression of bentonites. Canadian Geotechnical Journal, 39(4), 812-820.

Mitchell, J.K., 1976. Fundamentals o f Soil Behaviour. 1st edition. J. Wiley and Sons Publishers, Toronto.

Mitchell, J.K., 1993. Fundamentals of soil behaviour, 2nd edn. John Wiley and sons, New York.

Middelhoff, M., 2020. Hydro-mechanical behavior of claystone-based backfill materials under geo-environmental conditions. PhD thesis, Universit éde lorraine.

Nguyen, X.P., Cui, Y.J., Tang, A.M., Deng, Y.F., Li, X.L., Wouters, L., 2013. Effects of pore water chemical composition on the hydro-mechanical behavior of natural stiff clays. Engineering geology, 166, 52-64.

Pusch, R., 1982. Mineral–water interactions and their influence on the physical behavior of highly compacted Na bentonite. Canadian Geotechnical Journal, 19(3): 381-387.

Pusch, R., Karnland, O., 1988. Geological evidence of smectite longevity: The Sardinian and Gotland cases. Svensk k ärnbr änslehantering.

Pusch, R., Yong, R.N., 2006. Microstructure of smectite clays and engineering performance. CRC Press.

Rao, S.M., Thyagaraj, T., Thomas, H.R., 2006. Swelling of compacted clay under osmotic gradients. G éotechnique, 56(10), 707–713.

Saiyouri, N., Hicher, P.Y., Tessier, D., 2000. Microstructural approach and transfer water modelling in highly compacted unsaturated swelling clays. Mechanics of Cohesive ‐ frictional Materials: An International Journal on Experiments, Modelling and Computation of Materials and Structures, 5(1), 41-60.

Saiyouri, N., Tessier, D., Hicher, P.Y., 2004. Experimental study of swelling in unsaturated compacted clays. Clay minerals, 39(4), 469-479.

S ánchez, L., Cuevas, J., Ram írez, S., De Le ón, D.R., Fern ández, R., Villa, R.V.D., Leguey, S., 2006. Reaction kinetics of FEBEX bentonite in hyperalkaline conditions resembling the cement–bentonite interface. Applied Clay Science, 33(2), 125-141.

Savage, D., Noy, D., Mihara, M., 2002. Modelling the interaction of bentonite with hyperalkaline fluids. Appl. Geochem. 17, 207–223.

Schanz, T., Tripathy, S., 2009. Swelling pressure of a divalent ‐ rich bentonite: Diffuse double ‐ layer theory revisited. Water Resources Research, 45(5).

Sellin, P. Leupin, O.X., 2013. The use of clay as an engineered barrier in radioactive-waste management–a review.Clays and Clay Minerals, 61(6), 477-498.

Siddiqua S, Blatz, J., Siemens, G., 2011. Evaluation of the impact of pore fluid chemistry on the hydromechanical behavior of claybased sealing materials. Can Geothech J, 48, 199–213.

Sun, Z., Chen, Y.G., Cui, Y.J., Xu, H.D., Ye, W.M., Wu, D.B., 2018. Effect of synthetic water and cement solutions on the swelling pressure of compacted Gaomiaozi (GMZ) bentonite: the Beishan site case, Gansu, China. Engineering Geology, 244, 66-74.

Sun, Z., Chen, Y.G., Cui, Y.J., Ye, W.M., Chen, B., 2019. Effect of synthetic Beishan site water and cement solutions on the mineralogy and microstructure of compacted Gaomiaozi (GMZ) bentonite. Soils and Foundations, 59 (6), 2056-2069.

Sun, Z., Chen, Y.G., Ye, W.M., Cui, Y.J., Wang, Q., 2020. Swelling deformation of Gaomiaozi bentonite under alkaline chemical conditions in a repository. Engineering Geology, 279, 105891.

Villar, M.V., 2006. Infiltration tests on a granite/bentonite mixture: Influence of water salinity. Applied Clay Science, 31(1-2), 96-109.

Villar, M.V., Lloret, A. 2008. Influence of dry density and water content on the swelling of a compacted bentonite. Appl. Clay Sci. 39(1–2), 38–49.

Vitale, E., Deneele, D., Russo, G., 2016. Multiscale analysis on the behaviour of a lime treated bentonite. Procedia Engineering, 158, 87-91.

Wang, Q., Cui, Y.J., Tang, A.M., Delage, P., Gatmiri, B., Ye, W.M., 2014. Long-term effect of water chemistry on the swelling pressure of a bentonite-based material. Applied clay science, 87, 157-162.

Wang, Y., Duc, M., Cui, Y.J., Tang, A.M., Benahmed, N., Sun, W.J., Ye, W.M., 2017. Aggregate size effect on the development of cementitious compounds in a lime-treated soil during curing. Applied Clay Science, 136, 58-66.

Wileveau, Y., Bernier, F. (2008). Similarities in the hydromechanical response of Callovo-Oxfordian clay and Boom Clay during gallery excavation. Physics and Chemistry of the Earth, Parts A/B/C, 33, S343-S349.

Ye, W.M., Chen, Y.G., Chen, B., Wang, Q., Wang, J., 2010. Advances on the knowledge of the buffer/backfill properties of heavily-compacted GMZ bentonite. Engineering Geology, 116(1-2), 12-20.

Yong, R.N., Warkentin, B.P., 1975. Soil Properties and Behaviour. Elsevier, Amsterdam.

Yotsuji, K., Tachi, Y., Sakuma, H., Kawamura, K., 2021. Effect of interlayer cations on montmorillonite swelling: Comparison between molecular dynamic simulations and experiments. Applied Clay Science, 204, 106034.

Yukselen-Aksoy, Y., Kaya, A., Ören, A.H., 2008. Seawater effect on consistency limits and compressibility characteristics of clays. Eng. Geol., 102, 54–61.

Zeng, Z.X., Cui, Y.J., Zhang, F., Conil, N., Talandier, J., 2019. Investigation of swelling

pressure of bentonite/claystone mixture in the full range of bentonite fraction. Applied Clay Science.

Zeng, Z., Cui, Y. J., Conil, N., Talandier, J., 2020a. Experimental Investigation and Modeling of the Hydraulic Conductivity of Saturated Bentonite–Claystone Mixture. International Journal of Geomechanics, 20(10), 04020184.

Zeng, Z., Cui, Y.J., Conil, N., Talandier, J., 2020b. Effects of technological voids and hydration time on the hydro-mechanical behaviour of compacted bentonite/claystone mixture. Géotechnique, 1-14.

Zhu, C.M., Ye, W.M., Chen, Y.G., Chen, B., Cui, Y.J., 2013. Influence of salt solutions on the swelling pressure and hydraulic conductivity of compacted GMZ01 bentonite. Eng. Geol., 166, 74–80.

Zeng, Z.X., Cui, Y.J., Talandier, J. 2021. Submitted to Engineering Geology.

Long-term effect of water chemistry on the swelling pressure and hydraulic conductivity of compacted claystone/bentonite mixture with technological gaps

Zhixiong Zeng[1], Yu-Jun Cui[1], Jean Talandier[2]

Abstract: A compacted mixture of Callovo-Oxfordian (COx) claystone/MX80 bentonite is a promising sealing material in the French Cigéo project for radioactive waste disposal at great depth. Over time, the sealing material will be saturated by the site water originating from the surrounding rock and the water chemistry can affect the performance of the sealing material. In this study, the effects of water chemistry and technological gaps on the hydro-mechanical property were investigated by performing hydration tests on the compacted claystone/bentonite mixture with technological gaps using deionised water and synthetic site solution for 10 and 590 days. After the tests, the dry density, water content and microstructure distributions were also determined to complement the program. Results show that the synthetic site solution did not affect the swelling pressure and hydraulic conductivity after a short term of 10 days. With the increase of hydration time, the specimens with technological gaps tended to be homogeneous, resulting in a reduction of hydraulic conductivity. Because of the cation exchanges and the decreased diffuse double layer thickness, the synthetic site solution reduced the swelling pressure and increased the hydraulic conductivity in long term, especially for the specimens with lower global dry densities.

Keywords: claystone/bentonite mixture; swelling pressure; hydraulic conductivity; technological gaps; water chemistry

1 Introduction

Bentonite-based materials are the most suitable sealing/backfill material in underground radioactive waste repositories because of the high swelling potential, low permeability and favorable retention property (Villar and Lloret, 2008; Sellin and Leupin, 2013). One of the possibilities is to pre-compact the bentonite-based materials into blocks and then installed into shafts and drifts. During the installation of compacted blocks, technological gaps inevitably remain between blocks and at the interfaces with the host rock. Upon hydration, the swelling

1 Laboratoire Navier/CERMES, Ecole des Ponts ParisTech, 6 et 8 avenue Blaise Pascal, 77455 Marne La Vallée cedex 2, France
2 Andra, 1/7, rue Jean Monnet, 92298 Châtenay-Malabry cedex, France

of the compacted blocks will close technological gaps and prevent polluted fluid migration. After that, a swelling pressure will be generated, confining the excavation damaged zone of host rock and thus reducing the fluid flow via this zone (Darde et al., 2020). To this end, the hydro-mechanical property developed by the compacted bentonite-based materials with technological gaps are key factors in the safety assessment of the underground repositories.

The hydro-mechanical property of bentonite-based materials with initial technological gaps has been investigated by many researchers (Villar et al., 2005; 2019; Bian et al., 2019; Jia et al., 2019; Watanabe et al., 2021). It has been found that the technological gaps led to a heterogeneous dry density distribution upon hydration (Bian et al., 2019). The heterogeneity of dry density distribution could decrease with the increase of hydration time (Zeng et al., 2020a) but it would remain over a long time due to the boundary friction with the host rock (Zeng et al., 2020b).

In addition, the pore water of the host rock is of certain salinity (Wang et al., 2014a). It has been documented that the cations in the pore water significantly affected the crystalline swelling process (Wang et al., 2014a) as well as the montmorillonite type through the cation exchanges (Sun et al., 2018). Given that other factors are the same, larger replacing power could be expected for the cation with a higher valence. Moreover, the cations in pore water could influence the diffuse double layer thickness during osmotic swelling process (Siddiqua et al., 2011; Castellanos et al., 2008). Generally, the larger the solution concentration, the lower the net repulsive stress and the smaller the final swelling pressure (Mitchell, 1976; Chen et al., 2018). The interaction of bentonite-based materials with the pore water could alter the size of the available channel for water flow and influence the hydraulic conductivity (Pusch, 2001; Villar et al., 2006; Chen et al., 2015). The diffuse double layer thickness would reduce with the increasing cation concentration of pore water (Yong and Warkentin, 1975; Zhu et al., 2013). Therefore, at a given void ratio, a higher hydraulic conductivity could be expected for a specimen hydrated with a higher cation concentration due to the poor development of diffuse double layers (Castellanos et al., 2008).

In France, a compacted mixture comprising crushed Callovo-Oxfordian (COx) claystone and a minor content of bentonite is a possible sealing material for the economical and environment reasons (Zhang, 2014; Middelhoff, 2020). Zeng et al. (2020a) studied the hydro-mechanical property of claystone/bentonite mixture with 10 and 20% technological gaps during 90-day hydration. They found that the heterogeneity because of the existent of technological gaps could

lead to a more significant aeolotropic swelling behaviour and a higher hydraulic conductivity compared to the case without technological gaps (Zeng et al., 2020a). Unfortunately, the effect of pore water chemistry was not addressed in their study. Wang et al. (2014a) examined the swelling pressure evolution of compacted COx claystone/MX80 bentonite at short and long time scales. They found that the synthetic site solution had no obvious influence on the swelling pressure at 100 h but a significant decrease (9%) was observed for the specimen saturated with site solution after 700 days. Note that their study was limited to the swelling behaviour of mixture with a bentonite content of 70%. For the mixture with less claystone, the influence of water chemistry can be different due to the lower content of clay mineral. Middelhoff (2020) conducted a series of hydration test on compacted COx claystone/MX80 bentonite mixture with a bentonite content of 30% (dry density of 1.72 Mg/m^3) and indicated that synthetic site solution had negligible impacts on swelling pressure after 7 days and on hydraulic conductivity after 1 year. However, few systematic studies have been focused on the long-term effect of site solution on the hydro-mechanical property of claystone/bentonite mixture at low amount of bentonite with technological gaps.

In the present work, hydration tests were first conducted on the COx claystone/MX80 bentonite mixture with various technological gaps for 10 and 590 days using deionised water and synthetic site solution. The long-term effects of site water chemistry and technological gaps on the hydro-mechanical property of compacted blocks were investigated. After that, water content, dry density and microstructure distributions of the specimen were measured, allowing better understanding the influence mechanism of site solution chemistry and technological gaps.

2 Materials and experimental methods

2.1 Materials

The material studied in the present study was a mixture comprising 70% COx claystone and 30% MX80 bentonite (Wyoming, USA) in weight. The COx claystone was produced by excavation of drifts in Andra URL at about -490 m (Bure, France). The bentonite and claystone were processed to maximum grain diameters of 2.0 m. Fig. 1 depicts the grain size distributions of bentonite and claystone obtained by dry-sieving and hydrometer methods. The respective average grain diameters D_{50} of dry bentonite and claystone are 0.55 and 0.58 mm. This similarity allows a relatively homogeneous state by mixing. The main physico-chemical characteristics of bentonite and claystone are presented in Table 1. The equivalent specific gravity and initial water content of the mixture are 2.72 and 7.7%, respectively.

Table 1. Physico-chemical characteristics of MX80 bentonite and COx claystone

Property	MX80 bentonite	COx claystone
Initial water content (%)	11.4	6.1
Specific gravity	2.76	2.76
Liquid limit (%)	494	520
Plastic limit (%)	46	42
Plasticity index (%)	448	478
CEC (meq/100 g)	78-85[a]	22[b]
Na+	62.4-66.8[a]	2.9[b]
K+	0.2-1.3[a]	2.6[b]
Mg2+	3-4[a]	4.6[b]
Ca2+	6.6-7.4[a]	11.7[b]
Main minerals	Montmorillonite (86%)	Interstratified illite/smectite (40-45%)[c]
	Quartz (7%)	Carbonates (30%)[c]

[a] Herbert et al. (2004; 2008); [b] Middelhoff (2020); [c] Fouché et al. (2004)

In this study, the specimens were hydrated with both deionised water and synthetic site solution. The synthetic site solution simulates the working conditions of the sealing material in the repository. The composition of synthetic site solution corresponds to the pore water of claystone formation. It was obtained by dissolving the chemical components (Table 2) in deionised water.

Table 2. Recipe for the synthetic site solution preparation

Component	NaCl	$NaHCO_3$	KCl	$CaSO_4$▪$2H_2O$	$MgSO_4$▪$7H_2O$	$CaCl_2$▪$2H_2O$	Na_2SO_4
Content (g/L)	1.950	0.130	0.035	0.630	1.020	0.080	0.700

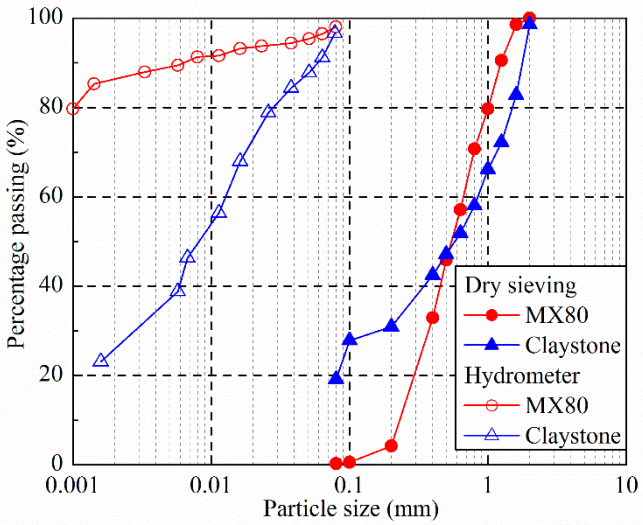

Fig. 1. Grain size distribution of MX80 bentonite and crushed COx claystone

2.2 Experimental methods

The mixture was first compacted statically in a rigid steel ring at a controlled rate of 0.05 mm/min. The compacted specimens are 50 mm in diameter and 10 mm in height and the target dry density is 2.0 Mg/m^3. Eight identical compacted specimens were prepared in total. Among

them, six compacted specimens were trimmed into smaller diameters of 44.72 mm (ST01 and LT05) and 47.43 mm (ST02-03 and LT06-07) (Table 3). Then, the trimmed specimens were installed and centered in the testing cell (a diameter of 50 mm) (Fig. 2). The specimens were placed between two metallic porous stones and filter papers. Afterwards, the cells were closed by placing the upper cap and the cap was then blocked with a screw to restrain the axial swell (Fig. 3). The lateral gaps between the trimmed specimens and cell wall were equal to 10 and 20% of the total volume, corresponding to 1.8 and 1.6 Mg/m^3 global dry densities. Afterwards, synthetic site solution was supplied from the bottom in tests ST01-02 and LT05-06, while specimens ST03 and LT07 were hydrated with deionised water. For comparison, specimens ST04 and LT08 were directly transferred into the testing cell and no gap was left at the interface with cell wall. Then, the specimens were saturated with site solution under a water head of about 1 m. As shown in Table 3, ST and LT stand for short and long terms, respectively. For tests ST, the specimens were hydrated for 10 days while for tests LT, the specimens were hydrated for about 590 days. During the hydration, the axial swelling force was measured with a force transducer. For tests ST01-02 and LT05-06, a pressure sensor was installed in the middle of specimens to monitor the radial pressure. At the end of swelling pressure tests, the hydraulic conductivity of all the specimens was determined using constant-head method, following the French standard AFNOR (2008). To minimise the disturbance on the microstructure, the respective water pressures were 40, 100 and 200 kPa for the specimens at 1.6, 1.8 and 2.0 Mg/m^3 global dry densities, which were smaller than a tenth of the maximum swelling pressures.

Table 3. Experimental programme

Test No.	Technological gaps (%)	Dry density (Mg/m^3)	Injected water	Swelling pressure	Duration (days)	MIP
ST01	20	1.6	Synthetic	Axial and radial	10	√
ST02	10	1.8	Synthetic	Axial and radial		√
ST03	10	1.8	Deionised	Axial only		-
ST04	0	2.0	Synthetic	Axial only		√
LT05	20	1.6	Synthetic	Axial and radial	590	√
LT06	10	1.8	Synthetic	Axial and radial		√
LT07	10	1.8	Deionised	Axial only		√
LT08	0	2.0	Synthetic	Axial only		√

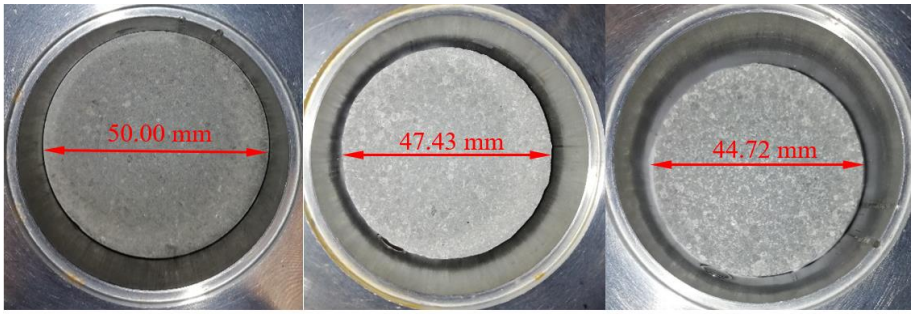

Fig. 2. Preparation of specimens with and without technological gaps

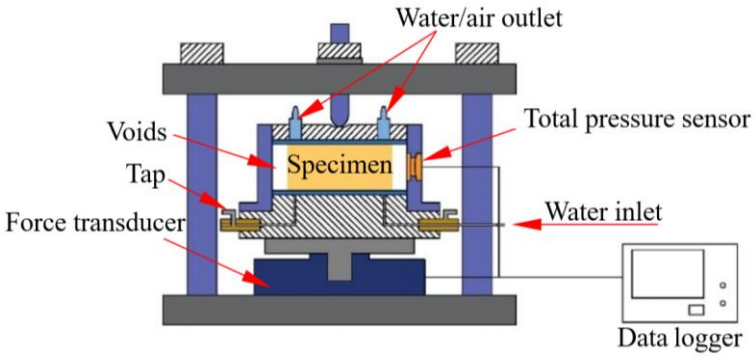

Fig. 3. Sketch of the experimental set-up used for the infiltration tests

After prescribed hydration times, the specimens were taken out of the cell for the determination of water content, dry density and microstructure feature. For the tests with initial technological gaps (ST01-03 and LT05-07), the specimens were divided into three zones, namely outer, middle and central (Fig. 4). Outer zone represents a ring with a 40 inner diameter and a 50 mm outer diameter, corresponding to the technological gaps; middle zone refers to a ring of 20 and 40 mm in inner and outer diameters, respectively; central zone is a cylinder of 20 mm in diameter. Afterwards, each zone was cut into several cubes. For the tests without gaps (ST04 and LT08), the specimens were directly cut into cubes. The water content of the soils was determined after drying in the oven at 105°C for 24 h and the dry density was derived from the Archimedes' buoyancy after immersion in an immiscible oil (commercial Kerdane). The microstructure observation was also carried out by the use of mercury intrusion porosimetry (MIP). The samples were first frozen with liquid nitrogen and dehydrated in a freeze-drier for 24 h. Subsequently, the freeze-dried samples were subjected to vacuum and filled with mercury, and then put into a pressure chamber with a maximum mercury pressure of 228 MPa. Correspondingly, the maximum and minimum intruded pore diameters were 350 and 0.006 μm, respectively.

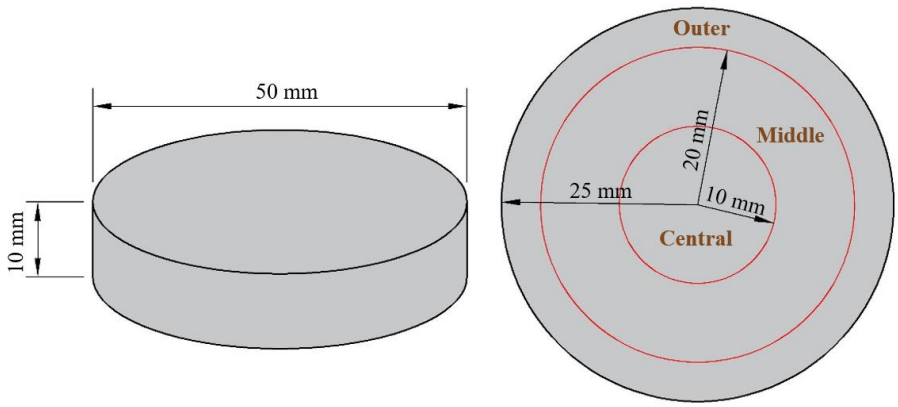

Fig. 4. Schematic view of the specimen cutting

3 Experimental results

3.1 Swelling pressures

Fig. 5 presents the kinetics of axial and radial swelling pressures for the specimens with initial technological gaps. The curves of identical specimens were quite similar, suggesting the excellent repeatability of the hydration tests. As shown in Fig. 5a, the axial swelling pressure started with an increase at the beginning of hydration. For the specimens without technological gaps or with 10% technological gaps, the axial swelling pressures stabilised after 58.3 and 7.4 h, respectively. For the specimens with 20% technological gaps, the axial swelling pressure increased until reaching a peak, then decreased, and stabilised at 5.8 h. By contrast, the radial swelling pressure was not detected at the beginning for the specimens with technological gaps. After 0.08 and 0.18 h, the radial swelling pressure became measurable and reached a first stability stage after about 7.5 and 5.7 h in the case of 10 and 20% gaps, respectively (Fig. 5b). As far as the water chemistry was concerned, the swelling pressure curves of the specimens hydrated with deionised water and synthetic site solution for 10 days were fairly similar, suggesting a negligible effect of water chemistry in short term (Fig. 5). Fig. 6 compares the axial swelling pressures of tests LT05-08 during 590 days. The axial swelling pressure for the specimens with initial gaps decreased from 10 to 590 days, especially for those hydrated with synthetic site solution. For clarity, the unified axial swelling pressure, the ratio of the axial swelling pressure to the value at 10 days, was calculated. Fig. 7 illustrates the kinetics of unified axial swelling pressure with the hydration time from 10 to 590 days. For the specimen without technological gaps (LT08) and the specimen hydrated with deionised water (LT07), the axial swelling pressure remained almost constant over this period. For the specimens with 10% and 20% technological gaps and hydrated with synthetic site solution, the axial swelling pressure decreased by 4 and 13% respectively. As the technological gaps increased, the decrease was

more significant. Additionally, the variations of axial and radial swelling pressures after 10 and 590 days of hydration with the global dry density are also summarised in Fig. 8. There were linear relationships between the axial and radial swelling pressures and global dry density. The fitted curved at 590 days lied below that at 10 days. The specimens with 10% technological gaps (LT06-07) hydrated with deionised water and synthetic site solution exhibited almost the same axial swelling pressure at 10 days. However, compared to that hydrated with deionised water, a remarkably lower axial swelling pressure was observed on the specimen hydrated synthetic site solution after 590 days.

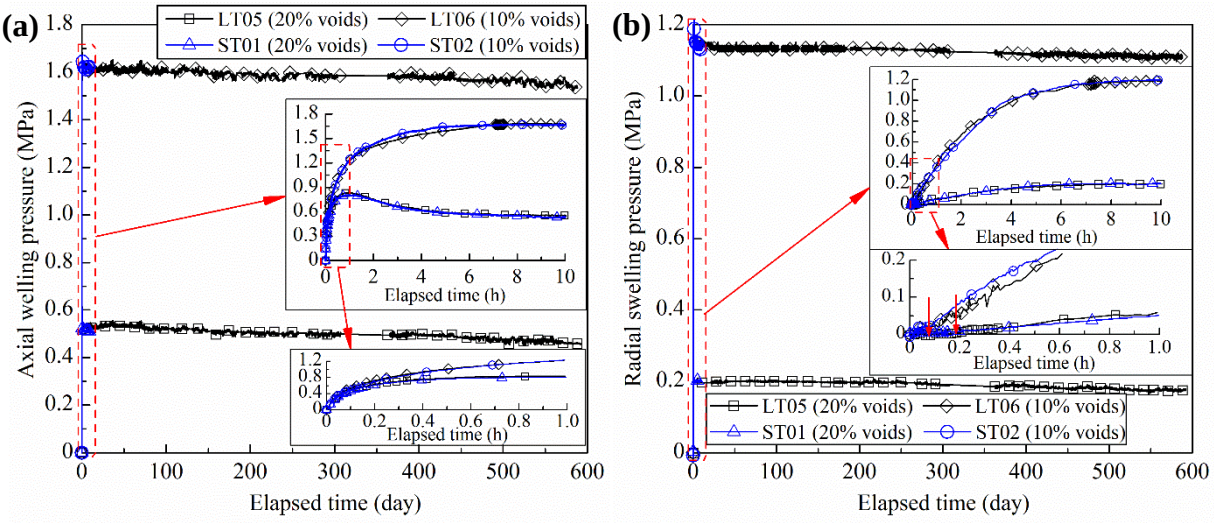

Fig. 5. Evolutions of axial and radial swelling pressures with elapsed time for the specimens with 10 and 20% technological gaps: (a) axial swelling pressure and (b) radial swelling pressure

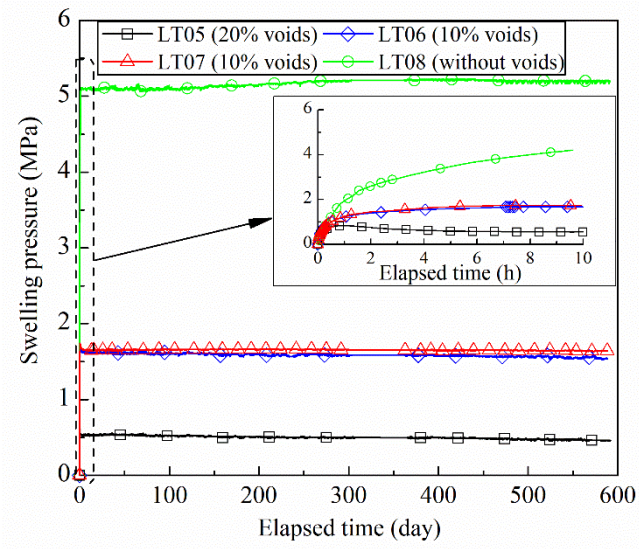

Fig. 6. Evolutions of axial swelling pressure with elapsed time for the specimens with and without technological gaps

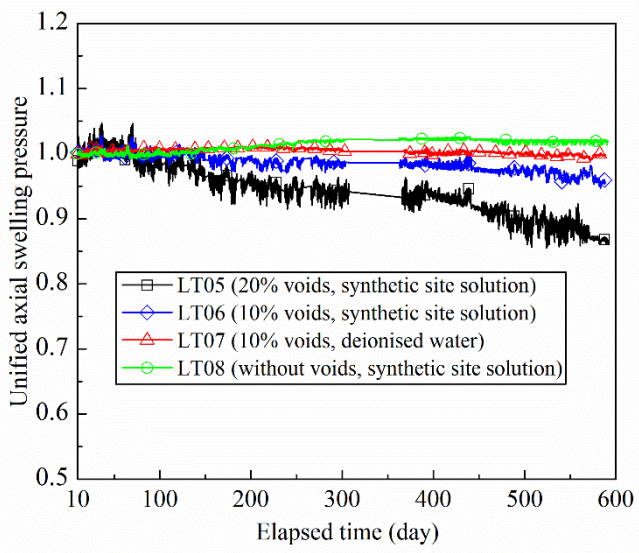

Fig. 7. Evolutions of unified axial swelling pressure with elapsed time for the specimens with and without technological gaps

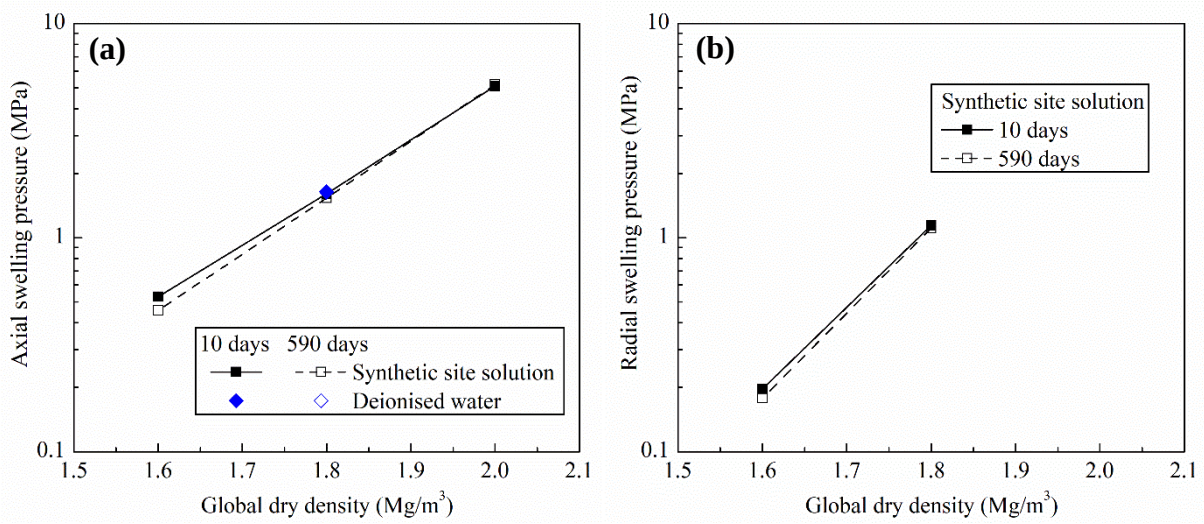

Fig. 8. Relationship between final axial and radial swelling pressures and global dry density: (a) axial swelling pressure and (b) radial swelling pressure

3.2 Hydraulic conductivity

Fig. 9 presents the hydraulic conductivities of specimens with various technological gaps after 10 and 590 days. After hydration with synthetic site solution for 10 days, the respective hydraulic conductivities of the specimens with 1.6, 1.8 and 2.0 Mg/m^3 global dry densities were 1.50×10^{-11}, 3.49×10^{-12} and 7.07×10^{-13} m/s. On the whole, the hydraulic conductivity reduced linearly as the global dry density increased. Under further hydration, the hydraulic conductivity decreased. After 590 days of hydration, the respective hydraulic conductivities decreased to 1.29×10^{-11}, 1.97×10^{-12} and 6.07×10^{-13} m/s for the specimens with 1.6, 1.8 and 2.0 Mg/m^3 global dry densities. This hydraulic conductivity reduction became more considerable as the

global dry density decreased. For the specimens with 10% technological gaps hydrated with synthetic site solution and deionised water, the hydraulic conductivity was quite close at 10 days. After 590 days, the specimen hydrated with synthetic site solution (LT06) exhibited a significantly larger hydraulic conductivity than that hydrated with deionised water (LT07).

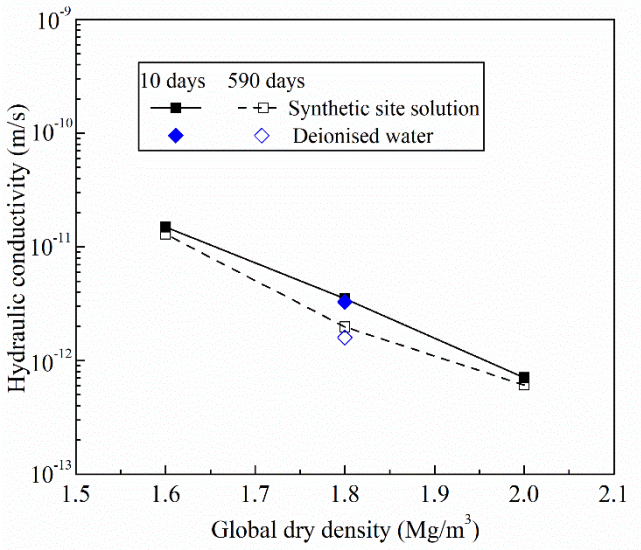

Fig. 9. Relationship between final hydraulic conductivity and global dry density

3.3 Water content and dry density distributions

After the hydration tests, the water content and dry density distributions of specimens with initial technological gaps were determined. As shown in Fig. 10, after 10-day hydration, the specimens with initial technological gaps exhibited significant heterogeneous distributions of water content and dry density. The outer zone which included the initial technological gaps had lower dry densities and larger water contents than the middle and central zones. While the technological gaps increased, the dry density and water content distributions were more heterogeneous. Moreover, the dry densities of middle and central zones were larger than the global one while the dry density of outer zone was lower, as shown in Fig10a. Upon further hydration, the denser zones (middle and central zones) could undergo further swelling which decreased the dry density, while the looser zone (outer zone) was compressed by the swelling pressure (Bian et al., 2019). As a result, the dry density heterogeneity decreased with further hydration. Although the heterogeneity decreased, it was still persistent after 590 days of hydration.

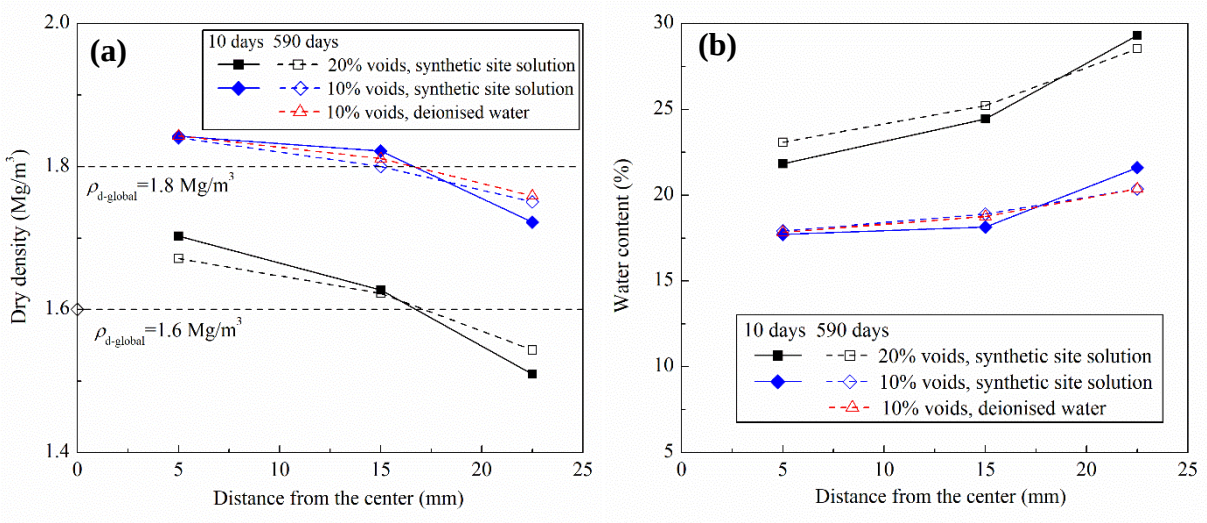

Fig. 10. Dry density and water content distributions of the specimens with technological gaps: (a) dry density and (b) water content

3.4 Microstructure features

The cumulative curves and corresponding density curves are presented in Fig. 11 for specimens with 20% gaps, Fig. 12 for specimens with 10% gaps and Fig. 13 for specimens without technological gaps. The specimens with initial technological gaps exhibited a heterogeneous distribution of microstructure. As shown in Figs. 11a and 12a, the cumulative curves of outer zone lie above those of middle and central zones. As the hydration time increased from 10 to 590 days, the cumulative curves of middle and central zones went up while that of outer zone went down, resulting in a more homogenous distribution of microstructure. Similarly, for the specimens without gaps, the cumulative curve of the specimen hydrated for 590 days (ST04) lied below that of the specimen hydrated for 10 days (LT08) (Fig. 13a). Comparison of the specimens hydrated with various solutions shows that the cumulative curve of the specimens with synthetic site solution (LT06) lied above those of the specimens with deionised water (LT07) after 590 days (Fig. 12a). For all the specimens, the total intruded void ratios were lower than that deduced from the measured dry density, which could be ascribed to the limitation of MIP technique.

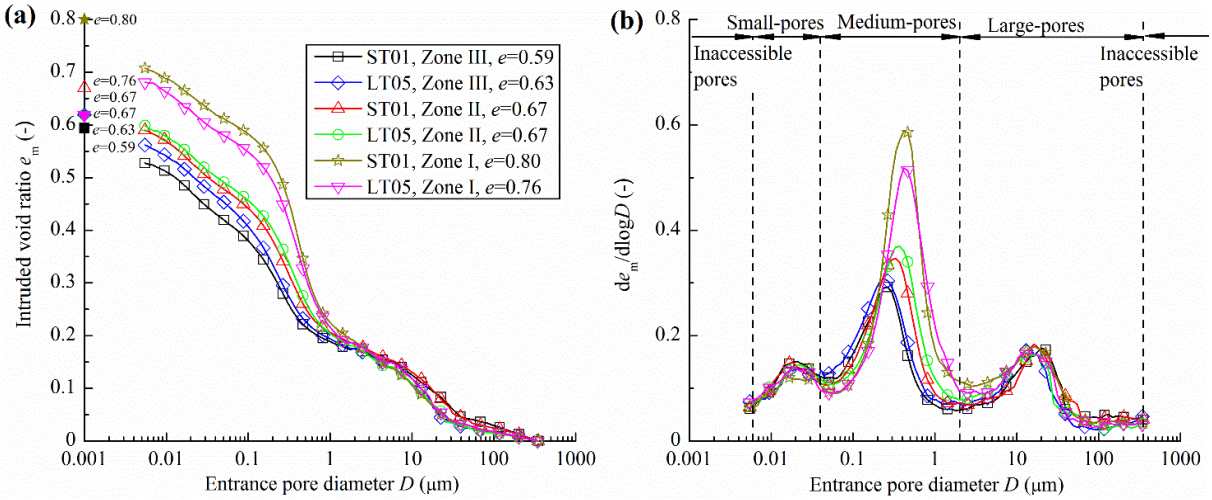

Fig. 11. MIP results of the specimens with 20% technological gaps: (a) cumulative curves and (b) density function curves

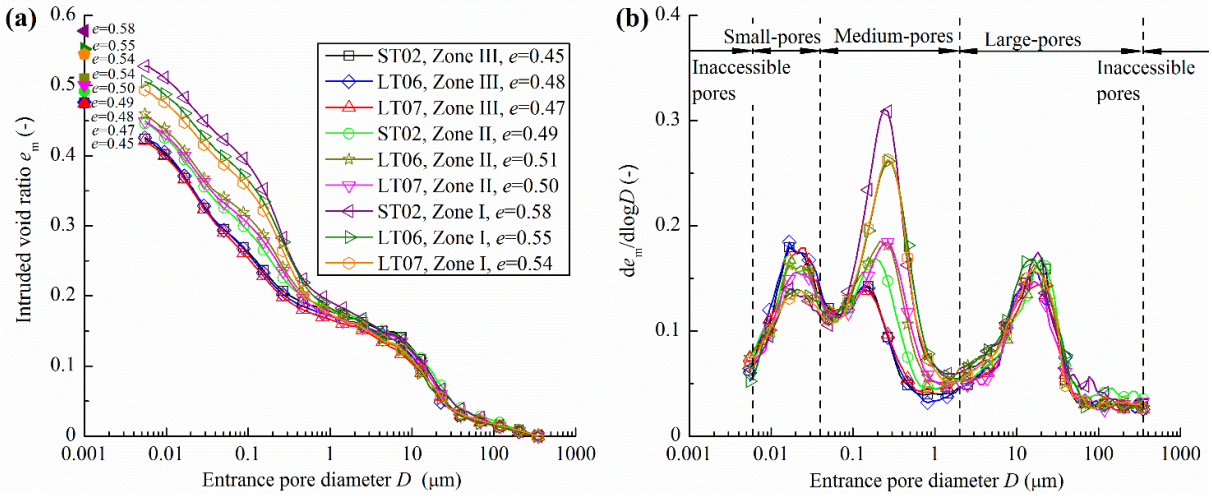

Fig. 12. MIP results of the specimens with 10% technological gaps: (a) cumulative curves and (b) density function curves

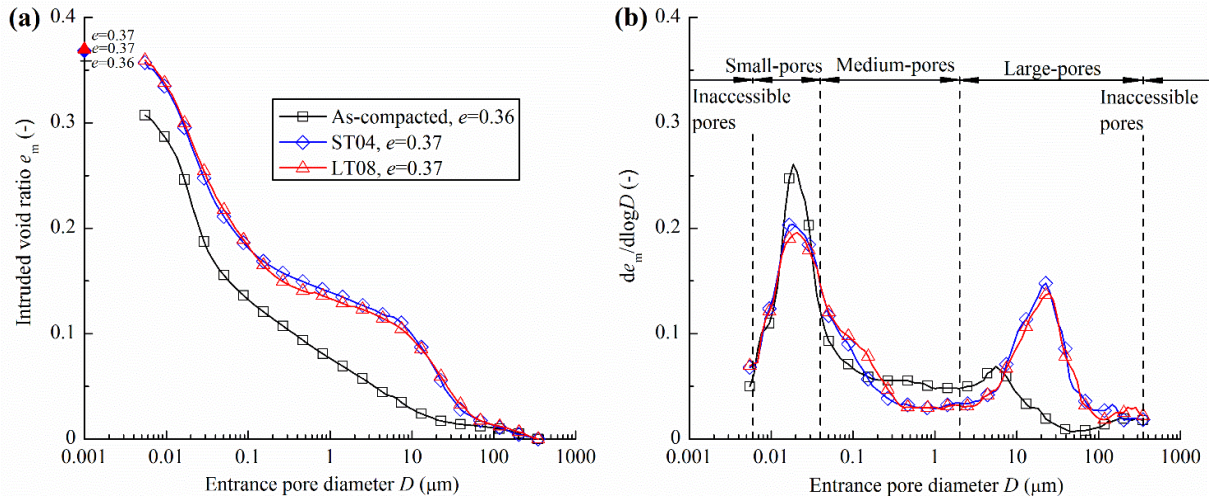

Fig. 13. MIP results of the specimens without technological gaps: (a) cumulative curves and (b) density function curves

From Fig. 13b, a bimodal pore distribution was identified for the as-compacted specimen at 2.0 Mg/m^3 dry density, with dominant large pores (around 6 μm) and dominant small pores (around 0.02 μm). For the specimens without technological gaps, the hydration was accompanied by an increase of the diameter of large pores and a decrease of the peak value of small pores, even though the distribution was still bimodal (Fig. 13b). For the specimens with technological gaps, the hydration not only increased the large-pore diameter and reduced the peak value of small pores, but also led to an additional population with a diameter of 0.17-0.40 μm between the two peaks (termed as medium pores) (Figs. 11b and 12b). As suggested by Wang et al. (2014b), 2 and 0.04 μm were taken as the delimiting diameters between large and medium pores and between medium and small pores, respectively. According to the cumulative curves and the delimiting diameters, the large-pore, medium-pore and small-pore void ratios of the specimens after different hydration times are summarised in Fig. 14. Also presented in Fig. 14 is the void ratio of inaccessible pores (<0.006 or >350 μm). The larger the technological gaps, the higher the large-pore, medium-pore and inaccessible-pore void ratios and the smaller the small-pore void ratio. On the whole, outer zone of the specimens with technological gaps (ST01-02) exhibited a smaller small-pore void ratio but higher inaccessible-pore, medium-pore and large-pore void ratios than middle and central zones at 10 days. As the hydration time increased from 10 to 590 days, the medium-pore and large-pore void ratios of outer zone decreased. By contrast, the large-pore void ratio of middle and central zones decreased and the medium-pore void ratio increased gradually. Additionally, the void ratios of pore populations of the specimens hydrated with synthetic site solution and deionised water for 590 days are also compared in Fig. 15. The specimen hydrated with synthetic site solution (LT06) showed slightly higher large-pore and small-pore void ratios but smaller medium-pore and inaccessible-pore void ratios compared to that hydrated with deionised water (LT07).

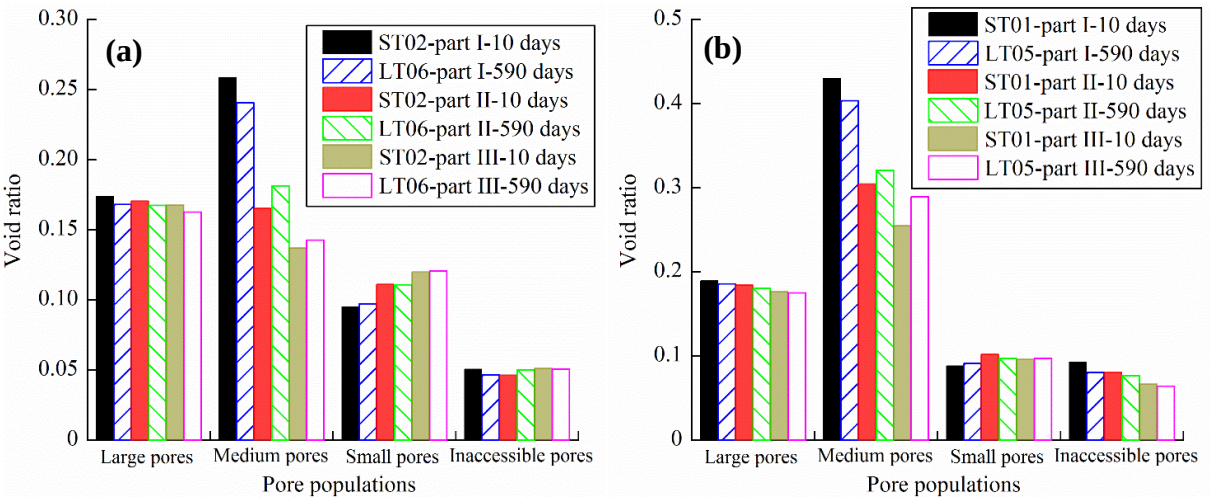

Fig. 14. Void ratios of different pore populations of the specimens with technological gaps after different times of hydration with synthetic site solution: (a) 10% technological gaps and (b) 20% technological gaps

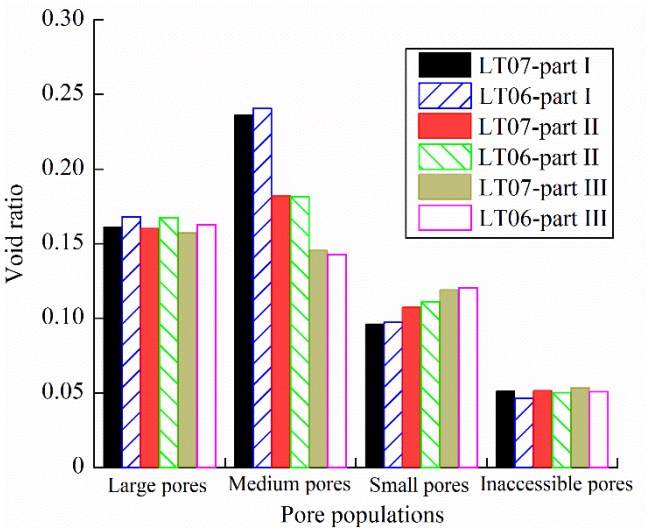

Fig. 15. Void ratios of different pore populations of the specimens with 10% technological gaps after 590 days of hydration with deionised water and synthetic site solution

4 Interpretation and discussion

When the hydration started, water rapidly filled the technological gaps. The compacted blocks imbibed water from the lateral side as well as the top and bottom. The hydration of compacted block with technological gaps could be characterised by two main processes: a filling process and a homogenization process (Zeng et al., 2020a). During the filling process, the dry density of the external zone of the compacted blocks decreased quickly while that of the internal zone decreased slowly due to the larger wetting distance. This resulted in a heterogeneous dry density distribution: the outer zone had a smaller dry density while the middle and central zones

exhibited larger ones (Fig. 10a). Upon further hydration, the specimen was subjected to a homogenisation process, with an increasing dry density in outer zone and a decreasing dry density in middle and central zones. However, after 590 days of hydration, the dry density distribution for the specimen with technological gaps was still heterogeneous (Fig. 10a). Zeng et al. (2020b) reported that the friction between specimens and porous stones resisted the homogenisation process and the heterogeneity could be persistent forever.

During the filling process, water molecules entered and intercalated between the clay layers of the side zone of the compacted blocks, increasing the inter-layer space. The clay aggregates swelled and increased the intra-aggregate pore size. Meanwhile, the swelling of clay aggregates could invade the pores between aggregates and reduce the inter-aggregate pore volume. The merging of increased intra-aggregate pores (small pores) and reduced inter-aggregate pores (large pores) corresponded to the appearance of medium pores. During the swelling of aggregates, fissure-like 2-dimensional (2-D) pores with an average diameter of 20 μm could appear with the division of clay aggregates into smaller ones (Wang et al., 2014b). This explained why the large-pore volume increased upon hydration. During the homogenization process, the large and medium pores for outer zone corresponding to the initial technological gaps would be compressed, resulting in decreases of the larger-pore and medium-pore volumes (Fig. 14). Contrastingly, middle and central zones further swelled with a decrease of small-pore volume and increases of medium-pore and large-pore volumes. In long term, the large-pore volume would slightly decrease due to the water redistribution (Delage et al., 2006). Commonly, fluid flow through soils was highly related to the large-pore volume (Cuisinier et al., 2011; Wang et al., 2013). While the large-pore volume of three zones increased from 10 to 590 days, a lower hydraulic conductivity was observed in the case of 590-day hydration (Fig. 9).

In addition to the technological gaps, the water chemistry of the site solution could also influence the hydro-mechanical property of claystone/bentonite mixture. The hydration of bentonite-based material mainly includes crystalline and osmotic swelling processes (Mitchell, 1993). The crystalline swelling process represents the stepwise insertion of water molecule layers in interlayer space. The maximum number of water molecules mainly depends on the type of clay. For instance, up to four water molecule layers can be adsorbed between clay layers for Na-montmorillonite under free-swell conditions but three for Ca- montmorillonite (Liu, 2013). When a montmorillonite was saturated with saline solution, cation exchange can occur, which is mainly controlled by the nature of exchangeable cation and the available cations in the

permeating water. A typically competitive order is: $Na^+<K^+<Mg^{2+}<Ca^{2+}$ (Mitchell, 1993; Wang et al., 2014a). In this study, when the claystone/MX80 bentonite mixture was saturated with synthetic site solution, the Na-bentonite could be transformed to K-, Mg- or Ca- bentonite. Subsequent to the adsorption of water molecules on clay surfaces, the electrical double-layer repulsion is the principal driving power for further swelling. Generally, with the increase of saline solution concentration, the diffuse double layer thickness and net repulsive stress would decrease (Yong and Warkentin, 1975; Mitchell, 1976). In the case of high specimen dry densities, the effect of water chemistry on crystalline and osmotic swelling processes could be less significant due to the lower permeability and the poor development of diffusion double layer (Pusch and Yong, 2006; Wang et al., 2014a), at least in short term. This explained why the synthetic site solution with lower salinity had a negligible influence on the hydro-mechanical property in the case of 10-day hydration. With further hydration, the cations in synthetic site solution could weaken the swelling process and lead to a lower a swelling pressure than that with deinoised water after 590 days of hydration (Fig. 7). Moreover, the smaller the global dry density, the more intensive the interaction between synthetic site solution and clay minerals due the higher permeability and the more remarkable the swelling pressure reduction. Owing to the constriction of interlayer space, a larger large-pore volume was observed on the specimen hydrated with synthetic solution (LT06), compared to that hydrated with deionised water (LT07) (Fig. 15). After 590 days of hydration, the specimen hydrated with synthetic site solution exhibited a larger hydraulic conductivity than that hydrated with deionised water (Fig. 9) because of the larger large-pore volume.

From Fig. 7, the axial swelling pressure decreased by 4 and 13% after 590 days of hydration with synthetic site solution in the case of 1.8 and 1.6 Mg/m^3 global dry densities respectively. Wang et al. (2014a) identified a decrease of 9% after 700 days of hydration while dealing with the swelling behaviour for COx claystone/MX80 bentonite with a proportion of 30/70 in weight and at 1.70 Mg/m^3 dry density. Additionally, similar microstructure changes after hydration were also observed on claystone/bentonite mixtures with proportions of 70/30 and 30/70 in weight. It appears that the synthetic site solution exerted a similar influence on the swelling behaviour of claystone/bentonite mixtures disregarding bentonite content. The influence of water chemistry on the swelling behaviour for claystone/bentonite mixture at a low bentonite content could not be ignored in long term thanks to its high permeability, even though the clay mineral content was low.

5 Conclusions

Hydration tests with different solutions were conducted on compacted claystone/bentonite mixtures with various technological gaps, allowing the effects of water chemistry and technological gaps on the hydro-mechanical property to be investigated. The involved mechanisms of the swelling pressure and hydraulic conductivity variations were further examined by analysing the microstructure features. According to the obtained results, the following conclusions were drawn.

In short term, the presence of technological gaps led to significant heterogeneity of dry density distribution. While the gaps increased, the swelling pressures reduced and the hydraulic conductivity increased. The synthetic site solution had a negligible influence on the swelling pressure and hydraulic conductivity for specimens with technological gaps.

As the hydration time increased, the heterogeneity because of the existent of technological gaps would decrease. It appears from the microstructure observation that the large pores of external zone were compressed by the swelling of the internal zones and the large-pore void ratio of internal zones decreased owing to the water redistribution, reducing the hydraulic conductivity.

In long term, the synthetic site solution weakened the swelling process and increased the large-pore volume due to cation exchange and diffuse double layer shrinking. A lower swelling pressure and a larger hydraulic conductivity were observed on specimens hydrated with synthetic site solution, especially for those at a low dry density.

The claystone/bentonite mixture at a low bentonite content was not immune to the water chemistry thanks to its high permeability, although the clay mineral content was low. The synthetic site solution could reduce the sealing property of claystone/bentonite mixtures regardless of bentonite content. It is recommended to take into account such water chemistry effect in assessing the long-term performance of sealing materials.

Acknowledgments

The authors gratefully thank Andra and Ecole des Ponts ParisTech for their support. The first author gratefully acknowledges China Scholarship Council for grant scholarship.

References

AFNOR, 2008. De´termination a` l'oedoperme´ame`tre des caracte´ristiques de gonflement – Flux et perme´abilite´ des ge´osynthe´tiques bentonitiques (GSB). (Oedopermeameter Determination of Swelling Characteristics – Flux and Permeability of Geosynthetic Clay Liners (GCL)). French standard NF P 84 705. French Association for Normalization, Paris.

Bian, X., Cui, Y.J., Li, X.Z., 2019. Voids effect on the swelling behaviour of compacted bentonite. Géotechnique, 69(7), 593-605.

Castellanos, E., Villar, M.V., Romero, E., Lloret, A., Gens, A., 2008. Chemical impact on the hydro-mechanical behaviour of high-density FEBEX bentonite. Physics and Chemistry of the Earth, Parts A/B/C 33, S516-S526.

Chen, Y.G., Zhu, C.M., Ye, W.M., Cui, Y.J., Wang, Q., 2015. Swelling pressure and hydraulic conductivity of compacted GMZ01 bentonite under salinization–desalinization cycle conditions. Applied Clay Science, 114, 454-460.

Chen, Y.G., Dong, X.X., Zhang, X.D., Ye, W.M., Cui, Y.J., 2018. Combined thermal and saline effects on the swelling pressure of densely compacted GMZ bentonite. Applied Clay Science, 166, 318-326.

Cuisinier, O., Auriol, J.C., Le Borgne, T. and Deneele, D., 2011. Microstructure and hydraulic conductivity of a compacted lime-treated soil. Engineering geology, 123(3), 187-193.

Darde, B., Dangla, P., Roux, J.N., Pereira, J.M., Talandier, J., Vu, M.N., Tang, A.M., 2020. Modelling the behaviour of bentonite pellet-powder mixtures upon hydration from dry granular state to saturated homogeneous state. Engineering Geology, 278, 105847.

Delage, P., Marcial, D., Cui, Y.J., Ruiz, X., 2006. Ageing effects in a compacted bentonite: a microstructure approach. Géotechnique, 56(5), 291-304.

Fouché, O., Wright, H., Le Cléac'h, J.M., Pellenard, P. 2004. Fabric control on strain and rupture of heterogeneous shale samples by using a non-conventional mechanical test. Applied Clay Science, 26(1-4), 367-387.

Herbert, H.J., Kasbohm, J., Moog, H.C., Henning, K.H. 2004. Long-term behaviour of the Wyoming bentonite MX-80 in high saline solutions. Applied Clay Science, 26(1-4), 275-291.

Herbert, H.J., Kasbohm, J., Sprenger, H., Fernández, A.M., Reichelt, C. 2008. Swelling pressures of MX-80 bentonite in solutions of different ionic strength. Physics and Chemistry of the Earth, Parts A/B/C, 33, S327-S342.

Jia, L.Y., Chen, Y.G., Ye, W.M., Cui, Y.J., 2019. Effects of a simulated gap on anisotropic swelling pressure of compacted GMZ bentonite. Engineering Geology, 248, 155-163.

Liu, L., 2013. Prediction of swelling pressures of different types of bentonite in dilute solutions. Colloids and Surfaces A: Physicochemical and Engineering Aspects, 434, 303-318.

Mitchell, J.K., 1976. Fundamentals of Soil Behaviour. 1st edition. J. Wiley and Sons Publishers, Toronto.

Mitchell, J.K., 1993. Fundamentals of soil behaviour, 2nd edn. John Wiley and sons, New York.

Middelhoff, M., 2020. Hydro-mechanical behavior of claystone-based backfill materials under geo-environmental conditions. PhD thesis, Université de lorraine.

Pusch, R., 2001. Experimental Study of the Effect of High Porewater Salinity on the Physical Properties of a Natural Smectitic Clay. SKB Technical Report TR-01-07, Stockholm.

Pusch, R., Yong, R.N., 2006,Microstructure of Smectite Clays and Engineering Performance, Taylor & Francis, London and New York.

Sellin, P. Leupin, O.X., 2013. The use of clay as an engineered barrier in radioactive-waste management–a review.Clays and Clay Minerals, 61(6), 477-498.

Siddiqua S, Blatz, J., Siemens, G., 2011. Evaluation of the impact of pore fluid chemistry on the hydromechanical behavior of claybased sealing materials. Can Geothech J, 48, 199–213.

Sun, Z., Chen, Y.G., Cui, Y.J., Xu, H.D., Ye, W.M., Wu, D.B., 2018. Effect of synthetic water and cement solutions on the swelling pressure of compacted Gaomiaozi (GMZ) bentonite: the Beishan site case, Gansu, China. Engineering Geology, 244, 66-74.

Villar, M.V., García-Siñeriz, J.L., Bárcena, I., Lloret, A., 2005. State of the bentonite barrier after five years operation of an in situ test simulating a high level radioactive waste repository. Engineering Geology, 80(3-4), 175-198.

Villar, M.V., 2006. Infiltration tests on a granite/bentonite mixture: Influence of water salinity. Applied Clay Science, 31(1-2), 96-109.

Villar, M.V., Lloret, A., 2008. Influence of dry density and water content on the swelling of a compacted bentonite. Appl. Clay Sci. 39(1–2), 38–49.

Villar, M.V., Iglesias, R.J., García-Siñeriz, J.L., Lloret, A., Huertas, F., 2019. Physical evolution of a bentonite buffer during 18 years of heating and hydration. Eng. Geol. doi: 10.1016/j.enggeo.2019.105408.

Wang, Q., Cui, Y.J., Tang, A.M., Barnichon, J.D., Saba, S., Ye, W.M., 2013. Hydraulic conductivity and microstructure changes of compacted bentonite/sand mixture during hydration. Engineering Geology, 164, 67-76.

Wang, Q., Cui, Y.J., Tang, A.M., Delage, P., Gatmiri, B., Ye, W.M., 2014a. Long-term effect of water chemistry on the swelling pressure of a bentonite-based material. Applied Clay Science, 87, 157-162.

Wang, Q., Cui, Y.J., Tang, A.M., Li, X.L., Ye, W.M., 2014b. Time-and density-dependent microstructure features of compacted bentonite. Soils and Foundations, 54(4), 657-666.

Watanabe, Y., Yokoyama, S., 2021. Self-sealing behavior of compacted bentonite–sand mixtures containing technological voids. Geomechanics for Energy and the Environment,

25, 100213.

Yong, R.N., Warkentin, B.P., 1975. Soil Properties and Behaviour. Elsevier, Amsterdam.

Zeng, Z.X., Cui, Y.J., Conil, N., Talandier, J., 2020a. Effects of technological voids and hydration time on the hydro-mechanical behaviour of compacted bentonite/claystone mixture. Géotechnique, 1-14.

Zeng, Z.X., Cui, Y.J., Conil, N., Talandier, J., 2020b. Analysis of boundary friction effect on the homogenization process of compacted bentonite/claystone mixture with technological voids upon hydration. Acta Geotechnica, 1-9.

Zhang, C.L., 2014. Characterization of excavated claystone and claystone–bentonite mixtures as backfill/seal material. Geological Society, London, Special Publications, 400(1), 323-337.

Zhu, C.M., Ye, W.M., Chen, Y.G., Chen, B., Cui, Y.J., 2013. Influence of salt solutions on the swelling pressure and hydraulic conductivity of compacted GMZ01 bentonite. Eng. Geol., 166, 74–80.

Chapter 6. Unsaturated hydraulic property

INTRODUCTION

The main function of sealing material is to fill up the technological voids and create a relatively impermeable zone to limit water flow. In the past decades, the hydraulic parameters (hydraulic diffusivity or conductivity) of saturated bentonite-based materials were largely studied. The saturated hydraulic conductivity of bentonite-based materials could be influenced by many factors: initial water content (Haug and Wong, 1992), dry density (Komine, 2004; Karnland et al., 2008), spatial distribution of dry density (Wang et al., 2013a), hydraulic gradient (Dixon et al., 1992, 1999) and temperature (Kanno et al., 1999; Villar and Lloret, 2004). However, the saturated hydraulic parameter alone is not enough for describing the water flow through the bentonite-based materials since the permeability of bentonite-based materials measured under unsaturated or dry conditions is quite different from that measured under saturated conditions. When placed in the galleries, the compacted bentonite-based materials are initially unsaturated at very high suctions. Thus, the unsaturated hydraulic parameter is an important factor to be accounted for.

In this chapter, the water flow in the compacted MX80 bentonite/COx claystone mixture was investigated by carrying out infiltration and water retention tests under constant-volume conditions alongside detailed microstructure observation. The total water hydraulic conductivity of the mixture was first experimentally determined by instantaneous profile method. Based on the pore structure of the mixtures at various suctions, a novel method considering the evolving pore structure was proposed to predict the hydraulic conductivity for both vapour and liquid phases. Further, a numerical model was set up to verify the feasibility of the proposed method and to investigate the contribution of vapour and liquid water flux.

The work presented in this chapter has been submitted to “Géotechnique” and now under the second revision.

Zeng, Z.X., Cui, Y.J., Talandier, J. 2020. Submitted to Géotechnique.

Investigation of the hydraulic conductivity of an unsaturated compacted bentonite/claystone mixture

Zhixiong Zeng[1], Yu-Jun Cui[1], Jean Talandier[2]

Abstract: The pre-compacted MX80 bentonite/Callovo-Oxfordian (COx) claystone mixture has been proposed as a candidate sealing material in a French deep geological repository for high-level radioactive waste. An in-depth understanding of the hydraulic property of this material is essential for accessing the over-pack corrosion and nuclide migration along the gallery. In this study, water flow in the compacted bentonite/claystone mixture was investigated by carrying out infiltration and water retention tests under constant-volume conditions alongside detailed microstructure observation. The evolution of total water hydraulic conductivity with suction was experimentally determined based on the instantaneous profile method. It was observed that the measured total hydraulic conductivity increased slowly at high suctions, then quickly at low suctions, and finally approached the saturated value. A new method was developed based on the evolving pore structure, accounting for both vapour and liquid-water hydraulic conductivities. The total hydraulic conductivity predicted by the proposed method agreed well with the measured one, indicating the reliability of the predictive method. The vapour hydraulic conductivity was larger than the liquid-water one at a suction larger than 15.2 MPa while liquid-water hydraulic conductivity became dominant at a suction lower than 15.2 MPa. In addition, based on the predicted vapour and liquid-water hydraulic conductivities, a numerical model was set up to simulate the water infiltration process. Comparison between the simulation and the measurement showed close agreement, validating the two-phase water flow mechanism in the bentonite/claystone mixture.

Keywords: expansive soils; fabric/structure of soils; laboratory tests; numerical modelling; partial saturation; permeability

1 Laboratoire Navier/CERMES, Ecole des Ponts ParisTech, 6 et 8 avenue Blaise Pascal, 77455 Marne La Vallée cedex 2, France
2 Andra, 1/7, rue Jean Monnet, 92298 Châtenay-Malabry cedex, France

1 Introduction

In most concepts of radioactive waste disposal at great depth, bentonites are considered as possible sealing materials on their own or in combination with other materials due to the high swelling characteristics, low permeability and radionuclides retention capacity (Pusch 1982; Yong et al., 1986). Because of the ease of controlling initial properties, the sealing materials are often compacted in blocks and placed in the drifts and shafts. When the local groundwater conditions are recovered, the compacted blocks will adsorb water and swell, filling up the technological voids. Then, the compacted blocks are further hydrated under constant-volume conditions and develop a swelling pressure against the host rock, with microstructure changes and subsequent changes in hydraulic properties (Cui et al., 2008). Therefore, the water flow through the compacted bentonite-based materials is a major concern in the design and safety assessment of deep geological repositories.

The hydraulic parameters (hydraulic diffusivity or conductivity) of bentonite-based materials have been largely studied, especially in saturated state. Generally, the saturated hydraulic conductivity was measured by monitoring the water inlet and/or outlet flows at constant water head (Cui et al., 2008). It was found that the saturated hydraulic conductivity of bentonite-based materials was influenced by many factors: initial water content (Haug and Wong, 1992), dry density (Komine, 2004), spatial distribution of dry density (Wang et al., 2013a), hydraulic gradient (Dixon et al., 1992; 1999) and temperature (Villar and Lloret, 2004). However, the compacted bentonite-based materials are initially unsaturated at very high suctions when placed in the gallery. Thus, the unsaturated hydraulic parameter is also an important factor to be accounted for. The unsaturated hydraulic parameter can be measured by either steady-state method (Lu et al., 2006) or unsteady-state method (Daniel, 1982). Very often, instantaneous profile method (unsteady-state method) is used for compacted clays. Kanno et al. (1999), Kröhn (2003), Börgesson et al. (2001) and Zhang et al. (2014) performed infiltration tests on compacted pure bentonite or a bentonite/sand mixture. At different times, the samples were extracted and sliced for the determination of water content profile. Due to the time-consuming testing process, the obtained data were quite limited and the water movement could occur during the cutting of samples after testing. To improve the accuracy, Daniel (1982), Lemaire et al. (2004), Cui et al. (2008) and Wang et al. (2013b) continuously measured the water content or suction profiles of soil columns upon wetting using dual-energy γ radiation technique or relative humidity sensors installed at various locations. It has been observed that the unsaturated

hydraulic conductivity of bentonite-based materials decreased and then increased after a certain suction (Cui et al., 2008; Wang et al., 2013b), unlike the hydraulic conductivity of low plasticity unsaturated soils which increased constantly with suction decrease (van Genuchten, 1980; Fredlund et al., 2012). Wang et al. (2013b) attributed this phenomenon to the variation of large-pore volume with hydration: the large pores were progressively invaded by the swollen clay aggregates at the beginning of hydration (Romero et al., 2011); contrastingly, while saturation was approached, the large-pore volume increased again due to the formation of 2-dmensional (2D) pores by division of clay aggregates. Note that the water flow includes liquid water flow and water vapour diffusion. In their analyses, the portions of water flow in liquid and vapour phases were not distinguished and the corresponding water flow mechanisms were not clarified.

In past decades, the contribution of vapour and liquid water flux to the global water flow was addressed by several researchers based on experimental results and numerical simulations (Kanno et al., 1999; Kröhn, 2003; 2019; Zhang et al., 2014). Kröhn et al. (2003) assumed that bentonite was exclusively hydrated by vapour diffusion in the pore space and proposed a constant diffusion coefficient to characterise the water infiltration process. However, the calculated value of the diffusion coefficient was found to be lower than the experimental one, suggesting that the contribution of liquid water flow could not be ignored. Additionally, the water diffusivity for both the vapour and liquid phases could vary with water content. To address this issue, Kanno et al. (1999) and Börgesson et al. (2001) proposed an empirical equation, attempting to distinguish the vapour and liquid flow processes. However, the fundamental physics of vapour and liquid flows were not examined.

Several empirical, macroscopic, and statistical models have also been developed to predict the hydraulic conductivity of unsaturated soils based on experimental findings and theoretical considerations (Leong and Rahardjo, 1997; Xu, 2004; Zou, 2012; Ye et al., 2014; Zhai and Rahardjo 2015). Among them, the statistical model provides the most reliable results (Leong & Rahardjo, 1997; Fredlund et al., 2012). By simplifying the pore structure as a bundle of capillaries, the relative hydraulic conductivity was estimated based on the Poiseuille's equation (Burdine, 1953; Watabe et al., 2006). With the statistical model, Romero et al. (1999) derived the relative hydraulic conductivity of Boom clay based on the pore size distribution. However, the pore structure was assumed to be unchanged upon wetting/drying in previous works. This assumption is not valid for high-plasticity soils. It has been reported that the pore structure of compacted bentonite-based materials could significantly evolve along with mechanical and hydraulic loading (Delage et al., 2006; Romero et al., 2011; Wang et al., 2013b). Therefore, it

becomes necessary to account for the evolutionary character of pore structure in hydraulic conductivity prediction.

In this study, infiltration and water retention tests under constant-volume conditions were carried out on a compacted MX80 bentonite/Callovo-Oxfordian (COx) claystone mixture, allowing the total water hydraulic conductivity of the mixture to be determined by instantaneous profile method. The microstructure evolution of the mixture upon wetting was also investigated using mercury intrusion porosimetry (MIP). Based on the test results, a novel method considering the evolving pore structure was proposed to predict the hydraulic conductivity for both vapour and liquid phases. Finally, a numerical model was set up to verify the feasibility of the proposed method and investigate the contribution of vapour and liquid water flux.

2 Materials and methods

2.1 Materials

The material used was a mixture of MX80 bentonite and COx claystone with a proportion of 30/70 in dry mass, which has been proposed as a candidate sealing material by the French National Radioactive Waste Management Agency (Andra, France). The MX80 bentonite was extracted from Wyoming, USA, while the COx claystone was taken at a depth of around 490 m in the Andra Underground Research Laboratory (URL) in Bure. Table 1 summarises the physico-chemical properties of bentonite and claystone. Fig. 1 shows the grain size distributions of bentonite and claystone determined by dry sieving method. The dry bentonite and claystone have mean grain diameters D_{50} of 0.55 and 0.58 mm, respectively. The bentonite and claystone were immersed into de-ionized water and wet-sieved through 80 μm sieve. The grain size distributions for the bentonite and claystone particles smaller than 80 μm were determined by hydrometer method (AFNOR, 2005) and the results are also shown in Fig. 1. The respective clay contents (< 2 μm) of bentonite and claystone are 86% and 26%.

Table 1. Physico-chemical properties of MX80 bentonite and COx claystone

Soil property	MX80 bentonite	COx claystone
Water content (%)	11.4	6.1
Specific gravity	2.76	2.70
Liquid limit (%)	494	41
Plastic limit (%)	46	24
Plasticity index (%)	448	17
Main minerals	Smectite (86%)	Interstratified illite/smectite (40-45%)[a]
	Quartz (7%)	Carbonate (30%)[a]
	Carbonate and feldspar (7%)	Quartz and feldspar (25-30%)[a]

[a] After Fouché et al. (2004)

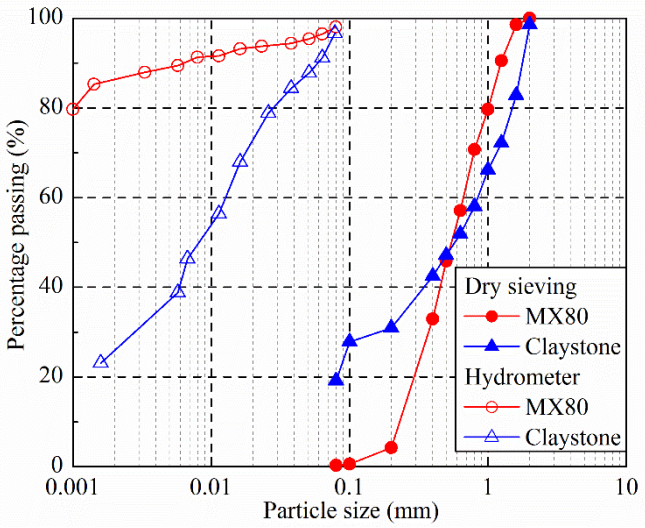

Fig. 1. Grain size distributions of MX80 bentonite and crushed COx claystone

To simulate the working environment of the mixture, synthetic water was used in the infiltration test. It was prepared by mixing the components with deionised water until full dissolution according to the chemical composition of pore water extracted from the Andra URL (Table 2).

Table 2. Recipe for the synthetic water preparation

Component	NaCl	$NaHCO_3$	KCl	$CaSO_4$·$2H_2O$	$MgSO_4$·$7H_2O$	$CaCl_2$·$2H_2O$	Na_2SO_4	Total
Content (g/L)	1.950	0.130	0.035	0.630	1.020	0.080	0.700	4.545

2.2 Water retention and MIP tests

The water retention property of the compacted bentonite/claystone mixture was determined under constant-volume conditions. The samples (50 mm in dia. and 5 mm in thick) were prepared by static compaction at a constant displacement rate of 0.05 mm/min to reach a dry density of 1.80 Mg/m^3. This value was selected to fulfil the requirements of Andra (swelling pressure is between 1 and 2 MPa and hydraulic conductivity is less than 10^{-11} m/s) (Zeng et al., 2020). After compaction, the initial suction of the mixture was measured by a chilled mirror dew point tensiometer (Decagon WP4), equal to 67.1 MPa (Table 3). To simulate the saturation process, the compacted samples were hydrated under constant-volume conditions at various suctions controlled using the osmotic (for suction of 1 MPa) and vapour equilibrium (for suctions equal to or higher than 4.2 MPa) techniques, as shown in Fig. 2. Six samples were placed into a special stainless steel cell (an inner diameter of 50 mm). To apply the osmotic technique, the semi-permeable membrane was placed between the porous stones and the sample and then installed between two perforated bases (Fig. 2a). Afterwards, the whole cell was immersed in a PEG 20000 (polyethylene glycol) solution corresponding to the target suction,

which was controlled by Brix index (Delage et al., 1998) using a refractometer in practice. To apply the vapour equilibrium technique, the compacted sample was sandwiched between metallic stainless porous stones and covered by two perforated bases (Fig. 2b). Then, two external bases with valves were added and a device containing a saturated salt solution was allowed to circulate for suction control. The different salt solutions used for controlling suctions are presented in Table 3. The whole apparatus was weighed regularly and the weight was found to increase rapidly at the beginning and become stable after about 25 days. Additionally, another sample sandwiched between metallic stainless porous stones was covered by two perforated bases and two external bases. Afterwards, synthetic water was injected into the sample from two valves to apply zero suction and the equilibration was achieved after approximately 2 days (Zeng et al., 2019). To ensure the equilibrium, all the samples were hydrated for 2 months and then extracted from the cell; the water content was determined by oven-drying at 105°C for 24 h. Note that the water content of the sample saturated with synthetic water (T07) was corrected by excluding the salt sediment from the dried samples, because the salts in synthetic water would precipitate out after oven-drying. The suction was measured using the WP4 potentiometer. The measured results were found to be close to the target suctions, confirming that the duration of hydration was long enough.

Table 3. Experimental programme

Test	Suction control method and duration		Suction (MPa)	MIP
T01	As-compacted		67.1	√
T02	Vapour equilibrium method (2 months)	NaCl	38	√
T03		$(NH_4)_2SO_4$	24.9	√
T04		KNO_3	9	√
T05		K_2SO_4	4.2	√
T06	Osmotic method (2 months)	PEG solution (0.302 g PEG/1 g water)	1	√
T07	Synthetic water (2 months)		0	√

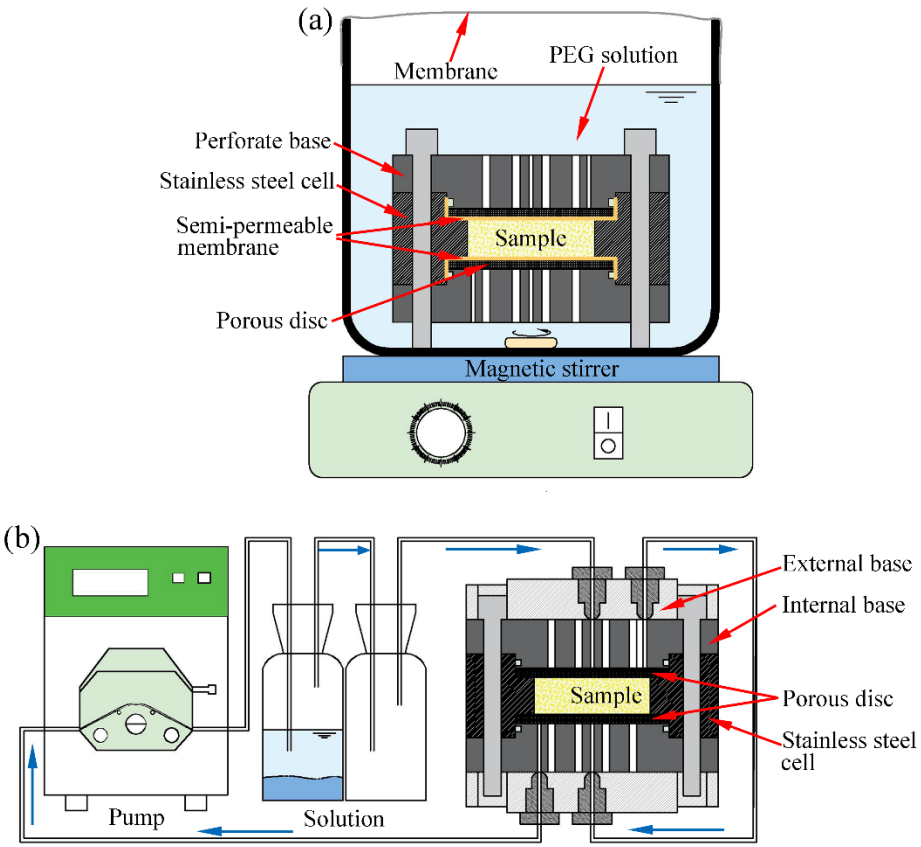

Fig. 2. Determination of the water retention curve under constant-volume conditions: (a) osmotic technique; (b) vapour equilibrium technique

MIP tests were also performed on the as-compacted and wetted samples after the water retention tests (Table 3). To minimise disturbance of the microstructure during dehydration, the samples were cut into small cubes with a side approximately equal to 1 cm and then freeze-dried following the procedure proposed by Delage and Pellerin (1984). Afterwards, an autopore IV 9500 mercury intrusion porosimeter with a maximum pressure of 230 MPa was employed to investigate the pore structure in the range from 350 to 0.006 μm pore diameter.

2.3 Infiltration test

To simulate the practical fabrication and construction processes of compacted blocks, identical discs of bentonite/claystone mixture with a diameter of 50 mm and a height of 50 mm were first statically compacted in a cylindrical mould at a constant displacement rate of 0.05 mm/min. Then, five discs were piled up inside a stainless steel cell 270 mm long, with 50 mm internal diameter and 80 mm outer diameter (Fig. 3). The total height of the discs was 250 mm and the total gaps between them were 0.21 mm. These gaps corresponded to 0.2% of the total void volume of the sample and their influence could be ignored. After placement of two porous stones at two sides, the sample was covered by the top and bottom stainless plugs. Next, the

two ends of the cell were tightly closed by metallic discs. Subsequently, four relative humidity sensors were installed in small holes at various heights along the cell: RH1 (50 mm), RH2 (100 mm), RH3 (150 mm) and RH4 (200 mm). To monitor the relative humidity at the top of the sample, another relative humidity sensor (RH5) was installed on the upper base. Afterwards, one valve on the lower base was connected to a burette and synthetic water was injected from the bottom of cell. The injected water volume was read from burette and the synthetic water in the burette was recharged regularly to keep the water head at the same level as the top of sample. For air evacuation, one valve on the upper base was kept open. The whole setup was placed in a constant temperature room (20 ± 1 °C). The test was conducted for 200 days.

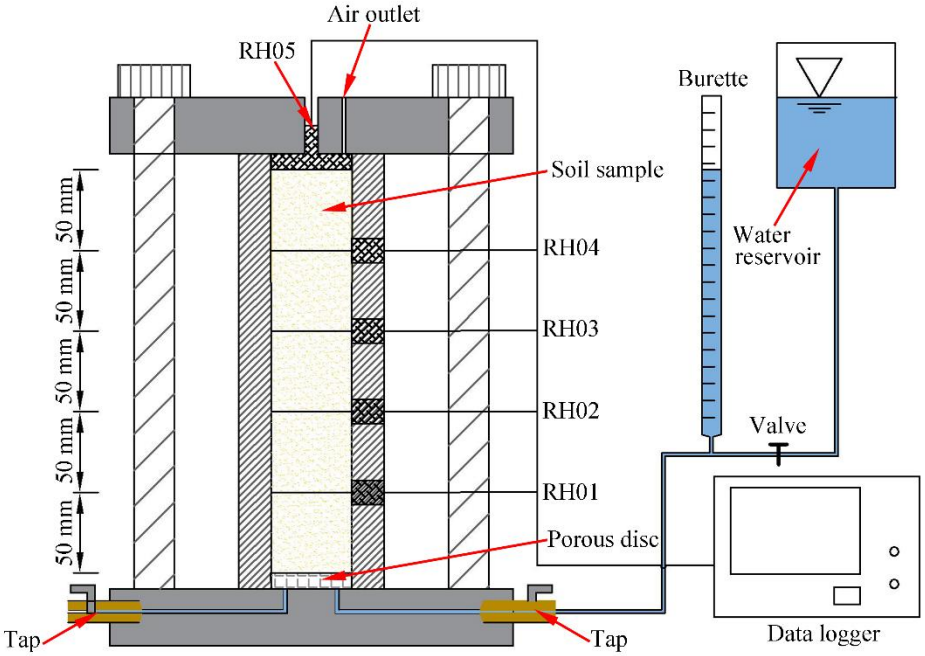

Fig. 3. Schematic layout of the infiltration test

3 Experimental results

3.1 Hydraulic conductivity

The evolution of the relative humidity at different locations is presented in Fig. 4. As the infiltration started, the relative humidity at RH1 increased rapidly and then tended to a stabilization value of 99.2% after 254 h. The increasing rate decreased with increasing distance from the wetting end and much more time was needed to reach a given relative humidity for the sensor at a more distant location. The relative humidity at RH5 kept almost constant at the beginning of hydration. After about 800 h, it started to increase and then reached 91.3% after 4800 h.

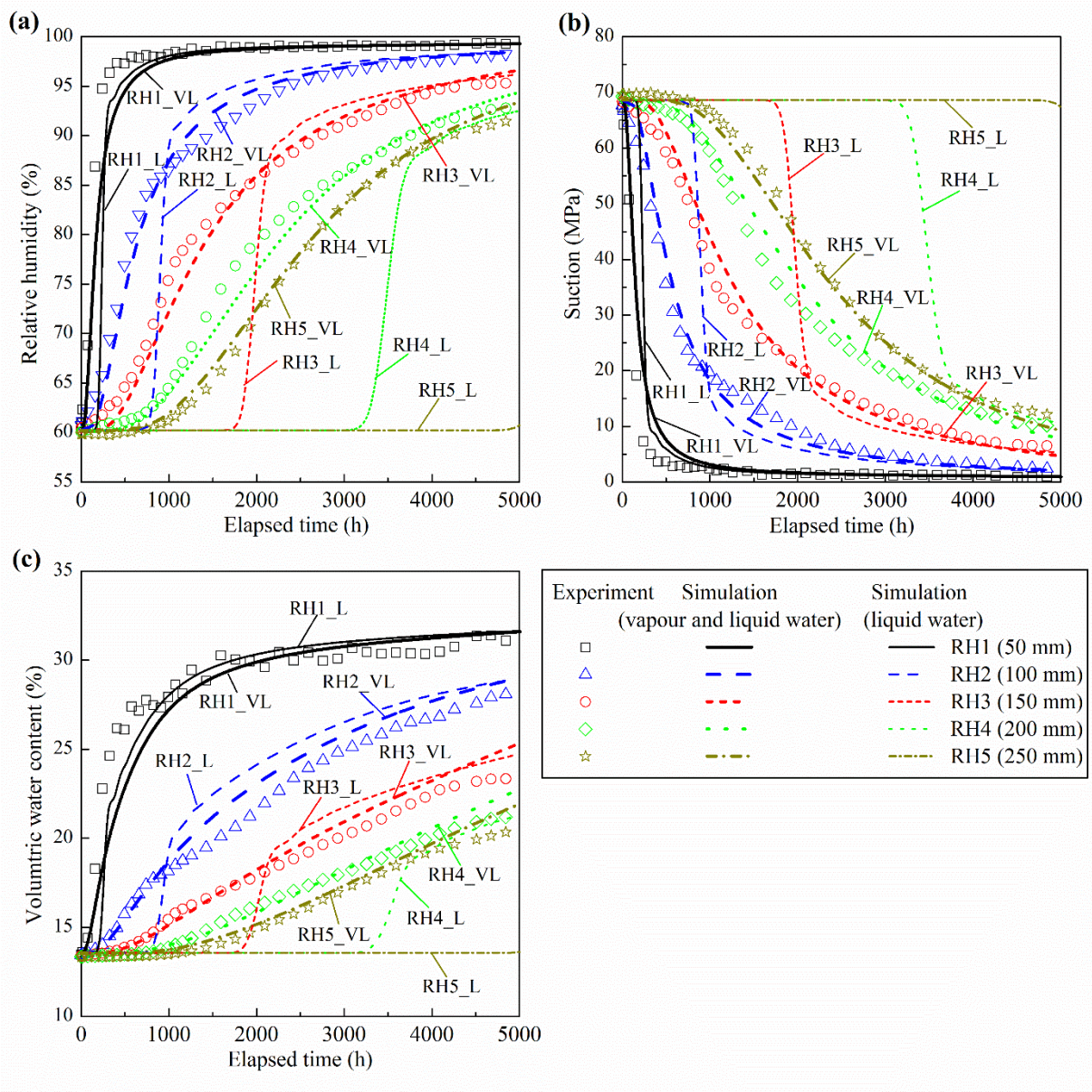

Fig. 4. Evolution of (a) relative humidity, (b) suction and (c) volumetric water content during water infiltration at different locations. Note: in the naming of curves, _VL and _L stand for the simulation results by considering both vapour and liquid water as well as only liquid water, respectively

Kelvin's law was used to convert the relative humidity (H_r) to suction (s expressed in MPa):

$$s=-\frac{10^{-6}\rho_w RT}{M}\ln H_r \tag{1}$$

where, R is the universal gas constant (8.314 J/(mol·K)), T is the absolute temperature (K), ρ_w is the water unit weight (1000 kg/m^3) and M is the molecular mass of water vapour (0.018016 kg/mol).

Figs. 4 and 5 present the evolution of suction and the suction profiles with a time interval of 300 h, respectively. The initial suctions at different positions were 68.2 ± 1.3 MPa,

corresponding to 60.4 ± 0.6 % initial relative humidity. As the hydration started, an instantaneous decrease was observed at the wetting end while the suctions at different heights decreased progressively at various rates, depending on the distances from the wetting end. With the hydration, the average slope of the suction profile increased gradually.

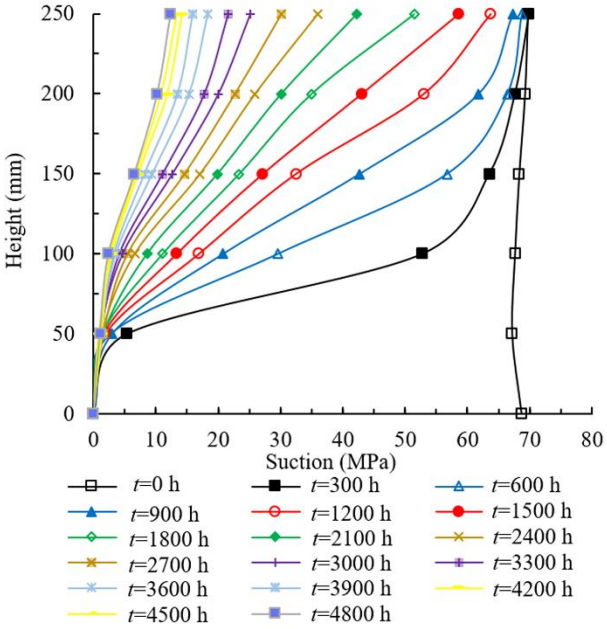

Fig. 5. Suction profiles at different infiltration times

Fig. 6 depicts the results of water retention tests. An almost bi-linear increase of volumetric water content was identified with suction decrease. As the suction was larger than 1 MPa, the volumetric water content (θ) increased sharply with decreasing suction. By contrast, as the suction was lower than 1 MPa, the water content stayed almost constant. The water retention curve could be fitted with the van Genuchten (1980) equation:

$$\theta=\frac{\theta_{sat}}{[1+(s/a)^c]^e} \tag{2}$$

where θ_{sat} is the saturated water content; a (MPa), c and e (e=1-1/c) are the fitting parameters.

From the measurement of suctions, the corresponding volumetric water contents were calculated using Eq. (2). Figs. 4 and 7 illustrate the evolution of volumetric water content at various locations and the volumetric water content profiles with a time interval of 300 h, respectively. The soils at the wetting end became saturated instantaneously and the average slope of volumetric water content profile tended to be vertical with the hydration time. The water flow volume passing through a cross section during a time period is equal to the total water volume change of the soils above this cross section, as indicated in Fig. 8. To validate the calculation of volumetric water content, the calculated water volume change of the whole

sample was compared to the injected water volume (Fig. 9). A close agreement was obtained between the measured and calculated values, suggesting a good reliability of computed evolution of water content at different locations.

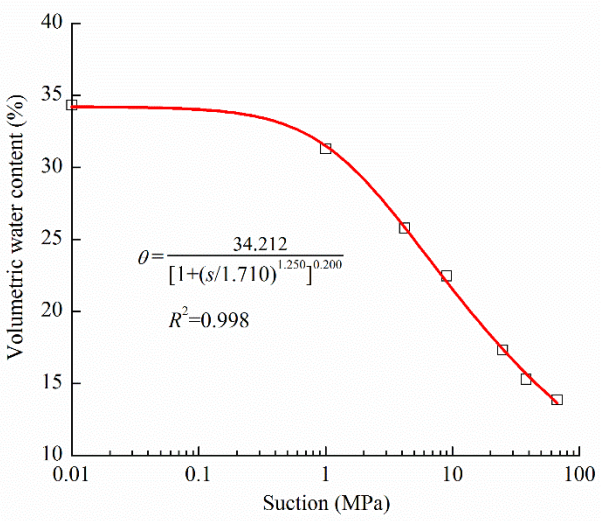

Fig. 6. Water retention curve of MX80 bentonite/COx claystone mixture under constant-volume conditions

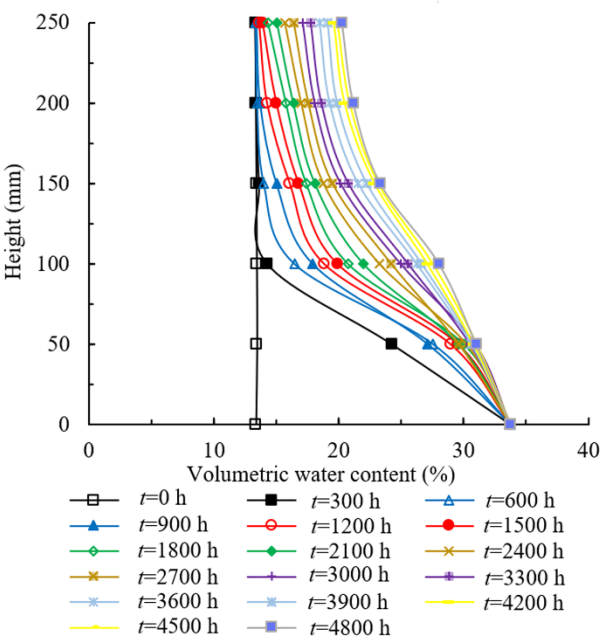

Fig. 7. Volumetric water content profiles at different infiltration times

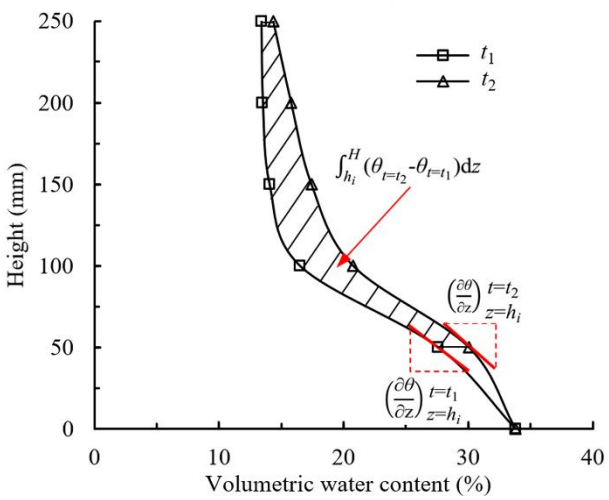

Fig. 8. Determination of water flow volume and volumetric water content gradient

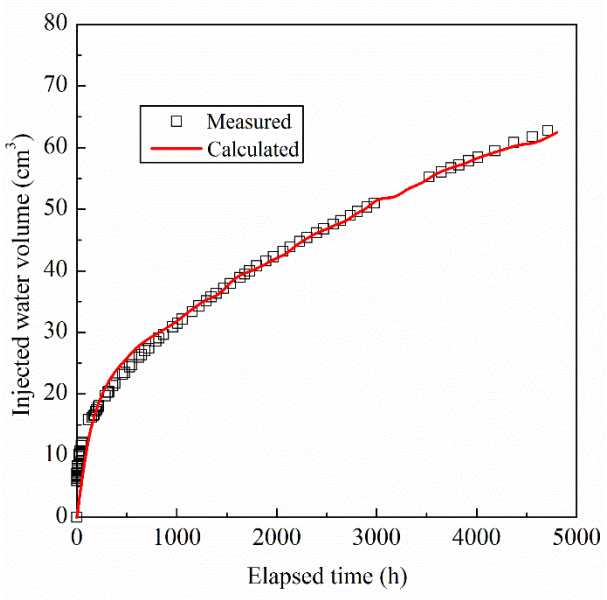

Fig. 9. Evolution of calculated and measured water volume injected into the samples with time

According to Kanno et al. (1999), the governing equation of water flow in a column of bentonite/claystone mixture under constant room temperature and atmospheric pressure can be expressed as:

$$q=-k\frac{d\psi}{d\theta}\frac{\partial\theta}{\partial z}=-D\frac{\partial\theta}{\partial z} \tag{3}$$

where ψ is the water potential in meter ($s=10^{-6}\rho_w g\psi$); z is the distance from the bottom of sample; q is the water flow rate (m/s); k is the hydraulic conductivity (m/s); D is the water diffusivity (m^2/s). Since the gravity and osmotic potentials were quite low, the matric potential was taken as the water potential in this study.

Accordingly, the water diffusivity can be calculated by the following equation based on the

volumetric water content profiles at different times (Kanno et al., 1999):

$$D=\frac{\int_{h_i}^{H}(\theta_{t=t_2}-\theta_{t=t_1})dz}{\frac{1}{2}\left\{\left(\frac{\partial\theta}{\partial z}\right)_{\substack{t=t_2\\z=h_i}}+\left(\frac{\partial\theta}{\partial z}\right)_{\substack{t=t_1\\z=h_i}}\right\}}\frac{1}{t_2-t_1} \quad (4)$$

where h_i is the height of the studied location; H is the total height of sample; $\theta_{t=t_1}$ and $\theta_{t=t_2}$ are the volumetric water contents at instants t_1 and t_2, respectively. $\int_{h_i}^{H}(\theta_{t=t_2}-\theta_{t=t_1})dz$ represents the water flow volume passing through the section at the studied location during a time period from t_1 to t_2. $\left(\frac{\partial\theta}{\partial z}\right)_{\substack{t=t_1\\z=h_i}}$ and $\left(\frac{\partial\theta}{\partial z}\right)_{\substack{t=t_2\\z=h_i}}$ are deduced from the tangents of volumetric water content profiles at instant t_1 and t_2, respectively (Fig. 8).

Then, the hydraulic conductivity is calculated using the following equation (Kanno et al., 1999):

$$k=D\frac{d\theta}{d\psi} \quad (5)$$

where $d\psi/d\theta$ is deduced from the water retention curve described by Eq. (2):

$$\frac{d\psi}{d\theta}=\frac{10^6 a}{ce\rho_w g\theta_{sat}}[1+(s/a)^c]^{(e+1)}(s/a)^{(1-c)} \quad (6)$$

where g is the gravitational acceleration (m/s^2). The variation of the measured hydraulic conductivity with suction at different locations is shown in Fig. 10. Note that the hydraulic conductivity derived by instantaneous method is the total one, which includes vapour and liquid-water hydraulic conductivities. The total hydraulic conductivity was about 4.56×10^{-15} m/s in the as-compacted state. As the suction decreased, it showed a slow increase (suction higher than 30 MPa) followed by a rapid increase (suction lower than 30 MPa). It finally approached the saturated value of 2.12×10^{-12} m/s (Zeng et al., 2020). The lower the suction, the higher the increasing rate of total hydraulic conductivity.

3.2 Microstructure

Fig. 11 presents the pore size distribution curves of the compacted bentonite/claystone mixture hydrated from as-compacted state (67.1 MPa) to 0 MPa. For the as-compacted sample, two populations were clearly identified: large pores with an entrance diameter of 2-50 μm and small pores with an entrance diameter of 0.006-0.04 μm. During wetting, the peak value of larger pores decreased as the suction decreased from 67.1 to 24.9 MPa and then increased as the suction decreased from 9 to 0 MPa. By contrast, the peak value of small pores (0.006–0.04 μm) decreased by 24%, although the mean diameter stayed always around 0.02 μm. Additionally,

another population with a diameter of 0.05-0.5 μm appeared (defined as medium pores) when the suction became smaller than 1 MPa. This phenomenon could be explained as follows: upon hydration, water molecules were progressively placed on the clay surfaces. During this process, the clay aggregates swelled, enlarging the small-pore space into the medium-pore population and progressively invading the initial large-pore space (Wang et al., 2013b; Zeng et al., 2020). When the large and small pores were transformed into the medium-pore population, a significant increase in medium-pore void ratio occurred. Meanwhile, the aggregates would be divided into smaller ones and fissure-like 2D pores with a mean diameter of 20 μm could appear (Wang et al., 2014). The variation of large-pore volume was due to the combined effects of the appearance of 2D pores and the invasion of swollen clay particles. This explained the decrease of large-pore volume with decreasing suction, followed by an increase when the suction was lower than 9 MPa.

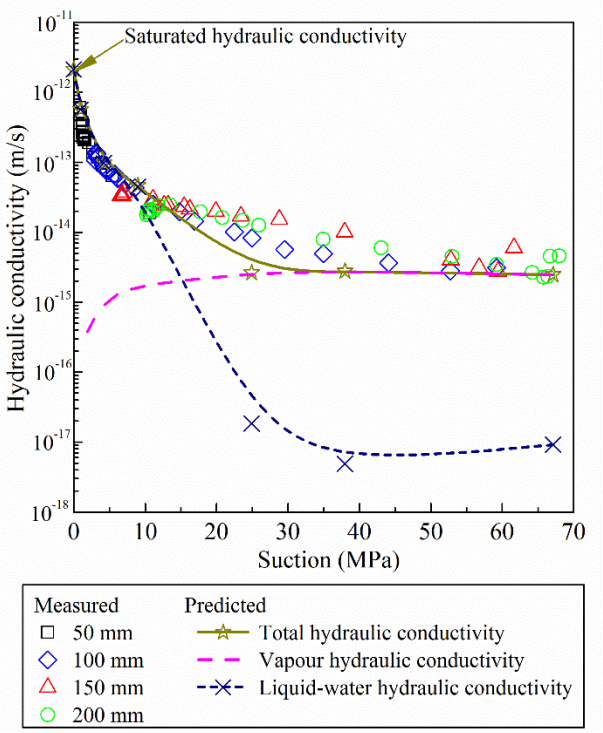

Fig. 10. Relationship between the measured and predicted hydraulic conductivities and suction

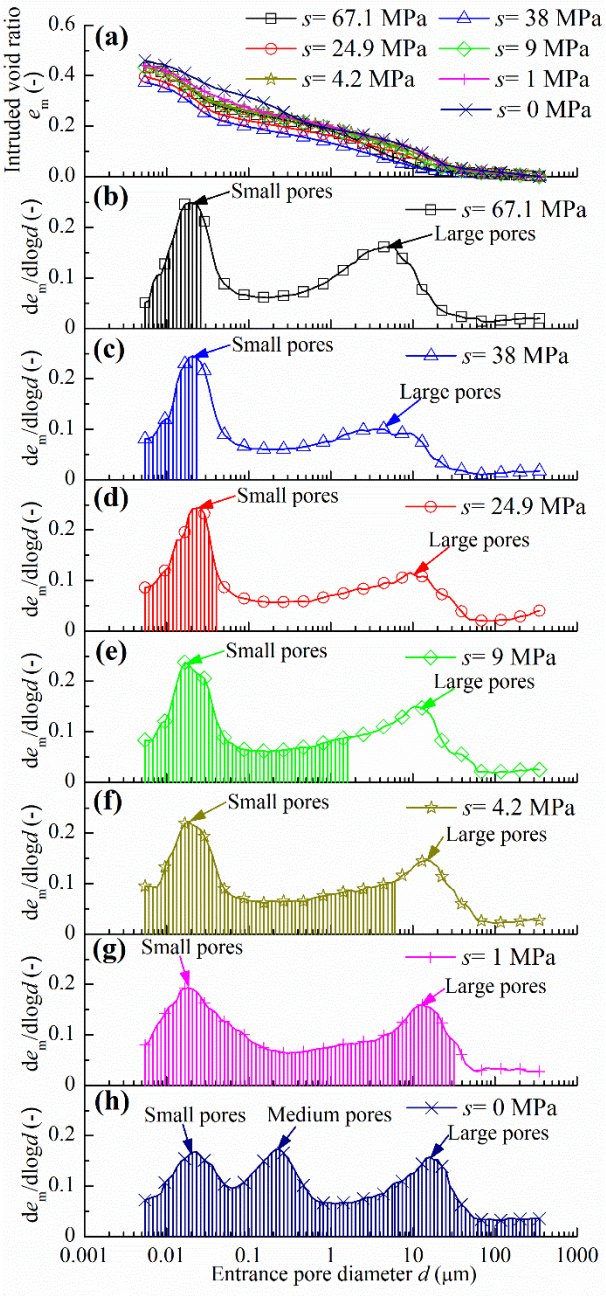

Fig. 11. Pore size distributions of the samples subjected to different suctions under constant-volume conditions: (a) cumulative curves, (b) density function curve of sample at a suction of 67.1 MPa, (c) density function curve of sample at a suction of 38 MPa, (d) density function curve of sample at a suction of 24.9 MPa, (e) density function curve of sample at a suction of 9 MPa, (f) density function curve of sample at a suction of 4.2 MPa, (g) density function curve of sample at a suction of 1 MPa and (h) density function curve of sample at a suction of 0 MPa. Note: the stripe zones represent the water-filled pores

4 Water infiltration modelling

4.1 Prediction of hydraulic conductivity

When a column of bentonite-based materials is wetted from one end, liquid water is driven to

the zone far from the wetting end through the water-filled pore space by suction gradient. Simultaneously, the water at the interface of liquid water evaporates to the air-filled space and is subsequently driven into the zone far from the wetting face by vapour pressure gradient (Börgesson et al., 2001; Kröhn, 2003). With hydration, the air-filled porosity space gradually decreases while the water-filled porosity increases. Moreover, the pore size distribution of bentonite-based materials can evolve (Fig. 11) and significantly influence the water flow. In previous works, the portions of water flow in liquid and vapour phases were not explicitly determined. Thus, the aim of this study is to propose a novel method for predicting the hydraulic conductivities in vapour and liquid phases based on the evolving pore structure.

4.1.1 Vapour phase

According to Philip and de Vries (1957), the vapour diffusivity in soil (D_v) can be calculated from that in air (D_a):

$$D_v=n_v\tau_g D_a \tag{7}$$

where n_v is the air-filled porosity and τ_g is the tortuosity factor. The vapour diffusivity in air can be estimated from the ambient temperature using the following equation (Šimunek et al., 2009):

$$D_a=2.12\times10^{-5}\left(\frac{T}{273.15}\right)^2 \tag{8}$$

The tortuosity factor in soil is mainly dependent on the air-filled porosity (Moldrup et al., 2001). Millington and Quirk (1961) suggested that the relationship between the tortuosity factor and air-filled porosity can be described by Eq. (9):

$$\tau_g=n_v^{1/3} \tag{9}$$

Afterwards, the vapour hydraulic conductivity is determined using the following equation (Šimunek et al., 2009):

$$k_v=D_v\rho_{vs}H_r\frac{Mg}{\rho_w RT} \tag{10}$$

where ρ_{vs} is the saturated vapour density (kg/m^3). It can be estimated from the ambient temperature using Eq. (11) (Šimunek et al., 2009):

$$\rho_{vs}=10^{-3}\frac{\exp(31.3716-\frac{6014.79}{T}-7.92495\times10^{-3}T)}{T} \tag{11}$$

4.1.2 Liquid phase

Based on the Poiseuille's equation for laminar flow through a capillary tube, the hydraulic conductivity for a distribution of capillary tubes (k_c) having different diameters d_i can be

expressed as (Lapierre et al., 1990):

$$k_c=\frac{\rho_w g n}{32\mu}\sum_{i=1}^{l} d_i^2 f(d_i) \tag{12}$$

where n is the porosity; μ is the water viscosity; i is the counter from 1 to l; d_i and $f(d_i)$ are the pore diameter and volumetric probability corresponding to i, respectively. According to Eq. (12), the following equation can be deduced to describe the ratio of the liquid-water hydraulic conductivity in unsaturated state to the saturated one (k_r) (Burdine, 1953; Watabe et al., 2006):

$$k_r=\frac{\sum_{j=1}^{m} d_j^2 f(d_j)}{\sum_{p=1}^{r} d_p^2 f(d_p)} \tag{13}$$

where m and r are the total numbers of pore intervals in unsaturated and saturated states, respectively; j and p are the counters from 1 to m and r, respectively; d_j and d_p are the diameters of pores filled by water in unsaturated and saturated states, respectively; $f(d_j)$ and $f(d_p)$ are the volumetric probabilities corresponding to the pore diameters of d_j and d_p, respectively. Then, the liquid-water hydraulic conductivity (k_l) of unsaturated soil can be derived from the saturated hydraulic conductivity (k_s):

$$k_l=k_r k_s \tag{14}$$

Notably, the pores were assumed to be cylindrical and all water was assumed to be mobile in this study. The influences of irregular pore shape (Tuller et al., 1999) and interlayer water immobility (Pusch et al., 1990) on the liquid-water hydraulic conductivity will be investigated in further studies.

4.1.3 Predicted hydraulic conductivity of bentonite/claystone mixture

According to Eq. (2), the air-filled porosities of the compacted bentonite/claystone mixture at various suctions are deduced using Eq. (15):

$$n_v=n\left\{1-\frac{1}{[1+(s/a)^c]^e}\right\} \tag{15}$$

The relative humidity values can be back-calculated from the suctions using Eq. (1). Using Eqs. (7)-(11), the vapour hydraulic conductivities at different suctions were predicted and the variation of the predicted vapour hydraulic conductivity of compacted bentonite/claystone mixture with suction is illustrated in Table 4 and Fig. 10. Overall, the vapour hydraulic conductivity decreased from 2.47×10^{-15} to 2.50×10^{-16} m/s as the suction decreased from 67.1 to 1 MPa.

In unsaturated states, the soil water is subjected to capillary force as a function of the pore size (Tang et al., 2009). The larger the pore size, the smaller the capillary force. Therefore, the soil

water is stored within the smaller pores while the larger pores are occupied by air (Watabe et al., 2006). According to the air-filled porosities and cumulative porosity curves (Fig. 11a) of samples at different suctions, the delimiting sizes of air-filled and water-filled pores could be identified and the results are summarised in Table 4. As illustrated in Fig. 11b-h, the stripe zones with a diameter smaller than delimiting sizes represent the water-filled pores while the non-stripe zones with a diameter larger than the delimiting sizes refer to the air-filled pores. Based on the water-filled pore size distributions at different suctions, the k_r value of compacted bentonite/claystone mixture was calculated. After substitution of k_r values and a saturated hydraulic conductivity (2.12×10^{-12} m/s) into Eq. (14), the liquid-water hydraulic conductivities at various suctions were obtained and the results are summarised in Table 4 and Fig. 10. The liquid-water hydraulic conductivity kept almost constant at 6.69×10^{-18} m/s when the suction was larger than 35 MPa. When the suction decreased to lower than 35 MPa, the liquid-water hydraulic conductivity increased sharply and approached the saturated one.

Table 4. Predicted liquid-water and vapour hydraulic conductivities at various suctions

Suction (MPa)	Delimiting size (μm)	k_r	Liquid-water hydraulic conductivity (m/s)	Vapour hydraulic conductivity (m/s)	Total hydraulic conductivity (m/s)
67.1	0.023	4.31×10^{-6}	9.13×10^{-18}	2.47×10^{-15}	2.48×10^{-15}
38	0.023	2.31×10^{-6}	4.90×10^{-18}	2.77×10^{-15}	2.77×10^{-15}
24.9	0.040	8.65×10^{-6}	1.83×10^{-17}	2.62×10^{-15}	2.63×10^{-15}
9	1.59	2.10×10^{-2}	4.46×10^{-14}	1.78×10^{-15}	4.64×10^{-14}
4.2	6.04	4.53×10^{-2}	9.60×10^{-14}	1.16×10^{-15}	9.71×10^{-14}
1	31.5	2.65×10^{-1}	5.62×10^{-13}	2.50×10^{-16}	5.63×10^{-13}
0	350	1.00	2.12×10^{-12}	0	2.12×10^{-12}

From Fig. 10, the liquid-water hydraulic conductivity was lower than 1% of the vapour hydraulic conductivity when the suction was larger than 24.9 MPa. As the suction decreased to about 15.2 MPa, the liquid-water hydraulic conductivity became comparable to the vapour hydraulic conductivity. In a nearly saturated state, the liquid-water hydraulic conductivity became 1000 times larger than the vapour hydraulic conductivity. Summarising, the vapour flow prevailed at the beginning of hydration, while the liquid water flow became more and more dominant with the hydration. Also plotted in Fig. 10 is the variation of the predicted total hydraulic conductivity k_T with suction. Overall, the predicted total hydraulic conductivity was in good agreement with the measured one. It kept almost constant as the suction was higher than 24.9 MPa and then increased considerably with the decrease of the suction from 24.9 to 0 MPa. It is worth noting that this phenomenon was different from that reported by Ye et al. (2009) on compacted GMZ bentonite at a dry density of 1.70 Mg/m^3, Wang et al. (2013b) on compacted

MX80 bentonite/sand mixture (a proportion of 70/30 in dry mass) at a dry density of 1.67 Mg/m^3 and Liu et al. (2020) on GMZ bentonite pellets mixture at a global dry density of 1.45 Mg/m^3. In their studies, an obvious decrease of total hydraulic conductivity with suction decrease was observed at a high suction level. This decreasing hydraulic conductivity was ascribed to the high porosities of samples. At high suctions, the soil water was stored within the aggregates and the microstructure of aggregates governed the suction level. The water volume ratio (the ratio of water volume to solid volume) only depended on suction, regardless of the sample porosity since the variation of porosity in the as-compacted state did not affect aggregates (Wang et al., 2013a). At the same suction, the samples with a larger porosity would exhibit a larger air-filled porosity. According to Eq. (7), a larger vapour hydraulic conductivity at high suctions and a steeper decrease of vapour hydraulic conductivity with suction decrease were expected for the samples with a larger porosity. Consequently, a significantly decreasing trend of hydraulic conductivity was observed at a high suction level.

4.2 Numerical simulation of the infiltration test

To simulate the water infiltration process in compacted bentonite/claystone mixture, a one-dimensional numerical model 0.25 m high (with a mesh size of 0.001 m) was set up with the aid of commercial software Geostudio/SEEP-W. The continuity equation is expressed as (Kanno et al., 1999):

$$\frac{\partial \theta}{\partial t}+\frac{\partial q}{\partial z}=0 \tag{16}$$

Combining Eqs. (3) and (16) yields:

$$\frac{\partial \theta}{\partial t}-\frac{\partial}{\partial z}\left(k\frac{\mathrm{d}\psi}{\mathrm{d}\theta}\frac{\partial \theta}{\partial z}\right)=0 \tag{17}$$

The initial and boundary conditions were the same as those in the infiltration test. The water retention property and the predicted vapour and liquid-water hydraulic conductivities (Fig. 10) were applied to the material. A transient seepage analysis was performed for the same period as the infiltration test (200 days). The numerical results were compared to the experimental ones in Fig. 4. On the whole, the experimental and numerical results matched quite well in terms of relative humidity, suction and volumetric water content, indicating the good reliability of the proposed methods for predicting both vapour and liquid-water hydraulic conductivities, and confirming the two-phase infiltration mechanism.

In addition, the contribution of vapour and liquid water flux to the water flow was also examined, by inputting the water retention property and the predicted liquid-water hydraulic conductivity.

The simulated results are compared to those with consideration of both vapour and liquid water flux in Fig. 4. Ignoring vapour transport significantly postponed the starting time of relative humidity increase and suction decrease while the increasing rate of relative humidity and decreasing rate of suction were more rapid. This phenomenon could be attributed to the liquid-water hydraulic conductivity being lower than the total hydraulic conductivity, especially at high suctions (Fig. 10). Without considering vapour diffusion, the volumetric water content increased slowly and a larger starting time of water content increase was observed. With the increase of water content, the liquid-water hydraulic conductivity of the soil close to the wetting end increased and the vapour hydraulic conductivity became negligible. By contrast, the liquid-water hydraulic conductivity of the soil far from the wetting end was still significantly lower than the total hydraulic conductivity. As a result, most water was left in the soil close to the wetting end and a more rapid increase in volumetric water content was observed, compared to that accounting for both vapour and liquid water flux. However, after a certain hydration time, the overall water content of the whole column after the same hydration time was still lower than that with consideration of both the vapour and liquid water flux (Fig. 10). These revealed that the vapour diffusion could facilitate the water infiltration, especially for the soil far from the wetting end.

5 Conclusions

Water flow in a compacted bentonite/claystone mixture was investigated by performing infiltration and water retention tests, allowing the total water hydraulic conductivity to be experimentally determined by instantaneous profile method. Based on the evolving pore structure of mixture upon wetting, vapour and liquid-water hydraulic conductivities were predicted and the infiltration process was numerically reproduced to investigate the contribution of vapour and liquid water flux. According to the obtained results, the following conclusions are drawn.

As the suction decreased from initial value (about 67.1 MPa) to zero, the measured total hydraulic conductivity increased slowly from 4.56×10^{-15} m/s (suction higher than 30 MPa), then rapidly (suction lower than 30 MPa), and finally approached the saturated hydraulic conductivity of 2.12×10^{-12} m/s.

According to the evolving pore structure of bentonite/claystone mixture, a method of predicting the vapour and liquid-water hydraulic conductivities was proposed based on the Philip and de

Vries' equation and capillary model, respectively. Overall, the predicted total hydraulic conductivity agreed well with the measured one. Additionally, as the suction was larger than 15.2 MPa, the vapour flow prevailed; by contrast, as the suction was lower than 15.2 MPa, the liquid water flow became dominant.

The results from numerical simulation using the predicted vapour and liquid-water hydraulic conductivities were in good agreement with the measurements, showing the relevance of proposed methods for vapour and liquid-water hydraulic conductivities. Ignoring vapour transport postponed the starting time of relative humidity increase or suction decrease, and underestimated the water content, especially for the soil far from the wetting end.

Acknowledgments

The authors thank Ecole des Ponts ParisTech for assistance with laboratory experiments. Z.X. Zeng acknowledges the China Scholarship Council (CSC) and the French National Radioactive Waste Management Agency (Andra) for providing funding to perform this study.

References

AFNOR (2005). Geotechnical investigating and testing, Laboratory testing of soils. Part 4: Determination of particle size distribution. AFNOR. P94.

Börgesson, L., Chijimatsu, M., Fujita, T., Nguyen, T.S., Rutqvist, J. & Jing, L. (2001). Thermo-hydro-mechanical characterisation of a bentonite-based buffer material by laboratory tests and numerical back analyses. International Journal of Rock Mechanics and Mining Sciences 38, No. 1, 95-104.

Burdine, N. (1953). Relative permeability calculations from pore size distribution data. Journal of Petroleum Technology 5, No. 3, 71-78.

Cui, Y.J., Tang, A.M., Loiseau, C. & Delage, P. (2008). Determining the unsaturated hydraulic conductivity of a compacted sand–bentonite mixture under constant-volume and free-swell conditions. Physics and Chemistry of the Earth, Parts A/B/C 33, S462-S471.

Daniel, D.E. (1982). Measurement of hydraulic conductivity of unsaturated soils with thermocouple psychrometers. Soil Science Society of America Journal 46, No. 6, 1125-1129.

Delage, P. & Pellerin, F. M. (1984). Influence de la lyophilisation sur la structure d'une argile sensible du Québec. Clay Minerals 19, No. 2, 151-160

Delage, P., Howat, M.D. & Cui, Y.J. (1998). The relationship between suction and swelling properties in a heavily compacted unsaturated clay. Engineering geology 50, No. 1-2, 31-

48.

Delage, P., Marcial, D., Cui, Y.J. & Ruiz, X. (2006). Ageing effects in a compacted bentonite: a microstructure approach. Géotechnique 56, No. 5, 291-304.Dixon, D.A., Gray, M.N. & Hnatiw, D. (1992). Critical gradients and pressures in dense swelling clays. Canadian Geotechnical Journal 29, No. 6, 1113-1119.

Dixon, D.A., Graham, J. & Gray, M.N. (1999). Hydraulic conductivity of clays in confined tests under low hydraulic gradients. Canadian Geotechnical Journal 36, No. 5, 815-825.

Fouché, O., Wright, H., Le Cléac'h, J. M. & Pellenard, P. (2004). Fabric control on strain and rupture of heterogeneous shale samples by using a non-conventional mechanical test. Appl. Clay Sci. 26, No. 1–4, 367–387.

Fredlund D.G., Rahardjo, H. & Fredlund, M.D. (2012). Unsaturated Soil Mechanics in Engineering Practice. Wiley, New York

Haug, M.D. & Wong, L.C. (1992). Impact of molding water content on hydraulic conductivity of compacted sand-bentonite. Canadian Geotechnical Journal 29, No. 2, 253-262.

Kanno, T., Fujita, T., Takeuchi, S., Ishikawa, H., Hara, K. & Nakano, M. (1999). Coupled thermo-hydro-mechanical modelling of bentonite buffer material. International journal for numerical and analytical methods in geomechanics 23 No. 12, 1281-1307.

Komine, H. (2004). Simplified evaluation on hydraulic conductivities of sand–bentonite mixture backfill. Applied clay science 26, No. 1-4, 13-19.

Kröhn, K.P. (2003). New conceptual models for the resaturation of bentonite. Applied clay science 23, No. 1-4, 25-33.

Kröhn, K.P. (2019). Re-saturation of compacted bentonite under repository-relevant flow conditions. Geomechanics for Energy and the Environment 17, 115-122.

Lapierre, C., Leroueil, S. & Locat, J. (1990). Mercury intrusion and permeability of Louiseville clay. Canadian Geotechnical Journal 27, No. 6, 761-773.

Lemaire, T., Moyne, C. & Stemmelen, D. (2004). Imbibition test in a clay powder (MX-80 bentonite). Applied clay science 26, No. 1-4, 235-248.

Leong, E.C. & Rahardjo, H. (1997). Review of soil-water characteristic curve equations. Journal of geotechnical and geoenvironmental engineering 123, No. 12, 1106-1117.

Liu, Z.R., Cui, Y.J., Ye, W.M., Chen, B., Wang, Q. & Chen, Y.G. (2020). Investigation of the hydro-mechanical behaviour of GMZ bentonite pellet mixtures. Acta Geotech. 15, No. 10, 2865-2875.

Lu, N., Wayllace, A., Carrera, J. & Likos, W.J. (2006). Constant flow method for concurrently measuring soil-water characteristic curve and hydraulic conductivity function. Geotechnical Testing Journal 29, No. 3, 230-241.

Millington, R.J. & Quirk, J.P. (1961). Permeability of porous solids. Transactions of the Faraday Society 57, 1200-1207.

Moldrup, P., Olesen, T., Komatsu, T., Schjønning, P. & Rolston, D.E. (2001). Tortuosity, diffusivity, and permeability in the soil liquid and gaseous phases. Soil Sci. Soc. Am. J. 65, No. 3, 613–623.

Philip, J.R. & de Vries, D.A. (1957). Moisture movement in porous materials under temperature gradients. Eos, Transactions American Geophysical Union 38 No. 2, 222-232.

Pusch, R. (1982). Mineral–water interactions and their influence on the physical behavior of highly compacted Na bentonite. Can. Geotech. J. 19, No. 3, 381-387

Romero, E., Gens, A. & Lloret, A. (1999). Water permeability, water retention and microstructure of unsaturated compacted Boom clay. Engineering Geology 54, No.1-2, 117-127.

Romero, E., Della Vecchia, G. & Jommi, C. (2011). An insight into the water retention properties of compacted clayey soils. Géotechnique 61, No.4, 313-328.

Šimunek, J., Sejna, M., Saito, H., Sakai, M. & van Genuchten, M.T. (2009). The Hydrus-1D software package for simulating the one-dimensional movement of water, heat and multiple solutes in variably-saturated media. Riverside, CA: Univ. of California

Tang, A.M., Cui, Y.J., Eslami, J. & Défossez, P. (2009). Analysing the form of the confined uniaxial compression curve of various soils. Geoderma 148, No. 3-4, 282-290.

Tuller, M., Or, D. & Dudley, L.M., (1999). Adsorption and capillary condensation in porous media: Liquid retention and interfacial configurations in angular pores. Water Resources Research 35, No.7, 1949-1964.

van Genuchten, M.T. (1980). A closed-form equation for predicting the hydraulic conductivity of unsaturated soils. Soil Sci. Soc. Am. J. 44, No. 5, 892–898.

Villar, M.V. & Lloret, A., (2004). Influence of temperature on the hydro-mechanical behaviour of a compacted bentonite. Applied Clay Science 26, No. 1-4, 337-350.

Wang, Q., Tang, A.M., Cui, Y.J., Delage, P., Barnichon, J.D. & Ye, W.M. (2013a). The effects of technological voids on the hydro-mechanical behaviour of compacted bentonite–sand mixture. Soils and Foundations 53, No. 2, 232-245.

Wang, Q., Cui, Y.J., Tang, A.M., Barnichon, J.D., Saba, S. & Ye, W.M. (2013b). Hydraulic conductivity and microstructure changes of compacted bentonite/sand mixture during hydration. Engineering Geology 164, 67-76.

Wang, Q., Cui, Y.J., Tang, A.M., Li., X.L. & Ye., W.M. (2014). Time-and density-dependent microstructure features of compacted bentonite. Soils and Foundations 54 No. 4, 657-666.

Watabe, Y., LeBihan, J.P. & Leroueil, S. (2006). Probabilistic modelling of saturated/unsaturated hydraulic conductivity for compacted glacial tills. Géotechnique 56, No. 4, 273-284.

Xu, Y.F. (2004). Calculation of unsaturated hydraulic conductivity using a fractal model for the pore-size distribution. Computers and Geotechnics 31, No. 7, 549-557.

Ye, W.M., Cui, Y.J., Qian, L.X. & Chen, B. (2009). An experimental study of the water transfer through confined compacted GMZ bentonite. Engineering Geology 108, No. 3-4, 169-176.

Ye, W.M., Wan, M., Chen, B., Chen, Y.G., Cui, Y.J. & Wang, J. (2014). An unsaturated hydraulic conductivity model for compacted GMZ01 bentonite with consideration of temperature. Environmental earth sciences 71, No. 4, 1937-1944.

Yong, R.N., Boonsinsuk, P. & Wong, G. (1986). Formulation of backfill material for a nuclear fuel waste disposal vault. Can. Geotech. J. 23, No. 2, 216-228.

Zeng, Z.X., Cui, Y.J., Zhang, F., Conil, N. & Talandier, J. (2019). Investigation of swelling pressure of bentonite/claystone mixture in the full range of bentonite fraction. Appl. Clay Sci. https://doi: 10.1016/j.clay.2019.105137.

Zeng, Z.X., Cui, Y.J., Conil, N. & Talandier, J. (2020). Effects of technological voids and hydration time on the hydro-mechanical behaviour of compacted bentonite/claystone mixture. Géotechnique. https://doi.org/10.1680/jgeot.19.P.220.

Zhai, Q. & Rahardjo, H. (2015). Estimation of permeability function from the soil–water characteristic curve. Engineering Geology 199, 148-156.

Zhang, M., Zhang, H.Y., Zhou, L., Wang, B.M. & Wang, S.J. (2014) Hydro-mechanical analysis of GMZ bentonite–sand mixtures in the water infiltration process as the buffer/backfill mixture in an engineered nuclear barrier. Applied clay science 97, 115-124.

Zou, Y. (2012). A macroscopic model for predicting the relative hydraulic permeability of unsaturated soils. Acta Geotechnica 7, No. 2, 129-137.

Conclusions and perspectives

CONCLUSIONS

In the French Cigéo project for deep geological disposal, a mixture of MX80 bentonite and excavated COx claystone in compacted blocks has been considered as a candidate sealing material by Andra. In general, the hydro-mechanical behaviour of such mixture depends on the material properties, such as mixing ratio and dry density. Additionally, the hydro-mechanical behavior of the mixture can be affected by environmental factors including swelling direction, technological voids, water chemistry and hydration path. In this study, a suitable mixture was preliminarily designed to fulfill the specifications in terms of swelling pressure and hydraulic conductivity. Then, the hydro-mechanical behaviour of the proposed mixture under different environmental conditions was further examined to gain more confidence in the long-term performance.

Preliminary design of the bentonite/claystone mixture

A series of compression, swelling pressure, hydraulic conductivity and MIP tests were performed on the compacted MX80 bentonite/COx claystone mixtures with various bentonite fractions, dry densities and water contents for the preliminary design of mixing ratio and dry density. In addition, the swelling pressure and hydraulic conductivity of the bentonite/claystone mixtures were then accessed from the binary composition and pore structure.

The experimental results show that the increase of bentonite fraction decreased the overall compressibility while the increase of water content increased the compressibility. During demoulding, the required pressure increased with the increase of bentonite fraction and the decreasing water content because of the increasing residual stress normal to the cell wall after compaction. To achieve a given final dry density, lower compaction pressure and demoulding pressure were required for the specimens with a lower bentonite fraction and a higher water content.

At a given dry density, the swelling pressure decreased and the hydraulic conductivity slightly increased with the decrease of bentonite fraction, suggesting that addition of claystone reduced the sealing performance of the mixture. To fulfill the specifications predefined by Andra in terms of swelling pressure and hydraulic conductivity, the dry density should be in the range of 1.72-1.82, 1.77-1.85 and 1.82-1.90 Mg/m^3 for the MX80 bentonite/COx claystone mixtures

with 30, 25 and 20% bentonite, respectively.

By considering the interaction between bentonite and claystone grains in the mixtures during hydration, the claystone void ratio after hydration was estimated based on the relationship between the swelling pressure and dry density of pure bentonite. Comparison of the claystone void ratio after hydration with the initial one allowed the volumetric strains of claystone grains under different stresses to be obtained and the mean swelling pressure of claystone grain was indirectly determined. In parallel, the mean swelling pressure of claystone grain was estimated according to the relationship between the vertical swelling pressure and the void ratio of intact COx claystone. The estimated value was found to be comparable to that indirectly determined from the swelling pressure tests on bentonite/claystone mixtures. This indicated that the claystone grains adsorbed water under the pressure applied by the previously swollen bentonite.

The claystone void ratio in the mixtures was lower than the initial one, suggesting that the swelling of claystone in the mixtures could be inhibited by bentonite. An inhibition factor was then introduced as a function of the bentonite fraction to describe the inhibition effect. According to two inflection points (40% and 70%), the inhibition effect can be divided into three zones (Zone I, $100 \geq B \geq 70$; Zone II, $70 > B \geq 40$; Zone III, $40 > B \geq 0$). In Zone I, the bentonite formed the continuous matrix, with claystone grain being the dispersed constituent; In Zone I, the swelling of claystone was almost totally inhibited by bentonite. The continuous matrix was formed by swollen claystone while the bentonite was dispersed in the matrix. In Zone III, the continuous matrix was formed by swollen claystone while the bentonite was dispersed. The matrix claystone fully swelled upon wetting and the claystone governed the global swelling pressure. In Zone II, both bentonite and claystone bentonite and claystone were randomly distributed, with neither constituent being continuous or dispersed. Additionally, according to the composite structures of bentonite/claystone mixtures with different bentonite fractions, two analytical methods were proposed to predict the swelling pressure and hydraulic conductivity. The good agreement between the estimation and measurement indicated the relevance of the proposed methods. From a practical point of view, these analytical methods would be helpful in designing the sealing/backfill elements with bentonite-based materials. If the properties of the bentonite and additive in the mixtures are known, the range of dry density at each bentonite fraction can be determined to satisfy the specifications in terms of swelling pressure and hydraulic conductivity.

From the MIP results, the bentonite/claystone mixtures exhibited a trimodal porosity after

hydration, with large pores with a mean pore diameter of 10-22 μm, medium pores with a mean diameter of 0.17-0.52 μm and small pores with a mean diameter of 0.025 μm. Because of the lower bentonite dry density, a larger medium-pore volume but a lower small-pore (0.006-0.04 μm) volume was observed on the specimens with lower bentonite fractions and larger void ratios after saturation. According to the pore size distribution, the total surface area of inter-particle pores was calculated assuming parallel and cylindrical pores, and the average the inter-particle distance was determined based on the total volume and the total surface area of inter-particle pores. It was found that there was a linear relationship between the swelling pressure and inter-particle distance, regardless of the bentonite fraction. Additionally, the relationship between hydraulic conductivity and pore size distribution was also interpreted using the general capillary model considering N_p pores in series. It was found that there was a unique relationship between the best value of N_p and plasticity index and an improved general capillary model was proposed for hydraulic conductivity prediction. In practice, the relationships elaborated between the hydro-mechanical behaviour with pore structure provide a way to characterise the hydro-mechanical behaviour of bentonite-based materials for radioactive waste repository and even for other types of applications.

Performance assessment under various environmental conditions

According to the above preliminary results, the mixture with a bentonite fraction of 30% and a global dry density of 1.8 Mg/m^3 was defined as a potential sealing material. To further examine the material performance during the long-term operation of underground radioactive waste repository, the influences of swelling direction, technological voids, hydration time, water chemistry and suction on the hydro-mechanical behaviour of compacted bentonite/claystone mixture with 30% bentonite were investigated.

(i) Effect of technological voids on aeolotropic swelling behaviour

For the compacted MX80 bentonite/COx claystone mixture with 30% bentonite, the radial swelling pressure was significantly lower than the axial one. The swelling aeolotropy (ratio of radial to axial swelling pressures) at low dry densities was mainly conditioned by the concentration of macro-pores in the border of specimens. By contrast, as the dry density decreased, the heterogeneous distribution of macro-pores decreased while the grain orientation increased. Thus, the aeolotropy coefficient increased and then decreased with the increasing dry density.

During the installation of compacted blocks, technological voids can remain between the surrounding rock and compacted blocks and between blocks. While taking into account average technological voids of 10%, the compacted blocks at a dry density of 2.0 Mg/m^3 are expected to fill up the technological voids and reach a required global dry density of 1.8 Mg/m^3. In this study, the effects of axial/radial technological voids on the aeolotropic swelling behaviour were experimentally studied. The MX80 bentonite/claystone mixture with 30% bentonite was compacted to a dry density of 2.0 mg/m^3 and both the axial and radial technological voids were designed to portray the voids between blocks and between the surrounding rock and compacted blocks, respectively. It was found that the axial technological voids could decrease the grain orientation and reduce the aeolotropy. By contrast, the radial technological voids would increase the heterogeneity and enhance the aeolotropy.

(ii) Effects of technological voids and hydration time

The evolution of hydro-mechanical behaviour of ompcated MX80 bentonite/COx claystone mixture with radial technological voids was also experimentally investigated. After the filling of technological voids, the water content and dry density distributions were heterogeneous, with a larger water content and a lower dry density in the compression zone while a lower water content and higher dry density in the swelling zone. Due to this heterogeneity, the specimens with initial voids exhibited slightly larger axial swelling pressure and hydraulic conductivity than those without voids at the same global dry density; on the contrary, their radial swelling pressure was slightly lower than that of the specimens without voids. Over time, the soil in the swelling zone underwent further swelling, while that in the compression zone was compressed by the swelling pressure. From microstructure observation, the global void ratio in the compression zone increased significantly after swelling at the filling stage, with increases in large-pore, medium-pore and inaccessible-pore void ratios but a decrease in small-pore void ratio. Over time, the large and medium pores were compressed by almost constant swelling pressure. By contrast, the large-pore volume of swelling zone increased until the suction decreased to below 1 MPa and then it decreased from 15 h to 2160 h owing to the water redistribution in the soil. These processes resulted in a decrease of heterogeneity due to the presence of technological voids with time.

However, the heterogeneity would remain forever according to the dry density evolution curves of different parts. It was suggested that the homogenization process would stop when the vector sum of swelling forces in the radial direction was lower than or equal to the boundary friction between the specimens and porous stones for all elements. Based on the force equilibrium in

the final state and the mass conservation, the final dry density distributions of specimens were estimated. The good agreement between the estimated and measured dry density distributions showed the relevance of the identified mechanism for the final heterogeneous dry density distribution.

(iii) Effect of water chemistry

The effect of water chemistry on the hydro-mechanical behaviour of Na^+ MX80 bentonite/claystone mixture with 30% bentonite was also studied. Additionally, an attempt was made to employ Ca^{2+} Sardinia bentonite in the mixture to adapt to the chemical environment. For the MX80 bentonite/claystone mixture hydrated with synthetic site solution for 90 days, the swelling capacity was reduced owing to the transformation of Na-montmorillonite to multi-cation dominant montmorillonite by cation exchanges. By contrast, for the Sardinia bentonite/claystone mixture, the similar increasing rate of swelling pressure was observed during the crystalline swelling process for different solutions, suggesting insignificant cation exchanges. During the osmotic swelling, the presence of cations reduced the repulsive force by diffuse double layer and thus swelling pressure for both the MX80 bentonite/claystone and Sardinia bentonite/claystone mixtures. Additionally, a smaller thickness of diffuse double layer and a greater large-pore volume could be expected for the specimens hydrated with synthetic site solution, leading to a higher hydraulic conductivity in that case, as compared to the case of deionised water. Furthermore, the decrease of swelling pressure and the increase of hydraulic conductivity were more significant in the case of low dry density due to the well-developed diffuse double layer and the higher permeability.

In addition to the cations, the hydroxide due to the degradation of concrete could dissolve the montmorillonite, reducing the swelling pressure, and increased the large-pore volume, facilitating the water flow for both the MX80 bentonite/claystone and Sardinia bentonite/claystone mixtures. Moreover, the lower the dry density, the more intensive the interaction between the montmorillonite and hydroxide and the more significant the changes in swelling pressure and hydraulic conductivity, due to the higher permeability.

In long term, the effect of water chemistry on the hydro-mechanical behaviour of bentonite/claystone mixture could become more significant. After a long period of 590 days, the synthetic site solution significantly weakened the swelling process and increased the large-pore void ratio, leading to a lower swelling pressure and a higher hydraulic conductivity of the MX80 bentonite/claystone mixture, especially at a low dry density.

(iv) Unsaturated hydraulic property

The hydraulic conductivity evolution of MX80 bentonite/COx claystone mixture with a bentonite fraction of 30% and a dry density of 1.8Mg/m^3 upon wetting was measured using instantaneous profile mtheod. As the suction decreased from initial value (about 67.1 MPa) to zero, the measured total hydraulic conductivity increased slowly at high suctions, then quickly at low suctions, and finally approached the saturated value.

Based on the evolving pore structure upon wetting, a new method was proposed to predict the vapour and liquid-water hydraulic conductivities. This predictive method considering the evolving pore structure was then verified by the good agreement between the simulated and experimental results. Overall, the predicted total hydraulic conductivity agreed well with the measured one. The vapour hydraulic conductivity was larger than the liquid-water one at a suction larger than 15.2 MPa while liquid-water hydraulic conductivity became dominant at a suction lower than 15.2 MPa.

Additionally, a numerical model was set up to simulate the water infiltration process. The results from numerical simulation using the predicted vapour and liquid-water hydraulic conductivities were in good agreement with the measurements. To examine the contribution of vapour and liquid water flux, only the predicted liquid-water hydraulic conductivity was applied to the material. It was found that ignoring vapour transport postponed the starting time of relative humidity increase or suction decrease, and underestimated the water content, especially for the soil far from the wetting end.

(v) Practical recommendations for the proposed bentonite/claystone mixture

Although the technological voids slightly affect the swelling aeolotropy and increase the hydraulic conductivity, both the final axial and radial swelling pressures and the hydraulic conductivity of the specimen at a global dry density of 1.8 Mg/m^3 after 90-day hydration satisfy the requirements of Andra in terms of swelling pressure and hydraulic conductivity. As far as the effect of water chemistry is concerned, both the Na^+ MX80 bentonite/claystone and Ca^{2+} Sardinia bentonite/claystone mixtures at dry density of 1.8 Mg/m^3 can fulfill the requirements of Andra after 90 days of hydration. It appears that the employment of Ca^{2+} Sardinia in the mixture does not reduce the detrimental effect of water chemistry on the hydro-mechanical behaviour of the mixture. Additionally, the sealing performance deterioration due to the water chemistry will last over a longer period owing to the slow interaction between the mixture and solutions. In the long-term performance assessment of the bentonite/claystone mixture, much

attention should be paid on this sealing performance deterioration.

PERSPECTIVES

This study allowed better understanding the hydro-mechanical behaviour of bentonite/claystone under relevant environmental conditions for the long-term safe storage of radioactive wastes in COx claystone formation. In light of the findings obtained, it appears interesting to address the following issues in future studies:

This study analysed the interaction between the bentonite and claystone grains in the mixtures with various dry densities and bentonite fractions based on the consideration of the great difference of swelling capacities of bentonite and claystone. However, this interaction has not been experimentally verified. It is thus necessary to clarify the microstructure of the binary mixtures before and after hydration using direct observations, using X-ray computed microtomography (μ-CT) for instance.

The specimens with technological voids were hydrated for predefined times and cut into slices for the determination of dry density profile at a given time. Since the testing process is time-consuming and tough, the obtained data are quite limited. It would be interesting to perform similar infiltration tests with simultaneous μCT scans. That will permit to continuously monitor the dry density distribution evolution over time and to confirm the homogenization process.

The swelling behaviour of compacted blocks with technological voids in the large field scale should be investigated. For the compacted blocks with a larger size, the water infiltration into the middle part is slower. Thus, the heterogeneity due to the presence of technological voids can be more remarkable and the homogenization process should last for a longer period.

Based on the experimental results obtained in this study, a constitutive model can be developed and then implemented in a numerical code for analyzing the hydro-mechanical behaviour of bentonite/claystone mixture in field conditions.

References

Abdullah, I., Mhaidib, A.l., 1999. Swelling behaviour of expansive shales from the middle region ofSaudi Arabia. Geotechnical and Geological Engineering. 16(4), 291–307.

Abichou, T., Benson, C.H., Edil, T.B., 2004. Network model for hydraulic conductivity of sand-bentonite mixtures. Canadian Geotechnical Journal, 41(4), 698-712.

Agus, S. S., Schanz T., 2005. Effect of shrinking and swelling on microstructures and fabric of a compacted bentonite-sand mixture. Proceedings of the international conference on problematic soils, Cyprus, 2, 543–550.

Agus, S.S., Schanz, T., 2008. A method for predicting the swelling pressure of compacted bentonites. Acta Geotech., 3(2), 125.

Ağbulut, Ü., 2019. Turkey's electricity generation problem and nuclear energy policy. Energy Sources, Part A: Recovery, Utilization, and Environmental Effects, 41(18), 2281-2298.

Andra, 2005. Dossier 2005 Argile - Synthesis: Evaluation of the Feasibility of a Geological Repository in an Argillaceous Formation (Meuse/ Haute-Marne Site). French National Radioactive Waste Management Agency, Chatenay-Malabry CEDEX 241 pp. Accessed 22 November 2018.

Baille, W., Tripathy, S., Schanz, T., 2010. Swelling pressures and one-dimensional compressibility behaviour of bentonite at large pressures. Applied Clay Science, 48(3), 324-333.

Barbour, S., Fredlund, D., 1989. Mechanisms of osmotic flow and volume change in clay soils. Can Geothec J, 26, 551–562.

Basma, A.A., Al-Homoud, A.S., Husein, A., 1995. Laboratory assessment of swelling pressure of expansive soils. Applied Clay Science, 9(5), 355-368.

Berner, U.R., 1992. Evolution of pore water chemistry during degradation of cement in a radioactive waste repository environment. Waste Manag. 12, 201–219.

Bian, X., Cui, Y.J., Li, X.Z., 2019a. Voids effect on the swelling behaviour of compacted bentonite. Géotechnique, 69(7), 593-605.

Bian, X., Cui, Y.J., Zeng, L.L., Li, X.Z., 2019b. Swelling behavior of compacted bentonite with the presence of rock fracture. Engineering Geology, 254, 25-33.

Bian, X., Cui, Y.J., Zeng, L.L., Li, X.Z., 2020. State of compacted bentonite inside a fractured granite cylinder after infiltration. Applied Clay Science, 186, 105438.

Börgesson, L., Chijimatsu, M., Fujita, T., Nguyen, T.S., Rutqvist, J., Jing, L., 2001. Thermo-hydro-mechanical characterisation of a bentonite-based buffer material by laboratory tests and numerical back analyses. International Journal of Rock Mechanics and Mining Sciences, 38(1), 95-104.

Börgesson, L., Johannesson, L.E., Gunnarsson, D., 2003. Influence of soil structure

heterogeneities on the behaviour of backfill materials based on mixtures of bentonite and crushed rock. Applied clay science, 23(1-4), 121-131.

Buzzi, O., Boulon, M., Deleruyelle, F., Besnus, F., 2008. Hydromechanical behaviour of rock-Bentonite interfaces under compression. Rock mechanics and rock engineering, 41(2), 343-371.

Bouazza, A., Abuel-Naga, H.M., Gates, W.P., Laloui, L., 2008. Temperature effects on volume change and hydraulic properties of geosynthetic clay liners. The First Pan American Geosynthetics Conference & Exhibition, 102–109 (2–5 March, Cancun, Mexico).

Carman P.C., 1956. Flow of gases through porous media. Butterworths, London.

Castellanos, E., Villar, M.V., Romero, E., Lloret, A., Gens, A., 2008. Chemical impact on the hydro-mechanical behaviour of high-density FEBEX bentonite. Physics and Chemistry of the Earth, Parts A/B/C 33, S516-S526.

Chen, Y.G., Cui, Y.J., Wang, Q., Ye, W.M., 2014. A preliminary study on hydraulic resistance of bentonite/host-rock seal interface. Géotechnique, 64(12), 997–1002.

Chen, Y.G., Zhu, C.M., Ye, W.M., Cui, Y.J., Wang, Q., 2015. Swelling pressure and hydraulic conductivity of compacted GMZ01 bentonite under salinization–desalinization cycle conditions. Applied Clay Science, 114, 454-460.

Chen, Y.G., Zhu, C.M., Ye, W.M., Cui, Y.J., Chen, B., 2016a. Effects of solution concentration and vertical stress on the swelling behavior of compacted GMZ01 bentonite. Applied Clay Science, 124, 11-20.

Chen, B., Guo, J.X., Zhang, H.X., 2016b. Alteration of compacted GMZ bentonite by infiltration of alkaline solution. Clay Minerals, 51(2), 237-247.

Chen, Y.G., Jia, L.Y., Ye, W.M., Chen, B., Cui, Y.J., 2016c. Advances in experimental investigation on hydraulic fracturing behavior of bentonite-based materials used for HLW disposal. Environmental Earth Sciences, 75(9), 787.

Chen, Y.G., Dong, X.X., Zhang, X.D., Ye, W.M., Cui, Y.J., 2018. Combined thermal and saline effects on the swelling pressure of densely compacted GMZ bentonite. Applied Clay Science, 166, 318-326.

Chen, Y.G., Sun, Z., Cui, Y.J., Ye, W.M., Liu, Q.H., 2019. Effect of cement solutions on the swelling pressure of compacted GMZ bentonite at different temperatures. Construction and Building Materials, 229, 116872.

Cho, W.J., Lee, J.O., Kang, C.H., 2000. Influence of temperature elevation on the sealing performance of a potential buffer material for a high-level radioactive waste repository. Annals of Nuclear Energy, 27(14), 1271-1284.

Cui, Y. J., Loiseau, C., Delage, P., 2002a. Microstructure changes of a confined swelling soil due to suction controlled hydration Unsaturated soils: proceedings of the Third International Conference on Unsaturated Soils, UNSAT 2002, 10-13 March 2002, Recife,

Brazil, 593.

Cui, Y.J., Yahia-Aissa, M., Delage, P., 2002b. A model for the volume change behavior of heavily compacted swelling clays. Engineering Geology, 64(2-3), 233-250.

Cui, Y.J., Tang, A.M., Loiseau, C., Delage, P., 2008. Determining the unsaturated hydraulic conductivity of a compacted sand–bentonite mixture under constant-volume and free-swell conditions. Physics and Chemistry of the Earth, Parts A/B/C, 33, S462-S471.

Cui, Y.J., 2017. On the hydro-mechanical behaviour of MX80 bentonite-based materials. Journal of Rock Mechanics and Geotechnical Engineering, 9(3), 565-574.

Cui, S.L., Zhang, H.Y., Zhang, M., 2012. Swelling characteristics of compacted GMZ bentonite–sand mixtures as a buffer/backfill material in China. Eng. Geol., 141, 65-73.

Cuisinier, O., Masrouri, F., 2005. Hydromechanical behaviour of a compacted swelling soil over a wide suction range. Engineering Geology, 81(3), 204-212.

Cuisinier, O., Masrouri, F., Pelletier, M., Villieras, F., Mosser-Ruck, R., 2008. Microstructure of a compacted soil submitted to an alkaline plume. Applied Clay Science, 40(1-4), 159-170.

Daniel, D.E., 1982. Measurement of hydraulic conductivity of unsaturated soils with thermocouple psychrometers. Soil Science Society of America Journal, 46(6), 1125-1129.

Dardé, B., 2019. Experimental and numerical study of the hydromechanical behavior of bentonite pellet-powder mixtures (Doctoral dissertation, Paris Est).

Delage, P., Marcial, D., Cui, Y.J., Ruiz, X., 2006. Ageing effects in a compacted bentonite: a microstructure approach. Géotechnique, 56(5), 291-304.

Delage, P., 2007. Microstructure features in the behaviour of engineered barriers for nuclearwaste disposal. In: Schanz, T. (Ed.), ExperimentalUnsaturated SoilMechanics. Springer, Berlin Heidelberg, 11–32.

Deng, Y.F., Tang, A.M., Cui, Y.J., Li, X.L., 2011. Study on the hydraulic conductivity of Boom clay. Can. Geotech. J., 48(10), 1461–1470.

Dixon, D.A., Gray, M.N., Graham, J., 1996. Swelling and hydraulic properties of bentonites from Japan, Canada and USA. In Proceedings of the second International Congress on Environmental Geotechnics, Osaka, Japan, 5-8.

Dunn, R.J., 1985. Laboratory measurement o f a fine-grained soil fluid conductivity. Engineering Geology, 21, 215-223.

Faucon, P., Adenot, F., Jacquinot, J.F., Petit, J.C., Cabrillac, R., Jorda, M., 1998. Longterm behavior of cement pastes used for nuclear waste disposal: review of physicochemical mechanisms of water degradation. Cem. Concr. Res. 28(6), 847–857.

Fernández, F., Quigley, R.M., 1988. Viscosity and dielectric constant controls on the hydraulic conductivity of clayey soils permeated with simple liquid hydrocarbons Canadian Geotechnical Journal, 22, 582-589.

Fernández, R., Cuevas, J., Sánchez, L., Vigil de la Villa, R., Leguey, S., 2006. Reactivity of the cement-bentonite interface with alkaline solutions using transport cells. Appl. Geochem. 21(6), 977–992.

Fernández, R., Mäder, U.K., Rodríguez, M., Vigil de la Villa, R., Cuevas, J., 2009. Alteration of compacted bentonite by diffusion of highly alkaline solutions. Eur. J. Mineral., 21, 725–735.

Garcia-Bengochea, I., Altschaeffl, A.G., Lovell, C.W., 1979. Pore distribution and permeability of silty clays. Journal of the Geotechnical Engineering Division, 105(7), 839-856.

Gatabin, C., Touze, G., Imbert, C., Guillot, W., Billaud, P., 2008. ESDRED Project, Module 1-Selection and THM characterization of the buffer material. In International conference underground disposal unit design&emplacement processes for a deep geological repository, 16-18 June, Prague.

Gatabin, C., Talandier, J., Collin, F., Charlier, R., Dieudonné, A.C. (2016). Competing effects of volume change and water uptake on the water retention behaviour of a compacted MX-80 bentonite/sand mixture. Applied Clay Science, 121, 57-62.

Glasser, F.P., Atkins, M., 1994. Cements in radioactive waste disposal. Mater. Res. Soc. Bull., 12, 33–39.

Gens, A., Guimaraes, L.N., Garcia-Molina, A., Alonso, E.E., 2002. Factors controlling rock-clay buffer interaction in a radioactive waste repository. Eng Geol., 64(2–3), 297–308.

Gens, A., Pomaro, B., Sánchez, M., Villar, M.V., 2018. On the hydration of unsaturated barriers for high-level nuclear waste disposal. In Unsaturated Soils: UNSAT 2018: The 7th International Conference on Unsaturated Soils, 55-60.

Harris, J., Hassall, M., Muriuki, G., Warnaar-Notschaele, C., McFarland, E., Ashworth, P., 2018. The demographics of nuclear power: Comparing nuclear experts', scientists' and non-science professionals' views of risks, benefits and values. Energy research & social science, 46, 29-39.

Herbert, H., Kasbohm, J., Sprenger, H., Fernández, A.M., Reichelt, C., 2008. Swelling pressures of MX-80 bentonite in solutions of different ionic strength. Phys. Chem. Earth, 33, S327–S342.

Heikola, T., Kumpulainen, S., Vuorinen, U., Kiviranta, L., Korkeakoski, P., 2013. Influence of alkaline (pH 8.3–12.0) and saline solutions on chemical, mineralogical and physical properties of two different bentonites. Clay Miner., 48(2), 309–329.

IAEA, 2009. Classification of radioactive waste. General safety guide. IAEA Safety Standards GSG-1, 68.

Jia, L.Y., Chen, Y.G., Ye, W.M., Cui, Y.J., 2019. Effects of a simulated gap on anisotropic swelling pressure of compacted GMZ bentonite. Engineering geology, 248, 155-163.

Karnland, O., Pusch, R., Sandén, T., 1992. The importance of electrolyte on the physical

properties of MX-80 bentonite. SKB Report AR 92-35, Stockholm (in Swedish).

Karnland, O., Olsson, S., Nilsson, U., 2006. Mineralogy and Sealing Properties of Various Bentonites and Smectite-Rich Clay Materials. SKB TR-06-30. Swedish Nuclear Fuel and Waste Management Co., Stockholm, Sweden, 34–41.

Karnland, O., Olsso, S., Nilsson, U., Sellin, P., 2007. Experimentally determined swelling pressures and geochemical interactions of compacted Wyoming bentonite with highly alkaline solutions. Phys. Chem. Earth, 32(1–7), 275–286.

Karnland, O., Nilsson, U., Weber, H., Wersin, P., 2008. Sealing ability of Wyoming bentonite pellets foreseen as buffer material–laboratory results. Phys. Chem. Earth Parts A/B/C, 33, S472-S475.

Kanno, T., Fujita, T., Takeuchi, S., Ishikawa, H., Hara, K., Nakano, M., 1999. Coupled thermo-hydro-mechanical modelling of bentonite buffer material. International journal for numerical and analytical methods in geomechanics, 23(12), 1281-1307.

Keller, L. M., Seiphoori, A., Gasser, P., Lucas, F., Holzer, L., Ferrari, A., 2014. The pore structure of compacted and partly saturated MX-80 bentonite at different dry densities. Clays and Clay Minerals, 62(3), 174–187.

Komine, H., Ogata, N., 1994. Experimental study on swelling characteristics of compacted bentonite. Can. Geotech. J., 31(4), 478-490.

Komine, H., Ogata, N., 1999. Experimental study on swelling characteristics of sand-bentonite mixture for nuclear waste disposal. Soils Found. 39(2), 83-97.

Komine, H., Ogata, N., 2003. New equations for swelling characteristics of bentonite-based buffer materials. Canadian Geotechnical Journal, 40(2), 460-475.

Komine, H., Ogata, N., 2004. Predicting swelling characteristics of bentonites. Journal of Geotechnical and Geoenvironmental engineering, 130(8), 818-829.

Komine, H., Yasuhara, K., Murakami, S., 2009. Swelling characteristics of bentonites in artificial seawater. Can. Geotech. J., 46, 177–189.

Kozeny, J., 1927. Uber kapillare Leitung des Wassers im Boden. Sitzungsber. Akad. Wiss. Wien 136:271–306.

Krõhn, K.P., 2003. New conceptual models for the resaturation of bentonite. Applied clay science, 23(1-4), 25-33.

Lang, L.Z., Baille, W., Tripathy, S., Schanz, T., 2018. Experimental study on the influence of preliminary desiccation on the swelling pressure and hydraulic conductivity of compacted bentonite. Clay Minerals, 53(4), 733-744.

Lee, J.O., Cho, W.J., Chun, K.S., 1999. Swelling pressures of a potential buffer material for high-level waste repository. J. Korean Nucl. Soc. 31(2), 139-150.

Lee, J.O., Lim, J.G., Kang, I.M., Kwon, S., 2012. Swelling pressures of compacted Cabentonite. Eng. Geol. 129-130, 20–26.

Lemaire, T., Moyne, C., Stemmelen, D., 2004. Imbibition test in a clay powder (MX-80 bentonite). Applied clay science, 26(1-4), 235-248.

Li, X.L., Bastiaens, W., Van Marcke, P., Verstricht, J., Chen, G.J., Weetjens, E., Sillen, X., 2010. Design and development of large-scale in-situ PRACLAY heater test and horizontal high-level radioactive waste disposal gallery seal test in Belgian HADES. Journal of Rock Mechanics and Geotechnical Engineering, 2(2), 103-110.

Liu, L., 2013. Prediction of swelling pressures of different types of bentonite in dilute solutions. Colloids and Surfaces A: Physicochemical and Engineering Aspects, 434, 303-318.

Liu, L.N., Chen, Y.G., Ye, W.M., Cui, Y.J., Wu, D.B., 2020a. Swelling pressure deterioration of compacted GMZ bentonite and its structural damage under heat combined with hyperalkaline conditions. Geomechanics and Geoengineering, 1-12.

Liu, Z.R., Cui, Y.J., Ye, W.M., Chen, B., Wang, Q., Chen, Y.G., 2020b. Investigation of the hydro-mechanical behaviour of GMZ bentonite pellet mixtures. Acta Geotechnica. https://doi.org/10.1007/s11440-020-00976-y.

Lloret, A., Villar, M.V., 2007. Advances on the knowledge of the thermo-hydro-mechanical behaviour of heavily compacted "FEBEX" bentonite. Physics and Chemistry of the Earth, 32(8–14), 701–715.

Loi n°2006-739; 2006. Loi de programme n° 2006-739 du 28 juin 2006 relative à la gestion durable des matières et déchets radioactifs, France.

Marcial, D., Delage, P., Cui, Y.J., 2006. A laboratory study of the self sealing behaviour of a compacted sand–bentonite mixture. Geomechanics and Geoengineering: An International Journal, 1(1), 73-85.

Martin, P.L., Barcala, J.M., Huertas, F., 2006. Large-scale and long-term coupled thermo-hydro-mechanic experiments with bentonite: the FEBEX mock-up test. J. Iberian Geol., 32(2), 259–282.

Massat, L., Cuisinier, O., Bihannic, I., Claret, F., Pelletier, M., Masrouri, F., Gaboreau, S., 2016. Swelling pressure development and inter-aggregate porosity evolution upon hydration of a compacted swelling clay. Applied Clay Science, 124–125, 197–210.

Mašín, D., Khalili, N., 2015. Swelling phenomena and effective stress in compacted expansive clays. Canadian Geotechnical Journal, 53(1), 134-147.

Mata, C., 2003. Hydraulic behaviour of bentonite based mixtures in engineered barriers: the Backfill and Plug Test at the A¨ spo¨ HRL (Sweden). (Ph. D. Thesis) Universitat Polite'cnica de Catalunya, Barcelona (257 pp.).

Mesri, G., Olson, R.E., 1971. Mechanisms controlling the permeability of clays. Clays and Clay Minerals, 19, 151-158.

Middelhoff, M., Cuisinier, O., Masrouri, F., Talandier, J., Conil, N., 2020. Combined impact of selected material properties and environmental conditions on the swelling pressure of

compacted claystone/bentonite mixtures. Applied Clay Science, doi: 10.1016/j.clay.2019.105389.

Mitchell, J.K., 1976. Fundamentals of Soil Behaviour. 1st edition. J. Wiley and Sons Publishers, Toronto.

Mitchell, J.K., 1993. Fundamentals of soil behaviour, 2nd edn. John Wiley and sons, New York

Molinero-Guerra, A., Mokni, N., Delage, P., Cui, Y. J., Tang, A. M., Aimedieu, P., Bernier, F., Bornert, M., 2017. In-depth characterisation of a mixture composed of powder/pellets MX80 bentonite. Applied Clay Science, 135, 538–546.

Molinero-Guerra, A., Aimedieu, P., Bornert, M., Cui, Y.J., Tang, A. M., Sun, Z., Mokni, N., Delage, P., Bernier, F., 2018. Analyses of the structural changes of a pellet/powder bentonite mixture upon wetting by X-ray computed microtomography. Applied Clay Science (165), 164-169.

Mollins, L.H., 1996. The Design of Bentonite-Sand Mixtures. PhD thesis, University of Leeds.

Mollins, L.H., Stewart, D.I., Cousens, T.W., 1996. Predicting the properties of bentonite-sand mixtures. Clay minerals, 31(2), 243-252.

Montes-Hernandez, G., Duplay, J., Martinez, L., Mendoza, C., 2003. Swelling-shrinkage kinetics of MX80 bentonite. Applied Clay Science, 22(6), 279–293.

Nakayama, S., Sakamoto, Y., Yamaguchi, T., Akai, M., Tanaka, T., Sato, T., Iida, Y.J.A.C.S., 2004. Dissolution of montmorillonite in compacted bentonite by highly alkaline aqueous solutions and diffusivity of hydroxide ions. Applied Clay Science, 27(1-2), 53-65.

NDA, 2013. Geological Disposal-How the world is dealing with its radioactive wastes.

NEA, 2008. Moving forward with geological disposal of radioactive waste, a collective statement by the NEA Radioactive Waste Management Commitee (RWMC). Technical report, OECD – Nuclear Energy Agency

Nguyen, X.P., Cui, Y.J., Tang, A.M., Deng, Y.F., Li, X.L. and Wouters, L., 2013. Effects of pore water chemical composition on the hydro-mechanical behavior of natural stiff clays. Engineering geology, 166, 52-64.

Olsen, H.W. 1962. Hydraulic flow through saturated clays. Proceedings of the 9th National Conference on Clays and Clay Minerals, 131-161.

OECD/NEA, 1995. The environmental and ethical basis of geological disposal of long- lived radioactive wastes. ïA collective opinion of the Radioactive Waste Management Committee of the OECD Nuclear Energy Agency. Technical report, OECD – Nuclear Energy Agency.

Pusch, R., 1979. Highly compacted sodium bentonite for isolating rock-deposited radioactive waste products. Nucl. Technol. 45 (2), 153–157 (United states).

Pusch, R., 1982. Mineral–water interactions and their influence on the physical behavior of highly compacted Na bentonite. Can Geotech J, 19(3), 381–387.

Pusch, R., 2001. Experimental Study of the Effect of High Porewater Salinity on the Physical Properties of a Natural Smectitic Clay. SKB Technical Report TR-01-07, Stockholm.

Pusch, R., Yong, R.N., 2006. Microstructure of smectite clays and engineering performance. CRC Press.

Rao, M., Shivananda, P., 2005. Role of osmotic suction in swelling of salt amended clays. Can Geotech J, 42, 307–315.

Rao, S.M., Thyagaraj, T., Thomas, H.R., 2006. Swelling of compacted clay under osmotic gradients. Géotechnique, 56(10), 707–713.

Rao, S.M., Ravi, K., 2015. Influence of initial degree of saturation on swell pressures of compacted Barmer bentonite specimens. Annals of Nuclear Energy, 80, 303-311.

Ren, X., Zhao, Y., Deng, Q., Kang, J., Li, D., Wang, D., 2016. A relation of hydraulic conductivity-void ratio for soils based on Kozeny-Carman equation. Engineering geology, 213, 89-97.

Romero, E., Simms, P.H., 2008. Microstructure investigation in unsaturated soils: A review with special attention to contribution of mercury intrusion porosimetry and environmental scanning electron microscopy. Geotechnical and Geological Engineering, 26, 705–727.

Sánchez, L., Cuevas, J., Ramírez, S., De León, D.R., Fernández, R., Villa, R.V.D., Leguey, S., 2006. Reaction kinetics of FEBEX bentonite in hyperalkaline conditions resembling the cement–bentonite interface. Applied Clay Science, 33(2), 125-141.

Saba, S., 2013. Hydro-mechanical behaviour of bentonite-sand mixture used as sealing materials in radioactive waste disposal galleries (Doctoral dissertation, Université Paris-Est).

Saba, S., Barnichon, J.D., Cui, Y.J., Tang, A.M., Delage, P., 2014a. Microstructure and anisotropic swelling behaviour of compacted bentonite/sand mixture. J. Rock Mech. Geotech. Eng. 6(2), 126-132.

Saba, S., Delage, P., Lenoir, N., Cui, Y.J., Tang, A.M., Barnichon, J.D., 2014b. Further insight into the microstructure of compacted bentonite–sand mixture. Engineering geology, 168, 141-148.

Saiyouri, N., Hicher, P.Y., Tessier, D., 1998. Microstructural analysis of highly compacted clay swelling. Proc. 2nd Int. Conf. on Unsaturated Soils, Beijing 1, 119–124.

Saiyouri, N., Hicher, P.Y., Tessier, D., 2000. Microstructural approach and transfer water modelling in highly compacted unsaturated swelling clays. Mechanics of Cohesive-frictional Materials: An International Journal on Experiments, Modelling and Computation of Materials and Structures, 5(1), 41-60.

Saiyouri, N., Tessier, D., Hicher, P.Y., 2004. Experimental study of swelling in unsaturated compacted clays. Clay Minerals, 39(4), 469–479.

Savage, D., Noy, D., Mihara, M., 2002. Modelling the interaction of bentonite with

hyperalkaline fluids. Appl. Geochem. 17, 207–223.

Schanz, T., Tripathy, S., 2009. Swelling pressure of a divalent-rich bentonite: Diffuse double-layer theory revisited. Water Resources Research. doi: 10.1029/2007WR006495.

Seiphoori, A., Ferrari, A., Laloui, L., 2014. Water retention behaviour and microstructural evolution of MX-80 bentonite during wetting and drying cycles. Géotechnique, 64(9), 721–734.

Sellin, P. Leupin, O.X., 2013. The use of clay as an engineered barrier in radioactive-waste management–a review.Clays and Clay Minerals, 61(6), 477-498.

Shi, X.S., Yin, J., 2018. Estimation of hydraulic conductivity of saturated sand–marine clay mixtures with a homogenization approach. International Journal of Geomechanics, 18(7), 04018082.

Siddiqua S, Blatz, J., Siemens, G., 2011. Evaluation of the impact of pore fluid chemistry on the hydromechanical behavior of claybased sealing materials. Can Geothech J, 48, 199–213.

Sivapullaiah, P.V., Sridharan, A., Stalin, V.K., 2000. Hydraulic conductivity of bentonite-sand mixtures. Canadian geotechnical journal, 37 (2), 406-413.

Sposito, G., Prost, R., 1982. Structure of Water Adsorbed on Smectites. Chemical Reviews, 82(6), 553–573.

Sridharan, A., Rao, S., Sivapullaiah, P.V., 1986. Swelling pressure of clays. ASTM geotechnical testing journal, 9(1), 24–33.

Sun, D.A., Cui, H., Sun, W., 2009. Swelling of compacted sand–bentonite mixtures. Appl Clay Sci, 43(3-4), 485-492.

Sun, D.A., Zhang, J., Zhang, J., Zhang, L., 2013. Swelling characteristics of GMZ bentonite and its mixtures with sand. Appl Clay Sci, 83, 224-230.

Sun, D.A., Zhang, L., Li, J., Zhang, B.C., 2015. Evaluation and prediction of the swelling pressures of GMZ bentonites saturated with saline solution. Appl. Clay Sci., 105–106, 207–216.

Sun, Z., Chen, Y.G., Cui, Y.J., Xu, H.D., Ye, W.M., Wu, D.B., 2018. Effect of synthetic water and cement solutions on the swelling pressure of compacted Gaomiaozi (GMZ) bentonite: the Beishan site case, Gansu, China. Engineering Geology, 244, 66-74.

Sun, H., Mašín, D., Najser, J., Nedela, V., Navrátilová, E., 2019a. Bentonite microstructure and saturation evolution in wetting-drying cycles evaluated using ESEM, MIP and WRC measurements. Geotechnique, 69(8), 713–726.

Sun, Z., Chen, Y.G., Cui, Y.J., Ye, W.M., Chen, B., 2019b. Effect of synthetic Beishan site water and cement solutions on the mineralogy and microstructure of compacted Gaomiaozi (GMZ) bentonite. Soils and Foundations, 59 (6), 2056-2069.

Sun, Z., Chen, Y.G., Ye, W.M., Cui, Y.J., Wang, Q., 2020. Swelling deformation of Gaomiaozi

bentonite under alkaline chemical conditions in a repository. Engineering Geology, 279, 105891.

Tang, C.S., Tang, A.M., Cui, Y.J., Delage, P., Schroeder, C., Shi, B., 2011a. A study of the hydro-mechanical behaviour of compacted crushed argillite. Engineering geology, 118(3-4), 93-103.

Tang, C.S., Tang, A.M., Cui, Y.J., Delage, P., Schroeder, C., De Laure, E., 2011b. Investigating the swelling pressure of compacted crushed-Callovo-Oxfordian claystone. Physics and Chemistry of the Earth, Parts A/B/C, 36(17-18), 1857-1866.

Tripathy, S., Sridharan, A., Schanz, T., 2004. Swelling pressures of compacted bentonites from diffuse double layer theory. Canadian Geotechnical Journal, 41(3), 437-450.

Terzaghi, K., 1943. Theoretical soil mechanics. New York: Wiley.

van Olphen, H. 1977. An introduction to clay colloid chemistry. For clay technologists, geologists and soil scientists. 2nd edition. A Wiley - Interscience Publication.

Villar, M.V., Rivas, P., 1994. Hydraulic properties of montmorillonite-quartz and saponite-quartz mixtures. Applied Clay Science, 9(1), 1-9.

Villar, M.V., 1999. Investigation of the behaviour of bentonite by means of suction-controlled oedometer tests. Engineering Geology, 54(1-2), 67-73.

Villar, M.V., García-Siñeriz, J.L., Bárcena, I., Lloret, A., 2005. State of the bentonite barrier after five years operation of an in situ test simulating a high level radioactive waste repository. Engineering Geology, 80(3-4), 175-198.

Villar, M.V., 2006. Infiltration tests on a granite/bentonite mixture: Influence of water salinity. Applied Clay Science, 31(1-2), 96-109.

Villar, M.V., Lloret, A., 2008. Influence of dry density and water content on the swelling of a compacted bentonite. Applied Clay Science, 39(1-2), 38-49.

Villar, M.V., Gomez-Espina, R., Gutierrez-Nebot, L., 2012. Basal spacings of smectite in compacted bentonite. Appl. Clay Sci. 65–66, 95–105.

Villar, M.V., Iglesias, R.J., García-Siñeriz, J.L., Lloret, A., Huertas, F., 2019. Physical evolution of a bentonite buffer during 18 years of heating and hydration. Eng Geol doi: 10.1016/j.enggeo.2019.105408.

Watabe, Y., LeBihan, J.P., Leroueil, S., 2006. Probabilistic modelling of saturated/unsaturated hydraulic conductivity for compacted glacial tills. Géotechnique, 56(4), 273-284.

Watabe, Y., Yamada, K., Saitoh, K., 2011. Hydraulic conductivity and compressibility of mixtures of Nagoya clay with sand or bentonite. Géotechnique, 61(3), 211-219.

Watanabe, Y., Yokoyama, S., 2021. Self-sealing behavior of compacted bentonite–sand mixtures containing technological voids. Geomechanics for Energy and the Environment, 25, 100213.

Wang, L., 2009. Near-field Chemistry of a HLW/SF Repository in Boom Clay-Scoping Calculations Relevant to the Super Container Design. First full draft, SCK•CEN Report, SCK•CEN-ER-17, December, 2009, Mol, Belgium. 11–18.

Wang, Q., Tang, A.M., Cui, Y.J., Delage, P., Gatmiri, B., 2012. Experimental study on the swelling behaviour of bentonite/claystone mixture. Eng. Geol. 124, 59-66.

Wang, Q., Tang, A.M., Cui, Y.J., Delage, P., Barnichon, J.D., Ye, W.M., 2013a. The effects of technological voids on the hydro-mechanical behaviour of compacted bentonite-sand mixture. Soils and Foundations, 53(2), 232–245.

Wang, Q., Cui, Y.J., Tang, A.M., Barnichon, J.D., Saba, S., Ye, W.M., 2013b. Hydraulic conductivity and microstructure changes of compacted bentonite/sand mixture during hydration. Engineering Geology, 164, 67-76.

Wang, Q., Cui, Y.J., Tang, A.M., Delage, P., Gatmiri, B., Ye, W.M., 2014. Long-term effect of water chemistry on the swelling pressure of a bentonite-based material. Applied Clay Science, 87, 157-162.

Xu, L., Ye, W.M., Chen, B., Chen, Y.G., Cui, Y.J., 2016. Experimental investigations on thermo-hydro-mechanical properties of compacted GMZ01 bentonite-sand mixture using as buffer materials. Engineering Geology, 213, 46-54.

Yamaguchi, T., Sakamoto, Y., Akai, M., Takazawa, M., Iida, Y., Tanaka, T., Nakayama, S., 2007. Experimental and modeling study on long-term alteration of compacted bentonite with alkaline groundwater. Phys. Chem. Earth, 32(1–7), 298–310.

Yigzaw, Z.G., Cuisinier, O., Massat, L., Masrouri, F., 2016. Role of different suction components on swelling behavior of compacted bentonites. Applied Clay Science, 120, 81–90.

Ye, W.M., Schanz, T., Qian, L.X., Wang, J., Arifin, Y., 2007. Characteristics of swelling pressure of densely compacted Gaomiaozi bentonite GMZ01. Chin. J. Rock Mech. Eng. 26 (S2), 3861–3865 (in Chinese).

Ye, W.M., Cui, Y.J., Qian, L.X., Chen, B., 2009. An experimental study of the water transfer through confined compacted GMZ bentonite. Engineering Geology, 108(3-4), 169-176.

Ye, W.M., Wan, M., Chen, B., Chen, Y.G., Cui, Y.J., Wang, J., 2012. Temperature effects on the unsaturated permeability of the densely compacted GMZ01 bentonite under confined conditions. Eng. Geol. 126, 1–7.

Ye, W.M., Lai, X.L., Liu, Y., Chen, Y.G., Cui, Y.J., 2013. Ageing effects on swelling behaviour of compacted GMZ01 bentonite. Nuclear Engineering and Design, 265, 262-268.

Ye, W.M., Zhang, F., Chen, B., Chen, Y.G., Wang, Q., Cui, Y.J., 2014a. Effects of salt solutions on the hydro-mechanical behavior of compacted GMZ01 Bentonite. Environ. Earth Sci., 72 (7), 2621–2630.

Ye, W.M., Zheng, Z.J., Chen, B., Chen, Y.G., Cui, Y.J., Wang, J., 2014b. Effects of pH and

temperature on the swelling pressure and hydraulic conductivity of compacted GMZ01 bentonite. Appl. Clay Sci. 101, 192–198.

Yong, R.N., Warkentin, B.P., 1975. Soil Properties and Behaviour. Elsevier, Amsterdam.

Yong, R.N., Boonsinsuk, P., Wong, G., 1986. Formulation of backfill material for a nuclear fuel waste disposal vault. Canadian Geotechnical Journal, 23(2), 216-228.

Yukselen-Aksoy, Y., Kaya, A., Ören, A.H., 2008. Seawater effect on consistency limits and compressibility characteristics of clays. Eng. Geol., 102, 54–61.

Zhang, C.L., 2014. Characterization of excavated claystone and claystone–bentonite mixtures as backfill/seal material. Geological Society, London, Special Publications, 400(1), 323-337.

Zhang, C.L., Krohn, K.P., 2019. Sealing behaviour of crushed claystone–bentonite mixtures. Geomechanics for Energy and the Environment, 17, 90-105.

Zhu, C.M., Ye, W.M., Chen, Y.G., Chen, B., Cui, Y.J., 2013. Influence of salt solutions on the swelling pressure and hydraulic conductivity of compacted GMZ01 bentonite. Eng. Geol., 166, 74–80.

Zhang, M., Zhang, H.Y., Zhou, L., Wang, B.M., Wang, S.J., 2014. Hydro-mechanical analysis of GMZ bentonite–sand mixtures in the water infiltration process as the buffer/backfill mixture in an engineered nuclear barrier. Applied clay science 97, 115-124.